ABSTRACT

Title of Dissertation: ANALYTICAL MODELING OF COMPACT BINARIES IN GENERAL RELATIVITY AND MODIFIED GRAVITY THEORIES

Mohammed M. Khalil
Doctor of Philosophy, 2022

Dissertation Directed by: Professor Alessandra Buonanno
Department of Physics

Gravitational-wave (GW) signals from the coalescence of almost a hundred binary systems have been detected over the past few years. These observations have improved our understanding of binary black holes and neutron stars, their properties, and astrophysical formation channels. GWs also probe gravity in the nonlinear, strong-field regime, thus allowing us to search for, or constrain, deviations from general relativity.

The focus of this dissertation is improving the analytical description of binary dynamics, which is important for producing accurate waveform models that can be used in searching for GW signals, inferring their parameters, and testing gravity. The research presented here can be divided into three complementary parts: 1) extending the post-Newtonian (PN) approximation for spinning binaries to higher orders, 2) improving effective-one-body (EOB) waveform models, and 3) identifying some signatures of modified gravity theories in waveforms.

The PN approximation, valid for slow motion and weak gravitational field, is widely used to model the dynamics of comparable-mass binaries, which are the main GW sources for ground-

based detectors. We derive PN results for spinning binaries at the third- and fourth-subleading PN orders for the spin-orbit coupling, and at the third-subleading order for the spin$_1$-spin$_2$ coupling. We adopt an approach that combines several analytical approximation methods to obtain PN results valid for arbitrary mass ratios from gravitational self-force results at first order in the mass ratio. This is possible due to the simple mass dependence of the scattering angle in the post-Minkowskian approximation (weak field but arbitrary velocities).

The EOB formalism produces accurate waveforms by combining analytical results for the binary dynamics with numerical relativity information, while recovering the strong-field test-body limit. To improve EOB models, we include spin-precession effects in the Hamiltonian up to the fourth PN order, and extend the radiation-reaction force and waveform to eccentric orbits. We also assess the accuracy of post-Minkowskian results, for both bound and scattering orbits, and incorporate them in EOB Hamiltonians.

In the context of modified gravity theories, we derive the conservative and dissipative dynamics in Einstein-Maxwell-dilaton theory at the next-to-leading PN order, and compute the Fourier-domain gravitational waveform. We also develop a theory-agnostic effective-field-theory approach for describing spontaneous and dynamical scalarization: non-perturbative phenomena in which compact objects can undergo a phase transition and acquire scalar charge. We apply this approach to binary black holes in Einstein-Maxwell-scalar theory using a quasi-stationary approximation, then extend it to account for the dynamical evolution of the scalar charge, and apply it to binary neutron stars in a class of scalar-tensor theories.

Improving waveform models is important for current-generation GW detectors and necessary for future detectors, such as LISA, the Einstein telescope, and Cosmic Explorer. The results obtained in this work are important steps towards that goal.

ANALYTICAL MODELING OF COMPACT BINARIES IN GENERAL RELATIVITY AND MODIFIED GRAVITY THEORIES

by

Mohammed M. Khalil

Dissertation submitted to the Faculty of the Graduate School of the
University of Maryland, College Park in partial fulfillment
of the requirements for the degree of
Doctor of Philosophy
2022

Dissertation Committee:
Professor Alessandra Buonanno (Advisor, Committee Chair)
Professor Bei-Lok Bernard Hu
Professor Theodore A. Jacobson
Professor Michael Coleman Miller (Dean's Representative)
Professor Peter Shawhan

Acknowledgments

I am grateful to my advisor, Alessandra Buonanno, for her guidance and support throughout my PhD. She suggested interesting research directions, and encouraged me to develop my own. She also taught me the importance of writing good papers and giving good presentations. Her breadth of knowledge and attention to details provided me with an example to strive for in my research.

I am also grateful to my secondary advisors at the AEI, Jan Steinhoff and Justin Vines. They helped expand my research topics, introduced me to the exciting field of compact binary dynamics, and patiently guided me through the calculations. Their expertise, drive, and kindness continue to inspire me.

I would like to thank all my collaborators: Andrea Antonelli, Alessandra Buonanno, Chris Kavanagh, Raissa Mendes, Néstor Ortiz, Serguei Ossokine, Antoni Ramos-Buades, Noah Sennett, Jan Steinhoff, and Justin Vines. I learned a lot from them, and the research presented in this dissertation would not have been possible without them.

In addition, I thank my dissertation committee members—Bei-Lok Hu, Ted Jacobson, Cole Miller, and Peter Shawhan—for their interest in my work and their time.

I also thank my friends—Abdelrahman, Ahmed, Amr, Andrea, Basem, Hannes, Hector, Kaustubh, Lorenzo, Luca, Mahmoud, Mohamed, Moustafa, Nils, Noah, Ollie, Omar, Riccardo, Roberto, Sai Kanth, Saketh, and Stefano—for making the past few years more enjoyable.

Finally, I thank my parents and brother for their constant support and encouragement.

Table of Contents

List of Tables

List of Figures

List of Abbreviations

ADM	Arnowitt-Deser-Misner
BBH	binary black hole
BH	black hole
EFT	effective field theory
EMd	Einstein-Maxwell-dilaton
EMRI	Extreme-mass-ratio inspiral
EMS	Einstein-Maxwell-scalar
EOB	effective one body
GR	general relativity
GW	gravitational wave
GSF	gravitational self-force
ISCO	innermost stable circular orbit
LIGO	Laser Interferometer Gravitational-Wave Observatory
LISA	Laser Interferometer Space Antenna
LO	leading order
LR	light ring
MPD	Mathisson-Papapetrou-Dixon
NLO	next-to-leading order
NNLO	next-to-NLO
NR	numerical relativity
NS	neutron star
PN	post-Newtonian
PM	post-Minkowskian
QNM	quasi-normal mode

RR	radiation reaction
SNR	signal-to-noise ratio
SO	spin-orbit
SPA	stationary phase approximation
SSC	spin-supplementary condition
ST	scalar-tensor

Summary of Research Contributions

The research I present in this dissertation has been conducted in collaboration with my advisor and several co-authors, and was published in Refs. [1–11]. I had substantial contributions to nine of these papers, and thus included them as chapters 2 – 10. In Sec. 1.5, I summarize the topics covered in these chapters, while here, I describe my contributions to each chapter.

Chapter 1 provides an introduction to and overview of the research presented in the rest of the dissertation. I was the sole author of this chapter.

Chapters 2 and 3 were published as Refs. [1, 2], in which we derived the 4.5PN spin-orbit and 5PN spin_1-spin_2 dynamics. I derived almost all the results using a Hamiltonian approach, while A. Antonelli and J. Vines independently reproduced the results using a radial action approach. I also contributed to most of the writing in these Chapters, and was the sole contributor to Sec. 3.5. All authors had significant contributions to the discussions and ideas of this work, which is why the author list is in alphabetical order.

Chapter 4 was published as Ref. [3], in which I derived new results for the spin-orbit dynamics at the 5.5PN order. I was the sole author of this chapter.

Chapter 5 was published as Ref. [4], in which we obtained, and assessed the accuracy of, EOB Hamiltonians for precessing spins up to 4PN order. All authors had significant contributions to the discussions and ideas of this work, but I was the primary contributor to all the results, figures and text, and was thus listed as the first author.

Chapter 6 was published as Ref. [5], in which we derived PN results for the radiation-reaction force and waveform modes for eccentric orbits in the EOB formalism. All authors had significant contributions to the discussions and ideas of this work, but I was the primary contributor to all the results and text, and was thus listed as the first author.

Chapter 7 was published as Ref. [6], in which we assessed the accuracy of fourth post-Minkowskian results, and incorporated them in EOB Hamiltonians. All authors had significant contributions to the discussions and ideas of this work, but I was the primary contributor to all the results, figures and text, and was thus listed as the first author.

Chapter 8 was published as Ref. [7], in which we obtained results for the conservative and dissipative dynamics in Einstein-Maxwell-dilaton theory. I derived the next-to-leading order Lagrangian and energy flux with guidance from J. Steinhoff and J. Vines. I also derived the GW phase and number of cycles with help from N. Sennett. All authors had significant contributions to the discussions and ideas of this work, but I was the primary contributor to all the results, figures and text, except § 8.2.4 and Fig. 8.8, and was thus listed as the first author.

Chapter 9 was published as Ref. [8], in which we developed a theory-agnostic approach to spontaneous and dynamical scalarization. I performed the numerical calculations applying this approach to Einstein-Maxwell-scalar theory, and produced all figures except Fig. 9.5. All authors contributed to the discussions and ideas of this work. The first three authors had equally-significant contributions and were listed alphabetically.

Chapter 10 was published as Ref. [9], in which we extended the approach in Chapter 9 to account for the dynamical evolution of the scalar charge, and applied it to binary neutron stars in a scalar-tensor theory. I was the primary contributor to the results, figures and text in Sec. 10.3 and 10.5, in addition to appendices Q and R on the binary dynamics. All authors had significant contributions to this work, which is why the author list is in alphabetical order.

Chapter 11 summarizes the conclusions of the previous chapters, and discusses possible future work. I was the sole author of this chapter.

In the rest of the dissertation, I use the pronoun “we” instead of “I”, even when referring to work for which I was the sole author.

Chapter 1: Introduction and Overview

1.1 Gravitational waves in general relativity

General relativity (GR) predicts the existence of gravitational waves (GWs): wavelike perturbations in spacetime that carry energy and propagate at the speed of light. GWs were first detected from a binary black hole coalescence (BH) in 2015 [12], and since then, about a hundred GW signals have been observed [13–15], including from binary neutron stars (NS) [16] and BH-NS binaries [17]. These observations ushered in the era of GW physics and astronomy, and have revolutionized our understanding of compact binary systems, their properties, and astrophysical formation channels [18–20].

This section gives a brief introduction to how GWs are described in GR, and how they propagate in vacuum and interact with test masses. This section mostly follows Refs. [21–23].

1.1.1 Linearized gravity

In GR, gravity is described by the Riemann tensor $R_{\alpha\mu\beta\nu}$, with the metric $g_{\mu\nu}$ dynamically responding to matter according to the Einstein field equations[1]

$$R_{\mu\nu} - \frac{1}{2}g_{\mu\nu}R + \Lambda g_{\mu\nu} = 8\pi T_{\mu\nu}, \tag{1.1}$$

[1]We use the metric signature $(-,+,+,+)$, and the conventions of Ref. [24] for the Riemann tensor. We also use geometric units in which the speed of light $c = 1$, Newton's constant $G = 1$, and the vacuum permittivity $\varepsilon_0 = 1/4\pi$. However, in post-Newtonian expansions, we write c explicitly for clarity, and similarly for G in post-Minkowskian expansions.

where $R_{\mu\nu} \equiv g^{\alpha\beta} R_{\alpha\mu\beta\nu}$ is the Ricci tensor, $R \equiv g^{\mu\nu} R_{\mu\nu}$ is the Ricci scalar, Λ is a cosmological constant that we take to be zero, and $T_{\mu\nu}$ is the stress-energy tensor, which satisfies the conservation law $\nabla_\mu T^{\mu\nu} = 0$.

To understand how GWs arise in GR, we start by expanding the metric around a flat spacetime background

$$g_{\mu\nu} = \eta_{\mu\nu} + h_{\mu\nu}, \tag{1.2}$$

where $\eta_{\mu\nu}$ is the Minkowski metric and $h_{\mu\nu}$ is a small perturbation, $|h_{\mu\nu}| \ll 1$. Then, we expand the Einstein equations to linear order in $h_{\mu\nu}$, for which it is more convenient to use the trace-reversed metric perturbation

$$\bar{h}_{\mu\nu} \equiv h_{\mu\nu} - \frac{1}{2}\eta_{\mu\nu} h, \tag{1.3}$$

where the trace $h \equiv \eta^{\mu\nu} h_{\mu\nu}$.

The invariance of GR under a coordinate transformation introduces a gauge freedom that makes it possible to impose the *Lorenz* gauge (also referred to as the harmonic or De Donder gauge)

$$\partial^\nu \bar{h}_{\mu\nu} = 0, \tag{1.4}$$

which reduces the number of independent components of the symmetric tensor $h_{\mu\nu}$ from ten to six. Under this gauge choice, the Einstein field equations reduce to the simple wave equation

$$\Box \bar{h}_{\mu\nu} = -16\pi T_{\mu\nu}, \tag{1.5}$$

where $\Box$ is the D'Alambertian operator in flat spacetime, and the stress-energy tensor in linearized theory satisfies the conservation condition $\partial_\mu T^{\mu\nu} = 0$.

1.1.2 The transverse-traceless gauge

In vacuum, the wave equation (1.5) reduces to

$$\Box \bar{h}_{\mu\nu} = 0, \qquad\qquad \text{(in vacuum)}, \tag{1.6}$$

in which case, an additional gauge freedom exists under the coordinate transformation $x^\mu \rightarrow x^\mu + \xi^\mu$ with $\Box \xi_\mu = 0$. These four conditions can be chosen such that $h_{\mu\nu}$ is spatial, traceless, and transverse. That is,

$$h^{0\mu} = 0, \qquad h^i{}_i = 0, \qquad \partial^j h_{ij} = 0, \tag{1.7}$$

where we use Latin letters to denote spatial components.

This gauge is called the *transverse-traceless* (TT) gauge, and it reduces the number of degrees of freedom in $h_{\mu\nu}$ to two, corresponding to the two GW polarizations: the plus and cross polarizations, h_+ and $h_\times$, respectively. Equation (1.6) admits a plane-wave solution, which we assume propagates in the z direction with frequency ω, yielding

$$h_{ij}^{\mathrm{TT}}(t,z) = \begin{pmatrix} h_+ & h_\times & 0 \\ h_\times & -h_+ & 0 \\ 0 & 0 & 0 \end{pmatrix}_{ij} \cos[\omega(t-z)], \tag{1.8}$$

and the metric

$$\begin{aligned} \mathrm{d}s^2 = -\mathrm{d}t^2 + \mathrm{d}z^2 + [1 + h_+ \cos(\omega(t-z))]\, \mathrm{d}x^2 + [1 - h_+ \cos(\omega(t-z))]\, \mathrm{d}y^2 \\ + 2h_\times \cos(\omega(t-z))\mathrm{d}x\mathrm{d}y. \end{aligned} \tag{1.9}$$

A projector operator $\Lambda_{ij,kl}$ to the TT gauge can be defined such that $h_{ij}^{\mathrm{TT}} = \Lambda_{ij,kl}\bar{h}_{kl}$, where

$$\Lambda_{ij,kl} = P_{ik}P_{jl} - \frac{1}{2}P_{ij}P_{kl}, \qquad P_{ij} = \delta_{ij} - n_i n_j, \tag{1.10}$$

and $\boldsymbol{n}$ is a unit vector in the direction of propagation.

1.1.3 Effect of GWs on test masses

Point particles in GR move along geodesics described by the *geodesic equation*

$$\frac{\mathrm{d}^2 x^\mu}{\mathrm{d}\tau^2} + \Gamma^\mu_{\nu\rho}(x)\frac{\mathrm{d}x^\nu}{\mathrm{d}\tau}\frac{\mathrm{d}x^\rho}{\mathrm{d}\tau} = 0, \tag{1.11}$$

where $\Gamma^\mu_{\nu\rho}(x)$ is the Christoffel symbol, and τ is proper time.

For two nearby particles with worldlines $x^\mu(\tau)$ and $x^\mu(\tau) + \xi^\mu(\tau)$, the equation for the displacement vector ξ^μ can be obtained by expanding the geodesic equation around the position of one particle and subtracting it from the equation of the other particle, leading to

$$\frac{\mathrm{D}^2 \xi^\mu}{\mathrm{D}\tau^2} = -R^\mu{}_{\nu\rho\sigma}\xi^\rho \frac{\mathrm{d}x^\nu}{\mathrm{d}\tau}\frac{\mathrm{d}x^\sigma}{\mathrm{d}\tau}, \tag{1.12}$$

where $\mathrm{D}/\mathrm{D}\tau$ is the covariant derivative. That is, the two particles experience a tidal gravitational force proportional to the Riemann tensor.

For a test particle starting from rest at $\tau = 0$, with $\mathrm{d}x^i/\mathrm{d}\tau = 0$, the geodesic equation (1.11) becomes

$$\left.\frac{\mathrm{d}^2 x^i}{\mathrm{d}\tau^2}\right|_{\tau=0} = -\left[\Gamma^i_{00}\left(\frac{\mathrm{d}x^0}{\mathrm{d}\tau}\right)^2\right]_{\tau=0}. \tag{1.13}$$

In the TT gauge, $(\Gamma^i_{00})_{\tau=0} = 0$, and thus $\mathrm{d}^2 x^i/\mathrm{d}\tau^2 = 0$, which means that the TT coordinates respond to an incoming GW such that the particle remains at rest. However, the proper distance s changes as in Eq. (1.9), which implies that for a wave propagating in the z direction, the proper distance corresponding to a coordinate separation $L \equiv x_2 - x_1$ is given by

$$\begin{aligned} s &= (x_2 - x_1)\left[1 + h_+\cos(\omega t)\right]^{1/2} \\ &\simeq L\left[1 + \frac{1}{2}h_+\cos(\omega t)\right]. \end{aligned} \tag{1.14}$$

For a vector $\boldsymbol{L}$, the proper distance $s \simeq L + h_{ij}L_iL_j/(2L)$; defining $s \equiv s_iL_i/L$, we get

$$\ddot{s}_i \simeq \frac{1}{2}\ddot{h}_{ij}s_j. \tag{1.15}$$

In the frame of a detector, the coordinate distance between test masses coincides with the proper distance, and one can show that the geodesic deviation equation becomes

$$\ddot{\xi}^i = -R^i{}_{0j0}\xi^j. \tag{1.16}$$

In linearized gravity, the Riemann tensor is invariant, and is given in the TT frame by $R^i{}_{0j0} = -\ddot{h}^{\mathrm{TT}}_{ij}/2$, yielding

$$\ddot{\xi}^i = \frac{1}{2}\ddot{h}^{\mathrm{TT}}_{ij}\xi^j. \tag{1.17}$$

Hence, the effect of GWs on masses m in the detector's frame can be described by a simple Newtonian force $F_i = (m/2)\ddot{h}^{\mathrm{TT}}_{ij}\xi^j$.

1.1.4 GW detection and analysis

The Laser Interferometer Gravitational-wave Observatory (LIGO) [25, 26] consists of two detectors, each with two perpendicular 4 km arms with mirrors at the end of each arm acting as test masses (see Fig. 1.1). A laser beam is passed through a beam splitter into Fabry-Perot optical cavities along each arm, and the laser beams are reflected a few hundred times between the mirrors at the ends of each arm, effectively increasing the arm length. When the beams are recombined, the optical interference is accurately measured to detect changes in the relative difference of the arms' lengths due to GWs. In addition, signal recycling mirrors are used to amplify the laser power and produce sharper interference patterns.

Together with the LIGO detectors in the USA, the Virgo detector in Italy [27] and the

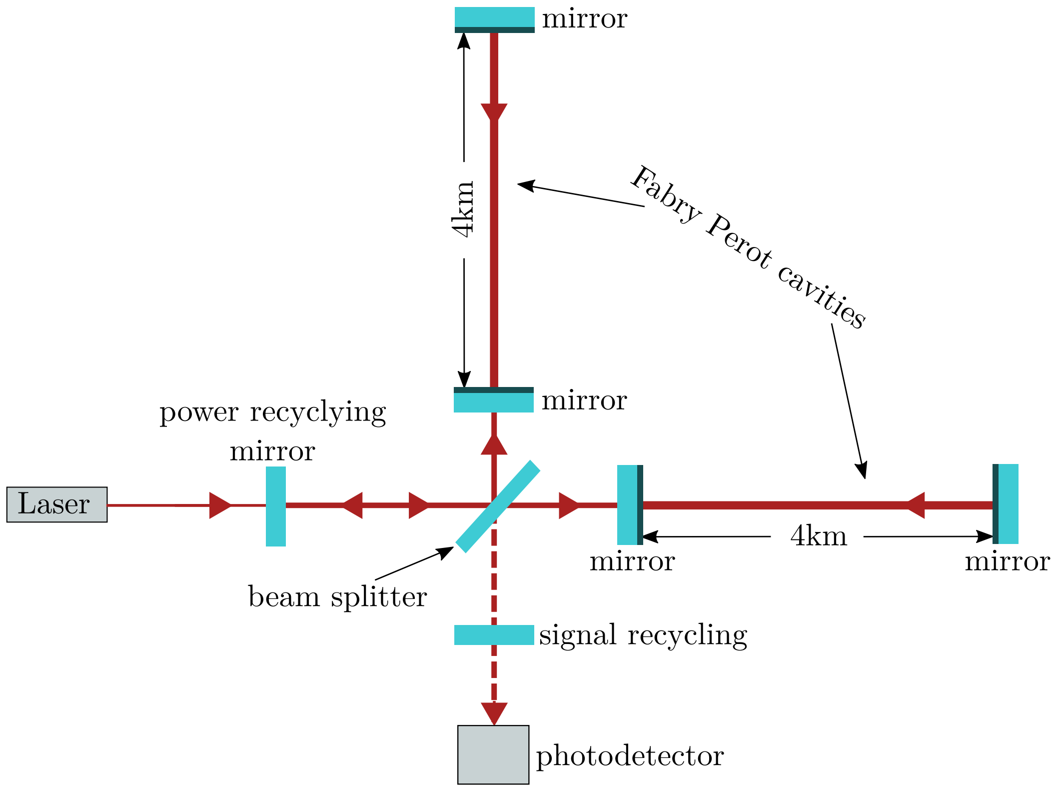

Figure 1.1: Simplified schematic of the laser interferometer used in LIGO. The mirrors act as test masses, and when a GW passes by the detector, the relative difference of the arms length changes, which causes an interference of the laser beams.

KAGRA detector in Japan [28, 29] form a network of GW detectors, which improves the sky localization of the source and increases the chances of detecting a GW signal [30].

The frequency band of Advanced LIGO ranges from 10 Hz to about 7 kHz, with a highest strain sensitivity of $10^{-23}/\sqrt{\mathrm{Hz}}$ around 100 Hz. A typical GW peak amplitude at 100 Hz is $h \sim 10^{-21}$, which causes a displacement in the arm length of about $\Delta L \sim 10^{-18}$ m. Such a weak signal has a smaller amplitude than the instrumental and environmental noise in the detector. However, since the sources and characteristics of the noise are well understood, one can use data analysis techniques to extract the signal from the noise.

The main technique used by ground-based detectors to observe GW signals from binary compact objects is *matched filtering*, in which a filter is applied to amplify the GW signal relative to the noise. The detector output can be written as $d(t) \equiv n(t) + h(t)$, where $n(t)$ is the noise and $h(t)$ is the GW signal. The noise is assumed to be stationary, with power spectral density $S_n(f)$, and is approximated by a Gaussian (normal) distribution $n(f) \sim \mathcal{N}(0; S_n(f)/2)$, with zero mean and $S_n(f)/2$ as the variance. Since the true GW signal $h(t)$ in the detector is unknown, we can use a template waveform $\tilde{h}(t)$ and check that $d(t) - \tilde{h}(t)$ is consistent with our model for the noise. To decide whether the data contain a GW signal, one uses Bayesian inference to compute the likelihood of the null hypothesis: the data are only noise, and that of the signal hypothesis: the data contain noise and GW signal. (See, e.g., Ref. [31] for details.)

Since the parameters of the signal are not known in advance, and producing a template waveform takes a long time, matched filtering requires comparing the detector data with a template bank that contains representative waveforms covering the range in parameter space of expected signals. More accurate waveform templates can lead to more confident detections and avoid missing signals with weak signal-to-noise ratio. Waveforms are also needed for parameter estimation studies, to extract the properties of the system, and for testing GR.

The research presented in this dissertation targets improving the accuracy of waveform models for spinning binaries, extending the range of parameter space they cover by including spin-precession and eccentricity effects, and identifying signatures of modified gravity theories on the binary dynamics and waveforms.

1.2 Analytical approximation methods for the binary dynamics

The most accurate waveforms, for comparable-mass binaries in the LIGO-Virgo frequency band, are produced in *numerical relativity* (NR) simulations, which are based on the 3+1 decomposition of spacetime within the Arnowitt-Deser-Misner (ADM) formalism [32, 33]. The first successful NR simulations were produced in 2005 by Pretorius [34] and soon after by Campanelli et al. [35] and Baker et al. [36]. Since then, thousands of NR simulations have been produced by several groups using different NR codes (see, e.g., Refs. [37–45] and for reviews Refs. [46–49]).

However, NR simulations are computationally very expensive, requiring weeks to months on supercomputers, making them impractical to cover the entire range of parameter space or to produce long waveforms. Hence, it is crucial to have accurate *analytical* waveform models that are much faster to compute, and can complement NR results. Analytical approximations also improve our understanding of the two-body dynamics and their GW emissions, and can help in characterizing modified gravity theories, which has been useful in experimental tests of GR [50].

GWs from binary systems can be divided into three phases: the *inspiral*, *merger*, and *ringdown*. The inspiral phase occurs when the binary components are well separated and are slowly coalescing on a time scale much larger than the orbital time scale. The early inspiral is well described by analytical approximation methods, but the accuracy of those approximations deteriorates in the late inspiral. At the innermost stable circular orbit, the binary components plunge towards each other at relativistic velocities; then, around the light ring, the merger phase begins, which can only be described using NR simulations. Finally, the ringdown phase is when the two compact objects merge into a single remnant with the perturbations being dissipated by GW emission. The ringdown can be described by BH perturbation theory [51–59], whose accuracy is confirmed by NR simulations.

The research in this dissertation focuses on the inspiral phase of the binary dynamics. Three main analytical methods are often used to describe the inspiral: the *post-Newtonian* (PN) approximation, the *post-Minkowskian* (PM) approximation, and *gravitational self-force* (GSF). The PN approximation is valid for small velocities and weak gravitational potential, which are of the same order for bound orbits, i.e. $v^2/c^2 \sim GM/c^2 r \ll 1$, where M is the total mass of the binary. The PM approximation is valid for arbitrary velocities in the weak field $GM/c^2 r \ll 1$, making it more applicable for scattering motion, since high velocities can be achieved. GSF provides an expansion in the small-mass ratio $q \equiv m_1/m_2 \ll 1$, and is most applicable for extreme-mass-ratio inspirals (EMRIs), which can reach millions of orbits within the frequency band of space-based detectors, thus requiring very accurate modeling of the phase.

The PM expansion encompasses the PN expansion, such that the $(n+1)$PM order includes all information up to the nPN order. For example, the 4PM conservative dynamics contains the full 3PN information for generic orbits. This is illustrated in Fig. 1.2, which shows how each term in PN and PM expansions depend on the velocity and separation for the conservative dynamics of nonspinning binaries.

Figure 1.3 provides a schematic representation of the binary systems for which each approximation is most suited, while Fig. 1.4 illustrates the regions of parameter space in which each approximation is applicable. These regions provide a rough estimate for where each approximation is more accurate, but the boundaries depend on the order in the expansion parameter used in each approximation. For small eccentricity $e \sim 0$ (bound orbits), the PN and PM approximations give comparable predictions, since from the virial theorem $v^2 \sim GM/r$, and the

		0PN	**1PN**	**2PN**	**3PN**	**4PN**	**5PN**	$\cdots$
0PM	1	v^2	v^4	v^6	v^8	v^{10}	v^{12}	$\cdots$
1PM		$1/r$	v^2/r	v^4/r	v^6/r	v^8/r	v^{10}/r	$\cdots$
2PM			$1/r^2$	v^2/r^2	v^4/r^2	v^6/r^2	v^8/r^2	$\cdots$
3PM				$1/r^3$	v^2/r^3	v^4/r^3	v^6/r^3	$\cdots$
4PM					$1/r^4$	v^2/r^4	v^4/r^4	$\cdots$
5PM						$1/r^5$	v^2/r^5	$\cdots$
6PM							$1/r^6$	$\cdots$

Figure 1.2: The relation between PN and PM results for the nonspinning conservative dynamics, and the dependence of each term in the expansions on the velocity v and separation r.

velocities are typically $\lesssim 0.4$ until the late inspiral. The PM approximation becomes more accurate than the PN approximation for scattering encounters at large velocities, or equivalently large eccentricities at fixed periastron distance, as illustrated in the right panel of Fig. 1.4. GSF can produce long waveforms that cover the entire range in eccentricity, for arbitrary velocities and separations, but for small mass ratios. NR, in principle, is valid for the entire parameter space, but due to the computational complexity involved, it is usually applied for short waveforms and comparable masses, with major difficulties for small mass ratios, since they lead to a large number of orbits. Furthermore, within the effective-one-body formalism, it is possible to combine several approximations methods with NR results to provide more accurate waveforms that cover the entire parameter space, as discussed in Sec. 1.3.

In the following subsections, we briefly discuss each of the approximation methods, while focusing on the topics most relevant to the research presented in this dissertation. We also discuss

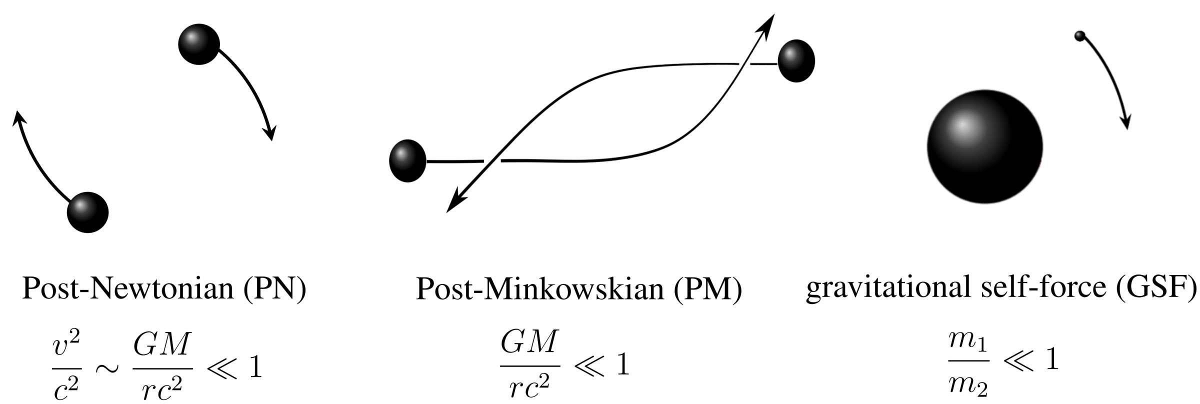

Figure 1.3: Illustration of the analytical approximation methods for the binary inspiral. The PN approximation is most suited for comparable-mass binaries in bound orbits, the PM approximation is suited for scattering motion, while GSF accurately describes EMRIs.

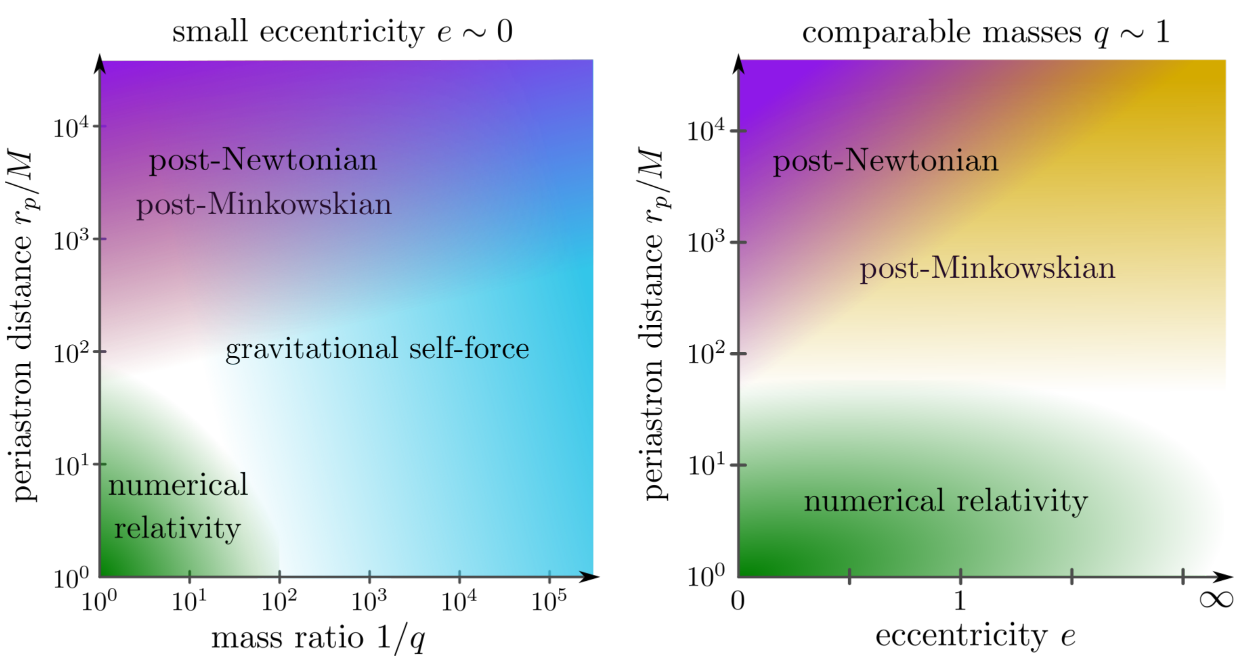

Figure 1.4: Regions of applicability of NR and the PN, PM, and GSF approximations, for small eccentricity $e \sim 0$ (left panel), and for comparable masses in generic orbits (right panel).

how spin is described in GR, since it enters all these methods, and is often treated as a small expansion parameter.

1.2.1 Post-Newtonian approximation

The PN approximation is the most commonly used analytical method for describing the motion of comparable-mass binaries in bound orbits, which are the main source of GWs for ground-based detectors. The first PN calculations were done by Einstein to study the perihelion precession [60], then the 1PN expansion for N-bodies was obtained by de Sitter, Lorentz and Droste [61–63], and later by Einstein, Infeld and Hoffman [64] by solving the vacuum field equations for two spherically-symmetric objects, showing that the internal structure of each body does not affect their dynamics. In the 1960's, Chandrasekhar extended PN calculations to hydrodynamics in a more systematic approach [65, 66], and paved the way to the 2PN expansion. PN research intensified in the 1970's after the discovery of the Hulse–Taylor binary pulsar [67]. Around that time, Ehlers et al. [68] published an important paper pointing out several problems in how the binary motion was treated in GR, which motivated further scrutiny by the community and by the 1990's, those problems were mostly addressed. (For a historical overview of the PN approximation, see Refs. [69–71].)

Over the past few decades, many studies have contributed to improving the PN approximation. For nonspinning binaries the conservative dynamics are known up to 4PN order [72–86], with partial results at 5PN [87–91] and 6PN [92–94]. Spin effects contribute to the conservative dynamics starting at 1.5PN order, and they have been derived for the spin-orbit (SO) coupling (linear in spin) up to 4.5PN [1, 2, 95–109], for the spin-spin coupling up to 4PN [110–122], and

PN order	0	1	1.5	2	2.5	3	3.5	4	4.5	5	5.5	6
no spin	N	1PN		2PN		3PN		4PN		5PN		6PN
spin-orbit			LO		NLO		N²LO		N³LO		N⁴LO	
spin²				LO		NLO		N²LO		N³LO		
spin³							LO		NLO		N²LO	
spin⁴								LO		NLO		
spin⁵											LO	
spin⁶												LO

1PM
2PM
3PM
4PM
5PM
6PM
7PM

Figure 1.5: Known PN results for the conservative dynamics of nonspinning and spinning binaries. PN orders written in black font are fully known, while those in gray are partially known. The shading of each PN order indicates the highest power in GM/r at that order.

at higher orders in spin [123–128]. (For reviews, see Refs. [129–134].) Chapters 2, 3 and 4, include the derivation of the PN results we obtained in Refs. [1–3] for the 4.5PN and 5.5PN SO coupling, and the 5PN aligned spin$_1$-spin$_2$ coupling. The table in Fig. 1.5 summarizes the current knowledge of PN results for the conservative dynamics, and the order at which spin contributions enter the PN expansion.

Radiative effects (energy and angular momentum losses due to GW emission) contribute to the equations of motion starting at 2.5PN, i.e., $\mathcal{O}(v^5/c^5)$; they appear as odd-in-velocity terms, since they are not time-symmetric. The radiative sector is known for nonspinning binaries up to 3.5PN relative (beyond the leading) order [135–161], and for spinning binaries up to 4PN [162–182]. In addition to the instantaneous contributions to the dissipative dynamics, nonlinear effects arise due to GWs scattered off spacetime curvature back onto the binary. These are called tail effects [183], and they start at 1.5PN relative order, with other nonlinear effects appearing at higher orders, such as tail-of-tails [184] (GWs scattered twice). In Chapter 6 (Ref. [5]), we derive the radiative dynamics for eccentric orbits at 2PN relative order, including the tail and spin contributions.

Finite-size effects, e.g. for NSs, appear in PN expansions at 5PN order, and are known up to 2PN relative order for the conservative dynamics [185–190] and 2.5PN relative order for the dissipative dynamics [191–196]. Despite appearing at such high PN orders, tidal effects in NSs can have a measurable effect on GW observations, since the numerical values of the PN coefficients are quite large. (See Ref. [197] for a review.)

The PN approach has also been useful in classifying and characterizing modified gravity theories through the parametrized post-Newtonian formalism [50, 198]. In addition, PN results were derived in specific modified gravity theories, such as scalar-tensor theories [199–210], quadratic gravity [211–214], and other theories [215–217]. In Chapter 8, based on Ref. [7], we derive the 1PN conservative and dissipative dynamics in Einstein-Maxwell-dilaton (EMd) theory.

In what follows, we demonstrate how PN results can be obtained by summarizing the derivation of the conservative and dissipative dynamics at next-to-leading PN order. But first, we begin by discussing the quadrupole approximation (at leading PN order). Throughout this subsection, we write c explicitly for clarity.

1.2.1.1 The quadrupole approximation

In PN calculations, we assume that the distance R from the source to the observer is much greater than the GW wavelength λ_{GW}. If d is the source's size and v its velocity, then $\lambda_{\text{GW}} \sim dc/v$, and thus slow motion $v \ll c$ implies $\lambda_{\text{GW}} \gg d$. The region around the source, extending to distance $\mathcal{R} \ll \lambda_{\rm GW}$, is denoted the *near zone*, while the region with $R \gg \lambda_{\rm GW}$ is denoted the *far zone*, as illustrated in Fig. 1.6. We use uppercase symbols for quantities in radiative coordinates $(T, \boldsymbol{X})$ (in the far zone), and use lowercase symbols $(t, \boldsymbol{x})$ for quantities in the near zone. The two coordinate systems are generally not the same, but they can be connected by matched-asymptotic expansions in the matching (or buffer) region [137–139]. However, this subtlety only matters at higher PN orders than what we consider in this section.

The linearized field equations (1.5) in the Lorenz gauge have the solution

$$\bar{h}_{\mu\nu}(T, \boldsymbol{X}) = \frac{4G}{c^4} \int \mathrm{d}^3 x \, \frac{T_{\mu\nu}\left(T_{\rm ret}, \boldsymbol{x}\right)}{|\boldsymbol{X} - \boldsymbol{x}|} \,, \tag{1.18}$$

where the retarded time $T_{\rm ret}$ is given by

$$T_{\rm ret} = T - \frac{|\boldsymbol{X} - \boldsymbol{x}|}{c} \,. \tag{1.19}$$

To evaluate this integral in the far zone (see Fig. 1.7), we use

$$|\boldsymbol{X} - \boldsymbol{x}| = R - \boldsymbol{x} \cdot \boldsymbol{N} + \mathcal{O}\left(\frac{d^2}{R}\right), \tag{1.20}$$

where $\boldsymbol{N} \equiv \boldsymbol{X}/R$ is the unit vector in the direction of propagation. Expanding Eq. (1.18) at leading order in $1/R$, we obtain

$$\bar{h}^{\rm TT}_{ij}(U, \boldsymbol{X}) = \frac{4G}{c^4 R} \Lambda_{ij,kl}(\boldsymbol{N}) \int \mathrm{d}^3 x \, T_{kl}\left(U + \frac{\boldsymbol{x} \cdot \boldsymbol{N}}{c}, \boldsymbol{x}\right) + \mathcal{O}\left(\frac{1}{R^2}\right) \,, \tag{1.21}$$

where we defined $U \equiv T - R/c$, and used the Λ operator from Eq. (1.10) to project to the TT gauge.

From the conservation law in linearized gravity of the stress-energy tensor $\partial_\mu T^{\mu\nu} = 0$, the spatial components of $T_{\mu\nu}$ can be related to the time component via

$$T^{ij} = \frac{1}{2} \frac{\partial^2}{\partial T^2} \left(x^i x^j T^{00}\right) + \text{boundary terms}, \tag{1.22}$$

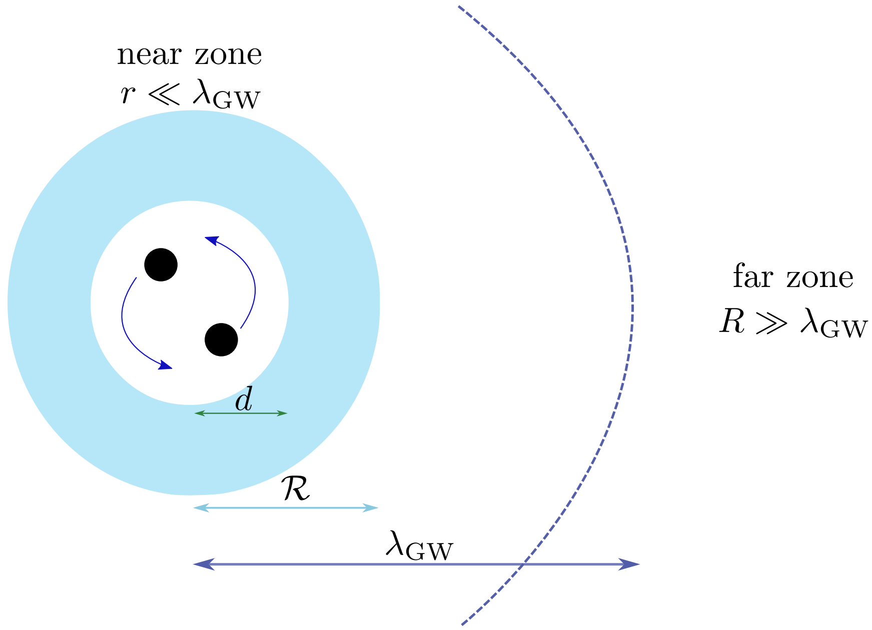

Figure 1.6: Schematic for the near zone ($r \ll \lambda_{\rm GW}$) and far zone ($R \gg \lambda_{\rm GW}$) used in the PN formalism. The shaded area is the matching region.

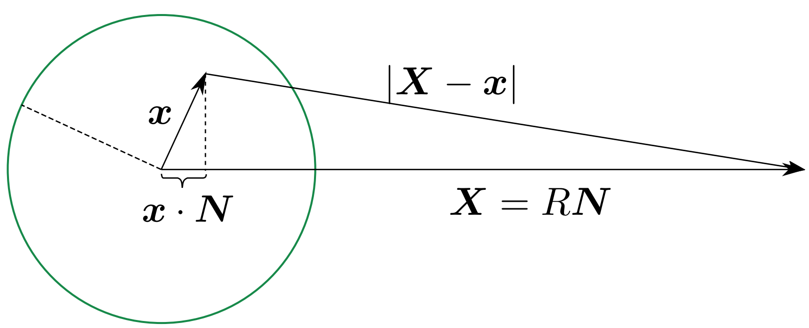

Figure 1.7: Illustration of the far zone expansion.

where the boundary terms involve spatial derivatives of T^{ij}, which can be dropped in the integral (1.21), leading to

$$\bar{h}_{ij}^{\mathrm{TT}}(U,\boldsymbol{X}) = \frac{2G}{c^4 R}\Lambda_{ij,kl}(\boldsymbol{N})\frac{\partial^2}{\partial T^2}\int \mathrm{d}^3x\, x^i x^j T^{00}\left(U+\frac{\boldsymbol{x}\cdot\boldsymbol{N}}{c},\boldsymbol{x}\right)+\mathcal{O}\left(\frac{1}{R^2}\right). \tag{1.23}$$

Assuming small velocities, the above equation can be expanded in v/c. At leading order, we obtain

$$\bar{h}_{ij}^{\mathrm{TT}}(U,\boldsymbol{X}) \simeq \frac{2G}{c^4 R}\Lambda_{ij,kl}(\boldsymbol{N})\frac{d^2 M^{ij}}{dT^2}\,, \tag{1.24}$$

with the quadrupole tensor

$$M^{ij} \equiv \int \mathrm{d}^3x\, x^i x^j T^{00}. \tag{1.25}$$

To make the quadrupole tensor trace-free, we define

$$\begin{aligned} Q^{ij} &\equiv M^{ij} - \frac{1}{3}\delta^{ij}M_{kk} \\ &= \int \mathrm{d}^3x\,\rho_g\left(x^i x^j - \frac{1}{3}\delta^{ij}\boldsymbol{x}^2\right), \end{aligned} \tag{1.26}$$

where T^{00} is identified as the Newtonian mass density ρ_g of the system. Then, the waveform in the quadrupolar approximation can be written as

$$\bar{h}_{ij}^{\mathrm{TT}}(U,\boldsymbol{X}) \simeq \frac{2G}{c^4 R}\Lambda_{ij,kl}(\boldsymbol{N})\frac{d^2 Q^{ij}}{dT^2}\,. \tag{1.27}$$

In the coordinate system covering the source, the total energy loss per unit solid angle can be expressed as [21]

$$\begin{aligned} \frac{\mathrm{d}E}{\mathrm{d}t\mathrm{d}\Omega} &= \frac{R^2 c^3}{32\pi G}\langle \dot{h}_{ij}^{\mathrm{TT}}\dot{h}_{ij}^{\mathrm{TT}}\rangle \\ &= \frac{G}{8\pi c^5}\Lambda_{ij,kl}(\boldsymbol{n})\langle \dddot{Q}^{ij}\dddot{Q}^{kl}\rangle, \end{aligned} \tag{1.28}$$

where the dots denote derivatives with respect to time t, and the angle brackets $\langle\ldots\rangle$ denote an appropriate time average, e.g., over an orbit for a binary. Integrating yields the total radiated power (or luminosity)

$$P = \frac{G}{5c^5}\langle \dddot{Q}^{ij}\dddot{Q}^{ij}\rangle, \tag{1.29}$$

which is the famous *quadrupole formula* derived by Einstein in 1918 [218]. The radiated angular momentum at leading order can also be expressed in terms of the quadrupole moment as

$$\frac{\mathrm{d}L^i}{\mathrm{d}t} = \frac{2G}{5c^5}\epsilon^{ijk}\langle \ddot{Q}^{jl}\dddot{Q}^{lk}\rangle. \tag{1.30}$$

For a binary system with masses m_1 and m_2 in a circular orbit, the relative coordinates in the center of mass are given by

$$x(t) = r\cos\Omega t, \qquad y(t) = r\sin\Omega t, \qquad z(t) = 0, \tag{1.31}$$

where r is the distance between the two bodies, and Ω is the orbital frequency. The nonzero components of the quadrupole tensor M_{ij} are

$$M_{11} = \frac{\mu}{2}r^2(1+\cos 2\Omega t), \quad M_{22} = \frac{\mu}{2}r^2(1-\cos 2\Omega t), \quad M_{12} = \frac{\mu}{2}r^2\sin 2\Omega t, \tag{1.32}$$

where $\mu \equiv m_1 m_2/(m_1+m_2)$ is the reduced mass. From Eq. (1.29), we obtain the total radiated power

$$P = \frac{32G}{5c^5}\mu^2 r^4 \Omega^6. \tag{1.33}$$

1.2.1.2 1PN expansion for the conservative dynamics

To obtain the equations of motion describing the binary dynamics, we need to work in the near zone, where the size of the source is much smaller than the GW wavelength, and we can neglect retardation effects. Here, we summarize the steps needed to derive the 1PN conservative dynamics, which are detailed in Appendix M in the context of EMd theory, which reduces to GR for zero charges.

The action is given by

$$S = S_g + S_m, \tag{1.34}$$

$$S_g = \frac{c^4}{16\pi G}\int \mathrm{d}t\mathrm{d}^3\boldsymbol{x}\,\sqrt{-g}g^{\mu\nu}\left(\Gamma^\rho_{\mu\lambda}\Gamma^\lambda_{\nu\rho} - \Gamma^\rho_{\mu\nu}\Gamma^\lambda_{\rho\lambda}\right), \tag{1.35}$$

$$S_m = -\sum_{\mathrm{i}}\int \mathrm{d}t m_{\mathrm{i}} c^2\sqrt{-g_{\mu\nu}\,v^\mu_{\mathrm{i}} v^\nu_{\mathrm{i}}/c^2}, \tag{1.36}$$

where S_g is the gravitational action written here in the (Einstein-)Landau-Lifshitz form[2] [219–221], and S_m is the matter action for point particles, from which the stress-energy tensor can be obtained via $T_{\mu\nu} = -2/\sqrt{-g}\,\delta S_m/\delta g^{\mu\nu}$.

To expand the action, we start by expanding the metric in powers of v/c, such that [222]

$$\begin{aligned} g_{00} &= -1 + 2V - 2V^2 + \dots, \\ g_{0i} &= -4V_i + \dots, \\ g_{ij} &= \delta_{ij} + 2V\delta_{ij} + \dots, \end{aligned} \tag{1.38}$$

where the potentials $V \sim \mathcal{O}(1/c^2)$, and $V_i \sim \mathcal{O}(1/c^3)$. The inverse metric satisfies $g^{\mu\lambda}g_{\lambda\nu} = \delta^\mu_{\ \nu}$, and the connection coefficients are given in terms of the metric by

$$\Gamma^\mu{}_{\nu\lambda} = \frac{1}{2}g^{\mu\rho}\left(\partial_\lambda g_{\rho\nu} + \partial_\nu g_{\rho\lambda} - \partial_\rho g_{\nu\lambda}\right). \tag{1.39}$$

Plugging the metric expansion (1.38) in the action (1.34), imposing the harmonic-gauge condition $g^{\mu\nu}\Gamma^\lambda_{\mu\nu} = 0$, and integrating by parts yields the 1PN action

$$S_g = \frac{c^4}{16\pi G}\int \mathrm{d}t\mathrm{d}^3\boldsymbol{x}\Big[-2\partial_i V\partial_i V + 2\partial_0 V\partial_0 V + 8\partial_i V_j\partial_i V_j\Big], \tag{1.40}$$

[2]The gravitational action can also be written in the more familiar Einstein-Hilbert form as

$$S_g = \frac{c^4}{16\pi G}\int \mathrm{d}t\mathrm{d}^3\boldsymbol{x}\,\sqrt{-g}R, \tag{1.37}$$

which differs from Eq. (1.35) by boundary terms, but Eq. (1.35) is more convenient for PN calculations.

$$S_m = \int \mathrm{d}t\mathrm{d}^3\boldsymbol{x} \left[\rho_g\Big(- c^2 + \frac{1}{2}v^2 + Vc^2 + \frac{1}{8}\frac{v^4}{c^2} + \frac{3}{2}Vv^2 - \frac{1}{2}V^2c^2 - 4V_iv^ic\Big)\right], \tag{1.41}$$

where the mass density ρ_g is defined by

$$\rho_g \equiv \sum_{\mathrm{i}} m_{\mathrm{i}}\delta^3(\boldsymbol{x} - \boldsymbol{x}_{\mathrm{i}}). \tag{1.42}$$

Varying the total action with respect to V_i and V yields the field equations

$$\nabla^2 V_i = -\frac{4\pi G}{c^3}\rho_g v^i, \tag{1.43}$$

$$\Box V = -\frac{4\pi G}{c^2}\rho_g - \frac{4\pi G}{c^4}\rho_g\left(\frac{3}{2}v^2 - Vc^2\right), \tag{1.44}$$

where $\Box \equiv -\partial_0^2 + \nabla^2$ is d'Alembertian in flat spacetime. The solution of these field equations is given by

$$V_i = \frac{G}{c^3}\left(\frac{m_1 v_1^i}{|\boldsymbol{x}-\boldsymbol{x}_1|} + \frac{m_2 v_2^i}{|\boldsymbol{x}-\boldsymbol{x}_2|}\right), \tag{1.45}$$

$$\begin{aligned} V = {}& \frac{G}{c^2}\left(\frac{m_1}{|\boldsymbol{x}-\boldsymbol{x}_1|} + \frac{m_2}{|\boldsymbol{x}-\boldsymbol{x}_2|}\right) + \frac{G}{2c^4}\left(m_1\frac{\partial^2}{\partial t^2}|\boldsymbol{x}-\boldsymbol{x}_1| + m_2\frac{\partial^2}{\partial t^2}|\boldsymbol{x}-\boldsymbol{x}_2|\right) \\ & + \frac{3G}{2c^4}\left(\frac{m_1 v_1^2}{|\boldsymbol{x}-\boldsymbol{x}_1|} + \frac{m_2 v_2^2}{|\boldsymbol{x}-\boldsymbol{x}_2|}\right) - \frac{G^2}{c^4}m_1 m_2\left(\frac{1}{r|\boldsymbol{x}-\boldsymbol{x}_1|} + \frac{1}{r|\boldsymbol{x}-\boldsymbol{x}_2|}\right), \end{aligned} \tag{1.46}$$

where $r \equiv |\boldsymbol{x}_1 - \boldsymbol{x}_2|$ and

$$\frac{\partial^2}{\partial t^2}|\boldsymbol{x}-\boldsymbol{x}_1| = \frac{v_1^2}{|\boldsymbol{x}-\boldsymbol{x}_1|} - \boldsymbol{n}_1\cdot\boldsymbol{a}_1 - \frac{(\boldsymbol{n}_1\cdot\boldsymbol{v}_1)^2}{|\boldsymbol{x}-\boldsymbol{x}_1|}, \tag{1.47}$$

with $\boldsymbol{n}_1 \equiv (\boldsymbol{x}-\boldsymbol{x}_1)/|\boldsymbol{x}-\boldsymbol{x}_1|$, and $\boldsymbol{a}_1 = d\boldsymbol{v}_1/dt$ is the acceleration.

Next, we use integration by parts in the gravitational action (1.40), and use the field equations (1.43) and (1.44) to get rid of the derivatives. The result for the total action is given by

$$S = \int \mathrm{d}t\mathrm{d}^3\boldsymbol{x}\left[\rho_g\left(-c^2 + \frac{1}{2}v^2 + \frac{v^4}{8c^2} + \frac{1}{2}Vc^2 + \frac{3}{4}Vv^2 - 2V_iv^ic\right)\right]. \tag{1.48}$$

Substituting the solution for V_i and V, and integrating over space, leads to the 1PN Lagrangian

$$\begin{aligned}\mathcal{L} = &-(m_1+m_2)c^2 + \frac{1}{2}m_1 v_1^2 + \frac{1}{2}m_2 v_2^2 + \frac{G m_1 m_2}{r} \\ &+ \frac{1}{c^2}\left[\frac{1}{8}m_1 v_1^4 + \frac{1}{8}m_2 v_2^4 + \frac{G m_1 m_2}{2r}\left[3(v_1^2+v_2^2) - 7(\boldsymbol{v_1}\cdot\boldsymbol{v_2}) - (\boldsymbol{n}\cdot\boldsymbol{v_1})(\boldsymbol{n}\cdot\boldsymbol{v_2})\right]\right. \\ &\left.\qquad - \frac{G^2 m_1 m_2 (m_1+m_2)}{2r^2}\right]. \end{aligned} \tag{1.49}$$

The Hamiltonian in the center-of-mass frame can be derived from the Lagrangian using a Legendre transformation [223]

$$H = \boldsymbol{v}\cdot\boldsymbol{p} - \mathcal{L}, \tag{1.50}$$

where the relative velocity $\boldsymbol{v} \equiv \boldsymbol{v}_1 - \boldsymbol{v}_2$ and the center-of-mass momentum $p_i = \partial\mathcal{L}/\partial v^i$. This leads to the Hamiltonian

$$\begin{aligned} H = &M + \frac{p^2}{2\mu} - \frac{GM\mu}{r} \\ &+ \frac{1}{c^2}\left[-\frac{1}{8}(1-3\nu)\frac{p^4}{\mu^3} - \frac{GM}{2\mu r}\left[(3+\nu)\,p^2 + \nu p_r^2\right] + \frac{G^2M^2\mu}{2r^2}\right] + \mathcal{O}\left(\frac{1}{c^4}\right), \end{aligned} \tag{1.51}$$

where $p_r = \boldsymbol{n}\cdot\boldsymbol{p}$ is the radial momentum, and we define the total mass M, reduced mass μ, and symmetric-mass ratio ν by

$$M \equiv m_1 + m_2\,, \qquad \mu \equiv \frac{m_1 m_2}{M}\,, \qquad \nu \equiv \frac{\mu}{M}\,. \tag{1.52}$$

1.2.1.3 Energy and angular momentum fluxes

In § 1.2.1.1, we expanded the metric in Eq. (1.23) at leading PN order to obtain the quadrupole formula. The metric in a radiative coordinate system is given to all orders in a multipolar expansion by [135]

$$h_{ij}^{\mathrm{TT}}(U,\boldsymbol{N}) = \frac{4G}{R}\sum_{\ell\geq 2}\frac{1}{\ell! c^{\ell+2}}\left[N_{L-2}M_{ijL-2}^{(\ell)}(U) - \frac{2\ell}{(\ell+1)c}N_{hL-2}\varepsilon_{hk(i}S_{j)kL-2}^{(\ell)}\right]^{\mathrm{TT}}, \tag{1.53}$$

where $U \equiv T - R/c$, M_L are the mass-type moments, and S_L are the current-type moments. In this notation, an uppercase index denotes a multi-index, such as $N^L \equiv N^{i_1} N^{i_2} \ldots N^{i_\ell}$, while a superscript in parentheses denotes derivatives, such as $\Psi^{(\ell)}(U) = d^\ell \Psi / dU^\ell$.

These radiative moments agree with the near-zone source moments I_L and J_L at low PN orders, such that [138, 139, 200]

$$M_L = I_L + \mathcal{O}(1/c^3), \qquad S_L = J_L + \mathcal{O}(1/c^2), \tag{1.54}$$

with

$$I_L(t) = \int \mathrm{d}^3 x \left[\widehat{x}_L \sigma + \frac{1}{2(2\ell+3)c^2} x^2 \widehat{x}_L \frac{\partial^2 \sigma}{\partial t^2} - \frac{4(2\ell+1)}{(\ell+1)(2\ell+3)c^2} \widehat{x}_{Ls} \frac{\partial \sigma^s}{\partial t} \right], \tag{1.55}$$

$$J_L(t) = \int \mathrm{d}^3 x \, \varepsilon_{hk\langle i_\ell} \widehat{x}_{L-1\rangle h} \sigma^k. \tag{1.56}$$

The source functions σ and σ^i are related to the stress-energy tensor by

$$\sigma \equiv \frac{T^{00} + T^{ss}}{c^2}, \qquad \sigma^i \equiv \frac{T^{0i}}{c}, \tag{1.57}$$

and the field equations (1.44) and (1.43) can be written in terms of them as

$$\Box V = -\frac{4\pi G}{c^2} \sigma, \qquad \Box V^i = -\frac{4\pi G}{c^3} \sigma^i, \tag{1.58}$$

from which it follows that

$$\sigma^i = m_1 v_1^i \delta^3(\boldsymbol{x} - \boldsymbol{x}_1) + m_2 v_2^i \delta^3(\boldsymbol{x} - \boldsymbol{x}_2), \tag{1.59}$$

$$\sigma = \left[m_1 + \frac{3}{2c^2} m_1 v_1^2 - \frac{G_{12} m_1 m_2}{c^2 r} \right] \delta^3(\boldsymbol{x} - \boldsymbol{x}_1) + 1 \leftrightarrow 2. \tag{1.60}$$

The multipole moments needed for the next-to-leading order fluxes and waveform are M_{ij}, M_{ijk}, and S_{ij}, which are given by

$$M_{ij} = \left(m_1 + \frac{3}{2c^2} m_1 v_1^2 - \frac{G_{12} m_1 m_2}{c^2 r} \right) x_1^{\langle ij \rangle} + \frac{m_1}{14c^2} \frac{d^2}{dt^2} x_1^2 x_1^{\langle ij \rangle}$$

$$-\frac{20m_1}{21c^2}\frac{d}{dt}v_1^k x_1^{\langle ijk\rangle} + 1 \leftrightarrow 2, \tag{1.61}$$

$$M_{ijk} = m_1 x_1^{\langle ijk\rangle} + m_2 x_2^{\langle ijk\rangle}, \tag{1.62}$$

$$S_{ij} = m_1 \varepsilon^{hk\langle j} x_1^{i\rangle} x_1^h v_1^k + m_2 \varepsilon^{hk\langle j} x_2^{i\rangle} x_2^h v_2^k. \tag{1.63}$$

where indices in angle brackets denote a symmetric trace-free projection; for example, $x^{\langle ij\rangle} \equiv x^i x^j - \frac{1}{3}x^2\delta_{ij}$.

In terms of the multipole moments, the energy flux is given by

$$\begin{aligned}
\Phi_E &= \frac{c^3}{32\pi G}\int \mathrm{d}\Omega \left(\frac{\partial h_{ij}^{\mathrm{TT}}}{\partial U}\right)^2 \\
&= \frac{G}{c^5}\left[\frac{1}{5}M_{ij}^{(3)}M_{ij}^{(3)} + \frac{1}{189c^2}M_{ijk}^{(4)}M_{ijk}^{(4)} + \frac{16}{45c^2}S_{ij}^{(3)}S_{ij}^{(3)} + \mathcal{O}\left(\frac{1}{c^4}\right)\right],
\end{aligned} \tag{1.64}$$

where the first term is the mass quadrupole flux, the second is the mass octopole, and the third is the current quadrupole. Taking the time derivatives of the multipole moments and squaring, we obtain the 1PN energy flux

$$\begin{aligned}
\Phi_E = {} & \frac{8G^3M^2\mu^2}{15c^5r^4}\left[12v^2 - 11\dot{r}^2\right] \\
& + \frac{8G^3M^2\mu^2}{420c^7r^4}\Bigg[(785 - 852\nu)v^4 - 2(1487 - 1392\nu)v^2\dot{r}^2 + 3(687 - 620\nu)\dot{r}^4 \\
& \quad - 160(17 - \nu)\frac{GMv^2}{r} + 8(367 - 15\nu)\frac{GM\dot{r}^2}{r} + 16(1 - 4\nu)\frac{G^2M^2}{r^2}\Bigg].
\end{aligned} \tag{1.65}$$

The angular momentum flux can be similarly expressed in terms of the source moments, which at next-to-leading order read [149, 224]

$$\begin{aligned}
\boldsymbol{\Phi}_J &= \frac{G}{c^5}\epsilon_{ijk}\left[\frac{2}{5}I_{jl}^{(2)}I_{kl}^{(3)} + \frac{32}{45c^2}J_{jl}^{(2)}J_{kl}^{(3)} + \frac{1}{63c^2}I_{jlm}^{(3)}I_{klm}^{(4)} + \mathcal{O}\left(\frac{1}{c^4}\right)\right] \\
&= \frac{8G^2M\mu^2}{5c^5r^3}\boldsymbol{L}_N\left[2v^2 - 3\dot{r}^2 + 2\frac{GM}{r}\right] \\
&\quad + \frac{8G^2M\mu^2}{420c^5r^3}\boldsymbol{L}_N\Bigg[(307 - 548\nu)v^4 - 6(74 - 277\nu)v^2\dot{r}^2 - 4(58 + 95\nu)v^2\frac{GM}{r}
\end{aligned}$$

$$+ 3(95 - 360\nu)\dot{r}^4 + 2(372 + 197\nu)\dot{r}^2 \frac{GM}{r} - 2(745 - 2\nu)\frac{G^2M^2}{r^2}\Bigg], \tag{1.66}$$

where $\boldsymbol{L}_N \equiv \boldsymbol{r} \times \boldsymbol{v}$.

In Chapter 8 (Ref. [7]), we extend the above derivation to obtain the next-to-leading order energy flux in EMd theory (see Appendix N for the details).

1.2.1.4 Gravitational waveform modes

The waveform propagating in the far zone is given in terms of multipole moments by Eq. (1.53), from which the two polarization states h_+ and $h_\times$ can be obtained using

$$h_+ = \frac{1}{2}\left(P_iP_j - Q_iQ_j\right) h_{ij}^{\rm TT}, \tag{1.67}$$

$$h_\times = \frac{1}{2}\left(P_iQ_j - P_jQ_i\right) h_{ij}^{\rm TT}, \tag{1.68}$$

where $\boldsymbol{P}$ and $\boldsymbol{Q}$ are the polarization unit vectors that form an orthonormal triad with the direction of propagation $\boldsymbol{N}$. Several conventions exist in the literature for the polarization triad; one common choice [158] is to use spherical coordinates with $\boldsymbol{P} \equiv -\boldsymbol{e}_\Phi$ and $\boldsymbol{Q} \equiv \boldsymbol{e}_\Theta$, for a wave propagating in the direction (Θ, Φ).

The complex polarization waveform $h \equiv h_+ - ih_\times$ is often decomposed in terms of spin-weighted $s = -2$ spherical harmonics $Y^{\ell m}_{-2}(\Theta, \Phi)$. These GW spherical harmonic modes are denoted $h^{\ell m}$ and are defined by

$$h = \sum_{\ell=2}^{\infty} \sum_{m=-\ell}^{\ell} h^{\ell m} Y^{\ell m}_{-2}(\Theta, \Phi). \tag{1.69}$$

The modes $h^{\ell m}$ can be computed from h via

$$h^{\ell m} = \int \mathrm{d}^2\Omega \, h \bar{Y}^{\ell m}_{-2}(\Theta, \Phi), \tag{1.70}$$

where $\bar{Y}_{-2}^{\ell m}$ is the complex conjugate, or they can be calculated directly from the radiative multipole moments via [158, 170, 225]

$$h^{\ell m} = \frac{1}{\sqrt{2} R c^{\ell+2}} \left[M^{\ell m} - \frac{i}{c} S^{\ell m} \right], \tag{1.71}$$

where R is the luminosity distance of the source, and the radiative multipole moments are related to the symmetric trace-free multipole moments M_L and S_L by

$$M^{\ell m} = \frac{16\pi}{(2\ell+1)!!} \sqrt{\frac{(\ell+1)(\ell+2)}{2\ell(\ell-1)}} \bar{\mathcal{Y}}_L^{\ell m} M_L, \tag{1.72}$$

$$S^{\ell m} = \frac{-32\pi}{(2\ell+1)!!} \sqrt{\frac{\ell(\ell+2)}{2(\ell+1)(\ell-1)}} \bar{\mathcal{Y}}_L^{\ell m} S_L, \tag{1.73}$$

where $\bar{\mathcal{Y}}_L^{\ell m}$ is the complex conjugate of the symmetric trace-free tensors relating the unit vectors $N_{\langle L \rangle}$ to the spherical harmonics basis $Y^{\ell m}(\Theta, \Phi)$ such that

$$Y^{\ell m}(\Theta, \Phi) = \mathcal{Y}_L^{\ell m} N_{\langle L \rangle}(\Theta, \Phi), \tag{1.74}$$

$$N_{\langle L \rangle}(\Theta, \Phi) = \frac{4\pi \ell!}{(2\ell+1)!!} \sum_{m=-\ell}^{\ell} \bar{\mathcal{Y}}_L^{\ell m} Y^{\ell m}(\Theta, \Phi), \tag{1.75}$$

$$\bar{\mathcal{Y}}_L^{\ell m} = \frac{(2\ell+1)!!}{4\pi \ell!} \int d\Omega \, N_{\langle L \rangle} \bar{Y}^{\ell m}, \tag{1.76}$$

$$\bar{\mathcal{Y}}_L^{\ell m} \mathcal{Y}_L^{\ell m'} = \frac{(2\ell+1)!!}{4\pi \ell!} \delta_{mm'}, \tag{1.77}$$

and we can express the unit vector $\boldsymbol{N}$ in terms of the angles Θ and Φ as

$$\boldsymbol{N} = \sin\Theta \cos\Phi \hat{\boldsymbol{e}}_x + \sin\Theta \sin\Phi \hat{\boldsymbol{e}}_y + \cos\Theta \hat{\boldsymbol{e}}_z. \tag{1.78}$$

For planar binaries, nonspinning or with aligned spins, it was shown in Ref. [158] that the modes can be determined using the mass-type multipole moments for even $\ell + m$, or the current-type multipole moments for odd $\ell + m$, i.e.,

$$h^{\ell m} = \begin{cases} M^{\ell m}/(\sqrt{2}Rc^{\ell+2}), & \ell + m \text{ even} \\ \\ -iS^{\ell m}/(\sqrt{2}Rc^{\ell+3}), & \ell + m \text{ odd} \end{cases}. \tag{1.79}$$

In addition, under a change in the sign of m, the modes are related via

$$h^{\ell m} = (-1)^\ell \bar{h}^{\ell,-m}, \tag{1.80}$$

and thus we can consider only positive integers for m.

The dominant mode is the $(\ell, m) = (2, 2)$ mode, since it is the only contribution to h at leading PN order, which is given by

$$h^{22} = -\frac{4\mu}{c^4 R}\sqrt{\frac{\pi}{5}}\mathrm{e}^{-2i\phi}\left[\left(\frac{1}{r} + p^2 - 2p_r^2\right) + i\frac{Lp_r}{r} + \mathcal{O}\left(\frac{1}{c^2}\right)\right]. \tag{1.81}$$

In Chapter 6 (Ref. [5]), we extend the calculation described above to derive the leading order spin-orbit and spin-spin contributions to the waveform modes for planar eccentric orbits.

1.2.2 Post-Minkowskian approximation

The PM approximation is valid for arbitrary velocities. So, unlike the PN approximation, it is applicable in situations in which large velocities can be achieved at large separations, such as scattering encounters.

PM approaches were pioneered in the 1950's by Bertotti and collaborators [226, 227] at 1PM order, then 2PM results were obtained in the 1980's in Refs. [136, 228–235], for the purpose of clarifying retarded interactions and radiation reaction in binary systems. Interest in the PM approximation was renewed recently, in part due to Refs. [236, 237], in which Damour showed that the dynamics of a binary system can be mapped at 1PM order to the motion of a test mass in a

Schwarzschild background. He also advocated for using quantum scattering amplitudes [238] to derive PM results, which was done soon after in, e.g., Refs. [239–250], including the calculation of the 3PM [243] and 4PM [246, 247] scattering angle. There has also been significant recent progress using classical [251–253], effective field theory [254–259], and worldline quantum field theory [260, 261] approaches. Spin effects were included in the PM approximation using all these approaches in Refs. [262–276], in addition to tidal [277–284], and radiative [285–298] effects.

PM expansions is often expressed in terms of the impulse (net change in momentum) or the gauge-invariant scattering angle (the angle by which the two bodies are deflected in the center-of-mass frame). In the following subsections, we briefly demonstrate how the PM expansion can be obtained by calculating the impulse at 1PM order. Then, we discuss the relation between the impulse and scattering angle, and their simple dependence on the mass ratio, which we exploited in Refs. [1–3] to derive novel PN results. Finally, we demonstrate how observables that describe unbound orbits, such as the scattering angle, can be related to bound-orbit observables, such as the periastron advance.

1.2.2.1 The impulse at 1PM order

In the PM approximation, one solves the Einstein equations and the geodesic equation in an expansion in Newton's constant G (or rather in the dimensionless quantity GM/c^2r). The metric, worldline, and momentum of nonspinning particles in a Schwarzschild background can be written in a PM expansion of the form

$$g_{\mu\nu}(x) = \eta_{\mu\nu} + G h^{(1)}_{\mu\nu}(x) + G^2 h^{(2)}_{\mu\nu}(x) + \cdots\,, \tag{1.82}$$

$$x^\mu_{\rm i}(\tau_{\rm i}) = x^\mu_{0{\rm i}}(\tau_{\rm i}) + G x^\mu_{1{\rm i}}(\tau_{\rm i}) + G^2 x^\mu_{2{\rm i}}(\tau_{\rm i}) + \cdots\,, \tag{1.83}$$

$$p^\mu_{\rm i}(\tau_{\rm i}) = p^\mu_{0{\rm i}}(\tau_{\rm i}) + Gp^\mu_{1{\rm i}}(\tau_{\rm i}) + G^2 p^\mu_{2{\rm i}}(\tau_{\rm i}) + \cdots\,, \tag{1.84}$$

where $\tau_{\rm i}$ is the proper time for each mass, and the subscript $\rm i = 1, 2, \ldots$ denotes the label of each particle.

At zeroth order, the metric is the flat spacetime metric $\eta_{\mu\nu}$, and the solution for the worldline and momentum are given by

$$x_{0{\rm i}}(\tau_{\rm i}) = y^\mu_{\rm i} + u^\mu_{\rm i}\tau_{\rm i}, \qquad p^\mu_{0{\rm i}}(\tau_{\rm i}) = m_{\rm i} u^\mu_{\rm i}, \tag{1.85}$$

where $y^\mu_{\rm i}$ is the displacement from the origin at $\tau = 0$, and $u^\mu_{\rm i}$ is the 4-velocity with $u^2_{\rm i} = -1$.

At linear order in G, the metric satisfies the linearized field equations (1.5), with the stress-energy tensor

$$T^{\mu\nu}(x) = \sum_{\rm i} \int {\rm d}\tau_{\rm i}\, p^{(\mu}_{\rm i} p^{\nu)}_{\rm i} \frac{\delta^4(x - x_{\rm i})}{\sqrt{-g}}\,. \tag{1.86}$$

Plugging the zeroth order solution in $T^{\mu\nu}$ and evaluating the integral gives the source term for the linearized equations, which can be solved for the first-order metric perturbation $h^{(1)}_{\mu\nu}$. The solution in harmonic gauge reads

$$\bar{h}^{\mu\nu}_1(x) = 4\sum_{\rm i} m_{\rm i} u^\mu_{\rm i} u^\nu_{\rm i} \frac{1}{r_{\rm i}}, \tag{1.87}$$

where $r_{\rm i} = \{(x - y_{\rm i})^2 + [u_{\rm i} \cdot (x - y_{\rm i})]^2\}^{1/2}$ is the (Minkowski) distance of the field point x from the worldline $x_{{\rm i}0} = y_{\rm i} + u_{\rm i}\tau_{\rm i}$ in its rest frame.

An important quantity that describes a scattering encounter is the impulse $\Delta p_{{\rm i}\mu} \equiv p'_{{\rm i}\mu} - p_{{\rm i}\mu}$. To obtain it, we use the equation of motion for the momentum

$$m_{\rm i} \frac{{\rm d}p_{{\rm i}\mu}}{{\rm d}\tau_{\rm i}} = -\frac{1}{2}\partial_\mu g^{\alpha\beta}(x_{\rm i}) p_{{\rm i}\alpha} p_{{\rm i}\beta}, \tag{1.88}$$

then integrate from $-\infty$ to $+\infty$. At 1PM order, the the total change in momentum reads [237]

$$\Delta p_{{\rm i}\mu} = \int_{-\infty}^{+\infty} {\rm d}\tau_{\rm i}\, \frac{{\rm d}p_{{\rm i}\mu}}{{\rm d}\tau_{\rm i}}$$

$$= -\frac{1}{2m_{\rm i}}\int_{-\infty}^{+\infty} \mathrm{d}\tau_{\rm i}\, \partial_\mu g^{\alpha\beta}(x_{\rm i}) p_{{\rm i}\alpha} p_{{\rm i}\beta}. \tag{1.89}$$

In terms of the impact parameter, defined as the separation between the zeroth-order worldlines $b^\mu \equiv y_1^\mu - y_2^\mu$, the 1PM impulse for a binary can be written as

$$\Delta p_1^\mu = -\frac{2Gm_1m_2}{\sqrt{\gamma^2-1}}(2\gamma^2-1)\frac{b^\mu}{b^2} + \mathcal{O}(G^2), \tag{1.90}$$

where γ is the dimensionless energy variable

$$\gamma \equiv -\frac{p_1^\mu p_{2\mu}}{m_1m_2}, \tag{1.91}$$

which can be written as $\gamma = 1/\sqrt{1-v^2}$ in terms of the asymptotic relative velocity.

1.2.2.2 Mass-ratio dependence of the scattering angle

Based on the structure of the PM expansion, Poincaré symmetry, and dimensional analysis, Ref. [252] (see also Refs. [255, 265, 299]) showed that the magnitude of the impulse, denoted $\mathsf{Q} \equiv (\Delta p_{1\mu}\Delta p_1^\mu)^{1/2}$, has the following dependence on the masses in the center-of-mass frame:

$$\begin{aligned}\mathsf{Q} = \frac{2Gm_1m_2}{b}\bigg[&\mathsf{Q}^{\rm 1PM} \\ &+ \frac{G}{b}\Big(m_1\mathsf{Q}^{\rm 2PM}_{m_1} + m_2\mathsf{Q}^{\rm 2PM}_{m_2}\Big) \\ &+ \frac{G^2}{b^2}\Big(m_1^2\mathsf{Q}^{\rm 3PM}_{m_1^2} + m_1m_2\mathsf{Q}^{\rm 3PM}_{m_1m_2} + m_2^2\mathsf{Q}^{\rm 3PM}_{m_2^2}\Big) + \cdots\bigg].\end{aligned} \tag{1.92}$$

That is, each PM order is a homogeneous polynomial in the two masses, with the leading order depending on m_1m_2 and each PM order adding another power in the masses. For nonspinning bodies, the functions $\mathsf{Q}^{\cdots}$ on the right-hand side depend only on the energy (or velocity).

The scattering angle χ, by which the two bodies are deflected in the center-of-mass frame,

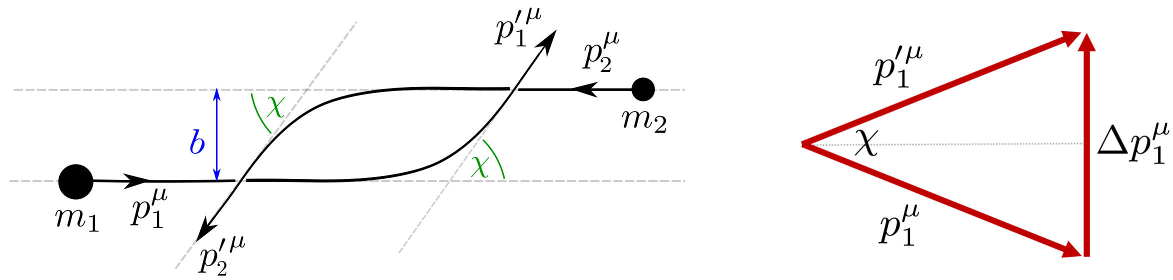

Figure 1.8: Illustration of the scattering angle χ and its relation to the impulse Δp_1^{μ}.

is related to Q via [252]

$$\sin\frac{\chi}{2} = \frac{\mathsf{Q}}{2P_{\text{c.m.}}}, \tag{1.93}$$

where $P_{\text{c.m.}}$ is the magnitude of the total linear momentum in the center-of-mass frame, which is the same as $|p_1^{\mu}|$ and $|p_2^{\mu}|$. This relation can be understood from Fig. 1.8, since from momentum conservation, the magnitude of p_1^{μ} is the same before and after scattering, and the difference between them is the impulse. From relativistic kinematics, we obtain the following relations for $P_{\text{c.m.}}$ and the total energy E:

$$P_{\text{c.m.}} = \frac{m_1 m_2}{E}\sqrt{\gamma^2 - 1}\,, \tag{1.94}$$

$$\begin{aligned} E &= \sqrt{m_1^2 + m_2^2 + 2m_1 m_2 \gamma} \\ &= M\sqrt{1 + 2\nu(\gamma - 1)}. \end{aligned} \tag{1.95}$$

Therefore, the scattering angle scaled by $E/m_1 m_2$ has the same mass dependence as Q. Equivalently, $M\chi/E$ has the same mass dependence as Q/μ.

Because of the symmetry under the exchange of the two bodies' labels, the mass dependence of $M\chi/E$ can be written as a polynomial in the symmetric mass ratio $\nu \equiv m_1 m_2/M^2$, since any homogeneous polynomial in the masses (m_1, m_2) of degree n can be written as a polynomial in ν of degree $\lfloor n/2 \rfloor$. For example, at 3PM and 4PM, the scattering angle contains quadratic and cubic polynomials in the masses, respectively, which can be written as

$$cm_1^2 + dm_1m_2 + cm_2^2 = M^2[c + (d - 2c)\nu], \tag{1.96}$$

$$cm_1^3 + dm_1^2m_2 + dm_1m_2^2 + cm_2^3 = M^3[c + (d - 3c)\nu], \tag{1.97}$$

for some mass-independent functions c and d. Thus, we find that the scattering angle, up to 5PM, has the following mass dependence:

$$\begin{aligned}
\frac{M}{E}\chi &= \frac{GM}{b}\mathsf{X}_1 + \left(\frac{GM}{b}\right)^2\mathsf{X}_2 \\
&\quad + \left(\frac{GM}{b}\right)^3\left[\mathsf{X}_3 + \nu\mathsf{X}_3^{\nu}\right] + \left(\frac{GM}{b}\right)^4\left[\mathsf{X}_4 + \nu\mathsf{X}_4^{\nu}\right] \\
&\quad + \left(\frac{GM}{b}\right)^5\left[\mathsf{X}_5 + \nu\mathsf{X}_5^{\nu} + \nu^2\mathsf{X}_5^{\nu^2}\right] + \dots,
\end{aligned} \tag{1.98}$$

where $\mathsf{X}_n^{\cdots}$ are functions only of energy/velocity.

This simple dependence of the scattering angle on the mass ratio has been used in Refs. [90–93] to derive PN results for nonspinning binaries from GSF results. We extended that approach in Refs. [1–3] to spinning binaries, as explained below in § 1.5.1.

1.2.2.3 From scattering to bound orbits

An important quantity that describes bound orbits is the *radial action*, which contains the same gauge-invariant information as the Hamiltonian. For planar orbits, it is defined by

$$I_r(E, L) = \frac{1}{2\pi}\oint p_r(r, E, L)\mathrm{d}r, \tag{1.99}$$

where the integral is evaluated over a bound orbit. By taking the integration bounds from $-\infty$ to $+\infty$, we obtain a radial action for hyperbolic orbits

$$I_r^{\mathrm{hyp}}(E, L) = \frac{1}{2\pi}\int_{-\infty}^{+\infty} p_r(r, E, L)\mathrm{d}r. \tag{1.100}$$

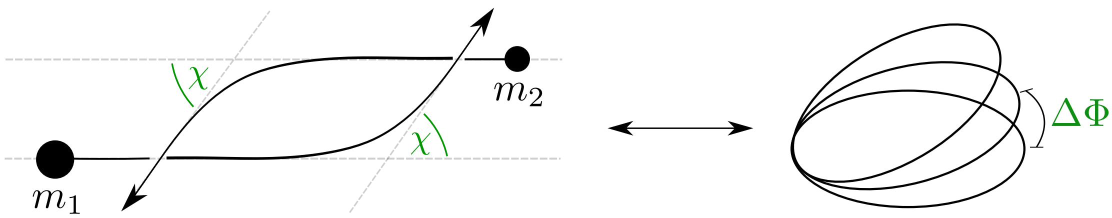

Figure 1.9: The scattering angle is related to the periastron advance via analytic continuation.

The periastron advance $\Delta\Phi$ and the scattering angle χ, which are depicted in Fig. 1.9, can be obtained from the radial action using

$$\Delta\Phi = -2\pi \frac{\partial I_r}{\partial L} - 2\pi, \tag{1.101}$$

$$\chi = -2\pi \frac{\partial I_r^{\text{hyp}}}{\partial L} - \pi, \tag{1.102}$$

which follow from Hamilton-Jacobi theory, since the derivative of the action $S_0 = \phi L + \int p_r \mathrm{d}r$ with respect to the angular momentum gives the azimuthal angle[3]

$$\phi = -\int \mathrm{d}r \frac{\partial p_r(r, E, L)}{\partial L} + \text{const.} \tag{1.103}$$

Integrating ϕ over a bound orbit yields the total angle swept over an orbit, leading to the periastron advance in Eq. (1.101). Similarly, integrating ϕ from $-\infty$ to $+\infty$ (and subtracting π) defines the scattering angle in Eq. (1.102).

The scattering angle and the periastron advance can be related to each other, for aligned spins, via analytic continuation, resulting in the following relation

$$\Delta\Phi(E, L, a_{\mathrm{i}}) = \chi(E, L, a_{\mathrm{i}}) + \chi(E, -L, -a_{\mathrm{i}}). \tag{1.104}$$

[3]The Hamilton-Jacobi equation for a conservative Hamiltonian is given by [300] $\partial S/\partial t = -H$, and the time dependence of the action can be written as $S = S_0 - Et$, where $S_0 = \phi L + \int p_r \mathrm{d}r$ is Hamilton's characteristic function. Hence, $\partial^2 S_0/\partial t \partial L = 0$, leading to Eq. (1.103).

where $a_{\rm i} \equiv S_{\rm i}/m_{\rm i}$ are the spins of the two bodies, with $\rm i = 1, 2$. This relation was derived in Refs. [255, 267] by relating the integration bounds of the integrals for χ and $\Delta\Phi$, which can be written as

$$\Delta\Phi = -2\int_{r_-}^{r_+} \frac{\partial p_r}{\partial L}\,\mathrm{d}r - 2\pi, \qquad \chi = -2\int_{r_-}^{\infty} \frac{\partial p_r}{\partial L}\,\mathrm{d}r - \pi. \tag{1.105}$$

For bound orbits ($E < M$), the integration bounds r_- and r_+ are the two roots of $p_r = 0$, which are positive at the turning points. For hyperbolic orbits ($E > M$), one root is positive and the other is negative, but the two roots are related by $r_-(E, -L, -a_{\rm i}) = r_+(E, L, a_{\rm i})$, similarly to the bound case. This was used in Refs. [255, 267] to relate the two integrals and obtain the relation (1.104).

A general map between bound and unbound observables was derived in Refs. [296, 297], following similar arguments. If a bound-orbit observable $\rm O_{bound}$ is given by

$$\mathrm{O}_{\rm bound}(E, L, a_{\rm i}) = 2\int_{r_-}^{r_+} f(r, E, L, a_{\rm i})\,\mathrm{d}r, \tag{1.106}$$

and an unbound observable $\rm O_{unbound}$ is given by

$$\mathrm{O}_{\rm unbound}(E, L, a_{\rm i}) = 2\int_{r_-}^{\infty} f(r, E, L, a_{\rm i})\,\mathrm{d}r, \tag{1.107}$$

then the two observables, for the local-in-time conservative dynamics, are related by

$$\mathrm{O}_{\rm bound}(E, L, a_{\rm i}) = \mathrm{O}_{\rm unbound}(E, L, a_{\rm i}) + \theta(f)\mathrm{O}_{\rm unbound}(E, -L, -a_{\rm i}), \tag{1.108}$$

where $\theta(f) = \pm 1$ if the function f is odd/even under a change in the sign of both L and $a_{\rm i}$. For example, the bound-orbit radial action I_r is even in L, i.e. $\theta(f) = -1$, and thus it is related to the unbound radial action $I_r^{\rm hyp}$ through the relation

$$I_r(E, L, a_{\rm i}) = I_r^{\rm hyp}(E, L, a_{\rm i}) - I_r^{\rm hyp}(E, -L, -a_{\rm i}). \tag{1.109}$$

Relations like these demonstrate how studying unbound observables can be useful in informing the bound-orbit dynamics. In Chapter 3 (Ref. [2]), we use such relations to relate the coefficients of the scattering angle to those of the radial action or Hamiltonian.

1.2.3 Gravitational self-force

Extreme-mass-ratio inspirals (EMRIs) are one of the most promising GW sources for space-based GW detectors, such as the Laser Interferometer Space Antenna (LISA) [301]. These systems consist of a stellar-mass object orbiting a supermassive BH, with mass ratios typically greater than 10^4. For EMRIs, the number of GW cycles detectable by LISA is the same order of magnitude as the mass ratio. Hence, it is important to use GSF to describe these systems, since it provides an expansion in the small-mass ratio that is valid for arbitrary velocities and gravitational potentials. Using the PN or PM approximations would not be sufficient, since they would result in a large accumulated phase error over months/years of observations.

When a small mass μ moves in the background of a Schwarzschild BH with mass $M \gg \mu$, that motion can be approximated, at zeroth order in the mass ratio, by the geodesic motion of a test mass. However, the small mass perturbs the background metric, and that perturbation can be incorporated in the acceleration of the small mass, which is said to move under the effect of its "self-force".

The equations of motion of a small body beyond the test-mass approximation are known as the MiSaTaQuWa equations, after Mino, Sasaki, and Tanaka [302], in addition to Quinn and Wald [303]. For a particle moving on a geodesic of the metric $g_{\mu\nu} = \bar{g}_{\mu\nu} + h_{\mu\nu}$, where $h_{\mu\nu}$ is the perturbation of the background metric $\bar{g}_{\mu\nu}$, the equations of motion follow from the geodesic equation, leading to

$$\frac{\mathrm{D}u^\mu}{\mathrm{d}\tau} = -\frac{1}{2}(\bar{g}^{\mu\nu} + u^\mu u^\nu)(2h_{\nu\lambda;\rho} - h_{\lambda\rho;\nu})u^\lambda u^\rho, \tag{1.110}$$

where u^μ is the 4-velocity and the covariant derivatives are evaluated on the background metric.

In Eq. (1.110), $h_{\mu\nu}$ are singular at the location of the small body, and have to be regularized. This is done by splitting the retarded metric perturbation $h^{\mathrm{ret}}_{\mu\nu}$ into singular-symmetric (in time) and regular-radiative pieces, i.e. $h^{\mathrm{ret}}_{\mu\nu} = h^{\mathrm{S}}_{\mu\nu} + h^{\mathrm{R}}_{\mu\nu}$. Detweiler and Whiting [304] showed that the radiative piece satisfies the homogeneous linearized Einstein equations, and argued that it is solely responsible for the self-force acting on the particle. The metric can then be written as $g_{\mu\nu} = \bar{g}_{\mu\nu} + h^{\mathrm{R}}_{\mu\nu}$, with the equations of motion given by Eq. (1.110) but with $h^{\mathrm{R}}_{\mu\nu}$ instead of $h_{\mu\nu}$, and

$$h^{\mathrm{R}}_{\mu\nu;\lambda} = -4\mu\left[u_{(\mu}R_{\nu)\rho\lambda\xi} + R_{\mu\rho\nu\xi}u_\lambda\right]u^\rho u^\xi + h^{\mathrm{tail}}_{\mu\nu\lambda}, \tag{1.111}$$

$$h^{\mathrm{tail}}_{\mu\nu\lambda} = 4\mu\int_{-\infty}^{\tau-\epsilon}\nabla_\lambda\left(G_{\mu\nu\mu'\nu'} - \frac{1}{2}g_{\mu\nu}G^{\rho}{}_{\rho\mu'\nu'}\right)(z,z')u^{\mu'}u^{\nu'}\mathrm{d}\tau', \tag{1.112}$$

where $z(\tau)$ is the instantaneous position of the particle, and we integrate over earlier positions $z(\tau')$ and take the limit $\epsilon \to 0^+$. The retarded Green function $G_{\mu\nu\mu'\nu'}$ is the solution of the wave equation

$$\Box\psi^{\mu\nu} + 2R^{\mu}{}_{\rho}{}^{\nu}{}_{\lambda}\psi^{\rho\lambda} = -16\pi T^{\mu\nu}, \tag{1.113}$$

where the trace-reversed potentials $\psi^{\mu\nu} \equiv h_{\mu\nu} - \frac{1}{2}g_{\mu\nu}g^{\lambda\rho}h_{\lambda\rho}$.

Numerical calculations of GSF at first order in the mass ratio have been performed using several methods, such as mode-sum regularization [305, 306] and puncture schemes [307, 308], both in Schwarzschild [309–314] and Kerr backgrounds [315–318]. There has also been significant progress towards second-order self-force [319–325], which resulted in the numerical calculation of the binding energy, energy flux, and waveform [326–328], for quasi-circular orbits and nonspinning BHs. For reviews on GSF see, e.g., Refs. [329–333].

There has also been analytical GSF results for gauge-invariant quantities in a PN expansion [334, 335], such as the Detweiler-Barack-Sago redshift [336–345] (defined as $z_\mathrm{i} \equiv \mathrm{d}\tau_\mathrm{i}/\mathrm{d}t = 1/u^t$), the spin-precession frequency [346–352] (see § 1.2.4 below), and tidal invariants [353–358]. In Appendix A, we show how the redshift and spin-precession frequency can be derived for a spinning test body in a Schwarzschild background. These quantities are very useful since they allow us to relate PN and GSF results, as we do in Chapters 2, 3, and 4 in a synergistic approach to derive PN results valid for arbitrary-mass ratios from GSF results.

1.2.4 Spinning binaries in general relativity

Astrophysical compact objects are generally spinning, with the spins having a significant effect on the orbital motion and the emitted GWs; for example, spin precession causes modulations in GW signals [359]. Measuring the spin magnitudes and directions from GW observations is useful in understanding the properties of compact binaries and their astrophysical formation channels [19]. Therefore, it is important to include spin in analytical approximations for the binary dynamics to produce accurate waveforms that can be used to correctly infer the parameters of the system.

In GR, the center-of-mass of a spinning body is not uniquely defined; this is illustrated in Fig. 1.10, where we see that for a spinning sphere, the hemisphere moving in the direction of motion is faster and thus heavier than the other hemisphere, causing the center-of-mass to shift, which depends on the reference frame. To quantify this, we begin by defining the antisymmetric

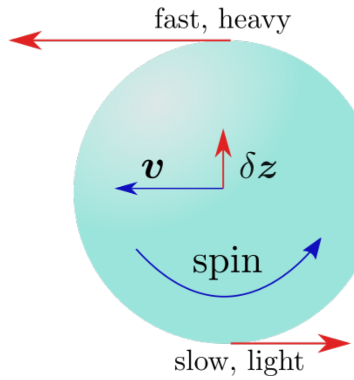

Figure 1.10: For a spinning sphere moving with velocity $\boldsymbol{v}$, the hemisphere moving in the direction of motion is faster and thus heavier than the other hemisphere, causing the center-of-mass to shift.

spin tensor $S^{\mu\nu}$ as the difference between the total angular momentum $J^{\mu\nu}$ and its orbital part, that is

$$J^{\mu\nu} = z^\mu p^\nu - p^\mu z^\nu + S^{\mu\nu}, \tag{1.114}$$

where p^μ is the linear momentum vector and z^μ is the spinning body's worldline. Under a center-of-mass shift $z^i \to z^i - \delta z^i$, the S^{i0} component of $S^{\mu\nu}$ transforms as [360]

$$S^{i0} \to S^{i0} + E\delta z^i, \tag{1.115}$$

where $E = p^0$ is the total energy, implying that S^{i0} is the mass dipole relative to the center z^i. However, it is always possible to choose the center z^i such that the mass dipole S^{i0} vanishes in a local Lorentz frame defined by the timelike vector f^μ, that is

$$S^{\mu\nu} f_\nu = 0. \tag{1.116}$$

This is called the spin-supplementary condition (SSC), and it ensures that $S^{\mu\nu}$ has three independent components only.

The most commonly used SSC is the covariant Tulczyjew-Dixon SSC [96, 361–363], which uses the body's rest frame with $f_\nu \equiv p_\nu$, yielding

$$\text{covariant SSC:} \qquad S^{\mu\nu} p_\nu = 0. \tag{1.117}$$

Another important choice is the canonical, or Newton-Wigner, SSC [364, 365]

$$\text{canonical SSC:} \qquad S^{\mu\nu} p_\nu + m S^{\mu\nu} n_\nu = 0, \tag{1.118}$$

where m is the mass and n_ν is any timelike unit vector. This condition leads to the following Poisson brackets [360]

$$\{z^i, p_j\} = \delta_{ij}, \qquad \{S_{ij}, S_{kl}\} = \delta_{ik} S_{jl} - \delta_{jk} S_{il} - \delta_{il} S_{jk} + \delta_{jl} S_{ik}, \tag{1.119}$$

implying that z^i, p_j, and S_{ij} are canonical variables, which is why this SSC is usually used when working in a Hamiltonian formulation of the spinning two-body dynamics. (For more details, see Refs. [360, 366].)

The motion of a spinning test body is governed by the Mathisson-Papapetrou-Dixon (MPD) equations [367–369], which to quadrupolar order in spin, read [366]

$$\frac{Dp^\mu}{d\tau} = -\frac{1}{2} R^\mu{}_{\nu\alpha\beta} \dot{z}^\nu S^{\alpha\beta} - \frac{1}{6} \nabla^\mu R_{\nu\rho\alpha\beta} J^{\nu\rho\alpha\beta}, \tag{1.120}$$

$$\frac{DS^{\mu\nu}}{d\tau} = 2p^{[\mu} \dot{z}^{\nu]} + \frac{4}{3} R^{[\mu}{}_{\rho\alpha\beta} J^{\nu]\rho\alpha\beta}, \tag{1.121}$$

where the tangent vector $\dot{z}^\mu = dz^\mu/d\tau$ and is normalized by $\dot{z}^\mu \dot{z}_\mu = -1$. The linear momentum p_μ and spin tensor $S^{\mu\nu}$ play the role of the monopole and dipole moment, while $J^{\nu\rho\alpha\beta}$ is the quadrupole tensor, which depends on the internal degrees of freedom of the body. These equations, together with the SSC fully determine the evolution of z^μ, p_μ, and $S_{\mu\nu}$. We use the MPD equations in Appendix A to obtain the redshift and spin-precession frequency. They can also be

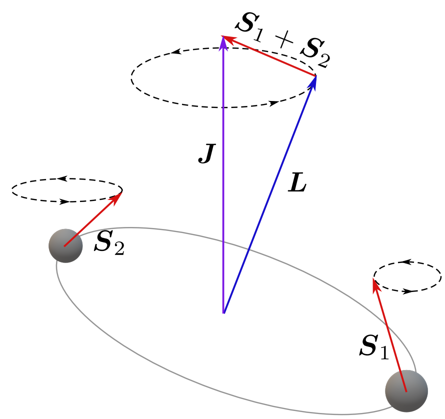

Figure 1.11: Illustration of spin precession in a binary system.

used to derive the scattering angle of a spinning test body in a Kerr background, which is needed in Chapters 3 and 4 when relating the coefficients of the Hamiltonian to those of the scattering angle.

Instead of the spin tensor $S^{\mu\nu}$, it is often convenient to work with the Pauli-Lubanski spin vector S^{μ}, defined by

$$S^{\mu} \equiv -\frac{1}{2}\eta^{\mu\nu\rho\lambda}u_{\nu}S_{\rho\lambda}, \qquad \Leftrightarrow \qquad S_{\mu\nu} = \eta_{\mu\nu\rho\lambda}u^{\rho}S^{\lambda}. \tag{1.122}$$

where u^{μ} is the 4-velocity, and $\eta_{\mu\nu\rho\lambda} = \sqrt{-g}\epsilon_{\mu\nu\rho\lambda}$ is the volume form with $\epsilon_{0123} = 1$. We also sometimes use the mass-rescaled spin $\boldsymbol{a} \equiv \boldsymbol{S}/m$ since it simplifies some equations, such as making the mass-ratio dependence of the scattering angle more evident, as discussed in § 1.5.1.2.

For a binary with spin vectors $\boldsymbol{S}_{\rm i}$ and masses $m_{\rm i}$, the total angular momentum $\boldsymbol{J}$ and spin magnitudes $|\boldsymbol{S}_{\rm i}|$ are constant (for the conservative dynamics). If the spins are aligned, or anti-aligned, with the angular momentum vector $\boldsymbol{L}$, which is perpendicular to the orbital plane, then the spin directions and orbital plane remain fixed. But if the spins are not aligned with $\boldsymbol{L}$, then both $\boldsymbol{L}$ and the spins precess around $\boldsymbol{J} = \boldsymbol{L} + \boldsymbol{S}_1 + \boldsymbol{S}_2$, such that $\dot{\boldsymbol{S}}_1 + \dot{\boldsymbol{S}}_2 = -\dot{\boldsymbol{L}}$, where the dot indicates a derivative with respect to coordinate time. (See Fig. 1.11 for an illustration.) The spin-precession frequency $\boldsymbol{\Omega}_{S_\mathrm{i}}$ can be defined through the relation

$$\frac{\mathrm{d}\boldsymbol{S}_\mathrm{i}}{\mathrm{d}t} = \boldsymbol{\Omega}_{S_\mathrm{i}} \times \boldsymbol{S}_\mathrm{i}. \tag{1.123}$$

For the spin-orbit (SO) dynamics, the leading PN order in the Lagrangian and equations of motion was derived in Refs. [95, 110, 163], and a Hamiltonian framework was developed in Refs. [100, 101, 360]. The Hamiltonian at leading order (1.5PN) reads

$$H_\mathrm{SO} = \left(2 + \frac{3m_2}{2m_1}\right)\frac{\boldsymbol{L}\cdot\boldsymbol{S}_1}{\mu r^3} + \left(2 + \frac{3m_1}{2m_2}\right)\frac{\boldsymbol{L}\cdot\boldsymbol{S}_2}{\mu r^3}, \tag{1.124}$$

from which the equations of motion for the spins are given by

$$\frac{\mathrm{d}\boldsymbol{S}_\mathrm{i}}{\mathrm{d}t} = \{\boldsymbol{S}_\mathrm{i}, H\} = \frac{\partial H}{\partial \boldsymbol{S}_\mathrm{i}} \times \boldsymbol{S}_\mathrm{i}. \tag{1.125}$$

Thus, at SO level, the Hamiltonian can be written as $H_\mathrm{SO} = \sum_\mathrm{i} \boldsymbol{\Omega}_{S_\mathrm{i}} \cdot \boldsymbol{S}_\mathrm{i}$.

The spin-spin contribution to the binary dynamics was first derived in the equations of motion in Refs. [110–112], and in a Hamiltonian framework in Refs. [117, 118, 370]. At leading order (2PN), the spin-spin part of the Hamiltonian reads

$$\begin{aligned} H_\mathrm{SS} = {} & \frac{C_{Q_1}}{2r^3}\frac{m_2}{m_1}\left[3(\boldsymbol{n}\cdot\boldsymbol{S}_1)^2 - \boldsymbol{S}_1^2\right] + \frac{C_{Q_2}}{2r^3}\frac{m_1}{m_2}\left[3(\boldsymbol{n}\cdot\boldsymbol{S}_2)^2 - \boldsymbol{S}_2^2\right] \\ & + \frac{1}{r^3}\left[3(\boldsymbol{n}\cdot\boldsymbol{S}_1)(\boldsymbol{n}\cdot\boldsymbol{S}_2) - \boldsymbol{S}_1\cdot\boldsymbol{S}_2\right], \end{aligned} \tag{1.126}$$

where $\boldsymbol{n} \equiv (\boldsymbol{x}_1 - \boldsymbol{x}_2)/r$ is a radial unit vector from one body to the other, and C_{Q_i} are the spin-induced quadrupole constants that equal one for BHs, but $C_{Q_\mathrm{i}} \simeq 4 - 8$ for NSs depending on their equation of state [371, 372]. The spin-spin interactions cause nutations of the spin directions, which are not present at SO level [359, 373, 374]. These nutations can reach 180 degrees in some configurations [375, 376], and have a significant effect on the binary dynamics and waveforms [374, 377–379].

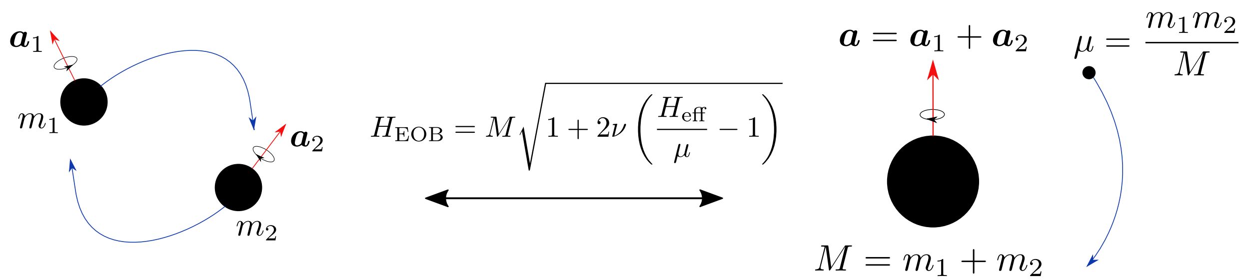

Figure 1.12: The EOB formalism maps the binary motion to that of a test mass in a deformed Kerr background.

1.3 The effective-one-body formalism

The effective-one-body (EOB) formalism [380, 381] combines information from several analytical approximations with NR results, while recovering the strong-field test-body limit, to provide an accurate description of the binary dynamics and waveform in a larger region of parameter space than each approximation separately.

In the nonspinning case, the EOB formalism maps the motion of a compact binary to that of a test mass in a deformed Schwarzschild background, as illustrated in Fig. 1.12. The mass of the background BH is the total mass of the binary $M \equiv m_1 + m_2$, while the mass of the test body is the reduced mass $\mu \equiv m_1 m_2/M$, and the deformation parameter of the background spacetime is the symmetric mass ratio $\nu \equiv \mu/M$.

For spinning binaries, with mass-rescaled spins $\boldsymbol{a}_1 \equiv \boldsymbol{S}_1/m_1$ and $\boldsymbol{a}_2 \equiv \boldsymbol{S}_2/m_2$, the mapping can be done to the effective metric of a deformed Kerr background with spin $\boldsymbol{a} \equiv \boldsymbol{a}_1 + \boldsymbol{a}_2$ and a nonspinning test mass. Alternatively, another mapping for the spins that is also used in the literature [382, 383] is to define the background spin as $\boldsymbol{S} \equiv \boldsymbol{S}_1 + \boldsymbol{S}_2$ and the test body's spin $\boldsymbol{S}_* \equiv \boldsymbol{S}_1 m_2/m_1 + \boldsymbol{S}_2 m_1/m_2 + \mathcal{O}(1/c^2)$.

EOB models have been constructed for nonspinning [80, 384–388], spinning [4, 370, 382, 383, 389–401], and eccentric binaries [5, 10, 402–404]. In addition, information from the post-Minkowskian [6, 236, 237, 405, 406] and small mass-ratio approximations [407–410] have been incorporated in EOB models.

The EOB approach consists of three main analytical components:

1. The Hamiltonian, which describes the conservative binary dynamics.

2. The radiation reaction (RR) force, which is added to the equations of motion, and accounts for the energy and angular momentum losses due to the emitted GWs.

3. The gravitational waveform, which is resummed to improve the accuracy of the PN expansion for the inspiral, includes a fit to NR results for the plunge, and models the ringdown part based on BH perturbation theory.

We discuss each of these components in the following subsections, while restricting to the case of nonspinning binaries for simplicity. Then, in § 1.5.2, we discuss precessing-spin binaries, and in § 1.5.3, explore the case of binaries in eccentric orbits.

1.3.1 EOB Hamiltonian for nonspinning binaries

EOB Hamiltonians for arbitrary mass ratios have been derived for nonspinning binaries up to 4PN order [80], with partial 5PN and 6PN information [88, 91, 93]. Here, we explain how such a Hamiltonian can be obtained, but for simplicity, restrict the explicit calculations to 2PN order, following Refs. [380, 381].

The effective background metric is defined by

$$g_{\mu\nu}^{\text{eff}}\mathrm{d}x^{\mu}\mathrm{d}x^{\nu} = -A\mathrm{d}t^2 + B\mathrm{d}r^2 + r^2\left(\mathrm{d}\theta^2 + \sin^2\theta\mathrm{d}\phi^2\right), \tag{1.127}$$

with the deformed mass-shell condition [384]

$$0 = g_{\text{eff}}^{\mu\nu}p_{\mu}p_{\nu} + \mu^2 + Q, \tag{1.128}$$

where Q is an additional term that contains quartic and higher-orders-in-momenta contributions. This relation can be solved for the effective energy/Hamiltonian $H_{\text{eff}} = E_{\text{eff}} = -p_0$ to obtain

$$H_{\text{eff}} = \sqrt{A\left(\mu^2 + \frac{p_r^2}{B} + \frac{L^2}{r^2} + Q\right)}, \tag{1.129}$$

where we recall that p_r is the radial momentum and L is the angular momentum. In the $\nu \to 0$ limit, H_{eff} reduces to the Schwarzschild Hamiltonian H_S for a test particle with mass μ, which is given by

$$H_S = \sqrt{\left(1 - \frac{2M}{r}\right)\left[\mu^2 + \left(1 - \frac{2M}{r}\right)p_r^2 + \frac{L^2}{r^2}\right]}, \tag{1.130}$$

i.e., with $A = 1 - 2M/r$, $B = 1/A$, and $Q = 0$. From the effective Hamiltonian H_{eff}, one defines a two-body Hamiltonian H_{EOB} via the energy map

$$H_{\text{EOB}} = M\sqrt{1 + 2\nu\left(\frac{H_{\text{eff}}}{\mu} - 1\right)}, \tag{1.131}$$

such that H_{EOB} is related to a PN-expanded two-body Hamiltonian through a canonical transformation. It was also found in Ref. [236] that the EOB map has the advantage of reproducing the full 1PM two-body Hamiltonian when $H_{\text{eff}} = H_S$.

To include high-order PN information in the EOB Hamiltonian, we write an ansatz for the A, B and Q potentials in Eq. (1.129), write an ansatz for a generating function of the canonical transformation, then match H^{EOB} to a PN-expanded Hamiltonian in some gauge, and finally solve for the unknown coefficients of the effective Hamiltonian and generating function.

To illustrate these steps at 2PN order, we use the following ansatz for the effective Hamiltonian

$$A = 1 - \frac{2M}{r} + \frac{a_2 M^2}{r^2} + \frac{a_3 M^3}{r^3}, \tag{1.132}$$

$$B = \left[1 - \frac{2M}{r} + \frac{b_2 M^2}{r^2}\right]^{-1}, \tag{1.133}$$

$$Q = 0, \tag{1.134}$$

with some unknown coefficients $a_2,\ a_3$, and b_2. Note that starting at 3PN order, we would need to assume a nonzero Q for a canonical transformation to exist.

The EOB Hamiltonian obtained with this ansatz has to agree, after a canonical transformation, with the 2PN two-body Hamiltonian in some gauge, such as ADM coordinates, in which the Hamiltonian in the center-of-mass frame is given by [380]

$$\begin{aligned} H_{\text{ADM}}^{\text{2PN}} = Mc^2 + \frac{p^2}{2\mu} - \frac{\mu M}{r} + \frac{1}{c^2}\left[\frac{\mu M^2}{2r^2} - \frac{(\nu+3)Mp^2}{2\mu r} - \frac{\nu M p_r^2}{2\mu r} + \frac{(3\nu-1)p^4}{8\mu^3}\right] \\ + \frac{1}{c^4}\Bigg[\frac{(8\nu+5)M^2p^2}{2\mu r^2} - \frac{\nu^2 M p^2 p_r^2}{4\mu^3 r} + \frac{3\nu M^2 p_r^2}{2\mu r^2} - \frac{(3\nu^2+20\nu-5)\,Mp^4}{8\mu^3 r} \\ - \frac{3\nu^2 M p_r^4}{8\mu^3 r} + \frac{(5\nu^2-5\nu+1)\,p^6}{16\mu^5} - \frac{(3\nu+1)\mu M^3}{4r^3}\Bigg]. \end{aligned} \tag{1.135}$$

Next, we write the following ansatz for the generating function of the canonical transformation:

$$\begin{aligned} \mathcal{G} = \frac{rp_r}{c^2}\left[g_1 p_r^2 + g_2\frac{L^2}{r^2} + \frac{g_3}{r}\right] \\ + \frac{rp_r}{c^4}\left[g_4 p_r^4 + \frac{g_5 L^2 p_r^2}{r^2} + \frac{g_6 L^4}{r^4} + \frac{g_7 p_r^2}{r} + \frac{g_8 L^2}{r^3} + \frac{g_9}{r^2}\right], \end{aligned} \tag{1.136}$$

perform the transformation using Poisson brackets, and match to the ansatz of the 2PN EOB Hamiltonian, i.e.

$$H_{\rm EOB}^{\rm 2PN} = H_{\rm ADM}^{\rm 2PN} + \{\mathcal{G}, H_{\rm ADM}^{\rm 2PN}\} + \frac{1}{2!}\{\mathcal{G}, \{\mathcal{G}, H_{\rm ADM}^{\rm 2PN}\}\} \tag{1.137}$$

where each bracket introduces a factor of $1/c^2$. Solving this equation for the unknowns yields

$$a_2 = 0, \qquad a_3 = 2\nu, \qquad b_2 = 6\nu, \tag{1.138}$$

for the coefficients of the effective Hamiltonian, and the following solution for the generating function:

$$\begin{aligned}\mathcal{G} = \frac{rp_r}{c^2}\left(\frac{L^2\nu}{2r^2} + \frac{\nu p_r^2}{2} - \frac{\nu+2}{2r}\right) + \frac{rp_r}{c^4}\Bigg[&-\frac{L^4\nu}{8r^4} - \frac{L^2\nu p_r^2}{4r^2} \\ &+ \frac{L^2(\nu-4)\nu}{4r^3} + \frac{(\nu-12)\nu p_r^2}{8r} - \frac{\nu p_r^4}{8} + \frac{-\nu^2+7\nu-1}{4r^2}\Bigg].\end{aligned} \tag{1.139}$$

1.3.2 Radiation-reaction force

The equations of motion are obtained from the EOB Hamiltonian, with RR force added to the right-hand side of those equations, such that

$$\begin{aligned}\dot{r} &= \frac{\partial H_{\rm EOB}}{\partial p_r}, & \dot{p}_r &= -\frac{\partial H_{\rm EOB}}{\partial r} + \mathcal{F}_r, \\ \dot{\phi} &= \frac{\partial H_{\rm EOB}}{\partial L}, & \dot{L} &= -\frac{\partial H_{\rm EOB}}{\partial \phi} + \mathcal{F}_\phi,\end{aligned} \tag{1.140}$$

where $\mathcal{F}_r$ and $\mathcal{F}_\phi$ are the radial and azimuthal components, respectively, of the RR force, and they start at 2.5PN order.

The RR force is related to the energy flux Φ_E and angular momentum flux Φ_J, but while the fluxes are gauge invariant, the RR force is *gauge dependent*. For quasi-circular orbits, the fluxes satisfy $\Phi_E = \Omega\Phi_J$ with $\Omega \equiv \dot{\phi}$ being the orbital frequency, and a possible gauge choice for the RR force is [374]

$$\mathcal{F}_\phi = -\frac{\Phi_E^{\rm qc}}{\Omega}, \qquad \mathcal{F}_r = \frac{p_r}{L}\mathcal{F}_\phi = -\frac{p_r}{L}\frac{\Phi_E}{\Omega}\,. \tag{1.141}$$

This force satisfies the balance equations between the energy/angular momentum losses by the system and the fluxes at infinity, that is

$$\dot{E}_{\rm system} = -\Phi_E, \qquad \dot{J}_{\rm system} = -\Phi_J, \tag{1.142}$$

where

$$\begin{aligned} \dot{E}_{\rm system} &\equiv \frac{{\rm d}H_{\rm EOB}}{{\rm d}t} = \dot{r}\mathcal{F}_r + \dot{\phi}\mathcal{F}_\phi, \\ \dot{J}_{\rm system} &\equiv \frac{{\rm d}L}{{\rm d}t} = \mathcal{F}_\phi. \end{aligned} \tag{1.143}$$

However, these balance equations are only valid approximately for quasi-circular orbits [402]. We discuss their generalization in § 1.5.3, which is important for the derivation of the RR force for eccentric orbits in Chapter 6.

A better agreement to NR results for the energy flux can be obtained by expressing the flux as a sum over waveform modes

$$\Phi_E = \frac{\Omega^2}{8\pi}\sum_{\ell=2}^{8}\sum_{m=1}^{\ell} m^2 \left|R h_{\ell m}\right|^2, \tag{1.144}$$

with the modes resummed and factorized as in the following subsection.

1.3.3 Factorized waveform modes

The GW spherical harmonic modes $h^{\ell m}$ are the expansion of the complex polarization waveform $h = h_+ - i h_\times$ into spin-weighted spherical harmonics (see § 1.2.1.4). The PN-expanded waveform does not give good agreement with NR, but the factorized waveform modes proposed in Refs. [386, 411–413] provide much better agreement, and are thus commonly used in EOB waveform models. For circular orbits, the factorized modes are given by

$$h^{\mathrm{F}}_{\ell m} = h^{\mathrm{N}}_{\ell m} S_{\mathrm{eff}} T_{\ell m} e^{i\delta_{\ell m}} f_{\ell m}, \tag{1.145}$$

where $h^{\mathrm{N}}_{\ell m}$ is the Newtonian part (leading PN order), while S_{eff} is an effective source term given by either the Hamiltonian or angular momentum such that

$$S_{\mathrm{eff}} = \begin{cases} H_{\mathrm{eff}}, & \ell + m \text{ even} \\ \Omega^{1/3} L, & \ell + m \text{ odd} \end{cases}. \tag{1.146}$$

This term is motivated by the Regge-Wheeler-Zerilli equation [51, 53], whose source term depends on the stress-energy tensor for a test body in a Schwarzschild background; since the EOB formalism maps the binary dynamics to a test body in a deformed black hole background, the source term can be viewed as the effective Hamiltonian or angular momentum. The third term in Eq. (1.145), $T_{\ell m}$, resums the infinite number of "leading logarithms" entering the tail effects for circular orbits [184, 414, 415], and thus contains more information than a PN expansion. The remaining part of the waveform modes is expressed as an amplitude $f_{\ell m}$ and a phase $\delta_{\ell m}$, such that the expansion of $h^{\mathrm{F}}_{\ell m}$ agrees with the known PN expansion for the modes. To improve the agreement with NR, $f_{\ell m}$ is further resummed to reduce the magnitude of the 1PN nonspinning coefficient, which grows linearly with ℓ, such that [386, 413]

$$f_{\ell m} = \begin{cases} \rho^{\ell}_{\ell m}, & m \text{ even} \\ (\rho^{\mathrm{NS}}_{\ell m})^{\ell} + f^{\mathrm{S}}_{\ell m}, & m \text{ odd} \end{cases}, \tag{1.147}$$

where $\rho^{\mathrm{NS}}_{\ell m}$ and $f^{\mathrm{S}}_{\ell m}$ contain the nonspinning and spin contributions, respectively. Explicit expressions for these quantities are lengthy and are provided in Refs. [394, 397, 398, 413]. In Chapter 6, we extend the factorized modes to eccentric orbits.

Since the accuracy of the PN waveform degrades near the plunge, EOB models multiply the factorized modes $h^{\mathrm{F}}_{\ell m}$ by a phenomenological function $N_{\ell m}$, called the non-quasicircular correction, such that the inspiral-plunge part of the waveform is given by [395]

$$h^{\text{insp-plunge}}_{\ell m} = h^{\mathrm{F}}_{\ell m} N_{\ell m}. \tag{1.148}$$

The ansatz for $N_{\ell m}$ is expressed in terms of p_r, such that $N_{\ell m} \to 1$ as $p_r \to 0$ in the early inspiral, and the coefficients of that function are fitted to NR waveforms.

The ringdown part of the waveform is well described by BH perturbation theory, and can be expressed as a superposition of quasi-normal modes (QNM)

$$h^{\mathrm{RD}}_{\ell m}(t) = \sum_{n=0}^{\infty} A_{\ell m n} e^{-i\sigma_{\ell m n} t}, \tag{1.149}$$

where $A_{\ell mn}$ are the complex amplitudes and $\sigma_{\ell mn}$ are the QNM frequencies, which only depend on the mass and spin of the perturbed BH, and can be matched to the masses and spins of the binary [416–418]. In the EOB approach, a simpler ansatz is used to model the merger-ringdown signal, using [397, 419]

$$h^{\text{merger-RD}}_{\ell m}(t) = \nu \tilde{A}_{\ell m}(t) e^{i\tilde{\phi}_{\ell m}(t)} e^{-i\sigma_{\ell m 0}\left(t - t^{\ell m}_{\text{match}}\right)}, \tag{1.150}$$

where $\sigma_{\ell m0}$ is the frequency of the dominant QNM, while $\tilde{A}_{\ell m}(t)$ and $\tilde{\phi}_{\ell m}(t)$ are tuned to NR waveforms by requiring continuity between $h^{\text{merger-RD}}_{\ell m}(t)$ and $h^{\text{insp-plunge}}_{\ell m}(t)$ in the amplitude and its first derivative, and in the GW frequency. The time $t^{\ell m}_{\text{match}}$, at which the two parts of the waveform are matched, is taken at the peak of the amplitude of the inspiral-plunge waveform. The full inspiral-merger-ringdown waveform is then given by

$$h_{\ell m}(t) = h^{\text{insp-plunge}}_{\ell m}(t)\theta(t^{\ell m}_{\text{match}} - t) + h^{\text{merger-RD}}_{\ell m}(t)\theta(t - t^{\ell m}_{\text{match}}), \tag{1.151}$$

where $\theta(t)$ is the Heaviside step function.

1.4 Modified gravity theories

General relativity is our most successful theory of gravity, and it has passed all experimental tests. However, GR is a classical theory that is not renormalizable, but modifications of GR with higher-curvature corrections can resolve this issue [420]. GR also includes singularities in gravitational collapse and cosmology [421], which could be resolved in a quantum theory of gravity. Therefore, it is expected that GR should be modified at high energies. Furthermore, it is possible that strong-field modifications of GR might leak out at low energies and leave an imprint on cosmological scales, thus providing an explanation for dark energy.

Many modifications of GR have been proposed in the literature, and they can all be classified based on which assumption of Lovelock theorem [422, 423] they violate. Lovelock's theorem states that GR is the unique theory of gravity under certain assumptions that can be expressed as follows [424]:

> "In four spacetime dimensions the only divergence-free symmetric rank-2 tensor constructed solely from the metric and its derivatives up to second differential order, and preserving diffeomorphism invariance, is the Einstein tensor plus a cosmological term."

Thus, modified gravity theories fall under one or more of the following classes: i) theories with extra field degrees of freedom; ii) theories that violate diffeomorphism invariance, either by violating Lorentz invariance or by including massive gravitons; iii) theories built in dimensions higher than four; and iv) theories that violate the weak equivalence principle. The diagram in Fig. 1.13 summarizes these possibilities.

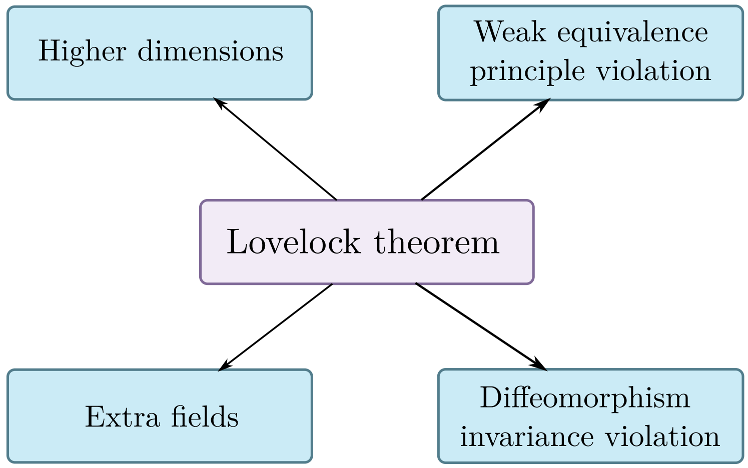

Figure 1.13: Diagram illustrating Lovelock's theorem. All modified gravity theories violate one or more of the four assumptions underlying the theorem.

The simplest and most natural extensions to GR are scalar-tensor theories, which include an extra scalar field non-minimally coupled to the metric, i.e. with a function of the scalar field multiplying the Ricci scalar. The action for the most widely studied class of scalar-tensor theories can be written in the Bergmann-Wagoner formulation as [424]

$$S_{\text{ST}} = \frac{1}{16\pi} \int \mathrm{d}^4x \sqrt{-\tilde{g}} \left[\phi\tilde{R} - \frac{\omega(\phi)}{\phi} \tilde{g}^{\mu\nu} \partial_\mu \phi \partial_\nu \phi - \tilde{U}(\phi) \right] + S_m[\Psi, \tilde{g}_{\mu\nu}], \tag{1.152}$$

where ω and $\tilde{U}$ are some functions of the scalar field ϕ, S_m is the matter part of the action, and Ψ are some matter fields that couple to the metric. The action written in this form is referred to as the *Jordan-frame* action, and we use tilde to refer to quantities in that frame.

Performing a field redefinition $\varphi = \varphi(\phi)$ and a conformal transformation of the metric $g_{\mu\nu} = \mathcal{A}^{-2}(\varphi)\tilde{g}_{\mu\nu}$, with $\mathcal{A}(\varphi) = \phi^{-1/2}$, defines the *Einstein-frame* action

$$S_{\text{ST}} = \frac{1}{16\pi} \int \mathrm{d}^4x \sqrt{-g} \left[R - 2g^{\mu\nu} \partial_\mu \varphi \partial_\nu \varphi - U(\varphi) \right] + S_m[\Psi, \mathcal{A}^2(\varphi) g_{\mu\nu}], \tag{1.153}$$

which simplifies the calculations because of the minimal coupling of the scalar field to R, at the expense of the non-minimal coupling to the metric in the matter action.

GWs emitted from compact binaries in scalar-tensor theories differ from GR due to the emission of scalar energy flux, including dipole radiation that vanishes in GR, and the existence of an additional polarization mode, namely a transverse breathing-mode.

In Chapters 8, 9 and 10, we consider some variations of scalar-tensor theories, and identify some of their signatures on GWs. This helps in testing GR with GW observations, which offer unprecedented opportunities to test gravity in the highly dynamical, strong-field regime, allowing us to test gravity in pure spacetime events (binary BH mergers) or with highly-dense matter (binary NS mergers).

1.5 Research Overview

This section summarizes the research presented in the rest of the dissertation, and it is structured as follows:

- § 1.5.1 summarizes Chapters 2, 3, and 4, which were published as Refs. [1–3]. We discuss a method for deriving PN results, which are valid for arbitrary mass ratios, from GSF results, by exploiting the simple mass dependence of the scattering angle in a PM expansion (see § 1.2.2.2). We use this method to derive new results for the spin-orbit (SO) dynamics at 4.5PN and 5.5PN orders, and for the aligned spin$_1$-spin$_2$ dynamics at 5PN order. We demonstrate the improvement in accuracy by comparing the binding energy with NR results.

- § 1.5.2 summarizes Chapter 5, which was published as Ref. [4]. We derive EOB Hamiltonians at 4PN order that are valid for precessing spins and generic compact objects, i.e., BHs or NSs. We also compare those Hamiltonians with NR results through the aligned-spin binding energy, finding good agreement.

- § 1.5.3 summarizes Chapter 6, which was published as Ref. [5]. We derive the RR force and gravitational waveform modes, in EOB coordinates, for aligned-spin binaries in eccentric orbits through 2PN order, including tail effects, and SO and spin-spin couplings. These PN results were used to extend the quasi-circular-orbit EOB multipolar waveform model `SEOBNRv4HM` [397, 398] to the eccentric one `SEOBNRv4EHM` [10].

- § 1.5.4 summarizes Chapter 7, which was published as Ref. [6]. We assess the accuracy of the 4PM conservative dynamics through comparisons with the PN approximation and NR simulations for the scattering angle and the circular-orbit binding energy. We also incorporate the PM results in EOB Hamiltonians, which significantly improves the accuracy over PM-expanded Hamiltonians.

- § 1.5.5 summarizes Chapter 8, which was published as Ref. [7]. We derive the conservative and dissipative binary dynamics in EMd theory at the next-to-leading PN order. We compute the Fourier-domain gravitational waveform and the number of useful GW cycles measurable by Advanced LIGO. We also construct two EOB Hamiltonians in EMd theory.

- § 1.5.6 summarizes Chapters 9 and 10, which were published as Refs. [8, 9]. We present a theory-agnostic effective-field-theory approach for describing spontaneous and dynamical scalarization, showing that all theories that exhibit spontaneous scalarization also manifest dynamical scalarization in binary systems. We apply this approach to BHs in Einstein-Maxwell-scalar theory, and to NSs in a particular class of scalar-tensor theories.

1.5.1 Synergies between PN and GSF approaches

As discussed in Sec. 1.2, the PN expansion is an approximation for small velocities but arbitrary mass ratios, while GSF provides an expansion in the mass ratio but for arbitrary velocities. References [90, 91] introduced a method, sometimes dubbed the "Tutti Frutti" method [286], that derives PN results valid for arbitrary mass ratios from GSF results at first order in the mass ratio. We extended this method in Refs. [1–3] to include spin.

The method splits the conservative dynamics into local and nonlocal-in-time contributions. The nonlocal part is calculated separately in a small-eccentricity expansion for bound orbits, or in a large-eccentricity expansion for scattering orbits. The local part is determined from gauge-invariant quantities—the redshift and spin-precession frequency—calculated at first order in the mass ratio. This is done by exploiting the simple mass-ratio dependence of the scattering angle in a PM expansion, as discussed in § 1.2.2.2, thus making it possible to derive the subleading PN order from test-body results, and the full third-subleading PN order from first-order self-force (1SF) results. The diagram in Fig. 1.14 illustrates this procedure, and the Table in Fig. 1.15 shows the relation between PN and GSF results for the local-in-time conservative dynamics.

This approach has been used to derive the 5PN conservative dynamics for nonspinning binaries except for two coefficients [90, 91], and the 6PN dynamics except for four coefficients [92, 93]. We extended that approach to spinning binaries, and derived the full 4.5PN SO and 5PN aligned spin$_1$-spin$_2$ dynamics [1, 2], and the 5.5PN SO dynamics except for one coefficient [3]. We explain these calculations in the following subsections, focusing on the 5.5PN SO dynamics as an example.

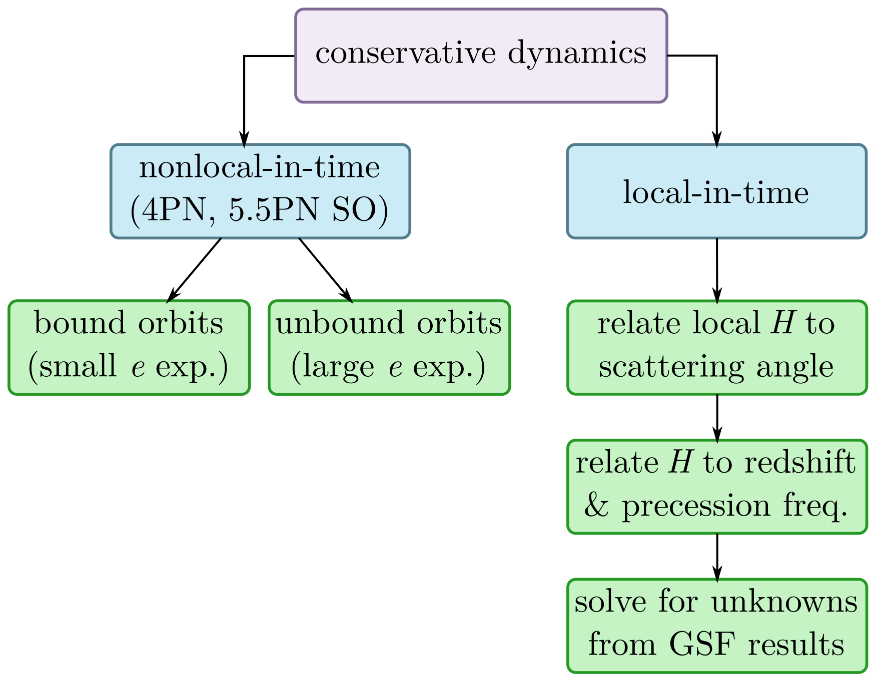

Figure 1.14: Overview of the "Tutti Frutti" method for deriving PN results from GSF. The conservative dynamics is split into local and nonlocal-in-time contributions, with the local part determined from gauge-invariant quantities calculated from GSF, by exploiting the simple mass-ratio dependence of the scattering angle.

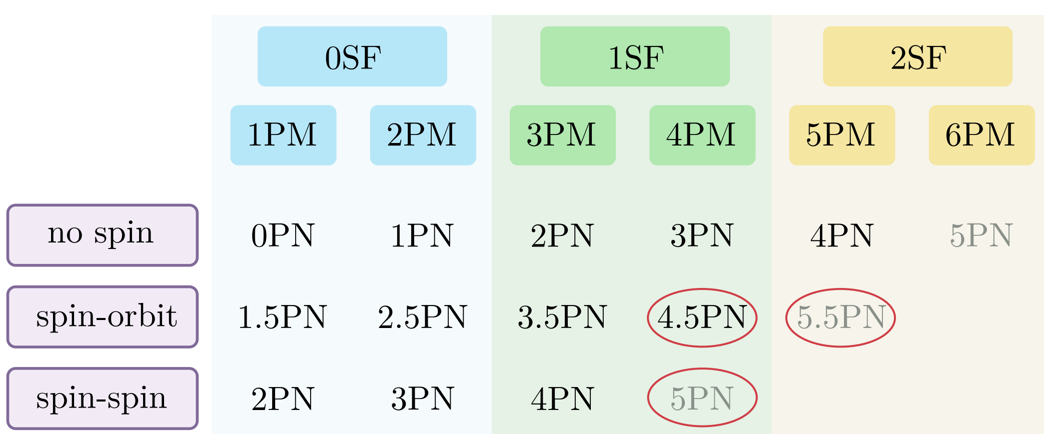

Figure 1.15: Relation between the PN, PM, and GSF approximations for the local-in-time conservative dynamics. Circled PN orders indicate the results we derived in Chapters 2, 3, and 4 using the "Tutti Frutti" method. PN orders in gray font are partially known.

1.5.1.1 Nonlocal-in-time contribution to the 5.5PN SO Hamiltonian

For an inspiraling binary, gravitational radiation emitted at earlier times can scatter off the spacetime curvature back onto the binary, thus affecting the conservative dynamics [79, 183, 425]. These are called *nonlocal-in-time* contributions, or *tail* effects, since they depend on the entire history of the binary. So far, there is no closed-form analytic solution for the nonlocal contributions that is valid for arbitrary eccentricities, but they can be calculated in an eccentricity expansion.

The total PN conservative action is split into local and nonlocal-in-time parts, such that

$$S_{\text{tot}}^{\text{nPN}} = S_{\text{loc}}^{\text{nPN}} + S_{\text{nonloc}}^{\text{nPN}}. \tag{1.154}$$

The nonlocal contribution starts at 4PN order for nonspinning binaries [79, 80], and at 5.5PN order for the SO dynamics [3]. It is given by the following integral:

$$S_{\text{nonloc}}^{\text{LO}} = \frac{GM}{c^3} \int \mathrm{d}t \, \text{Pf}_{2s/c} \int \frac{\mathrm{d}t'}{|t-t'|} \mathcal{F}_{\text{LO}}^{\text{split}}(t,t'), \tag{1.155}$$

which we evaluate at leading PN order, including both nonspinning and SO contributions. In that integral, $\mathcal{F}_{\text{LO}}^{\text{split}}(t,t')$ is the time-split (or time-symmetric) GW energy flux, which is explained below, and the Hadamard *partie finie* (Pf) operation is used since the integral is logarithmically divergent at $t' = t$.

It was shown in Refs. [79, 80] that the nonlocal part of the action can be written after a change of variables $\tau \equiv t' - t$ as

$$S_{\text{nonloc}}^{\text{LO}} = -\int \mathrm{d}t \, \delta H_{\text{nonloc}}^{\text{LO}}(t), \tag{1.156}$$

$$\delta H_{\text{nonloc}}^{\text{LO}}(t) \equiv -\frac{GM}{c^3} \text{Pf}_{2s/c} \int \frac{\mathrm{d}\tau}{|\tau|} \mathcal{F}_{\text{LO}}^{\text{split}}(t, t+\tau) + 2\frac{GM}{c^3} \mathcal{F}_{\text{LO}}^{\text{split}}(t,t) \ln\left(\frac{r}{s}\right). \tag{1.157}$$

The last term only depends on local time t, so we can simplify the local part by choosing the arbitrary length scale s to be the radial distance r between the two bodies in harmonic coordinates [91], thus removing the dependence of the local part on $\ln r$.

The time-split (or time-symmetric) GW energy flux $\mathcal{F}_{\text{LO}}^{\text{split}}(t,t')$ is expressed in terms of the source multipole moments as [79]

$$\mathcal{F}_{\text{LO}}^{\text{split}}(t,t') = \frac{G}{c^5}\left[\frac{1}{5}I_{ij}^{(3)}(t)I_{ij}^{(3)}(t') + \frac{16}{45c^2}J_{ij}^{(3)}(t)J_{ij}^{(3)}(t') + \dots\right], \tag{1.158}$$

and to obtain the nonlocal 5.5PN contribution to the Hamiltonian, we need the mass quadrupole moment I_{ij} at 1.5PN order, and the current quadrupole moment J_{ij} at 0.5PN order. These moments are given by [164, 426]

$$\begin{aligned}
I_{ij} &= m_1 x_1^{\langle i}x_1^{j\rangle} + \frac{3}{c^3}x_1^{\langle i}(\boldsymbol{v}_1\times\boldsymbol{S}_1)^{j\rangle} - \frac{4}{3c^3}\frac{d}{dt}x_1^{\langle i}(\boldsymbol{x}_1\times\boldsymbol{S}_1)^{j\rangle} + 1\leftrightarrow 2,\\
J_{ij} &= m_1 x_1^{\langle i}(\boldsymbol{x}_1\times\boldsymbol{v}_1)^{j\rangle} + \frac{3}{2c}x_1^{\langle i}S_1^{j\rangle} + 1\leftrightarrow 2.
\end{aligned} \tag{1.159}$$

The integral in Eq. (1.157) can be evaluated in an eccentricity expansion using the quasi-Keplerian parametrization [427], which is given for bound orbits, up to 1.5PN order, by

$$r = a_r(1 - e_r\cos u), \tag{1.160}$$

$$\ell = nt = u - e_t\sin u, \tag{1.161}$$

$$\phi = 2K\arctan\left[\sqrt{\frac{1+e_\phi}{1-e_\phi}}\tan\frac{u}{2}\right], \tag{1.162}$$

where a_r is the semi-major axis, u the eccentric anomaly, ℓ the mean anomaly, n the mean motion (radial angular frequency), K the periastron advance, and (e_r, e_t, e_ϕ) the radial, time, and phase eccentricities. Using that parametrization, we express the source multipole moments (1.159) in terms of the variables (a_r, e_t, t), and expand in eccentricity up to $\mathcal{O}(e_t^8)$. We then perform an orbit average of the time-split flux

$$\left\langle \mathcal{F}_{\text{LO}}^{\text{split}}(t, t+\tau) \right\rangle = \frac{n}{2\pi} \int_0^{2\pi/n} \mathcal{F}_{\text{LO}}^{\text{split}}(t, t+\tau) \mathrm{d}t, \tag{1.163}$$

and perform the Pf operation with time scale $2s/c$. The result of this calculation is the nonlocal part of the harmonic-coordinate Hamiltonian expanded in e_t, as given by Eq. (4.28) in Chapter 4.

It is more convenient to work with a Hamiltonian in EOB coordinates, since it leads to simpler expressions, and the results can be directly implemented in EOB waveform models. The effective Hamiltonian for nonspinning binaries was discussed in § 1.3.1, and the simplest way of extending it to include SO effects is to add a term proportional to LS/r^3, such that

$$\begin{aligned} H_{\text{eff}} = &\sqrt{A(r) \left[\mu^2 c^2 + A(r) \bar{D}(r) \frac{p_r^2}{c^2} + \frac{L^2}{c^2 r^2} + Q(r, p_r) \right]} \\ &+ \frac{1}{c^3 r^3} \boldsymbol{L} \cdot \left[g_S(r, p_r) \boldsymbol{S} + g_{S^*}(r, p_r) \boldsymbol{S}^* \right]. \end{aligned} \tag{1.164}$$

In this Hamiltonian, we use $\bar{D} \equiv 1/(AB)$, which is a more standard choice in the literature than $B(r)$ from Eq. (1.129). In addition, we define the spin combinations

$$\boldsymbol{S} \equiv \boldsymbol{S}_1 + \boldsymbol{S}_2, \qquad \boldsymbol{S}^* \equiv \frac{m_2}{m_1} \boldsymbol{S}_1 + \frac{m_1}{m_2} \boldsymbol{S}_2, \tag{1.165}$$

and include the PN SO corrections in the *gyro-gravitomagnetic* factors g_S and g_{S^*}, given by

$$g_S = 2 - \frac{1}{c^2} \left[\frac{27\nu}{16} \frac{p_r^2}{\mu^2} + \frac{5\nu M}{16 r} \right] + \dots + \frac{1}{c^8} \left(g_S^{\text{5.5PN,loc}} + g_S^{\text{5.5PN,nonloc}} \right), \tag{1.166}$$

$$g_{S^*} = \frac{3}{2} - \frac{1}{c^2} \left[\left(\frac{3\nu}{2} + \frac{5}{4} \right) \frac{p_r^2}{\mu^2} + \left(\frac{3}{4} + \frac{\nu}{2} \right) \frac{M}{r} \right] + \dots + \frac{1}{c^8} \left(g_{S^*}^{\text{5.5PN,loc}} + g_{S^*}^{\text{5.5PN,nonloc}} \right), \tag{1.167}$$

where we split the 5.5PN term into local and nonlocal parts. Note that the gyro-gravitomagnetic factors are the same for both aligned and precessing spins, since the spin vectors in Eq. (1.164) only couple to the angular momentum vector at SO level. Hence, even though the calculations that follow are specialized to aligned spins, the final result is valid for precessing spins.

Splitting the $A, \bar{D}$, and Q potentials in Eq. (1.164) into local and nonlocal pieces, and expanding the effective Hamiltonian to leading order in the nonlocal part, yields

$$H_{\text{eff}} = H_{\text{eff}}^{\text{loc}} + \frac{1}{c^8} H_{\text{eff}}^{\text{nonloc}} + \mathcal{O}(\text{5PN, 6.5PN SO}), \tag{1.168}$$

$$H_{\text{eff}}^{\text{nonloc}} = \frac{1}{2}\left(A^{\text{nonloc}} + \bar{D}^{\text{nonloc}} p_r^2 + Q^{\text{nonloc}}\right) + \frac{\boldsymbol{L}}{c^3 r^3} \cdot \left[\boldsymbol{S} g_S^{\text{5.5PN,nonloc}} + \boldsymbol{S}^* g_{S^*}^{\text{5.5PN,nonloc}}\right]. \tag{1.169}$$

To determine $g_S^{\text{5.5PN,nonloc}}$ and $g_{S^*}^{\text{5.5PN,nonloc}}$, we write them in terms of unknown coefficients, calculate the orbit average of $H_{\text{eff}}^{\text{nonloc}}$ in terms of (a_r, e_t), then match to the harmonic-coordinates nonlocal Hamiltonian, given by Eq. (4.28) in Chapter 4, to obtain Eq. (4.33).

1.5.1.2 Local-in-time contribution to the 5.5PN SO Hamiltonian

The magnitude of the impulse Q has a simple mass dependence in the PM expansion as in Eq. (1.92). We showed in Ref. [2] that this mass dependence holds when spin is included; we just need to replace the mass-independent functions $\mathsf{Q}^{n\text{PM}}_{m_1^i m_2^j}(v)$ in Eq. (1.92) by

$$\begin{aligned} \mathsf{Q}^{n\text{PM}}_{m_1^i m_2^j}(v) &\to \mathsf{Q}^{n\text{PM}}_{m_1^i m_2^j}\left(v, \frac{a_1}{b}, \frac{a_2}{b}\right) \\ &= \mathsf{Q}^{n\text{PM}}_{m_1^i m_2^j a^0}(v) + \frac{a_1}{b}\mathsf{Q}^{n\text{PM}}_{m_1^i m_2^j a_1}(v) + \frac{a_2}{b}\mathsf{Q}^{n\text{PM}}_{m_1^i m_2^j a_2}(v) + \frac{a_1 a_2}{b^2}\mathsf{Q}^{n\text{PM}}_{m_1^i m_2^j a_1 a_2}(v) + \mathcal{O}(a_i^2), \end{aligned} \tag{1.170}$$

where $a_{\text{i}} \equiv S_{\text{i}}/m_{\text{i}}$ are the mass-rescaled spins, and b is the covariant impact parameter defined as the orthogonal distance between the incoming worldlines when using the covariant (Tulczyjew-Dixon) SSC.

Thus, we find that the linear-in-spin part of the scattering angle, when scaled by E/M has the following mass dependence:

$$\begin{aligned} \frac{\chi_{\text{SO}}}{E/M} = \frac{a_1}{b}\Bigg\{ &\frac{GM}{b}\mathsf{X}_1 + \left(\frac{GM}{b}\right)^2\left[\mathsf{X}_2 + \delta \mathsf{X}_2^\delta\right] \\ &+ \left(\frac{GM}{b}\right)^3\left[\mathsf{X}_3 + \delta \mathsf{X}_3^\delta + \nu \mathsf{X}_3^\nu\right] + \left(\frac{GM}{b}\right)^4\left[\mathsf{X}_4 + \delta \mathsf{X}_4^\delta + \nu \mathsf{X}_4^\nu + \nu\delta \mathsf{X}_4^{\nu\delta}\right] \end{aligned}$$

$$+\left(\frac{GM}{b}\right)^5\left[\mathsf{X}_5+\delta\mathsf{X}_5^{\delta}+\nu\mathsf{X}_5^{\nu}+\nu\delta\mathsf{X}_5^{\nu\delta}+\nu^2\mathsf{X}_5^{\nu^2}\right]+\dots\Bigg\}+1\leftrightarrow 2, \tag{1.171}$$

where $\delta \equiv (m_2 - m_1)/M$, and $\mathsf{X}_n^{\cdots}$ are functions only of the energy, or equivalently the velocity. Terms independent of ν, i.e. $\mathsf{X}_n(v)$ and $\mathsf{X}_n^{\delta}(v)$, can be determined from the scattering angle of a spinning test particle in a Kerr background, which was calculated in Ref. [428]. We then write an ansatz for the other functions in terms of unknown coefficients in a 5.5PN expansion as in Eq. (4.45).

The scattering angle can be obtained, as explained in § 1.2.2.3, by integrating $\partial p_r/\partial L$ from $-\infty$ to $+\infty$. This means that it can be calculated from the local Hamiltonian by inverting the Hamiltonian for $p_r(H = E, L, r)$, and evaluating the integral

$$\chi = -2\int_{r_0}^{\infty}\frac{\partial p_r(E,L,r)}{\partial L}\mathrm{d}r - \pi\,, \tag{1.172}$$

where r_0 is the turning point, obtained from the largest root of $p_r(E,L,r) = 0$. We then relate the coefficients of the local Hamiltonian to those of the scattering angle ansatz, which reduces the number of unknowns in the Hamiltonian.

To determine the linear-in-ν coefficients in Eq. (1.171) from 1SF results, we calculate the redshift and spin-precession invariants from the *total* (local + nonlocal) Hamiltonian, since GSF does not differentiate between the two, then match their small-mass-ratio expansions to 1SF expressions known in the literature. A crucial component in this calculation is the first law of binary mechanics [2, 429–432], which reads

$$\mathrm{d}E = \Omega_r\mathrm{d}I_r + \Omega_\phi\mathrm{d}L + \sum_{\mathrm{i}}(z_{\mathrm{i}}\mathrm{d}m_{\mathrm{i}} + \Omega_{S_{\mathrm{i}}}\mathrm{d}S_{\mathrm{i}}), \tag{1.173}$$

where Ω_r and Ω_ϕ are the radial and azimuthal frequencies, I_r is the radial action, z_{i} is the redshift, and $\Omega_{S_{\mathrm{i}}}$ is the spin-precession frequency.

The orbit-averaged redshift can be calculated from the Hamiltonian using

$$z_1 = \left\langle \frac{\partial H}{\partial m_1} \right\rangle = \frac{1}{T_r} \oint \frac{\partial H}{\partial m_1} \mathrm{d}t, \tag{1.174}$$

where T_r is the radial period. The spin-precession frequency Ω_{S_1} is given by

$$\Omega_{S_1} = \left\langle \frac{\partial H}{\partial S_1} \right\rangle = \frac{1}{T_r} \oint \frac{\partial H}{\partial S_1} \mathrm{d}t. \tag{1.175}$$

Evaluating these integrals can be done in an eccentricity expansion using the Keplerian parametrization

$$r = \frac{1}{u_p(1 + e\cos\xi)}, \tag{1.176}$$

where u_p is the inverse semilatus rectum, e is the eccentricity, and ξ is the relativistic anomaly. This yields the redshift and spin-precession invariants in terms of the gauge-dependent u_p and e, i.e., $z_1(u_p, e)$ and $\psi_1(u_p, e)$. We then express them in terms of the gauge-independent variables

$$x \equiv (M\Omega_\phi)^{2/3}, \qquad \iota \equiv \frac{3x}{k}, \tag{1.177}$$

where $k \equiv T_\phi/(2\pi) - 1$ is the (fractional) periastron advance.

Next, we expand the redshift $z_1(x, \iota)$ and spin-precession frequency $\Omega_{S_1}(x, \iota)$ to first order in the mass ratio $q \equiv m_1/m_2$. In doing so, we make use of another set of variables (y, λ), defined by

$$y \equiv (m_2\Omega_\phi)^{2/3} = \frac{x}{(1+q)^{2/3}}, \tag{1.178}$$

$$\lambda \equiv \frac{3y}{k} = \frac{\iota}{(1+q)^{2/3}}, \tag{1.179}$$

which can be directly related to the variables used in GSF calculation, as explained in Appendix C. The result of this calculation can be schematically written as

$$z_1 = z_{1a^0}^{(0)} + a\, z_{1a}^{(0)} + q\left(z_{1a^0}^{\mathrm{1SF}} + a\, z_{1a}^{\mathrm{1SF}}\right) + \mathcal{O}(q^2, a^2), \tag{1.180}$$

$$\psi_1 = \psi^{(0)}_{1a^0} + q\psi^{\rm 1SF}_{1a^0} + \mathcal{O}(q^2, a)\,, \tag{1.181}$$

where the spin-precession invariant $\psi_1 \equiv \Omega_{S_1}/\Omega_\phi$, a is the Kerr spin, and each term is a PN expansion. Thus, by matching z_1 and ψ_1 computed from the Hamiltonian with the 1SF results derived in Refs. [341, 343, 349, 433], we can determine the remaining unknowns in the scattering angle and Hamiltonian, allowing us to solve for all coefficients up to 5.5PN order except for one coefficient at second-order in the mass ratio.

1.5.1.3 Comparison with numerical relativity

The binding energy $\bar{E}$ provides a good diagnostic for the conservative dynamics of the binary system [408, 434, 435]. In NR simulations, it is calculated by subtracting the total mass and radiated energy $E_{\rm rad}$ from the initial energy $E_{\rm in}$ at the beginning of the simulation [436]

$$\bar{E}_{\rm NR} \equiv E_{\rm in} - E_{\rm rad} - M. \tag{1.182}$$

Even without including $E_{\rm rad}$, it is informative to compare the binding energy calculated from the conservative Hamiltonian, while assuming exact circular orbits (i.e., not inspiraling). To compute the circular-orbit binding energy $\bar{E} \equiv H - M$, we set $p_r = 0$ in the Hamiltonian and numerically solve $\dot{p}_r = 0 = -\partial H/\partial r$ for the angular momentum L at different orbital separations. We can then obtain $\bar{E}$ as a function of the dimensionless parameter

$$v_\Omega \equiv (M\Omega)^{1/3}, \tag{1.183}$$

which is the velocity at leading PN order, where the orbital frequency $\Omega = \partial H/\partial L$.

To isolate the SO contribution $\bar{E}^{\rm SO}$ to the binding energy, we combine configurations with different spin orientations (parallel or anti-parallel to the orbital angular momentum direction),

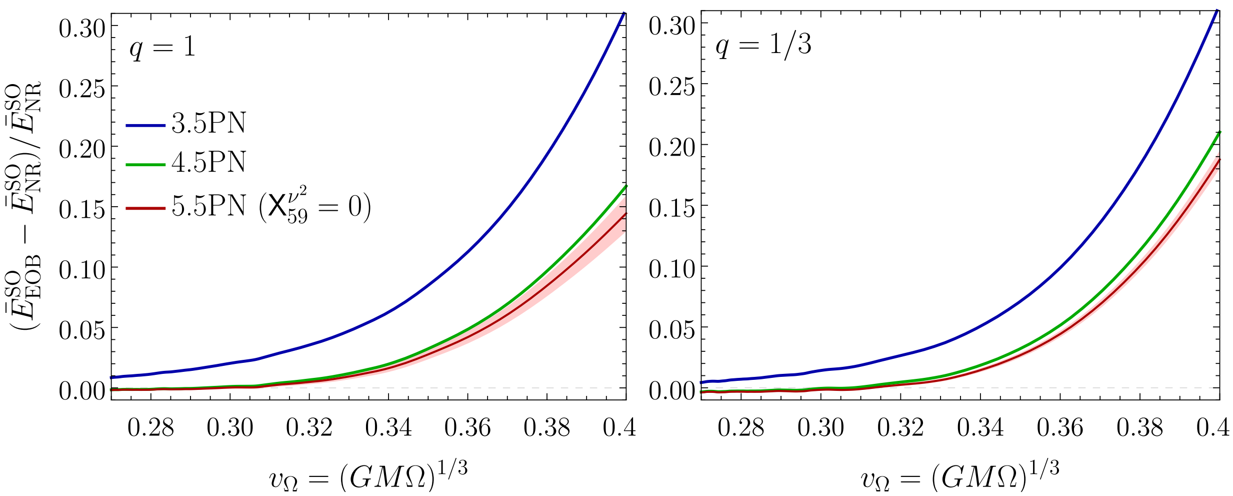

Figure 1.16: The relative difference in the SO contribution to the binding energy $\bar{E}^{\rm SO}$ between EOB and NR for equal masses (left panel) and $q = 1/3$ (right panel), plotted as a function of the frequency parameter v_Ω.

as explained in Refs. [437, 438]. One possibility is to use

$$\bar{E}^{\rm SO}(\nu, \hat{a}, \hat{a}) \simeq \frac{1}{2}\left[\bar{E}(\nu, \hat{a}, \hat{a}) - \bar{E}(\nu, -\hat{a}, -\hat{a})\right], \tag{1.184}$$

where $\hat{a}$ here is the magnitude of the dimensionless spin of each BH, which varies between -1 and 1. This relation subtracts the nonspinning and spin-spin parts, with corrections remaining at cubic order in spin, thus providing a good approximation for the SO contribution.

The binding energy was obtained from NR data in Ref. [438] for various spinning and nonspinning configurations. In Fig. 1.16, we show the relative difference in the SO contribution $\bar{E}^{\rm SO}$ between an EOB Hamiltonian and NR for two mass ratios, $q = 1$ and $q = 1/3$, as a function of v_Ω up to $v_\Omega = 0.4$, which corresponds to about an orbit before merger. We see that our 4.5PN SO result provides a significant improvement over the 3.5PN order, with smaller improvement at 5.5PN order. To produce the 5.5PN curve, we set the remaining quadratic-in-ν coefficient in the scattering angle, denoted $X_{59}^{\nu^2}$, to zero. Since this unknown is expected to be of $\mathcal{O}(10^2)$, based on the other coefficients at that order in the scattering angle, we also plot the energy for $\mathsf{X}_{59}^{\nu^2} = 500$ and $\mathsf{X}_{59}^{\nu^2} = -500$, demonstrating that the effect of that unknown is less than the difference between 4.5PN and 5.5PN, with decreasing effect for small mass ratios.

1.5.2 EOB Hamiltonians for precessing spins at 4PN order

In Ref. [4] (Chapter 5), we obtained EOB Hamiltonians that include the complete 4PN conservative dynamics for precessing spins. Such a Hamiltonian is also valid for generic compact objects, i.e. BHs or NSs, since we included the spin-induced multipole constants that parametrize the deformation of the spinning body. We considered four Hamiltonians that are extensions of the varieties found in the literature, and assessed their accuracy by comparing the binding-energy to NR simulations, finding good agreement. Here, we briefly discuss one Hamiltonian to show how it is constructed, and refer the reader to Chapter 5 for more details.

The Hamiltonian for a test mass in a Kerr background with spin $\boldsymbol{a}$ can be written in a 3-vector notation as follows: [4, 392]

$$H^{\text{Kerr}} = H^{\text{Kerr}}_{\text{odd}} + H^{\text{Kerr}}_{\text{even}} \tag{1.185}$$

$$H^{\text{Kerr}}_{\text{odd}} = \frac{2r}{\Lambda}\boldsymbol{L}\cdot\boldsymbol{a}, \tag{1.186}$$

$$H^{\text{Kerr}}_{\text{even}} = \left[A^{\text{Kerr}}\left(\mu^2 + B^{\text{Kerr}}_{p}\boldsymbol{p}^2 + B^{\text{Kerr}}_{np}(\boldsymbol{n}\cdot\boldsymbol{p})^2 + B^{\text{Kerr}}_{npa}(\boldsymbol{n}\times\boldsymbol{p}\cdot\boldsymbol{a})^2\right)\right]^{1/2}, \tag{1.187}$$

where $H^{\text{Kerr}}_{\text{odd}}$ contains odd-in-spin contributions while $H^{\text{Kerr}}_{\text{even}}$ is even-in-spin, and where

$$\begin{aligned} A^{\text{Kerr}} &= \frac{\Delta\Sigma}{\Lambda}, & B^{\text{Kerr}}_{p} &= \frac{r^2}{\Sigma}, \\ B^{\text{Kerr}}_{np} &= \frac{r^2}{\Sigma}\left[\frac{\Delta}{r^2} - 1\right], & B^{\text{Kerr}}_{npa} &= -\frac{r^2}{\Sigma\Lambda}(\Sigma + 2r), \end{aligned} \tag{1.188}$$

with

$$\Sigma \equiv r^2 + (\boldsymbol{n}\cdot\boldsymbol{a})^2, \qquad \Delta \equiv r^2 - 2r + a^2,$$
$$\Lambda \equiv (r^2+a^2)^2 - \Delta a^2 + \Delta(\boldsymbol{n}\cdot\boldsymbol{a})^2. \tag{1.189}$$

We take the effective Hamiltonian H^{eff} in the EOB description to be a deformation of the Kerr Hamiltonian H^{Kerr}, with the deformation parameter being the symmetric mass ratio $\nu \equiv \mu/M$. The masses of the Kerr BH and test mass are identified to be the total mass $M = m_1 + m_2$ and reduced mass $\mu = m_1 m_2/M$, respectively, while the Kerr spin $\boldsymbol{a}$ is mapped by $\boldsymbol{a} = \boldsymbol{a}_1 + \boldsymbol{a}_2$. This ensures that the Hamiltonian reproduces leading-order PN results for BHs at all even orders in spin [127, 264].

We write the effective Hamiltonian as

$$H^{\text{eff}} = H^{\text{eff}}_{\text{odd}} + H^{\text{eff}}_{\text{even}}, \tag{1.190}$$

with odd-in-spin PN corrections added in $H^{\text{eff}}_{\text{odd}}$ and even-in-spin PN corrections in $H^{\text{eff}}_{\text{even}}$. For the odd-in-spin part, we use the ansatz

$$H^{\text{eff}}_{\text{odd}} = \frac{GMr}{\Lambda}\left[\boldsymbol{L}\cdot(g_S \boldsymbol{S} + g_{S^*}\boldsymbol{S}^*) + \boldsymbol{L}\cdot\left(G^{(1)}_{S^3}\boldsymbol{S}_1 + G^{(2)}_{S^3}\boldsymbol{S}_2\right)\right], \tag{1.191a}$$

where $\boldsymbol{S} \equiv \boldsymbol{S}_1 + \boldsymbol{S}_2$ and $\boldsymbol{S}^* \equiv \boldsymbol{S}_1 m_2/m_1 + \boldsymbol{S}_2 m_1/m_2$. The gyro-gravitomagnetic factors include next-to-next-to-leading (3.5PN) SO corrections, while $G^{(1)}_{S^3}$ and $G^{(2)}_{S^3}$ include the leading order (3.5PN) cubic-in-spin corrections.

For the even-in-spin part of the effective Hamiltonian, we use the ansatz

$$H^{\text{eff}}_{\text{even}} = \left[A\Big(1 + B_p \boldsymbol{p}^2 + B_{np}(\boldsymbol{n}\cdot\boldsymbol{p})^2 + B_{npa}(\boldsymbol{n}\times\boldsymbol{p}\cdot\boldsymbol{a})^2 + Q\Big)\right]^{1/2}, \tag{1.192}$$

with the potentials chosen such that

$$A = A^{\text{Kerr}}\left(A^0 + A^{S^2} + A^{S^4}\right), \tag{1.193}$$

$$B_p = B_p^{\text{Kerr}}\left(1 + B_p^{S^2}\right), \tag{1.194}$$

$$B_{np} = \frac{\left(1 - \frac{2}{r} + \frac{a^2}{r^2}\right)\left(A^0 D^0 + B_{np}^{S^2}\right) - 1}{1 + (\boldsymbol{n}\cdot\boldsymbol{a})^2/r^2}, \tag{1.195}$$

$$B_{npa} = B_{npa}^{\text{Kerr}}, \tag{1.196}$$

$$Q = Q^0 + Q^{S^2}, \tag{1.197}$$

where $A^0(r),\ D^0(r)$ and $Q^0(r)$ include PN corrections for nonspinning binaries; A^{S^2}, $B_p^{S^2}$, $B_{np}^{S^2}$ and Q^{S^2} include next-to-next-to-leading (4PN) spin-spin corrections, while A^{S^4} includes the leading order (4PN) quartic-in-spin corrections.

Then, we write those potentials in terms of unknown coefficients in a PN expansion. For example, to include 4PN S^2 terms, we write

$$\begin{aligned}
A^{S^2} = \sum_{i,j=1,2} &\frac{1}{r^3}\left[\alpha_{ij}^{\text{2PN}}\boldsymbol{a}_i\cdot\boldsymbol{a}_j + \beta_{ij}^{\text{2PN}}(\boldsymbol{n}\cdot\boldsymbol{a}_i)(\boldsymbol{n}\cdot\boldsymbol{a}_j)\right] \\
&+ \frac{1}{r^4}\left[\alpha_{ij}^{\text{3PN}}\boldsymbol{a}_i\cdot\boldsymbol{a}_j + \beta_{ij}^{\text{3PN}}(\boldsymbol{n}\cdot\boldsymbol{a}_i)(\boldsymbol{n}\cdot\boldsymbol{a}_j)\right] \\
&+ \frac{1}{r^5}\left[\alpha_{ij}^{\text{4PN}}\boldsymbol{a}_i\cdot\boldsymbol{a}_j + \beta_{ij}^{\text{4PN}}(\boldsymbol{n}\cdot\boldsymbol{a}_i)(\boldsymbol{n}\cdot\boldsymbol{a}_j)\right],
\end{aligned} \tag{1.198}$$

where the unknown coefficients α_{ij} and β_{ij} are assumed to be symmetric under the exchange of the two bodies' labels. For the S^4 contribution, we write the ansatz

$$\begin{aligned}
A^{S^4} = \frac{1}{r^5}\sum_{i,j,k,l=1,2}\Big[&\alpha_{ijkl}(\boldsymbol{a}_i\cdot\boldsymbol{a}_j)(\boldsymbol{a}_k\cdot\boldsymbol{a}_l) + \beta_{ijkl}(\boldsymbol{a}_i\cdot\boldsymbol{a}_j)(\boldsymbol{n}\cdot\boldsymbol{a}_k)(\boldsymbol{n}\cdot\boldsymbol{a}_l) \\
&+ \gamma_{ijkl}(\boldsymbol{n}\cdot\boldsymbol{a}_i)(\boldsymbol{n}\cdot\boldsymbol{a}_j)(\boldsymbol{n}\cdot\boldsymbol{a}_k)(\boldsymbol{n}\cdot\boldsymbol{a}_l)\Big],
\end{aligned} \tag{1.199}$$

and similarly for the other potentials. We solve for these coefficients by matching the EOB Hamiltonian to a PN-expanded Hamiltonian written in a generic gauge after performing a canonical transformation, as explained in § 1.3.1. The results are given in Chapter 5 and Appendix E.

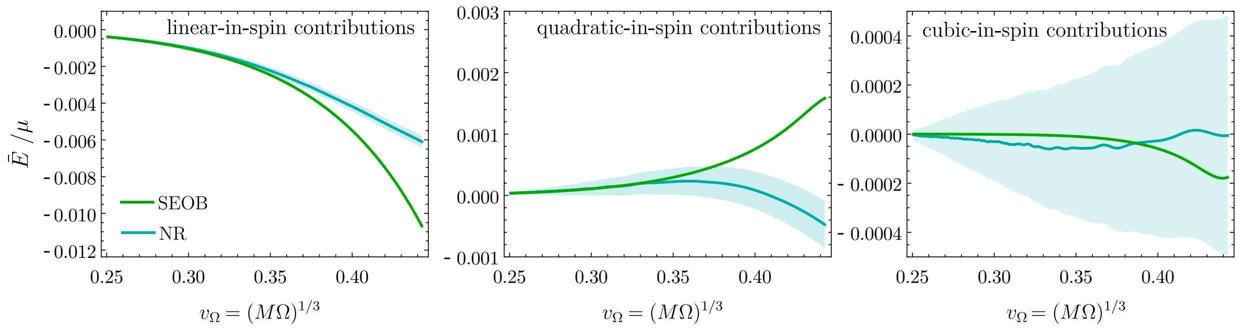

Figure 1.17: Linear-in-spin (left panel), quadratic-in-spin (central panel), and cubic-in-spin (right panel) contributions to the binding energy for the 4PN EOB Hamiltonian considered in this subsection. The NR error is indicated by the shaded regions. Figure adapted from Ref. [4] (Chapter 5).

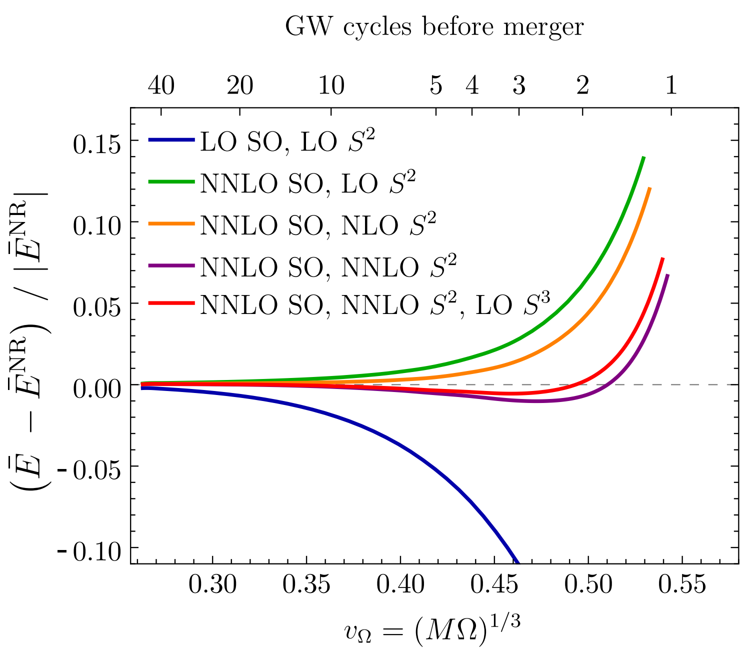

Figure 1.18: Comparing the effect of improving the PN information in the spin part of the EOB Hamiltonian on the binding energy, for a configuration with mass ratio $q = 3$ and equal dimensionless spins 0.85. Figure adapted from Ref. [4] (Chapter 5).

To assess the accuracy of this Hamiltonian, we compared its circular-orbit binding energy with NR simulations. Figure 1.17 shows the spin contributions at SO, S^2, and S^3 levels. These contributions were isolated by combining configurations with different spin orientations [437, 438]; for example, the SO contribution can be isolated using Eq. (1.184). We see from the figure that the SO contribution is almost an order of magnitude larger than the S^2 contribution, which is in turn an order of magnitude larger than the S^3 contribution. Figure 1.18 shows the effect of each spin PN order on the binding energy for a configuration with dimensionless spins $a_1/m_1 = a_2/m_2 = 0.85$ and mass ratio $q = 3$. We see that the higher PN orders for the spin contributions improve the agreement with NR results.

Because of the simplicity and accuracy of the Hamiltonian described above, it has been used to inform the Hamiltonian of the next-generation EOB model `SEOBNRv5`, which we are currently developing for use in the upcoming LIGO-Virgo-KAGRA runs.

1.5.3 Radiation reaction and waveform for eccentric orbits

GW observations have so far been consistent with binary coalescence in quasi-circular orbits [439–442], and it is expected that binaries would circularize before they enter the frequency band of ground-based detectors [443–445]. However, depending on their astrophysical formation channels, a small fraction of binaries could have non-negligible orbital eccentricity as they enter the LIGO-Virgo frequency band [446–448]. This can occur in dense stellar environments, such as globular clusters or galactic nuclei, where dynamic capture [446–451] or the Lidov-Kozai mechanism in hierarchical triples [452–455] can lead to eccentric binary inspirals at close separations. Interestingly, the signal-to-noise ratio is expected to be higher for eccentric binaries than quasi-circular ones [456], and Ref. [442] pointed out that GW190521 [457] could be consistent with an eccentric nonprecessing binary.

Even though the expected fraction of eccentric GW observations with current detectors is small, neglecting eccentricity for the parameter inference can cause significant bias [193]. Hence, it is important to develop accurate waveform models for eccentric binaries to detect them, infer their properties, and shed light on their astrophysical environment and formation channels.

In most EOB waveform models, the radiation-reaction (RR) force and waveform modes are specialized to quasi-circular orbits. In Ref. [5] (Chapter 6), we derived eccentric-orbit PN expressions for the RR force and the waveform modes in EOB coordinates through 2PN order, including tail effects, and SO and spin-spin couplings. We recast those results in a factorized form and included them in the state-of-the-art, quasi-circular-orbit model `SEOBNRv4HM` [397, 398] currently used in LIGO-Virgo analyses. In Ref. [10], we compared our eccentric model `SEOBNRv4EHM` with publicly-available NR simulations with initial orbital eccentricities $e \lesssim 0.3$ and mass ratios up to 3, finding good agreement.

1.5.3.1 Radiation-reaction force

The RR force accounts for the energy and angular momentum losses by the system, and is added to the right-hand side of the Hamilton equations (1.140). In general, the local energy and angular momentum losses by the system, which are gauge-dependent quantities, are not equal to the gauge-invariant energy and angular momentum fluxes, Φ_E and Φ_J, because of additional contributions due to interactions with the radiation field. The balance equations are modified by

Schott terms [402] that appear as total time derivatives in the balance equations, which read

$$\begin{aligned}
&\dot{E}_{\text{system}} + \dot{E}_{\text{Schott}} + \Phi_E = 0, \\
&\dot{J}_{\text{system}} + \dot{J}_{\text{Schott}} + \Phi_J = 0.
\end{aligned} \tag{1.200}$$

Substituting the expressions in Eqs. (1.143) for the energy and angular momentum losses yields

$$\begin{aligned}
&\dot{r}\mathcal{F}_r + \dot{\phi}\mathcal{F}_\phi + \dot{E}_{\text{Schott}} + \Phi_E = 0, \\
&\mathcal{F}_\phi + \dot{J}_{\text{Schott}} + \Phi_J = 0.
\end{aligned} \tag{1.201}$$

The coordinate gauge freedom in the RR force is related to the freedom in defining the Schott terms, and can be chosen such that the RR force for eccentric binaries reduces to the following quasi-circular-orbit expressions:

$$\begin{aligned}
&\mathcal{F}_\phi^{\text{qc}} = -\frac{\Phi_E^{\text{qc}}}{\Omega}, \\
&\mathcal{F}_r^{\text{qc}} = \mathcal{F}_\phi^{\text{qc}}\frac{p_r}{L} = -\frac{\Phi_E^{\text{qc}} p_r}{\Omega L},
\end{aligned} \tag{1.202}$$

where Ω is the orbital frequency and Φ_E^{qc} is the quasi-circular-orbits energy flux. These expressions were obtained in Refs. [374, 381], and have been used in the quasi-circular-orbit model `SEOBNRv4HM` [397, 398], which we extended to eccentric orbits.

Hence, the approach we use to obtain the RR force is to write a generic ansatz with unknown coefficients for the Schott terms, and calculate the RR force from the fluxes using the balance equations (1.201), which can be solved for the force components to give

$$\begin{aligned}
&\mathcal{F}_\phi = -\Phi_J - \dot{J}_{\text{Schott}}, \\
&\dot{r}\mathcal{F}_r = -\Phi_E + \dot{\phi}\Phi_J - \dot{E}_{\text{Schott}} + \dot{\phi}\dot{J}_{\text{Schott}}.
\end{aligned} \tag{1.203}$$

Then, we specify the free unknown coefficients in the Schott terms such that the force reduces to the conditions in Eq. (1.202) in the circular-orbit limit, i.e.,

$$\begin{aligned}
&\mathcal{F}_\phi = -\Phi_J + \mathcal{O}(\dot{p}_r) + \mathcal{O}(p_r^2), \\
&\frac{\mathcal{F}_r L}{\mathcal{F}_\phi p_r} = 1 + \mathcal{O}(p_r^2),
\end{aligned} \tag{1.204}$$

since both p_r and $\dot{p}_r$ are zero for circular orbits.

To illustrate this procedure at leading PN order (2.5PN), we start by writing the energy and angular momentum fluxes as

$$\Phi_E^{\rm inst} = \frac{8\nu^2 M^4}{15 r^4}\left(12\frac{p^2}{\mu^2} - 11\frac{p_r^2}{\mu^2}\right), \tag{1.205}$$

$$\Phi_J^{\rm inst} = \frac{8\nu^2 M^3 L}{5\mu r^3}\left(2\frac{p^2}{\mu^2} - 3\frac{p_r^2}{\mu^2} + \frac{2M}{r}\right), \tag{1.206}$$

and use the following ansatz for the Schott terms:

$$J_{\rm Schott}^{\rm inst} = \alpha_1 \frac{M^3 p_r L}{\mu^2 r^2}, \tag{1.207}$$

$$E_{\rm Schott}^{\rm inst} = \frac{M^2 p_r}{r^2}\left(\beta_1 \frac{p_r^2}{\mu^2} + \beta_2 \frac{p^2}{\mu^2} + \frac{M\beta_3}{r}\right). \tag{1.208}$$

Calculating the RR force with this ansatz using Eqs. (1.203) and requiring that $\mathcal{F}_r L/(\mathcal{F}_\phi p_r) - 1$ satisfies the condition in Eq. (1.204) gives the solution

$$\beta_1 = \frac{8}{5}, \qquad \beta_2 = -\frac{16}{3}, \qquad \beta_3 = 0, \qquad \alpha_1 = -\frac{128}{15}. \tag{1.209}$$

With that solution, we obtain the leading order RR force

$$\mathcal{F}_\phi^{\rm LO} = \frac{8\nu^2 M^3 L}{15\mu r^3}\left(10\frac{p^2}{\mu^2} - 39\frac{p_r^2}{\mu^2} - \frac{22M}{r}\right), \tag{1.210}$$

$$\mathcal{F}_r^{\rm LO} = -\frac{16\nu^2 M^3 p_r}{15\mu r^3}\left(-5\frac{p^2}{\mu^2} + 12\frac{p_r^2}{\mu^2} + \frac{11M}{r}\right). \tag{1.211}$$

The same procedure is performed in Chapter 6 up to 2PN relative order.

1.5.3.2 Initial conditions for eccentric orbits

To numerically evolve the equations of motion, we need to specify the initial conditions. In Ref. [5], we obtained initial conditions for eccentric orbits starting at periastron, and then generalized those conditions in Ref. [10] to start at an arbitrary point on the orbit.

We use the eccentricity e defined as in the Keplerian parametrization

$$r = \frac{1}{u_p(1 + e\cos\xi)}\,, \tag{1.212}$$

where u_p is the inverse semilatus rectum, and ξ is the relativistic anomaly, which equals 0 at periastron and π at apastron. Given an initial orbital frequency Ω_0, eccentricity e_0, relativistic anomaly ξ_0, masses, and spins, we obtain the initial conditions for r and L in absence of RR by solving the following equations:

$$\left[\frac{\partial H_{\rm EOB}}{\partial r}\right]_0 = -\left[\dot{p}_r(L,e,\xi)\right]_0\,, \qquad \left[\frac{\partial H_{\rm EOB}}{\partial L}\right]_0 = \Omega_0, \tag{1.213}$$

with $p_r(L,e,\xi)$ and $\dot{p}_r(L,e,\xi)$ given by the 2PN expansion given in Appendix C of Ref. [10].

Using the solution for r_0 and L_0, we obtain the initial condition for p_{r_0} by numerically solving

$$\left[\frac{\partial H_{\rm EOB}}{\partial p_r}\right]_0 = \left[\dot{r}^{(0)} + \dot{r}^{(1)}\right]_0\,, \tag{1.214}$$

where $\dot{r}^{(0)}$ is the 2PN expression for $\dot{r}$ in absence of RR, while $\dot{r}^{(1)}$ accounts for the effect of RR on $\dot{r}$, for which we use the quasi-circular expression derived in Ref. [374]

$$\dot{r}^{(1)} = -\frac{\Phi_E^{\rm qc}}{\Omega}\frac{\partial^2 H_{\rm EOB}/\partial r\partial L}{\partial^2 H_{\rm EOB}/\partial r^2}. \tag{1.215}$$

1.5.3.3 Waveform modes

We derived the waveform modes to 2PN order beyond the leading order of the $(2,2)$ mode, including the tail effects, and SO and spin-spin couplings for aligned spins. The instantaneous nonspinning part of the modes was derived for eccentric orbits in Refs. [151, 159] in harmonic coordinates and we converted their results to EOB coordinates using the transformations in

Ref. [402]. For the tail part, we extended the results of Ref. [403] to higher orders in the eccentricity expansion to $\mathcal{O}(e^6)$ and to higher modes using the Keplerian parametrization. The spin contributions to the modes were derived up to 2PN order for circular orbits in Ref. [173], and we extended that derivation to eccentric orbits following the steps discussed in § 1.2.1.4 while using the spin contributions to source moments from Refs. [166, 173].

We included the eccentric corrections in the factorized modes (1.145) as follows:

$$h^{\mathrm{F}}_{\ell m} = h^{\mathrm{N,qc}}_{\ell m} S_{\mathrm{eff}} (T^{\mathrm{qc}}_{\ell m} + T^{\mathrm{ecc}}_{\ell m}) e^{i\delta_{\ell m}} (f^{\mathrm{qc}}_{\ell m} + f^{\mathrm{ecc}}_{\ell m}), \tag{1.216}$$

where $h^{\mathrm{N,qc}}_{\ell m}$ is the quasi-circular leading PN order, the effective source term S_{eff} is given by

$$S_{\mathrm{eff}} = \begin{cases} H_{\mathrm{eff}}(r, p_r, L), & \ell + m \text{ even} \\ \Omega^{1/3} L, & \ell + m \text{ odd} \end{cases}, \tag{1.217}$$

$T^{\mathrm{ecc}}_{\ell m}$ contains the eccentric corrections to the tail contribution, $\delta_{\ell m}$ is the same as in the quasi-circular case, and $f^{\mathrm{ecc}}_{\ell m}$ contains the eccentric corrections to the instantaneous contributions (both spinning and nonspinning, including the Newtonian part).

1.5.3.4 Comparison with numerical relativity

In Ref. [10], we incorporated those PN results in an eccentric-orbit EOB model, denoted `SEOBNRv4EHM`, and compared its predictions with NR simulations. Since eccentricity is a gauge-dependent quantity, its value in the model does not necessarily agree with the eccentricity used in NR. Thus, to compare the waveforms produced by the model with NR results, we vary the initial eccentricity and frequency used to evolve the equations of motion, compute the waveform, then align it with the NR waveform to find the set of initial conditions giving the best match with NR. Figure 1.19 shows an example for an eccentric waveform with mass ratio $q = 2$

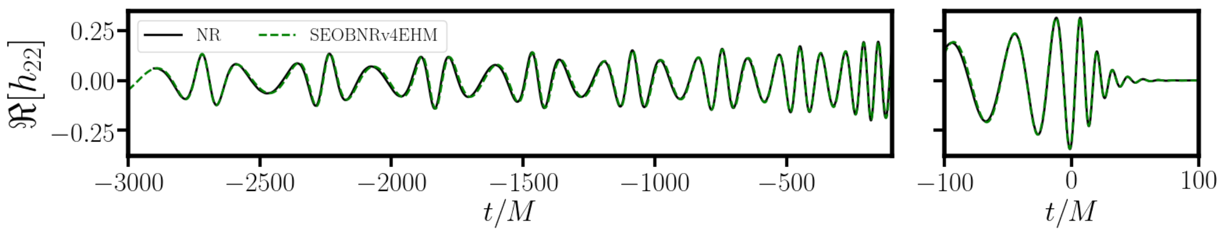

Figure 1.19: Comparison of the $(2, 2)$ waveform mode between `SEOBNRv4EHM` and an NR waveform with initial eccentricity $e_{\text{NR}} = 0.257$, mass ratio $m_2/m_1 = 2$, and zero spins. The mismatch is 0.35%. Figure from Ref. [10].

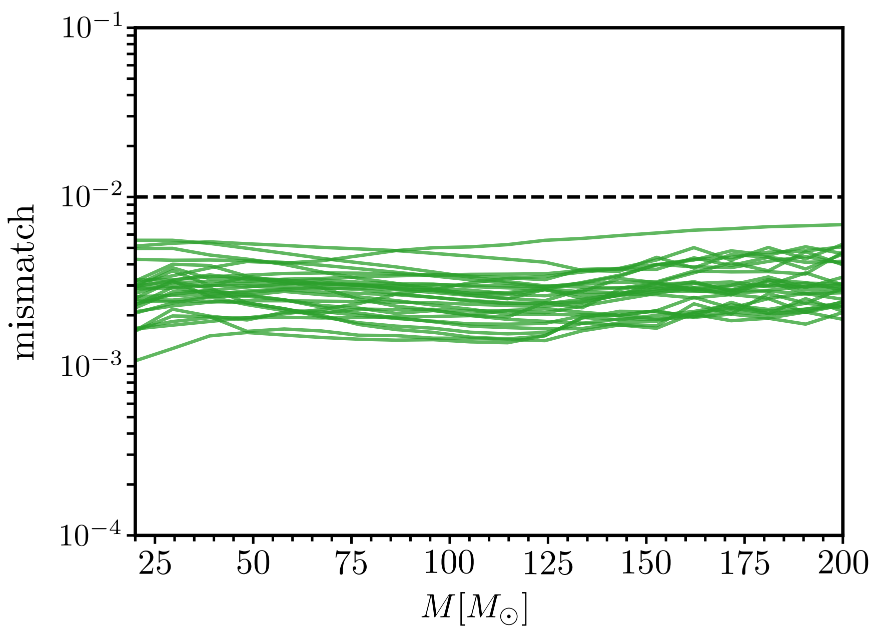

Figure 1.20: Mismatch between the `SEOBNRv4EHM` model and 28 NR simulations of eccentric binaries. The mismatch is less than 1%, indicating a good agreement. Figure adapted from Ref. [10].

and eccentricity $e_{\rm NR} = 0.257$, leading to a mismatch with the NR waveform of about 0.35%. The mismatch, also called unfaithfulness, is defined as a noise-weighted inner product between two waveforms maximized over a set of extrinsic parameters [398, 399].

We also compared our model with 28 publicly available NR simulations for eccentric orbits, which include configurations with mass ratios $m_2/m_1 \leq 3$, initial orbital eccentricity $e \leq 0.3$, and spin magnitudes ≤ 0.7. These NR waveforms were produced by the Simulating eXtreme Spacetimes (SXS) collaboration [41, 458]. For each waveform, we computed the mismatch between `SEOBNRv4EHM` and NR waveforms, finding it less than 1%, as shown in Fig. 1.20.

1.5.4 Energetics and scattering at fourth post-Minkowskian order

At 4PM (and 4PN) order, nonlocal-in-time (tail) effects contribute to the conservative dynamics. As discussed in § 1.5.1.1, these effects depend on the entire history of the binary, and are thus different between bound and unbound orbits. The 4PM conservative dynamics (including tail effects) was derived in Refs. [246, 247, 258, 259] for *hyperbolic orbits*. In Ref. [6] (Chapter 7), we assessed the accuracy of those results through comparisons with the PN approximation and NR simulations for the scattering angle and circular-orbit binding energy. We found that, while the 4PM and 3PN approximations give comparable results for bound orbits, the 4PM approximation becomes more accurate for hyperbolic orbits. We also incorporated the PM results in EOB Hamiltonians, which significantly improves the accuracy over PM-expanded Hamiltonians.

All GW detections so far have been consistent with bound-orbit inspirals, and there is no consensus in the literature [459–465] on the event rate for hyperbolic encounters, with the expected event rates varying between 0.001 to 0.39 per year for upcoming LIGO-Virgo-KAGRA runs, depending on the model [465]. Detecting GW bursts from hyperbolic orbits would have important implications on our understanding of dense stellar environments and the merger rate of compact objects. Therefore, studying the effect of scattering encounters on GWs and incorporating them in waveform models, may increase the likelihood of detecting them and inferring their parameters. We take a first step towards that goal by investigating the effect of hyperbolic-orbit PM results in the Hamiltonian on the scattering angle.

1.5.4.1 PM-expanded Hamiltonian and scattering angle

The 4PM Hamiltonian can be written in an isotropic gauge—depending explicitly on r and p^2 but not on the angular momentum L—as follows:

$$H_{\text{4PM}}^{\text{hyp}} = \sqrt{m_1^2 + p^2} + \sqrt{m_2^2 + p^2} + \sum_{n=1}^{4} \frac{G^n}{r^n} c_n, \tag{1.218}$$

where the 1PM and 2PM coefficients are given by [243]

$$\begin{aligned} c_1 &= \frac{\nu^2 M^2}{\Gamma^2 \xi}(1 - 2\gamma^2), \\ c_2 &= \frac{\nu^2 M^3}{\Gamma^2 \xi}\left[\frac{3}{4}(1 - 5\gamma^2) - \frac{4\nu\gamma(1 - 2\gamma^2)}{\Gamma\xi} - \frac{\nu^2(1 - \xi)(1 - 2\gamma^2)}{2\Gamma^3\xi^2}\right], \end{aligned} \tag{1.219}$$

with

$$\Gamma \equiv \frac{E}{M}, \qquad \xi \equiv \frac{E_1 E_2}{E^2}, \qquad \gamma \equiv \frac{p_1 \cdot p_2}{m_1 m_2} = \frac{E^2 - m_1^2 - m_2^2}{2 m_1 m_2}\,. \tag{1.220}$$

The 3PM and 4PM coefficients are lengthy and are given by Eq. (10) of Ref. [243] and Eq. (8) of Ref. [247]. The 3PM Hamiltonian is valid for both bound and unbound motion, but the nonlocal part of the 4PM coefficient c_4 has only been derived for hyperbolic orbits.

The radial action for hyperbolic orbits (see § 1.2.2.3) at 4PM order can be written schematically as

$$I_{r,4\text{PM}}^{\text{hyp}} = I_{r,3\text{PM}} - \frac{G^4 M^7 \nu^2 p^2}{16 E L^3} \left[\mathcal{M}_4^{\text{p}} + \nu \left(4\mathcal{M}_4^{\text{t}} \ln \frac{\sqrt{\gamma^2 - 1}}{2} + \mathcal{M}_4^{\pi^2} + \mathcal{M}_4^{\text{rem}} \right) \right], \tag{1.221}$$

where the 3PM part $I_{r,3\text{PM}}$ is valid for both bound and unbound motion. The terms $\mathcal{M}_4^{\cdot\cdot}$ are independent of the masses and are directly related to parts of the scattering amplitude [247]. The scattering angle can be obtained from the radial action using Eq. (1.102), which reads

$$\chi = -2\pi \frac{\partial I_r^{\text{hyp}}}{\partial L} - \pi. \tag{1.222}$$

To estimate the effect of the hyperbolic piece of the 4PM Hamiltonian, we calculate the PN-expanded circular-orbit binding energy and compare it to the energy calculated from a Hamiltonian valid for elliptic orbits. A 6PN bound-orbit EOB Hamiltonian was derived in Refs. [92, 93], which contains unknown coefficients at $\mathcal{O}(G^5)$ and higher orders, but is complete at $\mathcal{O}(G^4)$. Therefore, we can canonically transform the 6PN EOB Hamiltonian to isotropic gauge (the same as the 4PM Hamiltonian), truncate it at $\mathcal{O}(G^4)$, and analytically calculate the binding energy. We find that the difference between the elliptic- and hyperbolic-orbit binding energy at 4PM(4PN) order is given by

$$\begin{aligned} \bar{E}_{4\text{PM(4PN)}}^{\text{iso,hyp}} - \bar{E}_{4\text{PM(4PN)}}^{\text{iso,ell}} &= \nu x^5 \left[\frac{37933}{45} + \frac{1036\gamma_E}{45} - \frac{113847608 \ln 2}{45} \right. \\ &\qquad \left. - \frac{1472499 \ln 3}{20} + \frac{13671875 \ln 5}{12} \right] \\ &\simeq 14.94 \nu x^5 \,, \end{aligned} \tag{1.223}$$

where $x \equiv (M\Omega)^{2/3}$. That is, the disagreement is in the linear-in-ν coefficient, and is about 15% of the corresponding coefficient in $\bar{E}_{4\text{PM(4PN)}}^{\text{iso,ell}}$. In Fig. 1.21, we plot the fractional difference in the binding energy between hyperbolic and elliptic orbits at different PN orders, and for mass ratios

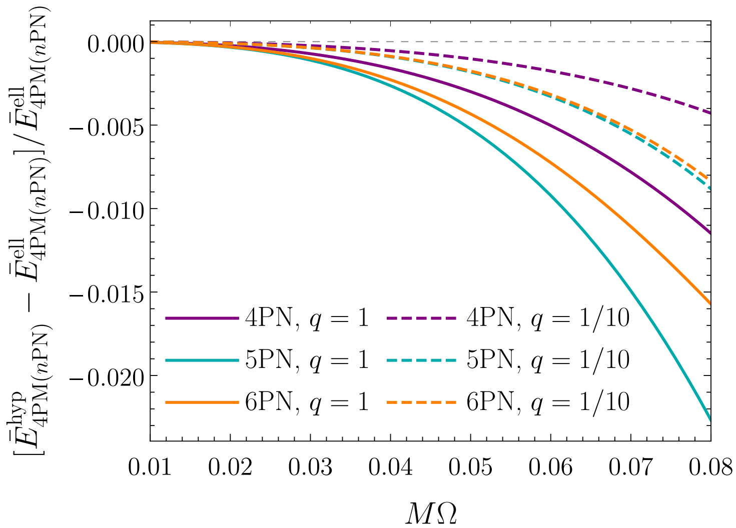

Figure 1.21: The fractional difference in the binding energy when computed from a hyperbolic-orbit Hamiltonian compared to an elliptic-orbit Hamiltonian. The energy is computed analytically at different PN orders, all truncated at 4PM order, and plotted for mass ratios $q = 1$ and $1/10$. Figure adapted from Ref. [6] (Chapter 7).

$q = 1$ and $q = 1/10$. We see that the fractional difference is $\lesssim 2\%$, which justifies applying the hyperbolic 4PM result to bound orbits. In Chapter 7 (see Fig. 7.3 there), we also complement the hyperbolic-orbit 4PM Hamiltonian with bound-orbit corrections at 4PN, 5PN, and 6PN orders, finding very small differences, further demonstrating that the hyperbolic piece has a small effect on the dynamics.

In the left panel of Fig. 1.22, we plot the binding energy calculated numerically from the Hamiltonian at different PM orders, and compare it with NR simulations for an equal-mass binary. We see that the 4PM Hamiltonian gives much better agreement with NR than Hamiltonians computed at lower PM orders. This is because the 4PM Hamiltonian contains the full 3PN information, which provides a significant improvement over the 2PN order.

A comparison of the 4PM results in the case of hyperbolic orbits can be performed through

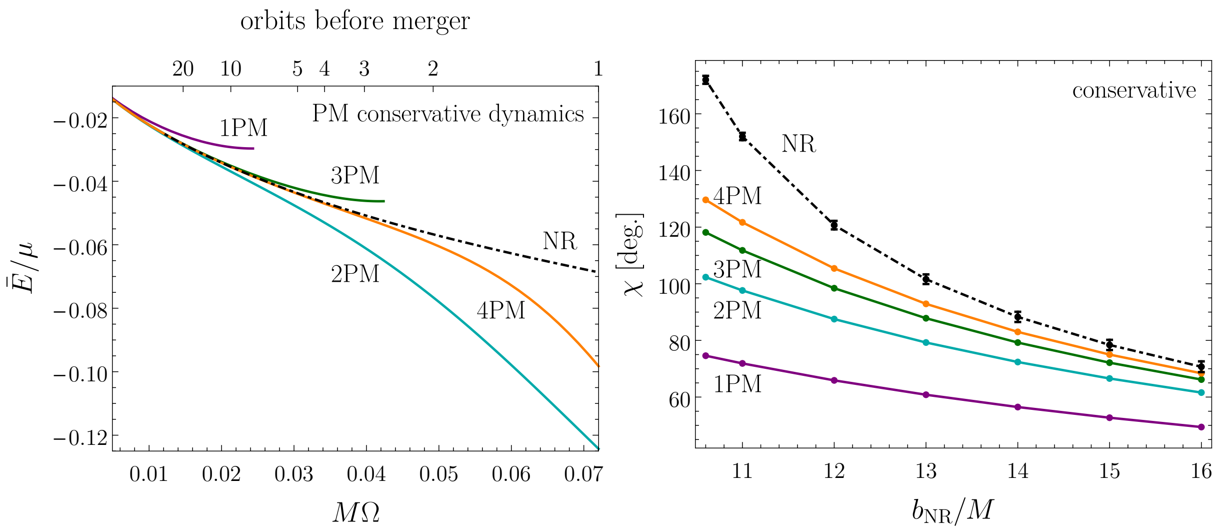

Figure 1.22: Binding energy for the PM-expanded Hamiltonian (left panel) and the PM-expanded scattering angle (right panel) compared with NR simulations for an equal-mass binary.

the scattering angle, which was computed from NR simulations in Ref. [466] for equal masses $q = 1$, initial asymptotic relative velocity $v \simeq 0.4$, and impact parameter $b_{\rm NR}$ ranging from $9M$ to $16M$. We see from the right panel of Fig. 1.22 that each PM order gives better agreement with NR than the lower orders, with an overall good agreement at 4PM, especially considering that these scattering angles are rather large while the PM expansion is an approximation away from a straight line.

1.5.4.2 PM-EOB Hamiltonians and scattering angle

Incorporating PM results in an EOB Hamiltonian has the advantage of improving the accuracy over PM-expanded Hamiltonians. We discussed in § 1.3.1 how to include PN results in an EOB Hamiltonian via a canonical transformation and matching to a PN-expanded Hamiltonian. For PM results, it is more convenient to calculate the gauge-invariant scattering angle from an ansatz for the EOB Hamiltonian, then match it to the PM-expanded scattering angle from Eq. (1.222).

We consider in Chapter 7 two ansatzes for a PM-EOB Hamiltonian: one based on the *post-Schwarzschild* (PS) gauge used in Refs. [237, 405], and another gauge, denoted PS* , that is given by

$$
\begin{aligned}
(H^{\text{eff,PS}^*})^2 = &\left(1 - \frac{2M}{r} + a_{2\text{PM}}\frac{M^2}{r^2} + a_{3\text{PM}}\frac{M^3}{r^3} + a_{4\text{PM}}\frac{M^4}{r^4}\right) \\
&\times \left[\mu^2 + \left(1 - \frac{2M}{r}\right)p_r^2 + \frac{L^2}{r^2}\right],
\end{aligned} \tag{1.224}
$$

with some unknown coefficients $a_{n\text{PM}}$ that are determined by matching to the scattering angle. In this ansatz, cf. Eq. (1.129), we choose the B potential to be the same as in the Schwarzschild metric, i.e., $B = 1/(1 - 2M/r)$, and include all the 4PM corrections into the A potential. The result for these coefficients is provided in Appendix L.

In the left panel of Fig. 1.23, we plot the binding energy calculated numerically from the PM-EOB Hamiltonian at different orders. We see that 4PM provides a significant improvement over the lower PM orders, even though the 4PM Hamiltonian is for hyperbolic orbits.

In the right panel of Fig. 1.23, we compute the scattering angle from the PM-EOB Hamiltonian by evolving the equations of motion without RR force, then reading off the final azimuthal angle after scattering. We find a very small disagreement with NR, which is why we plot the relative difference. Furthermore, since we are interested in assessing the accuracy of conservative results, we included the effect of RR as obtained from NR simulations through the initial conditions, as explained in Chapter 7 at the beginning of Sec. 7.5.

In both panels of Fig. 1.23, we also plot the binding energy and scattering angle obtained from an EOB Hamiltonian in the same gauge but with the a_{nPM} coefficients expanded up to 3PN

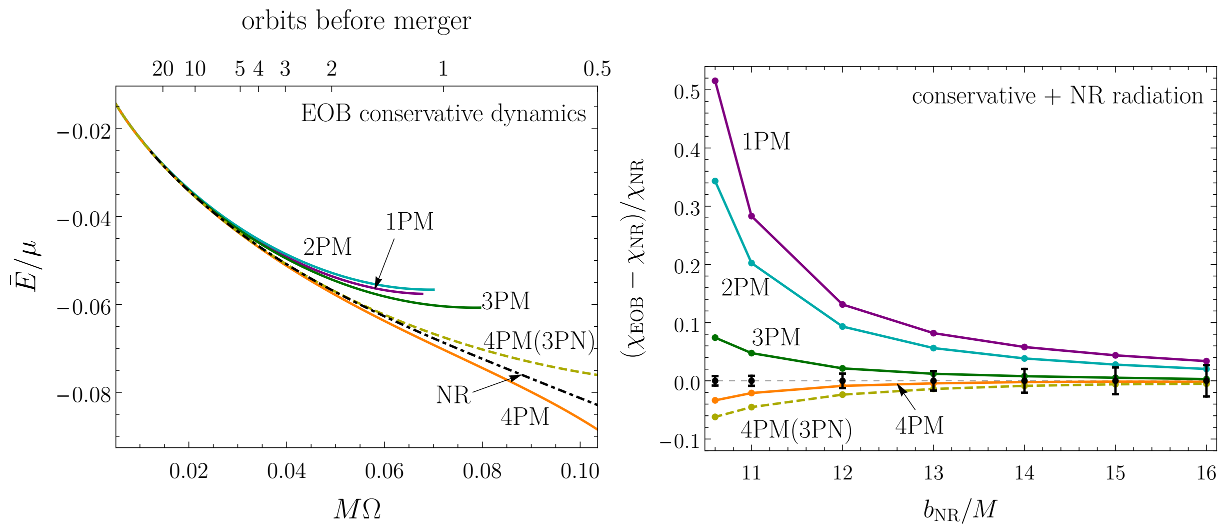

Figure 1.23: Binding energy (left panel) and scattering angle (right panel) for the PM-EOB Hamiltonian compared with NR.

order. We see that the 3PN expansion gives slightly better agreement with NR for the bound-orbit binding energy, while for scattering encounters, the full 4PM Hamiltonian leads to better results than the 3PN expansion of its coefficients.

1.5.5 Two-body dynamics in Einstein-Maxwell-dilaton theory

In Ref. [7] (Chapter 8), we studied the binary dynamics in Einstein-Maxwell-dilaton (EMd) theory, which originated as a low-energy limit of string theory [467, 468], and in which a massless scalar field can be generated by electrically-charged BHs. Astrophysical BHs are not expected to be electrically charged, since they would neutralize via spontaneous pair production [469] or interactions with astrophysical plasma [470] over timescales that grow with the mass-to-charge ratio of the fundamental particles. For electrons, this severely limits the charge that BHs can develop through accretion, and guarantees that any charged BH would discharge quickly. However, particles with much larger mass-to-charge ratios are predicted in models of minicharged dark matter [471–473] and dark photons [474–476]. It was argued in Ref. [477] that a charged BH in these models can acquire large electric charges and discharge on a much larger time scale than ordinary matter, under the assumption that the BH does not accrete ordinary charges. Studying EMd theory, and searching for its predictions in GW observations, can provide constraints on these dark matter models.

The action for EMd theory, in the Einstein frame, is given by

$$S = \frac{1}{16\pi} \int \mathrm{d}^4x \sqrt{-g} \left(R - 2g^{\mu\nu}\partial_\mu\varphi\partial_\nu\varphi - e^{-2a\varphi}F_{\mu\nu}F^{\mu\nu}\right) + S_m(\mathcal{A}(\varphi)g_{\mu\nu}, A_\mu, \Psi), \quad (1.225)$$

where φ is a scalar field (the dilaton), a is the dilaton coupling constant[4], $F_{\mu\nu} \equiv \nabla_\mu A_\nu - \nabla_\nu A_\mu$ is the electromagnetic field tensor, and S_m is the matter action. The action in the Jordan frame can be obtained after a conformal transformation $\tilde{g}_{\mu\nu} = \mathcal{A}^2(\varphi)g_{\mu\nu}$ with $\mathcal{A} = e^{a\varphi}$. Constraints on the theory were obtained from the spectra of accreting BHs [478] and the reflection spectrum of the disk [479], leading to $\mathcal{E}/Me^{a\varphi_0} \lesssim 0.1$, where $\mathcal{E}$ is the electric charge of the BH.

The metric for electrically-charged non-rotating BHs in EMd theory was derived in Ref. [467, 468]. Using that metric, we studied the geodesic motion of a test BH in the background metric of a more massive companion, wherein the scalar charge of the test BH decreases as it moves radially inwards. We found that the scalar charge exhibits a sharp transition, but we showed that it occurs very close to the horizon of the background BH and only if both BHs are nearly-extremally charged. Thus, we showed that binary BHs in EMd theory do not exhibit nonperturbative phenomena akin to dynamical scalarization (see Fig. 8.3 in Chapter 8).

[4]Not to be confused with the spin. We only consider nonspinning binaries in this subsection.

1.5.5.1 PN approximation for the conservative dynamics

To derive the 1PN conservative dynamics in EMd theory, we follow similar steps as in § 1.2.1.2, with a few changes. We start by splitting the action into the following pieces:

$$S = S_g + S_\varphi + S_{\text{em}} + S_m \,. \tag{1.226}$$

The gravitational action S_g is the same as in Eq. (1.34), while the dilaton part is given by

$$\begin{aligned} S_\varphi &\equiv -\frac{c^4}{8\pi G}\int \mathrm{d}t\mathrm{d}^3\boldsymbol{x}\sqrt{-g}g^{\mu\nu}\partial_\mu\varphi\partial_\nu\varphi \\ &\simeq -\frac{c^4}{8\pi G}\int \mathrm{d}t\mathrm{d}^3\boldsymbol{x}\left(-\partial_0\varphi\partial_0\varphi + \partial_i\varphi\partial_i\varphi\right), \end{aligned} \tag{1.227}$$

since φ is of order $1/c^2$. The electromagnetic part of the action, including the dilaton coupling, is given by

$$\begin{aligned} S_{\text{em}} &\equiv \frac{-1}{16\pi}\int \mathrm{d}t\mathrm{d}^3\boldsymbol{x}\sqrt{-g}e^{-2a\varphi}F_{\mu\nu}F^{\mu\nu} \\ &\simeq \frac{1}{8\pi}\int \mathrm{d}t\mathrm{d}^3\boldsymbol{x}\big[(1+2V-2a\varphi)\partial_i A_0\partial_i A_0 - \partial_j A_i\partial_j A_i - \partial_0 A_0\partial_0 A_0\big], \end{aligned} \tag{1.228}$$

where we used the Lorentz gauge condition $\partial_\mu A^\mu = 0$.

For the matter action S_m, each body is treated as a delta function with the dependence on the scalar field incorporated into the masses [200, 480], such that

$$S_m = -\sum_{\mathrm{i}}\int \mathrm{d}t\left[\mathfrak{m}_{\mathrm{i}}(\varphi)c^2\sqrt{-g_{\mu\nu}\,v_{\mathrm{i}}^\mu v_{\mathrm{i}}^\nu/c^2} - \frac{1}{c}\mathcal{E}_{\mathrm{i}}A_\mu v^\mu\right]. \tag{1.229}$$

where $\mathfrak{m}_{\mathrm{i}}(\varphi)$ is the field-dependent mass of particle i, $\mathcal{E}_{\mathrm{i}}$ is its electric charge, and $v_{\mathrm{i}}^\mu \equiv \mathrm{d}x_{\mathrm{i}}^\mu/\mathrm{d}t$. The field-dependent mass $\mathfrak{m}(\varphi)$ does not have a closed-form expression, but it can be expanded about the asymptotic/background value of the scalar field φ_0, such that

$$\mathfrak{m}(\varphi) = m\left[1 + \alpha\delta\varphi + \frac{1}{2}(\alpha^2+\beta)\delta\varphi^2 + \mathcal{O}\left(\frac{1}{c^6}\right)\right], \tag{1.230}$$

where $\delta\varphi \equiv \varphi - \varphi_0$, $m = \mathfrak{m}(\varphi_0)$ is the constant mass evaluated at φ_0, α is the (dimensionless) scalar charge given by

$$\alpha(\varphi) \equiv \frac{\mathrm{d}\ln\mathfrak{m}(\varphi)}{\mathrm{d}\varphi}\,, \qquad \beta(\varphi) \equiv \frac{\mathrm{d}\alpha(\varphi)}{\mathrm{d}\varphi}\,, \tag{1.231}$$

and to simplify the notation, we denote $\alpha \equiv \alpha(\varphi_0)$ and similarly for β.

Using the expansion of the field-dependent mass from Eq. (1.230), the matter action can be expanded as

$$\begin{aligned} S_m \simeq \int \mathrm{d}t\mathrm{d}^3\boldsymbol{x} \Bigg[\rho_g\bigg(- c^2 + \frac{1}{2}v^2 + Vc^2 + \frac{1}{8}\frac{v^4}{c^2} + \frac{3}{2}Vv^2 - \frac{1}{2}V^2c^2 - 4V_iv^ic\bigg) \\ + \rho_g\alpha\varphi\left(-c^2 + \frac{1}{2}v^2 + Vc^2\right) - \frac{1}{2}c^2\rho_g(\alpha^2+\beta)\varphi^2 + \rho_e\left(A_0 + \frac{1}{c}A_iv^i\right)\Bigg], \end{aligned} \tag{1.232}$$

where we define the mass density ρ_g and electric-charge density ρ_e by

$$\rho_g \equiv \sum_{\mathrm{i}} m_{\mathrm{i}}\delta^3(\boldsymbol{x} - \boldsymbol{x}_{\mathrm{i}}), \qquad \rho_e \equiv \sum_{\mathrm{i}} \mathcal{E}_{\mathrm{i}}\delta^3(\boldsymbol{x} - \boldsymbol{x}_{\mathrm{i}}). \tag{1.233}$$

From the expanded action, we obtain the field equations for V , V_i, φ, A_0 and A_i. Then, using these field equations and their solutions, the action can be written, after some simplifications, as

$$\begin{aligned} S = \int \mathrm{d}t\mathrm{d}^3\boldsymbol{x}\Bigg[\rho_g\left(-c^2 + \frac{1}{2}v^2 + \frac{v^4}{8c^2} + \frac{1}{2}Vc^2 + \frac{3}{4}Vv^2 - 2V_iv^ic\right) + \rho_e\left(\frac{1}{2}A_0 + \frac{1}{2c}A_iv^i\right) \\ + \frac{1}{2}\rho_g\alpha\varphi\left(-c^2 + \frac{1}{2}v^2\right) + \frac{1}{2}\rho_eA_0V - \frac{1}{2}a\rho_eA_0\varphi + \frac{G}{4c^2}\rho_g(1+a\alpha)A_0^2\Bigg]. \end{aligned} \tag{1.234}$$

Substituting the solution for the field equations gives the 1PN Lagrangian, from which we obtain the following center-of-mass Hamiltonian:

$$\begin{aligned} H_{\text{EMd}} = Mc^2 + \frac{p^2}{2\mu} - \frac{G_{12}M\mu}{r} \\ + \frac{1}{c^2}\Bigg\{ - \frac{1}{8}(1-3\nu)\frac{p^4}{\mu^3} - \frac{G_{12}M}{2\mu r}\left[\left(\frac{3-\alpha_1\alpha_2}{1+\alpha_1\alpha_2 - \frac{\mathcal{E}_1\mathcal{E}_2}{M\mu}} + \nu\right)p^2 + \nu p_r^2\right] \end{aligned}$$

$$
+\frac{M^2\mu}{2r^2}\left[(1+\alpha_1\alpha_2)^2+X_2\alpha_2^2\beta_1+X_1\alpha_1^2\beta_2+X_1\frac{\mathcal{E}_2^2}{M\mu}(1+a\alpha_1)+X_2\frac{\mathcal{E}_1^2}{M\mu}(1+a\alpha_2)\right.
$$

$$
\left.\left.-2\frac{\mathcal{E}_1\mathcal{E}_2}{M\mu}\left(1+a\alpha_1X_1+a\alpha_2X_2\right)\right]\right\}+\mathcal{O}\left(\frac{1}{c^4}\right), \tag{1.235}
$$

where $G_{12}\equiv 1+\alpha_1\alpha_2-\mathcal{E}_1\mathcal{E}_2/(M\mu)$, $X_1\equiv m_1/M$, and $X_2\equiv m_2/M$.

1.5.5.2 Dissipative dynamics at next-to-leading PN order

In § 1.2.1.3, we described how the energy flux is calculated in GR at 1PN order. The same steps can be performed in EMd theory but the final result also depends on the scalar and electric charges. In addition to the tensor flux, scalar and vector (electromagnetic) energy fluxes also exist in EMd theory. In a PN expansion, the leading-order terms are the scalar and vector dipole fluxes, which are $\mathcal{O}(1/c^3)$ (1.5PN), while the leading-order tensor flux is $\mathcal{O}(1/c^5)$ (2.5PN), which is the same as the next-to-leading order scalar and vector fluxes. The total energy flux is the sum of these fluxes, that is

$$
\Phi_E=\Phi_E^S+\Phi_E^V+\Phi_E^T. \tag{1.236}
$$

The details of the derivation of the total energy flux in EMd is provided in Appendix N; the leading orders read

$$
\Phi_E^S=\frac{1}{3c^3}\left(\frac{G_{12}M\mu}{r^2}\right)^2(\alpha_1-\alpha_2)^2+\mathcal{O}\left(\frac{1}{c^5}\right), \tag{1.237}
$$

$$
\Phi_E^V=\frac{2}{3c^3}\left(\frac{G_{12}M\mu}{r^2}\right)^2\left(\frac{\mathcal{E}_1}{m_1}-\frac{\mathcal{E}_2}{m_2}\right)^2+\mathcal{O}\left(\frac{1}{c^5}\right), \tag{1.238}
$$

$$
\Phi_E^T=\frac{8}{15c^5}\left(\frac{G_{12}M\mu}{r^2}\right)^2\left(12v^2-11\dot{r}^2\right)+\mathcal{O}\left(\frac{1}{c^7}\right), \tag{1.239}
$$

where we see that the scalar and vector fluxes vanish for equal charges at leading order.

From the energy flux and binding energy, we can compute the Fourier-domain gravitational waveform in the stationary-phase approximation (SPA), which can be used since the GW phase evolves much more rapidly than the amplitude during the inspiral. We begin by decomposing the waveform modes into an amplitude and a phase

$$h_{\ell m}(t) = A_{\ell m}(t) e^{im\phi(t)}, \tag{1.240}$$

where $\phi(t)$ is the orbital phase of the binary, then take the Fourier-transform

$$\tilde{h}_{\ell m}(f) = \int_{-\infty}^{\infty} \mathrm{d}t\, h_{\ell m}(t) e^{-2i\pi f t}. \tag{1.241}$$

Since the amplitude $A_{\ell m}$ and orbital frequency Ω evolve more slowly than the orbital phase, $|\dot{A}_{\ell m}/A_{\ell m}| \ll \Omega$ and $|\dot{\Omega}| \ll \Omega^2$, we can approximate the above integral by expanding the integrand about the time at which the complex phase is stationary. The SPA waveform for the $(2,2)$ mode can be written as

$$\tilde{h}_{22}^{\text{SPA}}(f) \equiv \mathcal{A}_{22}(f) e^{-i\psi_{22}(f) - i\pi/4}, \tag{1.242}$$

with the phase given by

$$\psi_{22}(f) = 2\pi f t_{\text{ref}} - \phi_{\text{ref}} + \frac{2}{G_{12}M} \int_{v_f}^{v_{\text{ref}}} \left(v_f^3 - v_\Omega^3\right) \frac{E'(v_\Omega)}{\Phi_E(v_\Omega)} \mathrm{d}v_\Omega, \tag{1.243}$$

where ϕ_{ref} and t_{ref} refer to an arbitrary reference point in the evolution of the binary, $v_\Omega \equiv (G_{12}M\Omega)^{1/3}$, and $v_f \equiv (\pi G_{12} M f)^{1/3}$, with f being the GW frequency.

To evaluate the integral in Eq. (1.243), we need to distinguish between two regimes: one in which the inspiral is driven by the tensor quadrupole flux, and another in which the inspiral is driven by the dipole flux. If the electric/scalar charges are small, then the tensor flux dominates and we can approximate the integrand in Eq. (1.243) by

$$\frac{E'(v_\Omega)}{\Phi_E(v_\Omega)} \simeq \frac{E'(v_\Omega)}{\Phi_E^T(v_\Omega)} \left[1 - \frac{\Phi_E^S(v_\Omega) + \Phi_E^V(v_\Omega)}{\Phi_E^T(v_\Omega)}\right]. \tag{1.244}$$

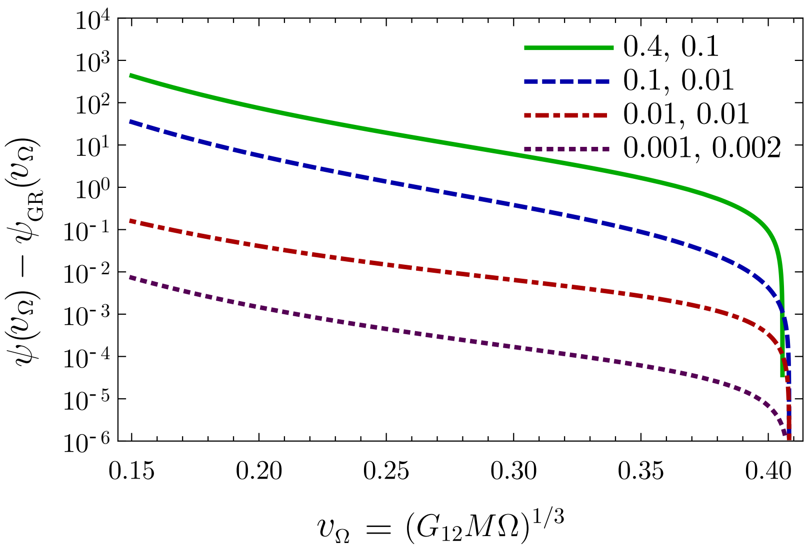

Figure 1.24: Phase difference in radians between EMd theory and GR as a function of v_Ω, computed in the quadrupole-driven regime, for equal masses, coupling constant $a = 1$, and various charge-to-mass ratios $\mathcal{E}_{\rm i}/m_{\rm i}$. Figure from Ref. [7] (Chapter 8).

Then, we expand the integrand using the next-to-leading order fluxes, and evaluate the integral, resulting in the quadrupole-driven phase

$$\psi^{\rm QD}(f) = 2\pi f t_{\rm ref} - \phi_{\rm ref} + \frac{1}{v_\Omega^5}\left[\frac{\rho_{-2}^{\rm QD}}{v_\Omega^2} + \rho_0^{\rm QD} + \rho_2^{\rm QD} v_\Omega^2 + \mathcal{O}\left(v_\Omega^4\right)\right], \tag{1.245}$$

with

$$\rho_{-2}^{\rm QD} = -\frac{5G_{12}}{7168\nu}\left[2\left(\frac{\mathcal{E}_1}{m_1} - \frac{\mathcal{E}_2}{m_2}\right)^2 + (\alpha_1 - \alpha_2)^2\right], \tag{1.246}$$

and the other lengthy coefficients given by Eq. (8.64a).

To see how the GW phase in EMd differs from GR, we plot in Fig. 1.24 the difference in phase between EMd theory with $a = 1$ and GR. We see that for dimensionless charge-to-mass ratios[5] $\mathcal{E}_i/m_i \lesssim 0.01$, the two waveforms differ by less than one radian over the frequency range of a ground-based GW detector. Furthermore, we checked that the phase difference from our PN

[5]The maximum charge for BHs in EMd theory is $\mathcal{E}_{\rm max} = e^{-a\varphi_0}\sqrt{1+a^2}M$, which is greater than the charge of an extremal Reissner-Nordström BH.

results is consistent with the results of Ref. [481], in which the authors performed NR simulations in EMd theory for charge-to-mass ratios $\mathcal{E}_i/m_i \lesssim 10^{-3}$.

1.5.6 Theory-agnostic approach to spontaneous and dynamical scalarization

Spontaneous scalarization [482] is a non-perturbative phenomenon in several modified theories of gravity [483–508], in which compact objects undergo a phase transition in the strong-field regime due to the spontaneous symmetry breaking of the scalar field, thus acquiring a scalar charge. This phenomenon is analogous to spontaneous magnetization, in which a ferromagnetic material undergoes a phase transition below a certain critical temperature, as illustrated in Fig. 1.25. In a binary system, scalar charges can similarly manifest as the separation between the binary components decreases (Fig. 1.26). This phenomenon is called *dynamical scalarization*, and it was shown to exist for binary NSs in scalar-tensor theories [484, 509] and for binary BHs in scalar-Gauss-Bonnet gravity [510–512].

An effective-action model for dynamical scalarization was introduced in Ref. [513] for a specific class of scalar-tensor theories [200, 202, 482]. Building on that model, we developed in Ref. [8] (Chapter 9) a *theory-agnostic* effective-field-theory approach for describing spontaneous scalarization, and showed that all theories that exhibit spontaneous scalarization also manifest dynamical scalarization. We applied this approach to Einstein-Maxwell-scalar (EMS) theory [514] as a simple example, while assuming the scalar field changes slowly (adiabatically). We later extended our effective-action model in Ref. [9] (Chapter 10) to account for the dynamical evolution of the scalar field during the phase transition, and applied it to binary NSs in a scalar-tensor theory, demonstrating how dynamical scalarization effects can be incorporated in GW models.

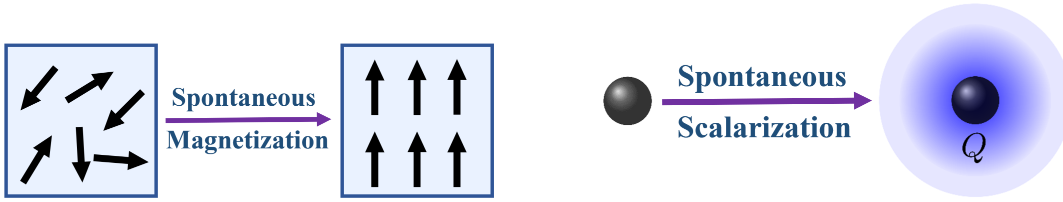

Figure 1.25: In the spontaneous magnetization of a ferromagnetic material, the spins align below a certain critical temperature. Analogously, spontaneous scalarization appears above a critical compactness (in scalar-tensor theories).

Figure 1.26: Illustration of dynamical scalarization in a binary system.

1.5.6.1 Effective-action model

The field part of the action in a generic gravity theory with an extra scalar field can be written, in the Einstein-frame, as

$$S_{\text{field}} = \int \mathrm{d}^4x \, \frac{\sqrt{-g}}{16\pi} \left(R - 2\partial_\mu \varphi \partial^\mu \varphi - f[g, \varphi^2, \dots] \right), \tag{1.247}$$

where f is some function of the metric, scalar field, and possibly matter degrees of freedom. The scalar field equation from that action reads

$$\Box \varphi = m_{\text{eff}}^2 \, \varphi, \qquad m_{\text{eff}}^2 \equiv \frac{1}{2} \frac{\partial f}{\partial \varphi^2}. \tag{1.248}$$

The scalar field φ can be decomposed into Fourier modes with frequency ω and wave vector $\boldsymbol{k}$, such that $\omega^2 \approx \boldsymbol{k}^2 + m_{\text{eff}}^2$. If m_{eff}^2 is sufficiently negative, then ω^2 is also negative, leading to a tachyonic instability that drives the system away from the unscalarized GR solution, breaking the scalar-inversion symmetry $\varphi \to -\varphi$. For a scalarized equilibrium configuration to exist, this mode instability must saturate in the nonlinear regime [515]. These two conditions, namely the instability due to $m_{\text{eff}}^2 < 0$ and its nonlinear saturation, are satisfied in the theories mentioned above that permit stable scalarized solutions.

The matter part of the action in scalar-tensor gravity for a compact object is given by a point-particle moving along a worldline $y^\mu(\tau)$, which reads

$$S_{\text{CO}}^{\text{inst}} = -\int \mathrm{d}\tau\, m_E(\varphi), \tag{1.249}$$

where m_E is the Einstein-frame mass depending on the external scalar field $\varphi(y^\mu)$. This action is valid for an instantaneous response of the compact object to the external scalar field φ.

A simple model for scalarization can be realized in an effective-theory approach. We split the fields of the full theory into short (UV) and long (IR) wavelength regimes, e.g. $\varphi = \varphi^{\text{IR}} + \varphi^{\text{UV}}$, then spatially average over the UV parts. This effectively shrinks the compact object to a point whose effective action is an integral over a worldline $y^\mu(\tau)$ (see Fig. 1.27 for an illustration). Dynamical variables representing the internal dynamics are evolved along the worldline, and we include in the effective action a dynamical variable $q(\tau)$ representing the monopolar scalar oscillation mode that becomes linearly unstable at scalarization.

The effective action can be constructed by writing an ansatz respecting certain symmetries: scalar-inversion, diffeomorphism, worldline-reparametrization, and time-reversal invariance. In addition, an oscillator equation for the mode $q(\tau)$ driven by the IR field φ^{IR} can be written, respecting these symmetries, as

$$c_{\dot{q}^2}\ddot{q} + V'(q) = \varphi^{\text{IR}}(y), \tag{1.250}$$

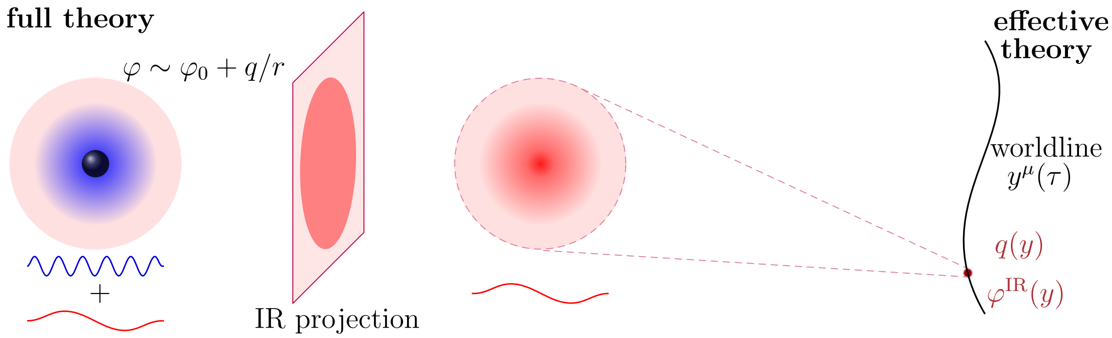

Figure 1.27: An illustration of the theory-agnostic approach of Ref. [8]. We split the fields of the full theory into small (UV) and long (IR) wavelength regimes, and integrate out the UV parts, effectively shrinking the compact object to a point whose effective action is an integral over a worldline. Then, we write an ansatz for an effective action respecting certain symmetries, and obtain a mapping between the quantities of the full and effective theories, such as identifying the scalar charge Q with a dynamical variable q.

where we assume the coefficient $c_{\dot{q}^2} > 0$. Scalar inversion in the effective theory reads $\varphi^{\text{IR}} \to -\varphi^{\text{IR}}$ and $q \to -q$, which means that the potential $V(q)$ must be even in q, and we can express it as a polynomial expansion, such that

$$V(q) = \frac{c_{(2)}}{2} q^2 + \frac{c_{(4)}}{4!} q^4 + \ldots , \tag{1.251}$$

where $c_{(2)}$ and $c_{(4)}$ are constant coefficients that can be matched to a specific theory, or constrained directly from observations.

A generic effective action that leads to the oscillator equation (1.250) around the critical point can thus be constructed as

$$S_{\text{NS}}^{\text{crit}} = \int d\tau \left[\frac{c_{\dot{q}^2}}{2} \dot{q}^2 + \varphi(y) q - m(q) + \mathcal{O}\left(\frac{d^2}{r^2}\right) \right] , \tag{1.252}$$

where we include terms up to a given power in the cutoff between IR and UV scales (the size of the compact object d). We also define

$$m(q) \equiv m_{(0)} - \varphi_0 q + \underbrace{\frac{c_{(2)}}{2!}q^2 + \frac{c_{(4)}}{4!}q^4 + \mathcal{O}\left(\frac{d^2}{r^2}\right)}_{V(q)}, \tag{1.253}$$

and include a possible cosmological/asymptotic value of the scalar field φ_0. The coefficient $m_{(0)}$ has the interpretation of the body's ADM mass in GR when $q = 0$.

If the external scalar field is not changing too rapidly, then $\dot{q} \approx 0$. In that case, varying the effective action with respect to q yields

$$\varphi = \frac{dm}{dq} = \frac{dV}{dq} = c_{(2)}q + \frac{c_{(4)}q^3}{3!} + \mathcal{O}\left(\frac{d^2}{r^2}\right), \tag{1.254}$$

then matching the UV and IR fields leads to the following relation:

$$m(q) = m_E(\varphi) + \varphi q, \tag{1.255}$$

which can be understood as a Legendre transformation. In analogy with thermodynamics, $m_E(\varphi)$ is the gravitational mass of the system, while $m(q)$ represents the "gravitational free energy" of the body, with $-\varphi q$ as the potential energy. This means that $m(q)$ serves as a better representation than $m_E(\varphi)$ for the behavior of the compact object near the critical point. In particular, we find that spontaneous scalarization occurs at $m'(q) = 0$ with nonzero q, i.e. the stable solutions for spontaneous scalarization occur at the minima of the potential $V(q)$.

1.5.6.2 Application to Einstein-Maxwell-scalar theory

As an example for how to apply the theory-agnostic approach described above, we consider Einstein-Maxwell-scalar (EMS) theory, in which electrically-charged BHs can spontaneously scalarize, and the action is given by [514]

$$S_{\text{field}} = \int \mathrm{d}^4x \, \frac{\sqrt{-g}}{16\pi}\left[R - 2\partial_\mu\varphi\partial^\mu\varphi - e^{-a\varphi^2}F^{\mu\nu}F_{\mu\nu}\right], \tag{1.256}$$

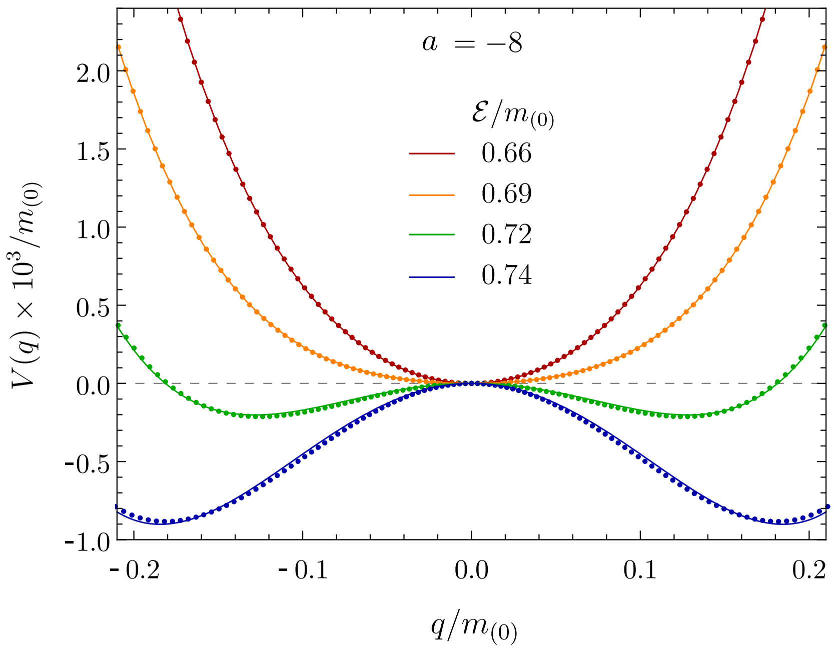

Figure 1.28: The potential $V(q)$ in EMS theory with coupling constant $a = -8$ and various electric charges. The numerical solutions and polynomial fits are indicated with points and lines, respectively. Figure adapted from Ref. [8] (Chapter 9).

where a is a coupling constant and $F_{\mu\nu}$ is the electromagnetic field tensor. The dependence on φ^2 allows for stable scalarized solutions, unlike the linear-in-φ dependence of EMd theory. Since the scalar field only couples to the electromagnetic field, this action can be considered a modified theory of electrodynamics, which makes it a simpler example than EMd or scalar-tensor theories, in which the scalar field couples non-minimally to gravity.

For an isolated BH in EMS theory, we numerically compute the ADM mass $m_E(\varphi_\infty)$ and scalar charge $q(\varphi_\infty)$ for different values of the asymptotic scalar field φ_∞, then compute $m(q)$ through $m(q) = m_E(\varphi_\infty) + \varphi_\infty q(\varphi_\infty)$. After that, we perform a numerical fit to the polynomial in Eq. (1.253) to determine the coefficients $c_{(2)}$ and $c_{(4)}$. In Fig. 1.28, we plot the potential $V(q)$ for different values of the electric charge $\mathcal{E}$ and for coupling constant $a = -8$. We see that for electric charges smaller than a certain value, the coefficient $c_{(2)} > 0$, which means that the minimum of $V(q)$ is at $q = 0$, implying that the GR solution is stable. For larger electric charges, $c_{(2)} < 0$ and the minima of $V(q)$ correspond to nonzero values of the scalar charge, implying that scalarized solutions are stable. Thus, our approach allows one to easily determine the values of the coupling constant and the electric charge at which spontaneous scalarization occurs without performing a perturbative stability analysis.

To describe dynamical scalarization in EMS theory, we derive from the effective action a two-body Lagrangian, at leading order, which is given by

$$
\begin{aligned}
L^{\mathrm{LO}} = & -m_A\left[1-\frac{\dot{\boldsymbol{y}}_A^2}{2}\right]-m_B\left[1-\frac{\dot{\boldsymbol{y}}_B^2}{2}\right]+\frac{c_{\dot{q}^2,A}}{2}\dot{q}_A^2+\frac{c_{\dot{q}^2,B}}{2}\dot{q}_B^2 \\
& +\frac{m_A m_B}{r}+\frac{\mathcal{E}_A\mathcal{E}_B}{r}+\frac{q_A q_B}{r},
\end{aligned}
\tag{1.257}
$$

where $m_A \equiv m_{(0),A} + \frac{c_{(2),A}}{2}q_A^2 + \frac{c_{(4),A}}{4!}q_A^4$, and similarly for m_B. Assuming $\dot{q} \approx 0$, we obtain the following Hamiltonian:

$$
H = m_A + m_B + \frac{\boldsymbol{p}_A^2}{2m_A} + \frac{\boldsymbol{p}_B^2}{2m_B} - \frac{m_A m_B}{r} + \frac{\mathcal{E}_A\mathcal{E}_B}{r} - \frac{q_A q_B}{r}. \tag{1.258}
$$

For identical bodies $q_A = q_B \equiv q$, and neglecting PN corrections, the equation of motion for q reads

$$
0 = \frac{\partial H}{\partial q} \simeq -2q\left[\frac{1}{r} - c_{(2)} - \frac{c_{(4)}}{6}q^2\right]. \tag{1.259}
$$

This equation has three solutions, and their stability is determined from the condition $\partial^2 H/\partial q^2 \geq 0$. Those stable solutions are given by

$$
q = \begin{cases} 0 & \text{for} \quad 1/r \leq c_{(2)} \\ \pm\sqrt{\dfrac{6}{c_{(4)}}}\sqrt{\dfrac{1}{r} - c_{(2)}} & \text{for} \quad 1/r \geq c_{(2)} \end{cases}, \tag{1.260}
$$

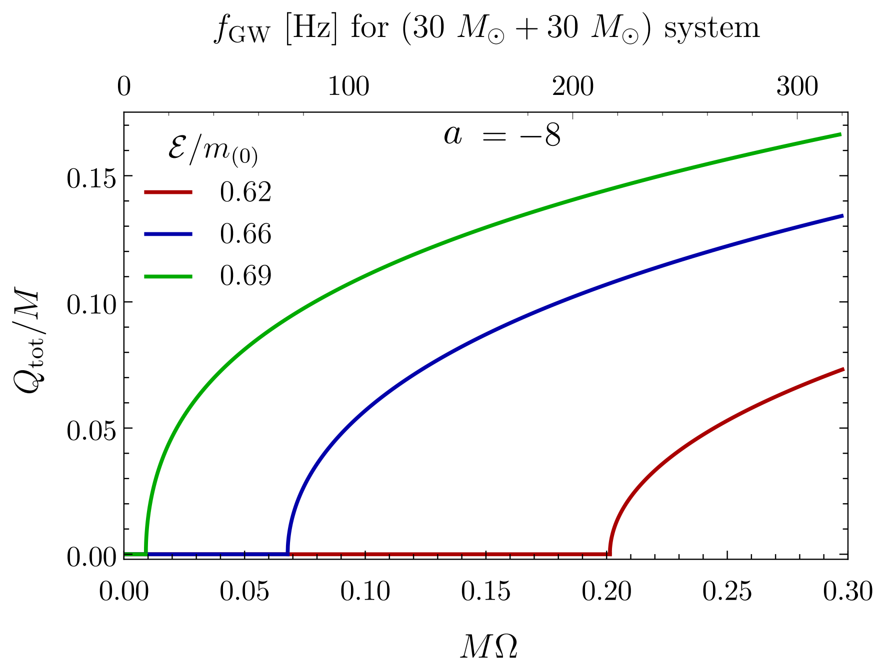

Figure 1.29: Total scalar charge $Q_{\rm tot}$ of an equal-mass binary as a function of the orbital frequency Ω, or GW frequency $f_{\rm GW} = \Omega/\pi$, for coupling constant $a = -8$. Figure adapted from Ref. [8] (Chapter 9).

which contains a phase transition at $r = 1/c_{(2)}$, with the GR solution stable at large separations, while the scalarized solution is stable for $r \leq 1/c_{(2)}$.

For circular orbits, the orbital frequency is given by Kepler's law as

$$\Omega^2 \simeq \frac{m_A + m_B}{r^3}\left(1 + \frac{q_A q_B}{m_A m_B} - \frac{\mathcal{E}_A \mathcal{E}_B}{m_A m_B}\right). \tag{1.261}$$

In Fig. 1.29, we plot the total scalar charge of the binary $Q_{\rm tot} \equiv q_A + q_B$ as a function of the orbital frequency, for coupling constant $a = -8$ and various electric charges. The scalar charge vanishes before the onset of dynamical scalarization, then increases abruptly at some critical frequency, and after that grows as $1/\sqrt{r}$.

1.5.6.3 Binary dynamics beyond the adiabatic approximation

In the previous subsection, we assumed that the external scalar field does not vary rapidly, so we used the quasi-stationary (adiabatic) approximation $\dot{q} \approx 0$. In Ref. [9] (Chapter 10), we incorporated the effect of $\dot{q}$ and explored the full dynamical evolution of q around the scalarization phase transition.

The two-body Hamiltonian, at leading order, is given by Eq. (1.258). In the center-of-mass frame, and for zero electric charges, the Hamiltonian reads

$$H = m_A + m_B + \frac{\boldsymbol{p}^2}{2\mu} + \frac{p_{q,A}^2}{2c_{\dot{q}^2,A}} + \frac{p_{q,B}^2}{2c_{\dot{q}^2,B}} - \frac{M\mu}{r} - \frac{q_A q_B}{r}, \tag{1.262}$$

where $\boldsymbol{p} \equiv \boldsymbol{p}_A = -\boldsymbol{p}_B$ is the center-of-mass momentum, $p_{q,A/B}$ are the canonical conjugates to the variables $q_{A/B}$, and the total and reduced masses are defined in terms of the constant masses $m^0_{A/B}$ by

$$M \equiv m_A^0 + m_B^0, \qquad \mu \equiv \frac{m_A^0 m_B^0}{M}. \tag{1.263}$$

The equations of motion are given by

$$\begin{aligned}
\dot{r} &= \frac{\partial H}{\partial p_r}, & \dot{p}_r &= -\frac{\partial H}{\partial r} + \mathcal{F}_r^{\text{quad}} + \mathcal{F}_r^{\text{dip}}, \\
\dot{\phi} &= \frac{\partial H}{\partial L}, & \dot{L} &= -\frac{\partial H}{\partial \phi} + \mathcal{F}_\varphi^{\text{quad}} + \mathcal{F}_\varphi^{\text{dip}}, \\
\dot{q}_A &= \frac{\partial H}{\partial p_{q,A}}, & \dot{p}_{q,A} &= -\frac{\partial H}{\partial q_A} + \mathcal{F}_{q_A}^{\text{mon}}, \\
\dot{q}_B &= \frac{\partial H}{\partial p_{q,B}}, & \dot{p}_{q,B} &= -\frac{\partial H}{\partial q_B} + \mathcal{F}_{q_B}^{\text{mon}},
\end{aligned} \tag{1.264}$$

where we include the RR forces at leading PN orders. The scalar monopole and dipole RR forces are derived in Appendix R, and are given by

$$\mathcal{F}_{q_A}^{\text{mon}} = \mathcal{F}_{q_B}^{\text{mon}} = -\dot{q}_A(t) - \dot{q}_B(t), \tag{1.265}$$

$$\mathcal{F}_r^{\rm dip} = \frac{2}{3}\frac{M}{\mu r^3} p_r \left(\frac{m_B^0}{M} q_A - \frac{m_A^0}{M} q_B\right)^2 \left(1 + \frac{q_A q_B}{M\mu}\right), \tag{1.266}$$

$$\mathcal{F}_\varphi^{\rm dip} = -\frac{1}{3}\frac{ML}{\mu r^3} \left(\frac{m_B^0}{M} q_A - \frac{m_A^0}{M} q_B\right)^2 \left(1 + \frac{q_A q_B}{M\mu}\right), \tag{1.267}$$

while the tensor quadrupole force reads [402]

$$\mathcal{F}_r^{\rm quad} = \frac{8}{15}\frac{M\mu^2}{r^3}\dot{r}\left(21 r^2 \dot{\phi}^2 - \frac{M}{r}\right), \tag{1.268}$$

$$\mathcal{F}_\varphi^{\rm quad} = -\frac{8}{15}\frac{M\mu^2}{r}\dot{\phi}\left(-\dot{r}^2 + 2r^2\dot{\phi}^2 + 2\frac{M}{r}\right). \tag{1.269}$$

The coefficients $c_{(2)}$ and $c_{(4)}$ can be determined from numerical solutions for an isolated object in the full theory, as described above, by fitting a polynomial of the form (1.253) to obtain $m(q)$. To determine the coefficient $c_{\dot{q}^2}$, we start from the oscillator equation for q, Eq. (1.250), which can be approximated in the force-free case by

$$\ddot{q} \simeq -\frac{c_{(2)}}{c_{\dot{q}^2}} q \equiv -\omega_0^2 q. \tag{1.270}$$

Then, we can match ω_0 to the (complex) scalar-led radial mode frequency ω_φ obtained from neutron-star perturbation theory [516], leading to

$$c_{\dot{q}^2} = \frac{c_{(2)}}{|\omega_\varphi|^2}. \tag{1.271}$$

As an application, we consider the Damour and Esposito-Farese (DEF) class of scalar-tensor theories. The action for DEF theory is given by Eq. (1.153) with the potential $U(\varphi) = 0$ and the coupling function $\mathcal{A}(\varphi) = \exp(\beta\varphi^2/2)$. We obtain numerical results for the three coefficients $c_{(2)}$, $c_{(4)}$, and $c_{\dot{q}^2}$ for NSs in DEF theory with $\beta = -5$. The values of these coefficients are shown in Figs. 10.2 and 10.4 in Chapter 10.

We then evolve the equations of motion (1.264), for an equal-mass binary with baryon mass $M_{bA} = M_{bB} = 1.18 M_\odot$, initial eccentricity $e = 0.3$, and initial radial separation at apastron $r_a \simeq$

$33.6M$. In Fig. 1.30, we plot $r(t)$ and $q(t)$, on a logarithmic and a linear scale. The horizontal and vertical dashed lines in the figure indicate the maximum radial separation allowing for dynamical scalarization $r_{\rm DS} \equiv 1/c_{(2)}$ and the time $t_{\rm DS}$ at which $r(t) = r_{\rm DS}$. We see that the scalar charge decreases until shortly after the mean separation $\bar{r}$ crosses $r_{\rm DS}$, then the scalar charge increases exponentially with small modulations until it reaches saturation, at which point the growth of q is proportional to $1/\sqrt{r}$. The small oscillations in the scalar charge before scalarization are due to the binary entering and exiting the dynamical scalarization region.

To compare the adiabatic approximation of the scalar charge with the full dynamical evolution, we plot both in Fig. 1.31. That is, we plot the approximate analytic solution from Eq. (1.260), and the result of numerically evolving the equations of motion (1.264). We see very good agreement between the two, except around the scalarization phase transition. This is because including the coefficient $c_{\dot{q}^2}$ accounts for the time scale of the exponential growth of the scalar charge, delaying reaching saturation.

We also plot in Fig. 1.32 the binding energy as a function of the orbital frequency for a configuration with baryon mass $M_{bA} = M_{bB} = 1.17 M_\odot$ on a quasi-circular orbit. We define the binding energy as the value of the Hamiltonian minus the constant ADM mass, i.e. $\bar{E} \equiv H - M$, which is given in terms of frequency by

$$\bar{E} = m_A + m_B - M + \frac{p_{q,A}^2}{2c_{\dot{q}^2,A}} + \frac{p_{q,B}^2}{2c_{\dot{q}^2,B}} - \frac{\mu}{2}(M\Omega)^{2/3}\left(1 + \frac{q_A q_B}{\mu M}\right)^{2/3}. \tag{1.272}$$

We see from the figure that the binding energy after scalarization decreases less rapidly than in GR, due to the sudden increase in the orbital frequency, causing the binary to become more tightly bound, which qualitatively agrees with the quasi-equilibrium numerical calculations of Ref. [485].

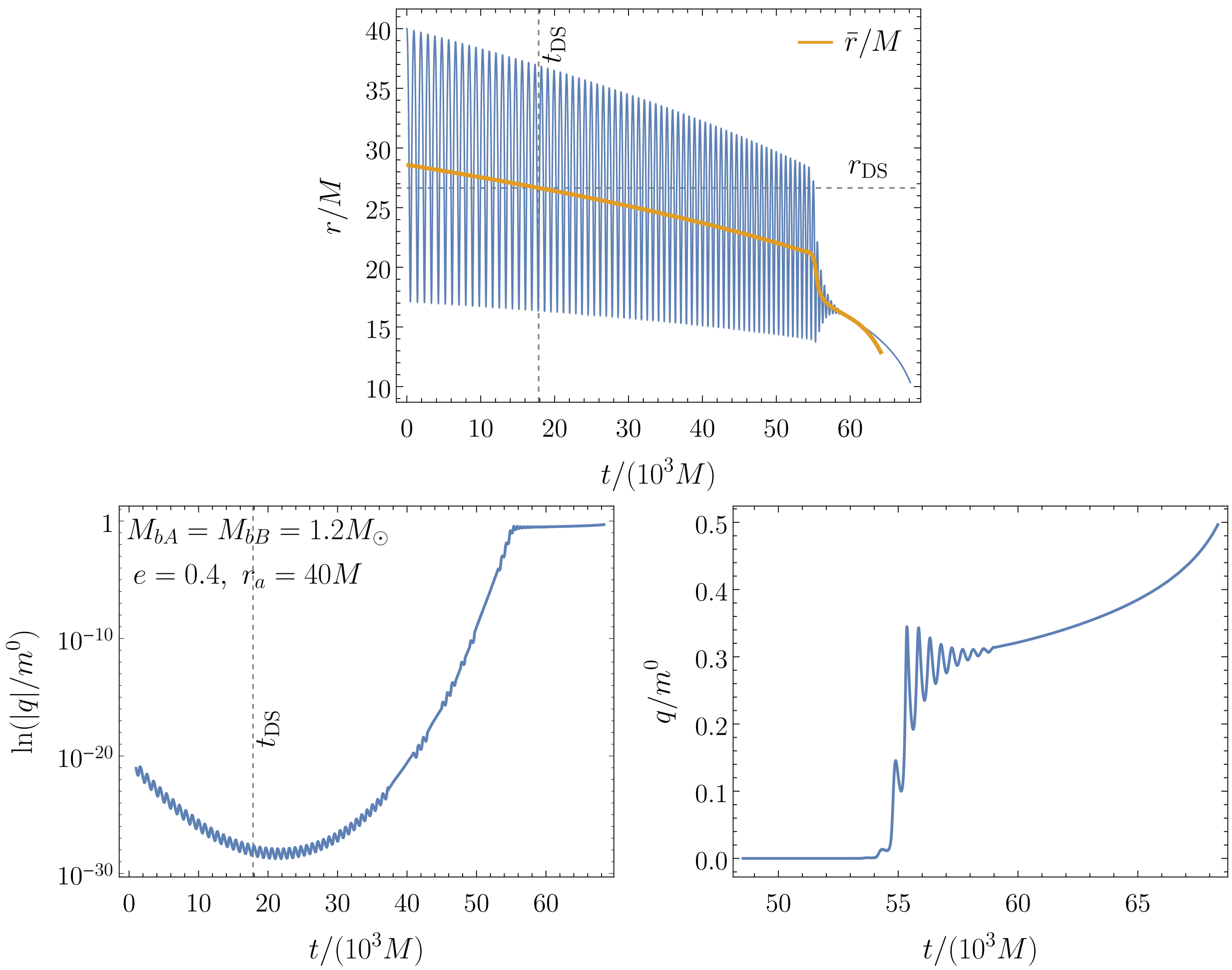

Figure 1.30: Effect of dynamical scalarization on the separation and scalar charge of an equal-mass binary with baryon mass $M_{bA} = M_{bB} = 1.2M_\odot$, initial eccentricity $e = 0.4$, and initial separation at apastron $r_a = 40M$. The oscillations in the scalar charge are due to the eccentric binary entering and exiting the dynamical scalarization region.

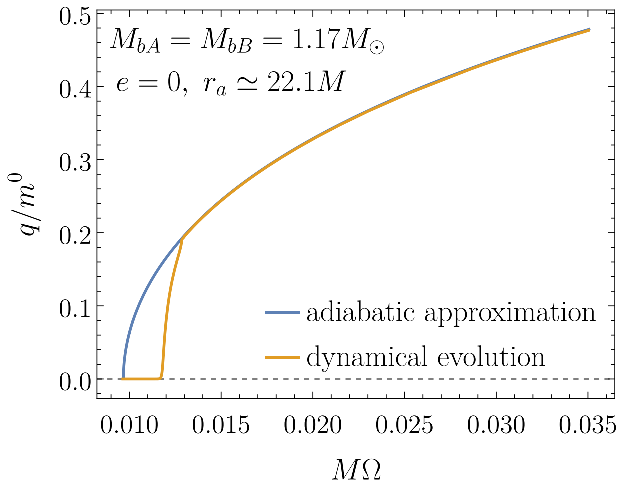

Figure 1.31: Comparison of the adiabatic approximation versus the full dynamical evolution of the scalar charge for an equal-mass binary in a quasi-circular inspiral, plotted versus the orbital frequency.

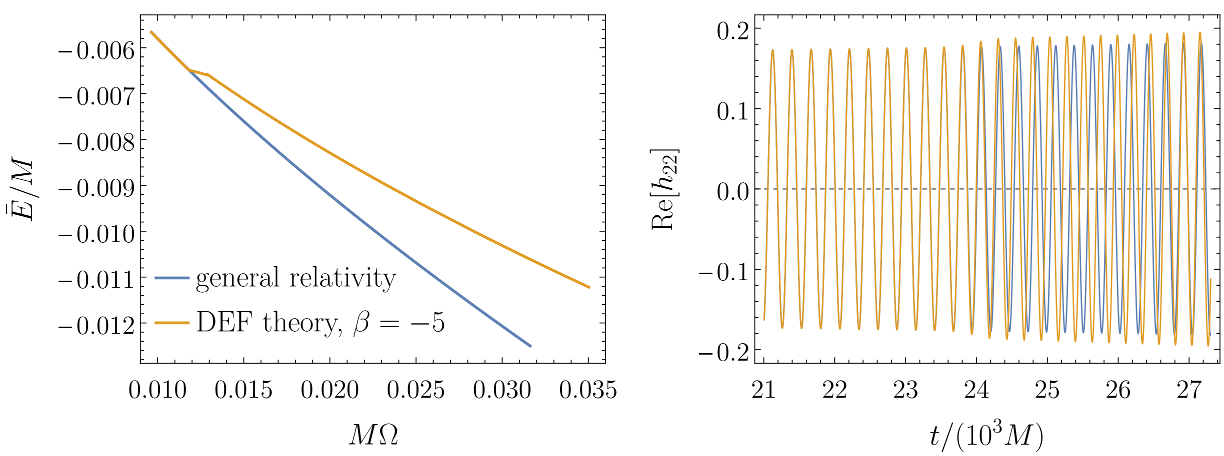

Figure 1.32: The leading-order binding energy as a function of the orbital frequency (left panel) and the real part of the (2,2) waveform mode at leading PN order around scalarization (right panel), for a binary in a quasi-circular inspiral with the same parameters as in Fig. 1.31.

In the right panel of Fig. 1.32, we plot the real part of the leading-order (2,2) waveform mode, which is given by Eq. (1.81). We see that the waveform in DEF theory agrees with GR until the onset of dynamical scalarization, which significantly changes the phase of the waveform, causing it to approach merger more quickly.

Thus, our approach demonstrates how dynamical-scalarization effects can be incorporated in PN waveform models for compact binaries in gravity theories that allow for scalarization. Alternatively, one could use the model to directly constrain the coefficients of the effective action from GW observations.

Chapter 2: Gravitational spin-orbit coupling through third-subleading post-Newtonian order: from first-order self-force to arbitrary mass ratios

Authors[1]: *Andrea Antonelli, Chris Kavanagh, Mohammed Khalil, Jan Steinhoff, and Justin Vines*

Abstract: Exploiting simple yet remarkable properties of relativistic gravitational scattering, we use first-order self-force (linear-in-mass-ratio) results to obtain arbitrary-mass-ratio results for the complete third-subleading post-Newtonian (4.5PN) corrections to the spin-orbit sector of spinning-binary conservative dynamics, for generic (bound or unbound) orbits and spin orientations. We thereby improve important ingredients of models of gravitational waves from spinning binaries, and we demonstrate the improvement in accuracy by comparing against aligned-spin numerical simulations of binary black holes.

2.1 Introduction

The success of gravitational-wave (GW) astronomy in the next decades relies on significantly improved theoretical predictions of GW signals from coalescing binaries of *spinning* compact objects such as black holes (BHs). A network of GW detectors [517, 518] has now observed dozens of signals from binary BHs, measuring distributions of the BHs' masses and

[1]Originally published as Phys. Rev. Lett. **125**, no.1, 011103 (2020)

spins and extrinsic properties, enabling diverse applications in astro- and fundamental physics [13, 18, 519, 520]: e.g., discerning binary BH formation channels [18], measurement of the Hubble constant [520], and tests of general relativity (GR) [519]. The search for and parameter estimation of GW signals require accurate predictions, from the inspiral (treated by analytic approximations) to the last orbits and merger of the binary (treated by numerical relativity, NR). The current accuracy of theoretical predictions, from combined analytic and numerical methods, will likely become insufficient when current detectors reach design sensitivity around 2022 [521]. More accurate predictions for gravitational waves are thus key to enable the physics applications mentioned above.

The primary relevant analytic approximation is the post-Newtonian (PN, weak-field and slow-motion) approximation. The conservative orbital dynamics is known for nonspinning binaries to the fourth-subleading PN order [79, 84–86, 522] (with partial results at the fifth [89, 90, 251, 253, 523] and sixth [93, 524, 525]), but only to second-subleading order (or next-to-next-to-leading order, N^{2}LO) in the spin-orbit sector [102, 107, 108]. The gravitational spin-orbit couplings, linear in the component bodies' spins, are analogous to those in atomic physics. Recently, the three-loop Feynman integrals at N^{3}LO in the spin-orbit case were calculated [109], leaving however plenty of tensorial lower-loop integrals as a comparably large computational task. Innovations that complement these massive algebraic manipulations are thus of great potential value.

In this paper, we follow a line of reasoning which leads to a complete result for the sought-after N^{3}LO-PN spin-orbit dynamics (at 4.5PN order for rapidly spinning binaries), requiring relatively little computational effort by building on a diverse array of previous results. We extend to the spinning case a novel approach based on special properties of the gauge-invariant scattering-angle function [90, 252, 265], which encodes the complete binary dynamics (both bound and unbound). The weak-field approximation of the scattering angle is strongly constrained by results in the small-mass-ratio approximation[2], as treated in the gravitational *self-force* paradigm [332]. The scattering-angle constraints imply that known first-order (linear-in-mass-ratio) self-force results with spin [341, 349, 433] uniquely fix the full N^{3}LO-PN spin-orbit dynamics for arbitrary mass ratios. This result completes the 4.5PN conservative dynamics of (rapidly) spinning binaries, together with the NLO cubic-in-spin couplings [125] (see also [128]).

As applications, we compute quantities which can be employed to improve waveform models for GW astronomy: the circular-orbit aligned-spin binding energy and the effective gyro-gravitomagnetic ratios. The former is a crucial ingredient in the construction of faithful models (together with the GW energy flux), for which we quantify the accuracy gain due to the present results by comparing to NR simulations. The latter parametrize spin effects in the `SEOBNR` waveform codes [396–399] used in LIGO-Virgo searches and inference analyses [13] and in the upcoming `TEOBResumS` waveform models [400, 401]. The gyro-gravitomagnetic ratios are analogous to the famous "g-factor" describing the anomalous magnetic dipole moment of the electron, where contributions at the fifth subleading order were obtained [526] and lead to spectacular agreement with experiment [527]. Regarding the gravitational analog, experimental constraints on the gyro-gravitomagnetic ratios are so far seemingly out of reach. In fact, only two GW events were observed to contain nonvanishing spin effects with 90% confidence [13] (see also Refs. [528, 529]). However, this will change, e.g., when systems with precessing spins are observed in the future, since the precession of the orbital plane leads to a characteristic modulation of the emitted GWs. This may allow improved tests of GR and inference of spins.

[2]We define the small-mass-ratio limit as $q = \frac{m_1}{m_2} \ll 1$, where $m_{1,2}$ are the masses of the compact objects.

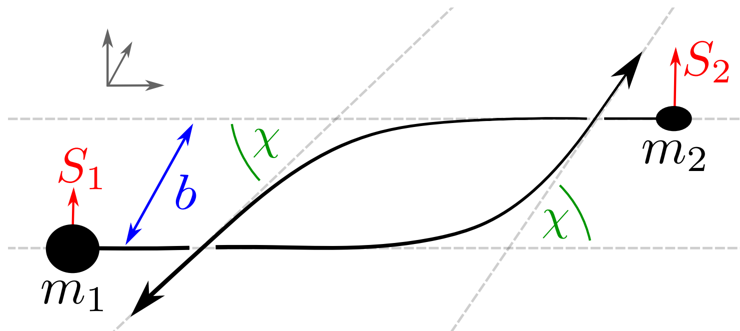

Figure 2.1: Illustration of aligned-spin scattering BHs.

Measuring BH spins and their orientations is also important for discriminating binary formation channels [18].

We begin by extending the link between weak-field scattering and the self-force approximation [90, 252, 265] to the spin-orbit sector. Using existing self-force results, we are then able to uniquely determine the N^{3}LO-PN spin-orbit dynamics, as encoded in the gauge-invariant scattering angle. We continue by calculating the gyro-gravitomagnetic ratios and circular-orbit aligned-spin binding energy. We compare to NR simulations to quantify the accuracy improvement and present our conclusions. G denotes Newton's constant, and c the speed of light.

2.2 The mass dependence of the scattering angle

The local-in-time conservative dynamics of a two-massive-body system (without spin or higher multipoles) is fully encoded in the system's gauge-invariant scattering-angle function $\chi(m_1, m_2, v, b)$ [236, 237]. This gives the angle χ by which both bodies are deflected in the center-of-mass frame, as a function of the masses m_{a} ($\mathsf{a} = 1, 2$), the asymptotic relative velocity v, and the impact parameter b. Based on the structure of iterative solutions in the weak-field (post-Minkowskian) approximation, it has been argued in Sec. II of Ref. [252] that this function exhibits the following simple dependence on the masses (at fixed v and b), through the total mass $M = m_1 + m_2$ and the symmetric mass ratio $\nu = m_1 m_2/M^2$,

$$\begin{aligned}\frac{\chi}{\Gamma} &= \frac{GM}{b} X^{\nu^0}_{G^1}(v) + \left(\frac{GM}{b}\right)^2 X^{\nu^0}_{G^2}(v) \\ &\quad + \left(\frac{GM}{b}\right)^3 \Big[X^{\nu^0}_{G^3}(v) + \nu X^{\nu^1}_{G^3}(v)\Big] \\ &\quad + \left(\frac{GM}{b}\right)^4 \Big[X^{\nu^0}_{G^4}(v) + \nu X^{\nu^1}_{G^4}(v)\Big] + \mathcal{O}\Big(\frac{GM}{b}\Big)^5,\end{aligned} \tag{2.1a}$$

where $\Gamma = E/Mc^2$, with $E^2 = (m_1^2 + m_2^2 + 2m_1 m_2 \gamma)c^4$ being the squared total energy, and $\gamma = (1 - v^2/c^2)^{-1/2}$ the asymptotic relative Lorentz factor. The remarkable fact to be noted here is that the $\mathcal{O}(\frac{GM}{b})^{1,2}$ terms are independent of ν, while the $\mathcal{O}(\frac{GM}{b})^{3,4}$ terms depend linearly on ν.

As will be argued in detail in future work [2],[3] this result generalizes straightforwardly to the case of spinning bodies in the aligned-spin configuration, i.e., spins pointing in the direction of the orbital angular momentum (as shown in Fig. 2.1). The aligned-spin dynamics is fully described by the aligned-spin scattering-angle function $\chi(m_{\mathsf{a}}, S_{\mathsf{a}}, v, b)$ [265]. Here, $S_{\mathsf{a}} = m_{\mathsf{a}} c a_{\mathsf{a}}$ are the signed spin magnitudes, positive if aligned as in Fig. 2.1, negative if anti-aligned. At the spin-orbit (linear-in-spin) level, the form of Eq. (2.1a) holds, with the X functions acquiring additional (linear) dependence on the spins *only* through the dimensionless ratios $a_{\mathsf{a}}/b = S_{\mathsf{a}}/m_{\mathsf{a}} cb$, as follows: [3]

$$X^{\nu^m}_{G^n} \to X^{\nu^m}_{G^n}(v) + \frac{a_+}{b} X^{\nu^m}_{G^n a_+}(v) + \delta \frac{a_-}{b} X^{\nu^m}_{G^n a_-}(v), \tag{2.1b}$$

[3]Note that our Eq. (2.1) is equivalent to Eqs. (2.14) and (2.15) of Ref. [252], but with all the functions $\mathsf{Q}^{n\mathrm{PM}}_{\dots}(\gamma)$ on the right-hand side of (2.15) replaced by functions $\mathsf{Q}^{n\mathrm{PM}}_{\dots}(\gamma, a_1/b, a_2/b)$ which are linear in a_1/b and a_2/b, and with the additional constraints imposed by symmetry under $(m_1, a_1) \leftrightarrow (m_2, a_2)$. The arguments leading to this result are very much analogous to those for the spinless case as given in Ref. [252] — using the structure of the PM expansion, Poincaré symmetry, dimensional analysis, etc. — with the given mass dependence holding at fixed "geometric quantities," except that these are now v, b, a_1, a_2 instead of just v (or γ) and b. The rescaled spins $a_{\mathsf{a}} = S_{\mathsf{a}}/m_{\mathsf{a}} c$ and the "covariant" (Tulczyjew-Dixon) worldlines (separated by the "covariant" impact parameter b) are identified as the appropriate geometrical (mass-independent) quantities, because it is in terms of these variables that the first-order metric perturbation is linear in the masses.

where $a_{\pm} = a_2 \pm a_1$ and $\delta = (m_2 - m_1)/M$, with the special constraints $X^{\nu^0}_{G^1 a_-} = 0 = X^{\nu^1}_{G^3 a_-}$; cf. Eq. (4.32) of Ref. [265], where this is seen to hold through N^{2}LO in the PN expansion. It is crucial to note that the impact parameter b in Eq. (2.1), is the ("covariant") one orthogonally separating the asymptotic worldlines defined by the Tulczyjew-Dixon condition [96, 361] for each spinning body [264, 265].

Now, the fourth order in GM/b encodes the complete spin-orbit dynamics at N^{3}LO in the PN expansion, and according to Eq. (2.1) only terms up to linear order in the mass ratio ν appear on the right-hand side (noting $\delta \to \pm 1$ as $\nu \to 0$)—that is, first-order self-force (linear-in-ν) results can be employed to fix the functions $X^{\nu^m}_{G^n \dots}(v)$ for $n \leq 4$.

2.3 Scattering angle, Hamiltonian, and binding energy

We now connect the scattering angle to an ansatz for a local-in-time binary Hamiltonian including spin-orbit interactions. If nonlocal-in-time (tail) effects are present, this step requires extra care [90], but this is not the case at the N^{3}LO-PN spin-orbit level. Crucially, the Hamiltonian describes the dynamics for both unbound (scattering) and bound orbits. The latter are not only most relevant for GW astronomy, but are also where the vast majority of self-force results are available. Hence, a gauge-dependent Hamiltonian allows us to connect the scattering angle (2.1) with known self-force results.

Let us parametrize our binary Hamiltonian $H(\boldsymbol{r}, \boldsymbol{p}, \boldsymbol{S}_1, \boldsymbol{S}_2)$ in the effective-one-body (EOB) [380] form,

$$H = Mc^2 \sqrt{1 + 2\nu \left(\frac{H_{\text{eff}}}{\mu c^2} - 1 \right)}, \tag{2.2}$$

where $H_{\text{eff}}(\boldsymbol{r}, \boldsymbol{p}, \boldsymbol{S}_1, \boldsymbol{S}_2)$ is the effective Hamiltonian and $\mu = M\nu$ is the reduced mass, with canonical Poisson brackets $\{r^i, p_i\} = \delta^i_j$, $\{S^i_{\mathsf{a}}, S^j_{\mathsf{a}}\} = \epsilon^{ij}{}_k S^k_{\mathsf{a}}$, and all others vanishing. At the spin-orbit level, to linear order in the spins, parity invariance implies that H can depend on the spins only through the scalars $\boldsymbol{L}\cdot\boldsymbol{S}_{\mathsf{a}}$, where $\boldsymbol{L} = \boldsymbol{r}\times\boldsymbol{p}$ is the canonical orbital angular momentum. Thus, a generic Hamiltonian ansatz is of the form

$$H_{\text{eff}} = H^{\text{ns}}_{\text{eff}} + \frac{1}{c^2 r^3}\boldsymbol{L}\cdot(g_S \boldsymbol{S} + g_{S^*}\boldsymbol{S}^*), \tag{2.3}$$

where $H^{\text{ns}}_{\text{eff}}(\boldsymbol{r}, \boldsymbol{p})$ is the nonspinning Hamiltonian. We use the conventional spin combinations $\boldsymbol{S} = \boldsymbol{S}_1 + \boldsymbol{S}_2$, $\boldsymbol{S}^* = \frac{m_2}{m_1}\boldsymbol{S}_1 + \frac{m_1}{m_2}\boldsymbol{S}_2$, while $g_S(\boldsymbol{r}, \boldsymbol{p})$ and $g_{S^*}(\boldsymbol{r}, \boldsymbol{p})$ are the effective gyro-gravitomagnetic ratios. In specializing to the case of aligned spins, in which $\boldsymbol{S}_{\mathsf{a}} = S_{\mathsf{a}}\hat{\boldsymbol{L}}$ are (anti)parallel to $\boldsymbol{L} = L\hat{\boldsymbol{L}}$ ($L = |\boldsymbol{L}|$), the motion is confined to the plane orthogonal to the angular momenta, and Eq. (2.3) simplifies to

$$H_{\text{eff}} = H^{\text{ns}}_{\text{eff}} + \frac{1}{c^2 r^3}L(g_S S + g_{S^*} S^*), \quad \text{(aligned)} \tag{2.4}$$

where, crucially, g_S and g_{S^*} are unmodified by this specialization (as they are independent of the spins). The aligned-spin Hamiltonian is therefore sufficient to reconstruct the generic-spin Hamiltonian, up to the spin-orbit level. We can adopt polar coordinates (r, φ) in the orbital plane, with canonically conjugate momenta (p_r, L), and the Hamiltonian is independent of φ due to rotation invariance. Then $H^{\text{ns}}_{\text{eff}}$, g_S, and g_{S^*} are each functions of (r, p_r, L). We take $H^{\text{ns}}_{\text{eff}}$ to be given to 4PN order by Eqs. (5.1) and (8.1) in Ref. [80]. Considering the freedom under canonical transformations, it can be shown that there exists a gauge in which g_S and g_{S^*} are independent of L [383, 389, 390]; we adopt this choice and parametrize our spin-orbit Hamiltonian with the undetermined gyro-gravitomagnetic ratios $g_S(r, p_r)$ and $g_{S^*}(r, p_r)$. Each term in a PN-expanded ansatz for g_S and g_{S^*} carries a certain power in c, from which the PN order can be read off; we include terms up to c^{-6} here. (c^{-2} corresponds to one PN order and $c \to \infty$ to the Newtonian limit.)

To ascribe physical significance to the spin-orbit Hamiltonian, we point to the striking similarity with the electromagnetic spin-orbit interactions in atomic physics, which makes g_S and g_{S^*} analogous to the "g-factor" of the electron (except that g_S and g_{S^*} depend on dynamical variables). This is no accident, since the gravito-magnetic field generated, e.g., by a rotating mass, can be interpreted to exert a Lorentz-like force. The relativistically preferred geometrical interpretation is that gravito-magnetic fields are dragging inertial/free-falling reference frames, as impressively demonstrated by the Gravity Probe B satellite experiment [530].

We constrain the ansatz for the Hamiltonian by requiring that it reproduces (i) the mass dependence of the scattering angle (2.1), (ii) the $\nu \to 0$ limit of the scattering angle, for a spinning test particle in a Kerr background, as obtained, e.g., by integrating Eq. (65) of Ref. [428], and (iii) certain gauge-invariant self-force observables, namely, the Detweiler-Barack-Sago redshift [314, 336, 338, 339, 341, 433, 531, 532] and the spin-precession frequency [346–350, 532–534] for bound eccentric aligned-spin orbits, to linear order in the mass ratio. The scattering angle χ is obtained from the Hamiltonian (2.2) via Eq. (4.10) of Ref. [265], with the translation from the total energy $E = H$ and canonical orbital angular momentum L to the asymptotic relative velocity v and "covariant" impact parameter b accomplished by Eqs. (4.13) and (4.17) of Ref. [265]. The redshifts z_{a} and spin-precession frequencies Ω_{a} ($\mathsf{a} = 1, 2$) are given by

$$z_{\mathsf{a}} = \left\langle \frac{\partial H}{\partial m_{\mathsf{a}}} \right\rangle, \qquad \Omega_{\mathsf{a}} = \left\langle \frac{\partial H}{\partial S_{\mathsf{a}}} \right\rangle, \tag{2.5}$$

where $\langle \cdots \rangle$ denotes an average over one period of the radial motion, following from a first law of binary mechanics for eccentric aligned-spin orbits [429–431, 535]. The procedure for expressing these quantities, in the small-mass-ratio limit, in terms of variables used in self-force calculations is detailed in Ref. [343]. In this process, to reach the N^{3}LO-PN accuracy in the spin-orbit sector, it is necessary to include the nonspinning 4PN part of the Hamiltonian, including the nonlocal tail part [79], given as an expansion in the orbital eccentricity as in Ref. [80]. After lengthy calculation, working consistently in the small-mass-ratio and PN approximations, we obtain, from our Hamiltonian ansatz, expressions for the redshift z_1 and precession frequency Ω_1 of the smaller body, which can be directly compared with the self-force results in Eq. (4.1) of Ref. [341], Eq. (23) of Ref. [433] and Eq. (20) of Ref. [343] for the redshift, and Eq. (3.33) of Ref. [349] for the precession frequency. The resultant constraints uniquely fix $g_S(r, p_r)$ and $g_{S^*}(r, p_r)$ at N^{3}LO, via an overdetermined system of equations.

From the Hamiltonian, we can finally calculate the *aligned-spin* circular-orbit binding energy $E_b = H - Mc^2$ as a function of the circular-orbit frequency $\omega = d\varphi/dt = \partial H/\partial L$. This is a gauge-invariant relation that can be compared to NR. We decompose E_b into nonspinning and spin-orbit (SO) parts, and further into PN orders, as in

$$E_b^{\text{SO}} = E_{b,\text{LO}}^{\text{SO}} + E_{b,\text{NLO}}^{\text{SO}} + E_{b,\text{N}^2\text{LO}}^{\text{SO}} + E_{b,\text{N}^3\text{LO}}^{\text{SO}} + \dots. \tag{2.6}$$

We can decompose the g_S, g_{S^*}, and χ_{SO} results from the previous discussion in the same way. The N^{3}LO pieces of all these quantities are the main results of this paper:

$$\begin{aligned}\frac{\chi_{\text{SO}}^{\text{N}^3\text{LO}}}{\Gamma} = \frac{v}{c\,b}\begin{pmatrix} a_+ & \delta a_- \end{pmatrix}\Bigg\{\Bigg[\frac{1}{4}\begin{pmatrix}177\nu\\ 0\end{pmatrix}\frac{v^6}{c^6}\Bigg]\left(\frac{GM}{v^2 b}\right)^3 + \pi\Bigg[\frac{3}{4}\begin{pmatrix}-91+13\nu\\ -21+\nu\end{pmatrix}\frac{v^2}{c^2}\\ -\frac{1}{8}\begin{pmatrix}1365-777\nu\\ 315-45\nu\end{pmatrix}\frac{v^4}{c^4} - \frac{1}{32}\begin{pmatrix}1365-\left(\frac{23717}{3}-\frac{733\pi^2}{8}\right)\nu\\ 315-\left(\frac{257}{3}+\frac{251\pi^2}{8}\right)\nu\end{pmatrix}\frac{v^6}{c^6}\Bigg]\left(\frac{GM}{v^2 b}\right)^4\Bigg\},\end{aligned} \tag{2.7}$$

$$
\begin{aligned}
c^6 g_S^{\mathrm{N^3LO}} &= \frac{\nu}{1152}\left(-80399+1446\pi^2+13644\nu-63\nu^2\right)\frac{(GM)^3}{r^3} \\
&+\frac{3\nu}{64}\left(-1761+2076\nu+23\nu^2\right)\frac{p_r^2}{\mu^2}\frac{(GM)^2}{r^2}+\frac{\nu}{128}\left(781+3324\nu-771\nu^2\right)\frac{p_r^4}{\mu^4}\frac{GM}{r} \\
&+\frac{7\nu}{128}\left(1-36\nu-95\nu^2\right)\frac{p_r^6}{\mu^6}, \qquad (2.8)
\end{aligned}
$$

$$
\begin{aligned}
c^6 g_{S^*}^{\mathrm{N^3LO}} &= -\frac{1}{384}\left[1215+2(7627-246\pi^2)\nu-4266\nu^2+36\nu^3\right]\frac{(GM)^3}{r^3} \\
&-\frac{3}{64}\left(15+558\nu-1574\nu^2-36\nu^3\right)\frac{p_r^2}{\mu^2}\frac{(GM)^2}{r^2} \\
&+\frac{1}{128}\left(-1105-106\nu+702\nu^2-972\nu^3\right)\frac{p_r^4}{\mu^4}\frac{GM}{r} \\
&-\frac{7}{128}\left(45+50\nu+66\nu^2+60\nu^3\right)\frac{p_r^6}{\mu^6}, \qquad (2.9)
\end{aligned}
$$

$$
\begin{aligned}
E_{b,\mathrm{N^3LO}}^{\mathrm{SO}} &= -\frac{\nu c^3}{GM}\frac{v_\omega^{11}}{c^{11}}\left[S\left(45-\frac{19679+174\pi^2}{144}\nu+\frac{1979}{36}\nu^2+\frac{265}{3888}\nu^3\right)\right. \\
&\left.+\frac{S^*}{8}\left(\frac{135}{2}-565\nu+\frac{1109}{3}\nu^2+\frac{50}{81}\nu^3\right)\right], \qquad (2.10)
\end{aligned}
$$

where $v_\omega = (GM\omega)^{1/3} = x^{1/2}c$. One needs to add our Eq. (2.7) to Eq. (4.32b) in Ref. [265] to obtain the complete spin-orbit scattering-angle contribution through N^{3}LO-PN and through $\mathcal{O}(\frac{GM}{b})^4$. The lower-order corrections to E_b^{SO} can be found in Eq. (5.4) of Ref. [108], and the lower-order gyro-gravitomagnetic ratios in Eqs. (55) and (56) of Ref. [390] (see also Ref. [383, 389]). Through the results for g_S and g_{S^*} presented above, one can straightforwardly improve the `SEOBNR` waveform models [396–399] used in contemporary gravitational-wave data analysis [13]. Likewise, one can use them to improve the upcoming `TEOBResumS` waveform models [400, 401]. The other main waveform model used by LIGO-Virgo data analysis [13] is the `IMRPhenom` family [536–542], which can also be improved using our results, though less directly.

2.4 Comparison to NR

We now quantify the improvement in accuracy from the new N^{3}LO spin-orbit correction. The circular-orbit aligned-spin binding energy is a particularly good diagnostic for this, since it encapsulates the conservative dynamics of analytical models, and can be obtained from accurate NR simulations [434, 435]. Of particular interest for us is the possibility to (approximately) isolate the linear-in-spin (spin-orbit) contribution by combining the binding energy for two configurations with spins parallel and anti-parallel to the direction of the angular momentum as follows [437, 438]

$$E_b^{\rm SO}(\nu, \hat{a}, \hat{a}) = \frac{1}{2}\left[E_b(\nu, \hat{a}, \hat{a}) - E_b(\nu, -\hat{a}, -\hat{a})\right], \tag{2.11}$$

with dimensionless spin $\hat{a} = \hat{a}_{\mathsf{a}} \equiv cS_{\mathsf{a}}/(Gm_{\mathsf{a}}^2)$. The result, based on recent NR simulations [438, 458], is shown in Fig. 2.2. The figure also shows the spin-orbit binding energy extracted numerically from the EOB Hamiltonian (2.2), combining two binding energies for different spin directions in the same way as in the NR case. The N^{3}LO spin-orbit result shows a clear advantage over the N^{2}LO one, and that improvement is more pronounced for equal masses than for slightly unequal masses. [The N^{3}LO PN binding energy (2.10) is very similar to the EOB one for the shown mass ratios.] This indicates that an inclusion of the N^{3}LO into existing waveform models may lead to improvements even in the strong-field regime, otherwise only accessible by computationally-expensive NR simulations. Recall that gravitational waves are observed from low frequencies (where approximation methods are applicable) to high frequencies (where PN theory is expected to break down).

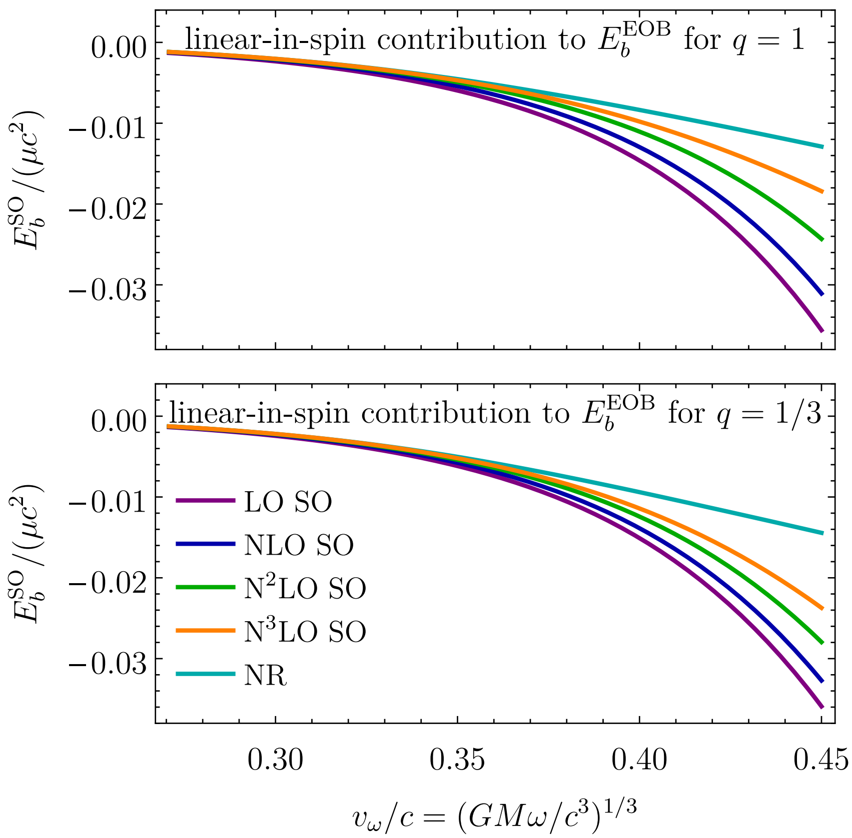

Figure 2.2: Comparison of the gauge-invariant relation between the circular-orbit aligned-spin spin-orbit binding energy E_b and v_ω. The figure shows results obtained numerically from the (PN-resummed) EOB Hamiltonian (2.2) and NR results from Refs. [438, 458]. The linear-in-spin contribution is isolated using Eq. (2.11) with spin magnitudes $\hat{a} = 0.6$ and for mass ratios $q = 1$ and $1/3$.

2.5 Conclusions

Currently-operating (second-generation) gravitational-wave detectors require accuracy improvements for GW predictions by the time they reach design sensitivity around 2022, which become even more stringent for future upgrades and the upcoming third generation of detectors [521]. The detector upgrades [543] in the coming years and a concurrent growing network of observatories [544, 545] also imply an increased number of detections [30], making it overall more likely to observe binaries oriented "edge on" instead of "face on," which allows measuring precession and extracting spin values with higher accuracy. The accurate modeling of GW modulations caused by precession, and also the phase accuracy in the aligned-spin case and the contingent improvement in the estimation of spin parameters, motivate us to push predictions for gravitational spin effects to higher orders.

For this purpose, we extended to spin-orbit couplings a link between the weak-field and small-mass-ratio approximations, via the scattering-angle function, as proposed in the nonspinning case in Ref. [90, 252] (see also Ref. [265]). We employed existing self-force results [341, 349, 433] to uniquely determine a N^{3}LO PN spin-orbit binary Hamiltonian. We calculated the effective gyro-gravitomagnetic ratios as they would enter the `SEOBNR` [396–399] and `TEOBResumS` [400, 401] waveform models, and we obtained the gauge-invariant scattering angle and circular-orbit binding energy for aligned spins. Since the spin-orbit interaction is universal, our results are applicable to generic spinning binaries, e.g., binaries containing neutron stars.

In Fig. 2.2 we compared the EOB-resummed binding energy against NR results. The EOB resummation shows a nice convergent behavior towards NR (for aligned spins) even in the strong field regime, which is usually not expected for asymptotic series expansions like the PN one. More importantly, the new contribution obtained in this paper roughly halves the gap to NR in the high-frequency regime compared to earlier N^{2}LO results for $q = 1$. This indicates that improved (resummed) analytical predictions based on our result can be trusted to higher frequencies, which may alleviate the need for longer and computationally very expensive NR waveforms. Hence, it is of particular value and urgency to improve the accuracy of the PN-approximate analytic part of GW models.

A clear avenue for future work is to consider higher orders in spin (and higher multipoles). In particular, in a forthcoming publication, we fix the S_1S_2 couplings at N^{3}LO (5PN order) for aligned spins using known self-force results. It seems reasonable to expect that complete quadratic-in-spin contributions at N^{3}LO, for BHs, for aligned and perhaps even generic spins, should be within reach of first-order self-force computations. These would require both further self-force observables and new conceptual developments, in particular, generalizations of first-law relations to include higher orders in spin and higher multipoles, and to the case of generic spin orientations (the precessing case). Future first-order self-force results for unbound orbits may also enable obtaining spin effects to fourth order in the weak-field (post-Minkowskian) approximation—for generic masses and velocities—for BH scattering events (only the second order is currently known [263]). While this scenario is unlikely to be of astrophysical relevance, it is still very interesting to consider from a conceptual point of view: after all, scattering encounters are the most elementary form of interaction.

Chapter 3: Gravitational spin-orbit and aligned spin$_1$-spin$_2$ couplings through third-subleading post-Newtonian orders

Authors[1]: *Andrea Antonelli, Chris Kavanagh, Mohammed Khalil, Jan Steinhoff, and Justin Vines*

Abstract: The study of scattering encounters continues to provide new insights into the general relativistic two-body problem. The local-in-time conservative dynamics of an aligned-spin binary, for both unbound and bound orbits, is fully encoded in the gauge-invariant scattering-angle function, which is most naturally expressed in a post-Minkowskian (PM) expansion, and which exhibits a remarkably simple dependence on the masses of the two bodies (in terms of appropriate geometric variables). This dependence links the PM and small-mass-ratio approximations, allowing gravitational self-force results to determine new post-Newtonian (PN) information to all orders in the mass ratio. In this paper, we exploit this interplay between relativistic scattering and self-force theory to obtain the third-subleading (4.5PN) spin-orbit dynamics for generic spins, and the third-subleading (5PN) spin$_1$-spin$_2$ dynamics for aligned spins. We further implement these novel PN results in an effective-one-body framework, and demonstrate the improvement in accuracy by comparing against numerical-relativity simulations.

[1]Originally published as Phys. Rev. D **102**, 124024 (2020)

3.1 Introduction

The burgeoning field of gravitational-wave (GW) astronomy has already shown its potential to revolutionize our understanding of our universe [520], gravity [519], and the nature of compact objects [13, 18], such as black holes (BHs) and neutron stars. The detection of compact-binary GW sources and the accurate inference of their parameters is contingent on having accurate theoretical predictions for their coalescence. As a result of this, a variety of techniques, both analytical and numerical, have been developed to understand the coalescence of binary compact objects, with the final goal of providing faithful waveform models that can be used in GW data analysis.

Post-Newtonian (PN) theory, the best known of the analytical techniques, has provided the foundation for the analytical studies of the two-body problem in general relativity which are most directly useful for gravitational-wave astronomy [129–131, 133, 134, 152, 546, 547]. In this approximation, most applicable to bound systems, one simultaneously assumes weak gravitational potential and small velocities, i.e., $GM/rc^2 \sim v^2/c^2 \ll 1$. The PN expansion is thus a powerful tool for describing the early inspiral of the binaries observed by LIGO and Virgo [13, 14]. PN studies have been carried out at high orders both in the nonspinning [79, 80, 82, 84–86, 89–93, 522, 523, 548] and in the spinning sectors, including spin-orbit (SO) [102, 105–109], bilinear-in-spin (spin_1-spin_2, S_1S_2) [120, 121, 549, 550] and spin-squared (S^2) [122, 124, 132, 550] couplings, as well as cubic and higher-in-spin corrections [123, 125–128]. PN information on the spin dynamics has also been included in effective-one-body (EOB) waveform models [4, 383, 390, 396–401].

In parallel to PN formalisms, the small-mass-ratio approximation, based on gravitational *self-force* (GSF) theory, has also seen rapid development (see Ref. [332] and references therein for a review). As suggested by the name, the expansion parameter in this limit is the mass ratio of the two bodies $q = m_1/m_2 \ll 1$. The leading order in this approximation is given by the geodesic motion of a test body in a Schwarzschild or Kerr background. Successive corrections, which can be interpreted as a force moving the body away from geodesic motion, are due to the perturbation of the background sourced by the small body's nonzero stress-energy tensor. This self-force effect on the motion of a nonspinning body has currently been numerically calculated to first order in q for generic orbits in Kerr spacetime [318]. In a recent breakthrough [326], the second-order-in-q binding energy in a Schwarzschild background has been calculated and compared to predictions from the first law of binary black-hole mechanics [429]. Meanwhile, much activity has led to the analytic calculation at very high PN orders (but at first order in q) of gauge-invariant quantities, such as the Detweiler redshift [336–344, 551] and the precession frequency [343, 346–350, 533], including effects of the smaller body's spin. This has quite naturally led to related activity in confronting and validating the PN and GSF approximations [429, 552, 553] in the domain which both are valid, i.e., for large orbital separations and small mass ratios, as well as in constructing EOB models based on both approximations [408–410, 554].

Recently, there has also been rapid advance in understanding and employing *post-Minkowskian* (PM) techniques, using a weak-field approximation $GM/rc^2 \ll 1$ in a background Minkowski spacetime, with no restriction on the relative velocity of the two bodies [236, 237, 239, 241, 243, 299]. This approximation most naturally applies to the weak-field scattering of compact objects, in which possibly relativistic velocities can be reached. Recent advances in PM gravity and in our understanding of the scattering of compact objects have been spearheaded by modern on-shell scattering-amplitude techniques, developed originally in the context of quantum particle physics (see, e.g., Ref. [299] and references therein).

Scattering amplitudes were used in Ref. [239] to calculate the nonspinning 2PM ($\mathcal{O}(G^2)$, one-loop) scattering angle, reproducing with astonishing efficiency the decades-old results of Westpfhal [228, 229] obtained by classical methods; an equivalent canonical Hamiltonian at 2PM order was derived from amplitudes in Ref. [241]. The scattering angle plays a key role in PM gravity: it encodes the complete local-in-time conservative dynamics of the system (at least in a perturbative sense) and it can be used to specify a Hamiltonian in a given unique gauge [237], which can in turn be used for unbound as well as *bound* systems (with potential relevance for improving waveform models [405]); see in particular Refs. [255, 267]. In Refs. [243, 299], the scattering angle and a corresponding Hamiltonian have been obtained at 3PM (two-loop) order for nonspinning systems, and the results have been confirmed and expounded upon in Refs. [91, 256, 524, 525].

The PM approximation for two-*spinning*-body systems was first tackled only very recently, with the SO dynamics at the 1PM and 2PM levels first derived by classical means in Refs. [262, 263]. These results have since been confirmed by amplitudes methods in Ref. [268], which also gave the 1PM and 2PM dynamics for the $\mathrm{S}_1\mathrm{S}_2$ sector, rounding out the current state of the art for generic-spin PM results beyond tree level. Several other works have also considered amplitudes methods in relation to spinning two-body systems, also beyond the SO and $\mathrm{S}_1\mathrm{S}_2$ sectors (beyond the dipole level in the bodies' multipole expansions), in particular for special cases such as bodies with black-hole-like spin-induced multipole structure and/or for the aligned-spin configuration (in which the bodies' spins are [anti-]parallel to the orbital angular momentum); see, e.g., [128, 269, 555] and references reviewed therein.

These works demonstrate that the study of gravitational scattering continues to provide novel results and useful insights on the relativistic two-body problem, with implications for precision gravitational-wave astronomy yet to be explored. A particularly powerful example of such an insight concerns the nontrivially simple dependence of the scattering-angle function on the masses [252] (see also [255, 265, 299]). This was exploited in Refs. [90, 91] to obtain almost all the 5PN dynamics (with the exception of 2 out of 36 coefficients in the EOB Hamiltonian; see also Refs. [89, 523]) from first-order self-force calculations (while appropriately dealing with nonlocal-in-time tail terms). This approach has also been used in Refs. [93, 548] to obtain most of the 6PN dynamics. An extension of this approach to spinning systems was used by the current authors in Ref. [1] to obtain the next-to-next-to-next-to-leading order (N^3LO) SO PN dynamics.

In this paper, we provide details for the calculation of the N^3LO-PN SO dynamics presented in Ref. [1], which completes the PN knowledge at 4.5PN order together with the NLO S^3 dynamics from Ref. [125] (see also [128]). Furthermore, we extend our analysis to include a derivation of the N^3LO S_1S_2 effects, contributing at 5PN order, for the case of spins aligned with the orbital angular momentum. We note that partial results of the N^3LO-PN SO and N^3LO S_1S_2 dynamics have previously been presented in Refs. [109, 550], where all terms at G^4 were calculated within the powerful effective field theory framework using Feynman integral calculus. The latter of these references gives further results for *all* quadratic-in-spin terms at N^3LO.

Our derivations are organized in the following procedures:

1. We argue that the scattering angle for an aligned-spin binary has a simple dependence on the masses (when expressed in terms of appropriate geometrical variables), which extends the result of Ref. [252] for nonspinning binaries. This mass dependence implies that the 4PM part of the scattering angle, which encodes the N^3LO PN dynamics, is determined by

terms up to linear order in the mass ratio. We use analytic results for the test-spin scattering angle to fix all terms at zeroth order in the mass ratio, leaving the linear terms to be fixed by first-order GSF results.

2. Assuming the existence of a PN Hamiltonian at the desired 4.5PN SO and 5PN S_1S_2 orders, and making use of its associated mass-shell constraint with undetermined coefficients, we calculate the scattering angle and match it to the constrained form from step 1. This procedure fixes its lower orders in velocity at 3PM and 4PM orders, leaving but half of the linear-in-mass-ratio coefficients to be determined by GSF calculations. We construct the bound-orbit radial action from the scattering angle (via the Hamiltonian dynamics), noting its simple dependence on the bodies' masses.

3. From the radial action, we calculate the redshift and spin-precession invariants and compare them with GSF results available in the literature to determine the remaining coefficients of the scattering angle. Vital to this step is the first law of spinning binary mechanics [429–431], which is used to relate the radial action to the redshift and precession frequency, and for which we herein discuss an extension to arbitrary-mass-ratio aligned-spin eccentric orbits.

(Although we work with aligned spins throughout, we note that the aligned SO result actually fixes the SO Hamiltonian also for precessing spins [1].)

The paper is organized as follows. Sections 3.2, 3.3 and 3.4 discuss points 1, 2 and 3, respectively. In Sec. 3.5, we implement the new PN results in the scattering angle in an EOB model, and use it to compare our results against NR simulations. We conclude in Sec. 3.6 with a discussion of results and potential future work. Finally, Appendix A contains expressions for tail terms in the radial action, while Appendix B contains explicit expressions for a certain mapping between variables used to connect redshift and precession-invariant results from the radial action to GSF results in the literature, which have been previously erroneously (yet innocuously) reported in the literature.

Notation

We use the metric signature $(-, +, +, +)$, and use units in which the speed of light is $c = 1$. For a binary of compact objects with masses m_1 and m_2, we use the following combinations of the masses

$$M = m_1 + m_2, \qquad \mu = \frac{m_1 m_2}{M}, \qquad \nu = \frac{\mu}{M}, \qquad q = \frac{m_1}{m_2}, \qquad \delta = \frac{m_2 - m_1}{M}, \tag{3.1}$$

with $m_1 < m_2$. We often make use of the rescaled versions of the canonical spins $\boldsymbol{S}_1$ and $\boldsymbol{S}_2$, i.e.,

$$\boldsymbol{a}_1 = \frac{\boldsymbol{S}_1}{m_1}, \qquad \boldsymbol{a}_2 = \frac{\boldsymbol{S}_2}{m_2}, \tag{3.2}$$

and define the following combinations of spins

$$\begin{aligned} \boldsymbol{S} = \boldsymbol{S}_1 + \boldsymbol{S}_2, \qquad \boldsymbol{S}_* = \frac{m_2}{m_1}\boldsymbol{S}_1 + \frac{m_1}{m_2}\boldsymbol{S}_2, \\ \boldsymbol{a}_{\rm b} = \frac{\boldsymbol{S}}{M}, \qquad \boldsymbol{a}_{\rm t} = \frac{\boldsymbol{S}_*}{M}. \end{aligned} \tag{3.3}$$

The relative position and momentum 3-vectors are denoted by $\boldsymbol{r}$ and $\boldsymbol{p}$, respectively. Using an implicit Euclidean background, it holds that

$$\boldsymbol{p}^2 = p_r^2 + \frac{L^2}{r^2}, \qquad p_r = \boldsymbol{n} \cdot \boldsymbol{p}, \qquad \boldsymbol{L} = \boldsymbol{r} \times \boldsymbol{p}, \tag{3.4}$$

where $\boldsymbol{n} = \boldsymbol{r}/r$ with $r = |\boldsymbol{r}|$, and $\boldsymbol{L}$ is the orbital angular momentum with magnitude L.

3.2 The mass dependence of the scattering angle

Here we argue that the structure of the PM expansion, applied to the conservative orbital dynamics of a two-massive-body system, leads to simple constraints on the dependence of the scattering-angle function on the bodies' masses, at fixed geometric quantities characterizing the incoming state. We closely follow the arguments given in Sec. II of Ref. [252] for the nonspinning case, considering only the local-in-time, conservative part of the dynamics, while generalizing to the case of spinning bodies, finally, in the aligned-spin configuration.

The motion of a two-point-mass system (the nonspinning case) is effectively governed by the coupled system of (i) geodesic equations for the worldlines of the two point masses, using the full two-body spacetime metric (with a suitable regularization or renormalization procedure), and (ii) Einstein's equations for the metric, sourced by effective point-mass energy-momentum tensors. In the case of spinning bodies, to dipolar order in the bodies' multipole expansions, the geodesic equations are replaced by the pole-dipole Mathisson-Papapetrou-Dixon (MPD) equations [367–369],

$$\frac{\mathrm{D}p_{\mathrm{i}\mu}}{\mathrm{d}\tau_{\mathrm{i}}} = -\frac{1}{2}R_{\mu\nu\rho\sigma}\dot{x}_{\mathrm{i}}^{\nu}S_{\mathrm{i}}^{\rho\sigma}, \tag{3.5a}$$

$$\frac{\mathrm{D}S_{\mathrm{i}}^{\mu\nu}}{\mathrm{d}\tau_{\mathrm{i}}} = 2p_{\mathrm{i}}^{[\mu}\dot{x}_{\mathrm{i}}^{\nu]}, \tag{3.5b}$$

$$0 = p_{\mathrm{i}\mu}S_{\mathrm{i}}^{\mu\nu}, \tag{3.5c}$$

where, for the ith body ($\mathrm{i} = 1,2$), $p_{\mathrm{i}}^{\mu}(\tau_{\mathrm{i}})$ is the linear momentum vector, $S_{\mathrm{i}}^{\mu\nu}(\tau_{\mathrm{i}})$ is the antisymmetric spin (intrinsic angular momentum) tensor, and $\dot{x}_{\mathrm{i}}^{\mu}(\tau_{\mathrm{i}})$ is the tangent to the body's worldline $x_{\mathrm{i}}(\tau_{\mathrm{i}})$. The constraint (3.5c), the "covariant" or Tulczyjew-Dixon spin supplementary condition [96, 361–363], combined with (3.5a) and (3.5b), uniquely determines a first-order equation of motion for the worldline, $\dot{x}_{\rm i}^\mu = \dot{x}_{\rm i}^\mu(x_{\rm i}, p_{\rm i}, S_{\rm i})[g]$. The corresponding effective energy-momentum tensor,

$$T^{\mu\nu}(x) = \sum_{\rm i} \int d\tau_{\rm i} \left[p_{\rm i}^{(\mu} \dot{x}_{\rm i}^{\nu)} \frac{\delta^4(x - x_{\rm i})}{\sqrt{-g}} + \nabla_\lambda \left(S_{\rm i}^{\lambda(\mu} \dot{x}_{\rm i}^{\nu)} \frac{\delta^4(x - x_{\rm i})}{\sqrt{-g}} \right) \right], \tag{3.6}$$

sources Einstein's equations,

$$R_{\mu\nu} - \frac{1}{2} R g_{\mu\nu} = 8\pi G T_{\mu\nu}. \tag{3.7}$$

In the PM scheme, an iterative solution to these equations is obtained as an expansion in G of the worldlines, momenta and spins,

$$\begin{aligned} x_{\rm i}^\mu(\tau_{\rm i}) &= x_{\rm i0}^\mu(\tau_{\rm i}) + G x_{\rm i1}^\mu(\tau_{\rm i}) + G^2 x_{\rm i2}^\mu(\tau_{\rm i}) + \cdots , \\ p_{\rm i}^\mu(\tau_{\rm i}) &= p_{\rm i0}^\mu(\tau_{\rm i}) + G p_{\rm i1}^\mu(\tau_{\rm i}) + G^2 p_{\rm i2}^\mu(\tau_{\rm i}) + \cdots , \\ S_{\rm i}^{\mu\nu}(\tau_{\rm i}) &= S_{\rm i0}^{\mu\nu}(\tau_{\rm i}) + G S_{\rm i1}^{\mu\nu}(\tau_{\rm i}) + G^2 S_{\rm i2}^{\mu\nu}(\tau_{\rm i}) + \cdots , \end{aligned} \tag{3.8}$$

and of the metric,

$$g_{\mu\nu}(x) = \eta_{\mu\nu} + G h_{1\mu\nu}(x) + G^2 h_{2\mu\nu}(x) + \cdots , \tag{3.9}$$

where $\eta_{\mu\nu}$ is the Minkowski metric, which we henceforth use instead of the full metric $g_{\mu\nu}$ for all 4-vector manipulations (index raising and lowering, dot products and squares of vectors, etc.).

At the leading orders in (3.8), given by the solutions to (3.5) with $g = \eta$, each body moves inertially in flat spacetime,

$$\begin{aligned} x_{\rm i0}^\mu(\tau_{\rm i}) &= y_{\rm i}^\mu + u_{\rm i}^\mu \tau_{\rm i}, \\ p_{\rm i0}^\mu(\tau_{\rm i}) &= m_{\rm i} u_{\rm i}^\mu, \\ S_{\rm i0}^{\mu\nu}(\tau_{\rm i}) &= m_{\rm i} \epsilon^{\mu\nu}{}_{\rho\sigma} u_{\rm i}^\rho a_{\rm i}^\sigma. \end{aligned} \tag{3.10}$$

Here, $y_{\rm i}^\mu$ are constant displacements from the origin at $\tau_{\rm i} = 0$, and $u_{\rm i}^\mu$ are constant 4-velocities, with $u_{\rm i}^2 = -1$, so that $\tau_{\rm i}$ are the (Minkowski) proper times, and $p_{\rm i}^2 = -m_{\rm i}^2$ where $m_{\rm i}$ are the constant rest masses. The zeroth-order spin tensors $S^{\mu\nu}_{\mathrm{i}0}$ are also constant, and, being orthogonal to $u_{\mathrm{i}\mu}$, have been parametrized in terms of a constant mass-rescaled (Pauli-Lubanski, "covariant") spin vector,

$$a^{\mu}_{\mathrm{i}} = -\frac{1}{2m_{\mathrm{i}}}\epsilon^{\mu}{}_{\nu\rho\sigma}u^{\nu}_{\mathrm{i}}S^{\rho\sigma}_{\mathrm{i}0}, \tag{3.11}$$

with dimensions of length, the magnitude of which would measure the radius of the ring singularity of a corresponding (linearized) Kerr black hole. We identify the zeroth-order geometric (mass-independent) quantities, y^{μ}_{i}, u^{μ}_{i} and a^{μ}_{i}, with those characterizing the asymptotic incoming state, along with the masses m_1 and m_2.

Inserting (3.10) into (3.6) (with $g = \eta$) yields the zeroth-order stress-energy tensor, which serves as a source for the first-order metric perturbation $h_{1\mu\nu}$ in the linearization of (3.7). The solution for the trace-reversed $\bar{h}^{\mu\nu}_1 = h^{\mu\nu}_1 - \frac{1}{2}\eta^{\mu\nu}h_{1\rho}{}^{\rho}$, in harmonic gauge ($\partial_\mu\bar{h}^{\mu\nu}_1 = 0$), reads

$$\bar{h}^{\mu\nu}_1(x) = 4\sum_{\mathrm{i}} m_{\mathrm{i}}\Big(u^{\mu}_{\mathrm{i}}u^{\nu}_{\mathrm{i}} + u^{(\mu}_{\mathrm{i}}\epsilon^{\nu)}{}_{\rho\sigma\lambda}u^{\rho}_{\mathrm{i}}a^{\sigma}_{\mathrm{i}}\partial^{\lambda}\Big)\frac{1}{r_{\mathrm{i}}}, \tag{3.12}$$

where $r_{\mathrm{i}} = \{(x-y_{\mathrm{i}})^2 + [u_{\mathrm{i}}\cdot(x-y_{\mathrm{i}})]^2\}^{1/2}$ is the (Minkowski) distance of the field point x from the (zeroth-order, flat geodesic) worldline $x_{\mathrm{i}0} = y_{\mathrm{i}} + u_{\mathrm{i}}\tau_{\mathrm{i}}$ in its rest frame, and ∂_μ is the flat covariant derivative. (Note that the result for the first-order field (3.12) would be the same whether we used the physical retarded Green's function or the time-symmetric Green's function, given the nature of the zeroth-order source, constant momentum and spin along a flat-spacetime geodesic.) A key property to be noted here is that h_1 is linear in the masses m_{i}, while having a more intricate dependence on the geometric quantities y^{μ}_{i}, u^{μ}_{i} and a^{μ}_{i}. (It is linear in the spins a^{μ}_{i} here only because we are working to linear order in the spins, to dipolar order in the multipole expansions.)

In the next step of the iterative scheme, one uses $g = \eta + h_1$ in the bodies' equations of motion (3.5) to solve for the first-order perturbations in (3.8) [for which it is sufficient to integrate the RHSs of (3.5a) and (3.5b) along the zeroth-order motion (3.10), and to regularize by simply dropping the divergent self-field contribution]. Importantly, one finds that $x^\mu_{\mathrm{i}1}$, $p^\mu_{\mathrm{i}1}/m_{\mathrm{i}}$ and $S^{\mu\nu}_{\mathrm{i}1}/m_{\mathrm{i}}$ are each linear functionals of $h_{1\mu\nu}(x)$, and are thus linear in the masses. From Poincaré symmetry, it follows that these results can depend on the positions y_{i} only through the vectorial impact parameter $b^\mu = y^\mu_1 - y^\mu_2$, where the y^μ_{i} here are chosen along the two zeroth-order worldlines by the conditions $u_1 \cdot b = u_2 \cdot b = 0$ (at mutual closest approach). For example, the impulse (net change in momentum) for body 1, $\Delta p^\mu_1 = G p^\mu_{11}(\tau_1 \to \infty) + \mathcal{O}(G^2)$, is given by[2]

$$\begin{aligned}\Delta p^\mu_1 = \frac{2Gm_1m_2}{\sqrt{\gamma^2-1}}\bigg[&-(2\gamma^2-1)\frac{b^\mu}{b^2} + \frac{2\gamma}{b^4}(2b^\mu b^\nu - b^2\eta^{\mu\nu})\epsilon_{\nu\rho\sigma\lambda}u^\rho_1 u^\sigma_2(a^\lambda_1 + a^\lambda_2) \\ &+ 2\frac{2\gamma^2-1}{b^6}(4b^\mu b^\nu b^\rho - 3b^2 b^{(\mu}\Pi^{\nu\rho)})a_{1\nu}a_{2\rho}\bigg] + \mathcal{O}(G^2),\end{aligned} \tag{3.13}$$

where

$$\gamma = -u_1 \cdot u_2 \tag{3.14}$$

is the asymptotic relative Lorentz factor, and $\Pi^\mu{}_\nu = \epsilon^{\mu\rho\alpha\beta}\epsilon_{\nu\rho\gamma\delta}u_{1\alpha}u_{2\beta}u^\gamma_1 u^\delta_2/(\gamma^2-1)$ is the projector into the plane orthogonal to both u_1 and u_2. Here, as below, we work to linear order in each spin, a_1 and a_2, keeping the cross term. We note again in (3.13) the simple dependence on the masses, with an overall factor of m_1m_2, at fixed geometric quantities b^μ, u^μ_{i} and a^μ_{i}.

In continuing the iterative PM solution, the $\mathcal{O}(G^n)$ terms in the bodies' degrees of freedom (3.8) correct the source (3.6) for the field equation (3.7), determining the $\mathcal{O}(G^{n+1})$ metric perturbation in (3.9); the latter, via the bodies' equations of motion (3.5), determines the $\mathcal{O}(G^{n+1})$ corrections in (3.8). As in Ref. [252] we are assuming here a systematic use of the time-symmetric

[2] Results equivalent to the first two lines of Eq. (3.13) were first derived in Ref. [262], and the last line results from an expansion in spins of the all-orders-in-spin results for black holes from Ref. [264], both references having worked from purely classical considerations; see also [266, 270] for derivations from quantum scattering amplitudes.

Green's function, to pick out the conservative sector of the dynamics. It becomes evident from the structure of these expansions that the $\mathcal{O}(G^n)$ metric perturbation $h_n^{\mu\nu}$ in (3.9) can be expressed as a homogeneous polynomial of degree n in the masses,

$$
\begin{aligned}
h_1^{\mu\nu}(x) &= m_1 h_{m_1}^{\mu\nu}(x) + m_2 h_{m_2}^{\mu\nu}(x), \\
h_2^{\mu\nu}(x) &= m_1^2 h_{m_1^2}^{\mu\nu}(x) + m_2^2 h_{m_2^2}^{\mu\nu}(x) + m_1 m_2 h_{m_1 m_2}^{\mu\nu}(x), \\
&\cdots
\end{aligned}
\tag{3.15}
$$

where the $h_{\cdots}^{\mu\nu}$ on the RHSs are functions only of the (asymptotic incoming) geometric quantities $(y_\mathrm{i}^\mu, u_\mathrm{i}^\mu, a_\mathrm{i}^\mu)$ and the field point x. The first line of (3.15) matches (3.12). Similarly, the $\mathcal{O}(G^n)$ corrections $x_{\mathrm{i}n}^\mu$, $p_{\mathrm{i}n}^\mu/m_\mathrm{i}$, $S_{\mathrm{i}n}^{\mu\nu}/m_\mathrm{i}$ for the body degrees of freedom (3.8) will be homogeneous polynomials of degree n in the masses; this is the crucial point for the following analysis (and for its conceivable extensions beyond the aligned-spin case). The zeroth-order quantities $x_{\mathrm{i}0}^\mu = y_\mathrm{i}^\mu + u_\mathrm{i}^\mu \tau_\mathrm{i}$, $p_{\mathrm{i}0}^\mu/m_\mathrm{i} = u_\mathrm{i}^\mu$ and $S_{\mathrm{i}0}^{\mu\nu}/m_\mathrm{i} = \epsilon^{\mu\nu}{}_{\rho\sigma} u_\mathrm{i}^\rho a_\mathrm{i}^\sigma$ from (3.10) are (taken to be) independent of the masses, as is the zeroth-order metric $h_0 = \eta$; they, along with the masses, both (i) fully parametrize the asymptotic incoming state and (ii) can be used to parametrize all the higher-order corrections.

Let us now specialize to the case of aligned spins, in which both spin vectors a_i^μ are (anti-)parallel to the orbital angular momentum, all of which remain constant throughout the scattering, while the orbital motion is confined to the fixed plane orthogonal to the angular momenta (just as for the nonspinning case). This entails $u_1 \cdot a_\mathrm{i} = u_2 \cdot a_\mathrm{i} = 0$ and $b \cdot a_\mathrm{i} = 0$. Choosing $\hat{z}^\mu$ (with $\hat{z}^2 = 1$) to be the direction of the orbital angular momentum ($\propto -\epsilon_{\mu\nu\rho\sigma} u_1^\nu u_2^\rho b^\sigma$), let us write $a_\mathrm{i}^\mu = a_\mathrm{i} \hat{z}^\mu$ for the constant rescaled spin vectors (equal to their incoming values), where the scalars a_i are positive for spins aligned with $\hat{z}^\mu$ and negative for anti-aligned. Crucially, in this case, the only nontrivial independent Lorentz-invariant scalars that can be constructed from the vectors $u_{\rm i}^{\mu}$, $a_{\rm i}^{\mu}$ and b^{μ} are the magnitude $b = (b^2)^{1/2}$ of the impact parameter and the two spin lengths a_1 and a_2, all three with dimensions of length, and the dimensionless Lorentz factor $\gamma = -u_1 \cdot u_2$.

Now consider the extension to higher orders in G of the impulse Δp_1^{μ} (3.13), which equals $-\Delta p_2^{\mu}$ (under the conservative dynamics) as the total momentum $p_1^{\mu} + p_2^{\mu}$ is conserved. Its magnitude $\mathsf{Q} := (\Delta p_{1\mu} \Delta p_1^{\mu})^{1/2}$ must be a Lorentz-invariant scalar. In the aligned-spin case, given the previous discussion, and due to Poincaré symmetry and dimensional analysis, it must be a function only of the dimensionless scalar γ and the dimension-length scalars b, a_1, a_2, Gm_1 and Gm_2. Given also the conclusion from above that, in (3.8) with $\rm i = 1$, p_{1n}^{μ}/m_1 is a homogeneous polynomial of degree n in the masses, with the leading $n = 1$ result seen in (3.13), it follows that the magnitude Q of the impulse must take the following form through fourth order in G (through 4PM order),

$$\begin{aligned}
\mathsf{Q} = \frac{2Gm_1m_2}{b}\Bigg[&\mathsf{Q}^{\rm 1PM} \\
&+ \frac{G}{b}\left(m_1\mathsf{Q}^{\rm 2PM}_{m_1} + m_2\mathsf{Q}^{\rm 2PM}_{m_2}\right) \\
&+ \frac{G^2}{b^2}\left(m_1^2\mathsf{Q}^{\rm 3PM}_{m_1^2} + m_2^2\mathsf{Q}^{\rm 3PM}_{m_2^2} + m_1m_2\mathsf{Q}^{\rm 3PM}_{m_1m_2}\right) \\
&+ \frac{G^3}{b^3}\left(m_1^3\mathsf{Q}^{\rm 4PM}_{m_1^3} + m_2^3\mathsf{Q}^{\rm 4PM}_{m_2^3} + m_1^2m_2\mathsf{Q}^{\rm 4PM}_{m_1^2m_2} + m_1m_2^2\mathsf{Q}^{\rm 4PM}_{m_1m_2^2}\right)\Bigg] + \mathcal{O}(G^5),
\end{aligned} \tag{3.16a}$$

where the Q's on the RHS are functions of the dimensionless scalars γ, a_1/b and a_2/b,

$$\begin{aligned}
\mathsf{Q}^{n\rm PM}_{m_1^im_2^j} &= \mathsf{Q}^{n\rm PM}_{m_1^im_2^j}(\gamma, \frac{a_1}{b}, \frac{a_2}{b}) \\
&= \mathsf{Q}^{n\rm PM}_{m_1^im_2^ja^0}(\gamma) + \frac{a_1}{b}\mathsf{Q}^{n\rm PM}_{m_1^im_2^ja_1}(\gamma) + \frac{a_2}{b}\mathsf{Q}^{n\rm PM}_{m_1^im_2^ja_2}(\gamma) + \frac{a_1a_2}{b^2}\mathsf{Q}^{n\rm PM}_{m_1^im_2^ja_1a_2}(\gamma)
\end{aligned} \tag{3.16b}$$

(with $i + j = n - 1$). In the second equality, we have expanded to linear order in each spin (assuming regular limits as the spins go to zero), and we are finally left with a set of undetermined functions depending only on the Lorentz factor γ.

Furthermore, Q must be invariant under an exchange of the two bodies' identities, $(m_1, a_1) \leftrightarrow (m_2, a_2)$. At 1PM order, this tells us that $\mathsf{Q}^{\mathrm{1PM}}(\gamma, a_1/b, a_2/b)$ is symmetric under $a_1 \leftrightarrow a_2$, and thus $\mathsf{Q}^{\mathrm{1PM}}_{a_1} = \mathsf{Q}^{\mathrm{1PM}}_{a_2}$, so that the third line of (3.16b) in this case is proportional to $a_1 + a_2$. Indeed, the explicit expression for $\mathsf{Q}^{\mathrm{1PM}}$ is given by the magnitude of the aligned-spin specialization of (3.13) (divided by $2Gm_1m_2/b$),[3]

$$\mathsf{Q}^{\mathrm{1PM}} = \frac{2\gamma^2 - 1}{\sqrt{\gamma^2 - 1}}\left(1 + 2\frac{a_1 a_2}{b^2}\right) - 2\gamma\frac{a_1 + a_2}{b}. \tag{3.18}$$

At 2PM order, the $1 \leftrightarrow 2$ symmetry tells us that each of the two functions in the second line of (3.16a) determines the other,

$$\mathsf{Q}^{\mathrm{2PM}}_{m_1}(\gamma, \frac{a_1}{b}, \frac{a_2}{b}) = \mathsf{Q}^{\mathrm{2PM}}_{m_2}(\gamma, \frac{a_2}{b}, \frac{a_1}{b}). \tag{3.19}$$

This function, like $\mathsf{Q}^{\mathrm{1PM}}$, is in fact fully determined by the (extended) test-body limit of $\mathsf{Q}/(m_1 m_2)$ — the limit where one of the masses, say, m_1, goes to zero, while keeping fixed m_2, a_2 and a_1 (and γ and b). The result for Q/m_1 in this limit can be consistently determined by solving the pole-dipole MPD equations (3.5) for a spinning test body in a stationary Kerr background; we will present explicit results from this procedure below in terms of the scattering-angle function. This test-body limit, with $m_1 \to 0$, determines all of the functions $\mathsf{Q}^{n\mathrm{PM}}_{m_2^{n-1}}$ with no powers of m_1, for all n, and the $1 \leftrightarrow 2$ symmetry also tells us that

$$\mathsf{Q}^{n\mathrm{PM}}_{m_1^{n-1}}(\gamma, \frac{a_1}{b}, \frac{a_2}{b}) = \mathsf{Q}^{n\mathrm{PM}}_{m_2^{n-1}}(\gamma, \frac{a_2}{b}, \frac{a_1}{b}). \tag{3.20}$$

[3] Note that this is the expansion to linear order in the spins of the result (80) from [264] for a two-black-hole system,

$$\mathsf{Q}^{\mathrm{1PM}} = \left(\frac{2\gamma^2 - 1}{\sqrt{\gamma^2 - 1}} - 2\gamma\frac{a_1 + a_2}{b}\right)\left(1 - \frac{(a_1 + a_2)^2}{b^2}\right)^{-1}, \tag{3.17}$$

to all orders in the spin-multipole expansion at 1PM order.

The only remaining functions in (3.16a), those not determined by the test-body limit and exchange symmetry, are $\mathsf{Q}^{3\mathrm{PM}}_{m_1m_2}$, $\mathsf{Q}^{4\mathrm{PM}}_{m_1^2m_2}$ and $\mathsf{Q}^{4\mathrm{PM}}_{m_1m_2^2}$. They are however still constrained by the exchange symmetry as follows. Firstly,

$$\mathsf{Q}^{3\mathrm{PM}}_{m_1m_2}(\gamma, \frac{a_1}{b}, \frac{a_2}{b}) = \mathsf{Q}^{3\mathrm{PM}}_{m_1m_2}(\gamma, \frac{a_2}{b}, \frac{a_1}{b}), \tag{3.21}$$

which implies that the third line of (3.16b) for $\mathsf{Q}^{3\mathrm{PM}}_{m_1m_2}$ (like for $\mathsf{Q}^{1\mathrm{PM}}$ above) is proportional to $a_1 + a_2$. Secondly,

$$\mathsf{Q}^{4\mathrm{PM}}_{m_1^2m_2}(\gamma, \frac{a_1}{b}, \frac{a_2}{b}) = \mathsf{Q}^{4\mathrm{PM}}_{m_1m_2^2}(\gamma, \frac{a_2}{b}, \frac{a_1}{b}), \tag{3.22}$$

so that one of these two functions determines the other.

Taking all of these constraints from exchange symmetry, we can eliminate all of the Q's with more m_1's in the subscript for those with more m_2's, while those with the same number of m_1's and m_2's must be symmetric under $a_1 \leftrightarrow a_2$. First focusing on the nonspinning (a^0) part of (3.16a), this becomes

$$\begin{aligned}\mathsf{Q}_{a^0} = \frac{2Gm_1m_2}{b}\Bigg[&\mathsf{Q}^{1\mathrm{PM}}_{a^0} + \frac{G}{b}(m_1+m_2)\mathsf{Q}^{2\mathrm{PM}}_{m_2a^0} + \frac{G^2}{b^2}\bigg((m_1^2+m_2^2)\mathsf{Q}^{3\mathrm{PM}}_{m_2^2a^0} + m_1m_2\mathsf{Q}^{3\mathrm{PM}}_{m_1m_2a^0}\bigg)\\ &+ \frac{G^3}{b^3}\bigg((m_1^3+m_2^3)\mathsf{Q}^{4\mathrm{PM}}_{m_2^3a^0} + m_1m_2(m_1+m_2)\mathsf{Q}^{4\mathrm{PM}}_{m_1m_2^2a^0}\bigg)\Bigg],\end{aligned} \tag{3.23}$$

recalling that all the Q's on the right-hand side are functions only of γ [henceforth dropping $+\mathcal{O}(G^5)$]. Introducing the total rest mass $M = m_1 + m_2$ and the symmetric mass ratio $\nu = m_1m_2/M^2 = \mu/M$ as in (3.1), and noting

$$\begin{aligned} m_1 + m_2 &= M,\\ m_1^2 + m_2^2 &= M^2(1-2\nu),\\ m_1^3 + m_2^3 &= M^3(1-3\nu),\end{aligned} \tag{3.24}$$

this becomes

$$
\begin{aligned}
\mathsf{Q}_{a^0} = \frac{2Gm_1m_2}{b}\Bigg[&\mathsf{Q}^{\text{1PM}}_{a^0} + \frac{GM}{b}\mathsf{Q}^{\text{2PM}}_{m_2a^0} + \left(\frac{GM}{b}\right)^2\left(\mathsf{Q}^{\text{3PM}}_{m_2^2a^0} + \nu\tilde{\mathsf{Q}}^{\text{3PM}}_{m_1m_2a^0}\right)\\
&+ \left(\frac{GM}{b}\right)^3\left(\mathsf{Q}^{\text{4PM}}_{m_2^3a^0} + \nu\tilde{\mathsf{Q}}^{\text{4PM}}_{m_1m_2^2a^0}\right)\Bigg],
\end{aligned}
\tag{3.25}
$$

where we defined $\tilde{\mathsf{Q}}^{\text{3PM}}_{m_1m_2a^0} := \mathsf{Q}^{\text{3PM}}_{m_1m_2a^0} - 2\mathsf{Q}^{\text{3PM}}_{m_2^2a^0}$ and $\tilde{\mathsf{Q}}^{\text{4PM}}_{m_1m_2^2a^0} := \mathsf{Q}^{\text{4PM}}_{m_1m_2^2a^0} - 3\mathsf{Q}^{\text{4PM}}_{m_2^3a^0}$, still functions only of γ. Remarkably, through 4PM order, this is just linear in the mass ratio ν at fixed M. Precisely the same manipulations go through for the a_1a_2 terms, replacing a^0 with a_1a_2 in all the subscripts and with an overall factor of a_1a_2/b^2 on the right-hand side.

Next consider just the 1PM and 2PM terms of the SO (a^1) part of (3.16a), after accounting for the exchange symmetry in the same way as in the previous paragraph (with $\mathsf{Q}^{\text{1PM}}_{a_1} = \mathsf{Q}^{\text{1PM}}_{a_2}$, $\mathsf{Q}^{\text{2PM}}_{m_1a_1} = \mathsf{Q}^{\text{2PM}}_{m_2a_2}$ and $\mathsf{Q}^{\text{2PM}}_{m_1a_2} = \mathsf{Q}^{\text{2PM}}_{m_2a_1}$); we find

$$
\mathsf{Q}_{a^1} + \mathcal{O}(G^3) = \frac{2Gm_1m_2}{b}\left[\frac{a_1+a_2}{b}\mathsf{Q}^{\text{1PM}}_{a_2} + \frac{G}{b}\left(\frac{m_1a_1+m_2a_2}{b}\mathsf{Q}^{\text{2PM}}_{m_2a_2} + \frac{m_2a_1+m_1a_2}{b}\mathsf{Q}^{\text{2PM}}_{m_2a_1}\right)\right].
\tag{3.26}
$$

We recognize the following spin combinations often used in the PN and EOB literature,

$$
\begin{aligned}
S &:= m_1a_1 + m_2a_2 = S_1 + S_2,\\
S_* &:= m_2a_1 + m_1a_2 = \frac{m_2}{m_1}S_1 + \frac{m_1}{m_2}S_2.
\end{aligned}
\tag{3.27}
$$

We will find it convenient to rescale each of these by the total rest mass M, defining

$$
\begin{aligned}
a_{\text{b}} &:= \frac{S}{M} = \frac{m_1a_1+m_2a_2}{m_1+m_2},\\
a_{\text{t}} &:= \frac{S_*}{M} = \frac{m_2a_1+m_1a_2}{m_1+m_2},
\end{aligned}
\tag{3.28}
$$

where b stands for background (or big) and t stands for test (or tiny). The (first) reason for these labels is that, in the extended test-body limit [$m_1 \to 0$ at fixed m_2 (or M) and fixed a_1 and a_2], we see that $a_{\text{b}} \to a_2$ becomes the spin-per-mass of the big background object with mass $M = m_2$, and $a_{\rm t} \to a_1$ becomes the spin-per-mass of the tiny spinning test body with negligible mass (with a further reason explained below). Note that $a_{\rm b} + a_{\rm t} = a_1 + a_2$. Now extending (3.26) to 4PM order, from (3.16a) accounting for exchange symmetry, using our new notation, we find

$$
\begin{aligned}
\mathsf{Q}_{a^1} = \frac{2Gm_1m_2}{b^2}\bigg[&\mathsf{Q}^{\rm 1PM}_{a_2}(a_{\rm b}+a_{\rm t}) + \frac{GM}{b}\Big(\mathsf{Q}^{\rm 2PM}_{m_2a_2}a_{\rm b} + \mathsf{Q}^{\rm 2PM}_{m_2a_1}a_{\rm t}\Big) \\
&+ \Big(\frac{GM}{b}\Big)^2\Big(\mathsf{Q}^{\rm 3PM}_{m_2^2a_2}a_{\rm b} + \mathsf{Q}^{\rm 3PM}_{m_2^2a_1}a_{\rm t} + \nu\tilde{\mathsf{Q}}^{\rm 3PM}_{m_1m_2a_2}(a_{\rm b}+a_{\rm t})\Big) \\
&+ \Big(\frac{GM}{b}\Big)^3\Big(\mathsf{Q}^{\rm 4PM}_{m_2^3a_2}a_{\rm b} + \mathsf{Q}^{\rm 4PM}_{m_2^3a_1}a_{\rm t} + \nu\Big[\tilde{\mathsf{Q}}^{\rm 4PM}_{m_1m_2^2a_2}a_{\rm b} + \tilde{\mathsf{Q}}^{\rm 4PM}_{m_1m_2^2a_2}a_{\rm t}\Big]\Big)\bigg],
\end{aligned}
\tag{3.29}
$$

where we defined $\tilde{\mathsf{Q}}^{\rm 3PM}_{m_1m_2a_2} = \mathsf{Q}^{\rm 3PM}_{m_1m_2a_2} - \mathsf{Q}^{\rm 3PM}_{m_2^2a_2} - \mathsf{Q}^{\rm 3PM}_{m_2^2a_1}$, $\tilde{\mathsf{Q}}^{\rm 4PM}_{m_1m_2^2a_2} := \mathsf{Q}^{\rm 4PM}_{m_1m_2^2a_2} - 2\mathsf{Q}^{\rm 4PM}_{m_2^3a_2} - \mathsf{Q}^{\rm 4PM}_{m_2^3a_1}$ and $\tilde{\mathsf{Q}}^{\rm 4PM}_{m_1m_2^2a_2} := \mathsf{Q}^{\rm 4PM}_{m_1m_2^2a_2} - \mathsf{Q}^{\rm 4PM}_{m_2^3a_2} - 2\mathsf{Q}^{\rm 4PM}_{m_2^3a_1}$, all still functions only of γ. We see that (3.29), like (3.25), is linear in the symmetric mass ratio ν (at fixed M, $a_{\rm b}$ and $a_{\rm t}$).

Now, just as in Eq. (2.14) of [252] — following from conservation of the total momentum $p_1^\mu + p_2^\mu$ and simple geometry and kinematics (which is identical for the nonspinning and aligned-spin cases) — the scattering angle χ, by which both bodies are deflected in the system's center-of-mass (cm) frame, is related to the magnitude Q of the impulse by

$$
\sin\frac{\chi}{2} = \frac{\mathsf{Q}}{2p_\infty},
\tag{3.30}
$$

where p_∞ (called "$P_{\rm c.m.}$" by Damour) is the magnitude of the bodies' equal and opposite spatial momenta in the cm frame, at infinity,

$$
p_\infty = \frac{m_1m_2}{E}\sqrt{\gamma^2-1}.
\tag{3.31}
$$

Here, E is the total energy in the cm frame,

$$
\begin{aligned}
E^2 &= m_1^2 + m_2^2 + 2m_1m_2\gamma \\
&= M^2(1+2\nu(\gamma-1)),
\end{aligned}
\tag{3.32}
$$

determined by the asymptotic Lorentz factor γ and the rest masses. Note also the definition of the asymptotic relative velocity v as used e.g. in [1, 128, 265],

$$v = \frac{\sqrt{\gamma^2 - 1}}{\gamma} \quad \Leftrightarrow \quad \gamma = \frac{1}{\sqrt{1 - v^2}}. \tag{3.33}$$

We will find it convenient to define yet another variable equivalent to γ or v, namely

$$\varepsilon := \gamma^2 - 1 = \gamma^2 v^2 = \left(\frac{p_\infty E}{m_1 m_2}\right)^2, \tag{3.34}$$

which, like v^2, can serve as a PN expansion parameter, and unlike v, is real for both unbound and bound orbits,

$$\begin{aligned} \text{unbound:} \quad E > M \quad &\Leftrightarrow \quad \varepsilon > 0, \\ \text{bound:} \quad E < M \quad &\Leftrightarrow \quad \varepsilon < 0, \end{aligned} \tag{3.35}$$

noting that $v = i\sqrt{1 - \gamma^2}/\gamma$ and p_∞ are imaginary for bound orbits. (Note that our $\varepsilon = \gamma^2 v^2$ is Damour's "$p_\infty^2 = p_{\text{eob}}^2$" [the squared momentum per mass of the effective test body], while our p_∞ is Damour's "$P_{\text{c.m.}}$".) We will also find it convenient to define a notation for the dimensionless ratio Γ (Damour's "h") between the total energy and the total rest mass,

$$\Gamma := \frac{E}{M} = \sqrt{1 + 2\nu(\gamma - 1)}, \tag{3.36}$$

with $\Gamma > 1$ ($\gamma > 1$) for unbound orbits, and $\Gamma < 1$ ($\gamma < 1$) for bound orbits. Then $p_\infty = \mu\gamma v/\Gamma = \mu\sqrt{\varepsilon}/\Gamma$.

With this notation in order, we can take our simplified result for the impulse magnitude Q (3.16a) [namely the sum of (3.25), its analogous $a_1 a_2$ version, and the SO part (3.29)], insert it into (3.30), and solve for the aligned-spin scattering angle χ. After this process, χ/Γ turns out to be linear in ν in the same way that Q is, thanks to the facts that the sine function is odd in its argument and that Γ^2 is linear in ν. The result can be expressed as follows,

$$\frac{\chi}{\Gamma} = \frac{GM}{b\sqrt{\varepsilon}}\mathsf{X}^{\nu^0}_{G^1} + \left(\frac{GM}{b\sqrt{\varepsilon}}\right)^2\mathsf{X}^{\nu^0}_{G^2} + \left(\frac{GM}{b\sqrt{\varepsilon}}\right)^3\left[\mathsf{X}^{\nu^0}_{G^3} + \nu\mathsf{X}^{\nu^1}_{G^3}\right]$$
$$+ \left(\frac{GM}{b\sqrt{\varepsilon}}\right)^4\left[\mathsf{X}^{\nu^0}_{G^4} + \nu\mathsf{X}^{\nu^1}_{G^4}\right] + \mathcal{O}\left(\frac{GM}{b}\right)^5, \tag{3.37a}$$

where each $\mathsf{X}^{\nu^m}_{G^k}$ takes the form

$$\mathsf{X}^{\nu^m}_{G^k} = \mathsf{X}^m_k(\varepsilon) + \frac{a_\mathrm{b}}{b\sqrt{\varepsilon}}\mathsf{X}^{m\mathrm{b}}_k(\varepsilon) + \frac{a_\mathrm{t}}{b\sqrt{\varepsilon}}\mathsf{X}^{m\mathrm{t}}_k(\varepsilon) + \frac{a_1a_2}{b^2\varepsilon}\mathsf{X}^{m\times}_k(\varepsilon), \tag{3.37b}$$

with $\times$ standing for the "cross term" a_1a_2, and with the special constraints

$$\mathsf{X}^{0\mathrm{b}}_1 = \mathsf{X}^{0\mathrm{t}}_1, \qquad \mathsf{X}^{1\mathrm{b}}_3 = \mathsf{X}^{1\mathrm{t}}_3, \tag{3.38}$$

recalling from (3.28) that $Ma_\mathrm{b} = m_1a_1 + m_2a_2$ and $Ma_\mathrm{t} = m_2a_1 + m_1a_2$. [4] All the X's on the right-hand side of (3.37b) are dimensionless and are functions *only* of the dimensionless $\varepsilon = \gamma^2 - 1$; they can be expressed in terms of the above $\mathsf{Q}(\gamma)$'s alone.

We see that the 1PM and 2PM terms in (3.37) are independent of the symmetric mass ratio ν and are thus fully preserved in the (*extended*) test-body limit $\nu \to 0$ (at fixed M, or equivalently $m_1 \to 0$ at fixed M, *and* at fixed a_1, a_2, b and γ), while the 3PM and 4PM terms are linear in ν. This allows us to deduce the complete 1PM and 2PM results for χ/Γ from its test-body limit, and the complete 3PM and 4PM results from first-order self-force (linear-in-mass-ratio) calculations.

The special constraints (3.38) are consequences of the $1 \leftrightarrow 2$ symmetry, as seen in the $G^1\nu^0$ and $G^3\nu^1$ SO terms in (3.29). This is a prediction of the above arguments which our considerations below will be able to test, rather than to rely on. For the case of the $G^3\nu^1$ SO terms, which

[4] In Ref. [1], the expression of the result (3.37) for the mass dependence of the scattering angle differed in that (i) we did not pull a factor of $1/\sqrt{\varepsilon}$ out of the X's for every factor of $1/b$, (ii) we used v instead of ε, and (iii) we used a_+ and $\delta\, a_-$ in place of a_b and a_t, with $a_\pm := a_2 \pm a_1$ and $\delta := (m_2 - m_1)/M$; the equivalence of the two expressions is apparent since

$$a_+ + \delta\, a_- = 2a_\mathrm{b}, \qquad a_+ - \delta\, a_- = 2a_\mathrm{t}. \tag{3.39}$$

we will determine (in a PN expansion) below from matching to first-order self-force calculations, we will allow $\mathsf{X}^1_{3\mathrm{b}}$ and $\mathsf{X}^1_{3\mathrm{t}}$ to be independent — in fact, $\mathsf{X}^1_{3\mathrm{b}}$ will be determined by the redshift invariant in a Kerr background and $\mathsf{X}^1_{3\mathrm{t}}$ by the spin-precession invariant in a Schwarzschild background — and we will find from the matching procedure that they are indeed equal through the considered PN orders. The fact that the complete content of Eqs. (3.37) holds through N^{2}LO in the PN expansion can be seen in Eqs. (4.32) of Ref. [265].

The ν^0 terms in (3.37) can be determined by solving the MPD equations of motion (3.5) for a spinning (pole-dipole) test body in a stationary background Kerr spacetime. An integrand for the test-spin-in-Kerr aligned-spin scattering angle function, to all PM orders, was derived in Ref. [428]; see, e.g., their Eq. (66) (which also includes pole-dipole-quadrupole terms for a test black hole). The results of the integration are as follows, to all orders in ε (to all PN orders at each PM order), extending Eq. (5.5) of Ref. [265] to 4PM order in the spin-orbit and bilinear-in-spin terms. The nonspinning parts are

$$\begin{aligned}
\mathsf{X}^0_1 &= 2\frac{1+2\varepsilon}{\sqrt{\varepsilon}} = 2\frac{2\gamma^2-1}{\sqrt{\gamma^2-1}} = 2\frac{1+v^2}{v\sqrt{1-v^2}}, \\
\mathsf{X}^0_2 &= \frac{3\pi}{4}(4+5\varepsilon) = \frac{3\pi}{4}(5\gamma^2-1), \\
\mathsf{X}^0_3 &= 2\frac{-1+12\varepsilon+72\varepsilon^2+64\varepsilon^3}{3\varepsilon^{3/2}}, \\
\mathsf{X}^0_4 &= \frac{105\pi}{64}(16+48\varepsilon+33\varepsilon^2),
\end{aligned} \tag{3.40a}$$

the SO parts are

$$\begin{aligned}
\mathsf{X}^{0\mathrm{b}}_1 a_\mathrm{b} + \mathsf{X}^{0\mathrm{t}}_1 a_\mathrm{t} &= -4\gamma\sqrt{\varepsilon}(a_\mathrm{b}+a_\mathrm{t}), \\
\mathsf{X}^{0\mathrm{b}}_2 a_\mathrm{b} + \mathsf{X}^{0\mathrm{t}}_2 a_\mathrm{t} &= -\frac{\pi}{2}\gamma(2+5\varepsilon)(4a_\mathrm{b}+3a_\mathrm{t}), \\
\mathsf{X}^{0\mathrm{b}}_3 a_\mathrm{b} + \mathsf{X}^{0\mathrm{t}}_3 a_\mathrm{t} &= -4\gamma\frac{1+12\varepsilon+16\varepsilon^2}{\sqrt{\varepsilon}}(3a_\mathrm{b}+2a_\mathrm{t}),
\end{aligned} \tag{3.40b}$$

$$\mathsf{X}_4^{0\mathrm{b}} a_\mathrm{b} + \mathsf{X}_4^{0\mathrm{t}} a_\mathrm{t} = -\frac{21\pi}{16}\gamma(8+36\varepsilon+33\varepsilon^2)(8a_\mathrm{b}+5\mathrm{a}_t),$$

and the bilinear-in-spin parts are

$$\begin{aligned}
\mathsf{X}_1^{0\times} &= 4\sqrt{\varepsilon}(1+2\varepsilon), \qquad (3.40c)\\
\mathsf{X}_2^{0\times} &= \frac{3\pi}{2}(2+19\varepsilon+20\varepsilon^2),\\
\mathsf{X}_3^{0\times} &= 8\frac{1+38\varepsilon+128\varepsilon^2+96\varepsilon^3}{\sqrt{\varepsilon}},\\
\mathsf{X}_4^{0\times} &= \frac{105\pi}{16}(24+212\varepsilon+447\varepsilon^2+264\varepsilon^3)
\end{aligned}$$

with $\gamma = \sqrt{1+\varepsilon}$.[5]

The ν^1 terms in (3.37), at 3PM and 4PM orders, can be determined in a PN expansion (here, an expansion in ε) from first-order self-force results (as well as from consistency with lower orders), as we will explicitly demonstrate below for the spin parts. We will use the known nonspinning coefficients through 4PM-3PN order [265],

$$\begin{aligned}
\mathsf{X}_3^1 &= -\frac{8+94\varepsilon+313\varepsilon^2+\mathcal{O}(\varepsilon^3)}{12\sqrt{\varepsilon}}, \qquad (3.41a)\\
\mathsf{X}_4^1 &= \pi\left[-\frac{15}{2}+\left(\frac{123}{128}\pi^2-\frac{557}{8}\right)\varepsilon+\mathcal{O}(\varepsilon^2)\right],
\end{aligned}$$

noting the transcendental $\zeta(2)$ contribution in the last term (the 4PM-3PN term). We will parametrize the SO coefficients as

$$\mathsf{X}_3^{1\mathrm{i}} = \frac{\gamma}{\sqrt{\varepsilon}}\Big(\mathsf{X}_{30}^{1\mathrm{i}}+\mathsf{X}_{31}^{1\mathrm{i}}\varepsilon+\mathsf{X}_{32}^{1\mathrm{i}}\varepsilon^2+\mathsf{X}_{33}^{1\mathrm{i}}\varepsilon^3+\mathcal{O}(\varepsilon^4)\Big),$$

[5] Note that, through 2PM order and up through the SO terms, the first two lines of the right-hand side of (3.37a), with (3.40a) and (3.40b) plugged into the first two lines of (3.37b), correctly give either (i) the aligned-spin scattering angle for a spinning test body with rescaled spin a_t in a Kerr background with mass M and rescaled spin a_b, or (ii) the rescaled aligned-spin scattering angle χ/Γ for the arbitrary-mass two-spinning-body system, using the "spin maps" (3.28); this is a further reason for the labels a_t and a_b. This gives a different "EOB scattering-angle mapping," an alternative to Eq. (3.16) of [265], which produces the 1PM and 2PM SO terms in the two-body scattering angle from its extended test-body limit. [Note however that this different mapping fails at quadratic order in the spins, while Eq. (3.16) of [265] still holds, according to all known results.]

$$\mathsf{X}_4^{1\mathrm{i}} = \pi\gamma\Big(\mathsf{X}_{41}^{1\mathrm{i}} + \mathsf{X}_{42}^{1\mathrm{i}}\varepsilon + \mathsf{X}_{43}^{1\mathrm{i}}\varepsilon^2 + \mathcal{O}(\varepsilon^3)\Big), \tag{3.41b}$$

with $\mathrm{i} = \mathrm{b}, \mathrm{t}$, and the bilinear-in-spin coefficients as

$$\begin{aligned} \mathsf{X}_3^{1\times} &= \frac{1}{\sqrt{\varepsilon}}\Big(\mathsf{X}_{30}^{1\times} + \mathsf{X}_{31}^{1\times}\varepsilon + \mathsf{X}_{32}^{1\times}\varepsilon^2 + \mathsf{X}_{33}^{1\times}\varepsilon^3 + \mathcal{O}(\varepsilon^4)\Big), \\ \mathsf{X}_4^{1\times} &= \pi\Big(\mathsf{X}_{41}^{1\times} + \mathsf{X}_{42}^{1\times}\varepsilon + \mathsf{X}_{43}^{1\times}\varepsilon^2 + \mathcal{O}(\varepsilon^3)\Big). \end{aligned} \tag{3.41c}$$

We have included all the same powers of ε present in the ν^0 coefficients (3.40), up to the orders in ε which will contribute at the N^{3}LO PN level. (We have also factored out $\gamma = \sqrt{1+\varepsilon}$ in the SO terms and π in the 4PM terms, following the patterns at ν^0.) For these $\mathsf{X}_{kn}^{1\cdots}$, which are all pure numbers, k gives the PM order, and n gives the maximum PN order (N^{n}LO) which determines that coefficient. This labeling and the consistency and sufficiency of this ansatz for the scattering angle will become evident in the matching between the scattering angle and a canonical Hamiltonian described in the following section.

Finally, it is important to note that the impact parameter b appearing everywhere in this section is the distance orthogonally separating the two spinning bodies' asymptotic incoming worldlines as defined by the "covariant" or Tulczyjew-Dixon condition [96, 361–363], Eq. (3.5c) above, for each body—the so-called "proper" or "covariant" impact parameter $b \equiv b_{\mathrm{cov}}$ [128, 265, 556]. This is crucial to the above argument because only with the covariant condition (3.5c) (or something equivalent to it at 0PM order) does it hold that the first-order field (3.12) is linear in the masses. Below, we will also work with the canonical orbital angular momentum $L \equiv L_{\mathrm{can}} = p_\infty b_{\mathrm{can}}$, where b_{can} is the impact parameter orthogonally separating the asymptotic incoming worldlines defined by cm-frame Newton-Wigner conditions [364, 365] for each body. This coincides with the conserved canonical orbital angular momentum L appearing in a canonical Hamiltonian formulation of aligned-spin two-body dynamics [366, 557]. [Note that, for the aligned-spin case, the covariant/Pauli-Lubanski spin vectors $m_{\rm i}a_{\rm i}^{\mu}$ used above coincide with the canonical spin vectors $S_{\rm i}^{\mu}$ (spatial vectors in the cm frame) which would be associated with the cm-frame Newton-Wigner conditions, and thus so do the aligned-spin (signed) magnitudes, $S_{\rm i} = m_{\rm i}a_{\rm i}$.] As shown in [264, 265], the canonical $L =: L_{\rm can}$ is related to the covariant b by

$$\begin{aligned} L &= L_{\rm cov} + \Delta L, \\ L_{\rm cov} &= p_\infty b = \frac{\mu}{\Gamma}\gamma v b = \frac{\mu}{\Gamma}\sqrt{\varepsilon} b, \\ \Delta L &= \left(\sqrt{m_1^2+p_\infty^2} - m_1\right)a_1 + \left(\sqrt{m_2^2+p_\infty^2} - m_2\right)a_2 \\ &= M\frac{\Gamma-1}{2}\left(a_{\rm b} + a_{\rm t} - \frac{a_{\rm b}-a_{\rm t}}{\Gamma}\right). \end{aligned} \tag{3.42}$$

Solving this for b, inserting the result into (3.37) [or (3.43)], and re-expanding to bilinear order in the (mass-rescaled) spins a_1 and a_2, one obtains the final parametrized form for the aligned-spin scattering angle function $\chi(E, L; m_{\rm i}, a_{\rm i})$ used in the following matching calculations.

Let us finally rewrite the scattering angle to include both the ν^0 and ν^1 terms in single coefficients (or which could allow mass dependence differing from that deduced above), and which would accommodate general quadratic-in-spin terms, with sums over i and j implied,

$$\frac{\chi}{\Gamma} = \sum_{k\geq 1}\left(\frac{GM}{b\sqrt{\varepsilon}}\right)^k \left[\mathsf{X}_k(\varepsilon,\nu) + \frac{a_{\rm i}}{b\sqrt{\varepsilon}}\mathsf{X}_k{}^{\rm i}(\varepsilon,\nu) + \frac{a_{\rm i}a_{\rm j}}{b^2\varepsilon}\mathsf{X}_k{}^{\rm ij}(\varepsilon,\nu)\right] \tag{3.43}$$

$+\mathcal{O}(a^3)$, with

$$\begin{aligned} a_{\rm i}\mathsf{X}_k{}^{\rm i} &= a_{\rm b}\mathsf{X}_k{}^{\rm b} + a_{\rm t}\mathsf{X}_k{}^{\rm t}, \\ a_{\rm i}a_{\rm j}\mathsf{X}_k{}^{\rm ij} &= a_1a_2\mathsf{X}_k{}^{\times} + \mathcal{O}(a_1^2, a_2^2). \end{aligned} \tag{3.44}$$

Our prediction for the mass-ratio dependence of the kPM coefficients $\mathsf{X}_k{}^{\rm A} = \{\mathsf{X}_k, \mathsf{X}_k{}^{\rm b}, \mathsf{X}_k{}^{\rm t}, \mathsf{X}_k{}^{\times}\}$

is that

$$\mathsf{X}_k{}^{\mathrm{A}}(\varepsilon,\nu) = \begin{cases} \mathsf{X}_k^{0\mathrm{A}}(\varepsilon), & k=1,2 \\ \mathsf{X}_k^{0\mathrm{A}}(\varepsilon) + \nu \mathsf{X}_k^{1\mathrm{A}}(\varepsilon), & k=3,4 \end{cases}. \tag{3.45}$$

The ν^0 coefficients $\mathsf{X}_k^{0\mathrm{A}}(\varepsilon)$ from the extended test-body limit are given explicitly in (3.40), and the ν^1 coefficients $\mathsf{X}_k^{1\mathrm{A}}(\varepsilon)$ which we will determine from self-force results are parametrized in a PN expansion in (3.41). Note that we will also be able to use the self-force results to test the fact that there are no ν^1 terms at 1PM and 2PM orders in this parametrization of the scattering angle. The fact that there are no ν^2 or higher terms through 4PM order cannot be probed with first-order self-force results, but has already been confirmed by arbitrary-mass PN results through N^{2}LO. Our prediction for the mass dependence will yield new arbitrary-mass results at the N^{3}LO PN level once we have fixed the PN expansions of the coefficients $\mathsf{X}_k^{1\mathrm{A}}$ from first-order self-force calculations.

3.3 From the unbound scattering angle to the bound radial action via canonical Hamiltonian dynamics

Besides the mass dependence of the scattering angle function established in the previous section, and the inputs of test-body results (discussed above) and first-order self-force results (discussed below), the other central ingredient in our derivation is the assumption of the existence of a (local-in-time) canonical Hamiltonian governing the aligned-spin conservative dynamics in the cm frame, for generic (*both* bound and unbound) orbits, with the Hamiltonian having well-defined (regular, polynomial) PN and PM expansions. Through the desired 4.5PN order in the SO sector and 5PN S_1S_2 one, we can safely ignore nonlocal-in-time (tail) contributions in the final dynamics/scattering angle. While these do appear at the 4PN level in the nonspinning sector [79] (see e.g., Ref. [558] for a translation into a nonlocal-in-time scattering angle), they only start appearing at 5.5PN order in the spinning one. This can most easily be seen in the first line of Eq.(68a) in Ref. [180], where the linear-in-spin tails are a relative 1.5PN order from the leading quadrupolar contributions to the tail. [As mentioned at the very end of this section, we find it necessary to include tail terms at 4PN order in the nonspinning sector to make contact with available results in the GSF literature.]

Our ultimate goal in this section is to take the gauge-invariant scattering-angle function χ for unbound orbits, parametrized in the previous section, and derive from it a parametrized expression for the gauge-invariant radial-action function I_r which characterizes bound orbits, from which we can derive all the bound-orbit gauge invariants to be compared with self-force results in Sec. 3.4.2 below.

We do this by passing through the gauge-dependent canonical Hamiltonian dynamics. It is to some extent true that this process (as we implement it here) can be bypassed by using relationships between gauge invariants for unbound and bound orbits found in [267], but not entirely. Those relationships yield I_r through $\mathcal{O}(G^4)$ from χ through $\mathcal{O}(G^4)$, but the complete PN expansion of I_r through N^{3}LO extends to $\mathcal{O}(G^8)$ (for the spin terms). The extra terms in I_r are obtained here via the canonical Hamiltonian dynamics, which determines them from (the PN re-expansion of) χ through $\mathcal{O}(G^4)$. Note that χ through $\mathcal{O}(G^4)$ does not contain the complete PN expansion of χ through N^{3}LO, nor through LO, since even the Newtonian scattering angle has contributions at all orders in G. But the PN expansion of the 4PM scattering angle, χ through $\mathcal{O}(G^4)$, does contain the complete information of the N^{3}LO PN Hamiltonian (contained in its $O(G^4)$ truncation), which determines the N^{3}LO PN radial action I_r (contained in its $O(G^8)$ truncation).

We begin in Sec. 3.3.1 by discussing canonical Hamiltonians for aligned-spin binaries, the resultant equations of motion, and their gauge freedom under canonical transformations, in a PM-PN expansion. We fix a unique gauge by imposing simplifying conditions not on the Hamiltonian function H itself, but on its corresponding "mass-shell constraint" (or "impetus formula"[255]), which is simply a rearrangement of the expression of the Hamiltonian, in which the squared momentum is given as a function of the Hamiltonian H (of the energy $E = H$). In Sec. 3.3.2, we describe how the scattering-angle function can be derived from the canonical mass-shell constraint, or vice versa (with our gauge-fixing for the mass shell), and derive the explicit relationships between the scattering-angle coefficients and the mass-shell coefficients. Finally, in Sec. 3.3.3, we compute the radial action I_r, and point out a hidden simplicity in its dependence on the mass ratio, when expressed in terms of appropriate (covariant rather than canonical) variables, which is a simple consequence of the mass dependence of the scattering angle χ and the relationship between χ and I_r discovered in [267].

3.3.1 The canonical Hamiltonian and/or the mass-shell constraint

For an aligned-spin binary canonical Hamiltonian,

$$H(r, \phi, p_r, L; m_{\rm i}, a_{\rm i}) = H(r, p_r, L; m_{\rm i}, a_{\rm i}) \tag{3.46}$$

the dynamical variables (depending on a time parameter t) are polar coordinates (r, ϕ) in the orbital plane, with r being the orbital separation, and their conjugate momenta $(p_r, p_\phi \equiv L)$. The Hamiltonian does not depend on the angular coordinate ϕ due to the system's axial symmetry, and it otherwise depends only on the constant masses and spins $(m_{\rm i}, a_{\rm i}) = (m_1, m_2, a_1, a_2)$. The

Hamiltonian equations of motions read

$$\begin{aligned}\dot{r} &= \frac{\partial H}{\partial p_r}, \qquad \dot{p}_r = -\frac{\partial H}{\partial r}, \\ \dot{\phi} &= \frac{\partial H}{\partial L}, \qquad \dot{L} = -\frac{\partial H}{\partial \phi} = 0,\end{aligned} \tag{3.47}$$

where we note that the canonical orbital angular momentum L is a constant of motion.

Such a Hamiltonian is not unique, but is subject to a type of gauge freedom, namely under canonical transformations: diffeomorphisms of the phase space which preserve the canonical form (3.47) of the equations of motion. In a quite general gauge (one which encompasses all gauges encountered in previous PN or PM aligned-spin Hamiltonians), the Hamiltonian takes the following form through quadratic order in the spins, through 4PM order,

$$\begin{aligned}H = H_0(\boldsymbol{p}^2; m_{\mathrm{i}}) + \sum_{k=1}^{4} \frac{G^k}{r^k} \Bigg[& c_k(\boldsymbol{p}^2, \frac{L^2}{r^2}; m_{\mathrm{i}}) \\ & + \frac{L a_{\mathrm{i}}}{r^2} c_k^{\mathrm{i}}(\boldsymbol{p}^2, \frac{L^2}{r^2}; m_{\mathrm{j}}) + \frac{a_{\mathrm{i}} a_{\mathrm{j}}}{r^2} c_k^{\mathrm{ij}}(\boldsymbol{p}^2, \frac{L^2}{r^2}; m_{\mathrm{k}}) \Bigg] + \mathcal{O}(G^5),\end{aligned} \tag{3.48}$$

where

$$\boldsymbol{p}^2 = p_r^2 + \frac{L^2}{r^2}, \tag{3.49}$$

is the total squared canonical linear momentum. Here, H_0 is the 0PM (free) Hamiltonian, and the functions c_k, c_k^{i} and c_k^{ij} encode respectively the nonspinning, spin-orbit, and quadratic-in-spin gravitational couplings at the kPM orders. The c's are assumed to have regular Taylor series around $L^2 = 0$ and $\boldsymbol{p}^2 = 0$. We will work here with the standard (gauge) choice for the free Hamiltonian in the cm frame,

$$H_0 = \sqrt{m_1^2 + \boldsymbol{p}^2} + \sqrt{m_2^2 + \boldsymbol{p}^2}, \tag{3.50}$$

such that, as $r \to \infty$, the magnitude $\sqrt{\boldsymbol{p}^2}$ of the canonical linear momentum corresponds to the two bodies' physical equal and opposite spatial momenta in the cm frame.

The expression (3.48) of the Hamiltonian can be solved, working perturbatively in G, for $\boldsymbol{p}^2(r, E, L; m_\mathrm{i}, a_\mathrm{i})$, where $E \equiv H(r, p_r, L; m_\mathrm{i}, a_\mathrm{i})$ is the total energy; one finds

$$\begin{aligned}\boldsymbol{p}^2 = p_\infty^2(E; m_\mathrm{i}) + \sum_{k\geq 1} \frac{G^k}{r^k}\bigg[& f_k(E, \frac{L^2}{r^2}; m_\mathrm{i}) \\ & + \frac{La_\mathrm{i}}{r^2} f_k^\mathrm{i}(E, \frac{L^2}{r^2}; m_\mathrm{j}) + \frac{a_\mathrm{i} a_\mathrm{j}}{r^2} f_k^\mathrm{ij}(E, \frac{L^2}{r^2}; m_\mathrm{k})\bigg],\end{aligned} \tag{3.51}$$

where the 0PM part p_∞^2 is found by (exactly) inverting (3.50), $H_0(\boldsymbol{p}^2) = E \;\Leftrightarrow\; p_\infty^2(E) = \boldsymbol{p}^2$,

$$p_\infty^2 = \frac{(E^2 - m_1^2 - m_2^2)^2 - 4m_1^2 m_2^2}{4E^2} = \mu^2 \frac{\gamma^2 - 1}{\Gamma^2}, \tag{3.52}$$

which we recognize as the same p_∞ from (3.31). The functions f_k, f_k^i and f_k^ij are determined by (and carry all of the information of) the $c_k^{\cdots}$ coefficients in the Hamiltonian (3.48). Importantly, the $f_k^{\cdots}$ functions will have regular limits as $\gamma^2 - 1 = \varepsilon \to 0$ (as $p_\infty \to 0$) and as $L^2 \to 0$, given our assumption that the $c_k^{\cdots}$ functions were regular as $\boldsymbol{p}^2 \to 0$ and $L^2 \to 0$. The quantities γ, ε and Γ are all defined in terms of the energy E and the rest masses just as in the previous section.

As discussed in Ref. [265] (through N^{2}LO in the PN expansion, and as we have explicitly verified through N^{3}LO), it is possible to find a perturbative canonical transformation which brings the Hamiltonian (3.48) into a "quasi-isotropic" form, i.e., a form in which the c's depend only $\boldsymbol{p}^2$ and not on L^2/r^2. Furthermore, the freedom in canonical transformations [among Hamiltonians of the form (3.48)] is completely fixed once one imposes this quasi-isotropic-Hamiltonian condition *and* uniquely specifies a 0PM Hamiltonian H_0, as we have done in (3.50). For such a quasi-isotropic Hamiltonian, one finds that the corresponding "mass shell constraint," the expression for $\boldsymbol{p}^2$ (3.51), has nonspinning and SO coefficients f_k f_k^i which are independent of L^2/r^2, but its quadratic-in-spin coefficients f_k^ij have terms at zeroth and first orders in L^2/r^2. However, there also exists a different (non-quasi-isotropic) gauge for the Hamiltonian (3.48) (one with

L^2/r^2 terms in $c_k^{\rm ij}$) such that its mass shell constraint (3.51) is quasi-isotropic, with the f_k, $f_k^{\rm i}$ and $f_k^{\rm ij}$ *all* depending only on E (and the masses) and not on L^2/r^2. Because both the scattering angle and the radial action are more directly related to the f coefficients in the mass shell, we will find it convenient to adopt this quasi-isotropic-mass-shell gauge (which is also unique with a given choice for H_0), specializing (3.51) to the form

$$\boldsymbol{p}^2 = p_\infty^2(E; m_{\rm i}) + \sum_{k\geq 1} \frac{G^k}{r^k}\left[f_k(E; m_{\rm i}) + \frac{La_{\rm i}}{r^2} f_k^{\rm i}(E; m_{\rm j}) + \frac{a_{\rm i}a_{\rm j}}{r^2} f_k^{\rm ij}(E; m_{\rm k})\right]. \tag{3.53}$$

Regrouping in terms of powers of r instead of powers of G, we have

$$p_r^2 + \frac{L^2}{r^2} = \boldsymbol{p}^2 = p_\infty^2 + \sum_{k\geq 1} \frac{G^k}{r^k} \tilde{f}_k, \tag{3.54}$$

where we define

$$\tilde{f}_k = f_k + \frac{La_{\rm i}}{G^2} f_{k-2}^{\rm i} + \frac{a_{\rm i}a_{\rm j}}{G^2} f_{k-2}^{\rm ij}, \tag{3.55}$$

with $f_{-1}^{\cdots} = f_0^{\cdots} = 0$, and we need to extend the sum to $k = 6$ (while dropping the nonspinning f_5 and f_6). Our starting point for the following calculations will be this ansatz for the mass shell constraint, which is fully equivalent to an ansatz for a Hamiltonian of the form (3.48) modulo gauge freedom. Our fundamental assumption is the existence of such a canonical Hamiltonian. We will find that the coefficients $f_k^{\cdots}(E; m_{\rm i})$ are uniquely determined by the expansion of the scattering-angle function to kPM order.

3.3.2 The scattering angle

As shown in [237], the scattering angle $\chi(E, L; m_{\rm i}, a_{\rm i})$ for an unbound orbit can be found directly from the canonical mass-shell constraint as follows. The constraint (3.54) can be solved for the radial momentum $p_r(r, E, L; m_\mathrm{i}, a_\mathrm{i})$, and then the scattering angle is given by the integral

$$\begin{aligned} \pi + \chi(E, L) &= -\int_\infty^\infty \mathrm{d}r \, \frac{\partial}{\partial L} p_r(r, E, L) \\ &= -2\int_{r_\mathrm{min}}^\infty \mathrm{d}r \, \frac{\partial}{\partial L}\sqrt{p_\infty^2 - \frac{L^2}{r^2} + \sum_{k\geq 1}\frac{G^k}{r^k}\tilde{f}_k}, \end{aligned} \tag{3.56}$$

where r_min is the largest real root of $p_r = 0$. In the direct evaluation of this integral, it would matter that the $\tilde{f}_k$ in (3.55) depend on L (in the SO terms). But let us define an antiderivative of $\pi + \chi$ with respect to L to be "the unbound radial action,"

$$W = -\frac{1}{2\pi}\left(\frac{\partial}{\partial L}\right)^{-1}(\pi + \chi), \tag{3.57a}$$

which is essentially a *partie finie* of the radial action integral for unbound orbits,

$$W(E, L) = \frac{1}{2\pi}\mathrm{Pf}\int_\infty^\infty \mathrm{d}r \, p_r(r, E, L). \tag{3.57b}$$

The eikonal phase [239, 268, 559, 560] is $W/\hbar$ (up to a constant). For the expression of W in terms of the $\tilde{f}_k$, it does not matter that the $\tilde{f}_k$ depend on L. That expression will be identical to the L-antiderivative of the nonspinning scattering angle expressed in terms of the nonspinning f_k, with $f_k \to \tilde{f}_k$, so this reduces the evaluation of the integral for the spinning case to the nonspinning problem, using the coefficient mapping (3.55). The results of the nonspinning integral (for χ, from which constructing W is trivial) have been tabulated at high orders, e.g., in [244]. One finds

$$2\pi W = -\pi L - \frac{G \ln L}{p_\infty}\tilde{\chi}_1 + \sum_{k\geq 2}\frac{G^k}{p_\infty^k L^{k-1}}\frac{\tilde{\chi}_k}{k-1}, \tag{3.58}$$

where $\tilde{\chi}_k$ are the entries of Table 1 in [244] with $f_k \to \tilde{f}_k$; the first few read

$$\tilde{\chi}_1 = \tilde{f}_1, \tag{3.59}$$

$$\tilde{\chi}_2 = \frac{\pi}{2}p_\infty^2 \tilde{f}_2,$$

$$\tilde{\chi}_3 = 2p_\infty^4 \tilde{f}_3 + p_\infty^2 \tilde{f}_1 \tilde{f}_2 - \frac{\tilde{f}_1^3}{12},$$
$$\tilde{\chi}_4 = \frac{3\pi}{8} p_\infty^4 (2p_\infty^2 \tilde{f}_4 + \tilde{f}_2^2 + 2\tilde{f}_1 \tilde{f}_3),$$
$$\ldots$$

The scattering angle χ is then given by

$$\pi + \chi = -2\pi \frac{\partial W}{\partial L}, \tag{3.60}$$

with the L-derivative acting also inside the $\tilde{f}_k$ in (3.55). To obtain W or χ through quadratic order in spins and through 4PM order, $\mathcal{O}(G^4)$, counting both the G^k in (3.58) and the $1/G^2$ in (3.55), we must include parts of the contributions up to $\tilde{f}_6$ and up to $\tilde{\chi}_8$. The resultant explicit expression of the scattering angle χ in terms of the $f_k^{\cdots}$ coefficients up to 4PM order and quadratic order in spins is

$$\begin{aligned}
\chi = {} & \frac{G}{p_\infty L} f_1 + \frac{\pi G^2}{2L^2} f_2 + \frac{G^3}{p_\infty^3 L^3} \left[-\frac{1}{12} f_1^3 + p_\infty^2 f_1 f_2 + 2p_\infty^4 f_3 \right] + \frac{3\pi G^4}{8L^4} \left[f_2^2 + 2f_1 f_3 + 2p_\infty^2 f_4 \right] \\
& + a_{\mathrm{i}} \Bigg\{ \frac{G p_\infty}{L^2} f_1^{\mathrm{i}} + \frac{\pi G^2}{2L^3} \left[f_1 f_1^{\mathrm{i}} + p_\infty^2 f_2^{\mathrm{i}} \right] + \frac{G^3}{p_\infty L^4} \left[\frac{3}{4} f_1^2 f_1^{\mathrm{i}} + 3p_\infty^2 \left(f_2 f_1^{\mathrm{i}} + f_1 f_2^{\mathrm{i}} \right) + 2p_\infty^4 f_3^{\mathrm{i}} \right] \\
& \qquad + \frac{3\pi G^4}{4L^5} \left[2f_1 f_2 f_1^{\mathrm{i}} + f_1^2 f_2^{\mathrm{i}} + 2p_\infty^2 \left(f_3 f_1^{\mathrm{i}} + f_2 f_2^{\mathrm{i}} + f_1 f_3^{\mathrm{i}} \right) + p_\infty^4 f_4^{\mathrm{i}} \right] \Bigg\} \\
& + a_{\mathrm{i}} a_{\mathrm{j}} \Bigg\{ \frac{2G p_\infty}{L^3} f_1^{\mathrm{ij}} + \frac{3\pi G^2}{16L^4} \left[4f_1 f_1^{\mathrm{ij}} + p_\infty^2 \left(3f_1^{\mathrm{i}} f_1^{\mathrm{j}} + 4f_2^{\mathrm{ij}} \right) \right] \\
& \qquad + \frac{G^3}{p_\infty L^5} \left[f_1^2 f_1^{\mathrm{ij}} + 4p_\infty^2 \left(f_2 f_1^{\mathrm{ij}} + f_1 f_1^{\mathrm{i}} f_1^{\mathrm{j}} + f_1 f_2^{\mathrm{ij}} \right) + \frac{8}{3} p_\infty^4 \left(2f_1^{\mathrm{i}} f_2^{\mathrm{j}} + f_3^{\mathrm{ij}} \right) \right] \\
& \qquad + \frac{15\pi G^4}{64L^6} \Big[8f_1 f_2 f_1^{\mathrm{ij}} + 5f_1^2 f_1^{\mathrm{i}} f_1^{\mathrm{j}} + 4f_1^2 f_2^{\mathrm{ij}} + p_\infty^4 \left(5f_2^{\mathrm{i}} f_2^{\mathrm{j}} + 10f_1^{\mathrm{i}} f_3^{\mathrm{j}} + 4f_4^{\mathrm{ij}} \right) \\
& \qquad\qquad + 2p_\infty^2 \left(4f_3 f_1^{\mathrm{ij}} + 5f_2 f_1^{\mathrm{i}} f_1^{\mathrm{j}} + 4f_2 f_2^{\mathrm{ij}} + 10f_1 f_1^{\mathrm{i}} f_2^{\mathrm{j}} + 4f_1 f_3^{\mathrm{ij}} \right) \Big] \Bigg\} \\
& + \mathcal{O}(a^3) + \mathcal{O}(G^5).
\end{aligned} \tag{3.61}$$

We see that the kPM coefficients $f_k^{\cdots}$ first enter in the G^k terms; however, they do not enter those terms at the leading orders in p_∞ (in the PN expansion of each PM coefficient). Recalling that all of the f's are finite as $p_\infty \to 0$ ($\varepsilon \to 0$), we see that, within each set of square brackets multiplying G^k, the lowest orders in p_∞ do not depend on $f_k^{\cdots}$, rather only on the lower-PM-order f's (with some exceptions at G^1 and G^2). Similarly, for the scattering-angle coefficients at even higher orders in G (some of which will be relevant below), the lower orders in their PN expansions will be determined by coefficients from lower orders in G already appearing here.

This gives the scattering angle χ in terms of the mass-shell coefficients f_k, f_k^{i}, f_k^{ij}, as an expansion in the canonical orbital angular momentum L. Equating that expression to a parametrization of χ of the form (3.43) in terms of the covariant impact parameter b, using the translation (3.42) while re-expanding in spins, one can solve for the f coefficients in the mass shell in terms of the X coefficients in the scattering angle (or vice versa), order by order in the PM expansion. Recall $p_\infty = \mu\sqrt{\varepsilon}/\Gamma$. Rewriting $\Delta L = L - p_\infty b$ from (3.42) as a sum over (effective) spins,

$$\Delta L = \frac{\mu}{\Gamma}\xi^{\mathrm{i}} a_{\mathrm{i}} = \frac{\mu}{\Gamma}\Big(\xi^{\mathrm{b}} a_{\mathrm{b}} + \xi^{\mathrm{t}} a_{\mathrm{t}}\Big), \tag{3.62a}$$

with

$$\begin{aligned} \xi^{\mathrm{b}} &= \frac{(\Gamma-1)^2}{2\nu} = 2\nu\Big(\frac{\gamma-1}{\Gamma+1}\Big)^2 = \frac{\nu\varepsilon^2}{8} + \mathcal{O}(\varepsilon^3), \\ \xi^{\mathrm{t}} &= \frac{\Gamma^2-1}{2\nu} \quad = \gamma - 1 \qquad\quad = \frac{\varepsilon}{2} + \mathcal{O}(\varepsilon^2), \end{aligned} \tag{3.62b}$$

the results for the f's through 2PM order are as follows: nonspinning,

$$f_1 = \mu^2 M \frac{\sqrt{\varepsilon}}{\Gamma}\mathsf{X}_1, \qquad f_2 = \frac{2\mu^2 M^2}{\pi\Gamma}\mathsf{X}_2, \tag{3.63a}$$

spin-orbit,

$$f_1^{\mathrm{i}} = \frac{\mu M}{\sqrt{\varepsilon}}\Big(\mathsf{X}_1{}^{\mathrm{i}} + \mathsf{X}_1 \xi^{\mathrm{i}}\Big), \tag{3.63b}$$

$$f_2^{\mathrm{i}} = \frac{\mu M^2}{\varepsilon}\left[\frac{2}{\pi}\mathsf{X}_2{}^{\mathrm{i}} - \Gamma\mathsf{X}_1\mathsf{X}_1{}^{\mathrm{i}} + \left(\frac{4}{\pi}\mathsf{X}_2 - \Gamma(\mathsf{X}_1)^2\right)\xi^{\mathrm{i}}\right]$$

and quadratic in spin,

$$\begin{aligned}
f_1^{\mathrm{ij}} &= \frac{\mu^2 M}{2\Gamma\sqrt{\varepsilon}}\Big(\mathsf{X}_1{}^{\mathrm{ij}} + 2\mathsf{X}_1\mathsf{X}_1{}^{\mathrm{i}}\xi^{\mathrm{j}} + \mathsf{X}_1\xi^{\mathrm{i}}\xi^{\mathrm{j}}\Big), \qquad (3.63\mathrm{c})\\
f_2^{\mathrm{ij}} &= \frac{\mu^2 M^2}{\Gamma\varepsilon}\bigg[\frac{4}{3\pi}\mathsf{X}_2{}^{\mathrm{ij}} - \frac{1}{2}\Gamma\mathsf{X}_1\mathsf{X}_1{}^{\mathrm{ij}} - \frac{3}{4}\Gamma\mathsf{X}_1{}^{\mathrm{i}}\mathsf{X}_1{}^{\mathrm{j}}\\
&\qquad + \left(\frac{4}{\pi}\mathsf{X}_2{}^{\mathrm{i}} - \frac{5}{2}\Gamma\mathsf{X}_1\mathsf{X}_1{}^{\mathrm{i}}\right)\xi^{\mathrm{j}} + \left(\frac{4}{\pi}\mathsf{X}_2 - \frac{5}{2}\Gamma(\mathsf{X}_1)^2\right)\xi^{\mathrm{i}}\xi^{\mathrm{j}}\bigg],
\end{aligned}$$

with symmetrization over i and j understood. These 1PM and 2PM results are exact (to all orders in ε). With our predicted mass-ratio dependence from the previous section, we have, for $k = 1, 2$, $\mathsf{X}_k(\varepsilon,\nu) = \mathsf{X}_k^0(\varepsilon)$, $a_{\mathrm{i}}\mathsf{X}_k{}^{\mathrm{i}}(\varepsilon,\nu) = a_{\mathrm{b}}\mathsf{X}_k^{0\mathrm{b}}(\varepsilon) + a_{\mathrm{t}}\mathsf{X}_k^{0\mathrm{t}}(\varepsilon)$, and $a_{\mathrm{i}}a_{\mathrm{j}}\mathsf{X}_k{}^{\mathrm{ij}}(\varepsilon,\nu) = a_1 a_2\mathsf{X}_k^{0\times}(\varepsilon) + \mathcal{O}(a_1^2, a_2^2)$, all independent of ν, and the $\mathsf{X}_k^{0\cdots}(\varepsilon)$ from the extended test-body limit are given explicitly by (3.40). Though it is not immediately obvious here, each of these f's has a finite limit as $\varepsilon \to 0$, as is required by our Hamiltonian ansatz. We will need the expansions of the $f_1^{\cdots}$ up to $\mathcal{O}(\varepsilon^3)$, and of the $f_2^{\cdots}$ up to $\mathcal{O}(\varepsilon^2)$. Along with $f_3^{\cdots}$ up to $\mathcal{O}(\varepsilon^1)$ and $f_4^{\cdots}$ at $\mathcal{O}(\varepsilon^0)$, we will then have a complete mass-shell constraint (3.53) up to N^{3}LO in the PN expansion, which could be solved for the corresponding canonical Hamiltonian (3.48).

At 3PM and 4PM orders, one can also solve for the f's in terms of the X's, obtaining exact expressions analogous to the above. But we will now work in a PN expansion, an expansion in ε, while enforcing our predicted mass-ratio dependence [which (3.63) did not]. For the nonspinning coefficients, using the known results (3.40a) and (3.41a) for the X's, we find

$$\begin{aligned}
\frac{f_3}{\mu^2 M^3} &= \frac{17-10\nu}{2} + \frac{36 - 91\nu + 13\nu^2}{4}\varepsilon + \mathcal{O}(\varepsilon^2),\\
\frac{f_4}{\mu^2 M^4} &= 8 + \left(\frac{41}{32}\pi^2 - \frac{160}{3}\right)\nu + \frac{7}{2}\nu^2 + \mathcal{O}(\varepsilon), \qquad (3.64)
\end{aligned}$$

through the orders that contribute to the N^{3}LO PN level. Here again we note the finite limits as $\varepsilon \to 0$. For the spinning contributions, we must enforce that all the f's have finite limits as $\varepsilon \to 0$, which will fix some of the unknown coefficients in our parametrization (3.41) of the ν^1 parts of the scattering angle, or relationships between them, from consistency with the lower-order f's and X's [recall the discussion following (3.61)]. At the SO level, this determines or constrains the lower-PN-order scattering-angle coefficients,

$$\mathsf{X}_{30}^{1\mathrm{i}} a_{\mathrm{i}} = 0, \tag{3.65}$$

$$\begin{aligned}
\mathsf{X}_{31}^{1\mathrm{i}} a_{\mathrm{i}} &= 10(a_{\mathrm{b}} + a_{\mathrm{t}}), \\
\mathsf{X}_{41}^{1\mathrm{i}} a_{\mathrm{i}} &= \frac{21}{2} a_{\mathrm{b}} + 9 a_{\mathrm{t}}, \\
\mathsf{X}_{42}^{1\mathrm{i}} a_{\mathrm{i}} &= \frac{3}{4}\Big(68 a_{\mathrm{b}} + 49 a_{\mathrm{t}} + 2\mathsf{X}_{32}^{1\mathrm{i}} a_{\mathrm{i}}\Big),
\end{aligned}$$

and expressions for f_3^{i} and f_4^{i} which are explicitly regular as $\varepsilon \to 0$ and depend on the remaining unknowns $\mathsf{X}_{32}^{1\mathrm{i}}$, $\mathsf{X}_{33}^{1\mathrm{i}}$, and $\mathsf{X}_{43}^{1\mathrm{i}}$, with $\mathrm{i} = \mathrm{b}, \mathrm{t}$,

$$\begin{aligned}
\frac{f_3^{\mathrm{i}} a_{\mathrm{i}}}{\mu M^3} = {} & \frac{-6 + 4\nu - 5\nu^2}{2} a_{\mathrm{b}} + \frac{-3 - 31\nu - 9\nu^2}{4} a_{\mathrm{t}} + \frac{\nu}{2}\mathsf{X}_{32}^{1\mathrm{i}} a_{\mathrm{i}} \\
& + \Bigg[\frac{-24 + 172\nu - 276\nu^2 + 21\nu^3}{16} a_{\mathrm{b}} + \frac{-166\nu - 90\nu^2 + 9\nu^3}{8} a_{\mathrm{t}} \\
& \quad + \frac{\nu}{4}\Big(\mathsf{X}_{32}^{1\mathrm{i}} + 2\mathsf{X}_{33}^{1\mathrm{i}}\Big) a_{\mathrm{i}}\Bigg]\varepsilon + \mathcal{O}(\varepsilon^2),
\end{aligned} \tag{3.66a}$$

and

$$\begin{aligned}
\frac{f_4^{\mathrm{i}} a_{\mathrm{i}}}{\mu M^4} = {} & \left(-2 - \frac{811}{8}\nu - 4\nu^2 + \frac{13}{8}\nu^3\right) a_{\mathrm{b}} + \left(\frac{1}{8} - \frac{1577}{12}\nu + \frac{41}{16}\pi^2\nu + \frac{35}{4}\nu^2 + \frac{3}{2}\nu^3\right) a_{\mathrm{t}} \\
& + \nu\Big[(4+\nu)\mathsf{X}_{32}^{1\mathrm{i}} - 2\mathsf{X}_{33}^{1\mathrm{i}} + \frac{4}{3}\mathsf{X}_{43}^{1\mathrm{i}}\Big] a_{\mathrm{i}} + \mathcal{O}(\varepsilon).
\end{aligned} \tag{3.66b}$$

Similarly, for the bilinear-in-spin coefficients, we find

$$\mathsf{X}_{30}^{1\times} = 0, \qquad \mathsf{X}_{31}^{1\times} = 8, \qquad \mathsf{X}_{41}^{1\times} = \frac{15}{2}, \qquad \mathsf{X}_{42}^{1\times} = \frac{45}{32}\Big(-22 + \mathsf{X}_{32}^{1\times}\Big), \tag{3.67}$$

while $f_k^{\mathrm{ij}} a_{\mathrm{i}} a_{\mathrm{j}} = f_k^{\times} a_1 a_2 + \mathcal{O}(a_1^2, a_2^2)$ with $f_3^{\times}$ and $f_4^{\times}$ given in terms of the remaining unknowns $\mathsf{X}_{32}^{1\times}$, $\mathsf{X}_{33}^{1\times}$, and $\mathsf{X}_{43}^{1\times}$ (and remaining unknowns from the SO level) by

$$\begin{aligned}\frac{f_3^{\times}}{\mu^2 M^3} &= \frac{5}{2} + \left(\frac{9}{2} + \frac{3}{8}\mathsf{X}_{32}^{1\times}\right)\nu - \nu^2 \\ &\quad + \frac{3}{8}\left[4 - 15\nu - 16\nu^2 + 4\nu^3 + 2\nu(1-2\nu)\mathsf{X}_{32}^{1\mathrm{b}} + 4\nu^2\mathsf{X}_{32}^{1\mathrm{t}} - \frac{\nu^2}{2}\mathsf{X}_{32}^{1\times} + \nu\mathsf{X}_{33}^{1\times}\right]\varepsilon + \mathcal{O}(\varepsilon^2),\end{aligned} \tag{3.68a}$$

and

$$\begin{aligned}\frac{f_4^{\times}}{\mu^2 M^4} &= 2 + \frac{187}{4}\nu - 21\nu^2 + \frac{13}{8}\nu^3 + \frac{\nu}{4}(19+2\nu)\mathsf{X}_{32}^{1\mathrm{b}} + \frac{\nu}{2}(10-\nu)\mathsf{X}_{32}^{1\mathrm{t}} \\ &\quad - \frac{3}{4}\nu(4+\nu)\mathsf{X}_{32}^{1\times} + \frac{3}{2}\nu\mathsf{X}_{33}^{1\times} + \frac{16}{15}\nu\mathsf{X}_{43}^{1\times} + \mathcal{O}(\varepsilon).\end{aligned} \tag{3.68b}$$

We now have a complete expression of the mass-shell constraint (3.53) through N^{3}LO in the PN expansion and through bilinear order in spins, which could be solved for the corresponding canonical Hamiltonian. It depends on the remaining unknown (dimensionless, numerical) coefficients $\mathsf{X}_{32}^{1\mathrm{A}}$, $\mathsf{X}_{33}^{1\mathrm{A}}$, and $\mathsf{X}_{43}^{1\mathrm{A}}$ with $\mathrm{A} = \{\mathrm{b}, \mathrm{t}, \times\}$, from (3.41). Recall, for $\mathsf{X}_{kn}^{1\mathrm{A}}$, k is the PM order, and n is the relative PN order.

3.3.3 The radial action

For a bound orbit ($\gamma^2 - 1 = \gamma^2 v^2 = \varepsilon < 0$), the same canonical mass-shell constraint (3.53) governs the motion. The (gauge-dependent) radial momentum function $p_r(r, E, L; m_{\mathrm{i}}, a_{\mathrm{i}})$ is still given by

$$p_r = \pm\sqrt{p_\infty^2 - \frac{L^2}{r^2} + \sum_k \frac{G^k}{r^k}\left[f_k + \frac{L a_{\mathrm{i}}}{r^2} f_k^{\mathrm{i}} + \frac{a_{\mathrm{i}} a_{\mathrm{j}}}{r^2} f_k^{\mathrm{ij}}\right]}, \tag{3.69}$$

but now $p_\infty^2 = (\mu/\Gamma)^2\varepsilon$ is negative. As a result, $p_r^2(r)$ has two positive real roots $r = r_\pm$ between which p_r^2 is positive, with r_+ being the largest real root, and the trajectory oscillates between these radial turning points $r_\pm$. The *canonical radial action* function $I_r(E, L, m_\mathrm{i}, a_\mathrm{i})$ is defined as the integral of $p_r \mathrm{d}r$ over one period of the radial motion,

$$\begin{aligned}
2\pi I_r := \oint \mathrm{d}r\, p_r &= \int_{r_-}^{r_+} \mathrm{d}r \Big(+\sqrt{p_r^2}\Big) + \int_{r_+}^{r_-} \mathrm{d}r \Big(-\sqrt{p_r^2}\Big) \\
&= 2\int_{r_-}^{r_+} \mathrm{d}r \sqrt{p_r^2},
\end{aligned} \tag{3.70}$$

and it is a gauge-invariant function, from which one can derive several other gauge-invariant functions physically characterizing bound orbits [255, 267]. Like the "unbound radial action" W (the L-antiderivative of the scattering-angle χ) (3.57), the bound radial action $I_r(E, L, m_\mathrm{i}, a_\mathrm{i})$ encodes the complete gauge-invariant information content of the canonical Hamiltonian (governing both unbound and bound orbits) (at least up to the N^{3}LO PN level) — though in a subtly different way, concerning orders in the PM-PN expansion of I_r versus that of W.

It was shown in [267] that the periastron-advance angle, $\Phi = 2\pi + \Delta\Phi = -2\pi\partial I_r/\partial L$, the angle swept out by a bound orbit during one period of the radial motion, is related to the scattering angle, $\pi + \chi = -2\pi\partial W/\partial L$, by

$$\Phi(E, L, m_\mathrm{i}, a_\mathrm{i}) = 2\pi + \chi(E, L, m_\mathrm{i}, a_\mathrm{i}) + \chi(E, -L, m_\mathrm{i}, -a_\mathrm{i}), \tag{3.71}$$

where the right-hand side requires an analytic continuation from $E > M$ (unbound, for which χ is real) to $E < M$ (bound, for which χ is complex), as detailed below. It follows from a straightforward extension of their argument that a particular L-antiderivative of this relation holds, giving the bound radial action I_r in terms of the unbound radial action W,

$$I_r(E, L, m_\mathrm{i}, a_\mathrm{i}) = W(E, L, m_\mathrm{i}, a_\mathrm{i}) - W(E, -L, m_\mathrm{i}, -a_\mathrm{i}), \tag{3.72}$$

as can also be verified by explicit calculation.

Consider the unbound radial action in the form (3.58), after replacing $\tilde{\chi}_1$ using (3.59) and (3.63a),

$$W = -\frac{L}{2} - GM\mu\frac{1+2\varepsilon}{\sqrt{\varepsilon}}\frac{\ln L}{\pi} + \frac{1}{2\pi}\sum_{k\geq 2}\frac{G^k}{p_\infty^k L^{k-1}}\frac{\tilde{\chi}_k}{k-1}. \tag{3.73}$$

In continuing this from the unbound case, $\varepsilon > 0$, $p_\infty^2 > 0$, to the bound case, $\varepsilon < 0$, $p_\infty^2 < 0$, the second term with $1/\sqrt{\varepsilon}$ becomes imaginary, as do all of the terms in the sum with k odd, having odd powers of $p_\infty = (\mu/\Gamma)\sqrt{\varepsilon}$. Note, from (3.59) and (3.55), and from the fact that all of the f's have regular Taylor series in ε about $\varepsilon = 0$, that all of the $\tilde{\chi}_k$ are still real for the bound case, and that the $\tilde{\chi}_k$ are unchanged by $(L, a_\mathrm{i}) \to (-L, -a_\mathrm{i})$. Thus, plugging the continuation of (3.73), with $\sqrt{\varepsilon} = i\sqrt{-\varepsilon}$, into (3.72), we see that all of the odd-k terms are canceled; after using $\ln L - \ln(-L) = \ln(-1) = -i\pi$ (choosing the branch which yields the physically sensible result), we are left with

$$I_r = -L + GM\mu\frac{1+2\varepsilon}{\sqrt{-\varepsilon}} + \frac{1}{\pi}\sum_{l\geq 1}\frac{G^{2l}}{p_\infty^{2l}L^{2l-1}}\frac{\tilde{\chi}_{2l}}{2l-1}, \tag{3.74}$$

which is real for bound orbits. Only the $\tilde{\chi}_k$ with k even ($k = 2l$) remain, and those with k odd are gone (except for $\tilde{\chi}_1$). This may make it seem as though we have lost information in passing from W to I_r, but in fact we have not, as long as we are sure to keep all terms in the consistent PN expansion of I_r (at least up to the N^{3}LO PN level); this is due to relationships between the $\tilde{\chi}_k$ as discussed below (3.61).

As we will make clearer below, the complete PN expansion of I_r up to N^{3}LO is contained in its PM expansion up to $\mathcal{O}(G^6)$ for the nonspinning terms and up to $\mathcal{O}(G^8)$ for the spin-orbit and quadratic-in-spin terms. This can be computed directly from (3.74), recalling that the $\tilde{\chi}_k$ are the entries of Table 1 of [244] with $f_k \to \tilde{f}_k$, as in (3.61) above, with the $\tilde{f}_k$ given by (3.55). We need again the contributions from f_k, f_k^i, f_k^ij up to $k = 4$, contained in the $\tilde{f}_k =$

$f_k + f^{\rm i}_{k-2} L a_{\rm i}/G^2 + f^{\rm ij}_{k-2} a_{\rm i} a_{\rm j}/G^2$ up to $k=6$. To reach the all the G^8 quadratic-in-spin terms, we must take the sum in (3.74) up to $l=6$, involving parts of $\tilde{\chi}_{12}$.

This process yields the radial action I_r through the N^{3}LO PN level as an expansion in the inverse canonical orbital angular momentum $L \equiv L_{\rm can}$. To express the results of that process, it will be advantageous to use the covariant orbital angular momentum $L_{\rm cov}$, which we define for the bound-orbit case by

$$L_{\rm cov} := L - \Delta L, \tag{3.75}$$

with $\Delta L(E, a_{\rm i})$ still given by the last two lines of (3.42) or by (3.62), in which we note that everything is still real for bound orbits [unlike in the second line of (3.42), where we would need to continue to imaginary b to keep $L_{\rm cov} = p_\infty b$ real].

In fact, the expression of the radial action (mostly) in terms of $L_{\rm cov}$ is simply related to the expression of the scattering angle in terms of $L_{\rm cov}$, as follows. Taking the form (3.43) for the scattering angle and eliminating b in favor of $L_{\rm cov} = (\mu/\Gamma)\sqrt{\varepsilon} b$,

$$\begin{aligned} \chi &= \Gamma \sum_{k\geq 1} \left(\frac{GM}{b\sqrt{\varepsilon}}\right)^k \left[\mathsf{X}_k + \frac{a_{\rm i}}{b\sqrt{\varepsilon}} \mathsf{X}_k{}^{\rm i} + \frac{a_{\rm i} a_{\rm j}}{b^2 \varepsilon} \mathsf{X}_k{}^{\rm ij}\right] \\ &= \Gamma \sum_{k\geq 1} \left(\frac{GM\mu}{\Gamma L_{\rm cov}}\right)^k \left[\mathsf{X}_k + \frac{\mu a_{\rm i}}{\Gamma L_{\rm cov}} \mathsf{X}_k{}^{\rm i} + \frac{\mu^2 a_{\rm i} a_{\rm j}}{\Gamma^2 L_{\rm cov}^2} \mathsf{X}_k{}^{\rm ij}\right], \end{aligned} \tag{3.76}$$

and then using (3.57a), being sure to match up the constant of integration with (3.73), we find

$$\begin{aligned} W = &-\frac{L}{2} - GM\mu \mathsf{X}_1 \frac{\ln L_{\rm cov}}{2\pi} + \frac{1}{2\pi} \sum_{k\geq 2} \frac{(GM\mu)^k}{(\Gamma L_{\rm cov})^{k-1}} \frac{\mathsf{X}_k}{k-1} \\ &+ \frac{1}{2\pi} \sum_{k\geq 1} \left(\frac{GM\mu}{\Gamma L_{\rm cov}}\right)^k \left[\mu a_{\rm i} \frac{\mathsf{X}_k{}^{\rm i}}{k} + \frac{\mu^2 a_{\rm i} a_{\rm j}}{\Gamma L_{\rm cov}} \frac{\mathsf{X}_k{}^{\rm ij}}{k+1}\right]. \end{aligned} \tag{3.77}$$

Then applying (3.72), as we did between (3.73) and (3.74), noting $L_{\rm cov} \to -L_{\rm cov}$ under $(L, a_{\rm i}) \to$

$(-L,-a_{\rm i})$, we are left with

$$I_r = -L + GM\mu\frac{1+2\varepsilon}{\sqrt{-\varepsilon}} + \frac{1}{\pi}\sum_{l\geq 1}\frac{(GM\mu)^{2l}}{(\Gamma L_{\rm cov})^{2l-1}}\left[\frac{\mathsf{X}_{2l}}{2l-1} + \frac{\mu a_{\rm i}}{\Gamma L_{\rm cov}}\frac{\mathsf{X}_{2l}{}^{\rm i}}{2l} + \frac{\mu^2 a_{\rm i}a_{\rm j}}{(\Gamma L_{\rm cov})^2}\frac{\mathsf{X}_{2l}{}^{\rm ij}}{2l+1}\right], \tag{3.78}$$

where these $\mathsf{X}_k{}^{\cdots}(\varepsilon,\nu)$ are precisely the same coefficients from the scattering angle in (3.76). These coefficients up through $k=2l=4$ are those we gave or parametrized above in (3.40) and (3.41), with (3.45). Recollecting them here, while using the constraints (3.65) and (3.67) obtained in matching between the scattering angle and the canonical mass shell, we have the G^2 coefficients which are independent of ν and are known exactly,

$$\begin{aligned}\mathsf{X}_2 &= \frac{3\pi}{4}(4+5\varepsilon),\\ \mathsf{X}_2{}^{\rm i}a_{\rm i} &= -\frac{\pi}{2}\gamma(2+5\varepsilon)(4a_{\rm b}+3a_{\rm t}),\\ \mathsf{X}_2{}^{\times} &= \frac{3\pi}{2}(2+19\varepsilon+20\varepsilon^2),\end{aligned} \tag{3.79a}$$

and the G^4 coefficients which are linear in ν,

$$\begin{aligned}\mathsf{X}_4 &= \frac{105\pi}{64}(16+48\varepsilon+33\varepsilon^2) + \pi\left[-\frac{15}{2} + \left(\frac{123}{128}\pi^2 - \frac{557}{8}\right)\varepsilon + \mathcal{O}(\varepsilon^2)\right]\nu,\\ \mathsf{X}_4{}^{\rm i}a_{\rm i} &= -\frac{21\pi}{16}\gamma(8+36\varepsilon+33\varepsilon^2)(8a_{\rm b}+5{\rm a}_t)\\ &\quad + \pi\gamma\left[\frac{21}{2}a_{\rm b} + 9a_{\rm t} + \frac{3}{4}\Big(68a_{\rm b}+49a_{\rm t}+2\mathsf{X}^{1\rm i}_{32}a_{\rm i}\Big)\varepsilon + \mathsf{X}^{1\rm i}_{43}a_{\rm i}\varepsilon^2 + \mathcal{O}(\varepsilon^3)\right]\nu,\\ \mathsf{X}_4{}^{\times} &= \frac{105\pi}{16}(24+212\varepsilon+447\varepsilon^2+264\varepsilon^3) + \pi\left[\frac{15}{2} + \frac{45}{32}\Big(-22+\mathsf{X}^{1\times}_{32}\Big)\varepsilon + \mathsf{X}^{1\times}_{43}\varepsilon^2 + \mathcal{O}(\varepsilon^3)\right]\nu.\end{aligned} \tag{3.79b}$$

As mentioned above, for the complete expression of the radial action at the N^{3}LO PN level, we need the low orders in the PN expansions of $\mathsf{X}_6{}^{\cdots}$ and (for the spin terms) $\mathsf{X}_8{}^{\cdots}$. We have obtained these from the procedure to compute the radial action described in the paragraph containing (3.74) and the following paragraph, in which the inputs are the $f_k^{\cdots}$ up to $k=4$ found in the previous subsection, finally changing variables using (3.75) to bring the result into the form (3.76). At G^6, we find the nonspinning

$$\frac{\mathsf{X}_6}{5\pi} = \frac{231}{4} + \Big(\frac{123}{128}\pi^2 - \frac{125}{2}\Big)\nu + \frac{21}{8}\nu^2 + \mathcal{O}(\varepsilon), \tag{3.79c}$$

spin-orbit,

$$\begin{aligned}\frac{\mathsf{X}_6{}^{\mathrm{i}}a_{\mathrm{i}}}{15\pi} &= \Big(-99 + \frac{127}{4}\nu - \frac{5}{4}\nu^2\Big)a_{\mathrm{b}} + \Big(-\frac{231}{4} + \frac{167}{8}\nu - \frac{9}{8}\nu^2\Big)a_{\mathrm{t}} + \frac{1}{4}\nu\mathsf{X}_{32}^{1\mathrm{i}}a_{\mathrm{i}} \\ &\quad + \bigg[\Big(-693 + \frac{4989}{16}\nu - \frac{123}{32}\pi^2\nu - \frac{225}{16}\nu^2\Big)a_{\mathrm{b}} + \Big(\frac{733}{4}\nu - \frac{1617}{4} - \frac{123}{64}\pi^2\nu - \frac{183}{16}\nu^2\Big)a_{\mathrm{t}} \\ &\quad + \nu\Big(\frac{7-3\nu}{8}\mathsf{X}_{32}^{1\mathrm{i}} - \frac{5}{4}\mathsf{X}_{33}^{1\mathrm{i}} + \mathsf{X}_{43}^{1\mathrm{i}}\Big)a_{\mathrm{i}}\bigg]\varepsilon + \mathcal{O}(\varepsilon^2),\end{aligned} \tag{3.79d}$$

and bilinear-in-spin,

$$\begin{aligned}\frac{\mathsf{X}_6{}^{\times}}{35\pi} &= \frac{495}{4} - \frac{123\nu}{16} - \frac{9}{8}\nu^2 + \frac{3}{32}\nu\mathsf{X}_{32}^{1\times} + \bigg[\frac{10197}{8} - \frac{4835}{32}\nu + \frac{123}{128}\pi^2\nu - \frac{399}{32}\nu^2 \\ &\quad - \frac{3}{8}\nu(1+2\nu)\mathsf{X}_{32}^{1\mathrm{b}} - \frac{3}{4}\nu(1-\nu)\mathsf{X}_{32}^{1\mathrm{t}} + \frac{9}{64}\nu(2-\nu)\mathsf{X}_{32}^{1\times} - \frac{15}{32}\nu\mathsf{X}_{33}^{1\times} + \frac{2}{5}\nu\mathsf{X}_{43}^{1\times}\bigg]\varepsilon + \mathcal{O}(\varepsilon^2).\end{aligned} \tag{3.79e}$$

At G^8, spin-orbit,

$$\begin{aligned}\frac{\mathsf{X}_8{}^{\mathrm{i}}a_{\mathrm{i}}}{35\pi} &= \Big(-715 + \frac{23947}{48}\nu - \frac{41}{8}\pi^2\nu - \frac{97}{2}\nu^2 + \frac{13}{16}\nu^3\Big)a_{\mathrm{b}} \\ &\quad + \Big(-\frac{6435}{16} + \frac{6883}{24}\nu - \frac{41}{16}\pi^2\nu - \frac{277}{8}\nu^2 + \frac{3}{4}\nu^3\Big)a_{\mathrm{t}} \\ &\quad + \nu\Big(\frac{2-\nu}{2}\mathsf{X}_{32}^{1\mathrm{i}} - \mathsf{X}_{33}^{1\mathrm{i}} + \frac{2}{3}\mathsf{X}_{43}^{1\mathrm{i}}\Big)a_{\mathrm{i}} + \mathcal{O}(\varepsilon),\end{aligned} \tag{3.79f}$$

and bilinear-in-spin

$$\frac{\mathsf{X}_8{}^{\times}}{315\pi} = \frac{5005}{16} - \frac{6599}{96}\nu + \frac{41}{128}\pi^2\nu - \frac{199}{32}\nu^2 + \frac{5}{16}\nu^3 - \frac{1}{8}\nu(1+2\nu)\mathsf{X}_{32}^{1\mathrm{b}} - \frac{1}{4}\nu(1-\nu)\mathsf{X}_{32}^{1\mathrm{t}} \tag{3.79g}$$

$$+ \frac{3}{64}\nu(2-\nu)\mathsf{X}_{32}^{1\times} - \frac{3}{32}\nu\mathsf{X}_{33}^{1\times} + \frac{1}{15}\nu\mathsf{X}_{43}^{1\times} + \mathcal{O}(\varepsilon). \tag{3.79h}$$

Note that the $\mathsf{X}_6{}^{\cdots}$ coefficients in (3.79d) and (3.79e) are exactly quadratic in ν, in spite of the fact that the f's from which they are constructed, in (3.66) and (3.68), are cubic in ν. Less surprisingly, the $\mathsf{X}_6{}^{\cdots}$ are cubic in ν, and more surprisingly the $\mathsf{X}_4{}^{\cdots}$ are linear in ν and the $\mathsf{X}_2{}^{\cdots}$ are independent of ν. This is all in fact a simple consequence of (i) the link (3.78) between the scattering-angle coefficients $\mathsf{X}_k{}^{\cdots}$ and the radial-action coefficients, and (ii) the (straightforward) extension of the predicted mass-ratio dependence (3.45) to kPM order: $\mathsf{X}_k{}^{\cdots}$ is a polynomial of degree $\lfloor\frac{k-1}{2}\rfloor$ in ν. This is the spinning analog of the "hidden simplicity" of the mass dependence of (the local-in-time part of) the radial action (which is the complete radial action through the N^{3}LO PN level) emphasized in Ref. [91]; here in the spin terms, this is crucially dependent on expressing I_r in (3.78) in terms the covariant $L_{\rm cov}$ rather than the canonical L.

Finally, we can make the PN order counting explicit by restoring factors of $1/c$. Through N^{3}LO, (3.78) reads

$$
\begin{aligned}
I_r = &\left[-L + GM\mu\frac{1+2\varepsilon}{c\sqrt{-\varepsilon}} + \frac{\mathsf{X}_2}{c^2}\frac{(GM\mu)^2}{\pi\Gamma L_{\rm cov}} + \frac{\mathsf{X}_4}{c^4}\frac{(GM\mu)^4}{3\pi(\Gamma L_{\rm cov})^3} + \frac{\mathsf{X}_6}{c^6}\frac{(GM\mu)^6}{5\pi(\Gamma L_{\rm cov})^5} + \mathcal{O}(\frac{1}{c^8})\right] \\
&+ \frac{\mu}{c}a_{\rm i}\left[\mathsf{X}_2{}^{\rm i}\frac{(GM\mu)^2}{2\pi(\Gamma L_{\rm cov})^2} + \frac{\mathsf{X}_4{}^{\rm i}}{c^2}\frac{(GM\mu)^4}{4\pi(\Gamma L_{\rm cov})^4} + \frac{\mathsf{X}_6{}^{\rm i}}{c^4}\frac{(GM\mu)^6}{6\pi(\Gamma L_{\rm cov})^6} + \frac{\mathsf{X}_8{}^{\rm i}}{c^6}\frac{(GM\mu)^8}{8\pi(\Gamma L_{\rm cov})^8} + \mathcal{O}(\frac{1}{c^8})\right] \\
&+ \mu^2 a_{\rm i}a_{\rm j}\left[\mathsf{X}_2{}^{\rm ij}\frac{(GM\mu)^2}{3\pi(\Gamma L_{\rm cov})^3} + \frac{\mathsf{X}_4{}^{\rm ij}}{c^2}\frac{(GM\mu)^4}{5\pi(\Gamma L_{\rm cov})^5} + \frac{\mathsf{X}_6{}^{\rm ij}}{c^4}\frac{(GM\mu)^6}{7\pi(\Gamma L_{\rm cov})^7} + \frac{\mathsf{X}_8{}^{\rm ij}}{c^6}\frac{(GM\mu)^8}{9\pi(\Gamma L_{\rm cov})^9} + \mathcal{O}(\frac{1}{c^8})\right],
\end{aligned}
\tag{3.80}
$$

with all the coefficients, to the orders in $\varepsilon = \gamma^2 - 1 = \mathcal{O}(c^{-2})$ contributing here at N^{3}LO, relative $\mathcal{O}(c^{-6})$, given explicitly by (3.79). These depend on the remaining unknowns $\mathsf{X}_{kn}^{1\rm A}$ from the parametrization of the scattering angle, at kPM order and relative nPN order.

In all the above manipulations, it was consistent to keep the nonspinning, spin-orbit, and bilinear-in-spin terms all through the same relative PN orders, here relative 3PN order, N^{3}LO. However, in matching to self-force results, due to certain changes of variables discussed below, the treatment of the N^{3}LO spin-orbit and bilinear-in-spin terms will require the inclusion of the 4PN nonspinning terms. We thus need to add to (3.80) the 4PN nonspinning part of the radial action for bound orbits, which includes contributions from the nonlocal-in-time tail integrals. We present in Appendix B the additional terms at 4PN order, which have been computed from (3.70) applied to the 4PN EOB Hamiltonian derived in [80], valid in an expansion in eccentricity (about the circular orbit limit) to sixth order. Replacing the first two lines of (3.80) with (B.1) yields the final form of the radial-action function which we will use to compute the gauge-invariant quantities to be compared with self-force calculations.

3.4 Third-subleading post-Newtonian spin-orbit and spin$_1$-spin$_2$ couplings

The remaining unknowns in the parametrization of the scattering-angle function (3.41) can be fixed with available self-force results. The key feature here is the existence of a Hamiltonian/radial action allowing us to connect the scattering-angle to the redshift and spin-precession invariants that, in the small-mass-ratio limit, can be matched to expressions independently calculated in GSF literature. A vital step in this calculation is the first law of BBH mechanics, which we extend to aligned-spins and eccentric orbits.

3.4.1 The first law of BBH mechanics

The first law of BBH mechanics [429] was first derived for nonspinning point particles in circular orbits in Ref. [429], then generalized to spinning particles on circular orbits in Ref. [430], to nonspinning particles in eccentric orbits in Refs. [431, 432], and to precessing eccentric orbits of a point mass in the small mass-ratio approximation [535]. In the following, we briefly review the arguments leading to these incarnations of the first law for binaries, making explicit how they apply to generic mass-ratio aligned-spin systems on eccentric orbits.

Let us follow Ref. [430] and start out with an action $\mathcal{S}$ for the binary,

$$\mathcal{S} = \mathcal{S}_{\text{grav}} + \mathcal{S}_1 + \mathcal{S}_2 \,, \tag{3.81}$$

where the compact objects are approximated by effective point-particles moving along worldlines $x_{\rm i}^\mu(\tau_{\rm i})$,

$$\mathcal{S}_{\rm i} = \int \mathrm{d}\tau_{\rm i} \left[-m_{\rm i} + \frac{1}{2} S_{{\rm i}\mu\nu} \Lambda_{{\rm i}c}{}^{\mu} \frac{D\Lambda_{\rm i}^{c\nu}}{d\tau} + \lambda_{\rm i}^{\mu} S_{{\rm i}\mu\nu} \dot{x}_{\rm i}^{\nu} + \dots \right], \tag{3.82}$$

and the gravitational action $\mathcal{S}_{\text{grav}}$ is given by the Einstein-Hilbert one with appropriate gauge-fixing and boundary terms. Here $\Lambda_{\rm i}^{c\mu}$ are frame transformations between the coordinate frame and a body-fixed frame (labeled by $c = 0, 1, 2, 3$) that is Lorentz-orthonormal ($\Lambda_{{\rm i}c}{}^{\mu} \Lambda_{{\rm i}d\mu} = \eta_{cd}$). We take $\tau_{\rm i}$ to be the (full-metric) proper times from now on. The equations of motion are obtained by varying the action with respect to the dynamical variables $X_A = \{x_{\rm i}, S_{\mu\nu}, \Lambda_{\rm i}^{c\mu}, \lambda_{\rm i}^{\mu}, g_{\mu\nu}\}$, leading to Eqs. (3.5)–(3.7), see, e.g., Refs. [362, 366]. The dots in Eq. (3.82) represent nonminimal (curvature) couplings to the worldline that may carry undetermined coefficients. These terms also include couplings of quadratic and higher orders in spin related to spin-induced multipole moments of the body [362].

Let us write the action as an integral of a Lagrangian L over coordinate time t as

$$\mathcal{S} = \int \mathrm{d}t \, L \,. \tag{3.83}$$

We can vary the Lagrangian L not only with respect to the dynamical variables X_A, but also vary certain constants appearing in the action, e.g., the masses $C_B = \{m_1, m_2\}$. Furthermore, taking the dynamical variables X_A on-shell (fulfilling their equations of motion) after variation, we arrive at (using summation convention for A, B)

$$\delta L = \frac{\partial L}{\partial C_B} \delta C_B + \underbrace{\frac{\delta L}{\delta X_A}}_{=0 \text{ (on-shell)}} \delta X_A + (\text{td}) \,, \tag{3.84}$$

with a total time derivative (td). Now, if one performs a transformation of the dynamical variables $X_A \to X'_{A'}$, which may depend on the C_B, then on-shell it holds

$$\delta L = \frac{\partial L}{\partial C_B}\delta C_B + \left[\underbrace{\frac{\delta L}{\delta X_A}}_{0}\frac{\delta X_A}{\delta X'_{A'}}\frac{\partial X'_{A'}}{\partial C_B} + (\text{td})\right]\delta C_B + \underbrace{\frac{\delta L}{\delta X_A}}_{0}\frac{\delta X_A}{\delta X'_{A'}}\delta X'_{A'} + (\text{td})\,. \tag{3.85}$$

Also allowing for changes of the Lagrangian of the form $L = L' + (\text{td})$, we arrive at

$$\left\langle \left(\frac{\partial L'}{\partial C_B}\right)_{X'_{A'}} \right\rangle = \left\langle \left(\frac{\partial L}{\partial C_B}\right)_{X_A} \right\rangle \quad (\text{on-shell})\,, \tag{3.86}$$

where the subscripts indicate quantities that are kept fixed during differentiation and with $\langle \dots \rangle$ an appropriate on-shell averaging that removes the total time derivatives.

For generic bound orbits, one can average the conservative motion in Eq. (3.86) over an infinite time in order to remove total time derivatives, which can be traded for a phase-space average in regions where the motion is ergodic; see, e.g., Refs. [535, 561]. For the aligned-spin case where the motion is confined to a plane, all oscillatory behavior can be removed by an average over a single orbit [431] (defined as an oscillation cycle of the radial distance r); this is the averaging used in the present paper. Further specializing to circular orbits, the radial distance is constant and hence the average becomes trivial [430]. Finally, note that another benefit of the averaging in Eq. (3.86) is that it helps to make expressions manifestly gauge invariant [535], which is important when matching PN Hamiltonians to (eccentric-orbit) self-force results.

It is straightforward to generalize the discussion from Lagrangians L' to Hamiltonians H'. Hamilton's dynamical equations for some pairs of canonical variables $(q^{\mathsf{c}}, p_{\mathsf{c}})$ are equivalently encoded by Hamilton's action principle,

$$0 = \delta\mathcal{S} = \delta\int \mathrm{d}t \Bigg[\underbrace{\sum_{\mathsf{c}} p_{\mathsf{c}}\frac{dq^{\mathsf{c}}}{dt} - H'}_{L'}\Bigg]\,. \tag{3.87}$$

Noting that the dynamical variables are now $X'_{A'} = \{q^{\mathsf{c}}, p_{\mathsf{c}}\}$, and that the kinematic $p\dot{q}$-terms in L' are independent of the C_B, we see that either Lagrangian in Eq. (3.86) can be replaced by *minus* a Hamiltonian (i.e., it can be applied also to canonical transformations between two Hamiltonians). The rather general on-shell relation (3.86) is interesting on its own, aside from facilitating the derivation of the first law of binary dynamics as demonstrated below.

We are now in a position to elaborate on the redshift variables z_{i} [429–431],

$$z_{\mathrm{i}} \equiv \left\langle \frac{\mathrm{d}\tau_{\mathrm{i}}}{\mathrm{d}t} \right\rangle = -\left\langle \frac{\partial L}{\partial m_{\mathrm{i}}} \right\rangle , \tag{3.88}$$

where the first equality is the definition of z_{i} adopted by us and the second equality is a consequence of the definition of L (3.83) together with the original point-particle action (3.82), $\int \mathrm{d}t\, L \sim -m_{\mathrm{i}} \int \mathrm{d}t\, \mathrm{d}\tau_{\mathrm{i}}/\mathrm{d}t$. We note that this relation holds to all orders in spin if the coefficients in the nonminimal couplings (the dots) in Eq. (3.82) are normalized such that no further explicit dependence on the masses m_{i} arises [344]. Now, several nontrivial transformations of the original action (3.81) are performed to arrive at a PN Hamiltonian (see, e.g., Refs. [132, 430, 432]): a transformation to SO(3)-canonical (Newton-Wigner) variables for the spin degrees of freedom, integrating out the orbital/near-zone metric or tetrad field (calculating the "Fokker action"), reduction of higher-order time derivatives via further variable transformations, a Legendre transform to the Hamiltonian H, specialization to the cm system, and eventually reducing nonlocal-in-time tail contributions to local ones. However, all of these transformations fall into the class of transformations $(X_A, L) \to (X'_{A'}, L')$ discussed above, so we may apply Eq. (3.86) (with $L' \to -H$) to Eq. (3.88) and conclude that the redshift variables z_{i} can be obtained from a PN Hamiltonian H via

$$z_{\mathrm{i}} = \left\langle \frac{\partial H}{\partial m_{\mathrm{i}}} \right\rangle . \tag{3.89}$$

Beside the redshift, let us introduce the (averaged) spin precession frequency $\Omega_{\rm i}$ as another important observable [430],

$$\Omega_{\rm i} \equiv \left\langle \left| \vec{\Omega}_{\rm i}^{\rm inst} \right| \right\rangle . \tag{3.90}$$

The (instantaneous, directed) precession frequency $\vec{\Omega}_{\rm i}^{\rm inst}$ can be read off from the equations of motion for the SO(3)-canonical spin vectors $S_{\rm i}^i$ generated by the Hamiltonian H,

$$\frac{{\rm d}\vec{S}_{\rm i}}{{\rm d}t} = \vec{\Omega}_{\rm i}^{\rm inst} \times \vec{S}_{\rm i} \,, \qquad \vec{\Omega}_{\rm i}^{\rm inst} \equiv \frac{\partial H}{\partial \vec{S}_{\rm i}} \,. \tag{3.91}$$

Indeed, this describes a precession of the spin vector; it is straightforward to see that the spin length $S_{\rm i} \equiv (\vec{S}_{\rm i} \cdot \vec{S}_{\rm i})^{1/2}$ is constant,

$$\frac{{\rm d}(\vec{S}_{\rm i} \cdot \vec{S}_{\rm i})}{{\rm d}t} = 2\vec{S}_{\rm i} \cdot \vec{\Omega}_{\rm i}^{\rm inst} \times \vec{S}_{\rm i} = 0 \,. \tag{3.92}$$

From now on, as in previous sections, we simplify the discussion to nonprecessing (aligned or anti-aligned) spins, so that $\vec{\Omega}_{\rm i}^{\rm inst} \parallel \vec{S}_{\rm i}$ and $d\vec{S}_{\rm i}/dt = 0$. That is, the spin degrees of freedom become nondynamical and can be dropped from the set of dynamical variables. [6] We can now include the spin lengths into our set of constants, $C_B = \{m_{\rm i}, S_{\rm i}\}$. Furthermore, the spin-direction component of the defining relation for $\vec{\Omega}_{\rm i}^{\rm inst}$ (3.91) reads $|\vec{\Omega}_{\rm i}^{\rm inst}| = \partial H/\partial S_{\rm i}$. Hence Eq. (3.90) becomes

$$\Omega_{\rm i} = \left\langle \frac{\partial H}{\partial S_{\rm i}} \right\rangle \qquad \text{(nonprecessing).} \tag{3.93}$$

We have now arrived at the important Eqs. (3.89) and (3.93) for the (gauge-invariant) observables $z_{\rm i}$ and $\Omega_{\rm i}$, that could be used to relate a PN Hamiltonian H to self-force results [343, 351]. But here, for the purpose of matching to self-force, we perform a canonical transformation to

[6] More precisely, their contribution to the kinematic terms in Hamilton's principle (3.87) (have to) vanish or turn into total time derivatives.

different phase-space variables that simplify explicit calculations and connects to the radial action introduced above.

As a first step in that direction, we choose the (nonprecessing) motion to be in the equatorial plane $\theta = \pi/2$, removing the polar angle θ and its canonical conjugate momentum p_θ from the phase space; the Hamiltonian is now of the form discussed in Sec. 3.3.1. Furthermore, since we consider a system where the Hamilton-Jacobi equation is separable, one can construct a special canonical transformation (for bound orbits) where the *constant* action variables

$$I_r = \frac{1}{2\pi} \oint \mathrm{d}r \, p_r, \qquad\qquad I_\phi = \frac{1}{2\pi} \oint \mathrm{d}\phi \, p_\phi = L\,, \tag{3.94}$$

are the new momenta [300], with the cm orbital angular momentum of the binary $p_\phi \equiv L = \text{const}$ conjugate to the azimuthal angle ϕ. The advantage of these variables for our purpose is that the averaging $\langle \ldots \rangle$ over one radial period becomes trivial due to the integral over one radial period $\oint$ in their definition. The canonical conjugates to I_r, I_ϕ are the so-called angle variables q_r, q_ϕ and evolve linear in time, i.e., their angular frequencies $\Omega_r = \dot{q}_r$, $\Omega_\phi = \dot{q}_\phi$ are constant [300]; overall Hamilton's equations of motion for the new, canonically transformed, Hamiltonian $H'(I_r, I_\phi = L; C_B)$ read

$$\Omega_r = \frac{\partial H'}{\partial I_r} = \text{const}\,, \qquad\qquad \Omega_\phi = \frac{\partial H'}{\partial L} = \text{const}\,, \tag{3.95}$$

$$\dot{I}_r = -\frac{\partial H'}{\partial q_r} = 0\,, \qquad\qquad \dot{L} = -\frac{\partial H'}{\partial q_\phi} = 0\,. \tag{3.96}$$

Recalling that $C_B = \{m_\mathrm{i}, S_\mathrm{i}\}$, we can apply Eq. (3.86) (with both Lagrangians replaced by Hamiltonians) for the canonical transformation to action-angle variables as well. Equations (3.89) and (3.93) then turn into

$$z_\mathrm{i} = \frac{\partial H'}{\partial m_\mathrm{i}}\,, \qquad \Omega_\mathrm{i} = \frac{\partial H'}{\partial S_\mathrm{i}}\,, \tag{3.97}$$

where the averaging over one radial period is inconsequential and can be dropped. Collecting Eqs. (3.95) and (3.97), we see that the differential of the cm energy $E \equiv H'$ can be written as

$$\mathrm{d}E = \Omega_r \mathrm{d}I_r + \Omega_\phi \mathrm{d}L + \sum_{\mathrm{i}} (z_{\mathrm{i}} \mathrm{d}m_{\mathrm{i}} + \Omega_{\mathrm{i}} \mathrm{d}S_{\mathrm{i}}). \tag{3.98}$$

In analogy to the first law of thermodynamics for the differential of the internal energy, this can be called the first law of conservative spinning binary dynamics for nonprecessing bound orbits (covering eccentric orbits and generic mass ratios). It also resembles the first law of BH thermodynamics, which provides a relation for the differential of the Arnowitt-Deser-Misner (ADM) energy $\mathrm{d}m_{\mathrm{i}}$ of an isolated BH and can be generalized to other compact objects as well [562]. Recall that Eq. (3.98) is valid to all orders in spin, if the coefficients of possible nonminimal coupling terms denoted by dots in Eq. (3.82) are normalized such that no additional dependence on m_{i} arises. It would be interesting to consider these coefficients as part of the constants C_B in future work.

Since the fundamental function introduced in the last section that generates observables for bound orbits is the radial action $I_r(E, L; m_{\mathrm{i}}, S_{\mathrm{i}})$, we consider the first law (3.98) in the form

$$2\pi \, \mathrm{d}I_r = T_r \mathrm{d}E - \Phi \mathrm{d}L - \sum_{\mathrm{i}} (\mathcal{T}_{\mathrm{i}} \mathrm{d}m_{\mathrm{i}} + \Phi_{\mathrm{i}} \mathrm{d}S_{\mathrm{i}}) \,, \tag{3.99}$$

where we have introduced

$$T_r = \frac{2\pi}{\Omega_r} = \oint \mathrm{d}t \,, \qquad \Phi = \Omega_\phi T_r = \oint \mathrm{d}\phi \,, \tag{3.100}$$

$$\mathcal{T}_{\mathrm{i}} = z_{\mathrm{i}} T_r = \oint \mathrm{d}\tau_{\mathrm{i}} \,, \qquad \Phi_{\mathrm{i}} = \Omega_{\mathrm{i}} T_r \,. \tag{3.101}$$

As a consequence of the first law, we hence obtain

$$\frac{T_r}{2\pi} = \left(\frac{\partial I_r}{\partial E}\right)_{L, m_{\mathrm{i}}, S_{\mathrm{i}}} , \qquad \frac{\Phi}{2\pi} = -\left(\frac{\partial I_r}{\partial L}\right)_{E, m_{\mathrm{i}}, S_{\mathrm{i}}} , \tag{3.102a}$$

$$\frac{\mathcal{T}_{\rm i}}{2\pi} = -\left(\frac{\partial I_r}{\partial m_{\rm i}}\right)_{E,L,m_{\rm j},S_{\rm i}}, \qquad \frac{\Phi_{\rm i}}{2\pi} = -\left(\frac{\partial I_r}{\partial S_{\rm i}}\right)_{E,L,m_{\rm i},S_{\rm j}}. \tag{3.102b}$$

Now the redshift variables can be calculated, from a given radial action I_r, as the ratio of proper and coordinate times,

$$z_{\rm i} = \frac{\mathcal{T}_{\rm i}}{T_r}, \tag{3.103}$$

which manifestly agrees with the (inverse of the) Detweiler-Barack-Sago redshift invariant calculated in GSF literature [314, 336]. The spin-precession frequency $\Omega_{\rm i}$ is given by $\Omega_{\rm i} = \Phi_{\rm i}/T_r$ from which we obtain the spin-precession invariant [346]

$$\psi_{\rm i} = \frac{\Omega_{\rm i}}{\Omega_\phi} = \frac{\Phi_{\rm i}}{\Phi}. \tag{3.104}$$

3.4.2 Comparison with self-force results

Starting from the radial action (3.78), we calculate the redshift z_1 and spin-precession invariants ψ_1 of the small body using Eqs. (3.103) and (3.104). To compare with results available in the literature, we express them in terms of the gauge-invariant variables[7]

$$x = (GM\Omega_\phi)^{2/3}, \quad \iota = \frac{3x}{\Phi/(2\pi) - 1}. \tag{3.105}$$

which are linked to (ε, L) via Eqs. (3.95) and (3.102). The expressions we obtain for $z_1(x,\iota)$ and $\psi(x,\iota)$ agree up to N^{2}LO with those in Eq. (50) of Ref. [343] and Eq. (83) of Ref. [351]. The full expressions up to N^{3}LO are lengthy, which is why we provide them as a `Mathematica` file in the Supplemental Material [**?**].

[7]Note that the denominator for ι in Eq. (3.105) is of 1PN order, which effectively scales down the PN ordering in such a way that manifestly nonlocal-in-time (4PN nonspinning) terms appear in the N^{3}LO correction to the spin-precession invariant. For this reason, we have included the 4PN nonspinning tail terms in the radial action as discussed at the end of the previous section.

Next, we expand $U_1 \equiv z_1^{-1}$ and ψ_1 to first order in the mass ratio q, first order in the massive body's spin a_2, and zeroth order in the spin of the smaller companion a_1,

$$U_1 = U^{(0)}_{1a^0} + \hat{a}\, U^{(0)}_{1a} + q\left(\delta U^{\rm GSF}_{1a^0} + \hat{a}\,\delta U^{\rm GSF}_{1a}\right) + \mathcal{O}(q^2, \hat{a}^2)\,, \tag{3.106a}$$

$$\psi_1 = \psi^{(0)}_{1a^0} + \hat{a}\, \psi^{(0)}_{1a} + q\left(\delta \psi^{\rm GSF}_{1a^0} + \hat{a}\,\delta \psi^{\rm GSF}_{1a}\right) + \mathcal{O}(q^2, \hat{a}^2)\,, \tag{3.106b}$$

with $\hat{a} = a_2/m_2$. In performing that expansion, we make use of the gauge-independent variables y and λ, which are related to x and ι via

$$y = (G m_2 \Omega_\phi)^{2/3} = \frac{x}{(1+q)^{2/3}}\,, \tag{3.107a}$$

$$\lambda = \frac{3y}{\Phi/(2\pi) - 1} = \frac{\iota}{(1+q)^{2/3}}\,. \tag{3.107b}$$

To compare the 1SF corrections $\delta U^{\rm GSF}_{1\cdots}$ and $\delta\psi^{\rm GSF}_{1\cdots}$ with those derived in the literature, we express the redshift and spin-precession invariants in terms of the Kerr-geodesic variables (u_p, e), where e is the eccentricity and u_p is the inverse of the dimensionless semilatus rectum (see Appendix C for details.) The terms needed to solve for the N^{3}LO SO unknowns are $\delta U^{\rm GSF}_{1a}$ and $\delta\psi^{\rm GSF}_{1\,a^0}$, for which we obtain

$$\begin{aligned}
\delta U^{\rm GSF}_{1a} &= \left(3 - \frac{7e^2}{2} - \frac{e^4}{8}\right) u_p^{5/2} + \left(18 - 4e^2 - \frac{117e^4}{4}\right) u_p^{7/2} + \left[\frac{251}{4} + \frac{1}{2}\mathsf{X}^{\rm 1b}_{32} + \frac{287e^2}{2}\right. \\
&\quad \left. - e^4\left(\frac{11099}{32} + \frac{15}{16}\mathsf{X}^{\rm 1b}_{32}\right)\right] u_p^{9/2} + \left[\frac{239}{2} - \frac{5}{4}\mathsf{X}^{\rm 1b}_{32} - \frac{5}{2}\mathsf{X}^{\rm 1b}_{33} + \frac{4}{3}\mathsf{X}^{\rm 1b}_{43}\right. \\
&\quad + e^2\left(\frac{35441}{24} - \frac{41\pi^2}{8} - \frac{11}{4}\mathsf{X}^{\rm 1b}_{32} - \frac{5}{2}\mathsf{X}^{\rm 1b}_{33} + 2\mathsf{X}^{\rm 1b}_{43}\right) \\
&\quad \left. + e^4\left(-\frac{230497}{96} + \frac{205\pi^2}{32} + \frac{195}{32}\mathsf{X}^{\rm 1b}_{32} + \frac{135}{16}\mathsf{X}^{\rm 1b}_{33} - 5\mathsf{X}^{\rm 1b}_{43}\right)\right] u_p^{11/2}\,,
\end{aligned} \tag{3.108a}$$

$$\begin{aligned}
\delta\psi^{\rm GSF}_{1\,a^0} &= -u_p + \left(\frac{9}{4} + e^2\right) u_p^2 + \left[\frac{933}{16} - \frac{123\pi^2}{64} - \frac{1}{4}\mathsf{X}^{\rm 1t}_{32} + e^2\left(\frac{79}{2} - \frac{123\pi^2}{256} - \frac{3}{8}\mathsf{X}^{\rm 1t}_{32}\right)\right] u_p^3 \\
&\quad + \Bigg[-\frac{277031}{2880} + \frac{1256\gamma_E}{15} + \frac{15953\pi^2}{6144} + \frac{11}{8}\mathsf{X}^{\rm 1t}_{32} + \frac{5}{4}\mathsf{X}^{\rm 1t}_{33} - \frac{2}{3}\mathsf{X}^{\rm 1t}_{43} + \frac{296}{15}\ln 2 + \frac{729}{5}\ln 3
\end{aligned}$$

$$
+\frac{628}{15}\ln u_p+e^2\bigg(\frac{20557}{480}+\frac{536\gamma_E}{5}-\frac{55217\pi^2}{4096}+\frac{55}{16}\mathsf{X}_{32}^{1\text{t}}+\frac{25}{8}\mathsf{X}_{33}^{1\text{t}}-2\mathsf{X}_{43}^{1\text{t}}
+\frac{11720}{3}\ln 2-\frac{10206}{5}\ln 3+\frac{268}{5}\ln u_p\bigg)\bigg]u_p^4\,. \tag{3.108b}
$$

These results can be directly compared with the GSF results in Eq. (4.1) of Ref. [341], Eq. (23) of Ref. [433] and Eq. (20) of Ref. [343] for the redshift, and Eq. (3.33) of Ref. [349] for the precession frequency. At N^{2}LO, as expected, our expressions depend on the scattering-angle coefficients. Upon matching these with the above-mentioned equations in the literature, we get the following four constraints (at each order in eccentricity):

$$
u_p^{9/2}\left[\frac{1}{2}\mathsf{X}_{32}^{1\text{b}}-\frac{97}{4}+e^4\left(\frac{1455}{32}-\frac{15}{16}\mathsf{X}_{32}^{1\text{b}}\right)\right]=0\,, \tag{3.109a}
$$

$$
u_p^{3}\left[\frac{97}{8}-\frac{1}{4}\mathsf{X}_{32}^{1\text{t}}+e^2\left(\frac{291}{16}-\frac{3}{8}\mathsf{X}_{32}^{1\text{t}}\right)\right]=0\,, \tag{3.109b}
$$

which can be consistently solved for the two unknowns

$$
\mathsf{X}_{32}^{1\text{b}}=\mathsf{X}_{32}^{1\text{t}}=\frac{97}{2}\,. \tag{3.110}
$$

Note that the special constraint (3.38), due to symmetry under interchanging the two bodies' labels $1\leftrightarrow 2$, is thus satisfied. Similarly, at N^{3}LO order, after substituting in the N^{2}LO coefficients, it holds that

$$
u_p^{11/2}\bigg[-\frac{26881}{72}+\frac{241\pi^2}{96}-\frac{5}{2}X_{33}^{1\text{b}}+\frac{4}{3}X_{43}^{1\text{b}}+e^2\bigg(-\frac{1846}{3}+\frac{241\pi^2}{64}-\frac{5}{2}X_{33}^{1\text{b}}+2X_{43}^{1\text{b}}\bigg)
+e^4\bigg(\frac{276775}{192}-\frac{1205\pi^2}{128}+\frac{135}{16}X_{33}^{1\text{b}}-5X_{43}^{1\text{b}}\bigg)\bigg]=0, \tag{3.111a}
$$

$$
u_p^4\bigg[\frac{8381}{48}-\frac{41\pi^2}{16}+\frac{5}{4}\mathsf{X}_{33}^{1\text{t}}-\frac{2}{3}\mathsf{X}_{43}^{1\text{t}}+e^2\bigg(\frac{17647}{32}-\frac{123\pi^2}{16}+\frac{25}{8}\mathsf{X}_{33}^{1\text{t}}-2\mathsf{X}_{43}^{1\text{t}}\bigg)\bigg]=0\,.
$$

These five equations can be consistently solved for the remaining four unknowns in the N^{3}LO SO scattering angle,

$$
\mathsf{X}_{33}^{1\text{b}}=\mathsf{X}_{33}^{1\text{t}}=\frac{177}{4}, \tag{3.112}
$$

$$\mathsf{X}_{43}^{1\mathrm{b}} = \frac{17423}{48} - \frac{241\pi^2}{128}, \qquad \mathsf{X}_{43}^{1\mathrm{t}} = \frac{2759}{8} - \frac{123}{32}\pi^2.$$

Again, the special constraint (3.38) is satisfied by $\mathsf{X}_{33}^{1\mathrm{b}}$ and $\mathsf{X}_{33}^{1\mathrm{t}}$. Considering the S_1S_2 dynamics, the relevant constraints can be obtained from the linear-in-spin correction to the spin-precession invariant, which in terms of the remaining unknown coefficients $\mathsf{X}_{ij}^{1\times}$ reads

$$\begin{aligned}\delta\psi_{1\,a^1}^{\mathsf{GSF}} = &-\frac{u_p^{3/2}}{2} - \left(\frac{41}{8} + \frac{e^2}{8}\right) u_p^{5/2} - \left[\frac{63}{32} + \frac{123\pi^2}{64} + \frac{3}{16}\mathsf{X}_{32}^{1\times}\right. \\ &\left. + e^2\left(\frac{71}{4} + \frac{123\pi^2}{256} + \frac{9}{32}\mathsf{X}_{32}^{1\times}\right)\right] u_p^{7/2} + \left[\frac{75841\pi^2}{6144} - \frac{4496717}{5760} + \frac{1256\gamma_E}{15} + \frac{39}{32}\mathsf{X}_{32}^{1\times}\right. \\ &+ \frac{15}{16}\mathsf{X}_{33}^{1\times} - \frac{8}{15}\mathsf{X}_{43}^{1\times} + \frac{296}{15}\ln 2 + \frac{729}{5}\ln 3 + \frac{628}{15}\ln u_p + e^2\Bigg(\frac{7703\pi^2}{4096} - \frac{1016249}{640} \\ &\left. + \frac{536\gamma_E}{5} + \frac{195}{64}\mathsf{X}_{32}^{1\times} + \frac{75}{32}\mathsf{X}_{33}^{1\times} - \frac{8}{5}\mathsf{X}_{43}^{1\times} + \frac{11720}{3}\ln 2 - \frac{10206}{5}\ln 3 + \frac{268}{5}\ln u_p\Bigg)\right] u_p^{9/2}.\end{aligned} \tag{3.113}$$

At N^{2}LO, this can be matched to Eqs. (52) and (56) of Ref. [351] to get the two constraints (at each order in e)

$$u_p^{7/2}\left[\frac{75}{8} + \frac{3}{16}\mathsf{X}_{32}^{1\times} + e^2\left(\frac{225}{16} + \frac{9}{32}\mathsf{X}_{32}^{1\times}\right)\right] = 0\,, \tag{3.114}$$

which can be solved for

$$\mathsf{X}_{32}^{1\times} = -50\,. \tag{3.115}$$

Similarly, at N^{3}LO it holds that

$$\begin{aligned}u_p^{9/2}\Bigg[&-\frac{6299}{16} + \frac{123\pi^2}{32} + \frac{15}{16}\mathsf{X}_{33}^{1\times} - \frac{8}{15}\mathsf{X}_{43}^{1\times} \\ &+ e^2\left(-\frac{41943}{32} + \frac{369\pi^2}{32} + \frac{75}{32}\mathsf{X}_{33}^{1\times} - \frac{8}{5}\mathsf{X}_{43}^{1\times}\right)\Bigg] = 0\,.\end{aligned} \tag{3.116}$$

Each order in eccentricity is solved for the remaining S_1S_2 unknown coefficients

$$\mathsf{X}_{33}^{1\times} = -\frac{1383}{5}, \qquad \mathsf{X}_{43}^{1\times} = -\frac{9795}{8} + \frac{1845\pi^2}{256}\,. \tag{3.117}$$

Combining the solutions obtained in this section with the results of Sec. 3.2 yields the scattering angle containing the complete local-in-time conservative SO and S_1S_2 dynamics through the third-subleading PN order

$$
\begin{aligned}
\frac{\chi}{\Gamma} = \quad & \left(\frac{GM}{b\sqrt{\varepsilon}}\right) 2\frac{1+2\varepsilon}{\sqrt{\varepsilon}} + \left(\frac{GM}{b\sqrt{\varepsilon}}\right)^2 \frac{3\pi}{4}(4+5\varepsilon) \\
& - \left(\frac{GM}{b\sqrt{\varepsilon}}\right)^3 \frac{1}{\sqrt{\varepsilon}} \left[2\frac{1-12\varepsilon-72\varepsilon^2-64\varepsilon^3}{3\varepsilon} + \nu\left(\frac{8+94\varepsilon+313\varepsilon^2}{12}\right)\right] \\
& + \left(\frac{GM}{b\sqrt{\varepsilon}}\right)^4 \pi \left[\frac{105}{64}(16+48\varepsilon+33\varepsilon^2) + \nu\left(-\frac{15}{2} + \left(\frac{123}{128}\pi^2 - \frac{557}{8}\right)\varepsilon\right)\right] \\
- \left(\frac{a_b}{b\sqrt{\varepsilon}}\right) \Bigg\{ & \left(\frac{GM}{b\sqrt{\varepsilon}}\right) 4\gamma\sqrt{\varepsilon} + \left(\frac{GM}{b\sqrt{\varepsilon}}\right)^2 2\pi\gamma\,(2+5\varepsilon) \\
& + \left(\frac{GM}{b\sqrt{\varepsilon}}\right)^3 \frac{\gamma}{\sqrt{\varepsilon}} \left[12(1+12\varepsilon+16\varepsilon^2) - \nu\left(10\varepsilon + \frac{97}{2}\varepsilon^2 + \frac{177}{4}\varepsilon^3\right)\right] \\
& + \left(\frac{GM}{b\sqrt{\varepsilon}}\right)^4 \pi\gamma \left[\frac{21}{2}(8+36\varepsilon+33\varepsilon^2) - \nu\left(\frac{21}{2} + \frac{495}{4}\varepsilon + \left(\frac{17423}{48} - \frac{241\pi^2}{128}\right)\varepsilon^2\right)\right] \Bigg\} \\
- \left(\frac{a_t}{b\sqrt{\varepsilon}}\right) \Bigg\{ & \left(\frac{GM}{b\sqrt{\varepsilon}}\right) 4\gamma\sqrt{\varepsilon} + \left(\frac{GM}{b\sqrt{\varepsilon}}\right)^2 \frac{3\pi}{2}\gamma\,(2+5\varepsilon) \\
& + \left(\frac{GM}{b\sqrt{\varepsilon}}\right)^3 \frac{\gamma}{\sqrt{\varepsilon}} \left[8(1+12\varepsilon+16\varepsilon^2) - \nu\left(10\varepsilon + \frac{97}{2}\varepsilon^2 + \frac{177}{4}\varepsilon^3\right)\right] \\
& + \left(\frac{GM}{b\sqrt{\varepsilon}}\right)^4 \pi\gamma \left[\frac{105}{16}(8+36\varepsilon+33\varepsilon^2) - \nu\left(9 + \frac{219}{2}\varepsilon + \left(\frac{2759}{8} - \frac{123}{32}\pi^2\right)\varepsilon^2\right)\right] \Bigg\} \\
+ \left(\frac{a_1a_2}{b^2\varepsilon}\right) \Bigg\{ & \left(\frac{GM}{b\sqrt{\varepsilon}}\right) \frac{4}{\sqrt{\varepsilon}}(\varepsilon+2\varepsilon^2) + \left(\frac{GM}{b\sqrt{\varepsilon}}\right)^2 \frac{3\pi}{2}(2+19\varepsilon+20\varepsilon^2) \\
& + \left(\frac{GM}{b\sqrt{\varepsilon}}\right)^3 \frac{1}{\sqrt{\varepsilon}} \left[8(1+38\varepsilon+128\varepsilon^2+96\varepsilon^3) + \nu\left(8\varepsilon - 50\varepsilon^2 - \frac{1383}{5}\varepsilon^3\right)\right] \\
& + \left(\frac{GM}{b\sqrt{\varepsilon}}\right)^4 \pi \Bigg[\frac{105}{16}(24+212\varepsilon+447\varepsilon^2+264\varepsilon^3) \\
& \qquad + \nu\left(\frac{15}{2} - \frac{405}{4}\varepsilon + \left(-\frac{9795}{8} + \frac{1845\pi^2}{256}\right)\varepsilon^2\right)\Bigg]\Bigg\}.
\end{aligned}
\tag{3.118}
$$

Importantly, we have checked that all the above results can be reproduced by starting from a Hamiltonian ansatz (rather than a radial action), constraining it via the mass-ratio dependence of the scattering angle (calculated via (3.56)), and obtaining the redshift and spin-precession invariants through Eqs. (3.89) and (3.93).

3.5 Effective-one-body Hamiltonian and comparison with numerical relativity

In this section, we quantify the improvement in accuracy from the new N^{3}LO SO and S_1S_2 corrections using numerical relativity (NR) simulations as means of comparison. We do this using an EOB Hamiltonian, calculated using the scattering angle obtained above, since the resummation of PN results it grants is expected to improve the agreement with NR in the high-frequency regime.

The EOB Hamiltonian is calculated from an effective Hamiltonian $H^{\rm eff}$ via the energy map

$$H^{\rm EOB} = M\sqrt{1 + 2\nu\left(\frac{H^{\rm eff}}{\mu} - 1\right)}, \tag{3.119}$$

where we use for the effective Hamiltonian an aligned-spin version of the Hamiltonian for a nonspinning test mass in a Kerr background (denoted SEOB$_{\rm TM}$ in Ref. [4]) with SO and S_1S_2 PN corrections. The effective Hamiltonian is given by

$$H^{\rm eff} = \left[A\left(\mu^2 + p^2 + B_{p_r}p_r^2 + B_L\frac{L^2a^2}{r^2} + \mu^2 Q\right)\right]^{1/2} + \frac{GMr}{\Lambda}L\left(g_S S + g_{S^*}S^*\right), \tag{3.120}$$

where $\Lambda = (r^2+a^2)^2 - \Delta a^2$ with $\Delta = r^2 - 2GMr + a^2$. The Kerr spin a is mapped to the binary's spins via $a = a_1 + a_2$, and the potentials are taken to be

$$A = \frac{\Delta r^2}{\Lambda}\left(A^0 + A^{\rm SS}\right), \tag{3.121a}$$

$$B_{p_r} = \left(1 - \frac{2GM}{r} + \frac{a^2}{r^2}\right)\left(A^0 D^0 + B_{p_r}^{\rm SS}\right) - 1, \tag{3.121b}$$

$$B_L = -\frac{r^2 + 2GMr}{\Lambda}, \tag{3.121c}$$

$$Q = Q^0 + Q^{\rm SS}, \tag{3.121d}$$

i.e., we factorize the PN corrections to the Kerr potentials. The zero-spin corrections $A^0(r),\ D^0(r)$ and $Q^0(r)$ are given by Eq. (28) of Ref. [4] and are based on the 4PN nonspinning Hamiltonian derived in Ref. [80]. The SO corrections are encoded in the gyro-gravitomagnetic factors g_S, and g_{S^*}, while the $\mathrm{S_1S_2}$ corrections are added through A^{SS}, $B^{\mathrm{SS}}_{p_r}$, and Q^{SS}.

For those PN corrections, we choose a gauge such that g_S, and g_{S^*} are independent of L [383, 389, 390]; we write an ansatz such that, up to N^{3}LO,

$$\begin{aligned}
g_S(r,p_r) &= 2\sum_{i=0}^{3}\sum_{j=0}^{i}\alpha_{ij}\frac{p_r^{2(i-j)}}{c^{2i}r^j},\\
g_{S^*}(r,p_r) &= \frac{3}{2}\sum_{i=0}^{3}\sum_{j=0}^{i}\alpha^*_{ij}\frac{p_r^{2(i-j)}}{c^{2i}r^j},
\end{aligned}\tag{3.122}$$

for some unknown coefficients α_{ij} and α^*_{ij}. For the $\mathrm{S_1S_2}$ corrections, A^{SS} and $B^{\mathrm{SS}}_{p_r}$ start at NLO and are independent of p_r, while Q^{SS} starts at NNLO and depends on p_r^4 or higher powers of p_r, i.e., we use an ansatz of the form

$$\begin{aligned}
A^{\mathrm{SS}} &= S_1S_2\left(\frac{\alpha_4^A}{c^6r^4}+\frac{\alpha_5^A}{c^8r^5}+\frac{\alpha_6^A}{c^{10}r^6}\right),\\
B^{\mathrm{SS}} &= S_1S_2\left(\frac{\alpha_3^B}{c^4r^3}+\frac{\alpha_4^B}{c^6r^4}+\frac{\alpha_5^B}{c^8r^5}\right),\\
Q^{\mathrm{SS}} &= S_1S_2\left(\alpha_{34}^Q\frac{p_r^4}{c^6r^3}+\alpha_{44}^Q\frac{p_r^4}{c^8r^4}+\alpha_{36}^Q\frac{p_r^6}{c^8r^3}\right).
\end{aligned}\tag{3.123}$$

To determine those unknowns, we calculate the scattering angle from such an ansatz using Eq. (3.56) (which entails inverting the EOB Hamiltonian for p_r in a PN expansion, differentiating with respect to L, and integrating with respect to r). We then match the result of that calculation to the scattering angle calculated in the previous section and solve for the unknown coefficients in the Hamiltonian ansatz. This uniquely determines all the coefficients of the spinning part of the Hamiltonian since our choice for the ansatz fixes the gauge dependence of the Hamiltonian. (See Sec. 3.3.1 for a discussion of the gauge freedom in the Hamiltonian.)

We obtain the gyro-gravitomagnetic factors

$$\begin{aligned}
g_S = 2\Bigg\{ & 1+\frac{\nu}{c^2}\left[-\frac{27}{16}\frac{p_r^2}{\mu^2}-\frac{5}{16}\frac{GM}{r}\right]+\frac{\nu}{c^4}\Bigg[\left(\frac{5}{16}+\frac{35\nu}{16}\right)\frac{p_r^4}{\mu^4}-\left(\frac{21}{4}-\frac{23\nu}{16}\right)\frac{p_r^2}{\mu^2}\frac{GM}{r} \\
& -\left(\frac{51}{8}+\frac{\nu}{16}\right)\frac{(GM)^2}{r^2}\Bigg]+\frac{\nu}{c^6}\Bigg[\left(-\frac{80399}{2304}+\frac{241\pi^2}{384}+\frac{379\nu}{64}-\frac{7\nu^2}{256}\right)\frac{(GM)^3}{r^3} \\
& +\left(-\frac{5283}{128}+\frac{1557\nu}{32}+\frac{69\nu^2}{128}\right)\frac{p_r^2}{\mu^2}\frac{(GM)^2}{r^2}+\left(\frac{781}{256}+\frac{831\nu}{64}-\frac{771\nu^2}{256}\right)\frac{p_r^4}{\mu^4}\frac{GM}{r} \\
& +\left(\frac{7}{256}-\frac{63\nu}{64}-\frac{665\nu^2}{256}\right)\frac{p_r^6}{\mu^6}\Bigg]\Bigg\},
\end{aligned} \tag{3.124a}$$

$$\begin{aligned}
g_{S^*} = \frac{3}{2}\Bigg\{ & 1+\frac{1}{c^2}\left[-\left(\frac{3\nu}{2}+\frac{5}{4}\right)\frac{p_r^2}{\mu^2}-\left(\frac{3}{4}+\frac{\nu}{2}\right)\frac{GM}{r}\right]+\frac{1}{c^4}\Bigg[\left(\frac{15\nu^2}{8}+\frac{5\nu}{3}+\frac{35}{24}\right)\frac{p_r^4}{\mu^4} \\
& +\left(\frac{19\nu^2}{8}-\frac{3\nu}{2}+\frac{23}{8}\right)\frac{p_r^2}{\mu^2}\frac{GM}{r}+\left(-\frac{\nu^2}{8}-\frac{13\nu}{2}-\frac{9}{8}\right)\frac{(GM)^2}{r^2}\Bigg] \\
& +\frac{1}{c^6}\Bigg[\left(-\frac{135}{64}+\frac{41\pi^2\nu}{48}-\frac{7627\nu}{288}+\frac{237\nu^2}{32}-\frac{\nu^3}{16}\right)\frac{(GM)^3}{r^3} \\
& +\left(-\frac{15}{32}-\frac{279\nu}{16}+\frac{787\nu^2}{16}+\frac{9\nu^3}{8}\right)\frac{p_r^2}{\mu^2}\frac{(GM)^2}{r^2} \\
& +\left(-\frac{1105}{192}-\frac{53\nu}{96}+\frac{117\nu^2}{32}-\frac{81\nu^3}{16}\right)\frac{p_r^4}{\mu^4}\frac{GM}{r} \\
& +\left(-\frac{105}{64}-\frac{175\nu}{96}-\frac{77\nu^2}{32}-\frac{35\nu^3}{16}\right)\frac{p_r^6}{\mu^6}\Bigg]\Bigg\},
\end{aligned} \tag{3.124b}$$

and the S_1S_2 corrections

$$\begin{aligned}
A^{\mathrm{SS}} = \frac{S_1S_2}{G^2M^2\mu^2}\Bigg\{ & \frac{(GM)^4}{c^6r^4}\left(2\nu-\nu^2\right)+\frac{(GM)^5}{c^8r^5}\left(\frac{17\nu}{2}+\frac{113\nu^2}{8}+\frac{3\nu^3}{4}\right) \\
& +\frac{(GM)^6}{c^{10}r^6}\left(\frac{61\nu}{2}-\frac{41\pi^2\nu^2}{16}+\frac{3791\nu^2}{48}+\frac{25\nu^3}{4}+\frac{21\nu^4}{32}\right)\Bigg\},
\end{aligned} \tag{3.125a}$$

$$\begin{aligned}
B_{p_r}^{\mathrm{SS}} = \frac{S_1S_2}{G^2M^2\mu^2}\Bigg\{ & \frac{(GM)^3}{c^4r^3}\left(6\nu+\frac{9}{2}\nu^2\right)+\frac{(GM)^4}{c^6r^4}\left(20\nu+26\nu^2+10\nu^3\right) \\
& +\frac{(GM)^5}{c^8r^5}\left(67\nu+328\nu^2-\frac{375\nu^3}{4}-\frac{37\nu^4}{16}\right)\Bigg\},
\end{aligned} \tag{3.125b}$$

$$\begin{aligned}
Q^{\mathrm{SS}} = \frac{S_1S_2}{G^2M^2\mu^2}\Bigg\{ & \frac{1}{c^6}\frac{p_r^4}{\mu^4}\frac{(GM)^3}{r^3}\left(+\frac{5\nu}{2}+\frac{45\nu^2}{8}-\frac{25\nu^3}{4}\right) \\
& +\frac{1}{c^8}\Bigg[\frac{p_r^6}{\mu^6}\frac{(GM)^3}{r^3}\left(-\frac{7\nu}{4}-\frac{63\nu^2}{16}-\frac{35\nu^3}{8}+\frac{245\nu^4}{32}\right)
\end{aligned}$$

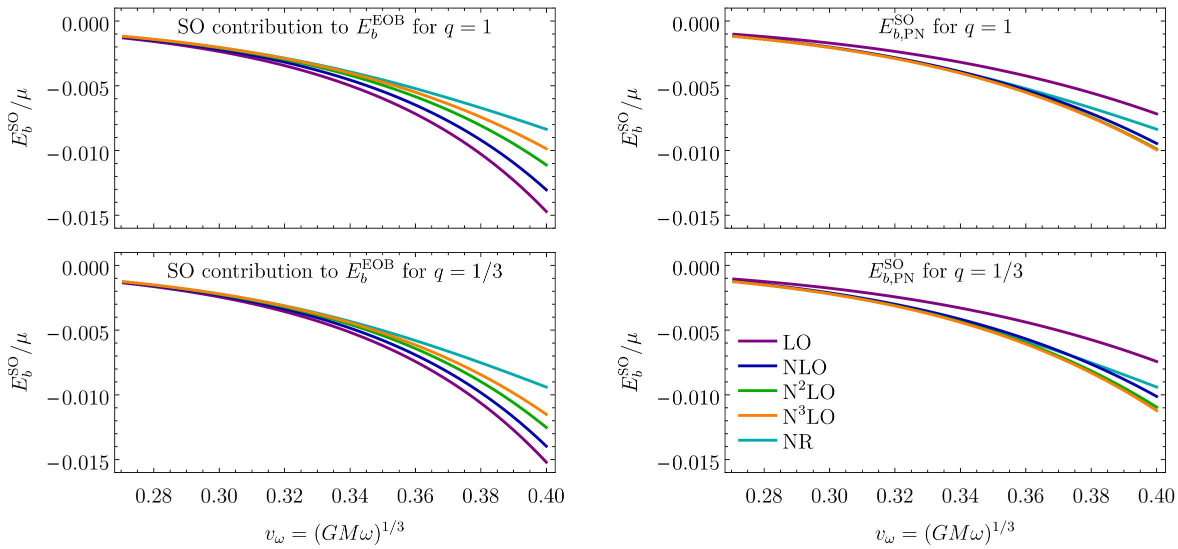

Figure 3.1: Binding energy versus the velocity parameter v_ω for the SO contribution to the EOB (left panels) and PN-expanded (right panels) binding energies for mass ratios $q = 1$ (top panels) and $q = 1/3$ (bottom panels).

$$+\frac{p_r^4}{\mu^4}\frac{(GM)^4}{r^4}\left(-13\nu+\frac{183\nu^2}{4}-63\nu^3-\frac{437\nu^4}{16}\right)\Bigg]\Bigg\}. \tag{3.125c}$$

Importantly, the factors g_S and g_{S^*}, obtained here for the aligned-spin case, also fix the generic-spin case by simply writing the odd-in-spin part of the effective Hamiltonian as

$$H_{\rm eff}^{\rm odd} = \frac{GMr}{\Lambda}\boldsymbol{L}\cdot\left(g_S\boldsymbol{S}+g_{S^*}\boldsymbol{S}^*\right), \tag{3.126}$$

with g_S and g_{S^*} unmodified since they are independent of the spins (see Ref. [1] for more details.) However, the spin$_1$-spin$_2$ corrections in Eq. (3.125) are only for aligned spins since the generic-spins case has additional contributions proportional to $(\boldsymbol{n}\cdot\boldsymbol{S}_1)(\boldsymbol{n}\cdot\boldsymbol{S}_2)$, where $\boldsymbol{n}=\boldsymbol{r}/r$. Such terms vanish for aligned spins and cannot be fixed from aligned-spin self-force results or be removed by canonical transformations.

For comparison with NR, a particularly good quantity to consider is the binding energy, since it encapsulates the conservative dynamics of analytical models, and can be obtained from

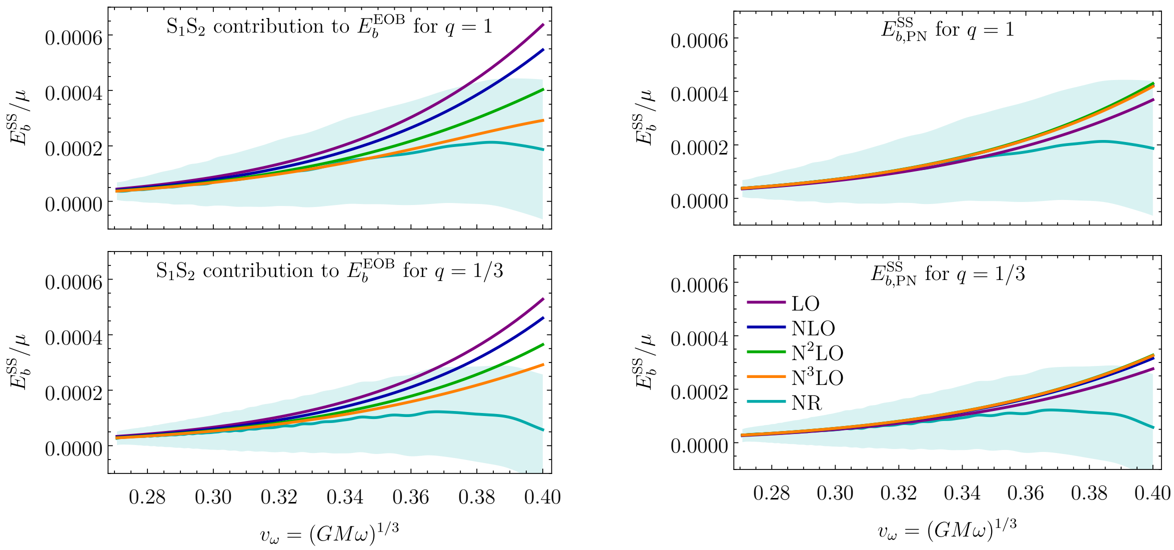

Figure 3.2: Binding energy versus the velocity parameter v_ω for the S_1S_2 contribution to the EOB (left panels) and PN-expanded (right panels) binding energies for mass ratios $q = 1$ (top panels) and $q = 1/3$ (bottom panels). The NR error is indicated by the shaded regions.

accurate NR simulations [434, 435]. The NR data for binding energy that we use were extracted in Ref. [438] from the Simulating eXtreme Spacetimes (SXS) catalog [458]. The binding energy calculated from NR simulations is defined by

$$E_b^{\rm NR} = E_{\rm ADM} - E_{\rm rad} - Mc^2, \tag{3.127}$$

where $E_{\rm rad}$ is the radiated energy, and $E_{\rm ADM}$ is the ADM energy at the beginning of the simulation. We then calculate the binding energy from the EOB conservative Hamiltonian using $E_b = H^{\rm EOB} - Mc^2$ for exact circular orbits at different orbital separations, i.e., we neglect the radiation reaction due to the emitted GWs. As a result of this assumption, the circular-orbit binding energy we calculate is not expected to agree with NR in the last few orbits.

To obtain the binding energy from a Hamiltonian in an analytical PN expansion, we set $p_r = 0$ for circular orbits and perturbatively solve $\dot{p}_r = 0 = -\partial H/\partial r$ for the angular momentum

L. The orbital frequency ω is given by $\omega = \partial H/\partial L$ from which we define the velocity parameter

$$v_\omega = (GM\omega)^{1/3}. \tag{3.128}$$

Expressing the PN-expanded Hamiltonian in terms of v_ω yields, for the SO part,

$$\begin{aligned}
E_{b,\text{PN}}^{\text{SO}} = \frac{\nu}{GM}\Bigg\{ & v_\omega^5 \left[-\frac{4}{3}S - S^*\right] + v_\omega^7 \left[S\left(\frac{31\nu}{18} - 4\right) + S^*\left(\frac{5\nu}{3} - \frac{3}{2}\right)\right] \\
& + v_\omega^9 \left[\frac{S}{24}\left(-324 + 633\nu - 14\nu^2\right) + \frac{S^*}{8}\left(-27 + 156\nu - 5\nu^2\right)\right] \\
& + v_\omega^{11}\Bigg[S\left(-45 + \frac{19679 + 174\pi^2}{144}\nu - \frac{1979}{36}\nu^2 - \frac{265}{3888}\nu^3\right) \\
& \quad - \frac{S^*}{8}\left(\frac{135}{2} - 565\nu + \frac{1109}{3}\nu^2 + \frac{50}{81}\nu^3\right)\Bigg]\Bigg\},
\end{aligned} \tag{3.129}$$

while for the S_1S_2 part,

$$\begin{aligned}
E_{b,\text{PN}}^{\text{SS}} = \frac{S_1 S_2}{G^2 M^3}\Bigg[& v_\omega^6 + v_\omega^8\left(\frac{5}{6} + \frac{5}{18}\nu\right) + v_\omega^{10}\left(\frac{35}{8} - \frac{1001}{72}\nu - \frac{371}{216}\nu^2\right) \\
& + v_\omega^{12}\left(\frac{243}{16} + \frac{123\pi^2 - 4214}{32}\nu + \frac{147}{8}\nu^2 + \frac{13}{16}\nu^3\right)\Bigg].
\end{aligned} \tag{3.130}$$

The same steps can be performed numerically to obtain the EOB binding energy without a PN expansion.

To examine the effect of the new N^3LO terms on the binding energy, we isolate the SO and the S_1S_2 contributions to the binding energy by combining configurations with different spin orientations (parallel or anti-parallel to the orbital angular momentum), as explained in Refs. [437, 438]. For the SO contribution, we use

$$E_b^{\text{SO}}(\nu, \hat{a}, \hat{a}) = \frac{1}{2}\left[E_b(\nu, \hat{a}, \hat{a}) - E_b(\nu, -\hat{a}, -\hat{a})\right] + \mathcal{O}(\hat{a}^3), \tag{3.131}$$

while for the S_1S_2 contribution, we use

$$E_b^{\text{SS}}(\nu, \hat{a}, \hat{a}) = E_b(\nu, \hat{a}, 0) + E_b(\nu, 0, -\hat{a}) - E_b(\nu, \hat{a}, -\hat{a}) - E_b(\nu, 0, 0) + \mathcal{O}(\hat{a}^3). \tag{3.132}$$

In Fig. 3.1, we plot the SO contribution to the EOB and PN-expanded binding energies versus the velocity parameter v_ω for spin magnitudes $\hat{a} = 0.6$. We also plot the NR results by combining the binding energies of configurations with different spins using results from Refs. [438, 458]. From the figure, we see that, adding each PN order improves agreement of the EOB binding energy with NR, especially in the high-frequency regime, with better improvement for equal masses than for unequal masses. In contrast, the PN binding energy, plotted using Eq. (3.129), seems *not* to converge towards NR in the high-frequency regime, with little difference between the N^{2}LO and N^{3}LO SO orders. Figure 3.2 shows the S_1S_2 contribution to the EOB and PN binding energies. As in the SO case, adding the new N^{3}LO significantly improves agreement of the EOB binding energy to NR, especially for equal masses, but there is little difference between PN orders for the PN binding energy.

Note that Figs. 3.1 and 3.2 should not be interpreted as a direct comparison between PN and EOB dynamics since our results were obtained for simplicity using exact circular-orbits, which leads to a very different behavior than for an *inspiraling* binary; Refs. [410, 435, 438], for example, show that EOB results are significantly better than PN when taking into account the binary evolution. Let us also stress that while the EOB and PN curves are based on the same PN information, the EOB Hamiltonian represents a particular resummation of the PN results. We leave the exploration of other resummations and a calibration to NR for future work.

3.6 Conclusions

GW astronomy allows a multitude of applications in fundamental and astrophysics [13, 18, 519, 520] that rely on accurate waveform models for inferring the source parameters. In this paper, we improved the PN description of spinning compact binaries using information from relativistic scattering and self-force theory, which is an extension of the approach introduced and used in Refs. [90, 91, 252] for the nonspinning case. We started by extending the arguments from Ref. [252] to show that the scattering angle for an aligned-spin binary has a simple dependence on the masses. This allowed us to determine the SO and aligned S_1S_2 couplings through N^3LO in a PN expansion using GSF results for the redshift and precession frequency of a small body on an eccentric orbit in a Kerr background. This result is neatly encapsulated in the gauge-invariant aligned-spin scattering-angle function, given explicitly in Eq. (3.118). The derivation presented here provides the full details for the recently reported result at SO level in Ref. [1], while extending the analysis to aligned S_1S_2 couplings.

Using these new PN results, we calculated the circular-orbit binding energy, the EOB gyro-gravitomagnetic factors, and implemented these results in an EOB Hamiltonian. To illustrate the effect of the new N^3LO terms, we compared the binding energy with NR simulations (see Figs. 3.1 and 3.2,) showing an improvement over the N^2LO. These results could be implemented in state-of-the-art `SEOBNR` [396–399] and `TEOBResumS` [400, 401] waveform models used in LIGO-Virgo searches and inference analyses [13].

While it is arguable whether PM results already provide a useful resummation of the PN ones [405], the present work shows that, with the crucial contribution of GSF theory, advances in PM theory already allow one to advance the PN knowledge in the spin sector. We thus beseech further research to explore synergies between GSF, PM, and PN theory, along the lines of Refs. [1, 90, 91, 93, 128, 548] and the present paper. One could, for instance, extend the results in this paper to N^3LO S^2 couplings, i.e. at quadratic order in each spin. This is an important step to complete the aligned-spin 5PN dynamics for BBHs. However, we leave such a calculation for future work, since it would require currently unavailable GSF results.

One can envision further important work at the interface between the PM and GSF approximations. With knowledge of first-order GSF theory, one can in principle determine the full 3PM and 4PM scattering angle in a completely independent way from techniques employed, e.g., in Ref. [243]. To this end, one could calculate the PM expansion of GSF gauge-invariant quantities for bound orbits directly (e.g., expansions in u_p valid at all orders in the eccentricity e). This enterprise would have to take great care in the inclusion of tail terms in the dynamics, as well as in the analytical continuation of such results to scattering systems. Should these quantities be calculated, one could exploit the method herein presented to fix the 3PM and 4PM scattering angles without further PN re-expansions. Even better would be a direct GSF treatment of scattering orbits and the scattering angle. This is likely to first come in the form of numerical calculations at first-order in the mass ratio. It will however be worth exploring whether "experimental mathematics" techniques can be used to obtain analytic expressions for the 4PM scattering angle by pushing such numerical calculations to extreme precision (see, e.g., Ref. [551] for an example along these lines in the GSF literature).

Finally, we stress that it is paramount to check our results with more established PN calculations (e.g., with the EFT approach, as was done partially at N^{3}LO in Refs. [109, 550]), as they have been obtained with a so-far completely unexplored method in the spinning sector that is begging to be further scrutinized.

Acknowledgments

We are grateful to Alessandra Buonanno and Maarten van de Meent for helpful discussions. We also thank Sergei Ossokine and Tim Dietrich for providing NR data for the binding energy and for related useful suggestions.

Chapter 4: Gravitational spin-orbit dynamics at the fifth-and-a-half post-Newtonian order

Author[1]: *Mohammed Khalil*

Abstract: Accurate waveform models are crucial for gravitational-wave data analysis, and since spin has a significant effect on the binary dynamics, it is important to improve the spin description in these models. In this paper, we derive the spin-orbit (SO) coupling at the fifth-and-a-half post-Newtonian (5.5PN) order. The method we use splits the conservative dynamics into local and nonlocal-in-time parts, then relates the local-in-time part to gravitational self-force results by exploiting the simple mass-ratio dependence of the post-Minkowskian expansion of the scattering angle. We calculate the nonlocal contribution to the 5.5PN SO dynamics to eighth order in the small-eccentricity expansion for bound orbits, and to leading order in the large-eccentricity expansion for unbound orbits. For the local contribution, we obtain all the 5.5PN SO coefficients from first-order self-force results for the redshift and spin-precession invariants, except for one unknown that could be fixed in the future by second-order self-force results. However, by incorporating our 5.5PN results in the effective-one-body formalism and comparing its binding energy to numerical relativity, we find that the remaining unknown has a small effect on the SO dynamics, demonstrating an improvement in accuracy at that order.

[1]Originally published as Phys. Rev. D **104**, no.12, 124015 (2021)

4.1 Introduction

Gravitational-wave (GW) observations [12–14] have improved our understanding of compact binary systems, their properties, and their formation channels [18, 19]. A crucial component in searching for GW signals and inferring their parameters is accurate analytical waveform models, in which spin is an important ingredient given its significant effect on the orbital dynamics.

Three main analytical approximation methods exist for describing the dynamics during the inspiral phase: the post-Newtonian (PN), the post-Minkowskian (PM), and the small-mass-ratio (gravitational self-force (GSF)) approximations.

The PN approximation is valid for small velocities and weak gravitational potential $v^2/c^2 \sim GM/rc^2 \ll 1$, and is most applicable for comparable-mass binaries in bound orbits. Many studies have contributed to improving the description of the conservative PN dynamics, for nonspinning binaries [74, 76, 79–88, 152, 563, 564], at spin-orbit (SO) level [96–100, 102–109, 166, 172], spin-spin [113–116, 119–122, 181], and higher orders in spin [123–128]. For reviews, see Refs. [129–134].

The PM approximation is valid for arbitrary velocities in the weak field $GM/rc^2 \ll 1$, and is most applicable for scattering motion since relativistic velocities can be achieved. It was pioneered by the classic results of Westpfahl [228, 229], with rapid progress using classical methods [232, 233, 236, 237, 251–253], scattering amplitudes [238–246, 289], effective field theory [254–258], and worldline quantum field theory [260, 261]. Spin effects were included in PM expansions using all these approaches in Refs. [262–275], and radiative contributions in Refs. [285–287, 296, 565].

The small-mass-ratio approximation $m_1/m_2 \ll 1$ is based on GSF theory, and is most applicable for extreme-mass-ratio inspirals (see, e.g., Refs. [302–304, 309, 310, 312, 314, 315, 317–323, 325, 561, 566–569] and the reviews [330–333].) Analytic GSF calculations to high PN orders were performed at first order in the mass ratio for the gauge-invariant redshift [336–344] and the spin-precession frequency [346–351]. There has also been recent important work on numerically calculating the binding energy and energy flux at second order in the mass ratio [326, 327].

The effective-one-body (EOB) formalism [380, 381] combines information from different analytical approximations with numerical relativity (NR) results, while recovering the strong-field test-body limit, thereby extending each approximation's domain of validity and improving the inspiral-merger-ringdown waveforms. EOB models have been constructed for nonspinning [80, 384–388], spinning [4, 382, 383, 389–401], and eccentric binaries [5, 402–404]. In addition, information from the post-Minkowskian [236, 237, 405, 406] and small mass-ratio approximations [407–410] have been incorporated in EOB models.

Recently, a method [90], sometimes dubbed the "Tutti Frutti" method [286], that combines all these formalisms has been used to derive PN results valid for arbitrary mass ratios from GSF results at first order in the mass ratio. The method relies on the simple mass-ratio dependence of the PM-expanded scattering angle [252] (see also Ref. [265]), making it possible to relate the local-in-time part of the Hamiltonian, or radial action, to GSF invariants, such as the redshift and precession frequency. The nonlocal-in-time part of the conservative dynamics, due to backscattered radiation emitted at earlier times, is derived separately, since it is calculated in an eccentricity expansion that differs between bound and unbound orbits. This approach has been used to derive the 5PN conservative dynamics for nonspinning binaries except for two coefficients [90, 91], the 6PN dynamics except for four coefficients [92, 93], and the full 4.5PN SO and 5PN aligned spin$_1$-spin$_2$ dynamics [1, 2].

In this paper, we determine the 5.5PN SO coupling for the two-body dynamics, which is the fourth-subleading PN order, except for one coefficient at second order in the mass ratio. Throughout, we perform all calculations for spins aligned, or antialigned, with the direction of the orbital angular momentum. However, the results are valid for precessing spins [1], since at SO level, the spin vector only couples to the angular momentum vector.

The results of this paper and the procedure used can be summarized as follows:

1. In Sec. 4.2, we calculate the nonlocal contribution to the 5.5PN SO Hamiltonian for bound orbits, in a small-eccentricity expansion up to eighth order in eccentricity. We do this for a harmonic-coordinates Hamiltonian, then incorporate those results into the gyro-gravitomagnetic factors in an EOB Hamiltonian.

2. In Sec. 4.3, we determine the local contribution by relating the coefficients of the local Hamiltonian to those of the PM-expanded scattering angle. We then calculate the redshift and spin-precession invariants from the total Hamiltonian, and match their small-mass-ratio expansion to first-order self-force (1SF) results. This allows us to recover all the coefficients of the local part except for one unknown. However, by computing the EOB binding energy and comparing it to NR, we show that the effect of the remaining unknown on the dynamics is small.

3. In Sec. 4.4, we complement our results for unbound orbits by calculating the nonlocal part of the gauge-invariant scattering angle, to leading order in the large-eccentricity expansion.

4. In Sec. 4.5, we provide two gauge-invariant quantities that characterize bound orbits: the radial action as a function of energy and angular momentum, and the circular-orbit binding

energy as a function of frequency.

We conclude in Sec. 4.6 with a discussion of the results, and provide in Appendix D a summary of the quasi-Keplerian parametrization at leading SO order. The main results of this paper are provided in the Supplemental Material as a MATHEMATICA file [3].

Notation

We use the metric signature $(-,+,+,+)$, and units in which $G = c = 1$, but sometimes write them explicitly in PM and PN expansions for clarity.

For a binary with masses m_1 and m_2, with $m_2 \geq m_1$, and spins $\boldsymbol{S}_1$ and $\boldsymbol{S}_2$, we define the following combinations of the masses:

$$M = m_1 + m_2, \qquad \mu = \frac{m_1 m_2}{M}, \qquad \nu = \frac{\mu}{M}, \qquad q = \frac{m_1}{m_2}, \qquad \delta = \frac{m_2 - m_1}{M}, \tag{4.1}$$

define the mass-rescaled spins

$$\boldsymbol{a}_1 = \frac{\boldsymbol{S}_1}{m_1}, \qquad \boldsymbol{a}_2 = \frac{\boldsymbol{S}_2}{m_2}, \tag{4.2}$$

the dimensionless spin magnitudes

$$\chi_1 = \frac{|\boldsymbol{S}_1|}{m_1^2}, \qquad \chi_2 = \frac{|\boldsymbol{S}_2|}{m_2^2}, \tag{4.3}$$

and the spin combinations

$$\begin{aligned} \boldsymbol{S} &= \boldsymbol{S}_1 + \boldsymbol{S}_2, \qquad & \boldsymbol{S}^* &= \frac{m_2}{m_1}\boldsymbol{S}_1 + \frac{m_1}{m_2}\boldsymbol{S}_2, \\ \chi_S &= \frac{1}{2}(\chi_1 + \chi_2), \qquad & \chi_A &= \frac{1}{2}(\chi_2 - \chi_1). \end{aligned} \tag{4.4}$$

We use several variables related to the total energy E of the binary system: the binding energy $\bar{E} = E - Mc^2$, the mass-rescaled energy $\Gamma = E/M$, and the effective energy E_{eff} defined by the energy map

$$E = M\sqrt{1 + 2\nu\left(\frac{E_{\text{eff}}}{\mu} - 1\right)}. \tag{4.5}$$

We also define the asymptotic relative velocity v and Lorentz factor γ via

$$\gamma = \frac{E_{\text{eff}}}{\mu},$$

$$v = \frac{\sqrt{\gamma^2 - 1}}{\gamma}, \quad \leftrightarrow \quad \gamma = \frac{1}{\sqrt{1 - v^2}}, \tag{4.6}$$

and define the dimensionless energy variable

$$\varepsilon = \gamma^2 - 1 = \gamma^2 v^2. \tag{4.7}$$

(Note that ε used here is denoted p_∞^2 in Ref. [91].)

The magnitude of the orbital angular momentum is denoted L, and is related to the relative position r, radial momentum p_r, and total linear momentum p via

$$p^2 = p_r^2 + \frac{L^2}{r^2}. \tag{4.8}$$

We often use dimensionless rescaled quantities, such as

$$r = \frac{r^{\text{phys}}}{M}, \qquad L = \frac{L^{\text{phys}}}{M\mu}, \qquad p_r = \frac{p_r^{\text{phys}}}{\mu}, \qquad E = \frac{E^{\text{phys}}}{\mu}, \qquad H = \frac{H^{\text{phys}}}{\mu}, \tag{4.9}$$

and similarly for related variables, e.g. $\bar{E} = \bar{E}^{\text{phys}}/\mu$, etc. It should be clear from the context whether physical or rescaled quantities are being used.

4.2 Nonlocal 5.5PN SO Hamiltonian for bound orbits

The total conservative action at a given PN order can be split into local and nonlocal-in-time parts, such that

$$S_{\text{tot}}^{\text{nPN}} = S_{\text{loc}}^{\text{nPN}} + S_{\text{nonloc}}^{\text{nPN}}, \tag{4.10}$$

where the nonlocal part is due to tail effects projected on the conservative dynamics [79, 183, 425], i.e., radiation emitted at earlier times and backscattered onto the binary. The nonlocal contribution starts at 4PN order, and has been derived for nonspinning binaries up to 6PN order [80, 91, 92]. In this section, we derive the leading-order spin contribution to the nonlocal part, which is at 5.5PN order.

The nonlocal part of the action can be calculated via the following integral:

$$S^{\text{LO}}_{\text{nonloc}} = \frac{GM}{c^3} \int dt\, \text{Pf}_{2s/c} \int \frac{dt'}{|t-t'|} \mathcal{F}^{\text{split}}_{\text{LO}}(t,t'), \tag{4.11}$$

where the label 'LO' here means that we include the *leading-order* nonspinning and SO contributions, and where the Hadamard *partie finie* (Pf) operation is used since the integral is logarithmically divergent at $t' = t$. The time-split (or time-symmetric) GW energy flux $\mathcal{F}^{\text{split}}_{\text{LO}}(t,t')$ is written in terms of the source multipole moments as [79]

$$\mathcal{F}^{\text{split}}_{\text{LO}}(t,t') = \frac{G}{c^5} \left[\frac{1}{5} I^{(3)}_{ij}(t) I^{(3)}_{ij}(t') + \frac{16}{45c^2} J^{(3)}_{ij}(t) J^{(3)}_{ij}(t') \right]. \tag{4.12}$$

The mass quadrupole I^{ij} and the current quadrupole J^{ij} (in harmonic coordinates and using the Newton-Wigner spin-supplementary condition [364, 365]) are given by [164, 426]

$$\begin{aligned}
I_{ij} &= m_1 x_1^{\langle i} x_1^{j\rangle} + \frac{3}{c^3} x_1^{\langle i} (\boldsymbol{v}_1 \times \boldsymbol{S}_1)^{j\rangle} - \frac{4}{3c^3} \frac{d}{dt} x_1^{\langle i} (\boldsymbol{x}_1 \times \boldsymbol{S}_1)^{j\rangle} + 1 \leftrightarrow 2, \\
J_{ij} &= m_1 x_1^{\langle i} (\boldsymbol{x}_1 \times \boldsymbol{v}_1)^{j\rangle} + \frac{3}{2c} x_1^{\langle i} S_1^{j\rangle} + 1 \leftrightarrow 2,
\end{aligned} \tag{4.13}$$

where the indices in angle brackets denote a symmetric trace-free part.

As was shown in Refs. [79, 80], the nonlocal part of the action can be written in terms of $\tau \equiv t' - t$ as

$$S^{\text{LO}}_{\text{nonloc}} = -\int dt\, \delta H^{\text{LO}}_{\text{nonloc}}(t),$$

$$\delta H^{\rm LO}_{\rm nonloc}(t) = -\frac{GM}{c^3}\mathrm{Pf}_{2s/c}\int \frac{d\tau}{|\tau|}\mathcal{F}^{\rm split}_{\rm LO}(t,t+\tau) + 2\frac{GM}{c^3}\mathcal{F}^{\rm split}_{\rm LO}(t,t)\ln\left(\frac{r}{s}\right). \tag{4.14}$$

Following Ref. [91], we choose the arbitrary length scale s entering the *partie finie* operation to be the radial distance r between the two bodies in harmonic coordinates. This has the advantage of simplifying the local part by removing its dependence on $\ln r$.

4.2.1 Computation of the nonlocal Hamiltonian in a small-eccentricity expansion

The integral for the nonlocal Hamiltonian in Eq. (4.14) can be performed in a small-eccentricity expansion using the quasi-Keplerian parametrization [427], which can be expressed, up to 1.5PN order, by the following equations:

$$r = a_r(1 - e_r\cos u), \tag{4.15}$$

$$\ell = nt = u - e_t\sin u, \tag{4.16}$$

$$\phi = 2K\arctan\left[\sqrt{\frac{1+e_\phi}{1-e_\phi}}\tan\frac{u}{2}\right], \tag{4.17}$$

where a_r is the semi-major axis, u the eccentric anomaly, ℓ the mean anomaly, n the mean motion (radial angular frequency), K the periastron advance, and (e_r, e_t, e_ϕ) the radial, time, and phase eccentricities.

The quasi-Keplerian parametrization was generalized to 3PN order in Ref. [570], and including SO and spin-spin contributions in Refs. [571, 572]. We summarize in Appendix D.1 the relations between the quantities used in the quasi-Keplerian parametrization and the energy and angular momentum at leading SO order. Using the quasi-Keplerian parametrization, we express the source multipole moments in terms of the variables (a_r, e_t, t), and expand the moments in eccentricity.

In the center-of-mass frame, the position vectors of the two bodies, $\boldsymbol{x}_1$ and $\boldsymbol{x}_2$, are related to $\boldsymbol{x} \equiv \boldsymbol{x}_1 - \boldsymbol{x}_2$ via [165]

$$
\begin{aligned}
x_1^i &= \frac{m_2}{M} x^i - \frac{\nu}{2c^3 \delta M} \epsilon^i{}_{jk} v^j (S^k - S^{*k}), \\
x_2^i &= -\frac{m_1}{M} x^i - \frac{\nu}{2c^3 \delta M} \epsilon^i{}_{jk} v^j (S^k - S^{*k}),
\end{aligned} \tag{4.18}
$$

where $\boldsymbol{v} \equiv \boldsymbol{v}_1 - \boldsymbol{v}_2$, and hence the source moments from Eq. (4.13) can be written as

$$
\begin{aligned}
I_{ij} &= M\nu x^{\langle i} x^{j\rangle} + \frac{1}{3c^3}\left[\frac{m_2^2}{M^2}\Big(4v^{\langle i}(\boldsymbol{S}_1 \times \boldsymbol{x})^{j\rangle} - 5x^{\langle i}(\boldsymbol{S}_1 \times \boldsymbol{v})^{j\rangle}\Big) + 1 \leftrightarrow 2\right], \qquad (4.19) \\
J_{ij} &= M\delta\nu x^{\langle i}(\boldsymbol{v} \times \boldsymbol{x})^{j\rangle} + \frac{3}{2c}\left[\frac{m_2}{M} x^{\langle i} S_1^{j\rangle} - \frac{m_1}{M} x^{\langle i} S_2^{j\rangle}\right].
\end{aligned}
$$

In polar coordinates,

$$
\begin{aligned}
\boldsymbol{x} &= r(\cos\phi,\, \sin\phi), \\
\boldsymbol{v} &= \dot{r}(\cos\phi,\, \sin\phi) + r\dot{\phi}(-\sin\phi,\, \cos\phi),
\end{aligned} \tag{4.20}
$$

with r and ϕ given by Eqs. (4.15) and (4.17), e_r and e_ϕ related to e_t via Eqs. (D.12) and (D.13), while $\dot{r}$ and $\dot{\phi}$ are given by

$$
\begin{aligned}
\dot{r} &= \frac{e_t \sin u}{\sqrt{a_r}\,(1 - e_t \cos u)}\,, \\
\dot{\phi} &= \frac{\sqrt{a_r - a_r e_t^2}}{a_r^2\,(1 - e_t \cos u)^2}\,,
\end{aligned} \tag{4.21}
$$

which are only needed at leading order. We then write the eccentric anomaly u in terms of time t using Kepler's equation (4.16), which has a solution in terms of a Fourier-Bessel series expansion

$$
u = nt + \sum_{k=1}^{\infty} \frac{2}{k} J_k(k e_t) \sin(knt)
$$

$$\simeq nt + e_t \sin(nt) + \frac{1}{2} e_t^2 \sin(2nt) + \dots . \tag{4.22}$$

We perform the eccentricity expansion for the nonlocal part up to $\mathcal{O}(e_t^8)$ since it corresponds to an expansion to $\mathcal{O}(p_r^8)$, which is the highest power of p_r in the 5.5PN SO local part. However, to simplify the presentation, we write the intermediate steps only expanded to $\mathcal{O}(e_t)$.

Plugging the expressions for $(r, \phi, \dot{r}, \dot{\phi})$ in terms of (a_r, e_t, t) into the source moments used in the time-split energy flux (4.12) and expanding in eccentricity yields

$$\begin{aligned}
\mathcal{F}_{\text{LO}}^{\text{split}}(t, t+\tau) &= \nu^2 a_r^4 n^6 \bigg\{ \frac{32}{5} \cos(2n\tau) + \frac{12}{5} e_t \Big[9\cos(nt + 3n\tau) + 9\cos(nt - 2n\tau) \\
&\quad - \cos(nt - n\tau) - \cos(nt + 2n\tau) \Big] \bigg\} + \frac{8\nu^2}{15} n^6 a_r^{5/2} \bigg\{ 48 n\tau \sin(2n\tau) \left(2\delta\chi_A - \nu\chi_S + 2\chi_S \right) \\
&\quad - 32\cos(2n\tau) \left(9\delta\chi_A - 5\nu\chi_S + 9\chi_S \right) - \cos(n\tau) \left(\delta\chi_A - 4\nu\chi_S + \chi_S \right) \\
&\quad + e_t \cos\left(nt + \frac{n\tau}{2} \right) \bigg[\cos\left(\frac{3n\tau}{2} \right) \left(352\delta\chi_A + 352\chi_S - 157\nu\chi_S \right) \\
&\qquad - 27\cos\left(\frac{5n\tau}{2} \right) \left(84\delta\chi_A - 47\nu\chi_S + 84\chi_S \right) \\
&\qquad - 36 n\tau \left(\sin\left(\frac{3n\tau}{2} \right) - 9\sin\left(\frac{5n\tau}{2} \right) \right) \left(2\delta\chi_A - \nu\chi_S + 2\chi_S \right) \bigg] \bigg\} + \mathcal{O}\left(e_t^2 \right),
\end{aligned} \tag{4.23}$$

the orbit average of which is given by

$$\begin{aligned}
\left\langle \mathcal{F}_{\text{LO}}^{\text{split}}(t, t+\tau) \right\rangle &= \frac{n}{2\pi} \int_0^{2\pi/n} \mathcal{F}_{\text{LO}}^{\text{split}}(t, t+\tau) dt \\
&= \frac{32}{5} \nu^2 n^6 a_r^4 \cos(2n\tau) + \frac{8}{15} \nu^2 n^6 a_r^{5/2} \Big[48 n\tau \sin(2n\tau) \left(2\delta\chi_A - \nu\chi_S + 2\chi_S \right) \\
&\qquad - \cos(n\tau) \left(\delta\chi_A - 4\nu\chi_S + \chi_S \right) \\
&\qquad - 32\cos(2n\tau) \left(9\delta\chi_A - 5\nu\chi_S + 9\chi_S \right) \Big] + \mathcal{O}\left(e_t^2 \right).
\end{aligned} \tag{4.24}$$

In the limit $\tau = 0$, this equation agrees with the eccentricity expansion of the energy flux from Eq. (64) of Ref. [572].

Then, we perform the *partie finie* operation with time scale $2s/c$ using Eq. (4.2) of Ref. [79], which reads

$$\mathrm{Pf}_T \int_0^\infty \frac{dv}{v} g(v) = \int_0^T \frac{dv}{v}[g(v)-g(0)] + \int_T^\infty \frac{dv}{v} g(v). \tag{4.25}$$

The first line of Eq. (4.14) yields

$$\begin{aligned}
-\mathrm{Pf}_{2s/c}\int \frac{d\tau}{|\tau|}\left\langle \mathcal{F}^{\mathrm{split}}_{\mathrm{LO}}(t,t+\tau)\right\rangle &= \frac{64}{5}\nu^2 n^6 a_r^4\left[\ln(4ns)+\gamma_E\right] \\
&- \frac{16}{15}\nu^2 n^6 a_r^{5/2}\Big\{\left[289\delta\chi_A + (289-164\nu)\chi_S\right]\ln(ns) + \left[289\gamma_E + 48 + 577\ln 2\right]\delta\chi_A \\
&+ \left[\gamma_E(289-164\nu) - 12\nu(2+27\ln 2) + 48 + 577\ln 2\right]\chi_S\Big\} + \mathcal{O}\left(e_t^2\right),
\end{aligned} \tag{4.26}$$

while the second line

$$\begin{aligned}
2\left\langle \mathcal{F}^{\mathrm{split}}_{\mathrm{LO}}(t,t)\right\rangle \ln\left(\frac{r}{s}\right) &= \frac{64}{5}\nu^2 n^6 a_r^4 \ln\left(\frac{a_r}{s}\right) \\
&- \frac{16}{15}\nu^2 n^6 a_r^{5/2}\ln\left(\frac{a_r}{s}\right)\left[289\delta\chi_A + (289-164\nu)\chi_S\right] + \mathcal{O}\left(e_t^2\right).
\end{aligned} \tag{4.27}$$

Adding the two expressions removes the dependence on s.

When performing the calculation to $\mathcal{O}\left(e_t^8\right)$, we obtain the following Delaunay-averaged nonlocal Hamiltonian:

$$\begin{aligned}
\left\langle \delta H^{\mathrm{LO}}_{\mathrm{nonloc}}\right\rangle &= \frac{\nu^2}{a_r^5}\left[\mathcal{A}^{\mathrm{4PN}}(e_t) + \mathcal{B}^{\mathrm{4PN}}(e_t)\ln a_r\right] \\
&+ \frac{\nu^2\delta\chi_A}{a_r^{13/2}}\Bigg\{\frac{584}{15}\ln a_r - \frac{64}{5} - \frac{464}{3}\ln 2 - \frac{1168}{15}\gamma_E \\
&+ e_t^2\left[\frac{2908}{5}\ln a_r - \frac{5816}{5}\gamma_E + \frac{2172}{5} - \frac{3304}{15}\ln 2 - \frac{10206}{5}\ln 3\right] \\
&+ e_t^4\left[\frac{43843}{15}\ln a_r - \frac{87686}{15}\gamma_E + \frac{114991}{30} - \frac{201362}{5}\ln 2 + \frac{48843}{4}\ln 3\right] \\
&+ e_t^6\Bigg[\frac{55313}{6}\ln a_r - \frac{55313}{3}\gamma_E + \frac{961807}{60} + \frac{6896921}{45}\ln 2 - \frac{3236031}{160}\ln 3 \\
&- \frac{24296875}{288}\ln 5\Bigg] + e_t^8\Bigg[\frac{134921}{6}\ln a_r - \frac{134921}{3}\gamma_E + \frac{135264629}{2880}
\end{aligned}$$

$$
\begin{aligned}
&\quad -\frac{94244416}{135}\ln 2+\frac{12145234375}{27648}\ln 5-\frac{1684497627}{5120}\ln 3\Bigg]\Bigg\} \\
&+\frac{\nu^2\chi_S}{a_r^{13/2}}\Bigg\{-\frac{64}{5}+\frac{32\nu}{5}+\left(\frac{896\nu}{15}-\frac{1168}{15}\right)\gamma_E+\left(\frac{576\nu}{5}-\frac{464}{3}\right)\ln 2 \\
&\quad+\left(\frac{584}{15}-\frac{448\nu}{15}\right)\ln a_r+e_t^2\Bigg[\frac{2172}{5}-\frac{4412\nu}{15}+\left(\frac{4216\nu}{5}-\frac{5816}{5}\right)\gamma_E \\
&\quad+\left(\frac{5192\nu}{15}-\frac{3304}{15}\right)\ln 2+\left(\frac{6561\nu}{5}-\frac{10206}{5}\right)\ln 3+\left(\frac{2908}{5}-\frac{2108\nu}{5}\right)\ln a_r\Bigg] \\
&\quad+e_t^4\Bigg[\frac{114991}{30}-\frac{38702\nu}{15}+\left(\frac{62134\nu}{15}-\frac{87686}{15}\right)\gamma_E+\left(\frac{386414\nu}{15}-\frac{201362}{5}\right)\ln 2 \\
&\quad+\left(\frac{48843}{4}-\frac{28431\nu}{4}\right)\ln 3+\left(\frac{43843}{15}-\frac{31067\nu}{15}\right)\ln a_r\Bigg] \\
&\quad+e_t^6\Bigg[\frac{961807}{60}-\frac{215703\nu}{20}+\left(\frac{193718\nu}{15}-\frac{55313}{3}\right)\gamma_E+\left(\frac{6896921}{45}-\frac{12343118\nu}{135}\right)\ln 2 \\
&\quad+\left(\frac{3768201\nu}{320}-\frac{3236031}{160}\right)\ln 3+\left(\frac{92421875\nu}{1728}-\frac{24296875}{288}\right)\ln 5 \\
&\quad+\left(\frac{55313}{6}-\frac{96859\nu}{15}\right)\ln a_r\Bigg]+e_t^8\Bigg[\frac{135264629}{2880}-\frac{45491177\nu}{1440} \\
&\quad+\left(\frac{93850\nu}{3}-\frac{134921}{3}\right)\gamma_E+\left(\frac{118966123\nu}{270}-\frac{94244416}{135}\right)\ln 2 \\
&\quad+\left(\frac{537837489\nu}{2560}-\frac{1684497627}{5120}\right)\ln 3+\left(\frac{12145234375}{27648}-\frac{3790703125\nu}{13824}\right)\ln 5 \\
&\quad+\left(\frac{134921}{6}-\frac{46925\nu}{3}\right)\ln a_r\Bigg]\Bigg\}+\mathcal{O}\left(e_t^{10}\right),
\end{aligned}\tag{4.28}
$$

where the functions $\mathcal{A}^{\text{4PN}}(e_t)$ and $\mathcal{B}^{\text{4PN}}(e_t)$ in the 4PN part are given in Table I of Ref. [91].

4.2.2 Nonlocal part of the EOB Hamiltonian

The (dimensionless) EOB Hamiltonian is given by the energy map

$$
H_{\text{EOB}}=\frac{1}{\nu}\sqrt{1+2\nu\left(H_{\text{eff}}-1\right)},\tag{4.29}
$$

where the effective Hamiltonian

$$
H_{\text{eff}}=\sqrt{A(r)\left[1+p^2+\left(A(r)\bar{D}(r)-1\right)p_r^2+Q(r,p_r)\right]}
$$

$$+\frac{1}{c^3 r^3}\boldsymbol{L}\cdot\left[g_S(r,p_r)\boldsymbol{S}+g_{S^*}(r,p_r)\boldsymbol{S}^*\right]. \tag{4.30}$$

The nonspinning potentials $A, \bar{D}$, and Q were obtained at 4PN order in Ref. [80]. The 4.5PN gyro-gravitomagnetic factors, g_S and g_{S^*}, are given by Eq. (5.6) of Ref. [2], and are in a gauge such that they are independent of the angular momentum. Note that the gyro-gravitomagnetic factors are the same for both aligned and precessing spins, since the spin vector only couples to the angular momentum vector at SO level. Hence, even though the calculations are specialized to aligned spins, the final result for the gyro-gravitomagnetic factors is valid for precessing spins.

Splitting the potentials $A, \bar{D}, Q$ into a local and a nonlocal piece, and writing the gyro-gravitomagnetic factors as

$$\begin{aligned} g_S &= 2+\cdots+\frac{1}{c^8}\left(g_S^{\text{5.5PN,loc}}+g_S^{\text{5.5PN,nonloc}}\right), \\ g_{S^*} &= \frac{3}{2}+\cdots+\frac{1}{c^8}\left(g_{S^*}^{\text{5.5PN,loc}}+g_{S^*}^{\text{5.5PN,nonloc}}\right) \end{aligned} \tag{4.31}$$

yields the following LO nonlocal part of the PN-expanded effective Hamiltonian

$$\begin{aligned} H_{\text{eff}} &= H_{\text{eff}}^{\text{loc}}+\frac{1}{c^8}H_{\text{eff}}^{\text{nonloc}}+\mathcal{O}(\text{5PN, 6.5PN SO}), \\ H_{\text{eff}}^{\text{nonloc}} &= \frac{1}{2}\left(A^{\text{nonloc}}+\bar{D}^{\text{nonloc}}p_r^2+Q^{\text{nonloc}}\right)+\frac{\nu\boldsymbol{L}}{c^3 r^3}\cdot\left[\boldsymbol{S}g_S^{\text{5.5PN,nonloc}}+\boldsymbol{S}^* g_{S^*}^{\text{5.5PN,nonloc}}\right]. \end{aligned} \tag{4.32}$$

Then, we write the nonlocal piece of the potentials and gyro-gravitomagnetic factors in terms of unknown coefficients, calculate the Delaunay average of $H_{\text{eff}}^{\text{nonloc}}$ in terms of the EOB coordinates (a_r, e_t), and match it to the harmonic-coordinates Hamiltonian from Eq. (4.28). Since harmonic and EOB coordinates agree at leading SO order, no canonical transformation is needed between the two at that order.

This yields the results in Table IV of Ref. [91] for the 4PN nonspinning part, and the following SO part expanded to $\mathcal{O}\left(p_r^8\right)$:

$$
\begin{aligned}
g_S^{\text{5.5PN,nonloc}} &= 2\nu\Bigg\{\left(\frac{292}{15}\ln r - \frac{32}{5} - \frac{584}{15}\gamma_E - \frac{232}{3}\ln 2\right)\frac{1}{r^4} \\
&\quad + \left(\frac{12782}{15} - 104\gamma_E + \frac{32744}{15}\ln 2 - \frac{11664}{5}\ln 3 + 52\ln r\right)\frac{p_r^2}{r^3} \\
&\quad + \left(\frac{12503}{15} - \frac{635456}{9}\ln 2 + \frac{218943}{5}\ln 3\right)\frac{p_r^4}{r^2} \\
&\quad + \left(\frac{38246}{25} + \frac{176799232}{225}\ln 2 - \frac{2517237}{10}\ln 3 - \frac{3015625}{18}\ln 5\right)\frac{p_r^6}{r} \\
&\quad + \left(\frac{503099}{350} - \frac{898982848}{189}\ln 2 + \frac{6352671875}{3024}\ln 5 - \frac{31129029}{400}\ln 3\right)p_r^8 + \mathcal{O}\left(p_r^{10}\right)\Bigg\}, \\
g_{S^*}^{\text{5.5PN,nonloc}} &= \frac{3}{2}\nu\Bigg\{\left(16\ln r - \frac{32}{5} - 32\gamma_E - \frac{2912}{45}\ln 2\right)\frac{1}{r^4} \\
&\quad + \left(\frac{35024}{45} - \frac{1024\gamma_E}{15} + \frac{93952}{45}\ln 2 - \frac{10692}{5}\ln 3 + \frac{512}{15}\ln r\right)\frac{p_r^2}{r^3} \\
&\quad + \left(\frac{9232}{15} - \frac{2978624}{45}\ln 2 + \frac{206064}{5}\ln 3\right)\frac{p_r^4}{r^2} \\
&\quad + \left(\frac{33048}{25} + \frac{1497436672}{2025}\ln 2 - \frac{1199934}{5}\ln 3 - \frac{12593750}{81}\ln 5\right)\frac{p_r^6}{r} \\
&\quad + \left(\frac{651176}{525} - \frac{9076395968}{2025}\ln 2 + \frac{2226734375}{1134}\ln 5 - \frac{697653}{14}\ln 3\right)p_r^8 \\
&\quad + \mathcal{O}\left(p_r^{10}\right)\Bigg\}. \qquad (4.33)
\end{aligned}
$$

4.3 Local 5.5PN SO Hamiltonian and scattering angle

In this section, we determine the local part of the Hamiltonian and scattering angle from 1SF results by making use of the simple mass dependence of the PM-expanded scattering angle.

4.3.1 Mass dependence of the scattering angle

Based on the structure of the PM expansion, Poincaré symmetry, and dimensional analysis, Ref. [252] (see also Ref. [265]) showed that the magnitude of the impulse (net change in momentum), for nonspinning systems in the center-of-mass frame, has the following dependence on the masses:

$$\begin{aligned}
\mathsf{Q} &= (\Delta p_{1\mu}\Delta p^{1\mu})^{1/2} \\
&= \frac{2Gm_1m_2}{b}\left[\mathsf{Q}^{\rm 1PM} + \frac{G}{b}\left(m_1\mathsf{Q}^{\rm 2PM}_{m_1} + m_2\mathsf{Q}^{\rm 2PM}_{m_2}\right)\right. \\
&\quad \left. + \frac{G^2}{b^2}\left(m_1^2\mathsf{Q}^{\rm 3PM}_{m_1^2} + m_1m_2\mathsf{Q}^{\rm 3PM}_{m_1m_2} + m_2^2\mathsf{Q}^{\rm 3PM}_{m_2^2}\right) + \cdots\right],
\end{aligned} \tag{4.34}$$

where each PM order is a homogeneous polynomial in the two masses. For nonspinning bodies, the Q's on the right-hand side are functions only of energy (or velocity v). This mass dependence has been extended in Ref. [2] to include spin, such that

$$\begin{aligned}
\mathsf{Q}^{n\rm PM}_{m_1^im_2^j} &= \mathsf{Q}^{n\rm PM}_{m_1^im_2^j}\left(v, \frac{a_1}{b}, \frac{a_2}{b}\right) \\
&= \mathsf{Q}^{n\rm PM}_{m_1^im_2^ja^0}(v) + \frac{a_1}{b}\mathsf{Q}^{n\rm PM}_{m_1^im_2^ja_1}(v) + \frac{a_2}{b}\mathsf{Q}^{n\rm PM}_{m_1^im_2^ja_2}(v) + \mathcal{O}(a_i^2),
\end{aligned} \tag{4.35}$$

where b is the *covariant* impact parameter defined as the orthogonal distance between the incoming worldlines when using the covariant (Tulczyjew-Dixon) spin-supplementary condition [96, 361] $p_{\mathrm{i}\mu}S_{\mathrm{i}}^{\mu\nu} = 0$. (See Refs. [2, 264, 265, 366] for more details.)

The scattering angle χ by which the two bodies are deflected in the center-of-mass frame is related to Q via [252]

$$\sin\frac{\chi}{2} = \frac{\mathsf{Q}}{2P_{\rm c.m.}}, \tag{4.36}$$

where $P_{\rm c.m.}$ is the magnitude of the total linear momentum in the center-of-mass frame and is given by

$$P_{\rm c.m.} = \frac{m_1m_2}{E}\sqrt{\gamma^2-1}\,, \tag{4.37}$$

where we recall that

$$E^2 = m_1^2 + m_2^2 + 2m_1m_2\gamma$$

$$
\begin{aligned}
&= M^2\left[1+2\nu(\gamma-1)\right], \\
\gamma &= \frac{1}{\sqrt{1-v^2}}.
\end{aligned}
\tag{4.38}
$$

Therefore, the scattering angle scaled by E/m_1m_2 has the same mass dependence as Q. (Equivalently, χ/Γ has the same mass dependence as Q/μ, where $\Gamma \equiv E/M$.)

For nonspinning binaries, and because of the symmetry under the exchange of the two bodies' labels, the mass dependence of χ/Γ can be written as a polynomial in the symmetric mass ratio ν. This is because any homogeneous polynomial in the masses (m_1, m_2) of degree n can be written as polynomial in ν of degree $\lfloor n/2 \rfloor$. For example,

$$
c_1 m_1^3 + c_2 m_1^2 m_2 + c_2 m_1 m_2^2 + c_1 m_2^3 = M^3[c_1 + (c_2 - 3c_1)\nu], \tag{4.39}
$$

for some mass-independent factors c_i. Hence, at each nPM order, χ/Γ is a polynomial in ν of degree $\lfloor (n-1)/2 \rfloor$.

When including spin, we also obtain a dependence on the antisymmetric mass ratio $\delta \equiv (m_2 - m_1)/M$, since

$$
a_1\left(c_1 m_1^3 + c_2 m_1^2 m_2 + c_3 m_1 m_2^2 + c_4 m_2^3\right) = M^3 a_1\left(\alpha_1 + \alpha_2\delta + \alpha_3\nu + \alpha_4\nu\delta\right), \tag{4.40}
$$

where α_i are some linear combinations of c_i.

Thus, we find that the scattering angle, up to 5PM and to linear order in spin, has the following mass dependence:

$$
\begin{aligned}
\chi &= \chi_{a^0} + \chi_a + \mathcal{O}(a^2), \qquad (4.41)\\
\frac{\chi_{a^0}}{\Gamma} &= \frac{GM}{b}\mathsf{X}_1^0 + \left(\frac{GM}{b}\right)^2 \mathsf{X}_2^0 \\
&\quad + \left(\frac{GM}{b}\right)^3\left[\mathsf{X}_3^0 + \nu\mathsf{X}_3^{0,\nu}\right] + \left(\frac{GM}{b}\right)^4\left[\mathsf{X}_4^0 + \nu\mathsf{X}_4^{0,\nu}\right]
\end{aligned}
$$

$$
\begin{aligned}
&+\left(\frac{GM}{b}\right)^5\left[\mathsf{X}_5^0+\nu\mathsf{X}_5^{0,\nu}+\nu^2\mathsf{X}_5^{0,\nu^2}\right]+\dots \qquad (4.42)\\
\frac{\chi_a}{\Gamma} &= \frac{a_1}{b}\bigg\{\frac{GM}{b}\mathsf{X}_1+\left(\frac{GM}{b}\right)^2\left[\mathsf{X}_2+\delta\mathsf{X}_2^\delta\right]\\
&+\left(\frac{GM}{b}\right)^3\left[\mathsf{X}_3+\delta\mathsf{X}_3^\delta+\nu\mathsf{X}_3^\nu\right]+\left(\frac{GM}{b}\right)^4\left[\mathsf{X}_4+\delta\mathsf{X}_4^\delta+\nu\mathsf{X}_4^\nu+\nu\delta\mathsf{X}_4^{\nu\delta}\right]\\
&+\left(\frac{GM}{b}\right)^5\left[\mathsf{X}_5+\delta\mathsf{X}_5^\delta+\nu\mathsf{X}_5^\nu+\nu\delta\mathsf{X}_5^{\nu\delta}+\nu^2\mathsf{X}_5^{\nu^2}\right]+\dots\bigg\}+1\leftrightarrow 2, \qquad (4.43)
\end{aligned}
$$

where the $\mathsf{X}_\mathsf{i}^{\cdots}$ are functions only of energy/velocity. Since ν and $\nu\delta$ are of order q when expanded in the mass ratio, their coefficients can be recovered from 1SF results.

This mass-ratio dependence holds for the *total* (local + nonlocal) scattering angle. However, by choosing the split between the local and nonlocal parts as we did in Sec. 4.2, i.e., by choosing the arbitrary length scale s to be the radial distance r, we get the same mass-ratio dependence for the *local* part of the 5.5PN SO scattering angle. This is confirmed by the independent calculation of the nonlocal part of the scattering angle in Eq. (4.92) below, which is linear in ν. (In Ref. [91], the authors introduced a 'flexibility' factor in the relation between s and r to ensure that this mass-ratio dependence continues to hold at 5PN order for both the local and nonlocal contributions separately.)

Terms independent of ν in the scattering angle can be determined from the scattering angle of a spinning test particle in a Kerr background, which was calculated in Ref. [428]. For a test body with spin s in a Kerr background with spin a, the 5PM test-body scattering angle to all PN orders and to linear order in spins can be obtained by integrating Eq. (65) of Ref. [428], leading to

$$
\begin{aligned}
\chi_\text{test} &= \frac{GM}{b}\left[\frac{2v^2+2}{v^2}-\frac{4(a+s)}{bv}\right]+\pi\left(\frac{GM}{b}\right)^2\left[\frac{3\left(v^2+4\right)}{4v^2}-\frac{\left(3v^2+2\right)(4a+3s)}{2bv^3}\right]\\
&+\left(\frac{GM}{b}\right)^3\left[\frac{2\left(5v^6+45v^4+15v^2-1\right)}{3v^6}-\frac{4\left(5v^4+10v^2+1\right)(3a+2s)}{bv^5}\right]
\end{aligned}
$$

$$
\begin{aligned}
&+\pi\Big(\frac{GM}{b}\Big)^4\left[\frac{105\,(v^4+16v^2+16)}{64v^4}-\frac{21\,(5v^4+20v^2+8)\,(8a+5s)}{16bv^5}\right]\\
&+\Big(\frac{GM}{b}\Big)^5\left[\frac{2\,(21v^{10}+525v^8+1050v^6+210v^4-15v^2+1)}{5v^{10}}\right.\\
&\qquad\left.-\frac{4\,(63v^8+420v^6+378v^4+36v^2-1)\,(5a+3s)}{3bv^9}\right]\\
&+\mathcal{O}\left(G^6\right)+\mathcal{O}(a^2,as,s^2).
\end{aligned}
\tag{4.44}
$$

Plugging this into Eq. (4.43) determines all the $\mathsf{X}_\mathsf{i}(v)$ and $\mathsf{X}_\mathsf{i}^\delta(v)$ functions. Hence, we can write the 5PM SO part of the local scattering angle, expanded to 5.5PN order, as follows:

$$
\begin{aligned}
\frac{\chi_a^{\rm loc}}{\Gamma}=\frac{a_1}{b}\Bigg\{&\left(\frac{GM}{v^2b}\right)(-4v)+\pi\left(\frac{GM}{v^2b}\right)^2\left[\left(\frac{\delta}{2}-\frac{7}{2}\right)v+\left(\frac{3\delta}{4}-\frac{21}{4}\right)v^3\right]\\
&+\left(\frac{GM}{v^2b}\right)^3\Big[(2\delta-10+\mathsf{X}_{31}^\nu\nu)v+(20\delta-100+\mathsf{X}_{33}^\nu\nu)v^3\\
&\qquad+(10\delta-50+\mathsf{X}_{35}^\nu\nu)v^5+\mathsf{X}_{37}^\nu\nu v^7+\mathsf{X}_{39}^\nu\nu v^9\Big]\\
&+\pi\left(\frac{GM}{v^2b}\right)^4\Bigg[\left(\mathsf{X}_{41}^{\delta\nu}\delta\nu+\mathsf{X}_{41}^\nu\nu\right)v+\left(\frac{63}{4}\delta-\frac{273}{4}+\mathsf{X}_{43}^{\delta\nu}\delta\nu+\mathsf{X}_{43}^\nu\nu\right)v^3\\
&\qquad+\left(\frac{315}{8}\delta-\frac{1365}{8}+\mathsf{X}_{45}^{\delta\nu}\delta\nu+\mathsf{X}_{45}^\nu\nu\right)v^5+\left(\frac{315\delta}{32}-\frac{1365}{32}+\mathsf{X}_{47}^{\delta\nu}\delta\nu+\mathsf{X}_{47}^\nu\nu\right)v^7\\
&\qquad+\left(\mathsf{X}_{49}^{\delta\nu}\delta\nu+\mathsf{X}_{49}^\nu\nu\right)v^9\Bigg]\\
&+\left(\frac{GM}{v^2b}\right)^5\Bigg[\left(-\frac{4\delta}{3}+\frac{16}{3}+\mathsf{X}_{51}^{\delta\nu}\delta\nu+\mathsf{X}_{51}^\nu\nu+\mathsf{X}_{51}^{\nu^2}\nu^2\right)v\\
&\qquad+\left(48\delta-192+\mathsf{X}_{53}^{\delta\nu}\delta\nu+\mathsf{X}_{53}^\nu\nu+\mathsf{X}_{53}^{\nu^2}\nu^2\right)v^3\\
&\qquad+\left(504\delta-2016+\mathsf{X}_{55}^{\delta\nu}\delta\nu+\mathsf{X}_{55}^\nu\nu+\mathsf{X}_{55}^{\nu^2}\nu^2\right)v^5\\
&\qquad+\left(560\delta-2240+\mathsf{X}_{57}^{\delta\nu}\delta\nu+\mathsf{X}_{57}^\nu\nu+\mathsf{X}_{57}^{\nu^2}\nu^2\right)v^7\\
&\qquad+\left(84\delta-336+\mathsf{X}_{59}^{\delta\nu}\delta\nu+\mathsf{X}_{59}^\nu\nu+\mathsf{X}_{59}^{\nu^2}\nu^2\right)v^9\Bigg]\Bigg\}+1\leftrightarrow 2,
\end{aligned}
\tag{4.45}
$$

where the X_{ij}^ν and $\mathsf{X}_{ij}^{\delta\nu}$ coefficients are independent of the masses, and can be determined, as explained below, from 1SF results. The coefficient $\mathsf{X}_{59}^{\nu^2}$ could be determined from future second-order self-force results.

4.3.2 Relating the local Hamiltonian to the scattering angle

The scattering angle can be calculated from the Hamiltonian by inverting the Hamiltonian and solving for $p_r(E, L, r)$, then evaluating the integral

$$\chi = -2 \int_{r_0}^{\infty} \frac{\partial p_r(E, L, r)}{\partial L} dr - \pi \,, \tag{4.46}$$

where r_0 is the turning point, obtained from the largest root of $p_r(E, L, r) = 0$. E and L represent the physical center-of-mass energy and *canonical* angular momentum, respectively.

As noted above, we express the scattering angle in terms of the *covariant* impact parameter b, but use the *canonical* angular momentum L in the Hamiltonian (corresponding to the Newton-Wigner spin-supplementary condition). The two are related via [264, 265]

$$\begin{aligned} L &= L_{\text{cov}} + \Delta L, \\ L_{\text{cov}} &= P_{\text{c.m.}} b = \frac{\mu}{\Gamma} \gamma v b, \\ \Delta L &= M \frac{\Gamma - 1}{2} \left[a_1 + a_2 - \frac{\delta}{\Gamma} (a_2 - a_1) \right], \end{aligned} \tag{4.47}$$

which can be used to replace L with b in the scattering angle. We can also replace E with v using Eq. (4.38).

Starting from the 4.5PN SO Hamiltonian, as given by Eq. (5.6) of Ref. [2], determines all the unknown coefficients in the scattering angle in Eq. (4.45) up to that order. Writing an ansatz for the local 5.5PN part in terms of unknown coefficients, such as

$$g_S^{\text{5.5PN,loc}} = \frac{g_{04}}{r^4} + g_{23} \frac{p_r^2}{r^3} + g_{42} \frac{p_r^4}{r^2} + g_{61} \frac{p_r^6}{r} + g_{80} p_r^8,$$

$$g_{S^*}^{\text{5.5PN,loc}} = \frac{g_{04}^*}{r^4} + g_{23}^*\frac{p_r^2}{r^3} + g_{42}^*\frac{p_r^4}{r^2} + g_{61}^*\frac{p_r^6}{r} + g_{80}^* p_r^8, \tag{4.48}$$

calculating the scattering angle, and matching to Eq. (4.45) allows us to relate the 10 unknowns in that ansatz to the 6 unknowns in the scattering angle at that order. This leads to

$$\begin{aligned}
g_S^{\text{5.5PN,loc}} &= 2\Bigg\{\frac{1}{r^4}\Bigg[\nu\left(\frac{3\mathsf{X}_{59}^{\delta\nu}}{32} - 2\mathsf{X}_{49}^{\delta\nu} - \frac{35\mathsf{X}_{39}^{\nu}}{16} + 2\mathsf{X}_{49}^{\nu} - \frac{3\mathsf{X}_{59}^{\nu}}{32} + \frac{309077}{1152} - \frac{35449\pi^2}{3072}\right) \\
&\qquad + \nu^2\left(\frac{235111}{2304} - \frac{3\mathsf{X}_{59}^{\nu^2}}{32} - \frac{583\pi^2}{192}\right) - \frac{\nu^4}{64} - \frac{413\nu^3}{512}\Bigg] \\
&\quad + \frac{p_r^2}{r^3}\left[\frac{3\nu^4}{8} - \frac{8259\nu^3}{128} + \left(\frac{198133}{384} - \frac{1087\pi^2}{128}\right)\nu^2 + \nu\left(2\mathsf{X}_{49}^{\delta\nu} + \frac{35\mathsf{X}_{39}^{\nu}}{8} - 2\mathsf{X}_{49}^{\nu} + \frac{1125}{16}\right)\right] \\
&\quad + \frac{p_r^4}{r^2}\left[-\frac{107\nu^4}{64} - \frac{73547\nu^3}{512} + \frac{31913\nu^2}{256} + \nu\left(\frac{8597}{128} - \frac{35\mathsf{X}_{39}^{\nu}}{24}\right)\right] \\
&\quad + \frac{p_r^6}{r}\left[\frac{1577\nu^4}{320} - \frac{11397\nu^3}{512} - \frac{2553\nu^2}{256} - \frac{893\nu}{256}\right] + p_r^8\left[\frac{189\nu^4}{64} + \frac{945\nu^3}{512} + \frac{99\nu^2}{256} - \frac{27\nu}{128}\right]\Bigg\}, \\
g_{S^*}^{\text{5.5PN,loc}} &= \frac{3}{2}\Bigg\{\frac{1}{r^4}\Bigg[-\frac{1701}{512} - \frac{15\nu^4}{512} - \frac{111\nu^3}{128} + \nu^2\left(-\frac{3\mathsf{X}_{59}^{\nu^2}}{32} - \frac{123\pi^2}{64} + \frac{29081}{512}\right) \\
&\qquad + \nu\left(2\mathsf{X}_{49}^{\delta\nu} - \frac{3\mathsf{X}_{59}^{\delta\nu}}{32} - \frac{35\mathsf{X}_{39}^{\nu}}{16} + 2\mathsf{X}_{49}^{\nu} - \frac{3\mathsf{X}_{59}^{\nu}}{32} + \frac{131519}{576} - \frac{90149\pi^2}{12288}\right)\Bigg] \\
&\quad + \frac{p_r^2}{r^3}\Bigg[-\frac{27}{64} + \nu\left(-2\mathsf{X}_{49}^{\delta\nu} + \frac{35\mathsf{X}_{39}^{\nu}}{8} - 2\mathsf{X}_{49}^{\nu} + \frac{86897}{768} - \frac{27697\pi^2}{2048}\right) \\
&\qquad \frac{171\nu^4}{256} - \frac{489\nu^3}{8} + \left(\frac{77201}{256} - \frac{123\pi^2}{16}\right)\nu^2\Bigg] + \frac{p_r^4}{r^2}\Bigg[-\frac{1377\nu^4}{512} - \frac{13905\nu^3}{128} + \frac{12135\nu^2}{512} \\
&\qquad + \nu\left(\frac{10569}{256} - \frac{35\mathsf{X}_{39}^{\nu}}{24}\right) + \frac{2525}{512}\Bigg] + \frac{p_r^6}{r}\left[\frac{16077\nu^4}{2560} - \frac{2391\nu^3}{640} - \frac{879\nu^2}{512} + \frac{77\nu}{32} + \frac{3555}{512}\right] \\
&\quad + p_r^8\left[\frac{945\nu^4}{512} + \frac{315\nu^3}{128} + \frac{1053\nu^2}{512} + \frac{189\nu}{128} + \frac{693}{512}\right]\Bigg\},
\end{aligned} \tag{4.49}$$

where we switched to dimensionless variables. We see that the 5 unknowns $(\mathsf{X}_{39}^{\nu}, \mathsf{X}_{49}^{\nu}, \mathsf{X}_{49}^{\delta\nu}, \mathsf{X}_{59}^{\nu}, \mathsf{X}_{59}^{\delta\nu})$ from the scattering angle only appear in the linear-in-ν coefficients of the gyro-gravitomagnetic factors up to order p_r^4, while the unknown $\mathsf{X}_{59}^{\nu^2}$ only appears in the quadratic-in-ν coefficients of the circular-orbit ($1/r^4$) part. All other coefficients have been determined, due to the structure of the PM-expanded scattering angle, and from lower-order and test-body results.

4.3.3 Redshift and precession frequency

To determine the linear-in-ν coefficients in the local Hamiltonian from 1SF results, we calculate the redshift and spin-precession invariants from the *total* (local + nonlocal) Hamiltonian, since GSF calculations do not differentiate between the two, then match their small-mass-ratio expansion to 1SF expressions known in the literature.

An important step in this calculation is the first law of binary mechanics, which was derived for nonspinning particles in circular orbits in Ref. [429], generalized to spinning particles in circular orbits in Ref. [430], to nonspinning particles in eccentric orbits in Refs. [431, 432], and to spinning particles in eccentric orbits in Ref. [2]. It reads

$$\mathrm{d}E = \Omega_r \mathrm{d}I_r + \Omega_\phi \mathrm{d}L + \sum_{\mathrm{i}} (z_{\mathrm{i}} \mathrm{d}m_{\mathrm{i}} + \Omega_{S_{\mathrm{i}}} \mathrm{d}S_{\mathrm{i}}), \tag{4.50}$$

where Ω_r and Ω_ϕ are the radial and azimuthal frequencies, I_r is the radial action, z_{i} is the redshift, and $\Omega_{S_{\mathrm{i}}}$ is the spin-precession frequency.

The orbit-averaged redshift is a gauge-invariant quantity that can be calculated from the Hamiltonian using

$$z_1 = \left\langle \frac{\partial H}{\partial m_1} \right\rangle = \frac{1}{T_r} \oint \frac{\partial H}{\partial m_1} dt, \tag{4.51}$$

where T_r is the radial period. The spin-precession frequency Ω_{S_1} and spin-precession invariant ψ_1 are given by

$$\begin{aligned} \Omega_{S_1} &= \left\langle \frac{\partial H}{\partial S_1} \right\rangle = \frac{1}{T_r} \oint \frac{\partial H}{\partial S_1} dt, \\ \psi_1 &\equiv \frac{\Omega_{S_1}}{\Omega_\phi}. \end{aligned} \tag{4.52}$$

In evaluating these integrals, we follow Refs. [343, 351] in using the Keplerian parametrization for the radial variable

$$r = \frac{1}{u_p\,(1 + e\cos\xi)}, \tag{4.53}$$

where u_p is the inverse of the semi-latus rectum, e is the eccentricity, and ξ is the relativistic anomaly. The radial and azimuthal periods are calculated from the Hamiltonian using

$$T_r \equiv \oint dt = 2\int_0^\pi \left(\frac{\partial H}{\partial p_r}\right)^{-1} \frac{dr}{d\xi} d\xi, \tag{4.54}$$

$$T_\phi \equiv \oint d\phi = 2\int_0^\pi \frac{\partial H}{\partial L} \left(\frac{\partial H}{\partial p_r}\right)^{-1} \frac{dr}{d\xi} d\xi. \tag{4.55}$$

Performing the above steps yields the redshift and spin-precession invariants in terms of the gauge-dependent u_p and e, i.e., $z_1(u_p, e)$ and $\psi_1(u_p, e)$. We then express them in terms of the gauge-independent variables

$$x \equiv (M\Omega_\phi)^{2/3}, \quad \iota \equiv \frac{3x}{k}, \tag{4.56}$$

where $k \equiv T_\phi/(2\pi) - 1$ is the fractional periastron advance. The expressions we obtain for $z_1(x,\iota)$ and $\psi(x,\iota)$ agree up to 3.5PN order with those in Eq. (50) of Ref. [343] and Eq. (83) of Ref. [351], respectively.

Note that the denominator of ι in Eq. (4.56) is of order 1PN, which effectively scales down the PN ordering such that, to obtain the spin-precession invariant at fourth-subleading PN order, we need to include the 5PN nonspinning part of the Hamiltonian, which is given in Refs. [90, 91].

4.3.4 Comparison with self-force results

Next, we expand the redshift $z_1(x,\iota)$ and spin-precession invariant $\psi_1(x,\iota)$ to first order in the mass ratio q, first order in the massive body's spin $a_2 \equiv a$, and zeroth order in the spin of the smaller companion a_1. In doing so, we make use of another set of variables (y, λ), defined by

$$
\begin{aligned}
y &\equiv (m_2\Omega_\phi)^{2/3} = \frac{x}{(1+q)^{2/3}}, \\
\lambda &\equiv \frac{3y}{T_\phi/(2\pi)-1} = \frac{\iota}{(1+q)^{2/3}}\,,
\end{aligned}
\tag{4.57}
$$

where the mass ratio $q = m_1/m_2$.

Schematically, those expansions have the following dependence on the scattering-angle unknowns:

$$
\begin{aligned}
z_1(y,\lambda) &= \cdots + q\left[\cdots + a\left\{\mathsf{X}_{39}^{\nu}, \mathsf{X}_{49}^{\nu} - \mathsf{X}_{49}^{\delta\nu}, \mathsf{X}_{59}^{\nu} - \mathsf{X}_{59}^{\delta\nu}\right\}\right], \\
\psi_1(y,\lambda) &= \cdots + q\left\{\mathsf{X}_{39}^{\nu}, \mathsf{X}_{49}^{\nu} + \mathsf{X}_{49}^{\delta\nu}, \mathsf{X}_{59}^{\nu} + \mathsf{X}_{59}^{\delta\nu}\right\},
\end{aligned}
\tag{4.58}
$$

which can be seen from the structure of the scattering angle in Eq. (4.45). In those expressions, the $\mathcal{O}(a)$ part of the redshift depends on the unknown X_{39}^{ν} and the *difference* of the two pairs of unknowns $(\mathsf{X}_{49}^{\nu}, \mathsf{X}_{49}^{\delta\nu})$ and $(\mathsf{X}_{59}^{\nu}, \mathsf{X}_{59}^{\delta\nu})$, while the spin-precession invariant depends on X_{39}^{ν} and the *sum* of the two pairs of unknowns. This means that solving for X_{39}^{ν} requires 1SF result for *either* z_1 or ψ_1, while solving for the other unknowns requires *both*.

Hence, to solve for all five unknowns, we need at least three (or two) orders in eccentricity in the redshift, at first order in the Kerr spin, and two (or three) orders in eccentricity in the spin-precession invariant, at zeroth order in both spins. Equivalently, instead of the spin-precession invariant, one could use the redshift at linear order in the spin of the smaller body a_1, but that is known from 1SF results for circular orbits only [342]. Incidentally, the available 1SF results are just enough to solve for the five unknowns, since the redshift is known to $\mathcal{O}(e^4)$ [341, 343, 433] and the spin-precession invariant to $\mathcal{O}(e^2)$ [349].

The last unknown $\mathsf{X}_{59}^{\nu^2}$ in the 5.5PN scattering angle appears in both the redshift and spin-precession invariants at *second* order in the mass ratio, thus requiring second-order self-force results for circular orbits.

To compare $z_1(y,\lambda)$ and $\psi_1(y,\lambda)$ with GSF results, we write them in terms of the Kerr background values of the variables (y,λ) expressed in terms of (u_p, e). The relations between the two sets of variables are explained in detail in Appendix B of Ref. [2], and we just need to append to Eqs. (B16)-(B20) there the following PN terms

$$\begin{aligned}
y(u_p,e) &= y_0(u_p,e) + a\, y_a(u_p,e) + \mathcal{O}(a^2), \qquad (4.59)\\
\lambda(u_p,e) &= \lambda_0(u_p,e) + a\, \lambda_a(u_p,e) + \mathcal{O}(a^2),\\
y_a(u_p,e) &= \cdots + \left(\frac{4829e^4}{12} - 4984e^2\right) u_p^{13/2},\\
\lambda_a(u_p,e) &= \cdots + \left(\frac{4671}{8} + \frac{13959e^2}{8} - \frac{19657e^4}{12}\right) u_p^{11/2}.
\end{aligned}$$

We obtain the following 1SF part of the inverse redshift $U_1 \equiv 1/z_1$ and spin-precession invariant ψ_1

$$\begin{aligned}
U_1 &= U_{1a^0}^{(0)} + a\, U_{1a}^{(0)} + q\left(U_{1a^0}^{\rm 1SF} + a\, U_{1a}^{\rm 1SF}\right) + \mathcal{O}(q^2, a^2),\\
\psi_1 &= \psi_{1a^0}^{(0)} + q\psi_{1a^0}^{\rm 1SF} + \mathcal{O}(q^2, a)\,, \qquad (4.60)
\end{aligned}$$

$$\begin{aligned}
U_{1a}^{\rm 1SF} &= \left(3 - \frac{7e^2}{2} - \frac{e^4}{8}\right) u_p^{5/2} + \left(18 - 4e^2 - \frac{117e^4}{4}\right) u_p^{7/2} + \left(87 + \frac{287e^2}{2} - \frac{6277e^4}{16}\right) u_p^{9/2}\\
&+ \left[\frac{3890}{9} - \frac{241\pi^2}{96} + \left(\frac{5876}{3} - \frac{569\pi^2}{64}\right) e^2 + \left(\frac{2025\pi^2}{128} - 3547\right) e^4\right] u_p^{11/2}\\
&+ \Bigg[8\mathsf{X}_{49}^{\delta\nu} - \frac{3\mathsf{X}_{59}^{\delta\nu}}{8} + \frac{35\mathsf{X}_{39}^{\nu}}{4} - 8\mathsf{X}_{49}^{\nu} + \frac{3\mathsf{X}_{59}^{\nu}}{8} + \frac{17917\pi^2}{768} + \frac{2027413}{2880} + \frac{2336\gamma_E}{15} + \frac{928\ln 2}{3}\\
&\quad + \frac{1168\ln u_p}{15} + e^2\Bigg(\frac{4832\ln u_p}{15} + 24\mathsf{X}_{49}^{\delta\nu} - \frac{21\mathsf{X}_{59}^{\delta\nu}}{16} + \frac{175\mathsf{X}_{39}^{\nu}}{8} - 24\mathsf{X}_{49}^{\nu} + \frac{21\mathsf{X}_{59}^{\nu}}{16}\\
&\qquad + \frac{182411\pi^2}{1536} + \frac{31389241}{2880} + \frac{9664\gamma_E}{15} - 1728\ln 2 + 2916\ln 3\Bigg)
\end{aligned}$$

$$+e^4\biggl(-\frac{1248\ln u_p}{5}-42\mathsf{X}^{\delta\nu}_{49}+\frac{63\mathsf{X}^{\delta\nu}_{59}}{32}-\frac{175\mathsf{X}^{\nu}_{39}}{4}+42\mathsf{X}^{\nu}_{49}-\frac{63\mathsf{X}^{\nu}_{59}}{32}-\frac{2496\gamma_E}{5}$$
$$-\frac{200393\pi^2}{1024}-\frac{137249131}{7680}+\frac{782912\ln 2}{15}-\frac{328779\ln 3}{10}\biggr)\biggr]u_p^{13/2}\,, \tag{4.61}$$

$$\psi^{\rm 1SF}_{1\,a^0}=-u_p+\left(\frac{9}{4}+e^2\right)u_p^2+\left[\frac{739}{16}-\frac{123\pi^2}{64}+\left(\frac{341}{16}-\frac{123\pi^2}{256}\right)e^2\right]u_p^3$$
$$+\biggl[\frac{628\ln u_p}{15}+\frac{31697\pi^2}{6144}-\frac{587831}{2880}+\frac{1256\gamma_E}{15}+\frac{296}{15}\ln 2+\frac{729\ln 3}{5}$$
$$+e^2\biggl(\frac{268\ln u_p}{5}-\frac{164123}{480}-\frac{23729\pi^2}{4096}+\frac{536\gamma_E}{5}+\frac{11720\ln 2}{3}-\frac{10206\ln 3}{5}\biggr)\biggr]u_p^4$$
$$+\biggl[4\mathsf{X}^{\delta\nu}_{49}-\frac{3\mathsf{X}^{\delta\nu}_{59}}{16}-\frac{35\mathsf{X}^{\nu}_{39}}{8}+4\mathsf{X}^{\nu}_{49}-\frac{3\mathsf{X}^{\nu}_{59}}{16}+\frac{6793111\pi^2}{24576}-\frac{22306\gamma_E}{35}-\frac{115984853}{57600}$$
$$+\frac{22058\ln 2}{105}-\frac{31347\ln 3}{28}-\frac{11153}{35}\ln u_p+e^2\biggl(\frac{4248047}{4800}+18\mathsf{X}^{\delta\nu}_{49}-\frac{15\mathsf{X}^{\delta\nu}_{59}}{16}$$
$$-\frac{35\mathsf{X}^{\nu}_{39}}{2}+18\mathsf{X}^{\nu}_{49}-\frac{15\mathsf{X}^{\nu}_{59}}{16}+\frac{4895607\pi^2}{16384}-\frac{22682\gamma_E}{15}+\frac{4430133\ln 3}{320}$$
$$+\frac{9765625\ln 5}{1344}-\frac{4836254\ln 2}{105}-\frac{11341\ln u_p}{15}\biggr)\biggr]u_p^5\,. \tag{4.62}$$

These results can be directly compared with those derived in GSF literature. In particular, for the redshift, we match to Eq. (4.1) of Ref. [341], Eq. (23) of Ref. [433], and Eq. (20) of Ref. [343], while for the precession frequency, we match to Eq. (3.33) of Ref. [349] [2] . The matching to 1SF results leads to the following solution for the unknown coefficients in the scattering angle:

$$\begin{aligned}
\mathsf{X}^{\nu}_{39}&=\frac{26571}{1120},\\
\mathsf{X}^{\delta\nu}_{49}&=\frac{533669}{4800}-\frac{97585\pi^2}{8192},\\
\mathsf{X}^{\nu}_{49}&=-\frac{403129}{4800}+\frac{80823\pi^2}{8192},\\
\mathsf{X}^{\delta\nu}_{59}&=\frac{285673}{240}-\frac{2477\pi^2}{16},\\
\mathsf{X}^{\nu}_{59}&=\frac{402799}{270}-\frac{4135\pi^2}{144}.
\end{aligned}\tag{4.63}$$

[2] Note that the $\mathcal{O}(e^2u_p^5)$ term in Eq. (3.33) of Ref. [349] has a typo, but the correct expression is provided in the Black Hole Perturbation Toolkit [573].

Note that all the logarithms and Euler constants, which are purely nonlocal, cancel between GSF results and those in Eqs. (4.61) and (4.62), thus providing a good check for our calculations.

Another check would be possible once 1SF results are computed at higher orders in eccentricity, since one could directly compare them to our results for the redshift and spin-precession invariants that are provided in the Supplemental Material [3] expanded to $\mathcal{O}(e^8)$.

4.3.5 Local scattering angle and Hamiltonian

Inserting the solution from Eq. (4.63) into the scattering angle in Eq. (4.45), yields

$$
\begin{aligned}
\frac{\chi_a^{\rm loc}}{\Gamma} = \frac{a_1}{b}\Bigg\{ &\left(\frac{GM}{v^2 b}\right)(-4v) + \pi\left(\frac{GM}{v^2 b}\right)^2\left[\left(\frac{\delta}{2}-\frac{7}{2}\right)v + \left(\frac{3\delta}{4}-\frac{21}{4}\right)v^3\right] \\
&+\left(\frac{GM}{v^2 b}\right)^3\Bigg[(2\delta-10)v + (20\delta-100+10\nu)v^3 + \left(10\delta-50+\frac{77}{2}\nu\right)v^5 \\
&\quad + \frac{177}{4}\nu v^7 + \frac{26571}{1120}\nu v^9\Bigg] \\
&+\pi\left(\frac{GM}{v^2 b}\right)^4\Bigg[\left(\frac{63}{4}\delta - \frac{273}{4} - \frac{3}{4}\delta\nu + \frac{39}{4}\nu\right)v^3 + \left(\frac{315}{8}\delta - \frac{1365}{8} - \frac{45}{8}\delta\nu + \frac{777}{8}\nu\right)v^5 \\
&\quad + \left(\frac{315\delta}{32} - \frac{1365}{32} + \left(-\frac{257}{96} - \frac{251\pi^2}{256}\right)\delta\nu + \left(\frac{23717}{96} - \frac{733\pi^2}{256}\right)\nu\right)v^7 \\
&\quad + \left(\left(\frac{533669}{4800} - \frac{97585\pi^2}{8192}\right)\delta\nu + \left(\frac{80823\pi^2}{8192} - \frac{403129}{4800}\right)\nu\right)v^9\Bigg] \\
&+\left(\frac{GM}{v^2 b}\right)^5\Bigg[\left(-\frac{4\delta}{3}+\frac{16}{3}\right)v + (48\delta - 192 - 4\delta\nu + 32\nu)v^3 \\
&\quad + \left(504\delta - 2016 - 109\delta\nu + 1032\nu - 16\nu^2\right)v^5 \\
&\quad + \left(560\delta - 2240 + \left(-\frac{21995}{54} - \frac{80\pi^2}{9}\right)\delta\nu + \left(\frac{150220}{27} - \frac{2755\pi^2}{36}\right)\nu - 168\nu^2\right)v^7 \\
&\quad + \left(84\delta - 336 + \left(\frac{285673}{240} - \frac{2477\pi^2}{16}\right)\delta\nu + \left(\frac{402799}{270} - \frac{4135\pi^2}{144}\right)\nu + \mathsf{X}_{59}^{\nu^2}\nu^2\right)v^9\Bigg]\Bigg\} \\
&+ 1 \leftrightarrow 2.
\end{aligned}
\tag{4.64}
$$

For the gyro-gravitomagnetic factors, which are one of the main results of this paper, substituting the solution (4.63) in Eq. (4.49) yields the following local part:

$$
\begin{aligned}
g_S^{\text{5.5PN,loc}} &= 2\Bigg\{\Bigg[-\frac{\nu^4}{64}-\frac{413\nu^3}{512}+\nu^2\left(-\frac{3\mathsf{X}_{59}^{\nu^2}}{32}-\frac{583\pi^2}{192}+\frac{235111}{2304}\right) \\
&\qquad +\left(\frac{62041\pi^2}{3072}-\frac{11646877}{57600}\right)\nu\Bigg]\frac{1}{r^4} \\
&\quad +\left[\frac{3\nu^4}{8}-\frac{8259\nu^3}{128}+\left(\frac{198133}{384}-\frac{1087\pi^2}{128}\right)\nu^2+\left(\frac{3612403}{6400}-\frac{22301\pi^2}{512}\right)\nu\right]\frac{p_r^2}{r^3} \\
&\quad +\left[-\frac{107\nu^4}{64}-\frac{73547\nu^3}{512}+\frac{31913\nu^2}{256}+\frac{8337\nu}{256}\right]\frac{p_r^4}{r^2} \\
&\quad +\left[\frac{1577\nu^4}{320}-\frac{11397\nu^3}{512}-\frac{2553\nu^2}{256}-\frac{893\nu}{256}\right]\frac{p_r^6}{r} \\
&\quad +\left[\frac{189\nu^4}{64}+\frac{945\nu^3}{512}+\frac{99\nu^2}{256}-\frac{27\nu}{128}\right]p_r^8\Bigg\},
\end{aligned}
\tag{4.65}
$$

$$
\begin{aligned}
g_{S^*}^{\text{5.5PN,loc}} &= \frac{3}{2}\Bigg\{\Bigg[-\frac{5\nu^4}{128}-\frac{37\nu^3}{32}+\nu^2\left(-\frac{\mathsf{X}_{59}^{\nu^2}}{8}-\frac{41\pi^2}{16}+\frac{29081}{384}\right)+\left(\frac{23663\pi^2}{3072}-\frac{55}{2}\right)\nu \\
&\qquad -\frac{567}{128}\Bigg]\frac{1}{r^4}+\left[-\frac{459\nu^4}{128}-\frac{4635\nu^3}{32}+\frac{4045\nu^2}{128}+\frac{107\nu}{12}+\frac{2525}{384}\right]\frac{p_r^4}{r^2} \\
&\quad +\left[\frac{57\nu^4}{64}-\frac{163\nu^3}{2}+\left(\frac{77201}{192}-\frac{41\pi^2}{4}\right)\nu^2+\left(\frac{34677}{160}-\frac{4829\pi^2}{384}\right)\nu-\frac{9}{16}\right]\frac{p_r^2}{r^3} \\
&\quad +\left[\frac{5359\nu^4}{640}-\frac{797\nu^3}{160}-\frac{293\nu^2}{128}+\frac{77\nu}{24}+\frac{1185}{128}\right]\frac{p_r^6}{r} \\
&\quad +\left[\frac{315\nu^4}{128}+\frac{105\nu^3}{32}+\frac{351\nu^2}{128}+\frac{63\nu}{32}+\frac{231}{128}\right]p_r^8\Bigg\}.
\end{aligned}
\tag{4.66}
$$

4.3.6 Comparison with numerical relativity

To quantify the effect of the 5.5PN SO part on the dynamics, and that of the remaining unknown coefficient $\mathsf{X}_{59}^{\nu^2}$, we compare the binding energy calculated from the EOB Hamiltonian to NR. The binding energy provides a good diagnostic for the conservative dynamics of the binary system [408, 434, 435], and can be calculated from accurate NR simulations by subtracting the radiated energy E_{rad} from the ADM energy E_{ADM} at the beginning of the simulation [436], i.e.,

$$\bar{E}_{\text{NR}} = E_{\text{ADM}} - E_{\text{rad}} - M. \tag{4.67}$$

To isolate the SO contribution $\bar{E}^{\text{SO}}$ to the binding energy, we combine configurations with different spin orientations (parallel or anti-parallel to the orbital angular momentum), as explained in Refs. [437, 438]. One possibility is to use

$$\bar{E}^{\text{SO}}(\nu, \chi, \chi) \simeq \frac{1}{2}\left[\bar{E}(\nu, \chi, \chi) - \bar{E}(\nu, -\chi, -\chi)\right], \tag{4.68}$$

where χ here is the magnitude of the dimensionless spin. This relation subtracts the nonspinning and spin-spin parts, with corrections remaining at order χ^3, which provides a good approximation since the spin-cubed contribution to the binding energy is about an order of magnitude smaller than the SO contribution, as was shown in Ref. [438].

We calculate the binding energy for circular orbits from the EOB Hamiltonian using $\bar{E}_{\text{EOB}} = H_{\text{EOB}} - M$ while neglecting radiation reaction effects, which implies that $\bar{E}_{\text{EOB}}$ is not expected to agree well with $\bar{E}_{\text{NR}}$ near the end of the inspiral. We set $p_r = 0$ in the Hamiltonian and numerically solve $\dot{p}_r = 0 = -\partial H/\partial r$ for the angular momentum L at different orbital separations. Then, we plot $\bar{E}$ versus the dimensionless parameter

$$v_\Omega \equiv (M\Omega)^{1/3}, \tag{4.69}$$

where the orbital frequency $\Omega = \partial H/\partial L$. Finally, we compare the EOB binding energy to NR data for the binding energy that were extracted in Ref. [438] from the Simulating eXtreme Spacetimes (SXS) catalog [41, 458]. In particular, we use the simulations with SXS ID 0228 and 0215 for $q = 1$, 0291 and 0264 for $q = 1/3$, all with spin magnitudes $\chi = 0.6$ aligned and antialigned. The numerical error in these simulations is significantly smaller than the SO contribution to the binding energy.

In Fig. 4.1, we plot the relative difference in the SO contribution $\bar{E}^{\text{SO}}$ between EOB and NR for two mass ratios, $q = 1$ and $q = 1/3$, as a function of v_Ω up to $v_\Omega = 0.38$, which corresponds to about an orbit before merger. We see that the inclusion of the 5.5PN SO part (with the remaining unknown $\mathsf{X}_{59}^{\nu^2} = 0$) provides an improvement over 4.5PN, but the difference is smaller than that between 3.5PN and 4.5PN. In addition, since the remaining unknown $\mathsf{X}_{59}^{\nu^2}$ is expected to be about $\mathcal{O}(10^2)$, based on the other coefficients in the scattering angle, we plotted the energy for $\mathsf{X}_{59}^{\nu^2} = 500$ and $\mathsf{X}_{59}^{\nu^2} = -500$, demonstrating that the effect of that unknown is less than the difference between 4.5PN and 5.5PN, with decreasing effect for small mass ratios.

4.4 Nonlocal 5.5PN SO scattering angle

The local part of the Hamiltonian and scattering angle calculated in the previous section is valid for both bound and unbound orbits. However, the nonlocal part of the Hamiltonian from Sec. 4.2 is only valid for bound orbits since it was calculated in a small-eccentricity expansion. In this section, we complement these results by calculating the nonlocal part for unbound orbits in a large-eccentricity (or large-angular-momentum) expansion.

The nonlocal part of the 4PN scattering angle was first computed in Ref. [558], in both the time and frequency domains, at leading order in the large-eccentricity expansion. This was extended in Ref. [91] at 5PN at leading order in eccentricity, and in Ref. [92] at 6PN to next-to-next-to-leading order in eccentricity. In addition, Refs. [548, 574] recovered analytical expressions for the nonlocal scattering angle by using high-precision arithmetic methods.

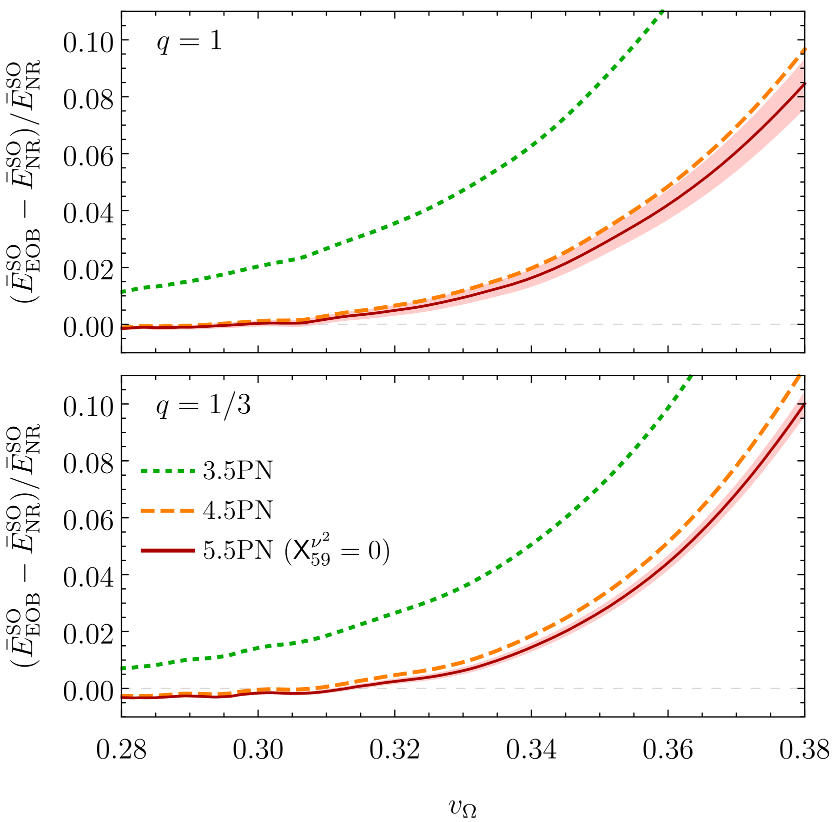

Figure 4.1: The relative difference in the SO contribution to the binding energy between EOB and NR, plotted versus the frequency parameter v_Ω. The 5.5PN curve corresponds to $\mathsf{X}^{\nu^2}_{59} = 0$, while the upper and lower edges of the shaded region around it correspond to $\mathsf{X}^{\nu^2}_{59} = -500$ and $\mathsf{X}^{\nu^2}_{59} = 500$, respectively.

It was shown in Ref. [558] that the nonlocal contribution to the scattering angle is given by

$$\chi_{\text{nonloc}} = \frac{1}{\nu}\frac{\partial}{\partial L} W_{\text{nonloc}}(E, L), \tag{4.70}$$

$$W_{\text{nonloc}} = \int dt\, \delta H_{\text{nonloc}}, \tag{4.71}$$

with δH_{nonloc} given by Eq. (4.14), leading to

$$W_{\text{nonloc}} = W^{\text{flux split}} + W^{\text{flux}}, \tag{4.72}$$

$$W^{\text{flux split}} = -\frac{GM}{c^3} \int dt\, \text{Pf}_{2s/c} \int \frac{d\tau}{|\tau|} \mathcal{F}^{\text{split}}_{\text{LO}}(t, t+\tau), \tag{4.73}$$

$$W^{\text{flux}} = \frac{2GM}{c^3} \int dt\, \mathcal{F}_{\text{LO}}(t,t) \ln\left(\frac{r}{s}\right). \tag{4.74}$$

To evaluate the integral in the large-eccentricity limit, we follow the steps used in Refs. [91, 558]. We use the quasi-Keplerian parametrization for hyperbolic motion [427, 575]

$$r = \bar{a}_r(e_r \cosh \bar{u} - 1), \tag{4.75}$$

$$\bar{n}t = e_t \sinh \bar{u} - \bar{u}, \tag{4.76}$$

$$\phi = 2K \arctan\left[\sqrt{\frac{e_\phi + 1}{e_\phi - 1}} \tanh \frac{\bar{u}}{2}\right], \tag{4.77}$$

which is the analytic continuation of the parametrization for elliptic orbits in Eqs. (4.15)–(4.17). In Appendix. D.2, we summarize the relations for these quantities in terms of the energy and angular momentum.

We begin by expressing the variables $(r, \dot{\phi}, \dot{r})$, which enter the multipole moments, in terms of (ϕ, L, e_t), such that

$$r = \frac{L^2}{1 + e_t \cos\phi} + \frac{2\delta\chi_A + (2-\nu)\chi_S}{L\left(e_t \cos\phi + 1\right)^2} \times \left(2\phi e_t \sin\phi + 4e_t \cos\phi + e_t^2 + 3\right),$$

$$\dot{\phi} = \frac{\left(e_t \cos\phi + 1\right)^2}{L^3} + \frac{\left(e_t \cos\phi + 1\right)\left(2\delta\chi_A + (2-\nu)\chi_S\right)}{2L^6}$$

$$\times \left(-8\phi e_t \sin\phi + e_t^2\cos(2\phi) - 12 e_t\cos\phi - 3e_t^2 - 10\right),$$

$$\dot{r} = \frac{e_t \sin\phi}{L} + \frac{e_t\left(2\delta\chi_A + (2-\nu)\chi_S\right)}{2L^4} \times \left(e_t \sin(2\phi) - 2\sin\phi + 4\phi\cos\phi\right). \tag{4.78}$$

We then use these relations to obtain an exact expression for the flux-split function $\mathcal{F}_{\mathrm{LO}}^{\mathrm{split}}(\phi,\phi')$, with no eccentricity expansion, which takes the form

$$\mathcal{F}_{\mathrm{LO}}^{\mathrm{split}}(\phi,\phi') = \frac{4\nu^2}{15L^{10}}(1+e_t\cos\phi)^2(1+e_t\cos\phi')^2 \times \left(F_0 + F_1 e_t + F_2 e_t^2\right)$$
$$+ \frac{\nu^2}{L^{13}}(1+e_t\cos\phi)(1+e_t\cos\phi') \times \left(F_0^s + F_1^s e_t + \cdots + F_6^s e_t^6\right), \tag{4.79}$$

where the functions $F_{\mathsf{i}}(\phi,\phi')$ are given by Eq. (92) of Ref. [262], but the functions $F_{\mathsf{i}}^s(\phi,\phi')$ in the SO part are too lengthy to write here. Instead, we expand $\mathcal{F}_{\mathrm{LO}}^{\mathrm{split}}(\phi,\phi')$ to leading order in a large-eccentricity expansion (in powers of $1/e_t$). To do that, we define the rescaled mean motion $\tilde{n} \equiv \bar{n}/e_t$, write the Kepler Eq. (4.76) as

$$\tilde{n}t = \sinh\bar{u} - \frac{\bar{u}}{e_t}, \tag{4.80}$$

and solve for $\bar{u}$ in a $1/e_t$ expansion

$$\bar{u} = \sinh^{-1}(t\tilde{n}) + \frac{\sinh^{-1}(t\tilde{n})}{e_t\sqrt{1+t^2\tilde{n}^2}} + \mathcal{O}(e_t^{-2}). \tag{4.81}$$

Substituting in Eq. (4.77) and expanding yields

$$\phi(t) = \tan^{-1}(t\tilde{n}) + \mathcal{O}\left(e_t^{-1}\right)$$
$$- \frac{t\tilde{n}e_t\left[2\delta\chi_A + (2-\nu)\chi_S\right]}{L^3\sqrt{t^2\tilde{n}^2+1}} + \mathcal{O}\left(e_t^0\right). \tag{4.82}$$

Defining $\tilde{t} \equiv \tilde{n}t$ and $\tilde{\tau} \equiv \tilde{n}\tau$, then substituting in Eq. (4.79) and expanding yields

$$\mathcal{F}^{\mathrm{split}}(t,t+\tau) = \frac{4\nu^2 e_t^6}{15L^{10}} \frac{\mathsf{f}_6(\tilde{t},\tilde{\tau})}{\left(\tilde{t}^2+1\right)^{5/2}\left(2\tilde{\tau}\tilde{t} + \tilde{t}^2 + \tilde{\tau}^2 + 1\right)^{5/2}} + \mathcal{O}(e_t^5)$$

$$+\frac{4\nu^2 e_t^8}{15L^{13}}\frac{\chi_S \mathsf{f}_8^S(\tilde{t},\tilde{\tau})+\delta\chi_A \mathsf{f}_8^A(\tilde{t},\tilde{\tau})}{\left(\tilde{t}^2+1\right)^{7/2}\left(2\tilde{\tau}\tilde{t}+\tilde{t}^2+\tilde{\tau}^2+1\right)^{7/2}}+\mathcal{O}(e_t^7), \tag{4.83}$$

with

$$\begin{aligned}
\mathsf{f}_6(\tilde{t},\tilde{\tau}) &= 2\tilde{t}^6+6\tilde{\tau}\tilde{t}^5+\left(6\tilde{\tau}^2+28\right)\tilde{t}^4+2\tilde{\tau}\left(\tilde{\tau}^2+28\right)\tilde{t}^3+\left(39\tilde{\tau}^2+50\right)\tilde{t}^2+\tilde{\tau}\left(11\tilde{\tau}^2+50\right)\tilde{t}\\
&\quad -12\left(\tilde{\tau}^2-2\right),\\
\mathsf{f}_8^S(\tilde{t},\tilde{\tau}) &= 4(9\nu-5)\tilde{t}^8+16(9\nu-5)\tilde{\tau}\tilde{t}^7+2\tilde{t}^6\left[18\nu\left(6\tilde{\tau}^2+5\right)-63\tilde{\tau}^2-67\right]\\
&\quad +2\tilde{\tau}\tilde{t}^5\left[18\nu\left(4\tilde{\tau}^2+15\right)-49\tilde{\tau}^2-201\right]\\
&\quad +\tilde{t}^4\left[18\nu\left(2\tilde{\tau}^4+35\tilde{\tau}^2+18\right)-2\left(19\tilde{\tau}^4+206\tilde{\tau}^2+141\right)\right]\\
&\quad -2\tilde{\tau}\tilde{t}^3\left[-36\nu\left(5\tilde{\tau}^2+9\right)+3\tilde{\tau}^4+77\tilde{\tau}^2+282\right]+22\tilde{\tau}^4-52\tilde{\tau}^2-74\\
&\quad -12\nu\left(3\tilde{\tau}^4+2\tilde{\tau}^2-6\right)+\tilde{t}^2\left[3\nu\left(35\tilde{\tau}^4+130\tilde{\tau}^2+84\right)-2\left(8\tilde{\tau}^4+169\tilde{\tau}^2+121\right)\right]\\
&\quad +\tilde{\tau}\tilde{t}\left[3\nu\left(5\tilde{\tau}^4+22\tilde{\tau}^2+84\right)-2\left(3\tilde{\tau}^4+28\tilde{\tau}^2+121\right)\right],\\
\mathsf{f}_8^A(\tilde{t},\tilde{\tau}) &= -2\left(\tilde{t}^2+1\right)\Big[40\tilde{\tau}\tilde{t}^5+\left(63\tilde{\tau}^2+57\right)\tilde{t}^4+7\tilde{\tau}\left(7\tilde{\tau}^2+23\right)\tilde{t}^3+\left(19\tilde{\tau}^4+143\tilde{\tau}^2+84\right)\tilde{t}^2\\
&\qquad +\tilde{\tau}\left(3\tilde{\tau}^4+28\tilde{\tau}^2+121\right)\tilde{t}+10\tilde{t}^6-11\tilde{\tau}^4+26\tilde{\tau}^2+37\Big].
\end{aligned} \tag{4.84}$$

Then, we evaluate the *partie finie* integral in Eq. (4.73), after writing it in terms of $\tilde{T}\equiv 2\tilde{n}s/c$, to obtain

$$\begin{aligned}
-\mathrm{Pf}_{\tilde{T}}\int\frac{d\tilde{\tau}}{|\tilde{\tau}|}\mathcal{F}_{\text{LO}}^{\text{split}}(t,t+\tau) &= \frac{8\nu^2 e_t^6}{15L^{10}\left(\tilde{t}^2+1\right)^3}\left[36+7\tilde{t}^2+2\left(\tilde{t}^2+12\right)\ln\left(\frac{\tilde{T}}{2\tilde{t}^2+2}\right)\right]\\
&\quad +\frac{16\nu^2 e_t^8}{15L^{13}\left(\tilde{t}^2+1\right)^4}\Bigg\{\chi_S\Bigg[60\nu+(3\nu-5)\tilde{t}^4-\left(2(5-9\nu)\tilde{t}^2-36\nu+37\right)\ln\left(\frac{\tilde{T}}{2\tilde{t}^2+2}\right)\\
&\quad +(36\nu+5)\tilde{t}^2-53\Bigg]-\delta\chi_A\left[\left(10\tilde{t}^2+37\right)\ln\left(\frac{\tilde{T}}{2\tilde{t}^2+2}\right)+5\tilde{t}^4-5\tilde{t}^2+53\right]\Bigg\}.
\end{aligned} \tag{4.85}$$

Integrating over t, we obtain the flux-split potential

$$W^{\text{flux split}}=\frac{2\pi\nu^2}{15e_t^3 a_r^{7/2}}\left[100+37\ln\left(\frac{s}{4e_t a_r^{3/2}}\right)\right]+\frac{\pi\nu^2}{30e_t^4 a_r^5}\Bigg\{31\delta\chi_A\left[-137-46\ln\left(\frac{s}{4a_r^{3/2}e_t}\right)\right]$$

$$+\chi_S\left[2774\nu-4247-2(713-457\nu)\ln\left(\frac{s}{4a_r^{3/2}e_t}\right)\right]\Bigg\}. \tag{4.86}$$

The second contribution W^{flux} in Eq. (4.74) can be easily integrated to yield

$$W^{\text{flux}}=\frac{2\pi\nu^2}{15e_t^3a_r^{7/2}}\left[-\frac{85}{4}-37\ln\left(\frac{s}{2a_re_t}\right)\right]+\frac{\pi\nu^2}{60e_t^4a_r^5}\Bigg\{\delta\chi_A\left[2255+2852\ln\left(\frac{s}{2a_re_t}\right)\right]$$
$$+\chi_S\left[2255-1365\nu+(2852-1828\nu)\ln\left(\frac{s}{2a_re_t}\right)\right]\Bigg\}, \tag{4.87}$$

where we used

$$r(t)=\frac{L^2\sqrt{\tilde{t}^2+1}}{e_t}+\frac{1}{L}\left[2\delta\chi_A+(2-\nu)\chi_S\right]. \tag{4.88}$$

Adding the two contributions leads to

$$W^{\text{nonloc}}=-\frac{\pi\nu^2}{30e_t^3a_r^{7/2}}\left[74\ln\left(4a_r\right)-315\right] \tag{4.89}$$
$$+\frac{\pi\nu^2}{60e_t^4a_r^5}\Big\{\chi_S\left[4183\nu-6239+2(713-457\nu)\ln(4a_r)\right]+\delta\chi_A\left[-6239+1426\ln\left(4a_r\right)\right]\Big\},$$

where we see that s cancels. In terms of the energy and angular momentum, and expanding in $1/L$ to leading order,

$$W^{\text{nonloc}}=\frac{2\pi\nu^2\bar{E}^2}{15L^3}\left[315+74\ln\left(\frac{\bar{E}}{2}\right)\right] \tag{4.90}$$
$$+\frac{2\pi\nu^2\bar{E}^3}{15L^4}\Bigg\{(4183\nu-6239)\chi_S-6239\delta\chi_A-2\left[713\delta\chi_A+(713-457\nu)\chi_S\right]\ln\left(\frac{E}{2}\right)\Bigg\},$$

and the nonlocal part of the scattering angle

$$\chi^{\text{nonloc}}=-\frac{2\pi\nu\bar{E}^2}{5L^4}\left[315+74\ln\left(\frac{\bar{E}}{2}\right)\right] \tag{4.91}$$
$$-\frac{8\pi\nu\bar{E}^3}{15L^5}\Bigg\{(4183\nu-6239)\chi_S-6239\delta\chi_A-2\left[713\delta\chi_A+(713-457\nu)\chi_S\right]\ln\left(\frac{E}{2}\right)\Bigg\}.$$

In terms of b and v, using Eqs. (4.47) and (4.38),

$$\chi^{\text{nonloc}}=-\frac{\pi\nu}{10b^4}\left[148\ln\left(\frac{v}{2}\right)+315\right] \tag{4.92}$$
$$-\frac{\pi\nu v}{15b^5}\Bigg\{4\ln\left(\frac{v}{2}\right)\left[(679\nu-824)\chi_S-824\delta\chi_A\right]+(6073\nu-7184)\chi_S-7184\delta\chi_A\Bigg\}.$$

4.5 Gauge-invariant quantities for bound orbits

In this section, we obtain two gauge-invariant quantities that characterize bound orbits: the radial action as a function of the energy and angular momentum, and the binding energy for circular orbits as a function of the orbital frequency.

4.5.1 Radial action

The radial action function contains the same gauge-invariant information as the Hamiltonian, and from it several other functions can be derived that describe bound orbits, such as the periastron advance, which can be directly related to the scattering angle via analytic continuation [255, 267]. This means that the entire calculation in Sec. 4.3 could be performed using the radial action instead of the Hamiltonian, as was done in Ref. [2].

The radial action is defined by the integral

$$I_r = \frac{1}{2\pi} \oint p_r dr, \tag{4.93}$$

and we split it into a local contribution and a nonlocal one, such that

$$I_r = I_r^{\text{loc}} + I_r^{\text{nonloc}}. \tag{4.94}$$

We calculate the local part from the local EOB Hamiltonian, i.e., Eq. (4.29) with the nonlocal parts of the potentials and gyro-gravitomagnetic factors set to zero. We invert the local Hamiltonian iteratively to obtain $p_r(\varepsilon, L, r)$ in a PN expansion, where we recall that

$$\begin{aligned} H_{\text{EOB}} &= \frac{1}{\nu}\sqrt{1+2\nu(\gamma-1)}, \\ \varepsilon &\equiv \gamma^2 - 1, \end{aligned} \tag{4.95}$$

with $\varepsilon < 0$, $\gamma < 1$ for bound orbits. Then, we integrate

$$I_r = \frac{1}{\pi} \int_{r_-}^{r_+} p_r(\varepsilon, L, r)\, dr, \tag{4.96}$$

where $r_\pm$ are the zeros of the Newtonian-order $p_r^{(0)} = \sqrt{\varepsilon + 2/r - L^2/r^2}$, which are given by

$$r_\pm = \frac{1 \pm \sqrt{1 + L^2 \varepsilon}}{-\varepsilon}. \tag{4.97}$$

It is convenient to express the radial action in terms of the *covariant* angular momentum $L_{\rm cov} = L - \Delta L$, with ΔL given by Eq. (4.47), since it can then be directly related to the coefficients of the scattering angle, as discussed in Ref. [2], and leads to slightly simpler coefficients for the SO part.

We obtain for the local part

$$\begin{aligned} I_r^{\rm loc} &= -L + I_0 + \frac{I_1}{\Gamma L_{\rm cov}} + \frac{I_2^s}{(\Gamma L_{\rm cov})^2} + \frac{I_3}{(\Gamma L_{\rm cov})^3} + \frac{I_4^s}{(\Gamma L_{\rm cov})^4} \\ &\quad + \frac{I_5}{(\Gamma L_{\rm cov})^5} + \frac{I_6^s}{(\Gamma L_{\rm cov})^6} + \frac{I_7}{(\Gamma L_{\rm cov})^7} + \frac{I_8^s}{(\Gamma L_{\rm cov})^8} + \frac{I_9}{(\Gamma L_{\rm cov})^9} + \frac{I_{10}^s}{(\Gamma L_{\rm cov})^{10}}, \end{aligned} \tag{4.98}$$

where each term starts at a given PN order, with 0.5PN order corresponding to each power in $1/L$. Also, as noted in Ref. [91], when the radial action is written in this form, in terms of Γ, the coefficients $I_{2n+1}^{(s)}$ become simple polynomials in ν of degree $\lfloor n \rfloor$.

The coefficients I_n for the nonspinning local radial action up to 5PN order are given by Eq. (13.20) of Ref. [91]. The SO coefficients I_n^s were derived in Ref. [2] to the 4.5PN order, but we list them here for completeness. The coefficients I_0, I_1, I_2^s are exact, and are given by

$$\begin{aligned} I_0 &= \frac{1 + 2\varepsilon}{\sqrt{-\varepsilon}}, \\ I_1 &= \frac{3}{4}(4 + 5\varepsilon), \\ I_2^s &= -\frac{1}{4}\gamma(5\varepsilon + 2)\left(4a_b + 3a_t\right), \end{aligned} \tag{4.99}$$

where $a_b \equiv S/M, a_t \equiv S^*/M$. The other SO coefficients, up to 5.5PN, read

$$
\begin{aligned}
I_4^s = & -\frac{21}{64}\gamma\left(33\varepsilon^2+36\varepsilon+8\right)\left(8a_b+5a_t\right)+\gamma\nu\Bigg\{\frac{21a_b}{8}+\frac{9a_t}{4}+\varepsilon\left(\frac{495a_b}{16}+\frac{219a_t}{8}\right) \\
& +\varepsilon^2\left[\left(\frac{17423}{192}-\frac{241\pi^2}{512}\right)a_b+\left(\frac{2759}{32}-\frac{123\pi^2}{128}\right)a_t\right] \\
& -\varepsilon^3\left[\left(\frac{156133}{3200}-\frac{22301\pi^2}{4096}\right)a_b+\left(\frac{8381\pi^2}{16384}-\frac{6527}{960}\right)a_t\right]+\mathcal{O}(\varepsilon^4)\Bigg\}, \\
I_6^s = & \left(-\frac{25\nu^2}{8}+\frac{1755\nu}{16}-\frac{495}{2}\right)a_b+\left(-\frac{45\nu^2}{16}+\frac{165\nu}{2}-\frac{1155}{8}\right)a_t \\
& -\varepsilon\Bigg\{\left[\frac{645\nu^2}{8}+\left(\frac{3665\pi^2}{256}-\frac{39715}{24}\right)\nu+\frac{3465}{2}\right]a_b \\
& +\left[\frac{1185\nu^2}{16}+\left(\frac{1845\pi^2}{128}-\frac{10305}{8}\right)\nu+\frac{8085}{8}\right]a_t\Bigg\} \\
& +\varepsilon^2\Bigg\{a_b\left(\left(\frac{10640477}{1920}-\frac{176785\pi^2}{2048}\right)\nu+\nu^2\left(\frac{45\mathsf{X}_{59}^{\nu^2}}{128}+\frac{2755\pi^2}{512}-\frac{176815}{384}\right)-\frac{121275}{32}\right) \\
& +a_t\left(\left(\frac{433715}{96}-\frac{1748755\pi^2}{16384}\right)\nu+\nu^2\left(\frac{45\mathsf{X}_{59}^{\nu^2}}{128}+\frac{5535\pi^2}{1024}-\frac{26175}{64}\right)-\frac{282975}{128}\right)\Bigg\} \\
& +\mathcal{O}(\varepsilon^3), \\
I_8^s = & \left[\frac{455\nu^3}{128}-\frac{10185\nu^2}{32}+\left(\frac{3755465}{1152}-\frac{42875\pi^2}{1536}\right)\nu-\frac{25025}{8}\right]a_b \\
& +\left[\frac{105\nu^3}{32}-\frac{16485\nu^2}{64}+\left(\frac{437605}{192}-\frac{1435\pi^2}{64}\right)\nu-\frac{225225}{128}\right]a_t \\
& +\varepsilon\Bigg\{\Bigg[\frac{4935\nu^3}{32}+\left(\frac{8263591}{180}-\frac{9948785\pi^2}{12288}\right)\nu+\nu^2\left(\frac{105\mathsf{X}_{59}^{\nu^2}}{64}-\frac{1583995}{192}+\frac{27895\pi^2}{256}\right) \\
& -\frac{225225}{8}\Bigg]a_b+\Bigg[\frac{1155\nu^3}{8}+\left(\frac{4594121}{144}-\frac{29957165\pi^2}{49152}\right)\nu \\
& +\nu^2\left(\frac{105\mathsf{X}_{59}^{\nu^2}}{64}-\frac{209195}{32}+\frac{47355\pi^2}{512}\right)-\frac{2027025}{128}\Bigg]a_t\Bigg\}+\mathcal{O}(\varepsilon^2), \\
I_{10}^s = & \Bigg[-\frac{63\nu^4}{16}+\frac{90405\nu^3}{128}+\left(\frac{88995311}{1280}-\frac{545853\pi^2}{512}\right)\nu-\frac{1322685}{32} \\
& +\nu^2\left(\frac{189\mathsf{X}_{59}^{\nu^2}}{128}+\frac{109515\pi^2}{512}-\frac{1119461}{64}\right)\Bigg]a_b+\Bigg[-\frac{945\nu^4}{256}+\frac{38115\nu^3}{64} \\
& +\left(\frac{14456349}{320}-\frac{11632089\pi^2}{16384}\right)\nu+\nu^2\left(\frac{189\mathsf{X}_{59}^{\nu^2}}{128}+\frac{167895\pi^2}{1024}-\frac{3292149}{256}\right)
\end{aligned}
$$

$$- \frac{2909907}{128}\Bigg] a_t + \mathcal{O}(\varepsilon). \tag{4.100}$$

The nonlocal part can be calculated similarly by starting from the total Hamiltonian, expanding Eq. (4.93) in eccentricity, then subtracting the local part. Alternatively, it can be calculated directly from the nonlocal Hamiltonian via [92]

$$I_r^{\text{nonloc}} = -\frac{H_{\text{nonloc}}}{\Omega_r}, \tag{4.101}$$

where $\Omega_r = 2\pi/T_r$ is the radial frequency given by Eq. (D.8).

The nonlocal Hamiltonian H_{nonloc} in Eq. (4.28) is expressed in terms of (e_t, a_r), but we can use Eqs. (D.6) and (D.12) to obtain $I_r^{\text{nonloc}}(E, L)$, i.e., as a function of energy and angular momentum. Then, we replace E with (e_t, L) using Eq. (D.10), expand in eccentricity to $\mathcal{O}(e_t^8)$, and revert back to (E, L). This way, we obtain an expression for I_r^{nonloc} in powers of $1/L$ that is valid to eighth order in eccentricity, and in which each ε^n contributes up to order e^{2n}.

The result for the 4PN and 5.5PN SO contributions reads

$$\begin{aligned}
\frac{I_r^{\text{nonloc}}}{\nu} &= \frac{1}{L_{\text{cov}}^7}\Bigg(\frac{170 \ln L_{\text{cov}}}{3} - \frac{170\gamma_E}{3} + \frac{18299}{96} - \frac{4777903}{90}\ln 2 + \frac{13671875 \ln 5}{512} \\
&\quad - \frac{15081309 \ln 3}{2560}\Bigg) + \frac{\varepsilon}{L_{\text{cov}}^5}\Bigg(\frac{244 \ln L_{\text{cov}}}{5} - \frac{244\gamma_E}{5} + \frac{157823}{360} - \frac{10040414}{45}\ln 2 \\
&\quad + \frac{126953125 \ln 5}{1152} - \frac{13542147 \ln 3}{640}\Bigg) + \frac{\varepsilon^2}{L_{\text{cov}}^3}\Bigg(\frac{74 \ln L_{\text{cov}}}{15} - \frac{74\gamma_E}{15} + \frac{89881}{240} \\
&\quad - \frac{5292281}{15}\ln 2 + \frac{130859375 \ln 5}{768} - \frac{35029179 \ln 3}{1280}\Bigg) \\
&+ \frac{\varepsilon^3}{L_{\text{cov}}}\Bigg(\frac{6187}{40} - \frac{11186786}{45}\ln 2 + \frac{44921875 \ln 5}{384} - \frac{1878147 \ln 3}{128}\Bigg) \\
&+ \varepsilon^4 L_{\text{cov}}\Bigg(\frac{40253}{1440} - \frac{1185023}{18}\ln 2 + \frac{138671875 \ln 5}{4608} - \frac{6591861 \ln 3}{2560}\Bigg) \\
&+ a_b\Bigg[\frac{1}{L_{\text{cov}}^{10}}\Bigg(-\frac{12579 \ln L_{\text{cov}}}{5} - \frac{24068101}{2880} + \frac{12579\gamma_E}{5} + \frac{398742736 \ln 2}{135} \\
&\quad + \frac{281496303 \ln 3}{1024} - \frac{40131484375 \ln 5}{27648}\Bigg) + \frac{\varepsilon}{L_{\text{cov}}^8}\Bigg(-2499 \ln L_{\text{cov}} - \frac{13345921}{720}
\end{aligned}$$

$$
\begin{aligned}
&+2499\gamma_E+\frac{1548980449\ln 2}{135}+\frac{1132984827\ln 3}{1280}-\frac{38230234375\ln 5}{6912}\bigg)\\
&+\frac{\varepsilon^2}{L_{\rm cov}^6}\bigg(-537\ln L_{\rm cov}-\frac{7268749}{480}+537\gamma_E+\frac{149780983\ln 2}{9}+\frac{2572548417\ln 3}{2560}\\
&-\frac{36141484375\ln 5}{4608}\bigg)+\frac{\varepsilon^3}{L_{\rm cov}^4}\bigg(13\gamma_E-13\ln L_{\rm cov}-\frac{4143337}{720}+\frac{1439288647\ln 2}{135}\\
&+\frac{116812287\ln 3}{256}-\frac{33865234375\ln 5}{6912}\bigg)+\frac{\varepsilon^4}{L_{\rm cov}^2}\bigg(-\frac{2608213}{2880}+\frac{342877711\ln 2}{135}\\
&+\frac{318592683\ln 3}{5120}-\frac{31401484375\ln 5}{27648}\bigg)\bigg]\\
&+a_t\bigg[\frac{1}{L_{\rm cov}^{10}}\bigg(\frac{8673\gamma_E}{5}-\frac{8673\ln L_{\rm cov}}{5}-\frac{16708517}{2880}+\frac{582216271\ln 2}{270}+\frac{980901819\ln 3}{5120}\\
&-\frac{29135234375\ln 5}{27648}\bigg)+\frac{\varepsilon}{L_{\rm cov}^8}\bigg(-\frac{5593\ln L_{\rm cov}}{3}-\frac{1921829}{144}+\frac{5593\gamma_E}{3}\\
&+\frac{231474971\ln 2}{27}+\frac{806618331\ln 3}{1280}-\frac{28420234375\ln 5}{6912}\bigg)+\frac{\varepsilon^2}{L_{\rm cov}^6}\bigg(-455\ln L_{\rm cov}\\
&-\frac{5444717}{480}+455\gamma_E+\frac{191532524\ln 2}{15}+\frac{1877210721\ln 3}{2560}-\frac{9203828125\ln 5}{1536}\bigg)\\
&+\frac{\varepsilon^3}{L_{\rm cov}^4}\bigg(-\frac{69\ln L_{\rm cov}}{5}-\frac{3226241}{720}+\frac{69\gamma_E}{5}+\frac{227762869\ln 2}{27}+\frac{87726159\ln 3}{256}\\
&-\frac{26708984375\ln 5}{6912}\bigg)+\frac{\varepsilon^4}{L_{\rm cov}^2}\bigg(-\frac{2112181}{2880}+\frac{562665401\ln 2}{270}+\frac{49433247\ln 3}{1024}\\
&-\frac{25712734375\ln 5}{27648}\bigg)\bigg].
\end{aligned}
\tag{4.102}
$$

4.5.2 Circular-orbit binding energy

Here, we calculate the gauge-invariant binding energy $\bar{E}$ analytically in a PN expansion, as opposed to the numerical calculation in Sec. 4.3.6 for the EOB binding energy.

For circular orbits and aligned spins, $\bar{E}$ can be calculated from the Hamiltonian (4.29) by setting $p_r=0$ and perturbatively solving $\dot{p}_r=0=-\partial H/\partial r$ for the angular momentum $L(r)$. Then, solving $\Omega=\partial H/\partial L$ for $r(\Omega)$, and substituting in the Hamiltonian yields $\bar{E}$ as a function of the orbital frequency. It is convenient to express $\bar{E}$ in terms of the dimensionless frequency parameter $v_\Omega \equiv (M\Omega_\phi)^{1/3}$.

The nonspinning 4PN binding energy is given by Eq. (5.5) of Ref. [79], and the 4.5PN SO part is given by Eq. (5.11) of Ref. [2]. We obtain for the 5.5PN SO part

$$\begin{aligned}\bar{E}^{\text{5.5PN,SO}} &= \nu v_\Omega^{13}\bigg\{S\bigg[-\frac{4725}{32}+\nu\left(\frac{1411663}{640}-\frac{10325\pi^2}{64}+\frac{352\gamma_E}{3}+\frac{2080\ln 2}{9}\right)+\frac{352}{3}\nu\ln v_\Omega \\ &\quad +\frac{310795\nu^3}{5184}+\frac{35\nu^4}{1458}+\nu^2\left(\frac{5\mathsf{X}_{59}^{\nu^2}}{8}+\frac{2425\pi^2}{864}-\frac{1975415}{5184}\right)\bigg] \\ &\quad +S^*\bigg[-\frac{2835}{128}+\nu\left(\frac{126715}{144}-\frac{102355\pi^2}{1536}+\frac{160\gamma_E}{3}+\frac{992\ln 2}{9}\right)+\frac{160}{3}\nu\ln v_\Omega \\ &\quad +\nu^2\left(\frac{5\mathsf{X}_{59}^{\nu^2}}{8}-\frac{205\pi^2}{576}-\frac{275245}{3456}\right)+\frac{46765\nu^3}{864}+\frac{875\nu^4}{31104}\bigg]\bigg\}. \qquad (4.103)\end{aligned}$$

4.6 Conclusions

Improving the spin description in waveform models is crucial for GW observations with the continually increasing sensitivities of the Advanced LIGO, Virgo, and KAGRA detectors [30], and for future GW detectors, such as the Laser Interferometer Space Antenna (LISA) [301], the Einstein Telescope (ET) [576], the DECi-hertz Interferometer Gravitational wave Observatory (DECIGO) [577], and Cosmic Explorer (CE) [578]. More accurate waveform models can lead to better estimates for the spins of binary systems, and for the orthogonal component of spin in precessing systems, which helps in identifying their formation channels [18, 19]. For this purpose, we extended in this paper the SO coupling to the 5.5PN level.

We employed an approach [2, 90] that combines several analytical approximation methods to obtain arbitrary-mass-ratio PN results from first-order self-force results. We computed the nonlocal-in-time contribution to the dynamics for bound orbits in a small-eccentricity expansion, Eq. (4.33), and for unbound motion in a large-eccentricity expansion, Eq. (4.92). To our knowledge, this is the first time that nonlocal contributions to the conservative dynamics have been computed in the spin sector. For the local-in-time contribution, we exploited the simple mass-ratio dependence of the PM-expanded scattering angle and related the Hamiltonian coefficients to those of the scattering angle. This allowed us to determine all the unknowns at that order from first-order self-force results, except for one unknown at second order in the mass ratio, see Eqs. (4.64)–(4.66). We also provided the radial action, in Sec. 4.5.1, and the circular-orbit binding energy, in Eq. (4.103), as two important gauge-invariant quantities for bound orbits. We stress again that, although all calculations in this paper were performed for aligned spins, the SO coupling is applicable for generic precessing spins.

The local part of the 5.5PN SO coupling still has an unknown coefficient, but as we showed in Fig. 4.1, its effect on the dynamics is smaller than the difference between the 4.5 and 5.5PN orders. Determining that unknown could be done through targeted PN calculations, as was illustrated in Ref. [286], in which the authors related the two missing coefficients at 5PN order to coefficients that can be calculated from an EFT approach. Alternatively, one could use analytical *second*-order self-force results, which might become available in the near future, given the recent work on numerically computing the binding energy and energy flux [326, 327]. Until then, one could still use the partial 5.5PN SO results in EOB waveform models complemented by NR calibration. Such an implementation would be straightforward, since we obtained the gyro-gravitomagnetic factors that enter directly into the `SEOBNR` [397–399] and `TEOBResumS` [388, 401, 404] waveform models, and less directly in the `IMRPhenom` models [536, 537, 539, 541], which are used in GW analyses.

Acknowledgments

I am grateful to Alessandra Buonanno, Jan Steinhoff, and Justin Vines for fruitful discussions and for their invaluable feedback on earlier drafts of this paper. I also thank Sergei Ossokine for providing NR data for the binding energy, and thank the anonymous referee for useful suggestions.

Chapter 5: Fourth post-Newtonian effective-one-body Hamiltonians with generic spins

Authors[1]: *Mohammed Khalil, Jan Steinhoff, Justin Vines, Alessandra Buonanno*

Abstract: In a compact binary coalescence, the spins of the compact objects can have a significant effect on the orbital motion and gravitational-wave (GW) emission. For generic spin orientations, the orbital plane precesses, leading to characteristic modulations of the GW signal. The observation of precession effects is crucial to discriminate among different binary formation scenarios, and to carry out precise tests of General Relativity. Here, we work toward an improved description of spin effects in binary inspirals, within the effective-one-body (EOB) formalism, which is commonly used to build waveform models for LIGO and Virgo data analysis. We derive EOB Hamiltonians including the complete fourth post-Newtonian (4PN) conservative dynamics, which is the current state of the art. We place no restrictions on the spin orientations or magnitudes, or on the type of compact object (e.g., black hole or neutron star), and we produce the first generic-spin EOB Hamiltonians complete at 4PN order. We consider multiple spinning EOB Hamiltonians, which are more or less direct extensions of the varieties found in previous literature, and we suggest another simplified variant. Finally, we compare the circular-orbit, aligned-spin binding-energy functions derived from the EOB Hamiltonians to

[1]Originally published as Phys. Rev. D **101**, no.10, 104034 (2020)

numerical-relativity simulations of the late inspiral. While finding that all proposed Hamiltonians perform reasonably well, we point out some interesting differences, which could guide the selection of a simpler, and thus faster-to-evolve EOB Hamiltonian to be used in future LIGO and Virgo inference studies.

5.1 Introduction

The observation of gravitational waves (GWs) from coalescing binaries [12, 13, 16, 579] using a continually improving network of GW detectors [517, 518, 544, 545] is a milestone in fundamental physics and astrophysics. As the detectors increase their sensitivity, we will observe more events, with larger signal-to-noise ratios, spanning a larger region of the parameter space. Thus, to faithfully recover the sources' properties, it is important to improve the accuracy of models of waveforms from binaries of compact objects (black holes and/or neutron stars) on generic orbits and with generic spin orientations. In the generic case, the orbital plane and the objects' spins precess about the direction of the system's total angular momentum, leading to modulations of the GW signal which are a smoking-gun signature of the dynamical influence of the spins. Including such precession effects in GW template models, as opposed to restricting to the simpler aligned-spin case with no precession, is important for more inclusive GW searches, more accurate inference studies and tests of General Relativity.

The effective-one-body (EOB) framework [380, 381] aims at providing a synergy between multiple analytical approximations and numerical-relativity (NR) simulations of relativistic inspiraling binaries. The core ingredient of the EOB approach is the EOB Hamiltonian, a canonical Hamiltonian describing the binary's (conservative) orbital dynamics, which both (i) agrees, in its post-Newtonian (PN) expansion,[2] with known results for arbitrary mass ratios from PN calculations (in the weak-field and low-speed regime), and (ii) becomes, in the extreme-mass-ratio limit, an exact Hamiltonian for a test (or probe) particle in an exact black-hole spacetime, valid for arbitrary separations and speeds. The EOB Hamiltonian is naturally expressed as a deformation of the zero-mass-ratio test-particle Hamiltonian, with the deformation determined by finite-mass-ratio results from the PN approximation. For example, the original (nonspinning) EOB Hamiltonian [380] becomes, as the mass ratio goes to zero, the exact Hamiltonian for a test mass undergoing geodesic motion in a Schwarzschild (nonspinning black hole) spacetime.

In generalizing to spinning black holes, the first natural replacement for the Schwarzschild-geodesic Hamiltonian is the Hamiltonian for geodesic (test-mass) motion in an exact Kerr (spinning black hole) spacetime. [3] A spinning EOB (SEOB) Hamiltonian incorporating the Kerr-geodesic limit was first constructed in Ref. [370] including leading-order (LO) spin-orbit and LO spin-squared effects in the PN expansion. This was later extended to the next-to-leading (NLO) [389] and next-to-NLO (NNLO) [390] spin-orbit levels, and to the NLO spin-squared level for aligned spins [580, 581] and then for generic (precessing) spins [392]. The Kerr-geodesic-based approach for aligned spins has been further developed in Refs. [391, 401, 435, 582–585], e.g., by including matter effects (for neutron stars) and calibration to NR simulations. A second category of SEOB Hamiltonians is based on the Hamiltonian for a *spinning* test-body (test spin) in a Kerr background [366, 557], first developed with NLO [382] and then NNLO [383] spin-orbit terms and with LO spin-squared terms. Such Hamiltonians have always been applicable for generic

[2] Recently, also the post-Minkowskian (weak-field) approximation for unbound orbits is considered; see below.

[3] With the aim of building a first inspiral-merger-ringdown waveform model for generic spins, Ref. [374] employed a spinning EOB Hamiltonian built by adding to the Schwarzschild-geodesic EOB Hamiltonian the PN-expanded spin Hamiltonian.

(precessing) spins. They have been generalized to include tidal effects in Refs. [586, 587], they have been used for studies of extreme-mass-ratio binaries in Ref. [588] and periastron advance in Ref. [589], and they have been refined and calibrated to NR simulations in Refs. [393–398]. EOB Hamiltonians have also been constructed to include information from gravitational self-force calculations [407–410] (for extreme mass ratios) and from the post-Minkowskian approximation [236, 237, 405] (assuming weak fields but allowing arbitrary speeds). A recent comparison of various SEOB waveform models is given in Ref. [590]. Waveform models constructed with the SEOB Hamiltonians based on a *spinning* test-body in a Kerr background [393, 395–398] have been employed in template banks of LIGO and Virgo, and inference studies of binary black holes [12, 13, 579]. For parameter estimation of binary neutron stars both classes of SEOB Hamiltonians have been employed in Ref. [13].

The goal of the present paper is to construct SEOB Hamiltonians for compact binaries (black holes or neutron stars) that include all known PN results to 4PN order for generic orbits and spin orientations. Beyond the up-to-NNLO spin-orbit and spin-squared contributions, the 4PN level includes also the LO cubic and quartic in spin terms. Previous work is not complete to 4PN order for generic spins [382, 383, 392] or complete to 4PN but valid for aligned spins only [391, 400, 401, 584]. We construct three SEOB Hamiltonians in this paper: (i) a Hamiltonian based on Ref. [392], which uses the idea of "centrifugal radius" r_c [391], while recovering the Kerr-geodesic limit; (ii) a simplified version of the Hamiltonian from Ref. [392] that does not use a centrifugal radius and has a different factorization for the PN spin corrections, similarly recovering the Kerr-geodesic limit; and (iii) one Hamiltonian following Refs. [382, 383, 557] which recovers the dynamics of a spinning test-body in the Kerr spacetime in the small-mass-ratio limit (see Table 5.1 for a summary of the differences between these Hamiltonians). As we wish to somewhat fairly compare different treatments of spin effects in the EOB formalism, we have modified some details of the original proposals of Refs. [383, 392] such that all the Hamiltonians agree in the zero-spin limit. We compare the aligned-spin circular-orbit binding energy functions from the different Hamiltonians with NR simulations and with the aligned-spin Hamiltonian from Refs. [391, 400, 401]. This enables one to assess compromises between accuracy and simplicity of the SEOB Hamiltonians.

The paper is organized as follows. In Sec. 5.2 we provide an overview of SEOB Hamiltonians and their construction. Sections 5.3 and 5.4 present the ansätze of the SEOB Hamiltonians, with explicit results matched to 4PN in Appendix E. We then compare the aligned-spin circular-orbit binding energy of the Hamiltonians against NR in Sec. 5.5. Our conclusions are given in Sec. 5.6.

Table 5.1: The SEOB Hamiltonians used in this paper and the differences between them. All Hamiltonians include complete 4PN results for generic spins and compact objects, except for the last Hamiltonian, which is for aligned spins.

SEOB	definition	references
$\mathrm{SEOB}_{\mathrm{TS}}$	based on the Hamiltonian for a test spin (TS) in Kerr spacetime	[382, 383]
$\mathrm{SEOB}_{\mathrm{TM}}^{r_c}$	based on the Hamiltonian for a test mass (TM) in Kerr spacetime; it uses the centrifugal radius r_c	[392]
$\mathrm{SEOB}_{\mathrm{TM}}$	simplified version of $\mathrm{SEOB}_{\mathrm{TM}}^{r_c}$; it does not use r_c; it uses different factorization for spin corrections	[this paper]
$\mathrm{SEOB}_{\mathrm{TM}}^{r_c,\mathrm{align}}$	similar to $\mathrm{SEOB}_{\mathrm{TM}}^{r_c}$, but for aligned spins and includes S^2 and S^4 corrections, differently	[391, 400, 401]

Notation

We use geometric units such that the speed of light c and the Newton constant G are equal to 1. We utilize various combinations of the masses m_1, m_2 of the binary's components,

$$\begin{gathered} M = m_1 + m_2, \quad \mu = \frac{m_1 m_2}{M}, \quad \nu = \frac{\mu}{M}, \\ q = \frac{m_1}{m_2}, \quad X_1 = \frac{m_1}{M}, \quad X_2 = \frac{m_2}{M}. \end{gathered} \tag{5.1}$$

For the spins $\boldsymbol{S}_1$, $\boldsymbol{S}_2$, we define the dimensionless versions

$$\boldsymbol{\chi}_1 = \frac{\boldsymbol{a}_1}{m_1} = \frac{\boldsymbol{S}_1}{m_1^2}, \qquad \boldsymbol{\chi}_2 = \frac{\boldsymbol{a}_2}{m_2} = \frac{\boldsymbol{S}_2}{m_2^2}, \tag{5.2}$$

along with the intermediate $\boldsymbol{a}_1$, $\boldsymbol{a}_2$. The relative position and momentum are denoted by $\boldsymbol{r}$ and $\boldsymbol{p}$, respectively. Using an implicit Euclidean background, it holds

$$\boldsymbol{p}^2 = p_r^2 + \frac{L^2}{r^2}, \quad p_r = \boldsymbol{n} \cdot \boldsymbol{p}, \quad \boldsymbol{L} = \boldsymbol{r} \times \boldsymbol{p}, \tag{5.3}$$

where $\boldsymbol{n} = \boldsymbol{r}/r$ with $r = |\boldsymbol{r}|$, and $\boldsymbol{L}$ is the orbital angular momentum with magnitude L. For convenience, we also introduce rescaled dimensionless variables,

$$\hat{\boldsymbol{r}} = \frac{\boldsymbol{r}}{M}, \quad \hat{\boldsymbol{p}} = \frac{\boldsymbol{p}}{\mu}, \quad \hat{H} = \frac{H}{\mu}, \quad \hat{\boldsymbol{L}} = \frac{\boldsymbol{L}}{M\mu}, \quad \hat{\boldsymbol{a}} = \frac{\boldsymbol{a}}{M}, \tag{5.4}$$

and similarly for the magnitudes $\hat{r} = |\hat{\boldsymbol{r}}|$, etc.; here, H is any of several Hamiltonians encountered below, and $\boldsymbol{a} = \boldsymbol{S}_{\text{Kerr}}/M$ is the rescaled spin of an effective Kerr black hole.

5.2 Spinning effective-one-body Hamiltonians

In this section, we give an overview of spinning EOB Hamiltonians and their construction [370, 380, 382, 383, 389–392, 400, 401, 557, 580, 581], on which current EOB waveform models are built [381, 386, 393–397, 401, 435, 583, 585]. The EOB Hamiltonians are constructed such that (i) they describe geodesic motion in Kerr spacetime in the limit of vanishing mass ratio and that (ii) they agree (up to a canonical transformation) with a PN approximate Hamiltonian describing the conservative binary motion up to a certain order (here the 4PN order [124]). A certain class of EOB Hamiltonians [382, 383, 557] also incorporates the (nongeodesic) motion of spinning test particles in Kerr spacetime in the small mass-ratio limit, as described by the Matthisson-Papapetrou-Dixon equations [361, 367, 368, 591, 592].

We consider a spinning binary in the center-of-mass frame. The orbital dynamics is described by the relative separation $\boldsymbol{r}$ and linear momentum $\boldsymbol{p}$ vectors, and the internal dynamics is assumed to be captured by the spins $\boldsymbol{S}_1$ and $\boldsymbol{S}_2$ of each body. The Poisson brackets between these dynamical variables are the standard ones,

$$\{r^i, p_j\} = \delta_{ij}, \tag{5.5a}$$

$$\{S_1^i, S_1^j\} = \epsilon_{ijk} S_1^k, \tag{5.5b}$$

$$\{S_2^i, S_2^j\} = \epsilon_{ijk} S_2^k, \tag{5.5c}$$

with all others vanishing. The dynamics on phase space is generated by a Hamiltonian function $H(\boldsymbol{r}, \boldsymbol{p}, \boldsymbol{S}_1, \boldsymbol{S}_2)$. The equation of motion of a generic phase-space function A reads

$$\frac{dA}{dt} = \{A, H\} + \frac{\partial A}{\partial t}. \tag{5.6}$$

Here the Hamiltonian is either the PN H^{PN} or the EOB H^{EOB} one. The EOB Hamiltonian H^{EOB} itself is given in terms of another Hamiltonian, the effective Hamiltonian H^{eff}, via the energy map,

$$H^{\text{EOB}} = M\sqrt{1 + 2\nu\left(\frac{H^{\text{eff}}}{\mu} - 1\right)}. \tag{5.7}$$

The utility of this energy map was demonstrated, e.g., in Refs. [236, 380, 384]. For instance, if for H^{eff} one just takes the Hamiltonian of geodesics in Schwarzschild spacetime, then H^{EOB} correctly describes both the 1PN and first post-Minkowskian dynamics [236, 380].

5.2.1 The effective Hamiltonian

The central idea of the EOB Hamiltonian is to combine the dynamics in the test-body limit (with no restriction on the speed or field strength) with the PN dynamics (not restricted in the mass ratio). In this way, one might overcome some of the limitations of the individual approximations. This can be achieved by making an ansatz for H^{eff} as a deformation of the test-body-limit Hamiltonian (deforming it such that PN results are recovered), which is the purpose of this section. Note that in the test-body limit $H^{\text{EOB}} \approx H^{\text{eff}} + \text{const}$.

Let us review the Hamiltonian of a spinning test-body in Kerr spacetime [366, 557]. One can easily specialize this to the nonspinning (geodesic) case, which is the basis of some SEOB models. These test-body Hamiltonians are the basis for all SEOB models. The (inverse) Kerr metric $g^{\mu\nu}_{\text{Kerr}}$ in Boyer-Lindquist coordinates $(x^\mu) = (t, r, \theta, \phi)$ is given by the line element

$$\begin{aligned} -d\tau^2 &= g^{\mu\nu}_{\text{Kerr}} \partial_\mu \partial_\nu \\ &= -\frac{\Lambda}{\Delta\Sigma}\partial_t^2 + \frac{\Delta}{\Sigma}\partial_r^2 + \frac{1}{\Sigma}\partial_\theta^2 + \frac{\Sigma - 2Mr}{\Sigma\Delta\sin^2\theta}\partial_\phi^2 - \frac{4Mra}{\Sigma\Delta}\partial_t\partial_\phi, \end{aligned} \tag{5.8}$$

where M is the mass of the black hole, $\sigma = Ma$ is its spin, and

$$\Sigma \equiv r^2 + a^2\cos^2\theta, \qquad \Delta \equiv r^2 - 2Mr + a^2, \tag{5.9a}$$

$$\Lambda \equiv (r^2 + a^2)^2 - a^2\Delta\sin^2\theta. \tag{5.9b}$$

The Hamiltonian of a spinning test-body H^{Kerr} can be obtained as a solution of the mass-shell constraint (see, e.g., Ref. [366])

$$-\mu^2 = g^{\mu\nu}_{\text{Kerr}} \left(p_\mu - \frac{1}{2}\omega_{\mu ab} S^{ab}_*\right)\left(p_\nu - \frac{1}{2}\omega_{\mu ab} S^{ab}_*\right) + \mathcal{O}(S^2_*), \tag{5.10}$$

where $p_\mu = (-H^{\text{Kerr}}, p_r, p_\theta, p_\phi)$, μ is the mass of the test-body, $S^{ab}_* = -S^{ab}_*$ is its spin tensor in a local Lorentz frame ($e_a{}^\mu e^{a\nu} = g^{\mu\nu}_{\text{Kerr}}$), $\omega_{\mu ab} = e_{b\nu}\nabla_\mu e_a{}^\nu$ are the Ricci rotation coefficients, and ∇_μ is the covariant derivative. The canonical spin vector of the test-body $\boldsymbol{S}_*$ is given by $S^i_* = \frac{1}{2}\epsilon^{ijk} S^{jk}_*$ and the components S_{0i} are fixed by the supplementary condition $S^{ab}(e_b{}^\mu p_\mu + \mu^2\delta^0_b) = 0 + \mathcal{O}(S^2_*)$, all in the local frame.

Let us split H^{Kerr} into a part dependent on the test-spin $\boldsymbol{S}_*$ and the remaining S_*-independent terms into parts even and odd in the Kerr spin a,

$$H^{\text{Kerr}} = H^{\text{Kerr}}_{\text{even}} + H^{\text{Kerr}}_{\text{odd}} + H^{\text{Kerr}}_{S_*}. \tag{5.11}$$

Following the procedure outlined above, and choosing the local frame from Ref. [382], this leads to

$$H^{\text{Kerr}}_{\text{even}} = \alpha^{\text{Kerr}}\sqrt{\mu^2 + \gamma^{\phi\phi}_{\text{Kerr}} p^2_\phi + \gamma^{rr}_{\text{Kerr}} p^2_r + \gamma^{\theta\theta}_{\text{Kerr}} p^2_\theta}, \tag{5.12a}$$

$$H^{\text{Kerr}}_{\text{odd}} = \beta^{\text{Kerr}} p_\phi \tag{5.12b}$$

$$\begin{aligned} H^{\text{Kerr}}_{S_*} = &\left[\boldsymbol{F}_t + \left(\beta^{\text{Kerr}} + \frac{\alpha^{\text{Kerr}}\gamma^{\phi\phi}_{\text{Kerr}} p_\phi}{\sqrt{q^{\text{Kerr}}}}\right)\boldsymbol{F}_\phi\right]\cdot \boldsymbol{S}_* \\ &+ \frac{\alpha^{\text{Kerr}}}{\sqrt{q^{\text{Kerr}}}}\left(\gamma^{rr}_{\text{Kerr}} p_r \boldsymbol{F}_r + \gamma^{\theta\theta}_{\text{Kerr}} p_\theta \boldsymbol{F}_\theta\right)\cdot \boldsymbol{S}_* + \mathcal{O}(S^2_*), \end{aligned} \tag{5.12c}$$

with

$$\alpha^{\text{Kerr}} = \frac{1}{\sqrt{-g^{tt}_{\text{Kerr}}}} = \sqrt{\frac{\Delta\Sigma}{\Lambda}}, \tag{5.13a}$$

$$\beta^{\text{Kerr}} = \frac{g^{t\phi}_{\text{Kerr}}}{g^{tt}_{\text{Kerr}}} = \frac{2aMr}{\Lambda}, \tag{5.13b}$$

$$\gamma^{\phi\phi}_{\rm Kerr} = g^{\phi\phi}_{\rm Kerr} - \frac{g^{t\phi}_{\rm Kerr} g^{t\phi}_{\rm Kerr}}{g^{tt}_{\rm Kerr}} = \frac{\Sigma}{\Lambda \sin^2\theta}, \tag{5.13c}$$

$$\gamma^{rr}_{\rm Kerr} = g^{rr}_{\rm Kerr} = \frac{\Delta}{\Sigma}, \tag{5.13d}$$

$$\gamma^{\theta\theta}_{\rm Kerr} = g^{\theta\theta}_{\rm Kerr} = \frac{1}{\Sigma}, \tag{5.13e}$$

$$\sqrt{q^{\rm Kerr}} = \frac{H^{\rm Kerr}_{\rm even}}{\alpha^{\rm Kerr}}, \tag{5.13f}$$

and with explicit expressions for the fictitious gravito-magnetic (frame-dragging) force interacting with the test-spin $\boldsymbol{S}_*$ given in Ref. [589] in terms of the vectors $\boldsymbol{F}_\mu$ (reproduced here in Sec. 5.4). A simplified version of this Hamiltonian for aligned spins and motion in the equatorial plane can be found in Ref. [593]. Simplifications for the generic-spin case are possible by making a different choice for the local frame which may simplify the Ricci rotation coefficients, see, e.g., Appendix C of Ref. [366].

The Hamiltonian above is written in terms of components instead of vectors, which is a disadvantage for some purposes. Following Ref. [392], we transform to a 3-vector notation (with an implicit flat Euclidean background) by treating (r, θ, ϕ) as spherical coordinates, with $\boldsymbol{r} = (x, y, z) = r(\sin\theta\cos\phi, \sin\theta\sin\phi, \cos\theta)$ and $\boldsymbol{a} = (0, 0, a)$. This is accompanied by a transformation of the momenta p_r, p_θ, p_ϕ to the new momenta $\boldsymbol{p}$,

$$p_r = \boldsymbol{n}\cdot\boldsymbol{p}, \quad p_\phi = L_z = (\boldsymbol{r}\times\boldsymbol{p})_z \tag{5.14a}$$

$$\frac{p_\theta^2}{r^2} = \boldsymbol{p}^2 - p_r^2 - \frac{p_\phi^2}{r^2\sin^2\theta} \tag{5.14b}$$

which makes it an overall canonical transformation. Noting that $a^2 p_\phi^2/r^2 = (\boldsymbol{n}\times\boldsymbol{p}\cdot\boldsymbol{a})^2$, $a\cos\theta = \boldsymbol{n}\cdot\boldsymbol{a}$, and $a^2\sin^2\theta = a^2 - (\boldsymbol{n}\cdot\boldsymbol{a})^2$, this results in the even-in-a Hamiltonian

$$H^{\rm Kerr}_{\rm even} = \left[A^{\rm Kerr}\left(\mu^2 + B^{\rm Kerr}_p \boldsymbol{p}^2 + B^{\rm Kerr}_{np}(\boldsymbol{n}\cdot\boldsymbol{p})^2 + B^{\rm Kerr}_{npa}(\boldsymbol{n}\times\boldsymbol{p}\cdot\boldsymbol{a})^2\right)\right]^{1/2}, \tag{5.15}$$

with

$$A^{\rm Kerr} = (\alpha^{\rm Kerr})^2 = \frac{\Delta\Sigma}{\Lambda}, \tag{5.16a}$$

$$B_p^{\rm Kerr} = r^2\gamma^{\theta\theta}_{\rm Kerr} = \frac{r^2}{\Sigma}, \tag{5.16b}$$

$$B_{np}^{\rm Kerr} = \gamma^{rr}_{\rm Kerr} - r^2\gamma^{\theta\theta}_{\rm Kerr} = \frac{r^2}{\Sigma}\left[\frac{\Delta}{r^2} - 1\right], \tag{5.16c}$$

$$B_{npa}^{\rm Kerr} = \frac{r^2}{a^2}\left[\gamma^{\phi\phi}_{\rm Kerr} - \frac{\gamma^{\theta\theta}_{\rm Kerr}}{\sin^2\theta}\right] = -\frac{r^2}{\Sigma\Lambda}(\Sigma + 2Mr), \tag{5.16d}$$

and

$$\Sigma = r^2 + (\boldsymbol{n}\cdot\boldsymbol{a})^2, \qquad \Delta = r^2 - 2Mr + a^2, \tag{5.17a}$$

$$\Lambda = (r^2+a^2)^2 - \Delta a^2 + \Delta(\boldsymbol{n}\cdot\boldsymbol{a})^2. \tag{5.17b}$$

Similarly, the odd-in-a part reads

$$H^{\rm Kerr}_{\rm odd} = \beta^{\rm Kerr} p_\phi = \frac{2Mr}{\Lambda}\boldsymbol{L}\cdot\boldsymbol{a}. \tag{5.18}$$

We now have all ingredients in order to discuss how an ansatz for the effective Hamiltonian can be built. In general, one takes the effective Hamiltonian to be a deformation of the Kerr Hamiltonian (the deformation parameter being the symmetric mass ratio ν), either for a test spin or a test mass. While all EOB models agree on the identification of the masses between the test-body and comparable mass case ($M = m_1 + m_2$, $\mu = m_1 m_2/M$), different choices are made for mapping the spins $\boldsymbol{a}$ and $\boldsymbol{S}_*$ to $\boldsymbol{S}_1$ and $\boldsymbol{S}_2$. Let us consider a simple explicit example. We could write the even-in-a part of the effective Hamiltonian as

$$H^{\rm eff}_{\rm even} = \left[A\Big(\mu^2 + B_p\boldsymbol{p}^2 + B_{np}(\boldsymbol{n}\cdot\boldsymbol{p})^2 + B_{npa}(\boldsymbol{n}\times\boldsymbol{p}\cdot\boldsymbol{a})^2 + \mu^2 Q\Big)\right]^{1/2}, \tag{5.19}$$

where the momentum-independent potentials A, B_p, B_{np}, B_{npa} are the Kerr potentials given above modified by PN corrections (to be determined). The quantity Q is a momentum-dependent potential introduced in Ref. [384], which may accommodate PN terms that do not fit into the momentum-independent potentials. (In cases where Q vanishes, the deformed Hamiltonian can be interpreted as describing geodesic motion in a ν-deformed Kerr metric.) The mentioned potentials should all be of even order in spin, while terms of odd order in spin should be included via a deformation of $H^{\text{Kerr}}_{\text{odd}}$. More explicit ansätze for the PN-corrected SEOB Hamiltonians and their potentials are discussed below.

5.2.2 Matching to post-Newtonian results

To fix the potentials in the ansatz for an effective Hamiltonian, one demands that the EOB Hamiltonian H^{EOB} agrees with the Hamiltonian in the PN approximation H^{PN} up to a canonical transformation. This will eventually not uniquely fix the potentials, but leave some (gauge) freedom.

Here we use the spinning PN Hamiltonian derived in the framework and gauges introduced in Ref. [132], since it is available to 4PN order in the spinning sector [124]. Broken up into leading order (LO), next-to-LO (NLO), next-to-NLO (NNLO) PN parts and into powers of spin, it reads

$$H^{\text{PN}}_{\text{spin}} = \begin{array}{ccccccc}
H^{\text{LO}}_{S} & & +H^{\text{NLO}}_{S} & & +H^{\text{NNLO}}_{S} & & \\
 & +H^{\text{LO}}_{S^2} & & +H^{\text{NLO}}_{S^2} & & +H^{\text{NNLO}}_{S^2} & \\
 & & & & +H^{\text{LO}}_{S^3} & & \\
 & & & & & +H^{\text{LO}}_{S^4} & \\
 & & & & & & \ddots \\
 & & & & & & \\
\mathcal{O}(\frac{1}{c^3}) & +\,\mathcal{O}(\frac{1}{c^4}) & +\,\mathcal{O}(\frac{1}{c^5}) & +\,\mathcal{O}(\frac{1}{c^6}) & +\,\mathcal{O}(\frac{1}{c^7}) & +\,\mathcal{O}(\frac{1}{c^8}) &
\end{array} \tag{5.20}$$

where columns correspond to PN orders counted by the inverse of the speed of light c (one PN order is $\mathcal{O}(c^{-2})$). Except for the self-spin-squared interactions in $H_{S^2}^{\rm NNLO}$ calculated in Ref. [122], these results have been derived in different frameworks and checked against each other: $H_S^{\rm LO}$ in Refs. [96, 110, 111, 162, 594–597], $H_S^{\rm NLO}$ in Refs. [97, 99–101, 103, 104, 598], $H_S^{\rm NNLO}$ in Refs. [102, 105–108], $H_{S^2}^{\rm LO}$ in Refs. [110, 111, 162, 595, 599], $H_{S^2}^{\rm NLO}$ in Refs. [114–117, 119, 177, 600–602], $H_{S^2}^{\rm NNLO}$ in Refs. [105, 120–122, 549], $H_{S^3}^{\rm LO}$ in Refs. [113, 123, 176, 603, 604], and $H_{S^4}^{\rm LO}$ in Refs. [113, 123, 603, 604]. These Hamiltonians are valid for both black holes and neutron stars. They depend on coefficients ($\tilde{C}_{(\rm ES^2)}$, $\tilde{C}_{(\rm BS^3)}$, $\tilde{C}_{(\rm ES^4)}$) which are the proportionality constants between the spin-induced multipoles (quadrupole, octupole, hexadecapole) and symmetric-tracefree tensors built out of (two, three, four) spin vectors (respectively). The proportionality constants depend on the type of compact object (and on the equation of state in case of a neutron star); here they are normalized to 0 for black holes (in the original paper [124], they are normalized to 1 and denoted without a tilde; see also Appendix E). This normalization makes sense here since we base the EOB Hamiltonian on a deformation of the Kerr one. Of course, the PN Hamiltonian $H^{\rm PN} = H_{\rm ns}^{\rm PN} + H_{\rm spin}^{\rm PN}$ must be supplemented by its nonspinning (ns) part $H_{\rm ns}^{\rm PN}$, which we only need to 2PN order here in order to construct the canonical transformation of the spin sector; it can be derived, e.g., from the Lagrangian in Ref. [605]. The nonspinning part was derived to 4PN order using independent methods [79, 84, 86, 522] and partial results at 5PN have already been obtained [89, 90, 523].

The condition that the EOB Hamiltonian $H^{\rm EOB}$ must coincide with results for the PN-approximate binary Hamiltonian $H^{\rm PN}$ up to a canonical transformation reads

$$H^{\rm EOB} = H^{\rm PN} + \{\mathcal{G}, H^{\rm PN}\} + \frac{1}{2!}\{\mathcal{G}, \{\mathcal{G}, H^{\rm PN}\}\} + \frac{1}{3!}\{\mathcal{G}, \{\mathcal{G}, \{\mathcal{G}, H^{\rm PN}\}\}\} + \dots \tag{5.21}$$

where $\mathcal{G}$ is the generating function of the canonical transformation. If $\mathcal{G}$ is small in the PN approximation, then the series in Eq. (5.21) terminates after a finite number of terms at a given PN order. In practice, one makes a PN-approximate and manifestly rotation invariant ansatz for $\mathcal{G}$ in terms of the canonical variables; we provide an explicit expression for $\mathcal{G}$ as `Mathematica` code in the supplementary material. Equation (5.21) then leads to constraints on the coefficients in the ansatz for $\mathcal{G}$ and H^{eff}. The remaining freedom in the coefficients is a gauge freedom within the EOB formalism.

Let us note some general considerations about how part of this gauge freedom can be fixed in SEOB models. Since binaries are expected to be on almost circular orbits during their last orbits, it makes sense to fix the gauge freedom of the EOB Hamiltonian such that it simplifies for circular orbits, for which $p_r \equiv \boldsymbol{n} \cdot \boldsymbol{p} = 0$ [384]. Taking the ansatz in Eq. (5.19) as an example, this means that—using the canonical transformation discussed above—one should transform as many PN terms as possible into a form such that they can be included in the potential B_{np}^{Kerr}, which drops out of the Hamiltonian for circular orbits. In the nonspinning case, it is additionally possible to require that the potential Q depends on the momentum only via p_r, and this uniquely fixes all EOB gauge freedom [380, 384]. For the example in Eq. (5.19), following the structure of the nonspinning Hamiltonian, it is natural to require that: (i) the momentum-dependence of $H_{\text{odd}}^{\text{Kerr}}$ is expressed in terms of p_r whenever possible [389], (ii) $B_{npa} = B_{npa}^{\text{Kerr}}$ [392], and (iii) terms in Q have a power in p_r that is as high as possible. The last requirement ensures that Q vanishes for circular orbits, as in the nonspinning case.

These considerations still leave some remaining gauge freedom in the spinning case, which we fix such to simplify the EOB Hamiltonian also for *aligned* spins. For example, it is possible to choose PN corrections in the potential B_p such that it only depends on terms of the form $\boldsymbol{n} \cdot \boldsymbol{S}$ but not $\boldsymbol{S} \cdot \boldsymbol{S}$. Any remaining gauge freedom beyond that may be chosen arbitrarily.

5.3 Spinning effective-one-body Hamiltonians with test mass

In this section we present different ansätze for effective Hamiltonians based on the Kerr geodesic one. That is, we do not include the Kerr test-spin Hamiltonian $H_{S_*}^{\text{Kerr}}$ here and instead make an ansatz of the form

$$H^{\text{eff}} = H_{\text{even}}^{\text{eff}} + H_{\text{odd}}^{\text{eff}}. \tag{5.22}$$

The explicit lengthy results from the matching at 4PN order against PN results (and fixing of the remaining gauge freedom) are given in Appendix E. We start with an extension of the SEOB Hamiltonian from Ref. [392], which we call $\text{SEOB}_{\text{TM}}^{r_c}$, to 4PN order, here including spin effects at LO S^3, and NNLO S^2. We also extend that Hamiltonian from black holes to generic compact objects, e.g., neutron stars. We proceed with a simplified version of the $\text{SEOB}_{\text{TM}}^{r_c}$ Hamiltonian to 4PN order that does not make use of the "centrifugal radius" introduced in Ref. [391]. For completeness, we also summarize the $\text{SEOB}_{\text{TM}}^{r_c,\text{align}}$ Hamiltonian from Refs. [391, 400, 401, 584] which is valid for aligned spins only. We do not include additional PN terms in the $\text{SEOB}_{\text{TM}}^{r_c,\text{align}}$ Hamiltonian since it is already 4PN complete for generic bodies. For convenience we summarize the Hamiltonians in Table 5.1.

5.3.1 Effective-one-body Hamiltonian with test-mass limit and centrifugal radius: $\text{SEOB}_{\text{TM}}^{r_c}$

Reference [392] was the first to construct an SEOB Hamiltonian with NLO spin-squared terms for generic spin orientations (but omitting a subtle contribution, included here, see Appendix A of Ref. [4]). Here we extend the Hamiltonian to include NNLO spin-squared and LO spin-cubed terms, and add multipole constants to make it applicable to generic bodies like neutron stars.

For the even-in-spin part of the $\text{SEOB}^{r_c}_{\text{TM}}$ Hamiltonian, we use the ansatz in Eq. (5.19),

$$H^{\text{eff}}_{\text{even}} = \left[A\Big(\mu^2 + B_p \boldsymbol{p}^2 + B_{np}(\boldsymbol{n}\cdot\boldsymbol{p})^2 + B_{npa}(\boldsymbol{n}\times\boldsymbol{p}\cdot\boldsymbol{a})^2 + \mu^2 Q\Big)\right]^{1/2}, \tag{5.23}$$

where the Kerr spin is mapped according to

$$\boldsymbol{a} = \boldsymbol{a}_1 + \boldsymbol{a}_2\,. \tag{5.24}$$

This ensures that the Hamiltonian reproduces leading-order PN results at all even orders in spin [127]. The effective Hamiltonian further uses the "centrifugal radius" r_c, which was introduced in Ref. [391] and is defined such that the Kerr Hamiltonian for aligned spins and equatorial orbits can be written as $H^{\text{Kerr}}_{\text{even}} = \sqrt{A^{\text{Kerr}}\left(\mu^2 + p_\phi^2/r_c^2 + p_r^2/B(r)\right)}$, which implies the definition

$$r_c = \sqrt{r^2 + a^2 + \frac{2Ma^2}{r}}\,. \tag{5.25}$$

The centrifugal radius was generalized to generic spin orientations in Ref. [392]. In terms of r_c, the Kerr potential A^{Kerr} from Eq. (5.16a) can be written equivalently as

$$A^{\text{Kerr}} = \left(1 - \frac{2M}{r_c}\right)\frac{\left(1+\frac{2M}{r_c}\right)}{\left(1+\frac{2M}{r}\right)}\frac{1+\frac{(\boldsymbol{n}\cdot\boldsymbol{a})^2}{r^2}}{1+\Delta\frac{(\boldsymbol{n}\cdot\boldsymbol{a})^2}{r^2 r_c^2}}\,. \tag{5.26}$$

In the nonspinning limit, only the first term above remains, which reduces to the Schwarzschild A-potential. This is the reason why Ref. [392] adds the zero-spin PN corrections to $1 - 2M/r_c$. However, in this paper we intend to investigate spin effects across different Hamiltonian descriptions, so we need to make sure that the nonspinning Hamiltonians are identical. That is, we need to choose a method for adding zero-spin corrections that can be applied to all four EOB Hamiltonians considered here. We simply multiply the Kerr potential A^{Kerr} by zero-spin PN corrections denoted A^0 below (without performing a Padé or $\log$ resummation[4] of A^0). For the spin-squared corrections, we follow Ref. [392] and add spin-squared corrections of the form $\boldsymbol{n}\cdot\boldsymbol{S}$ to the term $1+(\boldsymbol{n}\cdot\boldsymbol{a})^2/r^2$, and add corrections of the form $\boldsymbol{S}\cdot\boldsymbol{S}$ to $1+2M/r_c$, since it has an expansion of the form $1+2M/r-Ma^2/r^3+\ldots$. One employs similar considerations for adding PN corrections to the B-potentials in Eq. (5.23), leading to the following ansatz:

$$A = \left(1-\frac{2M}{r_c}\right)\frac{\left(1+\frac{2M}{r_c}+A^{SS}+A^{S^4}\right)}{\left(1+\frac{2M}{r}\right)}\frac{\left(1+\frac{(\boldsymbol{n}\cdot\boldsymbol{a})^2}{r^2}+A^{nS}\right)}{\left(1+\Delta\frac{(\boldsymbol{n}\cdot\boldsymbol{a})^2}{r^2 r_c^2}\right)}A^0(r_c)\,, \tag{5.27a}$$

$$B_p = \left[1+\frac{(\boldsymbol{n}\cdot\boldsymbol{a})^2}{r^2}+B_p^{nS}\right]^{-1}, \tag{5.27b}$$

$$B_{np} = \frac{1}{1+\frac{(\boldsymbol{n}\cdot\boldsymbol{a})^2}{r^2}}\left[\left(1-\frac{2M}{r}+\frac{a^2}{r^2}\right)\left(A^0(r_c)\,D^0(r_c)+B_{np}^{SS}+B_{np}^{nS}\right)-1\right], \tag{5.27c}$$

$$B_{npa} = B_{npa}^{\rm Kerr}\,, \tag{5.27d}$$

$$Q = Q^0(r_c)+Q^{S^2}. \tag{5.27e}$$

Note that we use the gauge choice from Ref. [392], i.e., there are no corrections of the form $\boldsymbol{S}\cdot\boldsymbol{S}$ in the potential B_p, which simplifies the Hamiltonian for aligned spins and circular orbits.

The 4PN corrections to the nonspinning effective Hamiltonian were obtained in Ref. [80]. Since we factor the PN corrections in $A^0(r_c)$, we choose it such that the PN expansion of the A potential agrees, in the nonspinning limit, with the results of Ref. [80]. Writing the PN corrections using scaled variables (5.4) to simplify notation, we obtain

$$\begin{aligned} A^0(r_c) = 1 + \nu\Bigg[&\frac{2}{\hat{r}_c^3}+\left(\frac{106}{3}-\frac{41}{32}\pi^2\right)\frac{1}{\hat{r}_c^4}+\left(\frac{1}{20}+\frac{41}{32}\pi^2\nu-\frac{221}{6}\nu+\frac{963}{512}\pi^2+\frac{128}{5}\gamma_E\right.\\ &\left.+\frac{256}{5}\ln 2+\frac{64}{5}\ln\frac{1}{\hat{r}_c}\right)\frac{1}{\hat{r}_c^5}\Bigg] \end{aligned} \tag{5.28a}$$

$$D^0(r_c) = 1+6\nu\frac{1}{\hat{r}_c^2}+\left(52\nu-6\nu^2\right)\frac{1}{\hat{r}_c^3}+\left[\frac{592}{15}\nu\ln\frac{1}{\hat{r}_c}+\left(\frac{123}{16}\pi^2-260\right)\nu^2\right.$$

[4] The justification for the Padé or $\log$ resummations is that they improve agreement with NR in some models and may hence be seen as an implicit calibration. In this paper, however, we consider EOB Hamiltonians with no calibration to NR, so we try to avoid such resummations, in particular in the nonspinning part.

$$+\,\nu\left(-\frac{23761}{1536}\pi^2-\frac{533}{45}+\frac{1184}{15}\gamma_E-\frac{6496}{15}\ln 2+\frac{2916}{5}\ln 3\right)\Bigg]\frac{1}{\hat{r}_c^4}, \tag{5.28b}$$

$$Q^0(r_c)=\left[2(4-3\nu)\nu\frac{1}{\hat{r}_c^2}+\left(\left(-\frac{5308}{15}+\frac{496256}{45}\ln 2-\frac{33048}{5}\ln 3\right)\nu-83\nu^2+10\nu^3\right)\frac{1}{\hat{r}_c^3}\right]\hat{p}_r^4 \\ +\left[\left(-\frac{827}{3}-\frac{2358912}{25}\ln 2+\frac{1399437}{50}\ln 3+\frac{390625}{18}\ln 5\right)\nu-\frac{27}{5}\nu^2+6\nu^3\right]\frac{\hat{p}_r^6}{\hat{r}_c^2}, \tag{5.28c}$$

where the corrections are expressed in terms of the centrifugal radius r_c, with $\hat{r}_c = r_c/M$, and $\hat{p}_r = p_r/\mu$. Note that here and in the SEOB models discussed below, we are using Taylor-expanded and not resummed versions of these potentials—we want to compare the different ansätze of the Hamiltonians irrespective of possible resummations for the potentials (see also footnote 4).

Spin-squared contributions, up to NNLO, are added to the Hamiltonian using the following ansatz

$$A^{SS}=\frac{c_n}{\hat{r}_c^3}\boldsymbol{\chi}_i\cdot\boldsymbol{\chi}_j+\frac{c_n}{\hat{r}_c^4}\boldsymbol{\chi}_i\cdot\boldsymbol{\chi}_j+\frac{c_n}{\hat{r}_c^5}\boldsymbol{\chi}_i\cdot\boldsymbol{\chi}_j, \tag{5.29a}$$

$$A^{nS}=\frac{c_n}{\hat{r}_c^3}(\boldsymbol{n}\cdot\boldsymbol{\chi}_i)(\boldsymbol{n}\cdot\boldsymbol{\chi}_j)+\frac{c_n}{\hat{r}_c^4}(\boldsymbol{n}\cdot\boldsymbol{\chi}_i)(\boldsymbol{n}\cdot\boldsymbol{\chi}_j)+\frac{c_n}{\hat{r}_c^5}(\boldsymbol{n}\cdot\boldsymbol{\chi}_i)(\boldsymbol{n}\cdot\boldsymbol{\chi}_j), \tag{5.29b}$$

$$B_p^{nS}=\frac{c_n}{\hat{r}_c^3}(\boldsymbol{n}\cdot\boldsymbol{\chi}_i)(\boldsymbol{n}\cdot\boldsymbol{\chi}_j)+\frac{c_n}{\hat{r}_c^4}(\boldsymbol{n}\cdot\boldsymbol{\chi}_i)(\boldsymbol{n}\cdot\boldsymbol{\chi}_j), \tag{5.29c}$$

$$B_{np}^{nS}=\frac{c_n}{\hat{r}_c^3}(\boldsymbol{n}\cdot\boldsymbol{\chi}_i)(\boldsymbol{n}\cdot\boldsymbol{\chi}_j)+\frac{c_n}{\hat{r}_c^4}(\boldsymbol{n}\cdot\boldsymbol{\chi}_i)(\boldsymbol{n}\cdot\boldsymbol{\chi}_j), \tag{5.29d}$$

$$B_{np}^{SS}=\frac{c_n}{\hat{r}_c^3}\boldsymbol{\chi}_i\cdot\boldsymbol{\chi}_j+\frac{c_n}{\hat{r}_c^4}\boldsymbol{\chi}_i\cdot\boldsymbol{\chi}_j, \tag{5.29e}$$

$$Q^{S^2}=\frac{\hat{p}_r^4}{\hat{r}_c^3}\left[c_n\boldsymbol{\chi}_i\cdot\boldsymbol{\chi}_j+c_n(\boldsymbol{n}\cdot\boldsymbol{\chi}_i)(\boldsymbol{n}\cdot\boldsymbol{\chi}_j)\right]+\frac{\hat{p}_r^3}{\hat{r}_c^3}c_n(\boldsymbol{p}\cdot\boldsymbol{\chi}_i)(\boldsymbol{n}\cdot\boldsymbol{\chi}_j), \tag{5.29f}$$

where we followed Ref. [392] in expressing the corrections in terms of r_c. We employ notation such that, e.g., $c_n\boldsymbol{\chi}_i\cdot\boldsymbol{\chi}_j\equiv c_n\boldsymbol{\chi}_1^2+c_n\boldsymbol{\chi}_1\cdot\boldsymbol{\chi}_2+c_n\boldsymbol{\chi}_2^2$. Each c_n stands for an independent undetermined coefficient in our ansatz, i.e., we use the same symbol c_n for all coefficients to simplify notation. The full expressions after matching to PN results are provided in Appendix E. Note that we added LO S^2 corrections to the A-potential above (which vanish for black holes) to account for the multipole constants of neutron stars.

The NLO S^2 contributions were included in the effective Hamiltonian in Ref. [392], however the authors missed a contribution in matching the EOB Hamiltonian to PN results, namely from the LO S^2 generating function applied to the LO SO Hamiltonian, i.e., from the Poisson bracket $\{\mathcal{G}^{\rm LO}_{S^2}, H^{\rm LO}_{S}\}$. (See Appendix A of Ref. [400].)

The leading-order quartic-in-spin terms A^{S^4} are zero for black holes, since the Kerr Hamiltonian, with the mapping $\boldsymbol{a} = \boldsymbol{a}_1 + \boldsymbol{a}_2$, automatically reproduces them, but they are nonzero for other types of compact objects. We take the most generic expression for the S^4 corrections

$$A^{S^4} = \frac{1}{\hat{r}_c^5}\Big[c_n(\boldsymbol{\chi}_i\cdot\boldsymbol{\chi}_j)(\boldsymbol{\chi}_k\cdot\boldsymbol{\chi}_l) + c_n(\boldsymbol{\chi}_i\cdot\boldsymbol{\chi}_j)(\boldsymbol{n}\cdot\boldsymbol{\chi}_k)(\boldsymbol{n}\cdot\boldsymbol{\chi}_l) \\ + c_n(\boldsymbol{n}\cdot\boldsymbol{\chi}_i)(\boldsymbol{n}\cdot\boldsymbol{\chi}_j)(\boldsymbol{n}\cdot\boldsymbol{\chi}_k)(\boldsymbol{n}\cdot\boldsymbol{\chi}_l)\Big], \tag{5.30}$$

where a summation over the spins of the two bodies is implied, and terms symmetric under the exchange of the two bodies' labels are only included once.

The spin-orbit and spin-cubed PN corrections are added to the odd-in-spin part of the Kerr Hamiltonian $H^{\rm Kerr}_{\rm odd}$. For the SO part we use the ansatz in Refs. [391, 392], and we add to it S^3 corrections,

$$\hat{H}^{\rm eff}_{\rm odd} = \frac{G_S}{\hat{r}\hat{r}_c^2\left(1+\Delta\frac{(\boldsymbol{n}\cdot\boldsymbol{a})^2}{r^2r_c^2}\right)}\left(X_1^2\hat{\boldsymbol{L}}\cdot\boldsymbol{\chi}_1 + X_2^2\hat{\boldsymbol{L}}\cdot\boldsymbol{\chi}_2\right) + \frac{G_{S^*}}{\hat{r}_c^3}\nu\left(\hat{\boldsymbol{L}}\cdot\boldsymbol{\chi}_1 + \hat{\boldsymbol{L}}\cdot\boldsymbol{\chi}_2\right) \\ + \frac{G_{S^3}}{\hat{r}_c^4}\hat{\boldsymbol{L}}\cdot\boldsymbol{\chi}_1 + \frac{\tilde{G}_{S^3}}{\hat{r}_c^4}\hat{\boldsymbol{L}}\cdot\boldsymbol{\chi}_2\,, \tag{5.31a}$$

where

$$G_S = 2\left[1 + \frac{c_n}{\hat{r}_c} + c_n\hat{p}_r^2 + \frac{c_n}{\hat{r}_c^2} + c_n\frac{\hat{p}_r^2}{\hat{r}_c} + c_n\hat{p}_r^4\right]^{-1},$$

$$G_{S^*} = \frac{3}{2}\left[1 + \frac{c_n}{\hat{r}_c} + c_n\hat{p}_r^2 + \frac{c_n}{\hat{r}_c^2} + c_n\frac{\hat{p}_r^2}{\hat{r}_c} + c_n\hat{p}_r^4\right]^{-1} \tag{5.32a}$$

$$\begin{aligned}
G_{S^3} = {} & \frac{1}{\hat{r}_c}\Big[c_n\boldsymbol{\chi}_1\cdot\boldsymbol{\chi}_1 + c_n\boldsymbol{\chi}_2\cdot\boldsymbol{\chi}_2 + c_n\boldsymbol{\chi}_1\cdot\boldsymbol{\chi}_2 + c_n(\boldsymbol{n}\cdot\boldsymbol{\chi}_1)^2 + c_n(\boldsymbol{n}\cdot\boldsymbol{\chi}_2)^2 + c_n(\boldsymbol{n}\cdot\boldsymbol{\chi}_1)(\boldsymbol{n}\cdot\boldsymbol{\chi}_2)\Big] \\
& + \hat{p}_r^2\Big[c_n(\boldsymbol{n}\cdot\boldsymbol{\chi}_1)^2 + c_n(\boldsymbol{n}\cdot\boldsymbol{\chi}_2)^2 + c_n(\boldsymbol{n}\cdot\boldsymbol{\chi}_1)(\boldsymbol{n}\cdot\boldsymbol{\chi}_2)\Big] \\
& + \frac{\hat{L}^2}{\hat{r}^2}\Big[c_n(\boldsymbol{n}\cdot\boldsymbol{\chi}_1)^2 + c_n(\boldsymbol{n}\cdot\boldsymbol{\chi}_2)^2 + c_n(\boldsymbol{n}\cdot\boldsymbol{\chi}_1)(\boldsymbol{n}\cdot\boldsymbol{\chi}_2)\Big],
\end{aligned}$$

$$\tilde{G}_{S^3} = G_{S^3} \quad \text{with} \quad 1 \leftrightarrow 2. \tag{5.32b}$$

Note that an inverse-Taylor resummation is used for G_S and G_{S^*}, which improves the description of the binary dynamics for aligned spins [391]. In the spin-cubed corrections G_{S^3} and $\tilde{G}_{S^3}$, a gauge freedom exists which we chose such that terms of the form $p_r^2\boldsymbol{\chi}_i\cdot\boldsymbol{\chi}_j$ or $L^2\boldsymbol{\chi}_i\cdot\boldsymbol{\chi}_j$ are not included. Explicit results after matching at 4PN can be found in Appendix E.1.

5.3.2 A simplified effective-one-body Hamiltonian with test-mass limit: SEOB$_{\text{TM}}$

Since it is important to have fast and simple EOB waveform models, in this section, we consider a simplified version of the SEOB$^{r_c}_{\text{TM}}$ Hamiltonian that uses r instead of r_c for the PN corrections. In order to assess the effect of this simplification, we also avoid resummations that are not motivated by the structure of the interactions, i.e., we factorize spin corrections to the Kerr potentials and do not use an inverse-Taylor resummation for the spin-orbit part.

The potentials of the effective Hamiltonian are simply taken to be

$$A = A^{\text{Kerr}}\left(A^0 + A^{SS} + A^{nS} + A^{S^4}\right), \tag{5.33a}$$

$$B_p = B_p^{\text{Kerr}}\left(1 + B_p^{nS}\right), \tag{5.33b}$$

$$B_{np} = \frac{\left(1 - \frac{2}{\hat{r}} + \frac{\hat{a}^2}{\hat{r}^2}\right)\left(A^0 D^0 + B_{np}^{SS} + B_{np}^{nS}\right) - 1}{1 + (\boldsymbol{n}\cdot\hat{\boldsymbol{a}})^2/\hat{r}^2}, \tag{5.33c}$$

$$B_{npa} = B_{npa}^{\text{Kerr}}, \tag{5.33d}$$

$$Q = Q^0 + Q^{S^2}, \tag{5.33e}$$

where the zero-spin corrections $A^0(r)$, $D^0(r)$ and $Q^0(r)$ are given by Eq. (5.28) but in terms of r instead of r_c. The ansätze for the S^2 and S^4 corrections are given by the corresponding expressions from the previous section, i.e., Eqs. (5.29) and (5.30), but using r instead of r_c (and with different coefficients c_n). For $H_{\text{odd}}^{\text{Kerr}}$, we modify the odd-in-$a$ part of the Kerr Hamiltonian by the SO and S^3 PN corrections, that is

$$\begin{aligned}\hat{H}_{\text{odd}}^{\text{eff}} = \frac{1}{\hat{r}\hat{r}_c^2\left(1+\Delta\frac{(\boldsymbol{n}\cdot\boldsymbol{a})^2}{r^2r_c^2}\right)}\Big[G_S\left(X_1^2\hat{\boldsymbol{L}}\cdot\boldsymbol{\chi}_1 + X_2^2\hat{\boldsymbol{L}}\cdot\boldsymbol{\chi}_2\right) + G_{S*}\nu\left(\hat{\boldsymbol{L}}\cdot\boldsymbol{\chi}_1 + \hat{\boldsymbol{L}}\cdot\boldsymbol{\chi}_2\right) \\ + \frac{G_{S^3}}{\hat{r}}\hat{\boldsymbol{L}}\cdot\boldsymbol{\chi}_1 + \frac{\tilde{G}_{S^3}}{\hat{r}}\hat{\boldsymbol{L}}\cdot\boldsymbol{\chi}_2\Big],\end{aligned} \tag{5.34a}$$

with the ansätze for the coefficients given in Eqs. (5.32a) and (5.32b), but again written with r instead of r_c (and different c_n). Explicit results after matching at 4PN can be found in Appendix E.2.

5.3.3 Aligned effective-one-body Hamiltonian with test-mass limit and centrifugal radius: $\text{SEOB}_{\text{TM}}^{r_c,\text{align}}$

In this section, we consider the aligned-spin EOB Hamiltonian proposed by Damour and Nagar in Ref. [391] and extended in Refs. [400, 401, 584], which we denote $\text{SEOB}_{\text{TM}}^{r_c,\text{align}}$. That Hamiltonian is similar to the aligned-spin limit of the $\text{SEOB}_{\text{TM}}^{r_c}$ Hamiltonian from above, except that the even-in-spin PN corrections are added to the centrifugal radius.

The even-in-spin effective Hamiltonian is given by

$$\hat{H}^{\text{eff}}_{\text{even}} = \sqrt{A\left(1 + \frac{\hat{L}^2}{\hat{r}_c^2} + \frac{\hat{p}_r^2}{B} + Q^0\right)}. \tag{5.35}$$

The EOB potentials A and B are given in Ref. [391], but we do not use Padé resummation and we modify how the zero-spin PN corrections are added such that they agree with the other Hamiltonians in this paper, that is

$$A = \left(1 - \frac{2}{\hat{r}_c}\right)\frac{1 + \frac{2}{\hat{r}_c}}{1 + \frac{2}{\hat{r}_c}} A^0(r_c), \tag{5.36a}$$

$$B = \frac{r^2}{r_c^2}\frac{1}{A\, D^0(r_c)}, \tag{5.36b}$$

where A^0, D^0 and Q^0 are given by Eq. (5.28). Note that Refs. [400, 401, 590] use $Q \equiv 2\nu(4 - 3\nu)p_r^4/r_c^2$ instead of Q^0, and use $p_{r_*} \equiv p_r\sqrt{A/B}$ instead of p_r.

The spin-squared and spin-quartic corrections are added to the centrifugal radius, which is here defined by

$$\hat{r}_c^2 = \hat{r}^2 + \hat{a}_Q^2\left(1 + \frac{2}{\hat{r}}\right) + \frac{\delta a^2_{\text{NLO}}}{\hat{r}} + \frac{\delta a^2_{\text{NNLO}}}{\hat{r}^2} + \frac{\delta a^4_{\text{LO}}}{\hat{r}^2}, \tag{5.37}$$

and where $\hat{a}_Q$ depends on the compact object's multipolar constants

$$\hat{a}_Q^2 \equiv \hat{a}^2 + \tilde{C}_{1(ES^2)}\hat{a}_1^2 + \tilde{C}_{2(ES^2)}\hat{a}_2^2, \tag{5.38}$$

where $\hat{a}_i = a_i/M$, $\hat{a} = |\boldsymbol{a}|/M$, and recalling Eq. (5.24).

The spin-orbit part was obtained in Ref. [391] with NNNLO ν-independent spinning-test-body contributions and ν-dependent contributions calibrated to NR. We do not include those higher-order corrections here, but we follow Ref. [391] in using an inverse-Taylor resummation/calibration of the coefficients G_S and G_{S^*} in

$$\hat{H}^{\text{eff}}_{\text{odd}} = \frac{G_S}{\hat{r}\hat{r}_c^2}\left(X_1^2\hat{L}\chi_1 + X_2^2\hat{L}\chi_2\right) + \frac{G_{S^*}}{\hat{r}_c^3}\nu\left(\hat{L}\chi_1 + \hat{L}\chi_2\right) + \frac{G_{S^3}}{\hat{r}_c^4}\hat{L}\,\chi_1 + \frac{\tilde{G}_{S^3}}{\hat{r}_c^4}\hat{L}\,\chi_2\,, \tag{5.39}$$

see Eqs. (E.7a), and where G_{S^3} and $\tilde{G}_{S^3}$ for aligned spins take the simple form

$$
\begin{aligned}
G_{S^3} &= \frac{1}{\hat{r}_c}\left(c_n \chi_1^2 + c_n \chi_1 \chi_2\right), \\
\tilde{G}_{S^3} &= \frac{1}{\hat{r}_c}\left(c_n \chi_2^2 + c_n \chi_1 \chi_2\right).
\end{aligned} \tag{5.40}
$$

Including spin-cubic contributions was discussed in Appendix A of Ref. [400], which we implement here so that the effective Hamiltonian includes all PN information at the same order as the other Hamiltonians considered in this paper. Explicit results after matching at 4PN can be found in Appendix E.3.

5.4 Effective-one-body Hamiltonian with test-spin limit: SEOB$_{\text{TS}}$

The SEOB Hamiltonian proposed in Refs. [382, 383] is based on the Hamiltonian of a *spinning* test body in the background of a Kerr black hole, which we here denote by SEOB$_{\text{TS}}$ (see Table 5.1). In this section, we extend that Hamiltonian to 4PN order; compared to previous results, we add NLO S^2, NNLO S^2 LO S^3, and LO S^4 PN corrections, for generic compact objects and spin orientations.

The SEOB$_{\text{TS}}$ Hamiltonian, as expressed in Ref. [589], is given by

$$\hat{H}^{\text{eff}} = \hat{H}^{\text{eff}}_{\text{even}} + \hat{H}^{\text{eff}}_{\text{odd}} + \hat{H}^{\text{eff}}_{S_*}, \tag{5.41a}$$

$$\hat{H}^{\text{eff}}_{\text{even}} = \alpha\sqrt{q + Q^0}, \tag{5.41b}$$

$$\hat{H}^{\text{eff}}_{\text{odd}} = \beta \hat{p}_\phi, \tag{5.41c}$$

$$
\begin{aligned}
\hat{H}^{\text{eff}}_{S_*} = {} & \left[\hat{\boldsymbol{F}}_t + \left(\beta + \frac{\alpha \gamma^{\phi\phi}\hat{p}_\phi}{\sqrt{q}}\right)\hat{\boldsymbol{F}}_\phi\right]\cdot \hat{\boldsymbol{S}}_* + \frac{\alpha}{\sqrt{q}}\left(\gamma^{rr}\hat{p}_r \hat{\boldsymbol{F}}_r + \gamma^{\theta\theta}\hat{p}_\theta \hat{\boldsymbol{F}}_\theta\right)\cdot \hat{\boldsymbol{S}}_* \\
& + \frac{1}{2\hat{r}^3}\left[3(\hat{\boldsymbol{S}}_* \cdot \boldsymbol{n})^2 - \hat{\boldsymbol{S}}_* \cdot \hat{\boldsymbol{S}}_*\right],
\end{aligned} \tag{5.41d}
$$

where

$$q = 1 + \gamma^{\phi\phi}\hat{p}_\phi^2 + \gamma^{rr}\hat{p}_r^2 + \gamma^{\theta\theta}\hat{p}_\theta^2, \tag{5.42}$$

and $\hat{\boldsymbol{S}}_* \equiv \boldsymbol{S}_*/M\mu$ is a rescaling of the spin of the test body. The spins are mapped according to

$$\boldsymbol{S}_* = \boldsymbol{\sigma}_* \left[1 + \nu f_*(r, \mathbf{p})\right] + \nu g_*(r, \mathbf{p})\boldsymbol{\sigma}, \tag{5.43a}$$

$$\boldsymbol{\sigma} = \boldsymbol{S}_1 + \boldsymbol{S}_2\ , \tag{5.43b}$$

$$\boldsymbol{\sigma}_* = \frac{m_2}{m_1}\boldsymbol{S}_1 + \frac{m_1}{m_2}\boldsymbol{S}_2, \tag{5.43c}$$

where the functions f_* and g_* are given by Eqs. (50)-(52) of Ref. [383], and that $\boldsymbol{\sigma} = M\boldsymbol{a}$ is the spin of the background Kerr metric; it does not hold $\boldsymbol{a} = \boldsymbol{a}_1 + \boldsymbol{a}_2$ as for the models discussed above. The spin maps are analogous to the mapping of the masses M, μ according to Eq. (5.1), with the difference that the spin maps relate dynamical variables. The deformed metric is obtained by substituting Δ, Σ, and Λ in the Kerr metric by

$$\Delta_t = \hat{r}^2 A(r) + \hat{\sigma}^2, \tag{5.44a}$$

$$\Delta_r = \Delta_t D^0(r), \tag{5.44b}$$

$$\hat{\Sigma} = \hat{r}^2 + \hat{\sigma}^2\cos^2\theta, \tag{5.44c}$$

$$\Lambda_t = (\hat{r}^2 + \hat{\sigma}^2)^2 - \hat{\sigma}^2\Delta_t\sin^2\theta, \tag{5.44d}$$

as in

$$\alpha = \frac{\sqrt{\Delta_t\hat{\Sigma}}}{\sqrt{\Lambda_t}}, \qquad \beta = \frac{2\hat{\sigma}\hat{r}}{\Lambda_t}, \tag{5.45a}$$

$$\gamma^{\phi\phi} = \frac{\hat{\Sigma}}{\Lambda_t\sin^2\theta}, \quad \gamma^{rr} = \frac{\Delta_r}{\hat{\Sigma}}, \quad \gamma^{\theta\theta} = \frac{1}{\hat{\Sigma}}. \tag{5.45b}$$

The potential $D^0(r)$ is given by Eq. (5.28b), and the potential A is given by

$$A = \hat{a}^2\left(\frac{1}{\hat{r}} - \frac{1}{\hat{r}_{H,+}}\right)\left(\frac{1}{\hat{r}} - \frac{1}{\hat{r}_{H,-}}\right)A^0(r) - \frac{\hat{a}^2}{\hat{r}^2}, \tag{5.46}$$

where A^0 is given by Eq. (5.28a), and $\hat{r}_{H,\pm}$ are the scaled inner and outer radii of a Kerr black hole, i.e.,

$$\hat{r}_{H,\pm} = 1 \pm \sqrt{1-\hat{a}^2}\,. \tag{5.47}$$

Finally, the vectors $\hat{\boldsymbol{F}}_t$, $\hat{\boldsymbol{F}}_r$, $\hat{\boldsymbol{F}}_\theta$, and $\hat{\boldsymbol{F}}_\phi$ describe the fictitious force acting on the test-body spin $\hat{\boldsymbol{S}}_*$ (frame dragging) in the deformed Kerr metric. They are given by Eq. (6) in Ref. [589], which we rewrite here for convenience,

$$\hat{\boldsymbol{F}}_\phi = \cos\theta\,\hat{\boldsymbol{n}} + \hat{\boldsymbol{v}}, \tag{5.48a}$$

$$\begin{aligned}\hat{\boldsymbol{F}}_t = {}& \hat{\boldsymbol{n}}\,\frac{\sqrt{\gamma^{\phi\phi}}\sqrt{\gamma^{\theta\theta}}}{\sqrt{q}}\left[\frac{\hat{p}_\phi\alpha_{,\theta}(1+2\sqrt{q})}{(1+\sqrt{q})} - \alpha\hat{p}_\phi\cot\theta - \frac{(1-2\sqrt{q})\beta_{,\theta}}{2\gamma^{\phi\phi}}\right]\\ &+\hat{\boldsymbol{v}}\,\frac{\csc\theta\sqrt{\gamma^{rr}}}{\sqrt{\gamma^{\phi\phi}}}\left[\frac{\gamma^{\phi\phi}\hat{p}_\phi\alpha_{,r}}{(1+\sqrt{q})} + \frac{(2\sqrt{q}-1)\beta_{,r} + \alpha\hat{p}_\phi\gamma^{\phi\phi}_{,r}}{2\sqrt{q}}\right],\end{aligned} \tag{5.48b}$$

$$\begin{aligned}\hat{\boldsymbol{F}}_r = {}& -\hat{\boldsymbol{n}}\,\frac{\sqrt{\gamma^{\theta\theta}}(\beta_{,\theta}\hat{p}_r + \beta_{,r}\hat{p}_\theta)}{2\alpha\sqrt{\gamma^{\phi\phi}}(1+\sqrt{q})} - \hat{\boldsymbol{v}}\,\frac{\csc\theta\left(\beta_{,\theta}\gamma^{\theta\theta}\hat{p}_\theta + 2\hat{p}_r\gamma^{rr}\beta_{,r}\right)}{2\alpha\sqrt{\gamma^{\phi\phi}}\sqrt{\gamma^{rr}}(1+\sqrt{q})}\\ &-\hat{\boldsymbol{\xi}}\,\frac{\csc\theta\sqrt{\gamma^{\theta\theta}}}{2\alpha\sqrt{\gamma^{rr}}}\left[\frac{2\sqrt{q}\alpha_{,\theta} + \hat{p}_\phi\beta_{,\theta}}{(1+\sqrt{q})} + \frac{\alpha\gamma^{\theta\theta}_{,\theta}}{\gamma^{\theta\theta}}\right],\end{aligned} \tag{5.48c}$$

$$\begin{aligned}\hat{\boldsymbol{F}}_\theta = {}& -\hat{\boldsymbol{n}}\,\frac{\sqrt{\gamma^{\theta\theta}}\beta_{,\theta}\hat{p}_\theta}{\alpha\sqrt{\gamma^{\phi\phi}}(1+\sqrt{q})} - \hat{\boldsymbol{v}}\,\frac{\csc\theta\sqrt{\gamma^{rr}}\hat{p}_\theta\beta_{,r}}{2\alpha\sqrt{\gamma^{\phi\phi}}(1+\sqrt{q})}\\ &+\hat{\boldsymbol{\xi}}\csc\theta\left[1 + \frac{\sqrt{\gamma^{rr}}}{2\alpha\sqrt{\gamma^{\theta\theta}}}\left(\frac{2\sqrt{q}\alpha_{,r} + \hat{p}_\phi\beta_{,r}}{(1+\sqrt{q})} + \frac{\alpha\gamma^{\theta\theta}_{,r}}{\gamma^{\theta\theta}}\right)\right].\end{aligned} \tag{5.48d}$$

Here, the unit vectors $(\hat{\boldsymbol{n}}, \hat{\boldsymbol{\xi}}, \hat{\boldsymbol{v}})$ are defined by $\hat{\boldsymbol{n}} = \frac{\boldsymbol{x}}{r}$, $\hat{\boldsymbol{\xi}} = \hat{e}^\sigma_{\rm Z}\times\hat{\boldsymbol{n}}$, and $\hat{\boldsymbol{v}} = \hat{\boldsymbol{n}}\times\hat{\boldsymbol{\xi}}$, where $\hat{e}^\sigma_{\rm Z} = \boldsymbol{\sigma}/\sigma$ denotes the direction of the (deformed) Kerr spin.

For the purpose of extending the SEOB$_{\rm TS}$ Hamiltonian to 4PN in the spinning sector, we deviate from the original philosophy of Refs. [382, 383] in that we do not modify the spin maps or deform the metric entering $H^{\rm eff}_{S_*}$ with terms of quadratic and higher order in spin. Instead, we only slightly modify the ansatz for the effective Hamiltonian (keeping $H^{\text{eff}}_{S_*}$ unchanged) as

$$\hat{H}^{\text{eff}}_{\text{even}} = \sqrt{\alpha^2 + A^{SS} + A^{nS} + A^{S^4}}\sqrt{q + B_p^{nS}\hat{\boldsymbol{p}}^2 + (B_{np}^{SS} + B_{np}^{nS})\hat{p}_r^2 + Q^0 + Q^{S^2} + Q^{S^4}} \tag{5.49a}$$

$$\hat{H}^{\text{eff}}_{\text{odd}} = \beta\hat{p}_\phi + \frac{G_{S^3}}{\hat{r}^4}\hat{\boldsymbol{L}}\cdot\boldsymbol{\chi}_1 + \frac{\tilde{G}_{S^3}}{\hat{r}^4}\hat{\boldsymbol{L}}\cdot\boldsymbol{\chi}_2, \tag{5.49b}$$

where we introduced potentials into $H^{\text{eff}}_{\text{even}}$ at quadratic and higher order in spin following the structure of Eq. (5.19). These potentials A^{SS}, A^{nS}, B_p^{nS}, B_{np}^{SS}, B_{np}^{nS}, Q^{S^2} and A^{S^4} are given by Eqs. (5.29) and (5.30) but with r instead of r_c (and different c_n), and similarly for the spin-cubic corrections G_{S^3} and $\tilde{G}_{S^3}$ from Eq. (5.32b). We take the function Q^{S^4} to have the form

$$\begin{aligned}
Q^{S^4} = \frac{\hat{p}_r^2}{\hat{r}^4}\Big[& c_n(\boldsymbol{n}\cdot\boldsymbol{\chi}_1)^3(\boldsymbol{n}\cdot\boldsymbol{\chi}_2) + c_n(\boldsymbol{n}\cdot\boldsymbol{\chi}_1)^2(\boldsymbol{\chi}_1\cdot\boldsymbol{\chi}_2) + c_n(\boldsymbol{\chi}_1\cdot\boldsymbol{\chi}_1)(\boldsymbol{n}\cdot\boldsymbol{\chi}_1)(\boldsymbol{n}\cdot\boldsymbol{\chi}_2)\\
&+ c_n(\boldsymbol{n}\cdot\boldsymbol{\chi}_2)^3(\boldsymbol{n}\cdot\boldsymbol{\chi}_1) + c_n(\boldsymbol{n}\cdot\boldsymbol{\chi}_2)^2(\boldsymbol{\chi}_1\cdot\boldsymbol{\chi}_2) + c_n(\boldsymbol{\chi}_2\cdot\boldsymbol{\chi}_2)(\boldsymbol{n}\cdot\boldsymbol{\chi}_1)(\boldsymbol{n}\cdot\boldsymbol{\chi}_2)\\
&+ c_n(\boldsymbol{n}\cdot\boldsymbol{\chi}_1)^2(\boldsymbol{n}\cdot\boldsymbol{\chi}_2)^2 + c_n(\boldsymbol{n}\cdot\boldsymbol{\chi}_1)^2(\boldsymbol{\chi}_2\cdot\boldsymbol{\chi}_2) + c_n(\boldsymbol{\chi}_1\cdot\boldsymbol{\chi}_1)(\boldsymbol{\chi}_2\cdot\boldsymbol{\chi}_2)\\
&+ c_n(\boldsymbol{\chi}_1\cdot\boldsymbol{\chi}_1)(\boldsymbol{n}\cdot\boldsymbol{\chi}_2)^2\Big]\\
+ \boldsymbol{p}\cdot\boldsymbol{\chi}_1\frac{\hat{p}_r}{\hat{r}^4}\Big[& c_n(\boldsymbol{\chi}_2\cdot\boldsymbol{\chi}_2)(\boldsymbol{n}\cdot\boldsymbol{\chi}_2) + c_n(\boldsymbol{n}\cdot\boldsymbol{\chi}_2)^3 + c_n(\boldsymbol{n}\cdot\boldsymbol{\chi}_1)^2(\boldsymbol{n}\cdot\boldsymbol{\chi}_2)\\
&+ c_n(\boldsymbol{n}\cdot\boldsymbol{\chi}_1)(\boldsymbol{\chi}_1\cdot\boldsymbol{\chi}_2) + c_n(\boldsymbol{n}\cdot\boldsymbol{\chi}_1)(\boldsymbol{n}\cdot\boldsymbol{\chi}_2)^2 + c_n(\boldsymbol{n}\cdot\boldsymbol{\chi}_1)(\boldsymbol{\chi}_2\cdot\boldsymbol{\chi}_2)\Big]\\
+ \boldsymbol{p}\cdot\boldsymbol{\chi}_2\frac{\hat{p}_r}{\hat{r}^4}\Big[& c_n(\boldsymbol{\chi}_1\cdot\boldsymbol{\chi}_1)(\boldsymbol{n}\cdot\boldsymbol{\chi}_1) + c_n(\boldsymbol{n}\cdot\boldsymbol{\chi}_1)^3 + c_n(\boldsymbol{n}\cdot\boldsymbol{\chi}_2)^2(\boldsymbol{n}\cdot\boldsymbol{\chi}_1)\\
&+ c_n(\boldsymbol{n}\cdot\boldsymbol{\chi}_2)(\boldsymbol{\chi}_1\cdot\boldsymbol{\chi}_2) + c_n(\boldsymbol{n}\cdot\boldsymbol{\chi}_2)(\boldsymbol{n}\cdot\boldsymbol{\chi}_1)^2 + c_n(\boldsymbol{n}\cdot\boldsymbol{\chi}_2)(\boldsymbol{\chi}_1\cdot\boldsymbol{\chi}_1)\Big].
\end{aligned} \tag{5.50}$$

Out of 38 possible terms in the most general expression for Q^{S^4}, 16 terms were removed via a gauge choice. We started by removing the three terms that do not vanish for aligned spins, but the other 13 terms were chosen arbitrarily. Explicit results after matching at 4PN can be found in Appendix E.4.

5.5 Comparison with numerical relativity

In this section, we compare the four SEOB Hamiltonians considered in this paper to NR simulations through the binding energy for circular orbits and aligned spins. The NR binding energy data we use here were extracted from the Simulating eXtreme Spacetimes (SXS) catalog [458] in Ref. [438]. Hereafter, in this section, we use the term "aligned spins" to mean spins parallel to, and in the same direction as, the orbital angular momentum $\boldsymbol{L}$, but we use the term "antialigned spins" to mean spins opposite to the direction of $\boldsymbol{L}$.

The binding energy is calculated by evaluating the EOB Hamiltonian for circular orbits ($p_r = 0$) and solving numerically $\dot{p}_r = -\partial H_{\text{EOB}}/\partial r = 0$ for the angular momentum p_ϕ at some radius. The orbital frequency Ω is obtained from

$$\Omega = \frac{\partial H_{\text{EOB}}}{\partial p_\phi}\,. \tag{5.51}$$

We then calculate the binding energy and orbital frequency as r goes from the beginning of the NR simulation to the innermost-stable circular orbit (ISCO) of the Hamiltonian, which marks the end of the inspiral phase of the binary coalescence and the beginning of the plunge. The ISCO is calculated by setting both the first and second derivatives of the Hamiltonian with respect to r to zero, i.e., $\partial H_{\text{EOB}}/\partial r = 0 = \partial^2 H_{\text{EOB}}/\partial r^2$.

It should be noted that the binding energy is extracted from NR simulations from an evolving binary, tracking the radiated energy in GWs. From the EOB Hamiltonians, however, we obtain the binding energy here by assuming exact circular orbits at different orbital separations, neglecting the orbital decay (radiation-reaction) due to the emitted GWs. The NR and EOB binding energies are thus not expected to agree exactly here during the last few orbits (see discussions in Ref. [405]).

In Fig. 5.1, we plot the binding energy for nonspinning configurations with different mass ratios q as a function of the "velocity" parameter $v \equiv (M\Omega)^{1/3}$, and we see that the binding energy increases with increasing mass ratio. The top axis of the figure indicates the number of GW cycles before merger, computed from the SXS waveform, for the case of $q = 1$, which is close to the other values of q; for example, at 2 GW cycles before merger, $v = 0.416$ for $q = 1$ while $v = 0.415$ for $q = 10$. Since all SEOB Hamiltonians considered here agree in the nonspinning limit by construction, this figure gives a rough estimate for the zero-spin contributions to the binding energy. In all plots of this section the number of GW cycles from merger is always computed from the SXS waveforms, and the merger is defined as the peak of the (2,2) gravitational mode.

The different spin contributions to the binding energy are depicted in Fig. 5.2. They can be extracted by combining results for various spin combinations as (see Refs. [437, 438])

$$
\begin{aligned}
E_{\mathrm{SO}} &= -\frac{1}{6}(-0.6,0) + \frac{8}{3}(0.3,0) - 2(0,0) - \frac{1}{2}(0.6,0), \\
E_{S^2} &= \frac{3}{2}(-0.6,0) - 2(0,0) + \frac{3}{2}(0.6,0) - (0.6,-0.6), \\
E_{S^3} &= -\frac{5}{6}(-0.6,0) - \frac{8}{3}(0.3,0) + 3(0,0) - \frac{1}{2}(0.6,0) + \frac{1}{2}(0.6,-0.6) + \frac{1}{2}(0.6,0.6), \quad \text{(5.52a)}
\end{aligned}
$$

where the numbers in brackets refer to the values of the dimensionless spins of the two bodies (χ_1, χ_2). The spin-squared contributions to the binding energy E_{S^2} refer to both S_i^2 and $S_1 S_2$ interactions. Similarly, spin-cubic contributions E_{S^3} refer to both S_i^3 and $S_i^2 S_j$. We see that the spin-orbit contribution is about an order of magnitude larger than the spin-squared contribution, which in turn is an order of magnitude larger than the spin-cubic contribution. All SEOB Hamiltonians give comparable results for the spin-orbit part, however for the spin-squared con-

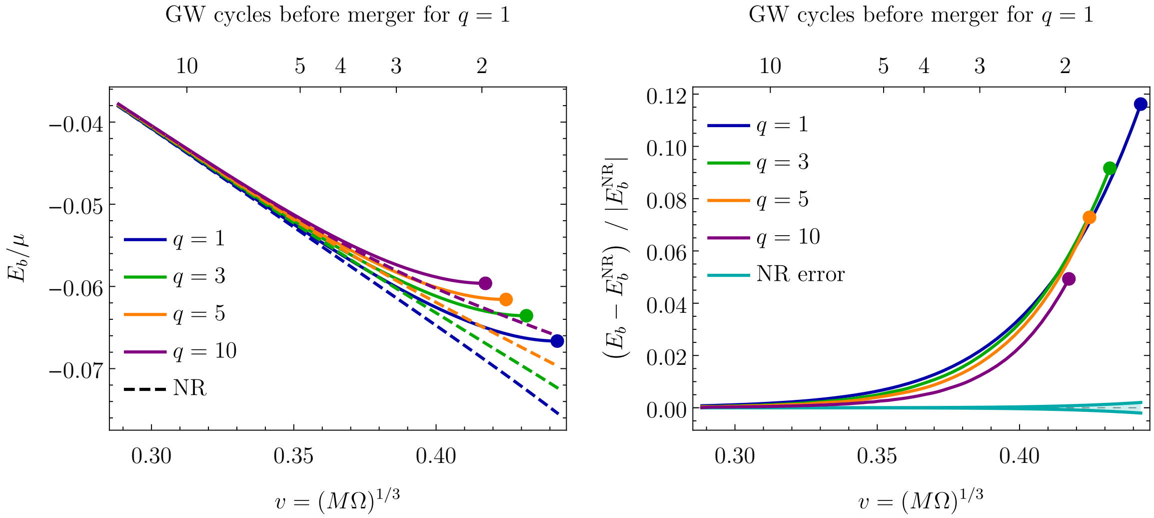

Figure 5.1: Binding energy (left panel) and fractional binding energy (right panel) versus the "velocity" parameter v for nonspinning binary–black-hole configurations with different mass ratios. The four SEOB Hamiltonians considered here are identical for zero spin. The relative NR error shown in the right panel is a conservative 1.1% estimate. The initial value of v (the left end of the plots' domain) here is determined by the beginning of the NR simulation with $q = 10$; those with lower mass ratios have several cycles at lower frequencies not shown here. We stress that the SEOB Hamiltonians at 4PN order are not calibrated to NR simulations.

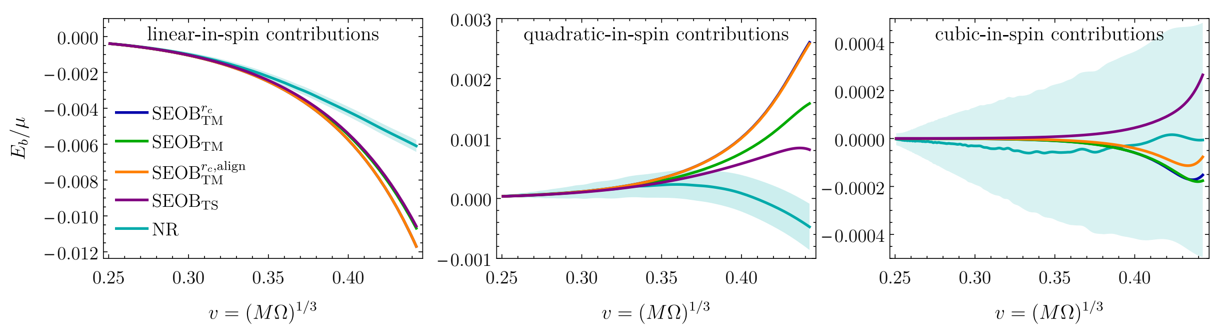

Figure 5.2: Binding energy versus the "velocity" parameter v for the linear-in-spin (left panel), quadratic-in-spin (central panel) and cubic-in-spin (right panel) contributions of the four SEOB Hamiltonians. The NR error is indicated by the shaded regions. In the left panel, the blue and orange curves overlap since the $\mathrm{SEOB}_{\mathrm{TM}}^{r_c}$ and $\mathrm{SEOB}_{\mathrm{TM}}^{r_c,\mathrm{align}}$ Hamiltonians are identical in the spin-orbit limit.

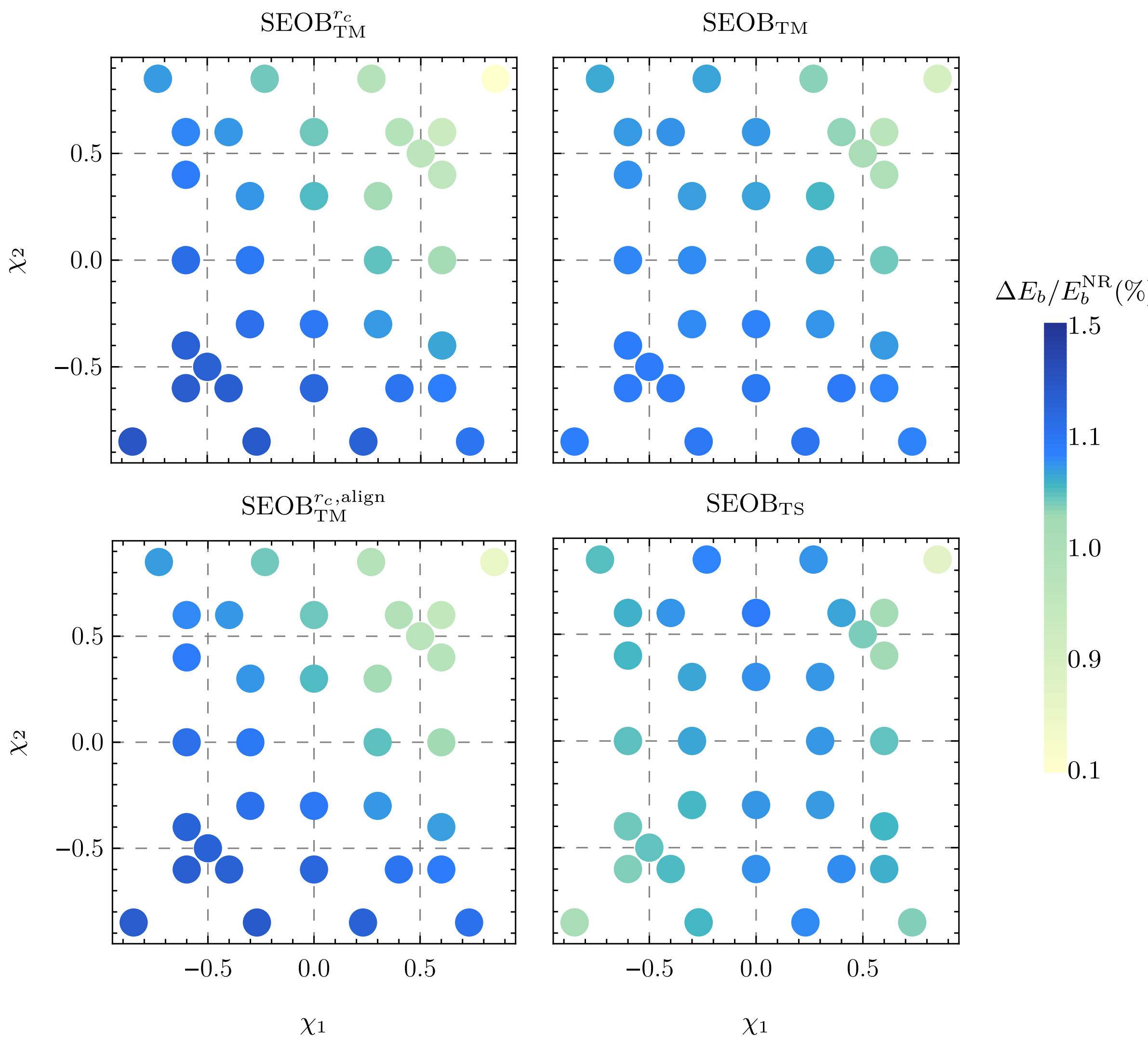

Figure 5.3: Fractional difference in the binding energy between NR and SEOB Hamiltonians for different spin configurations with mass ratio $q = 3$ at 4 GW cycles before merger.

tribution, the SEOB_{TS} and SEOB_{TM} Hamiltonians give better agreement with NR than the other two Hamiltonians. For the cubic-in-spin contributions, the NR error is larger than the EOB values for the binding energy, and hence we cannot conclude which Hamiltonian is better in terms of S^3 contributions.

In Fig. 5.3, we compare the fractional energy difference $|E_b - E_b^{\text{NR}}|/E_b^{\text{NR}}$ at four GW cycles (i.e., two orbits) before merger for various spin configurations with mass ratio $q = 3$. We see that, for all configurations at that frequency, the relative difference with NR is around 1%. For aligned spins, all Hamiltonians give comparable results, but the SEOB_{TS} Hamiltonian gives better agreement with NR for antialigned spins.

We also compare the binding energy as a function of velocity for some configurations with aligned spins (Fig. 5.4) and antialigned spins (Fig. 5.5). The curves in these figures start at the beginning of the available NR simulations and end at the ISCO of the EOB Hamiltonians. All effective Hamiltonians considered here have an ISCO for arbitrary spins, except that the SEOB_{TS} Hamiltonian does not have an ISCO for large aligned spins $\gtrsim 0.92$. From the three panels at the top of Fig. 5.4, we see that for large aligned spins ($\gtrsim 0.8$), the SEOB_{TS} Hamiltonian shows slightly better agreement with NR than the other Hamiltonians. However, for smaller spins ($\lesssim 0.6$), all Hamiltonians give very similar results. This is also the case when the two spins are both large but in opposite directions. For antialigned spins, the difference between the four Hamiltonians is smaller than in the aligned-spin case; the SEOB_{TS} Hamiltonian gives better agreement with NR than the other Hamiltonians, but the difference is small, even for spin magnitudes of 0.97, and becomes negligible for smaller spins.

Finally, in Fig. 5.6, we compare the effect of adding spin PN orders to the effective Hamiltonian for a configuration with mass ratio $q = 3$ and spins $\chi_1 = \chi_2 = 0.85$. For all Hamiltonians,

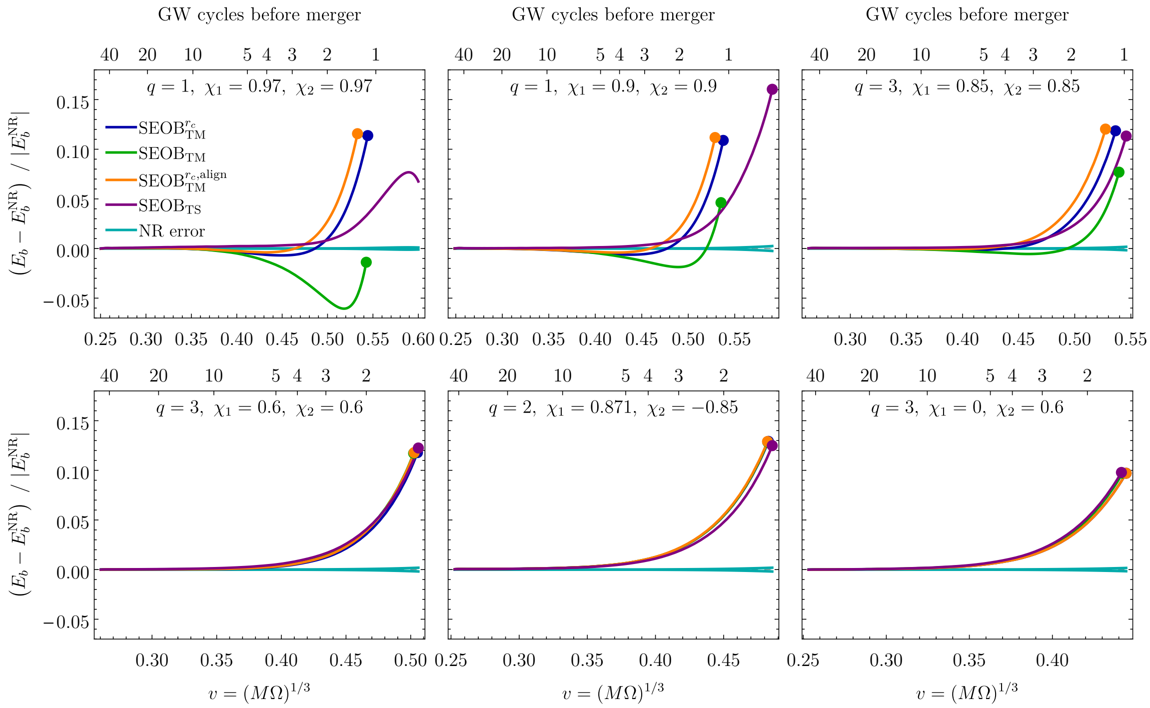

Figure 5.4: Binding energy comparison with NR for different aligned-spin configurations for the four SEOB Hamiltonians. Curves that end with a point indicate the location of the ISCO. For the NR error, we used 1.1% relative error as a very conservative estimate.

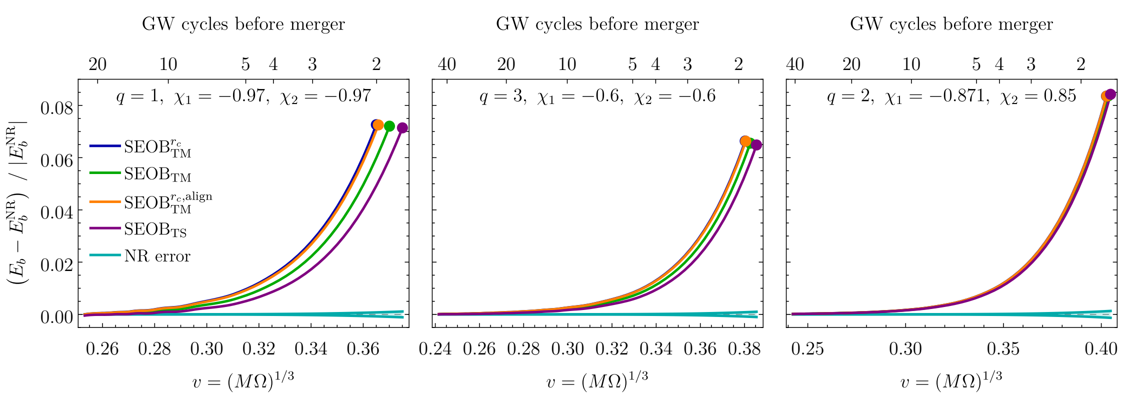

Figure 5.5: As in Fig. 5.4 but for configurations with antialigned spins.

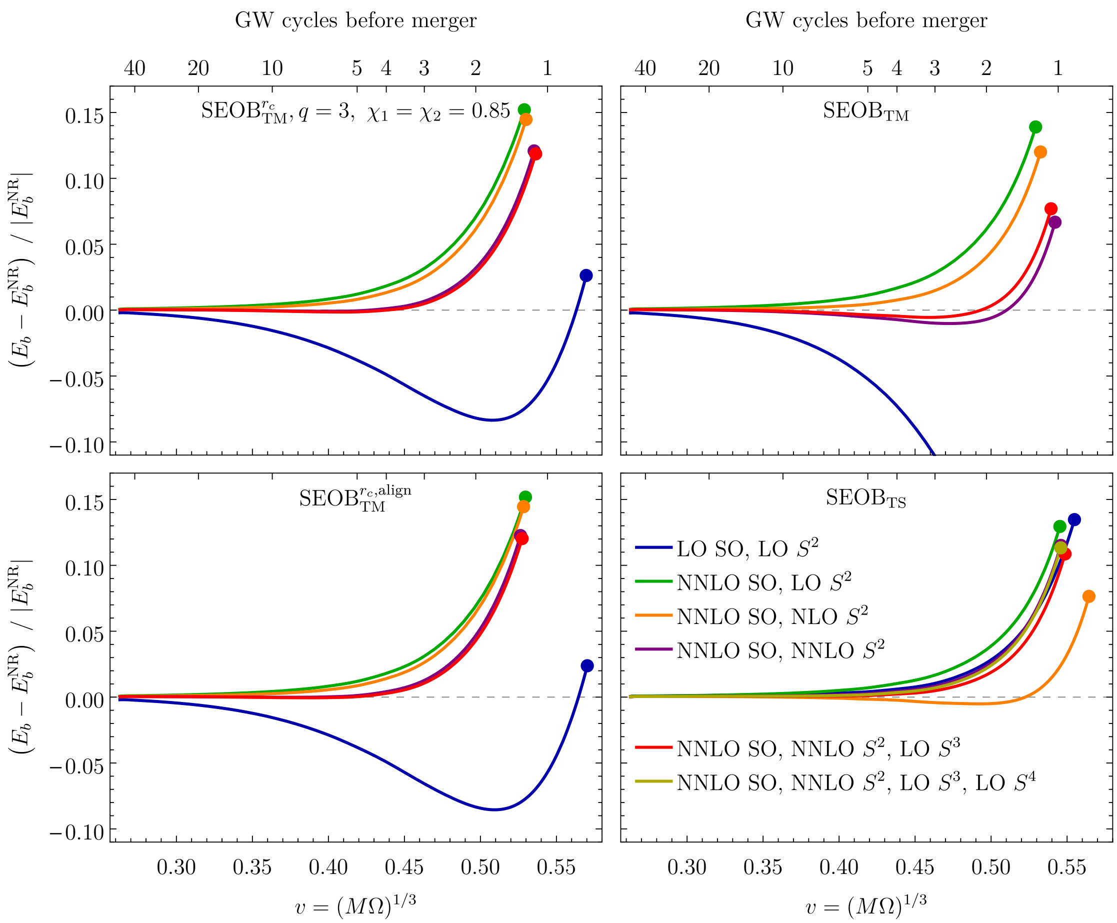

Figure 5.6: Comparing the effect of adding spin contributions to the binding energy at different PN orders for the four SEOB Hamiltonians.

adding higher spin orders improves agreement with NR, except for the $\mathrm{SEOB_{TS}}$ Hamiltonian where adding LO S^3 and LO S^4 gives slightly worse agreement. We checked that using different spin configurations gives qualitatively similar behavior.

Overall, beside the small differences pointed out above, all Hamiltonians perform reasonably well compared to NR simulations. One should expect that the differences that accumulate during the last orbits can be compensated by a calibration of the Hamiltonians, applying also further resummations to the potentials, which we leave for future work. This would be of particular interest for the simplified Hamiltonian, in order to prepare and evaluate it as a possible starting point for an EOB waveform model.

5.6 Conclusions

In this paper, we built spinning EOB Hamiltonians that include the complete fourth post-Newtonian conservative dynamics for generic (precessing) spins. These Hamiltonians are also valid for generic compact objects (e.g., black holes or neutron stars) since we included multipole constants that parametrize the deformation of the compact object due to its rotation.

In particular, we considered and extended four SEOB Hamiltonians: (i) an extension of the SEOB Hamiltonian from Ref. [392] by adding NNLO S^2 and LO S^3 contributions, in addition to adding the multipole constants; (ii) a simplified version of that Hamiltonian that differs in how the spin corrections are added to the Kerr metric, and that does not use the concept of centrifugal radius; (iii) the aligned-spin Hamiltonian from Refs. [391, 400, 401], which already includes complete 4PN information for generic compact objects, but considered here for comparison with the other Hamiltonians; (iv) an extension of the SEOB Hamiltonian from Refs. [382, 383], which uses a test spin, by adding NLO S^2, NNLO S^2, LO S^3, and LO S^4 contributions, in addition to adding the multipole constants. Since our goal in this paper was to improve the description of spin effects in the EOB formalism, we modified the zero-spin part of the above Hamiltonians such that they are identical in that limit. Furthermore, we did not include NR calibration parameters or resummations of the PN corrections (e.g., with Padé or $\log$ resummations of the zero-spin part) since they constitute an implicit calibration to NR that improves the performance of EOB Hamiltonians only in certain models.

We compared the four SEOB Hamiltonians considered here with NR simulations by calculating the binding energy for circular orbits and aligned spins. We found that all Hamiltonians show good agreement with NR, and that the difference between the Hamiltonians is quite small up to moderate values of the spins and a handful number of GW cycles before merger. For large spins, the SEOB_{TS} Hamiltonian performs better at large frequencies, but since all Hamiltonians have an error of about 1% compared to NR at about four GW cycles before merger, the simplest SEOB Hamiltonian SEOB_{TM} could be an excellent candidate for building an improved EOB waveform model with precessing spins. The simplicity will allow one to have a fast-to-evolve set of equations of motion, and could help in calibrating the EOB waveforms built with SEOB_{TM} to NR simulations. However, more analyses, which include dissipative effects, and a careful study of how the GW frequency approaches merger, are needed to pin down the more suitable SEOB Hamiltonian. Indeed, as several studies have shown [393–398], to attach robustly the merger-ringdown waveform to the inspiral-plunge one in the EOB formalism, dynamical quantities, such as the orbital frequency, radial separation and momentum vectors, have to behave regularly around and beyond the EOB photon orbit.

We leave for future work to complete the SEOB Hamiltonians to a gravitational waveform model, i.e., provide resummed expressions for GW modes and associated radiation-reaction forces. Once radiation-reaction forces are included in the model, it is important to perform comparisons with NR for precessing spins and to use those comparisons to study different resummation options and to add calibration parameters in order to improve the accuracy of EOB waveforms toward merger.

Acknowledgments

We thank Sergei Ossokine for providing us with the numerical-relativity data for the binding energy used in this paper.

Chapter 6: Radiation-reaction force and multipolar waveforms for eccentric, spin-aligned binaries in the effective-one-body formalism

Authors[1]: *Mohammed Khalil, Alessandra Buonanno, Jan Steinhoff, Justin Vines*

Abstract: While most binary inspirals are expected to have circularized before they enter the LIGO/Virgo frequency band, a small fraction of those binaries could have non-negligible orbital eccentricity depending on their formation channel. Hence, it is important to accurately model eccentricity effects in waveform models used to detect those binaries, infer their properties, and shed light on their astrophysical environment. We develop a multipolar effective-one-body (EOB) eccentric waveform model for compact binaries whose components have spins aligned or anti-aligned with the orbital angular momentum. The waveform model contains eccentricity effects in the radiation-reaction force and gravitational modes through second post-Newtonian (PN) order, including tail effects, and spin-orbit and spin-spin couplings. We recast the PN-expanded, eccentric radiation-reaction force and modes in factorized form so that the newly derived terms can be directly included in the state-of-the-art, quasi-circular–orbit EOB model currently used in LIGO/Virgo analyses (i.e., the `SEOBNRv4HM` model).

[1]Originally published as Phys. Rev. D **104**, no.2, 024046 (2021)

6.1 Introduction

The observation of gravitational waves (GWs) by the LIGO-Virgo detectors [13, 14] have corroborated the existence of binary black holes (BBHs) in our universe. But how and in which astrophysical environments these binaries form is not yet fully understood. However, the masses, spins (magnitude and orientation), and binary eccentricities inferred from GWs provide invaluable clues to determine BBH formation channels [18, 19]. So far, the observed GWs are consistent with binary coalescences of negligible eccentricity, i.e., on quasi-circular orbits [439–442].

In general, binaries are expected to circularize [443, 444] as they approach merger due to the emission of gravitational radiation. But depending on their astrophysical formation channel, a small fraction of binaries could have non-negligible orbital eccentricity, as they enter the frequency bands of current detectors. This can occur in dense stellar environments, such as globular clusters or galactic nuclei, where dynamic capture [446–451] or the Lidov-Kozai mechanism in hierarchical triples [452–454] can lead to eccentric binary inspirals at close separations.

In particular, Ref. [446] (and Ref. [447]) showed that $\sim 5\%$ (or $\sim 10\%$) of all mergers in globular clusters enter the LIGO band with eccentricity $e > 0.1$. Binaries formed via dynamic capture in galactic nuclei are expected to have high eccentricities [448], with 92% having $e > 0.1$ and $50\% - 85\%$ having $e > 0.8$ at 10 Hz. For a BBH around a supermassive BH, the Lidov-Kozai mechanism can secularly drive the BBH to eccentricities near unity for some orientations [454]. Hence, inferring those eccentricities from GWs is important for understanding the origin and environment of BBHs. Interestingly, Ref. [442] pointed out that GW190521 [457] could be consistent with either an eccentric nonprecessing or a quasi-circular precessing binary, which illustrates both the difficulties and prospects of further observations in the upcoming and future

LIGO, Virgo and KAGRA runs [30].

While the expected fraction of eccentric GW observations with current detectors is small, neglecting eccentricity for the parameter inference can cause significant bias [193]. This becomes more relevant for LISA where a large fraction of stellar-mass binaries is expected to be eccentric [606–610]. Hence, it is important to develop accurate waveform models for eccentric binaries to detect them, infer their properties, and shed light on their astrophysical environment and formation channels. Several studies developed post-Newtonian (PN) waveform models for eccentric orbits, such as Refs. [154, 570, 611–619], or hybrid models that use PN results for the inspiral and quasi-circular numerical-relativity (NR) simulations near merger [620–622]. Recently, NR simulations for eccentric binaries were reported in Refs. [41, 622, 623], and the first NR surrogate model for eccentric BBHs has been developed in Ref. [624].

The effective-one-body (EOB) formalism [80, 380, 381] improves inspiral-merger-ringdown waveforms by combining information from PN theory, NR simulations, and the strong-field test-body limit. EOB Hamiltonians have been constructed to include spin [4, 370, 382, 383, 389–392, 580], tidal effects [187, 586, 587, 625], information from the small mass-ratio [407–410, 588] and the post-Minkowskian approximations [236, 237, 405], and have been refined and calibrated to NR simulations [393–397, 399, 401, 413, 582]. While the EOB Hamiltonian is valid for generic orbits, most EOB waveform models use quasi-circular orbit results for the radiation-reaction (RR) force, gravitational waveform modes, and the calibration with NR simulations.

Recent approaches to extend the EOB formalism to eccentric orbits include Ref. [402], which derived the RR force with eccentricity up to 2PN order, but without tail effects and for nonspinning BHs. More recently, Ref. [403] incorporated eccentricity effects in the RR force and in the $(2, 2)$ waveform mode through 1.5PN order, including tail effects, using the Keplerian parametrization and phase variables that evolve only due to RR. References [626, 627] extended the quasi-circular SEOBNRv1 [394] model to eccentric orbits, while Ref. [628] added eccentric corrections in the SEOBNRv4 [397, 398] waveform model, notably in the $(2,2)$, $(2,1)$, $(3,3)$, $(4,4)$ modes through 2PN order, including spin-orbit (SO) and spin-spin (SS) couplings [2], but not tail effects. They employed these eccentric modes to construct a RR force for eccentric orbits, which however does not include the Schott terms. As argued in Ref. [402] and Sec. 6.2 below, these Schott terms are necessary for generic orbits to satisfy the flux-balance equations. Furthermore, Refs. [404, 629] incorporated noncircular effects in the TEOBResumS_SM [401, 630] model at leading PN order in the azimuthal component of the RR force, and used a quasi-circular 2PN-expanded radial RR force without spin or tail effects. They included eccentric corrections at leading PN order to all modes $m \neq 0$ up to $\ell = |m| = 5$.

In this paper, we develop a multipolar EOB waveform model for eccentric binaries with the compact-objects' spins aligned or antialigned (henceforth, for short aligned) with the orbital angular momentum. We derive the eccentric PN expressions for the RR force (including the Schott terms) and the gravitational modes up to $\ell = |m| = 6$, including the $m = 0$ mode, through 2PN order, including tail effects, and SO and SS couplings. We recast our results for the RR force and modes in a form that can be directly incorporated in the state-of-the-art, quasi-circular–orbit EOB model currently used in LIGO/Virgo analyses (SEOBNRv4HM [397, 398]).

The paper is structured as follows. In Sec. 6.2, we derive the RR force from the energy and angular momentum fluxes using the balance relations. We use the gauge freedom in the RR force to impose that it reduces to the relation used in SEOBNRv4HM in the quasi-circular–orbit

[2] Our results for those modes are mostly in agreement with Ref. [628] except for the SO part, where we disagree with their findings (their expressions contain two extra SO terms).

limit. In Sec. 6.3, we obtain initial conditions for eccentric orbits. In Sec. 6.4, we calculate all the gravitational waveform modes that contribute up to 2PN order relative to the leading order (LO) of the $(2,2)$ mode, i.e., up to the $\ell = |m| = 6$ mode. These higher-order modes are even more important for eccentric orbits than for quasi-circular ones [631]. We conclude in Sec. 6.5 with a discussion of results and potential future work. Finally, Appendix F provides the coordinate transformation from harmonic to EOB coordinates, Appendix G includes a derivation of the LO spin-squared contribution to the angular momentum flux, Appendix H lists the spin contributions to the waveform modes in harmonic coordinates, Appendix I provides some relations for dynamic quantities in the Keplerian parametrization, and Appendix J includes the transformation to tortoise coordinates.

Notation

We use the metric signature $(-,+,+,+)$, and use units in which $c = G = 1$, but write c explicitly in PN expansions.

We consider an aligned-spin binary with masses m_1 and m_2, with $m_1 \geq m_2$, and we define the following constants:

$$\begin{aligned} &M = m_1 + m_2, \quad \mu = \frac{m_1 m_2}{M}, \quad \nu = \frac{\mu}{M}, \\ &\delta = \frac{m_1 - m_2}{M}, \quad X_1 = \frac{m_1}{M}, \quad X_2 = \frac{m_2}{M}. \end{aligned} \tag{6.1}$$

In the binary's center of mass, we introduce the canonical phase-space variables (R, ϕ, P_R, P_ϕ), where R is the separation, ϕ the azimuthal angle, P_R the radial momentum, and P_ϕ the angular momentum. The total relative momentum P is given by $P^2 = P_R^2 + P_\phi^2/R^2$. We use the rescaled dimensionless variables

$$
\begin{aligned}
r = \frac{R}{M}, \quad t = \frac{T}{M}, \quad p_r = \frac{P_r}{\mu}, \quad p_\phi = \frac{P_\phi}{M\mu}, \\
\hat{H} = \frac{H}{\mu}, \quad \hat{S}_i = \frac{S_i}{M\mu}, \quad \chi_i = \frac{S_i}{m_i^2},
\end{aligned}
\tag{6.2}
$$

where the dimensionless quantities are denoted with either a hat or a lowercase letter.

The energy and angular momentum fluxes far away from the binary are denoted by Φ_E and Φ_J respectively, and scale as follows:

$$
\Phi_E = Gc^5 \tilde{\Phi}_E, \quad \Phi_J = c^5 \frac{\tilde{\Phi}_J}{M}, \tag{6.3}
$$

where quantities with a tilde are the physical dimensionful fluxes. The components of the RR force are denoted by $\mathcal{F}_r$ and $\mathcal{F}_\phi$, and are scaled similarly to Φ_E and Φ_J, respectively.

6.2 Radiation reaction force

The RR force accounts for the energy and angular momentum losses by the system, and is added to the right-hand side of the Hamilton equations of motion (EOMs) such that

$$
\begin{aligned}
\dot{r} = \frac{\partial \hat{H}}{\partial p_r}, \qquad \dot{p}_r = -\frac{\partial \hat{H}}{\partial r} + \mathcal{F}_r, \\
\dot{\phi} = \frac{\partial \hat{H}}{\partial p_\phi}, \qquad \dot{p}_\phi = -\frac{\partial \hat{H}}{\partial \phi} + \mathcal{F}_\phi,
\end{aligned}
\tag{6.4}
$$

where the leading order of $\mathcal{F}_{r,\phi}$ is of order $1/c^5$ (2.5 PN). From the EOMs, with $\partial H/\partial\phi = 0$, the time derivatives of energy and angular momentum are given by

$$
\begin{aligned}
\dot{E}_{\text{system}} &= \frac{d\hat{H}}{dt} = \dot{r}\mathcal{F}_r + \dot{\phi}\mathcal{F}_\phi, \\
\dot{J}_{\text{system}} &= \frac{dp_\phi}{dt} = \mathcal{F}_\phi.
\end{aligned}
\tag{6.5}
$$

The energy and angular momentum lost by the system are not equal to the energy and angular momentum fluxes, Φ_E and Φ_J, because of additional contributions to E and J due to interactions with the radiation field. The balance equations are modified by *Schott* terms, as in electrodynamics, that appear as total time derivatives in the balance equations [402]

$$\begin{aligned}
&\dot{E}_{\text{system}} + \dot{E}_{\text{Schott}} + \Phi_E = 0, \\
&\dot{J}_{\text{system}} + \dot{J}_{\text{Schott}} + \Phi_J = 0.
\end{aligned} \tag{6.6}$$

Substituting the expressions for the energy and angular momentum losses, we obtain

$$\begin{aligned}
&\dot{r}\mathcal{F}_r + \dot{\phi}\mathcal{F}_\phi + \dot{E}_{\text{Schott}} + \Phi_E = 0, \\
&\mathcal{F}_\phi + \dot{J}_{\text{Schott}} + \Phi_J = 0.
\end{aligned} \tag{6.7}$$

The energy and angular momentum fluxes are gauge-independent, but the RR force and Schott terms are gauge-dependent. This coordinate gauge freedom in the RR force was discussed by Iyer and Will in Refs. [146, 147], and by Gopakumar et. al. in Ref. [150]. Bini and Damour showed in Ref. [402] how the gauge freedom in $\mathcal{F}$ is related to the freedom in defining the Schott terms.

Note that while we only consider aligned spins in this paper, an extension to precessing spins is straightforward; the RR force $\boldsymbol{\mathcal{F}}$ is added to the EOM for the total momentum $\boldsymbol{p}$ and a RR contribution is added to the spin evolution equations, such that

$$\begin{gathered}
\frac{d\boldsymbol{r}}{dt} = \frac{\partial H}{\partial \boldsymbol{p}}, \qquad \frac{d\boldsymbol{p}}{dt} = -\frac{\partial H}{\partial \boldsymbol{r}} + \boldsymbol{\mathcal{F}}, \\
\frac{d\boldsymbol{S}_{\text{i}}}{dt} = \frac{\partial H}{\partial \boldsymbol{S}_{\text{i}}} \times \boldsymbol{S}_{\text{i}} + \dot{\boldsymbol{S}}_{\text{i}}^{\text{RR}}.
\end{gathered} \tag{6.8}$$

The balance equations are then given by

$$\dot{E}_{\text{system}} + \dot{E}_{\text{Schott}} + \Phi_E = 0$$

$$\dot{\boldsymbol{J}}_{\text{system}} + \dot{\boldsymbol{J}}_{\text{Schott}} + \boldsymbol{\Phi}_J = 0, \tag{6.9}$$

with

$$\begin{aligned}
\dot{E}_{\text{system}} &= \dot{\boldsymbol{r}} \cdot \boldsymbol{\mathcal{F}}, \\
\dot{\boldsymbol{J}}_{\text{system}} &= \boldsymbol{r} \times \boldsymbol{\mathcal{F}} + \dot{\boldsymbol{S}}_1^{\text{RR}} + \dot{\boldsymbol{S}}_2^{\text{RR}}.
\end{aligned} \tag{6.10}$$

See, e.g., Refs. [167, 168] for more details.

6.2.1 Summary of the approach used in this paper for the RR force

The aim of this paper is to extend the quasi-circular RR force and gravitational modes employed in the `SEOBNRv4HM` waveform model to eccentric orbits. The Hamilton equations that describe the dynamics of the `SEOBNRv4HM` model use the following relations between the RR force and the energy flux for quasi-circular orbits, which are based on results from Refs. [374, 381],

$$\begin{aligned}
\mathcal{F}_\phi^{\text{qc}} &= -\frac{\Phi_E^{\text{qc}}}{\Omega}, \\
\mathcal{F}_r^{\text{qc}} &= \mathcal{F}_\phi^{\text{qc}} \frac{p_r}{p_\phi} = -\frac{\Phi_E^{\text{qc}} p_r}{\Omega p_\phi},
\end{aligned} \tag{6.11}$$

with Ω being the (angular) orbital frequency. However, these two relations are only valid for quasi-circular orbits and are not consistent for generic orbits, since they use the circular-orbit relation $\Phi_E^{\text{qc}} = \Omega \Phi_J^{\text{qc}}$ and do not include the Schott terms.

Hence, the approach we use to obtain the RR force is to write a generic ansatz with unknown coefficients for the Schott terms, and calculate the RR force from the fluxes using the balance equations

$$\mathcal{F}_\phi = -\Phi_J - \dot{J}_{\text{Schott}},$$

$$\dot{r}\mathcal{F}_r = -\Phi_E + \dot{\phi}\Phi_J - \dot{E}_{\text{Schott}} + \dot{\phi}\dot{J}_{\text{Schott}}. \tag{6.12}$$

Then, we specify the free unknown coefficients in the Schott terms such that the force reduces to the conditions in Eq. (6.11) in the limit of quasi-circular orbits, i.e.,

$$\begin{aligned} \mathcal{F}_\phi &= -\Phi_J + \mathcal{O}(\dot{p}_r) + \mathcal{O}(p_r^2), \\ \frac{\mathcal{F}_r p_\phi}{\mathcal{F}_\phi p_r} &= 1 + \mathcal{O}(p_r^2), \end{aligned} \tag{6.13}$$

since both p_r and $\dot{p}_r$ are zero for circular orbits. Finally, we factorize the RR force into the quasi-circular part used in `SEOBNRv4HM` times eccentric corrections

$$\mathcal{F}_r = \mathcal{F}_r^{\text{qc}}\mathcal{F}_r^{\text{ecc}}, \qquad \mathcal{F}_\phi = \mathcal{F}_\phi^{\text{qc}}\mathcal{F}_\phi^{\text{ecc}}, \tag{6.14}$$

where the quasi-circular parts are given by Eq. (6.11), and the eccentric corrections scale as $\mathcal{F}_i^{\text{nc}} \sim 1 + \dot{p}_r + p_r^2 + \dots$. In the following subsections, we provide the details of these steps.

6.2.2 EOB Hamiltonian and angular momentum

The EOB Hamiltonian is calculated from an effective Hamiltonian H_{eff} via the energy map

$$H_{\text{EOB}} = M\sqrt{1 + 2\nu\left(\frac{H_{\text{eff}}}{\mu} - 1\right)}, \tag{6.15}$$

with H_{eff} given in Refs. [4, 382, 383]. When calculating the RR force to 2PN, we only need to work with the PN expansion of the EOB Hamiltonian. The nonspinning part to 2PN order is given by

$$\begin{aligned} \hat{H}^0_{\text{EOB}} = \frac{c^2}{\nu} + \frac{p^2}{2} - \frac{1}{r} + \frac{1}{c^2}\left[\frac{(\nu-1)p^2}{2r} - \frac{1+\nu}{8}p^4 - \frac{p_r^2}{r} - \frac{1+\nu}{2r^2}\right] \\ + \frac{1}{c^4}\left[\frac{1+\nu+\nu^2}{16}p^6 + \frac{(1+2\nu)p_r^2}{r^2} - \frac{(1+\nu-3\nu^2)\,p^2}{4r^2} + \frac{(1+\nu-3\nu^2)\,p^4}{8r}\right. \end{aligned}$$

$$
+\frac{(1+\nu)p^2p_r^2}{2r}-\frac{1-\nu+\nu^2}{2r^3}\Bigg], \tag{6.16}
$$

the LO (1.5PN) spin-orbit part

$$
\hat{H}^{\mathrm{SO}}_{\mathrm{EOB}}=\frac{p_\phi}{2c^3r^3}\left[\chi_1\left(2+2\delta-\nu\right)+\chi_2\left(2-2\delta-\nu\right)\right], \tag{6.17}
$$

and the LO (2PN) spin-spin part

$$
\begin{aligned}
\hat{H}^{\mathrm{SS}}_{\mathrm{EOB}}=\frac{1}{2c^4r^3}\Bigg\{&\chi_1^2\left[X_1^4\left(1-\frac{p_\phi^2}{r}+rp_r^2\right)-C_{1\mathrm{ES}^2}X_1^2\right]+\chi_2^2\left[X_2^4\left(1-\frac{p_\phi^2}{r}+rp_r^2\right)-C_{2\mathrm{ES}^2}X_2^2\right]\\
&+2\chi_1\chi_2\left[(\nu-1)\nu-\frac{\nu^2p_\phi^2}{r}+\nu^2rp_r^2\right]\Bigg\},
\end{aligned} \tag{6.18}
$$

where $C_{i\mathrm{ES}^2}$ are the spin quadrupole constants, which equal one for BHs.

The orbital frequency expanded to 2PN is given by

$$
\begin{aligned}
\Omega\equiv\dot{\phi}&=\frac{\partial\hat{H}_{\mathrm{EOB}}}{\partial p_\phi}\\
&=\frac{p_\phi}{r^2}+\frac{p_\phi}{c^2}\left[\frac{\nu-1}{r^3}-\frac{(\nu+1)p^2}{2r^2}\right]+\frac{1}{2c^3r^3}\left[\chi_1(2+2\delta-\nu)+\chi_1(2-2\delta-\nu)\right]\\
&\quad+\frac{p_\phi}{c^4}\left[\frac{3\left(\nu^2+\nu+1\right)p^4}{8r^2}+\frac{\left(-3\nu^2+\nu+1\right)p^2}{2r^3}+\frac{(\nu+1)p_r^2}{r^3}-\frac{-3\nu^2+\nu+1}{2r^4}\right]\\
&\quad-\frac{p_\phi}{c^4r^4}\left(2\nu^2\chi_1\chi_2+\chi_1^2X_1^4+\chi_2^2X_2^4\right)
\end{aligned} \tag{6.19}
$$

From the EOM $\dot{p}_r=-\partial\hat{H}/\partial r$, we can obtain an expression for $p_\phi(r,\dot{p}_r,p_r)$

$$
\begin{aligned}
\frac{p_\phi^2}{r}&=1+r^2\dot{p}_r+\frac{1}{2c^2r}\Big[6+(\nu+1)r^4\dot{p}_r^2-(\nu-5)r^2\dot{p}_r+rp_r^2\left((\nu+1)r^2\dot{p}_r+4\right)\Big]\\
&\quad-\frac{3\sqrt{r^3\dot{p}_r+r}}{2c^3r^2}\left[\chi_1(2+2\delta-\nu)+\chi_2(2-2\delta-\nu)\right]\\
&\quad+\frac{1}{8c^4r^2}\Big[\left(\nu^2+5\nu+1\right)r^6\dot{p}_r^3-\left(\nu^2-\nu+1\right)r^4p_r^4\dot{p}_r+2(5\nu+8)r^4\dot{p}_r^2-24(\nu-3)\\
&\qquad-\left(\nu^2+7\nu-63\right)r^2\dot{p}_r+2\left(8-24\nu+3\nu r^4\dot{p}_r^2\right)rp_r^2+2\left(\nu^2+\nu+3\right)p_r^2r^3\dot{p}_r\Big]\\
&\quad+\frac{1}{2c^4r^2}\Big\{\chi_1^2\left[3C_{1\mathrm{ES}^2}X_1^2+X_1^4\left(1+4r^2\dot{p}_r-2rp_r^2\right)\right]
\end{aligned}
$$

$$+\chi_2^2\left[3C_{2\mathrm{ES}^2}X_2^2+X_2^4\left(1+4r^2\dot{p}_r-2rp_r^2\right)\right]+\nu\chi_1\chi_2\left[2\left(\nu+4\nu r^2\dot{p}_r+3\right)-4\nu rp_r^2\right]\Bigg\}, \tag{6.20}$$

which we use to express the noncircular part of the RR force and modes in terms of p_r and $\dot{p}_r$. It will also be useful below, when taking the circular-orbit limit, to have an expression for p_ϕ as a function of r for circular orbits. Setting $\dot{p}_r = 0 = p_r$ in the previous equation yields

$$\begin{aligned}\frac{p_\phi^2}{r} \overset{\text{circ}}{=} & 1+\frac{3}{c^2 r}+\frac{3(3-\nu)}{c^4 r^2}-\frac{3}{2c^3 r^{3/2}}\left[\chi_1\left(-2\delta+\nu-2\right)+\chi_2\left(2\delta+\nu-2\right)\right] \\ & +\frac{1}{2c^4 r^2}\left[\chi_1^2\left(3C_{1\mathrm{ES}^2}X_1^2+X_1^4\right)+2\nu\chi_1\chi_2\left(3+\nu\right)+\chi_2^2\left(3C_{2\mathrm{ES}^2}X_2^2+X_2^4\right)\right].\end{aligned} \tag{6.21}$$

6.2.3 Energy and angular momentum fluxes

The energy and angular momentum fluxes for nonspinning binaries were derived to 3PN order in harmonic and Arnowitt-Deser-Misner (ADM) coordinates in Refs. [155–157]. The 2PN instantaneous part of the fluxes for nonspinning bodies is given in EOB coordinates in Appendix A of Ref. [402]. The leading order reads

$$\begin{aligned}\Phi_E^{\text{inst}} &= \frac{8\nu^2}{15r^4}\left(12p^2-11p_r^2\right)+\mathcal{O}\left(\frac{1}{c^2}\right), \\ \Phi_J^{\text{inst}} &= \frac{8\nu^2}{5r^3}p_\phi\left(2p^2-3p_r^2+\frac{2}{r}\right)+\mathcal{O}\left(\frac{1}{c^2}\right).\end{aligned} \tag{6.22}$$

The hereditary contributions to the fluxes can be expressed as an infinite sum over Bessel functions [156, 403] that can be evaluated numerically, or resummed analytically [160, 613]. Here, we follow the method from Ref. [403] to obtain the LO tail part (1.5 PN) of the orbit-averaged fluxes in an eccentricity expansion and we extend their derivation to $\mathcal{O}(e^6)$, which yields[3]

$$
\begin{aligned}
\left\langle\Phi_E^{\text{tail}}\right\rangle &= \frac{128\pi\nu^2}{5c^3}x^{13/2}\left[1+\frac{2335}{192}e^2+\frac{42955}{768}e^4+\frac{6204647}{36864}e^6+\mathcal{O}(e^8)\right],\\
\left\langle\Phi_J^{\text{tail}}\right\rangle &= \frac{128\pi\nu^2}{5c^3}x^{5}\left[1+\frac{209}{32}e^2+\frac{2415}{128}e^4+\frac{730751}{18432}e^6+\mathcal{O}(e^8)\right],
\end{aligned}
\tag{6.24}
$$

where $x \equiv \Omega^{2/3}$. The eccentricity e in these equations is defined using the Keplerian parametrization, which is given by

$$
r = \frac{1}{u_p(1+e\cos\chi)}\,,
\tag{6.25}
$$

where u_p is the inverse semilatus rectum and χ is the relativistic anomaly.

Since we are not using the adiabatic approximation and are not working with orbit-averaged fluxes, we can obtain an approximate expression for the tail contribution to the fluxes by writing an ansatz in terms of (r, p_r, p_ϕ) in a p_r expansion of the form

$$
\begin{aligned}
\Phi_E^{\text{tail}} &= \frac{128\pi\nu^2 p_\phi}{5c^3r^4}\left[\frac{1}{r^3}+c_1\frac{p_r^2}{r^2}+c_2\frac{p_r^4}{r}+c_3p_r^6+\mathcal{O}(p_r^8)\right],\\
\Phi_J^{\text{tail}} &= \frac{128\pi\nu^2}{5c^3r^2}\left[\frac{1}{r^3}+c_4\frac{p_r^2}{r^2}+c_5\frac{p_r^4}{r}+c_6p_r^6+\mathcal{O}(p_r^8)\right],
\end{aligned}
\tag{6.26}
$$

calculate the average of that ansatz in terms of (e, x) (see Appendix I), and then match it to the average flux in Eq. (6.24) to determine the unknowns c_n. This yields

$$
\begin{aligned}
\Phi_E^{\text{tail}} &= \frac{128\pi\nu^2 p_\phi}{5c^3r^4}\left[\frac{1}{r^3}+\frac{415p_r^2}{96r^2}+\frac{5p_r^4}{288r}-\frac{73p_r^6}{11520}+\mathcal{O}(p_r^8)\right],\\
\Phi_J^{\text{tail}} &= \frac{128}{5c^3r^2}\pi\nu^2\left[\frac{1}{r^3}+\frac{49p_r^2}{16r^2}-\frac{49p_r^6}{5760}+\mathcal{O}(p_r^8)\right].
\end{aligned}
\tag{6.27}
$$

[3] Calculating the tail contribution to the fluxes is similar to that for the waveform modes (see Sec. 6.4.2) except for using the integrals [130]

$$
\begin{aligned}
\Phi_E^{\text{tail}} &= \frac{4}{5}I_{ij}^{(3)}\int_0^\infty d\tau\, I_{ij}^{(5)}(t-\tau)\ln\left(\frac{\tau}{b}\right),\\
\Phi_J^{\text{tail}} &= \frac{4}{5}\epsilon_{zij}\left[I_{il}^{(2)}\int_0^\infty d\tau\, I_{jl}^{(5)}(t-\tau)\ln\left(\frac{\tau}{b}\right)+I_{jl}^{(3)}\int_0^\infty d\tau\, I_{il}^{(4)}(t-\tau)\ln\left(\frac{\tau}{b}\right)\right],
\end{aligned}
\tag{6.23}
$$

where I_{ij} is the mass quadrupole moment, and $b = 2r_0\mathrm{e}^{-11/12}$ with r_0 a gauge parameter.

The LO (1.5PN) SO fluxes for generic orbits and generic spins were derived in Refs. [164, 167]. (The next-to-leading-order (NLO) SO energy flux was derived in Ref. [174].) It should be noted that Ref. [164] used the Tulczyjew-Dixon (covariant) spin supplementary condition (SSC) [96, 361–363], while Ref. [167] used the Newton-Wigner (NW), or canonical, SSC [364, 365]. In this paper, we use the NW SSC since we are working in a canonical Hamiltonian formulation of the spinning two-body dynamics [366, 557]. Changing the velocities in Eq. (17) of Ref. [167] to momenta, which involves spin-orbit terms, the aligned-spin fluxes reduce to

$$\begin{aligned}
\Phi_E^{\rm SO} &= \frac{4\nu^2 p_\phi}{15c^3r^6}\left\{\chi_1\left[p^2(36\nu-37-37\delta)+\frac{4(9+9\delta-4\nu)}{r}+9p_r^2(3+3\delta-2\nu)\right]+1\leftrightarrow 2\right\},\\
\Phi_J^{\rm SO} &= \frac{4\nu^2}{15c^3r^3}\left\{\chi_1\left[p^4(8\nu-9\delta-9)+\frac{9+9\delta-4\nu}{r^2}+(9+9\delta-24\nu)p^2p_r^2\right.\right.\\
&\qquad\left.\left.-(17+17\delta+6\nu)\frac{p_r^2}{r}+15\nu p_r^4+(11+11\delta+10\nu)\frac{p^2}{r}\right]+1\leftrightarrow 2\right\}.
\end{aligned} \tag{6.28}$$

For the LO (2PN) SS contributions, the LO spin$_1$-spin$_2$ energy and angular momentum fluxes in harmonic coordinates were derived in Refs. [164, 168], while the spin-squared energy flux was derived in Refs. [177, 179], and we obtain in Appendix G the spin-squared angular momentum flux. Transforming from harmonic to EOB coordinates, using the transformations in Appendix F, we get the following SS contributions to the fluxes for aligned-spins:

$$\begin{aligned}
\Phi_E^{\rm SS} &= \frac{\nu^2}{15c^4r^6}\left\{\chi_1^2\Big[\left(149\delta-280\nu\delta+280\nu^2-578\nu+149\right)p_r^2+C_{1\rm ES^2}(\delta-2\nu+1)\right.\\
&\qquad\times\left(144p^2-156p_r^2\right)+3\left(96\nu\delta-47\delta-96\nu^2+190\nu-47\right)p^2\Big]\\
&\qquad\left.+\nu\chi_1\chi_2\left[10(28\nu-33)p_r^2-6(48\nu-47)p^2\right]+1\leftrightarrow 2\right\}.\\
\Phi_J^{\rm SS} &= \frac{\nu^2 p_\phi}{5c^4r^5}\left\{\chi_1^2\Big[\left(32\nu\delta-15\delta-32\nu^2+62\nu-15\right)\frac{1}{r}+\left(\delta-2\delta\nu+2\nu^2-4\nu+1\right)\right.\\
&\qquad\times\left(22p_r^2-20p^2\right)+C_{1\rm ES^2}(\delta-2\nu+1)\left(12p^2-30p_r^2+\frac{24}{r}\right)\Big]\\
&\qquad\left.+\nu\chi_1\chi_2\left[\frac{2(23-16\nu)}{r}-8(5\nu-3)p^2+4(11\nu-15)p_r^2\right]+1\leftrightarrow 2\right\}.
\end{aligned} \tag{6.29}$$

The total 2PN energy and angular momentum fluxes are the sum of all the above contributions, i.e.,

$$\Phi_E = \Phi_E^{\text{inst}} + \Phi_E^{\text{tail}} + \Phi_E^{\text{SO}} + \Phi_E^{\text{SS}},$$
$$\Phi_J = \Phi_J^{\text{inst}} + \Phi_J^{\text{tail}} + \Phi_J^{\text{SO}} + \Phi_J^{\text{SS}}. \tag{6.30}$$

6.2.4 Ansatz for the Schott terms

As an ansatz for the Schott terms E_{Schott} and J_{Schott}, we consider

$$\begin{aligned}
J_{\text{Schott}}^{\text{inst}} &= \frac{\nu^2 p_r p_\phi}{r^2}\bigg[\alpha_1 + \frac{1}{c^2}\left(\alpha_2 p_r^2 + \alpha_3 p^2 + \frac{\alpha_4}{r}\right) \\
&\quad + \frac{1}{c^4}\bigg(\alpha_5 p_r^4 + \alpha_6 p^2 p_r^2 + \alpha_7 \frac{p_r^2}{r} + \alpha_8 p^4 + \alpha_9 \frac{p^2}{r} + \frac{\alpha_{10}}{r^2}\bigg)\bigg], \\
E_{\text{Schott}}^{\text{inst}} &= \frac{\nu^2 p_r}{r^2}\bigg[\beta_1 p_r^2 + \beta_2 p^2 + \frac{\beta_3}{r} + \frac{1}{c^2}\bigg(\beta_4 p_r^4 + \beta_5 p^2 p_r^2 + \beta_6 \frac{p_r^2}{r} + \beta_7 p^4 + \beta_8 \frac{p^2}{r} + \frac{\beta_9}{r^2}\bigg) \\
&\quad + \frac{1}{c^4}\bigg(\beta_{10} p_r^6 + \beta_{11} p^2 p_r^4 + \beta_{12} \frac{p_r^4}{r} + \beta_{13} p^4 p_r^2 + \beta_{14} \frac{p^2 p_r^2}{r} + \beta_{15} \frac{p_r^2}{r^2} \\
&\qquad + \beta_{16} p^6 + \beta_{17} \frac{p^4}{r} + \beta_{18} \frac{p^2}{r^2} + \frac{\beta_{19}}{r^3}\bigg)\bigg].
\end{aligned} \tag{6.31}$$

Note that this ansatz for E_{Schott} is more general than the one used in Eq. (4.4) of Ref. [402], since we found that such an ansatz is needed for the RR force to satisfy the conditions in Eq. (6.11).

For the LO tail, we use the ansatz

$$\begin{aligned}
J_{\text{Schott}}^{\text{tail}} &= \frac{\pi \nu^2 p_r}{c^3 r^2}\left(\lambda_1 p_r^2 + \lambda_2 p^2 + \frac{\lambda_3}{r}\right), \\
E_{\text{Schott}}^{\text{tail}} &= \frac{\pi \nu^2 p_\phi p_r}{c^3 r^4}\left(\lambda_4 p_r^2 + \lambda_5 p^2 + \frac{\lambda_6}{r}\right),
\end{aligned} \tag{6.32}$$

while for the LO SO part,

$$J_{\text{Schott}}^{\text{SO}} = \frac{\nu^2 p_r}{c^3 r^2}\bigg[\chi_1\left(\sigma_1 p_r^2 + \sigma_2 p^2 + \frac{\sigma_3}{r}\right) + \chi_2\left(\sigma_4 p_r^2 + \sigma_5 p^2 + \frac{\sigma_6}{r}\right)\bigg],$$

$$E^{\rm SO}_{\rm Schott} = \frac{\nu^2 p_r p_\phi}{c^3 r^4}\left[\chi_1\left(\sigma_7 p_r^2 + \sigma_8 p^2 + \frac{\sigma_9}{r}\right) + \chi_2\left(\sigma_{10} p_r^2 + \sigma_{11} p^2 + \frac{\sigma_{12}}{r}\right)\right], \tag{6.33}$$

and for the SS part,

$$\begin{aligned}
J^{\rm SS}_{\rm Schott} &= \frac{\nu^2 p_\phi p_r}{c^4 r^4}\left[\chi_1^2\left(\zeta_1 + C_{1{\rm ES}^2}\zeta_2\right) + \chi_1\chi_2\zeta_3 + \chi_2^2\left(\zeta_4 + C_{2{\rm ES}^2}\zeta_5\right)\right],\\
E^{\rm SS}_{\rm Schott} &= \frac{\nu^2 p_r}{c^4 r^4}\left[\chi_1^2\left(\zeta_6 p_r^2 + \zeta_7 p^2 + \frac{\zeta_8}{r}\right) + \chi_1^2 C_{1{\rm ES}^2}\left(\zeta_9 p_r^2 + \zeta_{10} p^2 + \frac{\zeta_{11}}{r}\right)\right.\\
&\quad + \chi_1\chi_2\left(\zeta_{12} p_r^2 + \zeta_{13} p^2 + \frac{\zeta_{14}}{r}\right) + \chi_2^2\left(\zeta_{15} p_r^2 + \zeta_{16} p^2 + \frac{\zeta_{17}}{r}\right)\\
&\quad \left. + \chi_2^2 C_{2{\rm ES}^2}\left(\zeta_{18} p_r^2 + \zeta_{19} p^2 + \frac{\zeta_{20}}{r}\right)\right].
\end{aligned} \tag{6.34}$$

The total energy and angular momentum Schott terms are the sum of the above contributions, i.e.

$$\begin{aligned}
J_{\rm Schott} &= J^{\rm inst}_{\rm Schott} + J^{\rm tail}_{\rm Schott} + J^{\rm SO}_{\rm Schott} + J^{\rm SS}_{\rm Schott},\\
E_{\rm Schott} &= E^{\rm inst}_{\rm Schott} + E^{\rm tail}_{\rm Schott} + E^{\rm SO}_{\rm Schott} + E^{\rm SS}_{\rm Schott}.
\end{aligned} \tag{6.35}$$

Note that when taking the time derivative of these Schott terms using the EOMs, the LO nonspinning part contributes to the LO SO and SS parts of the RR force.

6.2.5 Solving for the eccentric-orbits RR force

Using the fluxes and the Schott terms, the RR force can be calculated from the balance equations (6.12), which fix some of the unknowns in the ansatz for the Schott terms. The remaining unknowns can be determined by requiring that the RR force satisfies the conditions (6.13) in the circular-orbits limit.

6.2.5.1 Leading order

At leading order, calculating the RR force with the ansatz in Eqs. (6.31) and expanding in p_r gives

$$\mathcal{F}_r = \frac{\nu^2}{5p_r r^3}\left(p^2 - \frac{1}{r}\right)\left[p^2\left(5\alpha_1 - 5\beta_2 + 16\right) - 5\frac{\beta_3}{r}\right] + \mathcal{O}(p_r). \tag{6.36}$$

Requiring that the $1/p_r$ term is zero, leads to the solution

$$\beta_3 = 0, \qquad \alpha_1 = \frac{1}{5}(5\beta_2 - 16). \tag{6.37}$$

Expanding $\mathcal{F}_r p_\phi/(\mathcal{F}_\phi p_r) - 1$ in p_r yields

$$\frac{\mathcal{F}_r p_\phi}{\mathcal{F}_\phi p_r} - 1 = \frac{9\left(5\beta_1 - 8\right)p^2 - \left(45\beta_1 + 30\beta_2 + 88\right)/r}{15\beta_2 p^2 + 3\left(32 - 5\beta_2\right)/r} + \mathcal{O}(p_r^2). \tag{6.38}$$

Requiring that the first term in that series expansion is zero gives the solution

$$\beta_1 = \frac{8}{5}, \quad \beta_2 = -\frac{16}{3}, \quad \alpha_1 = -\frac{128}{15}. \tag{6.39}$$

With that solution, we obtain the LO RR force

$$\begin{aligned}
\mathcal{F}_\phi^{\rm LO} &= \frac{8\nu^2}{15r^3}p_\phi\left(10p^2 - 39p_r^2 - \frac{22}{r}\right), \\
\mathcal{F}_r^{\rm LO} &= -\frac{16\nu^2}{15r^3}p_r\left(-5p^2 + 12p_r^2 + \frac{11}{r}\right).
\end{aligned} \tag{6.40}$$

This force satisfies the conditions in Eq. (6.13) for circular orbits since

$$\begin{aligned}
\mathcal{F}_\phi^{\rm LO} &= -\Phi_J^{\rm LO} - \frac{128}{15r^3}p_\phi\nu^2\left(2p_r^2 - \dot{p}_r r\right), \\
\frac{\mathcal{F}_r^{\rm LO}p_\phi}{\mathcal{F}_\phi^{\rm LO}p_r} &= 1 + \frac{15p_r^2}{10p^2 - 39p_r^2 - 22/r}.
\end{aligned} \tag{6.41}$$

6.2.5.2 1PN

Following the same steps as above, we obtain the following solution for the unknowns at 1PN:

$$\begin{aligned}
\beta_8 &= \frac{1}{15}\left(371 - 15\alpha_3 + 268\nu\right), \qquad \alpha_2 = \frac{1}{35}\left(35\beta_5 + 108\nu - 22\right), \\
\beta_6 &= \frac{2}{315}\left(105\alpha_3 - 1760\nu + 1743\right), \qquad \beta_9 = -\frac{32}{105}(4\nu - 1), \\
\beta_7 &= \alpha_3 + \frac{2}{35}(4\nu + 93), \qquad \alpha_4 = \frac{893}{21} - \alpha_3 + \frac{2924\nu}{105},
\end{aligned} \tag{6.42}$$

with 3 arbitrary coefficients out of 9 coefficients at that order. To simplify the resulting expressions for the RR force, we choose to set all arbitrary coefficients to zero, i.e. $\alpha_3 = \beta_4 = \beta_5 = 0$, which yields the following 1PN contribution to the RR force:

$$\begin{aligned}
\mathcal{F}_\phi^{\rm 1PN} &= \frac{\nu^2 p_\phi}{105 c^2 r^3}\Bigg[18(4\nu + 93)p_r^2 p^2 - 6(4\nu + 93)p^4 + 180(7\nu - 5)p_r^4 \\
&\quad + (9780\nu + 19198)\frac{p_r^2}{r} - (484\nu + 3833)\frac{p^2}{r} + \frac{1684\nu + 6213}{r^2}\Bigg], \\
\mathcal{F}_r^{\rm 1PN} &= \frac{\nu^2 p_r}{105 c^2 r^3}\Bigg[180(7\nu - 5)p_r^4 - 6(4\nu + 93)p^4 + 4(691\nu + 3958)\frac{p_r^2}{r} \\
&\quad - 198(6\nu - 13)p_r^2 p^2 - (484\nu + 3833)\frac{p^2}{r} + \frac{1684\nu + 6213}{r^2}\Bigg].
\end{aligned} \tag{6.43}$$

6.2.5.3 LO tail

Solving for the unknowns at the LO tail contribution leads to the solution

$$\begin{gathered}
\lambda_2 = -\frac{334}{15}, \quad \lambda_3 = \frac{128}{5}, \quad \lambda_4 = -\frac{334}{15} + \lambda_1, \\
\lambda_5 = -\frac{334}{15}, \quad \lambda_6 = \frac{128}{5},
\end{gathered} \tag{6.44}$$

with either λ_1 or λ_4 arbitrary. Choosing $\lambda_1 = 0$, the tail contribution to the RR forces becomes

$$\mathcal{F}_\phi^{\text{tail}} = \frac{\pi\nu^2}{c^3 r^2}\left(\frac{334p^4}{15r} - \frac{718p^2}{15r^2} - \frac{334p^2p_r^2}{5r} - \frac{308p_r^2}{15r^2} + \frac{49p_r^6}{225}\right),$$
$$\mathcal{F}_r^{\text{tail}} = \frac{\pi\nu^2 p_\phi p_r}{c^3 r^4}\left(\frac{334p^2}{15r} - \frac{p_r^4}{18} - \frac{7034p_r^2}{45r} - \frac{718}{15r^2}\right). \tag{6.45}$$

6.2.5.4 LO spin-orbit

At LO SO, we obtain the solution

$$\begin{aligned}
\sigma_5 &= \frac{1}{15}\left(-36\delta - 32\nu + 15\sigma_{11} + 36\right),\\
\sigma_6 &= \frac{1}{15}\left(-68\delta - 40\nu + 15\sigma_{12} + 68\right),\\
\sigma_2 &= \frac{1}{15}\left(36\delta - 32\nu + 15\sigma_8 + 36\right),\\
\sigma_3 &= \frac{1}{15}\left(68\delta - 40\nu + 15\sigma_9 + 68\right),\\
\sigma_{12} &= \frac{8}{15}(4\delta + 3\nu - 4),\\
\sigma_9 &= -\frac{8}{15}(4\delta - 3\nu + 4),\\
\sigma_4 &= \frac{1}{15}\left(-6\delta + 44\nu + 15\sigma_{10} + 6\right),\\
\sigma_1 &= \frac{1}{15}\left(6\delta + 44\nu + 15\sigma_7 + 6\right),\\
\sigma_{11} &= -\frac{2}{15}(9\delta + 22\nu - 9),\\
\sigma_8 &= \frac{2}{15}(9\delta - 22\nu + 9)
\end{aligned} \tag{6.46}$$

where either σ_1 or σ_7 is arbitrary, and either σ_4 or σ_{10} is arbitrary. Choosing $\sigma_7 = \sigma_{10} = 0$, we obtain

$$\mathcal{F}_\phi^{\text{SO}} = \frac{2\nu^2}{15c^3r^3}\chi_1\Bigg[p^4(22\nu - 9\delta - 9) + 5(3 + 3\delta + 16\nu)p_r^4 + (66\nu - 23\delta - 23)\frac{p_r^2}{r}$$
$$+ (179 + 179\delta - 146\nu)\frac{p^2}{r} + 6(9 + 9\delta - 22\nu)p^2p_r^2\Bigg] + 1 \leftrightarrow 2. \tag{6.47}$$

$$\mathcal{F}_r^{\rm SO} = \frac{2\nu^2 p_r p_\phi}{15c^3 r^5}\chi_1\left[\frac{179\delta - 146\nu + 179}{r} + (22\nu - 9\delta - 9)p^2 - 5(3+3\delta+16\nu)p_r^2\right] + 1 \leftrightarrow 2. \tag{6.48}$$

6.2.5.5 2PN no spin

At 2PN, we obtain

$$\begin{aligned}
\alpha_6 &= \beta_{13} - \frac{463\nu^2}{63} - \frac{1909\nu}{315} + \frac{922}{315}, \\
\beta_{15} &= -\frac{2\beta_{18}}{3} + \frac{1060\nu^2}{189} - \frac{12116\nu}{189} - \frac{347236}{2835}, \\
\beta_{16} &= -\beta_{17} - \beta_{18} - \frac{5276\nu^2}{315} - \frac{109609\nu}{630} + \frac{9175}{378}, \\
\beta_{14} &= \alpha_7 - \frac{2\beta_{17}}{3} - \frac{2\beta_{18}}{3} + \frac{244\nu^2}{45} - \frac{12466\nu}{135} - \frac{28204}{2835}, \\
\beta_{19} &= -\frac{640\nu^2}{189} + \frac{416\nu}{35} - \frac{2608}{945}, \\
\alpha_8 &= -\beta_{17} - \beta_{18} - \frac{5018\nu^2}{315} - \frac{105491\nu}{630} + \frac{52223}{1890}, \\
\alpha_{10} &= \beta_{18} - \frac{92\nu^2}{9} - \frac{309\nu}{5} - \frac{10019}{315}, \\
\alpha_9 &= \beta_{17} - \frac{78\nu^2}{7} + \frac{1201\nu}{90} + \frac{5711}{126},
\end{aligned} \tag{6.49}$$

with 8 arbitrary coefficients out of 16. Choosing $\alpha_5 = \alpha_7 = \beta_{10} = \beta_{11} = \beta_{12} = \beta_{13} = \beta_{17} = \beta_{18} = 0$ yields

$$\begin{aligned}
\mathcal{F}_\phi^{\rm 2PN} = \frac{\nu^2 p_\phi}{c^4 r^3}\Bigg\{&\left(\frac{5276\nu^2}{315} + \frac{109609\nu}{630} - \frac{9175}{378}\right)p^6 + \left(\frac{1519}{54} - \frac{9964\nu^2}{315} - \frac{100847\nu}{630}\right)\frac{p^4}{r} \\
&+ \left(\frac{3512\nu^2}{315} - \frac{4234\nu}{45} + \frac{3355}{21}\right)\frac{p^2}{r^2} + \left(\frac{9175}{126} - \frac{5276\nu^2}{105} - \frac{109609\nu}{210}\right)p^4 p_r^2 \\
&+ \left(\frac{104296}{945} - \frac{15121\nu^2}{105} - \frac{254732\nu}{315}\right)\frac{p_r^2 p^2}{r} + \left(\frac{52}{3} - \frac{152\nu^2}{9} - \frac{310\nu}{9}\right)p_r^6 \\
&+ \left(-\frac{185\nu^2}{63} + \frac{2171\nu}{63} - \frac{269}{63}\right)p_r^4 p^2 + \left(\frac{4112}{35} - \frac{278\nu^2}{45} + \frac{344\nu}{35}\right)\frac{p_r^4}{r} \\
&+ \left(-\frac{1604\nu^2}{315} - \frac{2054\nu}{7} - \frac{8803}{21}\right)\frac{p_r^2}{r^2} + \left(\frac{8\nu^2}{15} + \frac{9728\nu}{315} - \frac{190244}{2835}\right)\frac{1}{r^3}\Bigg\},
\end{aligned} \tag{6.50}$$

$$\mathcal{F}_r^{\text{2PN}} = \frac{\nu^2 p_r}{c^4 r^3}\left\{\left(\frac{5276\nu^2}{315} + \frac{109609\nu}{630} - \frac{9175}{378}\right)p^6 + \left(\frac{1519}{54} - \frac{9964\nu^2}{315} - \frac{100847\nu}{630}\right)\frac{p^4}{r}\right.$$
$$+ \left(\frac{3512\nu^2}{315} - \frac{4234\nu}{45} + \frac{3355}{21}\right)\frac{p^2}{r^2} + \left(\frac{9713}{126} - \frac{2129\nu^2}{45} - \frac{350537\nu}{630}\right)p^4 p_r^2$$
$$+ \left(\frac{26459}{945} - \frac{1745\nu^2}{63} - \frac{449227\nu}{315}\right)\frac{p_r^2 p^2}{r} + \left(\frac{52}{3} - \frac{152\nu^2}{9} - \frac{310\nu}{9}\right)p_r^6$$
$$+ \left(\frac{293\nu^2}{21} + \frac{1447\nu}{21} - \frac{1361}{63}\right)p_r^4 p^2 + \left(\frac{41612}{315} - \frac{1894\nu^2}{45} + \frac{28648\nu}{315}\right)\frac{p_r^4}{r}$$
$$\left. + \left(\frac{34528\nu^2}{945} - \frac{481624\nu}{945} - \frac{18761}{45}\right)\frac{p_r^2}{r^2} + \left(\frac{8\nu^2}{15} + \frac{9728\nu}{315} - \frac{190244}{2835}\right)\frac{1}{r^3}\right\}. \quad (6.51)$$

6.2.5.6 LO spin-spin

At LO SS, we obtain the unique solution

$$\zeta_1 = \frac{1}{30}\left[\delta(73 - 128\nu) + 128\nu^2 - 274\nu + 73\right],$$
$$\zeta_2 = -\frac{42}{5}(\delta - 2\nu + 1), \quad \zeta_3 = \frac{2}{15}\nu(64\nu - 261),$$
$$\zeta_4 = \frac{1}{30}\left[\delta(128\nu - 73) + 128\nu^2 - 274\nu + 73\right],$$
$$\zeta_5 = \frac{42}{5}(\delta + 2\nu - 1),$$
$$\zeta_6 = -\frac{74}{15}\left(-2\delta\nu + \delta + 2\nu^2 - 4\nu + 1\right),$$
$$\zeta_7 = \frac{1}{10}\left[\delta(43 - 80\nu) + 80\nu^2 - 166\nu + 43\right],$$
$$\zeta_8 = 0, \qquad \zeta_9 = 2(\delta - 2\nu + 1),$$
$$\zeta_{10} = -6(\delta - 2\nu + 1), \qquad \zeta_{11} = 0,$$
$$\zeta_{12} = \frac{8}{15}(15 - 37\nu)\nu, \qquad \zeta_{13} = \frac{2}{5}\nu(40\nu - 63),$$
$$\zeta_{14} = 0, \qquad \zeta_{15} = -\frac{74}{15}\left[\delta(2\nu - 1) + 2\nu^2 - 4\nu + 1\right],$$
$$\zeta_{16} = \frac{1}{10}\left[\delta(80\nu - 43) + 80\nu^2 - 166\nu + 43\right],$$
$$\zeta_{17} = 0, \qquad \zeta_{18} = -2(\delta + 2\nu - 1),$$

$$\zeta_{19} = 6(\delta + 2\nu - 1), \qquad \zeta_{20} = 0. \tag{6.52}$$

With that solution, we get

$$\begin{aligned}
\mathcal{F}_\phi^{\rm SS} = \frac{\nu^2 p_\phi}{30 c^4 r^5} \Bigg\{ & \chi_1^2 \Bigg[24 X_1^2 C_{1\rm ES^2} \left(15 p^2 - 90 p_r^2 - \frac{49}{r} \right) \\
& + \left(361\delta - 632\nu\delta + 632\nu^2 - 1354\nu + 361 \right) p_r^2 \\
& + \left(400\nu\delta - 209\delta - 400\nu^2 + 818\nu - 209 \right) p^2 \\
& + \left(355\delta - 704\nu\delta + 704\nu^2 - 1414\nu + 355 \right) \frac{1}{r} \Bigg] \\
& + \nu\chi_1\chi_2 \left[(378 - 400\nu) p^2 + (632\nu - 2250) p_r^2 + \frac{704\nu - 1182}{r} \right] + 1 \leftrightarrow 2 \Bigg\},
\end{aligned} \tag{6.53}$$

$$\begin{aligned}
\mathcal{F}_r^{\rm SS} = \frac{\nu^2 p_r}{30 c^4 r^5} \Bigg\{ & \chi_1^2 \Bigg[24 X_1^2 C_{1\rm ES^2} \left(15 p^2 - 55 p_r^2 - \frac{49}{r} \right) \\
& + \left(301\delta - 512\delta\nu + 512\nu^2 - 1114\nu + 301 \right) p_r^2 \\
& + \left(400\nu\delta - 209\delta - 400\nu^2 + 818\nu - 209 \right) p^2 \\
& + \left(355\delta - 704\delta\nu + 704\nu^2 - 1414\nu + 355 \right) \frac{1}{r} \Bigg] \\
& + \nu\chi_1\chi_2 \left[(378 - 400\nu) p^2 + (512\nu - 1410) p_r^2 + \frac{704\nu - 1182}{r} \right] + 1 \leftrightarrow 2 \Bigg\}.
\end{aligned} \tag{6.54}$$

6.2.6 Factorizing the RR force into circular and noncircular parts

The total RR force is the sum of the contributions calculated in the previous section, i.e.,

$$\begin{aligned}
\mathcal{F}_\phi &= \mathcal{F}_\phi^{\rm LO} + \mathcal{F}_\phi^{\rm 1PN} + \mathcal{F}_\phi^{\rm 2PN} + \mathcal{F}_\phi^{\rm tail} + \mathcal{F}_\phi^{\rm SO} + \mathcal{F}_\phi^{\rm SS}, \\
\mathcal{F}_r &= \mathcal{F}_r^{\rm LO} + \mathcal{F}_r^{\rm 1PN} + \mathcal{F}_r^{\rm 2PN} + \mathcal{F}_r^{\rm tail} + \mathcal{F}_r^{\rm SO} + \mathcal{F}_r^{\rm SS}.
\end{aligned} \tag{6.55}$$

We have checked that our gauge-dependent RR force agrees with that in Refs. [167, 168, 402] by using the balance equations. Denoting the RR force from those references by $(\bar{\mathcal{F}}_r, \bar{\mathcal{F}}_\phi)$ with corresponding Schott terms $(\bar{E}_{\text{Schott}}, \bar{J}_{\text{Schott}})$, Eqs. (6.7) lead to

$$\dot{\bar{r}}\bar{\mathcal{F}}_r + \dot{\bar{\phi}}\bar{\mathcal{F}}_\phi + \dot{\bar{E}}_{\text{Schott}} = \dot{r}\mathcal{F}_r + \dot{\phi}\mathcal{F}_\phi + \dot{E}_{\text{Schott}},$$
$$\bar{\mathcal{F}}_\phi + \dot{\bar{J}}_{\text{Schott}} = \mathcal{F}_\phi + \dot{J}_{\text{Schott}}. \tag{6.56}$$

Then, by writing an ansatz for $(\bar{E}_{\text{Schott}}, \bar{J}_{\text{Schott}})$ with unknown coefficients, we checked that a solution exists, implying that $(\mathcal{F}_r, \mathcal{F}_\phi)$ and $(\bar{\mathcal{F}}_r, \bar{\mathcal{F}}_\phi)$ are related via a coordinate transformation.

To implement our results in the `SEOBNRv4HM` model, we factorize the RR force into a quasi-circular part times eccentric corrections as in Eqs. (6.14) and (6.11), which read

$$\mathcal{F}_\phi = \mathcal{F}_\phi^{\text{qc}}\mathcal{F}_\phi^{\text{ecc}}, \qquad \mathcal{F}_r = \mathcal{F}_r^{\text{qc}}\mathcal{F}_r^{\text{ecc}},$$
$$\mathcal{F}_\phi^{\text{qc}} = -\frac{\Phi_E^{\text{qc}}}{\Omega}, \qquad \mathcal{F}_r^{\text{qc}} = -\frac{\Phi_E^{\text{qc}} p_r}{\Omega p_\phi}, \tag{6.57}$$

and for the quasi-circular part we use the unexpanded force used in `SEOBNRv4HM`, in which the energy flux has the following PN expansion in terms of the orbital velocity $v_\Omega \equiv \Omega^{1/3}$:

$$\begin{aligned}\frac{\Phi_E^{\text{qc}}}{\nu^2} &= \frac{32}{5}v_\Omega^{10} - \frac{2}{105c^2}(980\nu + 1247)v_\Omega^{12} + \frac{128\pi}{5c^3}v_\Omega^{13}\\ &+ \frac{4v_\Omega^{13}}{5c^3}\left[\chi_1(12\nu - 11\delta - 11) + \chi_2(12\nu + 11\delta - 11)\right]\\ &+ \frac{2}{2835c^4}v_\Omega^{14}\left(32760\nu^2 + 166878\nu - 44711\right)\\ &+ \frac{2}{5c^4}v_\Omega^{14}\left[(32C_{1\text{ES}^2} + 1)\chi_1^2X_1^2 + 62\nu\chi_1\chi_2 + (32C_{2\text{ES}^2} + 1)\chi_2^2X_2^2\right].\end{aligned} \tag{6.58}$$

This leads to the eccentric part

$$\mathcal{F}_\phi^{\text{ecc}} = \frac{29p_r^2r - 10\dot{p}_r r^2 + 12}{12\left(\dot{p}_r r^2 + 1\right)^{2/3}} + \frac{[\dots]}{c^2 r\left(\dot{p}_r r^2 + 1\right)^{5/3}} + \dots$$
$$\mathcal{F}_r^{\text{ecc}} = \frac{7p_r^2r - 5\dot{p}_r r^2 + 6}{6\left(\dot{p}_r r^2 + 1\right)^{2/3}} + \frac{[\dots]}{c^2 r\left(\dot{p}_r r^2 + 1\right)^{5/3}} + \dots \tag{6.59}$$

The full 2PN expressions are provided in the Supplemental Material to Ref. [5].

In these eccentric corrections to the RR force, we used $\dot{p}_r$ instead of p_ϕ because it improves the agreement of our model with `SEOBNRv4HM` in the quasi-circular orbit limit, in which $p_r = 0 = \dot{p}_r$ leading to $\mathcal{F}^{\text{ecc}}_{r,\phi} = 1$. However, having $\dot{p}_r$ on the right-hand side of the EOM for p_r would complicate solving the system of differential equations (6.4). Therefore, when evolving the EOMs, we simply replace $\dot{p}_r$ in the RR force with the derivative of the Hamiltonian with respect to r calculated numerically, i.e. $\dot{p}_r \to -\partial \hat{H}_{\text{EOB}}/\partial r$.

SEOBNR waveform models use p_{r_*} (the conjugate momentum to the tortoise radial coordinate r_*) instead of p_r since it improves stability of the EOMs near the EOB event horizon [411, 582]. The two momenta are related by Eq. (J.3). In Appendix J, we also obtain Eq. (J.8) for the transformation between $\dot{p}_r$ and $\dot{p}_{r_*}$.

6.3 Initial conditions

Having determined the RR force that enters the EOMs, we need to specify the initial conditions to be used in evolving the system of equations. In this section, we first review how the initial conditions are implemented in `SEOBNRv4HM` for quasi-circular orbits [374, 381], and then discuss a simple extension for eccentric orbits.

6.3.1 Initial conditions for quasi-circular orbits

Let us recapitulate the initial conditions for quasi-circular/spherical orbits in the `SEOBNRv4HM` model as derived in Refs. [374, 381]. We start by specifying an initial orbital frequency Ω_0, with initial orbital phase $\phi_0 = 0$, and solve

$$\left[\frac{\partial H}{\partial r}\right]_0 = 0, \qquad \left[\frac{\partial H}{\partial p_\phi}\right]_0 = \Omega_0 \tag{6.60}$$

for the initial values of r and p_ϕ, while neglecting RR, $p_r \approx 0$. The initial condition for p_r is then obtained by solving

$$[\dot{r}]_0 = \left[\frac{\partial H}{\partial p_r}\right]_0 \tag{6.61}$$

for p_r, after calculating $[\dot{r}]_0$ using the result from adiabatic evolution [381]

$$[\dot{r}]_0 = \left[\frac{dp_\phi/dt}{dp_\phi/dr}\right]_0 = \left[\frac{\dot{E}}{dE/dr}\right]_0, \tag{6.62}$$

where $\dot{E}$ is the circular-orbits energy flux, and the derivative $dE/dr = dH/dr$ can be determined using the following equations for circular orbits:

$$dH = \frac{\partial H}{\partial r}dr + \frac{\partial H}{\partial p_r}dp_r + \frac{\partial H}{\partial p_\phi}dp_\phi, \tag{6.63}$$

$$p_r = 0, \quad dp_r = 0, \quad d\left(\frac{\partial H}{\partial r}\right) = 0. \tag{6.64}$$

This leads to

$$\frac{d}{dr}\frac{\partial H}{\partial r} = 0 = \frac{\partial^2 H}{\partial r^2} + \frac{\partial^2 H}{\partial r \partial p_\phi}\frac{dp_\phi}{dr}, \tag{6.65}$$

which can be solved for dp_ϕ/dr to obtain

$$\frac{dp_\phi}{dr} = -\frac{\partial^2 H/\partial r^2}{\partial^2 H/\partial r \partial p_\phi}\,. \tag{6.66}$$

Plugging that solution into $dH/dr = (\partial H/\partial p_\phi)dp_\phi/dr$ yields the result in Eq. (4.14) of Ref. [374], which reads

$$\frac{dH}{dr} = -\frac{(\partial H/\partial p_\phi)(\partial^2 H/\partial r^2)}{\partial^2 H/\partial r \partial p_\phi}, \tag{6.67}$$

and hence

$$\left[\frac{\partial H}{\partial p_r}\right]_0 = [\dot{r}]_0 = \left[-\frac{dE}{dt}\frac{\partial^2 H/\partial r \partial p_\phi}{(\partial H/\partial p_\phi)(\partial^2 H/\partial r^2)}\right]_0. \tag{6.68}$$

The complete procedure to obtain the initial conditions for the orbital phase-space is now as follows. Given Ω_0, masses, and spins, we numerically solve the relations in Eq. (6.60) for the initial values r_0 and $p_{\phi 0}$, choosing $\phi_0 = 0$ and assuming $p_r \approx 0$. Using these values, we numerically solve Eq. (6.68) for the initial value p_{r0}.

6.3.2 Initial conditions for eccentric orbits

Since eccentricity is a gauge-dependent concept, we do not need to calculate accurate initial conditions for eccentric orbits in a specific gauge. Instead, we can choose a measure for eccentricity that can be adjusted to be as convenient as possible for numerical implementation. The only strict requirement is that for zero eccentricity $e = 0$ one recovers the quasi-circular case. Hence, we can start with very accurate initial conditions for quasi-circular orbits and perturb them for eccentric orbits.

We choose to specify an initial orbital frequency Ω_0 and an initial eccentricity e_0 using the Keplerian parametrization $1/r = u_p(1 + e\cos\chi)$. We also assume that the orbit starts with $\phi_0 = 0$ at *periastron* $(\chi = 0)$, where $p_r = 0$ in absence of RR, which simplifies calculating the initial conditions for r and p_ϕ. An advantage of starting at periastron instead of apastron is that the specified initial frequency is then the maximum orbital frequency (over the first orbit), and can be used to estimate the frequency at which the binary enters a GW detector's frequency band.

To obtain r_0 and $p_{\phi 0}$, we solve Eq. (6.60) with a nonzero $\dot{p}_r$, i.e.,

$$\left[\frac{\partial H}{\partial r}\right]_0 = -\left[\dot{p}_r(p_\phi, e)\right]_0, \qquad \left[\frac{\partial H}{\partial p_\phi}\right]_0 = \Omega_0, \tag{6.69}$$

with $p_r \approx 0$, and $[\dot{p}_r]_0$ given as a 2PN expansion in terms of p_ϕ and e. For quasi-circular orbits, these equations reduce exactly to Eqs. (6.60) since $\dot{p}_r \propto e$.

To obtain the PN expansion for $\dot{p}_r$ at periastron, we first invert the Hamiltonian at the turning points $r_\pm = 1/(u_p(1 \pm e))$ with $p_r = 0$ and solve for the energy and angular momentum as functions of e and u_p, which are given by Eqs. (I.2). Then, we invert $p_\phi(e, u_p)$ to obtain Eq. (I.3) for $u_p(p_\phi, e)$ and insert it into the PN expansion for $\dot{p}_r = -\partial H/\partial r$ at periastron ($r = 1/[u_p(1+e)]$). This yields

$$
\begin{aligned}
[\dot{p}_r]_0 = {}& \frac{e_0(e_0+1)^2}{p_{\phi 0}^4} + \frac{e_0(e_0+1)^2}{2c^2 p_{\phi 0}^6}\left[e_0^2(5-\nu) - 4e_0 + \nu + 7\right] \\
& + \frac{e_0(e_0+1)^2\,(3e_0^2 - 2e_0 + 3)}{2c^3 p_{\phi 0}^7}\Big[(\nu - 2\delta - 2)\chi_1 + (\nu + 2\delta - 2)\chi_2\Big] \\
& + \frac{e_0(e_0+1)^2}{8c^4 p_{\phi 0}^8}\Big[3\nu^2 - \nu + 95 - 6e_0^2\left(\nu^2 + 5\nu - 39\right) + 8e_0(\nu - 25) \\
& \quad + e_0^4\left(3\nu^2 - 17\nu + 55\right) + 8e_0^3(\nu - 7)\Big] \\
& + \frac{e_0(e_0+1)^2}{2c^4 p_{\phi 0}^8}\Big\{\chi_1^2\Big[C_{1\mathrm{ES}^2}\left(3e_0^2 - 2e_0 + 3\right)X_1^2 + \left(5e_0^2 - 6e_0 - 3\right)X_1^4\Big] \\
& \quad + \nu\chi_1\chi_2\Big[e_0^2(5\nu + 3) - 2e_0(3\nu + 1) - 3\nu + 3\Big] + 1 \leftrightarrow 2\Big\}.
\end{aligned}
\tag{6.70}
$$

The initial condition can now be obtained in analogy to the quasi-circular case: given Ω_0, e_0, masses, and spins, we obtain r_0 and p_{ϕ_0} from Eqs. (6.69) and (6.70) (assuming $p_r \approx 0$), p_{r0} then follows from Eq. (6.68) as before, and $\phi_0 = 0$ by convention. We can keep using the circular-orbits energy flux in Eq. (6.68), instead of replacing $\dot{E}$ with $\Omega\mathcal{F}_\phi$ for eccentric orbits, because the difference on the orbital dynamics is negligible since it involves p_r (which at periastron is numerically much smaller than r or p_ϕ).

To assess the accuracy of the initial conditions for eccentric orbits, we compare the specified value for the eccentricity in the Keplerian parametrization with the value calculated from the orbital frequency (or the frequency of the $(2,2)$ mode) at periastron Ω_p and apastron Ω_a, which is given by [632]

$$
e_\Omega = \frac{\sqrt{\Omega_p} - \sqrt{\Omega_a}}{\sqrt{\Omega_p} + \sqrt{\Omega_a}}\,, \tag{6.71}
$$

and to calculate it, we follow the steps explained after Eq. (2.8) of Ref. [622]. Since we evaluate

e_Ω by evolving the binary over one orbit (including RR), it only holds approximately that $\Omega_p \approx \Omega_a$ in the quasi-circular case. That is, e_Ω does not vanish exactly for quasi-circular orbits, in contrast to our e_0. Table 6.1 shows the value of the eccentricity e_Ω calculated from the orbital frequency compared to the specified eccentricity e_0, and we see good agreement between the two measures of eccentricity.

Table 6.1: Nonspinning initial conditions given the parameters (e_0, Ω_0, ν), and the eccentricity e_Ω measured from the orbital frequency using Eq. (6.71). The initial frequency Ω_0 was chosen to give ~ 30 GW cycles between r_0 and $r = 5$.

e_0	Ω_0	ν	r_0	$p_{\phi 0}$	p_{r0}	e_Ω
0.01	0.03	0.25	10.4	3.8	-0.0012	0.0087
0.2	0.045	0.25	8.1	3.7	-0.0024	0.19
0.7	0.065	0.25	6.7	4.0	-0.0033	0.69
0.2	0.058	0.1	6.8	3.6	-0.0011	0.20

6.4 Gravitational waveform modes

In this section, we obtain the 2PN waveform modes to 2PN order including LO tail effects, and SO and SS couplings for aligned spins. The instantaneous nonspinning part of the modes was derived for eccentric orbits in Refs. [151, 159] in harmonic coordinates and we convert their results to EOB coordinates. For the LO tail part, we extend the results of Ref. [403] to $\mathcal{O}(e^6)$ and to higher modes using the Keplerian parametrization, and then convert those results to an expansion in p_r and $\dot{p}_r$. The spin contributions to the modes were derived to 2PN order for circular orbits in Ref. [173], and here we derive them for eccentric orbits.

The GW spherical harmonic modes $h^{\ell m}$ are the expansion of the complex polarization waveform $h = h_+ - ih_\times$ into spin-weighted $s = -2$ spherical harmonics $Y_{-2}^{\ell m}(\Theta, \Phi)$ such that

$$h_+ - ih_\times = \sum_{\ell=2}^{\infty} \sum_{m=-\ell}^{\ell} h^{\ell m} Y_{-2}^{\ell m}(\Theta, \Phi). \tag{6.72}$$

The modes $h^{\ell m}$ can be calculated directly from the radiative multipole moments via [158, 170, 225]

$$h^{\ell m} = \frac{1}{\sqrt{2} D_L c^{\ell+2}} \left[U^{\ell m} - \frac{i}{c} V^{\ell m} \right], \tag{6.73}$$

where D_L is the luminosity distance of the source, and the radiative multipole moments are related to the symmetric trace-free (STF) moments U_L and V_L by

$$\begin{aligned} U^{\ell m} &= \frac{16\pi}{(2\ell+1)!!} \sqrt{\frac{(\ell+1)(\ell+2)}{2\ell(\ell-1)}} \bar{\mathcal{Y}}_L^{\ell m} U_L, \\ V^{\ell m} &= \frac{-32\pi}{(2\ell+1)!!} \sqrt{\frac{\ell(\ell+2)}{2(\ell+1)(\ell-1)}} \bar{\mathcal{Y}}_L^{\ell m} V_L, \end{aligned} \tag{6.74}$$

where $\bar{\mathcal{Y}}_L^{\ell m}$ is the complex conjugate of the STF tensors relating the unit vectors $N_{\langle L \rangle}$ (which point from the source to the detector) to the spherical harmonics basis $Y^{\ell m}(\Theta, \Phi)$ such that

$$Y^{\ell m}(\Theta, \Phi) = \mathcal{Y}_L^{\ell m} N_{\langle L \rangle}(\Theta, \Phi), \tag{6.75}$$

$$N_{\langle L \rangle}(\Theta, \Phi) = \frac{4\pi \ell!}{(2\ell+1)!!} \sum_{m=-\ell}^{\ell} \bar{\mathcal{Y}}_L^{\ell m} Y^{\ell m}(\Theta, \Phi), \tag{6.76}$$

$$\bar{\mathcal{Y}}_L^{\ell m} = \frac{(2\ell+1)!!}{4\pi \ell!} \int d\Omega \, N_{\langle L \rangle} \bar{Y}^{\ell m}, \tag{6.77}$$

$$\bar{\mathcal{Y}}_L^{\ell m} \mathcal{Y}_L^{\ell m'} = \frac{(2\ell+1)!!}{4\pi \ell!} \delta_{mm'}, \tag{6.78}$$

and we can express the unit vector $\boldsymbol{N}$ in terms of the angles Θ and Φ as

$$\boldsymbol{N} = \sin\Theta \cos\Phi \hat{\boldsymbol{e}}_x + \sin\Theta \sin\Phi \hat{\boldsymbol{e}}_y + \cos\Theta \hat{\boldsymbol{e}}_z. \tag{6.79}$$

For planar binaries, nonspinning or with aligned spins, it was shown in Ref. [158] that the modes can be determined using the mass-type multipole moments for even $\ell + m$, or the current-type multipole moments for odd $\ell+m$, i.e.,

$$\begin{aligned}
h^{\ell m} &= \frac{1}{\sqrt{2}D_L c^{\ell+2}}U^{\ell m}, \qquad && \ell+m \text{ even} \\
h^{\ell m} &= -\frac{i}{\sqrt{2}D_L c^{\ell+3}}V^{\ell m}, \qquad && \ell+m \text{ odd}.
\end{aligned} \tag{6.80}$$

We define $H^{\ell m}$ such that

$$h^{\ell m} = -\frac{8\mu}{c^4 D_L}\sqrt{\frac{\pi}{5}}\mathrm{e}^{-im\phi}H^{\ell m}, \tag{6.81}$$

which makes the LO part of $H^{22} = x$ for circular orbits. Note that different conventions for the phase origin contribute a factor of $(-i)^m$ to the modes [169].

In this paper, we compute the modes to 2PN order beyond the leading order of the $(2,2)$ mode, which means we consider modes up to the $\ell = 6,\ m =$ even modes. To 2PN order, the instantaneous contributions to the radiative multipole moments coincide with the source multipole moments. Including the hereditary terms that contribute to 2PN, the radiative multipole moments are given by [159, 170, 225]

$$\begin{aligned}
U_{ij} &= I_{ij}^{(2)} + \frac{2M}{c^3}\int_0^\infty d\tau\, I_{ij}^{(4)}(t-\tau)\ln\left(\frac{\tau}{b_1}\right) + \mathcal{O}\left(\frac{1}{c^5}\right), \\
U_{ijk} &= I_{ijk}^{(3)} + \frac{2M}{c^3}\int_0^\infty d\tau\, I_{ijk}^{(5)}(t-\tau)\ln\left(\frac{\tau}{b_2}\right) + \mathcal{O}\left(\frac{1}{c^5}\right), \\
U_L &= I_L^{(\ell)} + \mathcal{O}\left(\frac{1}{c^3}\right), \\
V_{ij} &= J_{ij}^{(2)} + \frac{2M}{c^3}\int_0^\infty d\tau\, J_{ij}^{(4)}(t-\tau)\ln\left(\frac{\tau}{b_3}\right) + \mathcal{O}\left(\frac{1}{c^5}\right), \\
V_L &= J_L^{(\ell)} + \mathcal{O}\left(\frac{1}{c^3}\right),
\end{aligned} \tag{6.82}$$

where the constants b_i are gauge parameters that will be eliminated via a phase shift as was done in Ref. [225]. The source multipole moments for nonspinning binaries are given in, e.g., Refs. [159, 225], while the spin contributions to the source moments are given in Refs. [166, 173].

6.4.1 Instantaneous nonspinning contributions

The instantaneous contributions to the modes for nonspinning binaries in eccentric orbits were derived in Ref. [151] to 2PN, and in Ref. [159] to 3PN. The results of Ref. [159] are in harmonic coordinates and in terms of the variables $(r, \phi, \dot{r}, \dot{\phi})$. Hence, we can simply transform their results from harmonic to EOB coordinates using the transformations in Appendix F. For the $(2,2)$ mode we obtain

$$
\begin{aligned}
\hat{H}^{22}_{\text{inst}} &= \frac{1}{2}\left(\frac{1}{r} + p^2 - 2p_r^2\right) + i\frac{p_\phi p_r}{r} + \frac{1}{c^2}\Bigg\{\left(\frac{\nu}{28} - \frac{5}{28}\right)p^4 + \left(\frac{31\nu}{28} - \frac{157}{84}\right)\frac{p^2}{r} \\
&\quad + \left(\frac{5}{14} - \frac{\nu}{14}\right)p_r^2 p^2 + \left(\frac{13}{3} - \nu\right)\frac{p_r^2}{r} + \left(\frac{\nu}{2} - 2\right)\frac{1}{r^2} \\
&\quad + i\frac{p_\phi p_r}{r}\left[\left(\frac{\nu}{14} - \frac{5}{14}\right)p^2 + \left(\frac{2\nu}{7} - \frac{185}{42}\right)\frac{1}{r}\right]\Bigg\} \\
&\quad + \frac{1}{c^4}\Bigg\{\left(-\frac{17\nu^2}{336} - \frac{13\nu}{336} + \frac{5}{48}\right)p^6 + \left(-\frac{671\nu^2}{1008} - \frac{1375\nu}{1008} + \frac{481}{504}\right)\frac{p^4}{r} \\
&\quad + \left(\frac{127\nu^2}{54} - \frac{1355\nu}{189} - \frac{5519}{3024}\right)\frac{p^2}{r^2} + \left(\frac{17\nu^2}{168} + \frac{13\nu}{168} - \frac{5}{24}\right)p_r^2 p^4 \\
&\quad + \left(-\frac{67\nu^2}{126} + \frac{20\nu}{9} - \frac{659}{504}\right)\frac{p_r^2 p^2}{r} + \left(-\frac{464\nu^2}{189} + \frac{2249\nu}{756} - \frac{811}{3024}\right)\frac{p_r^2}{r^2} \\
&\quad + \left(\frac{17\nu^2}{18} - \frac{25\nu}{36} - \frac{919}{1008}\right)\frac{p_r^4}{r} + \left(\frac{205\nu^2}{252} - \frac{49\nu}{36} + \frac{95}{63}\right)\frac{1}{r^3} \\
&\quad + i\frac{p_r p_\phi}{r}\Bigg[\left(-\frac{17\nu^2}{168} - \frac{13\nu}{168} + \frac{5}{24}\right)\frac{p^4}{r} + \left(-\frac{4\nu^2}{21} + \frac{29\nu}{28} + \frac{67}{56}\right)\frac{p^2}{r^2} \\
&\quad + \left(-\frac{523\nu^2}{378} + \frac{1226\nu}{189} + \frac{193}{54}\right)\frac{1}{r^3} + \left(\frac{43\nu^2}{63} - \frac{125\nu}{126} + \frac{787}{504}\right)\frac{p_r^2}{r^2}\Bigg]\Bigg\}.
\end{aligned} \tag{6.83}
$$

The expressions for the other modes that contribute to 2PN, i.e., up to $\ell = |m| = 6$, are provided as a *Mathematica* file in the Supplemental Material to Ref. [5]. Note that the $(\ell, 0)$ modes are zero for circular orbits but not for eccentric orbits. For example, the LO part of the $(2,0)$ mode is given by

$$\hat{H}^{20}_{\text{inst}} = \frac{1}{\sqrt{6}}\left(p^2 - \frac{1}{r}\right) + \mathcal{O}\left(\frac{1}{c^2}\right), \tag{6.84}$$

which is zero for circular orbits since $p^2 = 1/r + \ldots$.

6.4.2 Hereditary contributions

The hereditary contributions to the modes can be calculated analytically in an eccentricity expansion, as was done in Ref. [403] for the $(2,2)$ mode to $\mathcal{O}(e^2)$, and in Ref. [161] for all modes to 3PN order and to $\mathcal{O}(e^6)$. The results of Ref. [161] use the quasi-Keplerian parametrization, while here we use the Keplerian parametrization following the method developed in Ref. [403], which is based on results from Refs. [156, 225, 633], to derive the leading order tail effects that contribute to the modes up to 2PN order and to $\mathcal{O}(e^6)$. (See Ref. [403] for a discussion of the advantages of the Keplerian parametrization over the quasi-Keplerian parametrization.) We finally convert the eccentricity-expanded tail contributions to an expansion in p_r and $\dot{p}_r$.

6.4.2.1 Modes with even $\ell + m$

The LO mass-type multipole moments are given by [156]

$$I^L = \mu s_\ell r^\ell n^{\langle L\rangle}, \tag{6.85}$$

where $s_\ell \equiv X_2^{\ell-1} + (-1)^\ell X_1^{\ell-1}$, and the unit vectors $n^{\langle L\rangle}$ are related to spherical harmonics via Eq. (6.76), leading to

$$I^L = \sum_{m=-\ell}^{\ell} \mathcal{Y}^L_{\ell m} a_{\ell m} r^\ell \mathrm{e}^{-im\phi}, \tag{6.86}$$

with the coefficients (for equatorial orbits)

$$a_{\ell m} \equiv \frac{4\pi\mu s_\ell \ell!}{(2\ell+1)!!}\bar{Y}_{\ell m}\left(\frac{\pi}{2},0\right). \tag{6.87}$$

Decomposing the phase ϕ into an oscillatory part and a linearly growing part $\phi = \phi_0 + \omega_\phi t + \Delta\phi_r$ allows expressing the oscillatory part $\Delta\phi_r$ as a Fourier series expansion. Hence,

$$I^L = \sum_{m=-\ell}^{\ell} \mathcal{Y}^L_{\ell m} a_{\ell m} J_{\ell m} \mathrm{e}^{-im\psi_\phi}, \tag{6.88}$$

with the functions $J_{\ell m}$ defined by

$$J_{\ell m} = r^\ell \mathrm{e}^{-im\phi_0}\mathrm{e}^{-im\Delta\phi_r} = \sum_{k=-\infty}^{\infty} J_{\ell mk}\mathrm{e}^{-ik\psi_r}, \tag{6.89}$$

where ψ_r and ψ_ϕ are the radial and azimuthal angle variables associated with the frequencies $\omega_r = d\psi_r/dt$ and $\omega_\phi = d\psi_\phi/dt$. The coefficients $J_{\ell mk}$ are given by

$$\begin{aligned} J_{\ell mk} &= \frac{1}{2\pi}\int_0^{2\pi} d\psi_r\, \mathrm{e}^{ik\psi_r} J_{\ell m} \\ &= \frac{\omega_r}{2\pi}\int_0^{2\pi} \frac{d\chi}{\mathcal{P}} r^\ell \mathrm{e}^{-im\phi_0}\mathrm{e}^{-im\Delta\phi_r}\mathrm{e}^{ik\psi_r} \\ &= \frac{\omega_r}{2\pi} u_p^{-\ell-3/2}\int_0^{2\pi} \frac{d\chi}{(1+e\cos\chi)^{\ell+2}}\mathrm{e}^{-im\Delta\phi_r}\mathrm{e}^{ik\psi_r}, \end{aligned} \tag{6.90}$$

where, in the last line, we assume $\phi_0 = 0$. The function $\mathcal{P}$ denotes the conservative part of $\dot{\chi}$ and is related to the radial angle ψ_r via $d\psi_r/d\chi = \omega_r/\mathcal{P}$, with $\mathcal{P} = (1+e\cos\chi)^2 u_p^{3/2}$ at LO (see Ref. [403] for more details).

Thus, the Newtonian mass multipole moments can be expressed as

$$I^L = \sum_{m=-\ell}^{\ell}\sum_{k=-\infty}^{\infty} \mathcal{Y}^L_{\ell m} a_{\ell m} J_{\ell mk}\mathrm{e}^{-i(k\psi_r + m\psi_\phi)}, \tag{6.91}$$

where the azimuthal angle is related to the radial angle by $\psi_\phi = \phi - \Delta\phi_r$ with $\Delta\phi_r = \chi - \psi_r$ at LO. This allows us to write the LO tail contribution to the mass-type radiative moments as

$$U_L^{\text{tail}} = \frac{2M}{c^3}\int_0^\infty d\tau\, I_L^{(\ell+2)}(t-\tau)\ln\left(\frac{\tau}{b}\right),$$

$$= (-i)^{\ell+2}\frac{2M}{c^3}\sum_{m=-\ell}^{\ell}\sum_{k=-\infty}^{\infty}\mathcal{Y}_L^{\ell m}a_{\ell m}J_{\ell mk}\Omega_{mk}^{\ell+2}\mathrm{e}^{-i(k\psi_r+m\psi_\phi)}\mathcal{I}(\Omega_{mk}), \tag{6.92}$$

where $\Omega_{mk}\equiv m\omega_\phi + k\omega_r$ and

$$\begin{aligned}\mathcal{I}(x) &\equiv \int_0^\infty d\tau\,\mathrm{e}^{ix\tau}\ln\left(\frac{\tau}{b}\right)\\ &= -\frac{1}{x}\left[\frac{\pi}{2}\mathrm{sgn}(x) + i\ln(|x|b) + i\gamma_E\right].\end{aligned} \tag{6.93}$$

The exponential $\mathrm{e}^{-ik\psi_r}$ can be expressed in terms of χ and e by integrating $d\psi_r = \omega_r d\chi/\mathcal{P}$, with $\omega_r = (u_p - e^2 u_p)^{3/2}$, leading to Eq. (3.41) of Ref. [403], which reads

$$\mathrm{e}^{-ik\psi_r} = \mathrm{e}^{ik\frac{e\sqrt{1-e^2}\sin\chi}{1+e\cos\chi}}\left(\frac{1+\sqrt{1-e^2}+e\,\mathrm{e}^{i\chi}}{e+(1+\sqrt{1-e^2})\mathrm{e}^{i\chi}}\right)^k. \tag{6.94}$$

Hence, the modes with $\ell=2$ and m even are given by

$$h^{2m}_{\text{tail}} = \frac{\sqrt{24}Ma_{2m}}{c^7 R}\mathrm{e}^{-im\phi}\sum_{k=-\infty}^{\infty}J_{2mk}\Omega_{mk}^4\mathrm{e}^{im\chi}\mathrm{e}^{-i(k+m)\psi_r}\mathcal{I}(\Omega_{mk}), \tag{6.95}$$

while the modes with $\ell=3$ and m odd are given by

$$h^{3m}_{\text{tail}} = -i\frac{4\sqrt{5}Ma_{3m}}{3\sqrt{6}c^8 R}\mathrm{e}^{-im\phi}\sum_{k=-\infty}^{\infty}J_{3mk}\Omega_{mk}^5\mathrm{e}^{im\chi}\mathrm{e}^{-i(k+m)\psi_r}\mathcal{I}(\Omega_{mk}). \tag{6.96}$$

To obtain analytical expressions for the modes, we expand the above equations in eccentricity, where the infinite sum over k can be stopped at the order of the expansion in e. The result of that expansion is complicated, but we can perform a phase redefinition in the leading order instantaneous part[4] of the form $\phi \to \phi + x^{3/2}\delta_\phi$, and absorb in δ_ϕ all terms that are not proportional to $\pi^{3/2}$. This modifies the phase at 4PN relative order, which we can ignore when working

[4]One first needs to express the leading order part in terms of the variables (e, x, χ) instead of (r, p_r, p_ϕ) using the relations from Appendix I. For example, for the $(2,2)$ mode, we obtain

$$h^{22}_{\text{LO}} = \frac{-8\mu}{c^4 D_L}\sqrt{\frac{\pi}{5}}\mathrm{e}^{-2i\phi}\frac{x}{1-e^2}\left[1+\frac{e}{4}(\mathrm{e}^{-i\chi}+5\mathrm{e}^{i\chi})+\frac{e^2}{2}\mathrm{e}^{2i\chi}\right].$$

to 2PN order. (See Ref. [225] for more details.) The result for the $(2,2)$ mode to $\mathcal{O}(e^6)$ is given by

$$
\begin{aligned}
\hat{H}^{22}_{\text{tail}} = \frac{2\pi}{c^3}x^{5/2}\Bigg[&1 + e\left(\frac{11\mathrm{e}^{-i\chi}}{8} + \frac{13\mathrm{e}^{i\chi}}{8}\right) + e^2\left(\frac{5}{8}\mathrm{e}^{-2i\chi} + \frac{7}{8}\mathrm{e}^{2i\chi} + 4\right) \\
&+ e^3\left(\frac{121\mathrm{e}^{-i\chi}}{32} + \frac{143\mathrm{e}^{i\chi}}{32} + \frac{3}{32}\mathrm{e}^{-3i\chi} + \frac{1}{12}\mathrm{e}^{3i\chi}\right) + e^4\left(\frac{25}{16}\mathrm{e}^{-2i\chi} + \frac{203}{96}\mathrm{e}^{2i\chi} - \frac{5}{96}\mathrm{e}^{4i\chi} + \frac{65}{8}\right) \\
&+ e^5\left(\frac{55\mathrm{e}^{-i\chi}}{8} + \frac{6233\mathrm{e}^{i\chi}}{768} + \frac{15}{64}\mathrm{e}^{-3i\chi} + \frac{281\mathrm{e}^{3i\chi}}{1536} + \frac{53\mathrm{e}^{5i\chi}}{7680}\right) \\
&+ e^6\left(\frac{175}{64}\mathrm{e}^{-2i\chi} + \frac{1869}{512}\mathrm{e}^{2i\chi} - \frac{449\mathrm{e}^{4i\chi}}{3840} + \frac{31\mathrm{e}^{6i\chi}}{23040} + \frac{30247}{2304}\right)\Bigg], \qquad (6.97)
\end{aligned}
$$

while for the $(2,0)$ mode

$$
\begin{aligned}
\hat{H}^{20}_{\text{tail}} = \frac{\pi x^{5/2}}{2\sqrt{6}c^3}\Bigg[&e\left(\mathrm{e}^{-i\chi} + \mathrm{e}^{i\chi}\right) + e^2\left(\mathrm{e}^{-2i\chi} + \mathrm{e}^{2i\chi} + 2\right) + e^3\left(3\mathrm{e}^{-i\chi} + 3\mathrm{e}^{i\chi} + \frac{1}{4}\mathrm{e}^{-3i\chi} + \frac{1}{4}\mathrm{e}^{3i\chi}\right) \\
&+ e^4\left(\frac{29}{12}\mathrm{e}^{-2i\chi} + \frac{29}{12}\mathrm{e}^{2i\chi} + \frac{9}{2}\right) + e^5\left(\frac{179\mathrm{e}^{-i\chi}}{32} + \frac{179\mathrm{e}^{i\chi}}{32} + \frac{125}{192}\mathrm{e}^{-3i\chi} + \frac{125}{192}\mathrm{e}^{3i\chi}\right) \\
&+ e^6\left(\frac{805}{192}\mathrm{e}^{-2i\chi} + \frac{805}{192}\mathrm{e}^{2i\chi} - \frac{7}{960}\mathrm{e}^{-4i\chi} - \frac{7}{960}\mathrm{e}^{4i\chi} + \frac{121}{16}\right)\Bigg]. \qquad (6.98)
\end{aligned}
$$

The $(3,3)$ mode is given by

$$
\begin{aligned}
\hat{H}^{33}_{\text{tail}} = -\frac{9i\pi\delta}{4c^4}\sqrt{\frac{15}{14}}x^3\Bigg[&1 + e\left(\frac{47\mathrm{e}^{-i\chi}}{27} + \frac{19\mathrm{e}^{i\chi}}{9}\right) + e^2\left(\frac{61}{54}\mathrm{e}^{-2i\chi} + \frac{91}{54}\mathrm{e}^{2i\chi} + \frac{155}{27}\right) \\
&+ e^3\left(\frac{691\mathrm{e}^{-i\chi}}{108} + \frac{841\mathrm{e}^{i\chi}}{108} + \frac{35\mathrm{e}^{-3i\chi}}{108} + \frac{65\mathrm{e}^{3i\chi}}{108}\right) \\
&+ e^4\left(\frac{32}{9}\mathrm{e}^{-2i\chi} + \frac{287}{54}\mathrm{e}^{2i\chi} + \frac{5\mathrm{e}^{-4i\chi}}{144} + \frac{115\mathrm{e}^{4i\chi}}{1728} + \frac{3139}{216}\right) \\
&+ e^5\left(\frac{503\mathrm{e}^{-i\chi}}{36} + \frac{613\mathrm{e}^{i\chi}}{36} + \frac{35\mathrm{e}^{-3i\chi}}{36} + \frac{3095\mathrm{e}^{3i\chi}}{1728} - \frac{457\mathrm{e}^{5i\chi}}{25920}\right) \\
&+ e^6\left(\frac{131}{18}\mathrm{e}^{-2i\chi} + \frac{150503\mathrm{e}^{2i\chi}}{13824} + \frac{5}{48}\mathrm{e}^{-4i\chi} + \frac{151}{810}\mathrm{e}^{4i\chi} - \frac{41\mathrm{e}^{6i\chi}}{20736} + \frac{219}{8}\right)\Bigg], \qquad (6.99)
\end{aligned}
$$

and the $(3,1)$ mode

$$
\hat{H}^{31}_{\text{tail}} = \frac{i\pi\delta x^3}{12\sqrt{14}c^4}\Bigg[1 + e\left(\mathrm{e}^{i\chi} - 9\mathrm{e}^{-i\chi}\right) + e^2\left(-\frac{27}{2}\mathrm{e}^{-2i\chi} - \frac{5}{4}\mathrm{e}^{2i\chi} - 15\right)
$$

$$
\begin{aligned}
&+ e^3\left(-\frac{177}{4}\mathrm{e}^{-i\chi} - \frac{19\mathrm{e}^{i\chi}}{2} - \frac{25}{4}\mathrm{e}^{-3i\chi} - \frac{4}{3}e^{3i\chi}\right)\\
&+ e^4\left(-\frac{89}{2}\mathrm{e}^{-2i\chi} - \frac{125}{24}\mathrm{e}^{2i\chi} - \frac{15}{16}\mathrm{e}^{-4i\chi} - \frac{55\mathrm{e}^{4i\chi}}{192} - \frac{1703}{32}\right)\\
&+ e^5\left(-\frac{10141}{96}\mathrm{e}^{-i\chi} - \frac{2867\mathrm{e}^{i\chi}}{96} - \frac{75}{4}\mathrm{e}^{-3i\chi} - \frac{629}{192}\mathrm{e}^{3i\chi} - \frac{7}{960}\mathrm{e}^{5i\chi}\right)\\
&+ e^6\left(-\frac{142903\mathrm{e}^{-2i\chi}}{1536} - \frac{2965}{256}\mathrm{e}^{2i\chi} - \frac{45}{16}\mathrm{e}^{-4i\chi} - \frac{239}{240}\mathrm{e}^{4i\chi} + \frac{37\mathrm{e}^{6i\chi}}{23040} - \frac{16343}{144}\right)\Bigg].
\end{aligned} \tag{6.100}
$$

We checked that our results agree with those of Ref. [161] after converting between the quasi-Keplerian and Keplerian parametrization, and performing a phase shift.

To express the modes in terms of (r, p_r, p_ϕ) instead of (x, e, χ), we use the following leading order relations:

$$
p_\phi = \frac{1}{\sqrt{u_p}}, \qquad p_r = e\sqrt{u_p}\sin\chi, \qquad \frac{1}{r} = u_p(1 + e\cos\chi), \qquad x = u_p(1 - e^2). \tag{6.101}
$$

As explained above, it is advantageous to replace p_ϕ^2 with $\dot{p}_r$ using $\dot{p}_r = (p_\phi^2 - r)/r^3$ and expand in both p_r and $\dot{p}_r$ (since p_r and $\dot{p}_r$ are both of order e) to obtain

$$
\begin{aligned}
\hat{H}^{22}_{\text{tail}} = \frac{2\pi}{c^3}\Bigg\{&\frac{p_\phi}{r^3} + \frac{ip_r}{4r^2} + \left[\frac{7}{32}p_\phi p_r^2\dot{p}_r - \frac{7}{96}p_\phi r^3\dot{p}_r^3 + i\left(\frac{7p_r^3}{96r} - \frac{7}{32}r^2p_r\dot{p}_r^2\right)\right]\\
&+ \left[\frac{3p_\phi}{32}r^5\dot{p}_r^4 - \frac{p_\phi}{8}r^2p_r^2\dot{p}_r^2 + \frac{p_\phi p_r^4}{48r} + i\left(\frac{r^4}{12}p_r\dot{p}_r^3 - \frac{r}{96}p_r^3\dot{p}_r\right)\right]\\
&+ \left[\frac{31}{384}p_\phi r p_r^4\dot{p}_r - \frac{173p_\phi r^7\dot{p}_r^5}{1920} - \frac{1}{192}p_\phi r^4p_r^2\dot{p}_r^3 + i\left(\frac{r^6p_r}{768}\dot{p}_r^4 - \frac{49}{384}r^3p_r^3\dot{p}_r^2 + \frac{89p_r^5}{3840}\right)\right]\\
&+ \Bigg[\frac{97p_\phi r^9\dot{p}_r^6}{1152} + \frac{1}{16}p_\phi r^6p_r^2\dot{p}_r^4 - \frac{47}{384}p_\phi r^3p_r^4\dot{p}_r^2 + \frac{p_\phi p_r^6}{96}\\
&\quad + i\left(-\frac{1}{64}r^8p_r\dot{p}_r^5 + \frac{137r^5p_r^3\dot{p}_r^3}{1152} - \frac{23}{640}r^2p_r^5\dot{p}_r\right)\Bigg]\Bigg\},\\
\hat{H}^{20}_{\text{tail}} = \frac{\pi}{\sqrt{6}c^3}\Bigg\{&\frac{p_\phi\dot{p}_r}{r} - p_\phi r\dot{p}_r^2 + \left[\frac{3}{4}p_\phi r^3\dot{p}_r^3 - \frac{1}{4}p_\phi p_r^2\dot{p}_r\right] + \left[-\frac{7}{12}p_\phi r^5\dot{p}_r^4 - \frac{p_\phi p_r^4}{6r}\right]\\
&+ \left[\frac{95}{192}p_\phi r^7\dot{p}_r^5 + \frac{13}{96}p_\phi r^4p_r^2\dot{p}_r^3 + \frac{11}{192}p_\phi r p_r^4\dot{p}_r\right]
\end{aligned}
$$

$$
+ \left[-\frac{139}{320}p_\phi r^9\dot{p}_r^6 - \frac{11}{96}p_\phi r^6 p_r^2\dot{p}_r^4 + \frac{3}{64}p_\phi r^3 p_r^4\dot{p}_r^2 - \frac{p_\phi p_r^6}{480}\right]\Bigg\},
$$

$$
\hat{H}^{33}_{\text{tail}} = -\frac{9i\pi\delta}{4c^4}\sqrt{\frac{15}{14}}\Bigg\{\frac{1}{r^3} + \left[\frac{23\dot{p}_r}{27r} + \frac{10ip_\phi p_r}{27r^3}\right] - \frac{2p_r^2}{27r^2} + \Bigg[i\left(\frac{25}{432}p_\phi p_r^3\dot{p}_r - \frac{25}{432}p_\phi r^3 p_r\dot{p}_r^3\right)
$$

$$
- \frac{25r^5\dot{p}_r^4}{1728} + \frac{25}{288}r^2p_r^2\dot{p}_r^2 - \frac{25p_r^4}{1728r}\Bigg]
$$

$$
+ \left[i\left(\frac{109p_\phi r^5 p_r\dot{p}_r^4}{2592} + \frac{41p_\phi r^2 p_r^3\dot{p}_r^2}{1296} - \frac{41p_\phi p_r^5}{12960r}\right) + \frac{293r^7\dot{p}_r^5}{25920} + \frac{41r^4p_r^2\dot{p}_r^3}{1296} - \frac{157rp_r^4\dot{p}_r}{5184}\right]
$$

$$
+ \Bigg[\frac{2845r^3p_r^4\dot{p}_r^2}{41472} - \frac{1561r^9\dot{p}_r^6}{207360} - \frac{775r^6p_r^2\dot{p}_r^4}{13824} - \frac{653p_r^6}{69120}
$$

$$
+ i\left(\frac{4211p_\phi rp_r^5\dot{p}_r}{103680} - \frac{2173p_\phi r^7 p_r\dot{p}_r^5}{103680} - \frac{307p_\phi r^4p_r^3\dot{p}_r^3}{3456}\right)\Bigg]\Bigg\},
$$

$$
\hat{H}^{31}_{\text{tail}} = \frac{i\pi\delta}{12\sqrt{14}c^4}\Bigg\{\frac{1}{r^3} + \left[\frac{10ip_\phi p_r}{r^3} - \frac{11\dot{p}_r}{r}\right] - \left[\frac{11ip_\phi\dot{p}_r p_r}{2r} + \frac{13p_r^2}{4r^2} + \frac{11r\dot{p}_r^2}{4}\right]
$$

$$
+ \left[i\left(6p_\phi rp_r\dot{p}_r^2 - \frac{p_\phi p_r^3}{6r^2}\right) + \frac{35}{12}r^3\dot{p}_r^3 - \frac{p_r^2\dot{p}_r}{2}\right]
$$

$$
+ \left[i\left(\frac{45}{16}p_\phi p_r^3\dot{p}_r - \frac{61}{16}p_\phi r^3p_r\dot{p}_r^3\right) - \frac{269}{192}r^5\dot{p}_r^4 + \frac{37}{32}r^2p_r^2\dot{p}_r^2 - \frac{63p_r^4}{64r}\right]
$$

$$
+ \left[\frac{643}{960}r^7\dot{p}_r^5 + \frac{5}{16}r^4p_r^2\dot{p}_r^3 + \frac{101}{192}rp_r^4\dot{p}_r + i\left(\frac{83}{32}p_\phi r^5p_r\dot{p}_r^4 - \frac{43}{48}p_\phi r^2p_r^3\dot{p}_r^2 + \frac{379p_\phi p_r^5}{480r}\right)\right]
$$

$$
+ \Bigg[\frac{317}{768}r^3p_r^4\dot{p}_r^2 - \frac{5039r^9\dot{p}_r^6}{11520} - \frac{289}{768}r^6p_r^2\dot{p}_r^4 - \frac{297p_r^6}{1280}
$$

$$
+ i\left(\frac{151}{576}p_\phi r^4p_r^3\dot{p}_r^3 - \frac{4267p_\phi r^7p_r\dot{p}_r^5}{1920} + \frac{271}{640}p_\phi rp_r^5\dot{p}_r\right)\Bigg]\Bigg\}, \tag{6.102}
$$

where terms in each square bracket are the same order in eccentricity.

6.4.2.2 Modes with odd $\ell + m$

The Newtonian order current quadrupole moment is given by [156]

$$
J^{ij} = -\delta\mu r^2 n_k v_l \epsilon^{kl\langle i}n^{j\rangle} = -\delta r p_\phi\, \hat{e}_z^{\langle i}n^{j\rangle}, \tag{6.103}
$$

where $\hat{e}_z^i$ is the unit vector in the z-direction. The term $e_z^{\langle i}n^{j\rangle}$ can be expressed in terms of $\mathcal{Y}_{21}^{ij}$, as was done in Ref. [189], by defining the complex vector

$$\zeta^i = e_x^i + ie_y^i, \tag{6.104}$$

which leads to

$$\mathcal{Y}_{21}^{ij} = -\frac{1}{2}\sqrt{\frac{15}{2\pi}}\zeta^{\langle i}e_z^{j\rangle}. \tag{6.105}$$

Since, for equatorial orbits, $n^i = \cos\phi\,\hat{e}_x^i + \sin\phi\,\hat{e}_y^i$ and $\lambda^i = -\sin\phi\,\hat{e}_x^i + \cos\phi\,\hat{e}_y^i$, we obtain

$$n^i + i\lambda^i = e^{-i\phi}\zeta^i. \tag{6.106}$$

Hence,

$$\begin{aligned} e_z^{\langle i}n^{j\rangle} &= \text{Re}\left[\mathrm{e}^{-i\phi}e_z^{\langle i}\zeta^{j\rangle}\right] = -2\sqrt{\frac{2\pi}{15}}\text{Re}\left[\mathrm{e}^{-i\phi}\mathcal{Y}_{21}^{ij}\right] \\ &= -\sqrt{\frac{2\pi}{15}}\left(\mathrm{e}^{-i\phi}\mathcal{Y}_{21}^{ij} + \mathrm{e}^{i\phi}\bar{\mathcal{Y}}_{21}^{ij}\right). \end{aligned} \tag{6.107}$$

Since V_{ij} is contracted with $\bar{\mathcal{Y}}_{ij}^{\ell m}$ in Eq. (6.74), and $\bar{\mathcal{Y}}_{ij}^{\ell m}\bar{\mathcal{Y}}_{\ell m}^{ij} = 0$, only the term with $\mathcal{Y}_{21}^{ij}$ in the above equation contributes to the modes. Thus, we only need to consider the following part of the current quadrupole

$$J^{ij} = \mu\delta\sqrt{\frac{2\pi}{15}}\mathcal{Y}_{21}^{ij}p_\phi r e^{-i\phi} + \ldots. \tag{6.108}$$

Then, we follow the same steps as in the previous subsection. Decomposing the phase into $\phi = \omega_\phi t + \Delta\phi$ leads to

$$J^{ij} = \mu\delta\sqrt{\frac{2\pi}{15}}\mathcal{Y}_{21}^{ij}p_\phi \mathrm{e}^{-i\psi_\phi}J_{11} + \ldots, \tag{6.109}$$

with

$$J_{11} = r\mathrm{e}^{-i\Delta\phi} = \sum_{k=-\infty}^{\infty} J_{11k}\mathrm{e}^{-ik\psi_r}, \tag{6.110}$$

and

$$
\begin{aligned}
J_{11k} &= \frac{1}{2\pi}\int_0^{2\pi} d\psi_r\, J_{11}\mathrm{e}^{ik\psi_r} \\
&= \frac{\omega_r}{2\pi u_p^{5/2}}\int_0^{2\pi} \frac{d\chi}{(1+e\cos\chi)^3}\mathrm{e}^{-i\Delta\phi}\mathrm{e}^{ik\psi_r}.
\end{aligned} \tag{6.111}
$$

Thus, the current quadrupole source moment can be expressed as

$$
J^{ij} = \mu\delta\sqrt{\frac{2\pi}{15}}\mathcal{Y}_{21}^{ij}p_\phi \sum_{k=-\infty}^{\infty} J_{11k}\mathrm{e}^{-i(k\psi_r+\psi_\phi)} + \ldots, \tag{6.112}
$$

and the current quadrupole radiative moment

$$
V_{ij}^{\mathrm{tail}} = \frac{2M\mu\delta}{c^3}\sqrt{\frac{2\pi}{15}}\mathcal{Y}_{21}^{ij}p_\phi \sum_{k=-\infty}^{\infty} J_{11k}\Omega_{1k}^4 \times \mathrm{e}^{-i(k\psi_r+\psi_\phi)}\mathcal{I}(\Omega_{1k}), \tag{6.113}
$$

leading to the $(2,1)$ mode

$$
h_{\mathrm{tail}}^{21} = \frac{16i}{3}\sqrt{\frac{\pi}{5}}\frac{\delta M}{Rc^8}\mathrm{e}^{-i\phi}p_\phi \sum_{k=-\infty}^{\infty} J_{11k}\Omega_{1k}^4\mathrm{e}^{i\chi} \times \mathrm{e}^{-i(k+1)\psi_r}\mathcal{I}(\Omega_{1k}), \tag{6.114}
$$

with $p_\phi = 1/\sqrt{u_p} = \sqrt{(1-e^2)/x}$. Expanding in eccentricity yields

$$
\begin{aligned}
\hat{H}_{\mathrm{tail}}^{21} = \frac{i\pi\delta}{3c^4}x^3\Bigg[& 1 + e\left(3\mathrm{e}^{-i\chi} + \mathrm{e}^{i\chi}\right) + e^2\left(3\mathrm{e}^{-2i\chi} + \frac{1}{4}\mathrm{e}^{2i\chi} + 6\right) \\
& + e^3\left(\frac{45\mathrm{e}^{-i\chi}}{4} + 4\mathrm{e}^{i\chi} + \frac{5}{4}\mathrm{e}^{-3i\chi} + \frac{1}{6}\mathrm{e}^{3i\chi}\right) \\
& + e^4\left(\frac{19}{2}\mathrm{e}^{-2i\chi} + \frac{25}{24}\mathrm{e}^{2i\chi} + \frac{3}{16}\mathrm{e}^{-4i\chi} + \frac{17}{192}\mathrm{e}^{4i\chi} + \frac{493}{32}\right) \\
& + e^5\left(\frac{2375\mathrm{e}^{-i\chi}}{96} + \frac{865\mathrm{e}^{i\chi}}{96} + \frac{15}{4}\mathrm{e}^{-3i\chi} + \frac{91}{192}\mathrm{e}^{3i\chi} - \frac{7}{960}\mathrm{e}^{5i\chi}\right) \\
& + e^6\left(\frac{29957\mathrm{e}^{-2i\chi}}{1536} + \frac{593}{256}\mathrm{e}^{2i\chi} + \frac{9}{16}\mathrm{e}^{-4i\chi} + \frac{241}{960}\mathrm{e}^{4i\chi} + \frac{37\mathrm{e}^{6i\chi}}{23040} + \frac{8417}{288}\right)\Bigg],
\end{aligned} \tag{6.115}
$$

which is in agreement with the results of Ref. [161]. In terms of $(r, p_r, p_\phi, \dot{p}_r)$, we obtain

$$
\hat{H}_{\mathrm{tail}}^{21} = \frac{i\pi\delta}{3c^4}\Bigg\{\frac{1}{r^3} + \left[\frac{\dot{p}_r}{r} - \frac{2ip_\phi p_r}{r^3}\right] + \left[\frac{ip_\phi\dot{p}_r p_r}{2r} - \frac{p_r^2}{4r^2} + \frac{1}{4}r\dot{p}_r^2\right] + \left[-\frac{ip_\phi p_r^3}{6r^2} - \frac{1}{12}r^3\dot{p}_r^3 - \frac{1}{2}\dot{p}_r p_r^2\right]
$$

$$+\left[i\left(\frac{5}{16}p_\phi p_r^3\dot{p}_r-\frac{5}{16}p_\phi r^3p_r\dot{p}_r^3\right)-\frac{1}{192}5r^5\dot{p}_r^4+\frac{13}{32}r^2p_r^2\dot{p}_r^2-\frac{7p_r^4}{64r}\right]$$
$$+\left[i\left(\frac{11}{32}p_\phi r^5p_r\dot{p}_r^4-\frac{19}{48}p_\phi r^2p_r^3\dot{p}_r^2+\frac{19p_\phi p_r^5}{480r}\right)+\frac{43}{960}r^7\dot{p}_r^5-\frac{3}{16}r^4p_r^2\dot{p}_r^3+\frac{29}{192}rp_r^4\dot{p}_r\right]$$
$$+\left[i\left(-\frac{511p_\phi r^7p_r\dot{p}_r^5}{1920}+\frac{115}{576}p_\phi r^4p_r^3\dot{p}_r^3-\frac{61}{640}p_\phi rp_r^5\dot{p}_r\right)-\frac{79r^9\dot{p}_r^6}{2304}\right.$$
$$\left.\left.-\frac{13}{768}r^6p_r^2\dot{p}_r^4+\frac{17}{768}r^3p_r^4\dot{p}_r^2+\frac{59p_r^6}{1280}\right]\right\}. \tag{6.116}$$

6.4.3 Aligned-spin contributions

The spin contributions to the modes were derived for circular orbits in Refs. [169, 173, 180]. To derive the spin part of the modes to 2PN for eccentric orbits, we use the source moments from Refs. [166, 173], which are in harmonic coordinates and in terms of the covariant SSC. Differentiating the source moments to obtain the radiative moments (6.82), and plugging them into Eq. (6.73), we obtain the modes listed in Appendix H. Transforming from harmonic to EOB coordinates, and from the covariant to the NW SSC using the transformations in Appendix F, we obtain the following spin contributions to the modes:

$$\begin{aligned}
\hat{H}^{22}_{\text{spin}} &= \frac{1}{c^3}\left[\frac{\chi_1}{12r^3}\left[(6\delta+\nu+6)p_\phi+2i(3\delta-\nu+3)rp_r\right]\right.\\
&\quad\left.+\frac{\chi_2}{12r^3}\left[(-6\delta+\nu+6)p_\phi-2i(3\delta+\nu-3)rp_r\right]\right]\\
&\quad+\frac{1}{4c^4r^3}\Big\{\chi_1^2\left[3C_{1\text{ES}^2}X_1^2-X_1^4\left(2p^2r+1\right)\right]+\chi_2^2\left[3C_{2\text{ES}^2}X_2^2-X_2^4\left(2p^2r+1\right)\right]\\
&\quad-2\nu\chi_1\chi_2\left(\nu-3+2\nu p^2r\right)\Big\},\\
\hat{H}^{21}_{\text{spin}} &= \frac{i}{4c^2r^2}\left[-(1+\delta)\chi_1+(1-\delta)\chi_2\right]+\frac{\chi_1}{84c^4r^2}\left[\frac{ip_\phi^2}{r^2}(43\nu\delta-42\delta+153\nu-42)\right.\\
&\quad+\frac{p_rp_\phi}{r}(3\delta(2\nu+49)-104\nu+147)+\frac{i}{2}p_r^2(\delta(38\nu+105)+74\nu+105)\\
&\quad\left.+\frac{i}{r}(63\delta-38\nu\delta-74\nu+63)\right]
\end{aligned}$$

$$
\begin{aligned}
&+\frac{\chi_2}{84c^4r^2}\left[\frac{ip_\phi^2}{r^2}(43\nu\delta-42\delta-153\nu+42)+\frac{p_rp_\phi}{r}(3\delta(2\nu+49)+104\nu-147)\right.\\
&\left.+\frac{i}{2}p_r^2(38\nu\delta+105\delta-74\nu-105)+\frac{i}{r}(63\delta-38\nu\delta+74\nu-63)\right],\\
\hat{H}^{20}_{\text{spin}}&=\frac{\sqrt{3}p_\phi}{2\sqrt{2}c^3r^3}\left[(2\delta-\nu+2)\chi_1+(-2\delta-\nu+2)\chi_2\right]\\
&+\frac{\sqrt{3}}{2\sqrt{2}c^4r^3}\left\{\chi_1^2\left[\frac{X_1^4}{3r}\left(2r^2p_r^2-2p_\phi^2+r\right)-C_{1\text{ES}^2}X_1^2\right]\right.\\
&\left.+\chi_2^2\left[\frac{X_2^4}{3r}\left(2r^2p_r^2-2p_\phi^2+r\right)-C_{2\text{ES}^2}X_2^2\right]+\frac{2\nu\chi_1\chi_2}{3}\left[\nu-3-2\nu\frac{p_\phi^2}{r}+2\nu rp_r^2\right]\right\},\\
\hat{H}^{30}_{\text{spin}}&=\frac{-i\nu p_r}{\sqrt{42}c^3r^2}(\chi_1+\chi_2),\\
\hat{H}^{31}_{\text{spin}}&=\frac{1}{24\sqrt{14}c^4r^2}\left\{\chi_1\left[\frac{ip_\phi^2}{2r^2}(55\nu\delta-96\delta+375\nu-96)+i\left(p_r^2-\frac{2}{r}\right)(2\nu\delta-6\delta+23\nu-6)\right.\right.\\
&\left.+\frac{p_rp_\phi}{r}(-6\nu\delta+30\delta-127\nu+30)\right]+\chi_2\left[\frac{ip_\phi^2}{2r^2}(55\nu\delta-96\delta-375\nu+96)\right.\\
&\left.\left.+\frac{p_rp_\phi}{r}(-6\nu\delta+30\delta+127\nu-30)+i\left(p_r^2-\frac{2}{r}\right)(2\nu\delta-6\delta-23\nu+6)\right]\right\},\\
\hat{H}^{32}_{\text{spin}}&=\frac{\nu}{6c^3r^3}\sqrt{\frac{5}{7}}(4p_\phi+irp_r)(\chi_1+\chi_2),\\
\hat{H}^{33}_{\text{spin}}&=\frac{\sqrt{5}}{8\sqrt{42}c^4r^2}\left\{\left[-\frac{23i(\delta+1)\nu p_\phi^2}{2r^2}+\frac{(2\nu\delta+6\delta-19\nu+6)p_rp_\phi}{r}\right.\right.\\
&\left.+i\left(\frac{2}{r}-p_r^2\right)(2\nu\delta-6\delta+23\nu-6)\right]\chi_1+\left[\frac{(2\delta\nu+6\delta+19\nu-6)p_rp_\phi}{r}\right.\\
&\left.\left.-\frac{23i(\delta-1)\nu p_\phi^2}{2r^2}+i\left(\frac{2}{r}-p_r^2\right)(2\delta\nu-6\delta-23\nu+6)\right]\chi_2\right\},\\
\hat{H}^{41}_{\text{spin}}&=-i\sqrt{\frac{5}{2}}\frac{\nu}{336c^4r^4}\left(-10irp_rp_\phi+6r^2p_r^2-12r+11p_\phi^2\right)\left[(\delta-1)\chi_1+(\delta+1)\chi_2\right],\\
\hat{H}^{43}_{\text{spin}}&=\sqrt{\frac{5}{14}}\frac{\nu}{48c^4r^4}\left(10rp_rp_\phi+2ir^2p_r^2-4ir-23ip_\phi^2\right)\left[(\delta-1)\chi_1+(\delta+1)\chi_2\right].
\end{aligned}
\tag{6.117}
$$

The circular-orbit limit of these modes, when expressed in terms of the orbital frequency, agrees with the results of Refs. [173, 180]. The spin contributions to the $(2,2)$, $(2,1)$, and $(3,3)$ modes for eccentric orbits were calculated in Ref. [628]; however, we find a small disagreement with their results for the SO part.[5]

6.4.4 Factorized modes

The quasi-circular waveform modes used in SEOBNRv4HM are factorized as follows [386, 398, 412, 413]:

$$h_{\ell m}^{\text{F,qc}} = h_{\ell m}^{\text{N,qc}} \hat{S}_{\text{eff}}^{\text{qc}} T_{\ell m}^{\text{qc}} e^{i\delta_{\ell m}} f_{\ell m}^{\text{qc}}, \tag{6.118}$$

where $h_{\ell m}^{\text{N,qc}}$ is the Newtonian part of the mode, $\hat{S}_{\text{eff}}^{\text{qc}}$ is an effective source term given by

$$\hat{S}_{\text{eff}}^{\text{qc}} = \begin{cases} \hat{H}_{\text{eff}}(v_\Omega) & \ell + m \text{ even} \\ \hat{L}_{\text{eff}} \equiv v_\Omega \, p_\phi(v_\Omega) & \ell + m \text{ odd} \end{cases}, \tag{6.119}$$

$T_{\ell m}^{\text{qc}}$ resums the infinite number of "leading logarithms" entering the tail effects, $\delta_{\ell m}$ contains the part of the tail not included in $T_{\ell m}^{\text{qc}}$, and $f_{\ell m}$ contains PN corrections such that the expansion of $h_{\ell m}^{\text{F,qc}}$ agrees with the known PN expansion of the modes. See Refs. [398, 413] for more details and for expressions of these terms.

We include the eccentric corrections in the factorized modes as follows:

$$\begin{aligned} h_{\ell 0}^{\text{F}} &= \hat{S}_{\text{eff}} (1 + T_{\ell 0}^{\text{ecc}}) f_{\ell 0}^{\text{ecc}}, \\ h_{\ell m}^{\text{F}} &= h_{\ell m}^{\text{N,qc}} \hat{S}_{\text{eff}} (T_{\ell m}^{\text{qc}} + T_{\ell m}^{\text{ecc}}) e^{i\delta_{\ell m}} (f_{\ell m}^{\text{qc}} + f_{\ell m}^{\text{ecc}}), \end{aligned} \tag{6.120}$$

[5] The difference between the modes in Ref. [628] (denoted with a bar) and the modes in Eq. (6.117) (with $C_{1\text{ES}^2} = C_{2\text{ES}^2} = 1$) is given by

$$\begin{aligned} \hat{\bar{H}}_{\text{spin}}^{22} - \hat{H}_{\text{spin}}^{22} &= \frac{i\nu p_r}{2c^3 r^2} (\chi_1 + \chi_2), \\ \hat{\bar{H}}_{\text{spin}}^{21} - \hat{H}_{\text{spin}}^{21} &= \frac{i\delta\nu p_r}{6c^4 r^3} (r p_r + i p_\phi)(\chi_1 + \chi_2), \\ \hat{\bar{H}}_{\text{spin}}^{33} - \hat{H}_{\text{spin}}^{33} &= \frac{\sqrt{5}\delta\nu p_r}{8\sqrt{42} c^4 r^3} (17 p_\phi + 5 i r p_r)(\chi_1 + \chi_2), \end{aligned}$$

which is likely due to the coordinate/SSC transformations detailed in Appendix F.

where the effective source term is given by

$$\hat{S}_{\text{eff}} = \begin{cases} \hat{H}_{\text{eff}}(r, p_r, p_\phi) & \ell + m \text{ even} \\ \hat{L}_{\text{eff}} \equiv v_\Omega \, p_\phi & \ell + m \text{ odd} \end{cases}, \tag{6.121}$$

$T_{\ell m}^{\text{ecc}}$ contains the eccentric corrections to the hereditary contributions, $\delta_{\ell m}$ is the same as in the quasi-circular case, and $f_{\ell m}^{\text{ecc}}$ contains the eccentric corrections to the instantaneous contributions (both spinning and nonspinning, including the Newtonian part). For example, for the leading order of the $(2,2)$ mode, we obtain

$$f_{22}^{\text{ecc}} = \frac{1}{2(r^2\dot{p}_r + 1)^{1/3}} \left[2 + r^2\dot{p}_r - r p_r^2 - 2\left(r^2\dot{p}_r + 1\right)^{1/3} + 2ip_r\sqrt{r^3\dot{p}_r + r}\right] + \dots . \tag{6.122}$$

For the tail part, we simplified the results of Sec. 6.4.2 and eliminated the gauge parameter by using a phase shift, which led to the circular part of the tail contribution to the $(2,2)$ mode simply being $2\pi v_\Omega^5$; however, this phase redefinition is not done in `SEOBNRv4HM`, and the corresponding expression reads $v_\Omega^5 \left(2\pi + 12i\log\left(2\epsilon v_\Omega\right) - 17i/3 + 12i\gamma_E/3\right)$. Therefore, when including the eccentric corrections in $T_{\ell m}^{\text{ecc}}$, we assume that the phase redefinition was done only for the eccentric part and keep using the same circular part as in `SEOBNRv4HM`. In addition, since we expanded the tail part in eccentricity to $\mathcal{O}(e^6)$, when factorizing the modes as in Eq. (6.120) and writing the quasi-circular part in terms of frequency, we reexpand T_{lm}^{ecc} in eccentricity (or p_r and $\dot{p}_r$). For example, for the $(2,2)$ mode, we obtain

$$T_{22}^{\text{ecc}} = -\frac{\pi}{4r}\left[4r^{3/2}\dot{p}_r + ip_r\left(r^2\dot{p}_r + 6\right) + 2\sqrt{r}p_r^2 + \mathcal{O}(p_r^3)\right]. \tag{6.123}$$

The full expressions for T_{lm}^{ecc} and f_{lm}^{ecc} are provided in the Supplemental Material [**?**].

6.5 Conclusions

Extending the waveform models used today in GW astronomy from quasi-circular to eccentric orbits is important for future observations with LIGO, Virgo and KAGRA detectors [**?**], and with new facilities on the ground (Cosmic Explorer and Einstein Telescope), and in space (LISA). In fact, sources with non-negligible eccentricity might come into reach of observations soon and should routinely be included in searches and parameter inference. While this presents a challenge for waveform modeling and data analysis, it also offers the unique opportunity to unveil the formation channels of compact binaries and probe their environment (through eccentricity measurements). In this paper, we constructed an EOB waveform model for eccentric binaries. For this purpose, we obtained analytical results for the RR force and waveform modes to 2PN order, including the leading-order tail effects, and SO and SS couplings for aligned spins.

In particular, we first derived the RR force for eccentric orbits in PN expanded form, and then we recast it in a form that it can be directly incorporated in the quasi-circular RR force employed in the `SEOBNRv4HM` [397, 398] model, currently used in LIGO/Virgo analyses [14]. We then obtained initial conditions for the binary evolution which generalize those from Ref. [374] to eccentric orbits, and which allow starting the binary's evolution from a specified initial frequency at periastron and an initial eccentricity (in the Keplerian parametrization). We also calculated all the waveform modes that contribute up to 2PN order relative to the leading order of the $(2,2)$ mode. It should be noted that the $(\ell,0)$ modes are proportional to the eccentricity and are hence important for eccentric orbits, especially the $(2,0)$ mode since it starts at the same PN order as the $(2,2)$ mode. Also the gravitational modes were rewritten in a factorized form to be straightforwardly implemented in the `SEOBNRv4HM` model.

Our results for the RR force and modes are valid for moderate to high eccentricities during the inspiral phase, since we do not use an eccentricity expansion except for the tail part, which is known analytically as an infinite series expansion. We provided expressions for the tail part in an expansion to $\mathcal{O}(e^6)$, but we checked that expanding to $\mathcal{O}(e^{10})$ produces negligible difference on the waveform even for high eccentricities ($\lesssim 0.9$). If results for e close to 1 are needed, one could calculate the series expansion for the tail part numerically, or use analytical resummation methods as was done in Refs. [160, 613].

We are currently incorporating the eccentric RR force and gravitational modes of this paper in the inspiral-merger-ringdown quasi-circular–orbit `SEOBNRv4HM` waveform model (`SEOBNRv4EHM` [**?**]) and validating it against NR simulations with eccentricity. We leave to future work the extension of the model to higher PN orders and the inclusion of spin precession.

Acknowledgments

We are grateful to Serguei Ossokine, Harald Pfeiffer, Antoni Ramos-Buades, Hannes Rüter, and Maarten van de Meent for helpful discussions. We also thank Marco Stella, Marta Orselli, and Andrea Placidi for pointing out typos.

Chapter 7: Energetics and scattering of gravitational two-body systems at fourth post-Minkowskian order

Authors[1]: *Mohammed Khalil, Alessandra Buonanno, Jan Steinhoff, Justin Vines*

Abstract: Upcoming observational runs of the LIGO-Virgo-KAGRA collaboration, and future gravitational-wave (GW) detectors on the ground and in space, require waveform models more accurate than currently available. High-precision waveform models can be developed by improving the analytical description of compact binary dynamics and completing it with numerical-relativity (NR) information. Here, we assess the accuracy of the recent results for the fourth post-Minkowskian (PM) conservative dynamics through comparisons with NR simulations for the circular-orbit binding energy and for the scattering angle. We obtain that the 4PM dynamics gives better agreement with NR than the 3PM dynamics, and that while the 4PM approximation gives comparable results to the third post-Newtonian (PN) approximation for bound orbits, it performs better for scattering encounters. Furthermore, we incorporate the 4PM results in effective-one-body (EOB) Hamiltonians, which improves the disagreement with NR over the 4PM-expanded Hamiltonian from $\sim 40\%$ to $\sim 10\%$, or $\sim 3\%$ depending on the EOB gauge, for an equal-mass binary, two GW cycles before merger. Finally, we derive a 4PN-EOB Hamiltonian for hyperbolic orbits, and compare its predictions for the scattering angle to NR, and to the

[1]Originally published as Phys. Rev. D **106**, no.2, 024042 (2022)

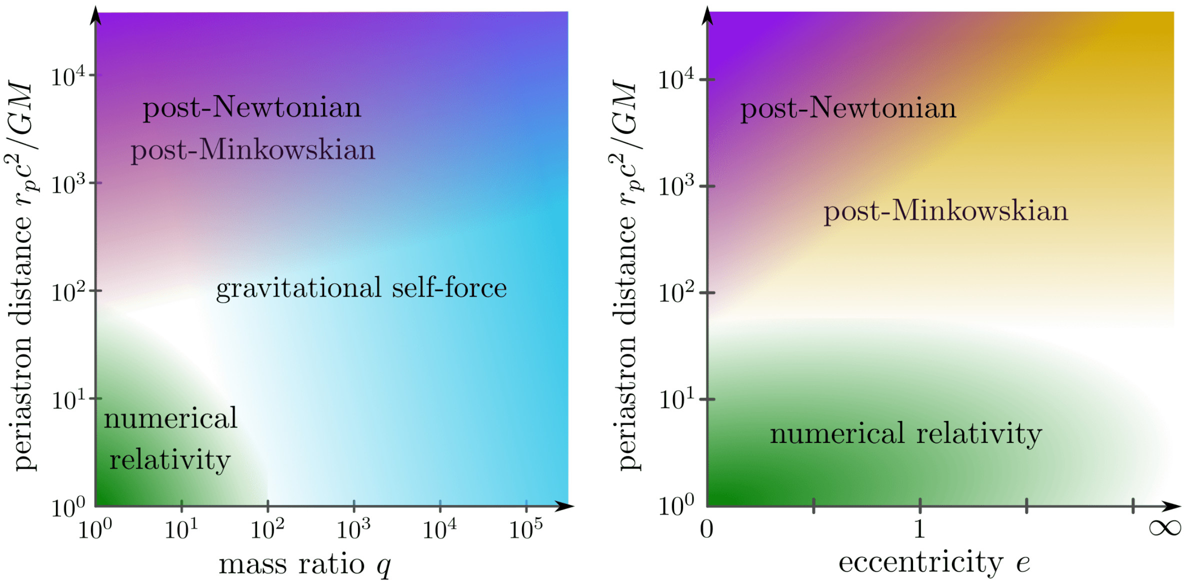

Figure 7.1: The left panel shows the region of applicability of NR and the PN, PM, and GSF approximations for small eccentricity $e \sim 0$, in which case the PN and PM approximations overlap. The right panel shows the range in eccentricity for which each approximation is applicable for comparable masses $q \sim 1$. The PM approximation is more accurate than the PN approximation for scattering encounters at large velocities, or equivalently large eccentricities at fixed periastron distance.

scattering angle of a 4PN-EOB Hamiltonian computed for elliptic orbits.

7.1 Introduction

Gravitational-wave (GW) observations [12–15] have improved our understanding of compact binaries, composed of black holes and/or neutron stars, their properties, and their astrophysical formation channels [18–20]. Searching for GW signals and estimating their parameters require accurate waveform models or templates. Since numerical-relativity (NR) simulations are computationally expensive, analytical approximation methods become essential for producing such waveforms.

The post-Newtonian (PN) approximation is valid for slow motion, $v^2/c^2 \ll 1$, and weak gravitational potential, $GM/rc^2 \ll 1$, making it most applicable for binaries in bound orbits where $v^2/c^2 \sim GM/rc^2$, which are the main sources observed by ground-based GW detectors, such as LIGO, Virgo and KAGRA [517, 518, 634]; for reviews, see Refs. [129–134].

Similarly, the post-Minkowskian (PM) approximation is a weak-field expansion, but places no restriction on the magnitude of velocities. Next to entirely classical approaches to the PM approximation [228, 229, 232, 233, 236, 237, 251–253], recent progress is pioneered by methods starting out from (quantum) scattering amplitudes [11, 238–250]. In addition, manifestly classical methods that make use of quantum-field-theory techniques show great promise for advancing the PM approximation, namely effective field theory [254–259] and worldline quantum field theory [260, 261] approaches. The PM approximation has also been applied to spin [262–275, 556, 635–639], tidal [277–284] and radiative effects [285–298, 640].

The PM expansion encompasses the PN expansion, such that the $(n+1)$PM order includes all the information up to the nPN order, making it potentially more accurate. Binaries in bound orbits can reach velocities on the order of 0.4 or larger when spiraling over the last orbits before merger. This means that the relativistic corrections become more and more important in the last stages of the inspiral and plunge. Thus, we might expect that at some high PM order, the PM expansion may start to become more accurate than the PN expansion. Furthermore, scattering encounters on hyperbolic trajectories can reach high velocities, for which the PM approximation becomes more relevant. The gravitational self-force (GSF) approximation [302, 303, 309, 315, 318, 320, 326, 332, 333, 336, 567, 568, 641] expands the Einstein's equations in power of the binary's mass ratio $m_2/m_1 \ll 1$. It is thus valid for any velocity and is not restricted to the weak fields. Figure 7.1 illustrates the regions of parameter space in which the PN, PM and GSF approximations are (roughly) applicable when generic orbits are considered.

Detecting GW bursts from hyperbolic encounters would have important implications on our understanding of dense stellar environments and the merger rate of compact objects formed through this astrophysical channel. Currently, there does not seem to be a consensus in the literature [459–465] on the event rate for scattering encounters, due to the high uncertainty in the astrophysical models; the expected event rates vary between 0.001 to 0.39 per year for upcoming LIGO-Virgo-KAGRA runs, depending on the model [465], with higher rates expected for future detectors. Gravitational waves from hyperbolic encounters would be expected at higher rates in the LIGO-Virgo-KAGRA frequency band if a large population of primordial black holes exists in dense stellar clusters, as was proposed in Refs. [642–645] based on some inflationary models. Other GW sources that could reach highly-relativistic velocities are binaries in galactic nuclei, where dynamical capture and three-body interactions can drive binaries to high eccentricities [445, 448, 450, 454, 455, 461, 646–651].

Most studies of hyperbolic and parabolic encounters use the PN approximation, for both the dynamics [402, 427, 565, 575] and the GW energy spectrum [462, 652–655]. The effective-one-body (EOB) formalism [380, 381] has also been applied to scattering, as in Refs. [10, 404, 466, 656–658]. EOB waveform models improve the inspiral-merger-ringdown waveforms by combining test-body, PN, black-hole perturbation, and NR results. PM results have been incorporated in EOB Hamiltonians in Refs. [236, 237, 405, 406].

In this paper, we study the results of Refs. [246, 247, 258, 259] for the 4PM conservative dynamics, both the "vanilla" 4PM Hamiltonians and the EOB Hamiltonians constructed with 4PM conservative information. Generally, the waveform models are evaluated on the two-body dynamics, which is derived from the Hamiltonian and the radiation-reaction (RR) force. The

Hamiltonian describes the conservative dynamics, while the RR force accounts for the energy and angular momentum losses due to GWs, and it is included in the right-hand side of the Hamilton equations. Since the RR force has not been computed in PM theory at sufficiently high PM order, in this paper, we restrict our study to the conservative sector, and therefore focus on the Hamiltonian. As shown in Refs. [408, 434, 435], a good diagnostic to assess the accuracy of models for the conservative dynamics is to compare the binding energy from the Hamiltonians and NR. The latter contains both conservative and dissipative effects. When augmenting the models' dynamics with RR effects, the binding energy can change (e.g., see Fig. 6 in Ref. [405]). However, it is still very informative to perform studies that compare to NR only the conservative dynamics at various orders of the perturbative expansion, and also develop different flavors of Hamiltonians, and explore their closeness to NR. Eventually, when RR effects in PM theory become available, one will be able to identify the most suitable model for the full dynamics that best represent the NR results. Quite interestingly, in the case of the scattering angle, for which we can add the RR effects to the models' predictions, we show that the radiative contribution is much smaller than the conservative one (see Fig. 7.6 below).

The paper is structured as follows. In Sec. 7.2 and Sec. 7.3, we summarize the 4PM results and incorporate them in EOB Hamiltonians. Then, in Sec. 7.4, we compare the circular-orbit binding energies with NR, while in Sec. 7.5, we compare the scattering angles. We conclude in Sec. 3.6, and write in Appendices K and L the expressions for the PN and EOB Hamiltonians.

Notation

We adopt units in which the speed of light $c = 1$.

For a binary with masses m_1 and m_2, with $m_1 \geq m_2$, we define the following quantities:

$$M \equiv m_1 + m_2, \quad \mu \equiv \frac{m_1 m_2}{M}, \quad \nu \equiv \frac{\mu}{M}, \quad q \equiv \frac{m_1}{m_2}. \tag{7.1}$$

From the total energy E, we define the binding energy:

$$\bar{E} \equiv \frac{E - M}{\mu}, \tag{7.2}$$

and the effective energy E_{eff} through the EOB energy map [380]

$$E = M\sqrt{1 + 2\nu\left(\frac{E_{\text{eff}}}{\mu} - 1\right)}. \tag{7.3}$$

We also introduce the following quantities:

$$\begin{aligned}\gamma &\equiv \frac{E_{\text{eff}}}{\mu} = \frac{E^2 - m_1^2 - m_2^2}{2m_1 m_2}, \\ \Gamma &\equiv \frac{E}{M} = \sqrt{1 + 2\nu(\gamma - 1)}\,,\end{aligned} \tag{7.4}$$

where γ is related to the asymptotic relative velocity v by

$$v \equiv \frac{\sqrt{\gamma^2 - 1}}{\gamma}, \quad \text{or} \quad \gamma = \frac{1}{\sqrt{1 - v^2}}. \tag{7.5}$$

When dealing with PN expansions, it is convenient to define the dimensionless energy variable [2]

$$\varepsilon \equiv \gamma^2 - 1 = \gamma^2 v^2. \tag{7.6}$$

The orbital angular momentum is denoted L, and is related to the relative position R, radial momentum P_R, and total linear momentum P via

$$P^2 = P_R^2 + \frac{L^2}{R^2}. \tag{7.7}$$

[2]Note that ε used here is denoted p_∞^2 in Refs. [91, 247].

We use $H_{\rm hyp}$ to denote a Hamiltonian with PM or PN information that is valid for unbound/hyperbolic motion, and use $H_{\rm ell}$ for a Hamiltonian valid for bound/elliptic orbits. A Hamiltonian written without a 'hyp' or 'ell' subscript is valid for generic motion.

We often use the following dimensionless rescaled quantities:

$$r \equiv \frac{R}{GM}, \quad u \equiv \frac{1}{r}, \quad p \equiv \frac{P}{\mu}, \quad p_r \equiv \frac{P_R}{\mu}, \quad l \equiv \frac{L}{GM\mu}, \quad \hat{H} \equiv \frac{H}{\mu}. \tag{7.8}$$

7.2 PM-expanded scattering angle and Hamiltonian

The 4PM conservative dynamics (including tail effects) has been derived recently in Refs. [246, 247, 258, 259] for *hyperbolic orbits* in a large-eccentricity expansion. We note that this 4PM result agrees with the 6PN result of Refs. [92, 93, 286], and exhibits a simple mass dependence, which is expected due to Lorentz invariance and dimensional analysis, as argued in Ref. [252]. The result of Refs. [246, 247, 258, 259] also agrees with the 5PN result of Refs. [87, 88, 564], except for a single term that does not have the expected mass dependence, and is proportional to ν^2. [3] Furthermore, Ref. [259] argued that conservative memory terms are still missing at 4PM order. However, at the PM order we are working, there is no unique definition of the conservative dynamics. In this paper, we follow the definition of the conservative dynamics of Refs. [92, 93, 286], which implies that memory effects at 4PM order will appear in the dissipative dynamics, and will be accounted for when they become available. Thus, here we assume that the conservative-dynamics results in Refs. [246, 247, 258, 259] are complete.

The two-body dynamics can be conveniently encoded in the gauge-invariant radial action,

[3] The difference in the 5PN conservative scattering angle between Refs. [91, 247] and [88], which is given by Eq. (69) of the latter, is proportional to $\nu^2 v^6/L^4$. In all configurations considered in this paper, the velocities reached by a binary system are typically $\lesssim 0.5$. As a consequence, such a difference has a very small effect in our study — for example on the order of 10^{-3} degrees for the range of parameters in Fig. 7.6.

I_r, which at 4PM order can be written schematically as

$$I_{r,\text{4PM}}^{\text{hyp}} = I_{r,\text{3PM}} - \frac{\pi G^4 M^7 \nu^2 P^2}{8EL^3}\left[\mathcal{M}_4^{\text{p}} + \nu\left(4\mathcal{M}_4^{\text{t}} \ln\frac{\sqrt{\gamma^2-1}}{2} + \mathcal{M}_4^{\pi^2} + \mathcal{M}_4^{\text{rem}}\right)\right], \tag{7.9}$$

which includes the lower PM orders, with the 3PM part $I_{r,\text{3PM}}$ valid for both bound and unbound motion. The terms $\mathcal{M}_4^{\cdot\cdot}$ are directly related to parts of the scattering amplitude; they are independent of the masses, and are written in Eq. (3) of Ref. [247]. An expression for these terms that is valid for generic orbits (bound and unbound) is difficult to derive and has not yet been found. The physical reason is that the tail effects [183] starts to enter at 4PM order, which is a nonlocal-in-time interaction depending on the entire history of the binary. Thus, it is different for bound and unbound orbits.

The scattering angle, by which the two bodies are deflected in the center-of-mass frame, is a gauge-invariant function that contains the same information as the radial action or the hyperbolic-orbit Hamiltonian. It can be obtained from the derivative of the radial action with respect to the angular momentum, that is,

$$\chi = -\frac{\partial I_r^{\text{hyp}}}{\partial L}. \tag{7.10}$$

The 3PM and 4PM pieces of the conservative scattering angle have a logarithmic divergence in the high-energy (massless) limit. However, that divergence at 3PM order was shown to cancel with a corresponding divergence in the radiative contribution [285, 288, 289, 293, 294, 640], and it is expected that such divergence also cancels at 4PM order [286]. In this paper, we only consider comparable-mass binaries, for which the singularity in the massless limit is irrelevant, and we demonstrate in Fig. 7.6 that the radiative contribution to the 3PM scattering angle is negligible for the range of parameters we consider.

Reference [247] also derives a two-body Hamiltonian from the radial action, following the steps in Refs. [241, 299]. The 4PM Hamiltonian in *isotropic* gauge, and for hyperbolic orbits, is given by

$$H_{\text{4PM}}^{\text{hyp}} = \sqrt{m_1^2 + P^2} + \sqrt{m_2^2 + P^2} + \sum_{n=1}^{4} \frac{G^n}{R^n} c_n, \tag{7.11}$$

where the c_n-coefficients are given by Eqs. (10) of Ref. [243] and Eq. (8) of Ref. [247]. Like the radial action, the 3PM part of $H_{\text{4PM}}^{\text{hyp}}$ is valid for generic motion, but the 4PM piece is for hyperbolic orbits. This Hamiltonian is determined in Ref. [247] from an ansatz that matches the scattering angle that follows from the radial action $I_{r,\text{4PM}}^{\text{hyp}}$, which is determined from the scattering amplitude.

To assess how close $H_{\text{4PM}}^{\text{hyp}}$ is to a bound-orbit 4PM Hamiltonian, we complement $H_{\text{4PM}}^{\text{hyp}}$ with bound-orbit corrections $\Delta H_{\text{4PM(nPN)}}^{\text{ell}}$, such that the nPN expansion of $H_{\text{4PM}}^{\text{hyp}} + \Delta H_{\text{4PM(nPN)}}^{\text{ell}}$ gives the correct nPN Hamiltonian up to $\mathcal{O}(G^4)$ for bound orbits in isotropic gauge. We obtain $\Delta H_{\text{4PM(nPN)}}^{\text{ell}}$ to 6PN order, as explained in Appendix K, since the 6PN Hamiltonian is fully known up to $\mathcal{O}(G^4)$ [92, 93]. In Sec. 7.4, we compare the binding energy calculated from these Hamiltonians with NR, finding a small difference between $H_{\text{4PM}}^{\text{hyp}}$ and its bound-orbit corrections.

7.3 Effective-one-body Hamiltonians

In the case of nonspinning compact objects, the EOB formalism [380, 381] maps the binary motion to that of a test mass in a deformed Schwarzschild background. The two-body Hamiltonian H^{EOB} is related to an effective Hamiltonian H^{eff} via the energy map

$$H^{\text{EOB}} = M\sqrt{1 + 2\nu\left(\frac{H_{\text{eff}}}{\mu} - 1\right)}. \tag{7.12}$$

The effective metric is defined by

$$g_{\mu\nu}^{\text{eff}} \mathrm{d}x^\mu \mathrm{d}x^\nu = -A\mathrm{d}T^2 + B\mathrm{d}R^2 + R^2\left(\mathrm{d}\theta^2 + \sin^2\theta\mathrm{d}\phi^2\right), \tag{7.13}$$

with the mass-shell condition [384]

$$0 = g_{\text{eff}}^{\mu\nu} P_\mu P_\nu + \mu^2 + Q, \tag{7.14}$$

leading to the effective Hamiltonian $H_{\text{eff}} = -P_0$,

$$H_{\text{eff}}^2 = A \left(\mu^2 + \frac{P_R^2}{B} + \frac{L^2}{R^2} + Q \right). \tag{7.15}$$

In the $\nu \to 0$ limit, H_{eff} reduces to the Schwarzschild Hamiltonian for a test mass, which is given by

$$\hat{H}_S^2 = (1 - 2u) \left[1 + (1 - 2u) p_r^2 + l^2 u^2 \right]. \tag{7.16}$$

To include higher PN information in an EOB Hamiltonian, we write an ansatz for the A, B and Q potentials in Eq. (7.15), perform a canonical transformation, then match H^{EOB} to the PN-expanded Hamiltonian. This procedure is explained in more detail in Appendix K. For PM results, it is more convenient to calculate the gauge-invariant scattering angle from the ansatz for H^{EOB}, then match it to the PM-expanded scattering angle in Eq. (7.10). These calculations will lead to the first derivation of 4PM-EOB Hamiltonians (and their nPN limits) for hyperbolic orbits.

As an ansatz, we choose the B potential to be the same as in the Schwarzschild metric, i.e., $B = 1/(1 - 2u)$, and include all the 4PM corrections into either Q or A. When included in Q, we get a 4PM generalization of the *post-Schwarzschild* (PS) Hamiltonian considered in Refs. [237, 405], which is given by

$$(\hat{H}^{\text{eff,PS}})^2 = \hat{H}_S^2 + (1 - 2u) \left(u^2 q_{\text{2PM}} + u^3 q_{\text{3PM}} + u^4 q_{\text{4PM}} + \Delta_{\text{4PN}}^Q \right), \tag{7.17}$$

where $q_{n\text{PM}}$ can in general be any scalar function of the energy or the dynamical variables. In this ansatz, we include a 4PN correction term Δ_{4PN}^Q as explained below.

The other gauge we consider in this paper incorporates PM corrections in the A potential, and reads

$$(\hat{H}^{\text{eff,PS}^*})^2 = \left(1 - 2u + u^2 a_{2\text{PM}} + u^3 a_{3\text{PM}} + u^4 a_{4\text{PM}} + \Delta^A_{4\text{PN}}\right)\left[1 + (1-2u)p_r^2 + l^2 u^2\right], \quad (7.18)$$

which is meant to more closely resemble, in the circular-orbit limit, the standard EOB gauge of Refs. [80, 380, 384], which is often used in EOB waveform models for LIGO-Virgo-KAGRA observations.

To determine the $q_{n\text{PM}}$ and $a_{n\text{PM}}$ coefficients, we calculate the scattering angle from the Hamiltonian. To achieve this, we invert the Hamiltonian $\hat{H}^{\text{EOB}}(l, r, p_r) = \bar{E} + 1/\nu$ to obtain $p_r(\bar{E}, l, r)$, then evaluate the integral

$$\chi = -2\int_{r_0}^{\infty} \frac{\partial p_r(\bar{E}, l, r)}{\partial l} dr - \pi\,, \quad (7.19)$$

where r_0 is the turning point obtained from the largest root of the unperturbed (1PM) radial momentum $p_r^{(0)}(\bar{E}, l, r) = 0$. To simplify evaluating this integral, we assume that a canonical transformation has been performed such that $q_{n\text{PM}}$ and $a_{n\text{PM}}$ are functions only of the effective energy E_{eff}, which is constant. However, since $q_{n\text{PM}}$ and $a_{n\text{PM}}$ themselves define H_{eff}, their dependence on E_{eff} should be understood perturbatively in the PM scheme. When working up to 3PM order, that energy can be taken to be the (1PM-accurate) Schwarzschild Hamiltonian $\hat{H}_S$ (see Refs. [237, 405] for more details). However, at 4PM order, we need to account for nonlinear effects by using the 2PM effective energy, as explained in Appendix L.

Since the scattering angle is gauge invariant, matching χ calculated from the EOB Hamiltonian to the PM-expanded scattering angle in Eq. (7.10) enables us to solve for the coefficients $q_{n\text{PM}}(\gamma)$ and $a_{n\text{PM}}(\gamma)$, where $\gamma \equiv E_{\text{eff}}/\mu$. (See Appendix L for the expressions of these coefficients.).

Table 7.1: Summary of the Hamiltonians considered in this paper.

Hamiltonian	definition
$H_{n\text{PN}}$	PN-expanded Hamiltonian to $\mathcal{O}(c^{-2n})$
$H_{n\text{PM}}$	PM-expanded Hamiltonian to $\mathcal{O}(G^{n})$
$H^{\text{hyp}}_{\text{4PM}} + \Delta H^{\text{ell}}_{\text{4PM}(n\text{PN})}$	4PM hyperbolic-orbit Hamiltonian plus a bound-orbit correction up to orders nPN and 4PM
$H^{\text{ell,iso}}_{\text{nPN(4PM)}}$	PN-expanded Hamiltonian truncated at $\mathcal{O}(G^4)$ in isotropic coordinates, valid for bound orbits
$H^{\text{EOB}}_{n\text{PN}}$	PN-EOB Hamiltonian in the gauge used in Refs. [80, 380, 384]
$H^{\text{EOB,PS}}_{\ldots}$	EOB Hamiltonian in Eq. (7.17), based on the PS gauge [237, 405]
$H^{\text{EOB,PS}^*}_{\ldots}$	EOB Hamiltonian in the gauge used in Eq. (7.18)
$H^{\text{EOB},\ldots}_{\text{4PM+4PN}}$	4PM-EOB Hamiltonian (for hyperbolic orbits) complemented with the missing 4PN part (for bound orbits).

We also complement the 4PM EOB Hamiltonians above with the missing 4PN(5PM) piece. This is done by writing an ansatz for Δ_{4PN}, such that

$$\Delta_{\text{4PN}} = \sum_{n=2}^{5} \alpha_n u^n \varepsilon^{5-n} + \left(\alpha_{4,\ln} u^4 \varepsilon + \alpha_{5,\ln} u^5\right) \ln u + \alpha_{4,\ln\varepsilon} u^4 \ln \varepsilon, \tag{7.20}$$

where we use the PN expansion parameters u and $\varepsilon \equiv \gamma^2 - 1$, each of one PN order. Then, we perform a canonical transformation and match the result to the elliptic 4PN Hamiltonian of Ref. [80]. Note that the $\ln \varepsilon$ term is there to cancel a corresponding term that appears in the 4PM hyperbolic-orbit Hamiltonian. The coefficients in Eq. (7.20) are written in Appendix L.

We summarize in Table 7.1 the different Hamiltonians considered in this paper.

7.4 Binding energy for circular orbits

The 4PM part of the Hamiltonian in Eq. (7.11) is valid in the large-eccentricity limit, which means it is not consistent with the circular-orbit binding energy at 4PN and higher orders. However, we show that the tail contribution to that Hamiltonian has a small effect on the dynamics, and so we use it to get an estimate for the 4PM contribution to the binding energy.

7.4.1 PN-expanded binding energy

We start by comparing the PN-expanded binding energy calculated from a bound-orbit Hamiltonian to the unbound case.

In Appendix K, we compute the bound-orbit 6PN Hamiltonian in isotropic coordinates, by canonically transforming the EOB Hamiltonian of Refs. [92, 93]. We truncate that Hamiltonian at 4PM, and calculate the binding energy, which at 4PN reads

$$\bar{E}^{\text{iso,ell}}_{\text{4PN(4PM)}} = \bar{E}_{\text{3PN}}(x) + x^5 \left[\frac{11795}{768} - \nu\frac{518}{45}\ln x + \nu\left(\frac{428071\pi^2}{36864} - \frac{7899659}{34560} + \frac{1036\ln 2}{45}\right) + \nu^2\left(\frac{1435\pi^2}{576} - \frac{122815}{6912}\right) - \frac{5341\nu^3}{3456} - \frac{77\nu^4}{62208}\right], \tag{7.21}$$

where $\bar{E}_{\text{3PN}}(x)$ is given by Eq. (232) of Ref. [130], and $x \equiv (M\Omega)^{2/3}$, with Ω being the orbital frequency. Note that the 4PN part of this result is *not* gauge-invariant, but is only valid for isotropic coordinates. The reason is that PN-accurate coordinate transformations — for example to isotropic coordinates — in general span several PM orders.

We find that the difference between the binding energy in Eq. (7.21) and the energy computed from the hyperbolic-orbit Hamiltonian (7.11) at 4PN is given by

$$\begin{aligned}\bar{E}^{\text{iso,hyp}}_{\text{4PN(4PM)}} - \bar{E}^{\text{iso,ell}}_{\text{4PN(4PM)}} &= \nu x^5 \left[\frac{37933}{45} + \frac{1036\gamma_E}{45} - \frac{113847608\ln 2}{45} - \frac{1472499\ln 3}{20} + \frac{13671875\ln 5}{12}\right] \\ &\simeq 14.94\nu x^5\,,\end{aligned} \tag{7.22}$$

where we see that the disagreement is in the non-logarithmic, linear-in-ν coefficient of Eq. (7.21). That coefficient is -112.96 in $\bar{E}^{\text{iso,ell}}_{\text{4PN(4PM)}}$, and is -98.01 in $\bar{E}^{\text{iso,hyp}}_{\text{4PN(4PM)}}$, with the difference being 14.94. (Note that the $\ln x$ term in Eq. (7.21) is the same for bound and unbound orbits, as was shown to all PN orders in Ref. [297].)

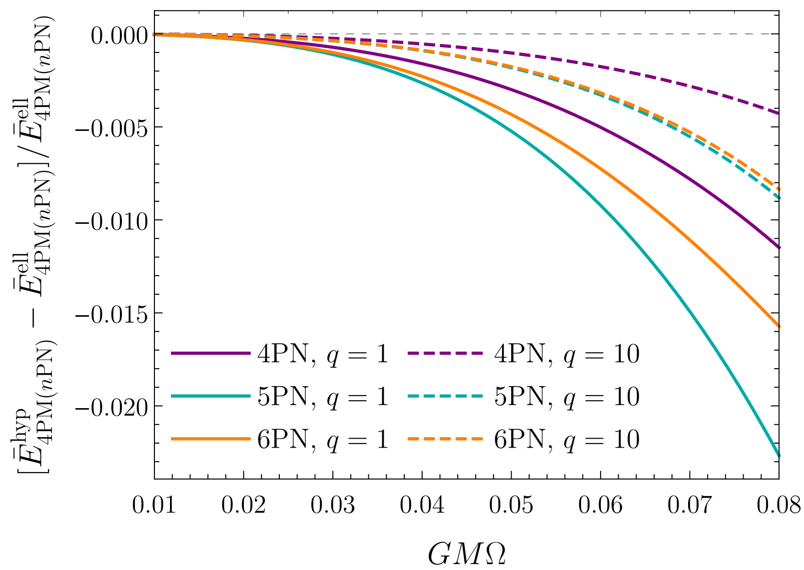

Figure 7.2: Relative difference in the circular-orbit binding energy, computed analytically from an elliptic versus a hyperbolic-orbit Hamiltonian.

In Fig. 7.2, we plot the relative difference in the binding energy at different PN orders, and for mass ratios $q = 1$ and $q = 10$, finding disagreement $\lesssim 2\%$, which justifies applying the hyperbolic 4PM result to bound orbits as we do below, since we find that the disagreement with NR is larger than 2%.

7.4.2 Binding energy from PM-expanded Hamiltonians

To compute the binding energy for circular orbits from the PM-expanded Hamiltonian in Eq. (7.11), we do so numerically by setting $p_r = 0$ in the Hamiltonian and solving $\dot{p}_r = -\partial\hat{H}/\partial r = 0$ for the angular momentum l at different orbital separations. We then plot $\bar{E} = \hat{H}_{n\text{PM}} - 1/\nu$ versus the orbital frequency $M\Omega = \partial\hat{H}/\partial l$ (see Ref. [405] for more details).

In Fig. 7.3, we compare the binding energy with NR data that were extracted in Ref. [438]

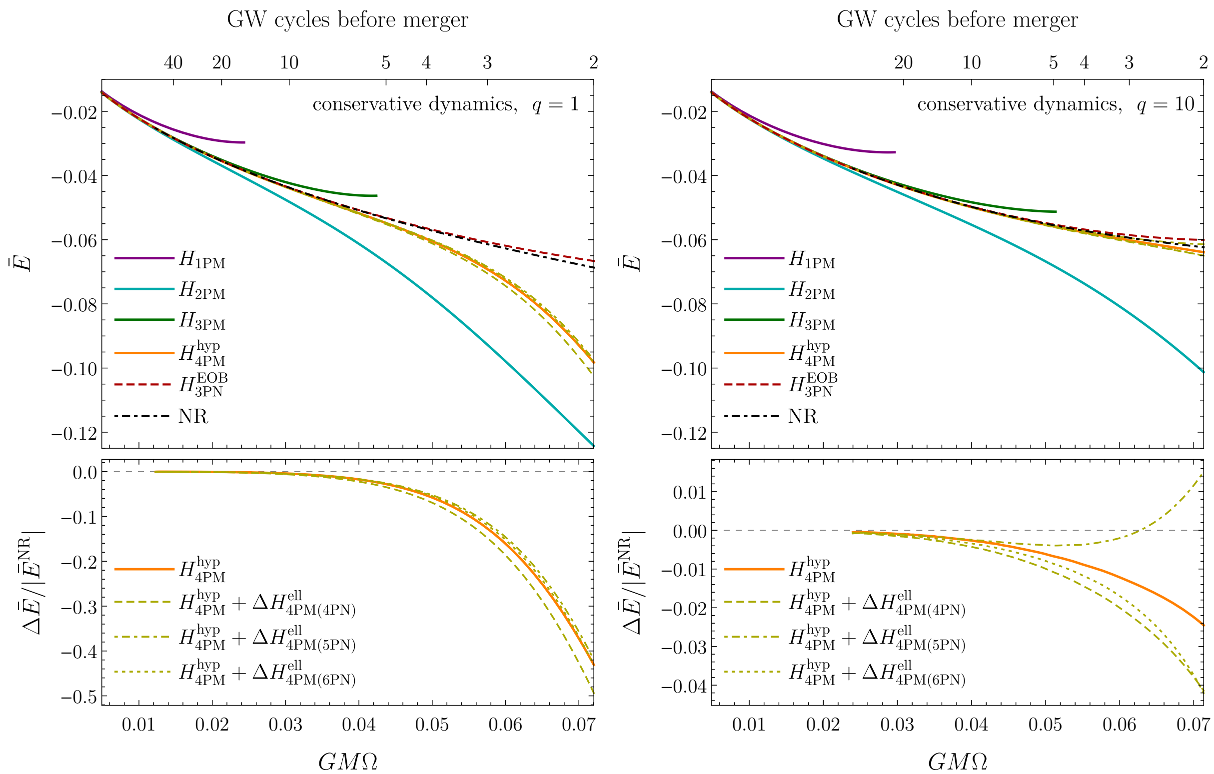

Figure 7.3: Binding energy versus orbital frequency for the PM-expanded Hamiltonians compared to the NR prediction for a nonspinning equal-mass (left panel) and mass-ratio $q = 10$ (right panel) binary black hole. The top axis gives the number of GW cycles before merger, which is twice the number of orbits. The lower panels show the relative difference of the 4PM curves with NR.

from numerical simulations produced by the Simulating eXtreme Spacetimes (SXS) collaboration [41, 458]. In particular, we use the simulations with SXS ID 0180 for mass ratio $q = 1$ and ID 0303 for $q = 10$, for which the numerical error is too small to show in the figure.

We see that the 4PM Hamiltonian gives much better agreement with NR toward merger than Hamiltonians computed at lower PM orders. This is because the 4PM Hamiltonian contains the full 3PN information, which is known to give considerably better results than 2PN. The improvement at 4PM is even more significant for mass ratio $q = 10$ than $q = 1$, because the 3PN coefficient in the binding energy increases significantly with increasing mass ratio. In addition, it seems that $H^{\rm hyp}_{\rm 4PM}$ is very close to what a bound-orbit 4PM Hamiltonian would be, as evidenced by how close the curves $H^{\rm hyp}_{\rm 4PM} + \Delta H^{\rm ell}_{\rm 4PM(nPN)}$, computed at 4PN, 5PN and 6PN orders, are to $H^{\rm hyp}_{\rm 4PM}$.

For comparison, the figure also shows the 3PN EOB Hamiltonian in the gauge of Refs. [80, 380, 384], which gives better agreement with NR (also when considering different mass ratios) because it includes the exact test-body limit, and the associated resummation of the PN results. In the plots, we stop the numerical evaluation of the energy either at the innermost-stable circular orbit (ISCO) or at two GW cycles (one orbit) before merger. We note that the EOB results on the figures do not contain any NR information, and the g_{00} effective metric contains PN terms in a Taylor-expanded form.

7.4.3 Binding energy from PM-EOB Hamiltonians

Similarly, computing the binding energy from the PM-EOB Hamiltonians leads to Fig. 7.4 for $q = 1$ and Fig. 7.5 for $q = 10$. In both figures, we plot the binding energy at each PM order, and complement 4PM with 4PN information. We stop the numerical evaluation either at

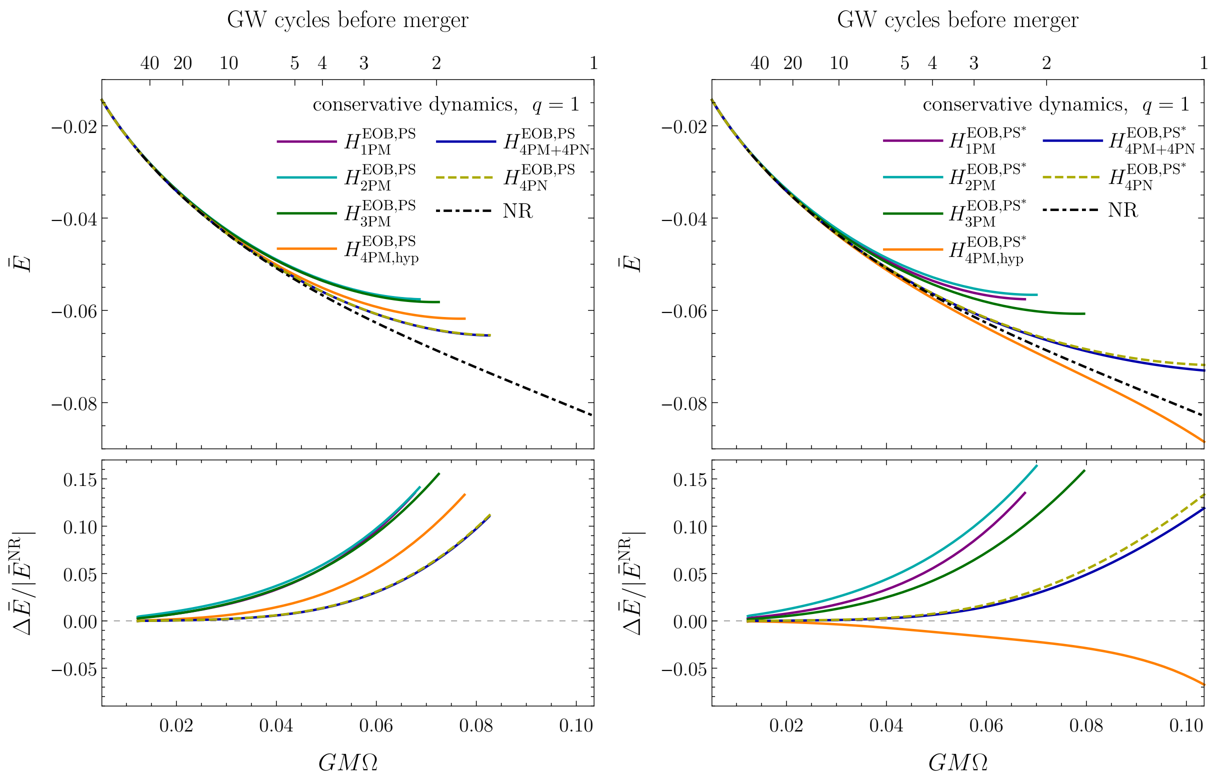

Figure 7.4: Binding energy versus orbital frequency for the PM-EOB Hamiltonians, compared to the NR prediction for $q = 1$. The left panels contain results for the EOB Hamiltonian in the PS gauge in Eq. (7.17), while the right panels are for the PS* gauge in Eq. (7.18).

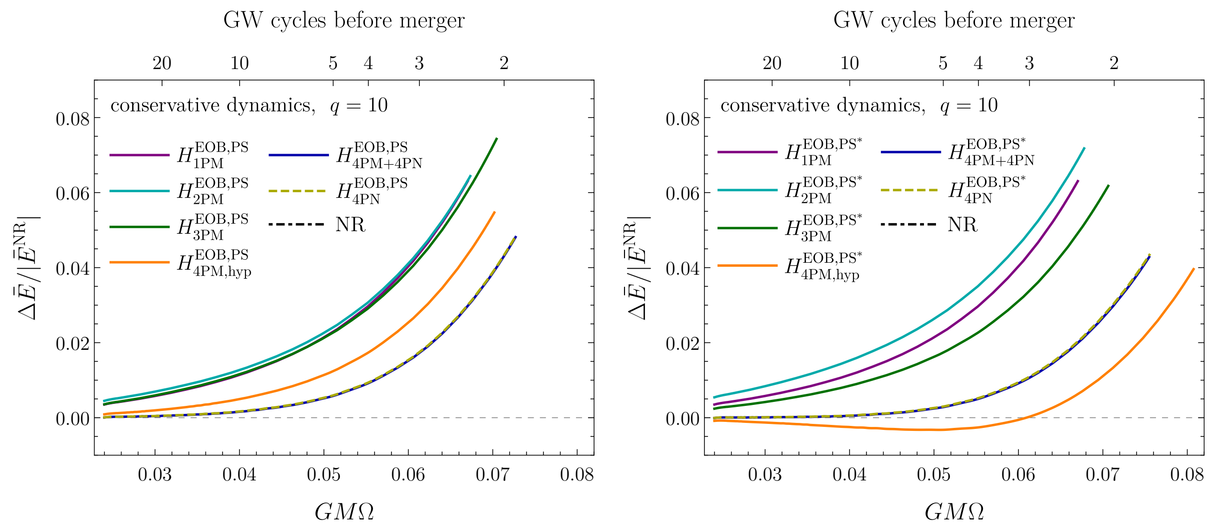

Figure 7.5: Similar to Fig. 7.4 but for mass ratio $q = 10$, and we only show the relative difference since the EOB curves are closer to the NR curve than for equal masses. All curves end at the ISCO.

the ISCO or at one GW cycle before merger.

From the figures, we observe the following:

- The 4PM order provides a significant improvement over the lower orders, even though the PM Hamiltonian is for hyperbolic orbits.
- The PS* gauge performs better than the PS gauge, for both equal and unequal masses. That difference is due to higher-order terms resulting from the resummation of the Hamiltonian coefficients. We expect that the more PN/PM orders are included, the closer different gauges would be to each other.
- Complementing 4PM with the missing 4PN information for bound orbits gives results for the PS* gauge that are comparable to the standard PN-EOB gauge.
- Using 4PN-expanded potentials in $H^{\rm EOB,...}_{\rm 4PN}$ gives almost the same result as the 4PM+4PN

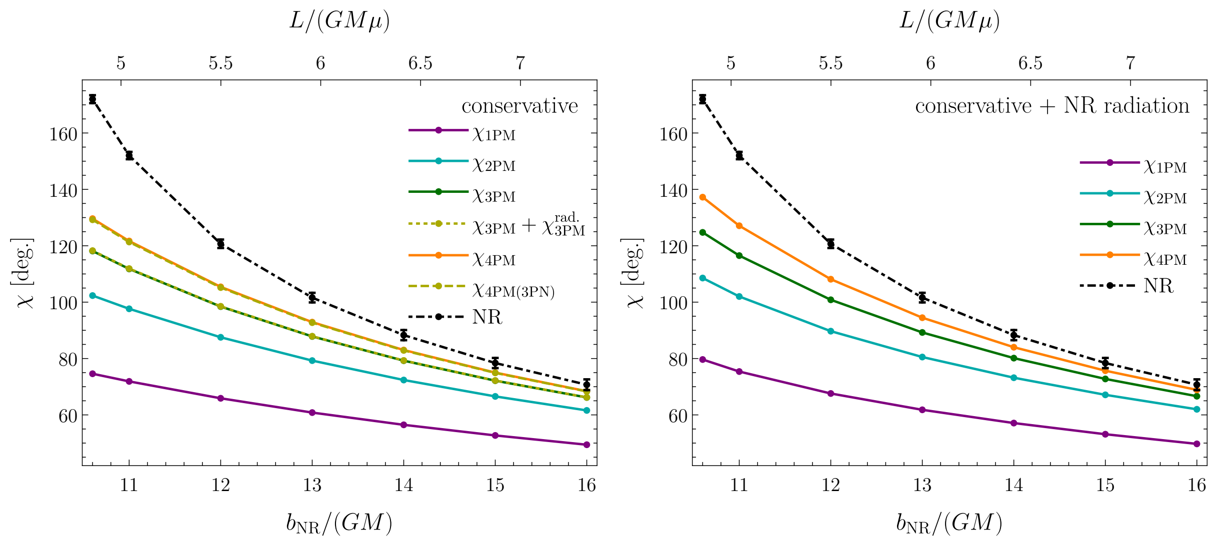

Figure 7.6: Comparison of the PM-expanded scattering angle with NR. The left panel shows the conservative scattering angle, except for the $\chi_{3PM} + \chi_{3PM}^{\text{rad.}}$ curve that also includes the leading-order (3PM) radiative contribution. The right panel incorporates the effect of the radiative losses from the NR simulations using Eq. (7.25).

Hamiltonian, although for the PS* gauge, the 4PM+4PN Hamiltonian is slightly better for equal masses than its 4PN expansion.

7.5 Scattering angle comparison with NR

Since the 4PM part of the radial action in Eq. (7.9) is valid for hyperbolic orbits, a better comparison with NR is through the scattering angle.

NR simulations for the scattering angle were reported in Ref. [466] for equal masses $q = 1$ and initial linear momentum $|\boldsymbol{p}| = 0.11456439M$. The initial energy in these simulations is approximately $E_{\text{in}}^{\text{NR}} \simeq 1.02259$ (corresponding to velocity $v \simeq 0.4$), and the initial angular momentum $L_{\text{in}}^{\text{NR}}$ is proportional to the impact parameter b_{NR}, which ranges between $9M$ to $16M$. The NR error in the scattering angle is $\sim 1 - 2$ degrees.

Reference [466] also reported the energy and angular momentum losses due to the emitted GWs, which can be used to account for the radiative contributions to the scattering angle. It was proven in Ref. [402] that when working to linear order in RR, the radiative contribution to the total scattering angle is half the difference of the conservative scattering angle evaluated as a function of the outgoing and incoming states, i.e.,

$$\chi^{\text{rad.}} = \frac{1}{2}\left[\chi^{\text{cons.}}(E_{\text{out}}, L_{\text{out}}) - \chi^{\text{cons.}}(E_{\text{in}}, L_{\text{in}})\right], \tag{7.23}$$

which means that the total scattering angle is given by

$$\begin{aligned}\chi^{\text{tot}}(E_{\text{in}}, L_{\text{in}}) &\equiv \chi^{\text{cons.}}(E_{\text{in}}, L_{\text{in}}) + \chi^{\text{rad.}}(E_{\text{in}}, L_{\text{in}}) \\ &= \frac{1}{2}\left[\chi^{\text{cons.}}(E_{\text{in}}, L_{\text{in}}) + \chi^{\text{cons.}}(E_{\text{out}}, L_{\text{out}})\right],\end{aligned} \tag{7.24}$$

which can be written as

$$\chi^{\text{tot}}(E_{\text{in}}, L_{\text{in}}) = \chi^{\text{cons.}}(E_{\text{avg}}, L_{\text{avg}}), \tag{7.25}$$

where

$$E_{\text{avg}} \equiv \frac{E_{\text{in}} + E_{\text{out}}}{2}, \qquad L_{\text{avg}} \equiv \frac{L_{\text{in}} + L_{\text{out}}}{2}. \tag{7.26}$$

We emphasize that the relation (7.25) holds when neglecting contributions quadratic in RR, which start at 5PN order.

7.5.1 PM-expanded scattering angle

In the left panel of Fig. 7.6, we plot the conservative PM-expanded scattering angle, calculated from Eq. (7.10), for the initial values of energy and angular momentum used in the NR simulations, which are written in Table I of Ref. [466]. We see that each PM order gives better agreement with NR than the lower orders, with an overall good agreement at 4PM, especially considering that these scattering angles are rather large while the PM expansion is an approximation away from a straight line.

We also plot the 3PN expansion of the 4PM scattering angle, finding that the difference with the full 4PM angle is only $\sim .1$ degrees. This is because the initial velocity is $v \simeq 0.4$, for which a PN expansion provides a good approximation. Higher velocities would lead to larger differences between the PM scattering angle and its PN expansion. Furthermore, the figure shows the 3PM conservative scattering angle plus the leading order (3PM) radiative contribution, which is given by Eq. (5.7) of Ref. [285], however the effect of that radiative contribution is so small that it is almost the same as the conservative 3PM curve.

In the right panel of Fig. 7.6, we plot the scattering angle taking into account the effect of RR by modifying the initial conditions, as explained above in Eq. (7.25). We see that all curves are shifted closer to the NR curve, but their order remains the same.

7.5.2 Scattering angle from PM-EOB Hamiltonians

To compute the scattering angle from the EOB Hamiltonians, we start with an initial azimuthal angle $\phi_{\text{in}} = 0$, evolve the equations of motion without RR force, then read off the final angle ϕ_{out}, leading to the scattering angle $\chi_{\text{EOB}} = \phi_{\text{out}} - \phi_{\text{in}} - \pi$. We start the evolution with initial separation $r_{\text{in}} = 10^4$, initial angular momentum $L_{\text{in}}^{\text{NR}}$, and solve $E_{\text{in}}^{\text{NR}} = H^{\text{EOB}}$ for the initial p_r.

In Fig. 7.7, we plot the relative difference in the conservative scattering angle between EOB and NR, finding much smaller difference than the PM-expanded angles in Fig. 7.6. Similarly, in Fig. 7.8, we plot the same quantity but using initial conditions that account for the NR energy

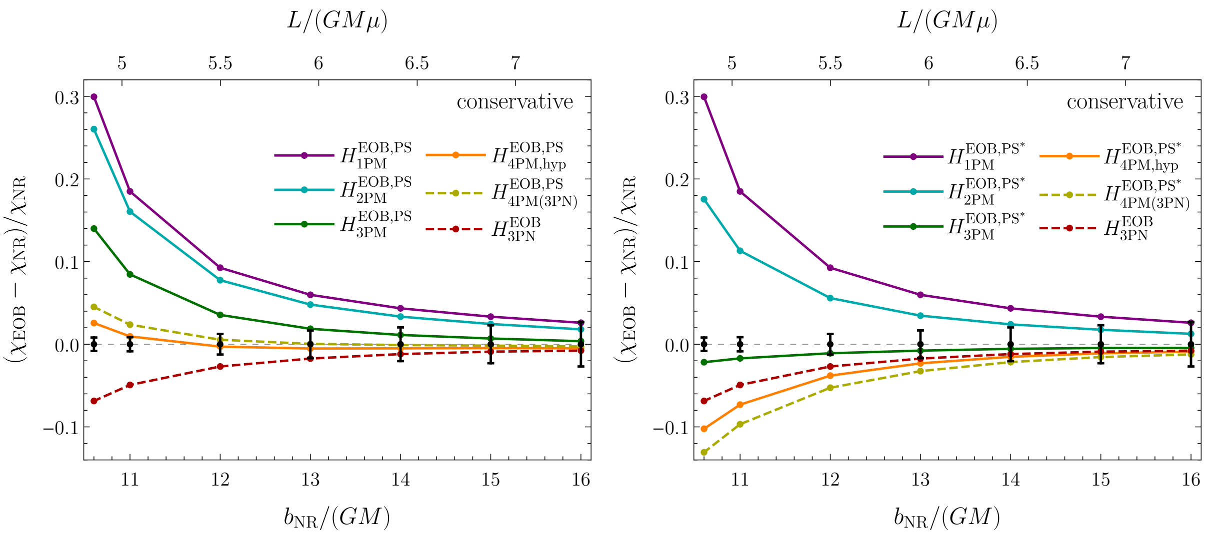

Figure 7.7: Comparison with NR of the conservative scattering angle computed from the EOB Hamiltonians in the PS gauge (left panel) and the PS* gauge (right panel).

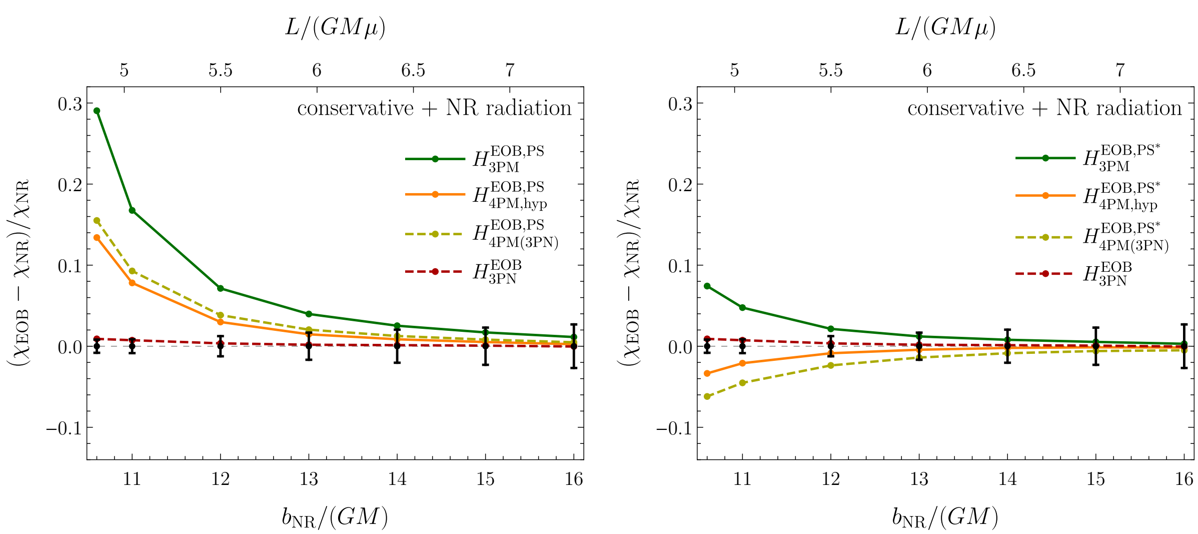

Figure 7.8: Scattering angle calculated from the EOB Hamiltonians in the PS gauge (left panel) and the PS* gauge (right panel) while incorporating radiative effects from NR through the initial conditions as in Eq. (7.25).

and angular momentum losses, as in Eq. (7.25). For comparison, both figures show the scattering angle calculated from a 3PN EOB Hamiltonian in the gauge of Refs. [80, 380, 384], which is valid for arbitrary trajectories since 3PN is purely local in time (no tails contributions).

From Fig. 7.7, we see that 4PM performs better than 3PM for the PS gauge, but 3PM is better for the PS* gauge. However, when including the NR RR in Fig. 7.8, 4PM becomes closer to NR than 3PM for both gauges. We also see that the PS* gauge gives better agreement with NR than the PS gauge.

For bound orbits, we saw in the previous section that PN-expanding the PM Hamiltonians gave almost the same results. For scattering encounters on the other hand, we see from both Fig. 7.7 and Fig. 7.8 that the 4PM Hamiltonians lead to better results than the 3PN expansion of their potentials, for both EOB gauges and whether or not RR is included.

7.5.3 4PN EOB Hamiltonian for hyperbolic orbits

The 4PN EOB Hamiltonian derived in Ref. [80] included the tail part in a small-eccentricity expansion, and is thus valid for bound orbits. The 4PN tail contribution for hyperbolic orbits was derived in Ref. [558], analytically at leading order in the large-eccentricity expansion, and numerically for eccentricity ≥ 1. However, it is not straightforward to translate the all-orders-in-eccentricity result of Ref. [558] to an EOB Hamiltonian in the form of Eq. (7.15). Therefore, here, we compute a hyperbolic-orbit 4PN EOB Hamiltonian at next-to-leading order in the large-eccentricity expansion. We use that Hamiltonian to compare the effect of using an elliptic versus a hyperbolic-orbit Hamiltonian on the scattering angle.

We start by writing an effective Hamiltonian of the form

$$\hat{H}_{\text{eff}}^{\text{4PN,hyp}} = \sqrt{A^{\text{hyp}}\left[1 + \frac{p_r^2}{B^{\text{hyp}}} + l^2u^2 + Q^{\text{hyp}}\right]}\,, \tag{7.27}$$

$$(B^{\text{hyp}})^{-1} \equiv A^{\text{hyp}}\bar{D}^{\text{hyp}}, \tag{7.28}$$

in which the potentials contain local and nonlocal-in-time contributions, starting at 4PN order. The local part is valid for generic motion, and is given by Eqs. (4.4), (9.6) and (9.7) of Ref. [91], which we follow in how the local and nonlocal parts are split.

We then write an ansatz for the potentials with unknown coefficients for the nonlocal contribution, that is

$$\begin{aligned}
A^{\text{hyp}} &= 1 - 2u + 2\nu u^3 + \left(\frac{94}{3} - \frac{41}{32}\pi^2\right)\nu u^4 \\
&\quad + \left[\left(\frac{41\pi^2}{32} - \frac{221}{6}\right)\nu^2 + \left(\frac{2275\pi^2}{512} - \frac{4237}{60}\right)\nu\right]u^5 \\
&\quad + \left(a_5^{\text{nloc}} + a_{5,\ln u}^{\text{nloc}}\ln u + a_{5,\ln p}^{\text{nloc}}\ln p^2\right)u^5,
\end{aligned} \tag{7.29}$$

$$\begin{aligned}
\bar{D}^{\text{hyp}} &= 1 + 6\nu u^2 + \left(52\nu - 6\nu^2\right)u^3 \\
&\quad + \left[\left(\frac{123\pi^2}{16} - 260\right)\nu^2 + \left(\frac{1679}{9} - \frac{23761\pi^2}{1536}\right)\nu\right]u^4 \\
&\quad + \left(d_4^{\text{nloc}} + d_{4,\ln u}^{\text{nloc}}\ln u + d_{4,\ln p}^{\text{nloc}}\ln p^2\right)u^4,
\end{aligned} \tag{7.30}$$

$$\begin{aligned}
Q^{\text{hyp}} &= 2\nu(4 - 3\nu)u^2p_r^4 + \left(10\nu^3 - 83\nu^2 + 20\nu\right)u^3p_r^4 \\
&\quad + \left(6\nu^3 - \frac{27\nu^2}{5} - \frac{9\nu}{5}\right)u^2p_r^6.
\end{aligned} \tag{7.31}$$

In this ansatz, the 4PM nonlocal coefficients in $\bar{D}^{\text{hyp}}$ are at leading order in the large-eccentricity expansion, while those at 5PM in A^{hyp} are at next-to-leading order, with no nonlocal contributions to Q^{hyp}. We also assume in the ansatz a dependence on $\ln p^2$ because it simplifies the result, but other possible choices include $\ln(l^2u^2)$ or $\ln E_{\text{N}}$, with E_{N} being the Newtonian energy.

To fix the unknown coefficients in the ansatz, we calculate the scattering angle from the Hamiltonian using Eq. (7.19), then match the result to the *total* 5PM(4PN) scattering angle, which schematically reads

$$\frac{\chi_{4\mathrm{PN}}}{2} = \frac{\chi_1}{L} + \frac{\chi_2}{L^2} + \frac{\chi_3}{L^3} + \frac{\chi_4^{\mathrm{loc}} + \chi_4^{\mathrm{nloc}}}{L^4} + \frac{\chi_5^{\mathrm{loc}} + \chi_5^{\mathrm{nloc}}}{L^5}\,, \tag{7.32}$$

where the local χ_n coefficients are given by Eq. (10.1) of Ref. [91], and the nonlocal part by Eq. (6.11) of Ref. [92]. After matching the scattering angle and solving for the Hamiltonian coefficients, we obtain the following solution

$$\begin{aligned}
a_5^{\mathrm{nloc}} &= \nu\left(\frac{2752}{15}\ln 2 - \frac{5464}{75}\right), \\
a_{5,\ln p}^{\mathrm{nloc}} &= \frac{64\nu}{5}, \qquad a_{5,\ln u}^{\mathrm{nloc}} = 0, \\
d_4^{\mathrm{nloc}} &= \nu\left(168 - \frac{1184}{15}\ln 2\right), \\
d_{4,\ln p}^{\mathrm{nloc}} &= \frac{592\nu}{15}, \qquad d_{4,\ln u}^{\mathrm{nloc}} = 0,
\end{aligned} \tag{7.33}$$

that is, with no dependence on $\ln u$.

In Fig. 7.9, we compare to NR the scattering angle computed from the elliptic-orbit Hamiltonian of Ref. [80] and the angle computed from the hyperbolic-orbit Hamiltonian in Eq. (7.27). We see that, unexpectedly, the elliptic-orbit Hamiltonian gives better agreement with NR. However, that result depends on the particular resummation of the potentials.

To illustrate this, we consider a simple factorization of the A potential given by

$$\begin{aligned}
A^{\text{hyp,fact.}} = (1-2u)\Bigg\{1 + 2\nu u^3 + \left(\frac{106}{3} - \frac{41\pi^2}{32}\right)\nu u^4 \\
+ \left[\left(\frac{963\pi^2}{512} - \frac{21841}{300} + \frac{2752\ln 2}{15}\right)\nu + \left(\frac{41\pi^2}{32} - \frac{221}{6}\right)\nu^2 + \frac{64}{5}\nu\ln p^2\right]u^5\Bigg\},
\end{aligned} \tag{7.34}$$

which agrees with Eq. (7.29) when Taylor expanded. Similarly, the factorized version of the

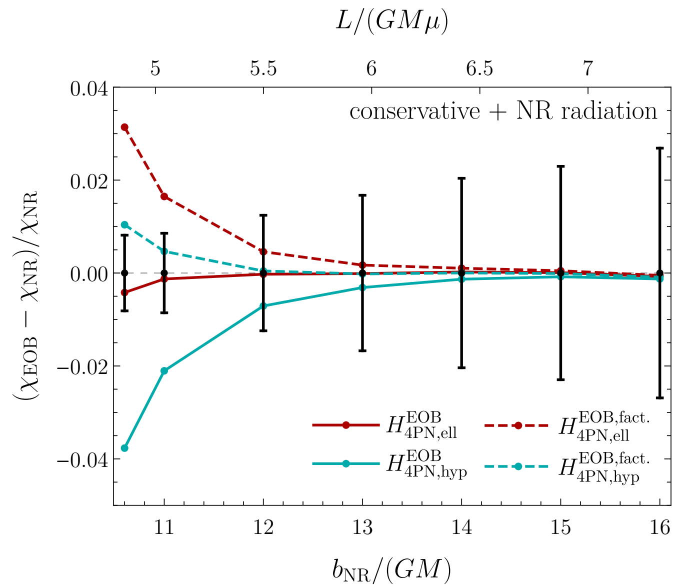

Figure 7.9: Scattering angle calculated from 4PN EOB Hamiltonians for elliptic and hyperbolic orbits. The solid lines are for Hamiltonians with Taylor-expanded potentials, while the dashed lines are for Hamiltonians with factorized potentials.

elliptic-orbits A potential in Eq. (8.1) of Ref. [80] reads

$$A^{\text{ell,fact.}} = (1-2u)\left\{1 + 2\nu u^3 + \left(\frac{106}{3} - \frac{41\pi^2}{32}\right)\nu u^4 \right. \tag{7.35}$$
$$\left. + \left[\left(\frac{1}{20} + \frac{963\pi^2}{512} + \frac{128\gamma_E}{5} + \frac{256\ln 2}{5}\right)\nu + \left(\frac{41\pi^2}{32} - \frac{221}{6}\right)\nu^2 + \frac{64}{5}\nu\ln u\right]u^5\right\}.$$

Comparing the scattering angle computed from Hamiltonians with these factorized potentials (dashed lines in Fig. 7.9), we see that the hyperbolic-orbit Hamiltonian now gives better agreement with NR than the one for elliptic orbits.

These results show that there can be differences between elliptic and hyperbolic-orbit Hamiltonians when applied to scattering encounters, but which performs better depends on the particular gauge of the Hamiltonian and the resummations of its coefficients.

7.6 Conclusions

In this paper, we investigated the conservative 4PM Hamiltonian with nonlocal-in-time (tail) effects for hyperbolic orbits, which was derived in Refs. [246, 247, 258, 259], by comparing it to NR simulations for the binding energy and scattering angle. We found an improvement over lower PM orders, which was expected since 4PM order contains the full 3PN information. In addition, even though the nonlocal part of the 4PM Hamiltonian is valid for hyperbolic motion, we showed that it performs well for bound orbits, and that the hyperbolic piece has a small effect on the dynamics. This was demonstrated by comparing the PN-expanded binding energy for bound versus unbound orbits (see Fig. 7.2), and by complementing the 4PM Hamiltonian with bound-orbit corrections at 4PN, 5PN, and 6PN orders (see Fig. 7.3).

As a first study, we incorporated the 4PM information in two EOB Hamiltonians, given by Eqs. (7.17) and (7.18). (The EOB Hamiltonians are not calibrated to NR simulations, and do not use resummations of the effective-metric components.) For bound orbits, we found that the PM Hamiltonians gave similar results to the same Hamiltonians with PN-expanded potentials. However, for the scattering angle, the PM-EOB Hamiltonians showed better agreement with NR than PN-EOB Hamiltonians in the same gauge (see Figs. 7.7 and 7.8).

In particular, we found that including 4PM results in EOB Hamiltonians improved the disagreement with the NR binding energy from about 40%, for equal masses at 2 GW cycles before merger, to about 10% for the PS gauge and 3% for the PS* gauge (see Figs. 7.3 and 7.4). These results have been obtained for the conservative dynamics, but will change, and likely improve, once RR is included and the equations of motion are evolved for an inspiraling trajectory. For the scattering angle, the difference with NR was 8% and 2%, respectively for the two EOB gauges, at impact parameter $b = 11GM$ and initial relative velocity $v \simeq 0.4$ (see Figs. 7.6 and 7.8). Our comparisons of the scattering angle also highlighted the importance of including RR effects even when comparing conservative results with NR. For example, the conclusions one draws would be different between Fig. 7.7, which is purely conservative, and Fig. 7.8, which includes the NR radiative losses.

Furthermore, we worked out a 4PN EOB Hamiltonian for hyperbolic orbits, which extends the elliptic-orbit Hamiltonian of Ref. [80]. We compared the scattering angles of the two Hamiltonians to NR and showed that the Hamiltonian gauge and the resummations of its coefficients can affect the agreement with NR.

The only NR simulations currently available in the literature for the scattering angle [466] are for equal masses and for a specific value of the energy corresponding to $v \simeq 0.4$. It would be interesting to see how PM and PN information compare with NR for unequal masses and higher velocities. Such studies would enable the construction of accurate waveform models over the whole binary parameters space including large eccentricities and large velocities.

Acknowledgments

We are grateful to Zvi Bern, Enrico Herrmann, Radu Roiban, and Mikhail Solon for fruitful discussions and valuable comments. We also thank Gregor Kälin, Julio Parra-Martinez, Rafael Porto, Michael Ruf, Chia-Hsien Shen, and Mao Zeng for useful discussions. We thank Sergei Ossokine for providing the NR data for the binding energy.

Chapter 8: Hairy binary black holes in Einstein-Maxwell-dilaton theory and their effective-one-body description

Authors[1]: *Mohammed Khalil, Noah Sennett, Jan Steinhoff, Justin Vines, Alessandra Buonanno*

Abstract: In General Relativity and many modified theories of gravity, isolated black holes (BHs) cannot source massless scalar fields. Einstein-Maxwell-dilaton (EMd) theory is an exception: through couplings both to electromagnetism and (non-minimally) to gravity, a massless scalar field can be generated by an electrically charged BH. In this work, we analytically model the dynamics of binaries comprised of such scalar-charged ("hairy") BHs. While BHs are not expected to have substantial electric charge within the Standard Model of particle physics, nearly-extremally charged BHs could occur in models of minicharged dark matter and dark photons. We begin by studying the test-body limit for a binary BH in EMd theory, and we argue that only very compact binaries of nearly-extremally charged BHs can manifest non-perturbative phenomena similar to those found in certain scalar-tensor theories. Then, we use the post-Newtonian approximation to study the dynamics of binary BHs with arbitrary mass ratios. We derive the equations governing the conservative and dissipative sectors of the dynamics at next-to-leading order, use our results to compute the Fourier-domain gravitational waveform in the stationary-phase approx-

[1]Originally published as Phys. Rev. D **98**, no.10, 104010 (2018)

imation, and compute the number of useful cycles measurable by the Advanced LIGO detector. Finally, we construct two effective-one-body (EOB) Hamiltonians for binary BHs in EMd theory: one that reproduces the exact test-body limit and another whose construction more closely resembles similar models in General Relativity, and thus could be more easily integrated into existing EOB waveform models used in the data analysis of gravitational-wave events by the LIGO and Virgo collaborations.

8.1 Introduction

The first observations of gravitational waves (GWs) from coalescing binary black holes (BHs) [12, 659–662] and neutron stars [16] offer unprecedented opportunities to test the highly dynamical, strong-field regime of General Relativity (GR) [50, 424, 663]. Leveraging the extraordinary precision of GW detectors to test gravity requires waveform models that incorporate potential deviations from GR. One can construct such models in a theory-independent way by considering phenomenological deviations to waveform models in GR and then constraining the magnitude of these corrections, see, e.g., the constructions of [664–667]. Such an approach has been used by the LIGO and Virgo collaborations to test GR with binary BHs [579, 660, 668]. Alternatively, one can compute the waveform produced in a particular alternative theory, which can then be used to measure directly the fundamental quantities that define that modified theory of gravity [50].

In this paper, we adopt the latter approach, focusing on the dynamics of binary BHs in Einstein-Maxwell-dilaton (EMd) theory. This theory originated as a low-energy limit of string theory [467, 468]. In EMd theory, a scalar field (the dilaton) couples to a vector field (the photon) such that BHs with electric charge also source the scalar; the BH develops a scalar charge, or hair. It has been shown that in GR (and some scalar extensions) isolated BHs cannot carry such a charge [669, 670]; these results are often referred to as "no-hair theorems." Analytic solutions exist in EMd theory for spherically symmetric BHs parameterized by the dilaton coupling constant a [see Eqs. (8.1) and (8.2) below for the action]. For $a = 0$, the theory reduces to Einstein-Maxwell (EM) theory and the BH solution is the Reissner-Nordström metric. For $a = 1$, the solution corresponds to the low energy limit of heterotic string theory. For $a = \sqrt{3}$, the solution corresponds to Kaluza-Klein BHs [671], and an analytic solution for charged spinning BHs in EMd theory is only known for that value of a [672].

In the absence of electric charge, isolated BHs in EMd theory behave as in GR. Within the Standard Model, astrophysical BHs are expected to be electrically neutral; however, there exist various theoretical mechanisms beyond the Standard Model that would allow BHs to accumulate non-negligible charge. For a BH with charge Q and mass M to accrete a particle with the same-sign charge q and mass m, gravitational attraction between the two bodies must overpower their electrostatic repulsion, i.e., $q\,Q \lesssim m\,M$, or equivalently $Q/M \lesssim m/q$.[2] Furthermore, a charged BH will neutralize via spontaneous pair production [469] or interactions with astrophysical plasmas [470] over timescales that grow with the mass-to-charge ratio of the available fundamental particles. For electrons, the dimensionless mass-to-charge ratio $m_e/q_e \sim 10^{-22}$ severely limits the charge that BHs can develop through accretion, and guarantees that any BH charged through other means will discharge quickly. However, particles with much larger mass-to-charge ratios are predicted in models of minicharged dark matter [471–473] and would allow BHs to acquire

[2] Throughout this work, we use geometric units, in which $G = c = 4\pi\epsilon_0 = 1$, where G is the bare gravitational constant.

and retain a much larger electric charge [477]. Similarly, models in which dark matter is charged under a hidden U(1) gauge field [474–476], a "dark photon," would allow for BHs to develop significant hidden charge, provided that the ratio of the dark-matter particle's mass to its (hidden) charge is sufficiently large [477]. These two types of dark matter models are consistent with laboratory experiments and cosmological observations [673–675]; current constraints restrict the new particles' mass to 1 GeV $\lesssim m \lesssim$ 10 TeV [476] and its charge to $\lesssim 10^{-14}(m/\text{GeV})q_e$ [676] (see also Fig. 1 in Ref. [477]).

The dynamical evolution of binary BHs in EMd theory has been studied in various contexts. Numerical-relativity simulations of single and binary BHs were performed in Ref. [481]. The authors considered small electric charges and found that the resulting gravitational waveforms are difficult to distinguish from those in GR. Numerical-relativity simulations of the collision of charged BHs with large electric charges in EM theory were performed in Refs. [677, 678], where it was found that a significant fraction of the energy is carried away by electromagnetic radiation.

In this work, we compute the conservative and dissipative dynamics of a binary BH, and the resulting gravitational waveform, in EMd theory, to first order in the (weak-field and slow-motion) post-Newtonian (PN) approximation. We also construct an effective-one-body (EOB) Hamiltonian description [380, 381] of the conservative dynamics, which provides an analytical resummation of the PN dynamics to exactly recover the test-body limit. In late 2017, the 1PN Lagrangian for a two-body system in EMd theory was derived independently in Ref. [210] using a method different from our own. In that work, the author also discussed an abrupt transition in the scalar charge of a BH as the external scalar field is varied. However, we show here that this transition occurs only in binaries composed of nearly-extremal charged BHs and only near the end of their coalescence. Although extremally charged BHs are excluded when restricting to the Standard Model of particle physics, they are still viable in minicharged dark matter and dark photons models, as we have discussed above.

The paper is structured as follows. In Sec. 8.2, we study the behavior of a small BH in the background of a much more massive companion. By exploring the response of this test BH to its external environment, we discuss whether non-perturbative, strong-field phenomena, akin to those seen in binary neutron stars in scalar-tensor (ST) theories, can occur in binary BHs in EMd theory. In Sec. 8.3, we use the PN approximation to study the dynamics of a binary system with an arbitrary mass ratio. We derive the two-body 1PN Lagrangian and Hamiltonian (with details relegated to Appendix M) and calculate the scalar charge of the two bodies. Further, we derive (with details in Appendix N) the next-to-leading order PN scalar, vector, and tensor energy fluxes emitted by the binary. Restricting our attention to quasi-circular orbits, we compute the Fourier-domain gravitational waveform at next-to-leading-order using the stationary-phase approximation. In Sec. 8.4, we work out an EOB description of the PN Hamiltonian in EMd theory. We construct two EOB Hamiltonians: one based on the exact BH solution, and the other based on an approximation to that solution. The former is more physical in the strong-gravity regime because it exactly reproduces the dynamics in the test-body limit; the latter uses the same gauge as EOB models in GR, and thus would be easier to integrate into existing data-analysis infrastructure. We compare these two EOB Hamiltonians by calculating the binding energy and the innermost stable circular orbit to determine the region of the parameter space in which they agree. Finally, we present some concluding remarks in Sec. 8.5.

8.2 Einstein-Maxwell-dilaton theory

8.2.1 Setup

We consider a generalization of EMd theory presented in Refs. [467, 468] in the Jordan frame

$$S=\int d^4x\,\frac{\sqrt{-\tilde{g}}}{16\pi}e^{-2a\varphi}\Big(\tilde{R}+(6a^2-2)\tilde{g}^{\mu\nu}\tilde{\nabla}_\mu\varphi\tilde{\nabla}_\nu\varphi$$

$$-F_{\mu\nu}F^{\mu\nu}\Big)+S_m(\tilde{g}_{\mu\nu},A_\mu,\psi), \tag{8.1}$$

where φ is a scalar field (the dilaton), a is the dilaton coupling constant, $F_{\mu\nu}\equiv\tilde{\nabla}_\mu A_\nu-\tilde{\nabla}_\nu A_\mu$ is the electromagnetic field tensor, and tildes signify quantities in the Jordan frame. We also include some matter fields ψ, which couple minimally to $\tilde{g}_{\mu\nu}$ and, through some fundamental electric charge, to A_μ; we represent this total matter action schematically with S_m. By construction, electrically neutral, non-self-gravitating matter configurations will follow geodesics of $\tilde{g}_{\mu\nu}$, and thus this theory respects the weak equivalence principle. However, self-gravitating systems are bound (in part) through non-linear interactions of the scalar field. The back-reaction of the scalar field on the metric exerts an additional force on such systems, causing them to no longer follow geodesics; thus, this theory violates the strong equivalence principle.

The Einstein frame provides a more convenient representation of EMd theory. Performing the conformal transformation $g_{\mu\nu}=\mathcal{A}^{-2}(\varphi)\tilde{g}_{\mu\nu}$ with $\mathcal{A}=e^{a\varphi}$, the action becomes

$$S=\int d^4x\,\frac{\sqrt{-g}}{16\pi}\left(R-2g^{\mu\nu}\partial_\mu\varphi\partial_\nu\varphi-e^{-2a\varphi}F_{\mu\nu}F^{\mu\nu}\right)$$

$$+S_m(\mathcal{A}^2(\varphi)g_{\mu\nu},A_\mu,\psi), \tag{8.2}$$

where $g_{\mu\nu}$ is the Einstein-frame metric. In this paper, we primarily work in the Einstein frame, but occasionally use quantities in the Jordan frame, denoted with tildes. For a discussion of the equivalence between the two frames see Ref. [679].

For the matter action S_m, we adopt the approach introduced by Eardley [480], in which each body is treated as a delta function and the dependence on the scalar field is incorporated into the masses. For charged monopolar point particles, neglecting dipoles/spins and higher multipoles, the matter action in the Einstein frame can be written as [200]

$$S_m = -\sum_A \int dt \left[\mathfrak{m}_A(\varphi)\sqrt{-g_{\mu\nu}\, v_A^\mu v_A^\nu} - q_A A_\mu v_A^\mu\right], \tag{8.3}$$

where $\mathfrak{m}_A(\varphi)$ is the field-dependent mass of particle A, q_A is the electric charge, $v_A^\mu \equiv u_A^\mu/u_A^0$ where u_A^μ is its four-velocity, and the fields are evaluated at the particle's location. The mass in the Einstein frame $\mathfrak{m}(\varphi)$ is related to the mass in the Jordan-Fierz frame $\tilde{\mathfrak{m}}(\varphi)$ by

$$\mathfrak{m}(\varphi) = \mathcal{A}(\varphi)\tilde{\mathfrak{m}}(\varphi), \tag{8.4}$$

where $\tilde{\mathfrak{m}}(\varphi)$ is generally not a constant except for bodies with negligible self-gravity.

In most cases, a closed-form expression for the field-dependent mass $\mathfrak{m}(\varphi)$ cannot be found. Instead, one expands the mass about the external/background value φ_0 of the scalar field

$$\ln \mathfrak{m}(\varphi) = \ln \mathfrak{m}(\varphi_0) + \left.\frac{d\ln \mathfrak{m}(\varphi)}{d\varphi}\right|_{\varphi_0} \delta\varphi + \frac{1}{2}\left.\frac{d^2 \ln \mathfrak{m}(\varphi)}{d\varphi^2}\right|_{\varphi_0} \delta\varphi^2 + \mathcal{O}\left(\frac{1}{c^6}\right), \tag{8.5}$$

where $\delta\varphi \equiv \varphi - \varphi_0$. The mass expansion can be parameterized in terms of

$$\alpha(\varphi) \equiv \frac{d\ln \mathfrak{m}(\varphi)}{d\varphi}, \qquad \beta(\varphi) \equiv \frac{d\alpha(\varphi)}{d\varphi}, \tag{8.6}$$

where α is referred to as the (dimensionless) scalar charge. With these parameters, the mass expansion can be written as

$$\mathfrak{m}(\varphi) = m\left[1 + \alpha\delta\varphi + \frac{1}{2}(\alpha^2+\beta)\delta\varphi^2 + \mathcal{O}\left(\frac{1}{c^6}\right)\right], \tag{8.7}$$

where the field-dependent mass is denoted by the Gothic script $\mathfrak{m}$, while the mass evaluated at the background value of the scalar field is denoted by m. We also drop the dependence of the parameters on the background value to simplify the notation, i.e., $\alpha \equiv \alpha(\varphi_0)$, and $\beta \equiv \beta(\varphi_0)$. For the field-dependent parameters, we always explicitly write $\alpha(\varphi)$ and $\beta(\varphi)$. The expression for $\alpha(\varphi)$ depends on the structure of the body; for static BHs, it depends only on the charge-to-mass ratio, whereas for baryonic matter, it also depends on the body's composition.

We note that Eq. (8.3) together with the expansion of the mass (8.7) provide a systematic construction of an effective source or action for an extended object in a PN expansion. We neglect couplings to derivatives of the field, which would correspond to dipole/spin and higher multipole interactions. Due to invariance under gauge transformations $A_\mu \to A_\mu + \partial_\mu \epsilon$, the charges q_A must be constant; they cannot depend on the scalar field like the masses.

8.2.2 Black-hole solution

The metric for an electrically-charged non-rotating BH in EMd theory is given by [467, 468]

$$ds^2 = -A(r)dt^2 + B(r)dr^2 + r^2 C(r) d\Omega^2, \tag{8.8}$$

with

$$A(r) = \left(1 - \frac{r_+}{r}\right)\left(1 - \frac{r_-}{r}\right)^{\frac{1-a^2}{1+a^2}}, \tag{8.9a}$$

$$B(r) = \frac{1}{A(r)}, \tag{8.9b}$$

$$C(r) = \left(1 - \frac{r_-}{r}\right)^{\frac{2a^2}{1+a^2}}, \tag{8.9c}$$

where the constants r_+ and r_- are given in terms of the Arnowitt-Deser-Misner mass M and electric charge Q by

$$M = \frac{r_+}{2} + \left(\frac{1-a^2}{1+a^2}\right)\frac{r_-}{2}, \tag{8.10}$$

$$Q^2 = \frac{r_+ r_-}{1+a^2}\, e^{-2a\varphi_0}\,. \tag{8.11}$$

The constant r_+ corresponds to the outer horizon, and r_- corresponds to the inner horizon. The surface area of the horizon (entropy of the BH) is proportional to $r_+^2 C(r_+)$. Here, we refer to the metric (8.8) as the GHS metric, after Garfinkle, Horowitz and Strominger who found the solution in that form in Ref. [468].

The electromagnetic four-potential A_μ, for an electrically-charged BH, is given by

$$A_0(r) = -\frac{Q}{r} e^{2a\varphi_0}, \qquad A_i(r) = 0\,, \tag{8.12}$$

and the scalar field φ is given by

$$\varphi(r) = \varphi_0 + \frac{a}{1+a^2} \ln\left(1 - \frac{r_-}{r}\right). \tag{8.13}$$

While we consider only electric charges in this paper, we note that the solution for a magnetically charged BH can be obtained from the above solution via the duality rotation that sends $F_{\mu\nu} \to \frac{1}{2} e^{-2a\varphi} \epsilon_{\mu\nu}{}^{\lambda\rho} F_{\lambda\rho}$ and $\varphi \to -\varphi$. [3] In addition to the electric charge, BHs in EMd theory can acquire scalar charge, also called dilaton charge, defined by [468]

$$D \equiv \frac{1}{4\pi} \int d^2\Sigma^\mu \nabla_\mu \varphi, \tag{8.14}$$

where the integral is over a two-sphere at spatial infinity, leading to

$$D = \frac{a}{1+a^2} r_-\,. \tag{8.15}$$

Far from the BH, we have $\varphi(r) \simeq \varphi_0 - D/r + \mathcal{O}(1/r^2)$, which means that D acts as the monopole charge sourcing the scalar field.

[3] The results of Sec. 8.2 hold also for magnetic charges if we flip the sign of φ. However, the PN and EOB results in the following sections would change in non-trivial ways for the magnetic case, since the BH's $F_{\mu\nu}$ is given by $F_{\theta\phi} = Q_m \sin\theta$ with a magnetic charge Q_m, as opposed to $F_{tr} = Q/r^2$ with an electric charge Q (all other components being zero in each case).

The constants r_+ and r_- can be expressed in terms of the mass and the dilaton charge, or the mass and electric charge, as

$$\begin{aligned} r_- &= \frac{1+a^2}{a} D \\ &= \frac{1+a^2}{1-a^2}\left(M - \sqrt{M^2-(1-a^2)Q^2e^{2a\varphi_0}}\right), \end{aligned} \tag{8.16a}$$

$$\begin{aligned} r_+ &= 2M - \frac{1-a^2}{a} D \\ &= M + \sqrt{M^2-(1-a^2)Q^2e^{2a\varphi_0}}\,. \end{aligned} \tag{8.16b}$$

Expressing quantities in terms of the dilaton charge D, rather than the electric charge Q, makes most equations simpler as it avoids the square root. Therefore, in most of the equations below, we use D instead of Q. The relation between Q and D can be read off from Eq. (8.16a), or Eq. (8.16b),

$$Q^2\, e^{2a\varphi_0} = \frac{2M}{a} D - \frac{1-a^2}{a^2} D^2\,. \tag{8.17}$$

The maximum electric charge of the BH occurs when $r_+ = r_-$, which leads to

$$Q_{\text{max}}\, e^{a\varphi_0} = \sqrt{1+a^2} M. \tag{8.18}$$

Hence, for nonzero values of a, an EMd BH can be more charged than an extremal Reissner-Nordström BH with the same mass. Since the dilaton charge is related to the electric charge via Eq. (8.17), the maximum electric charge (8.18) corresponds to the maximum dilaton charge $D_{\text{max}} = aM$.

Without loss of generality, we set the background scalar field to zero, i.e., $\varphi_0 = 0$. To recover the dependence on φ_0, one can simply rescale all electric charges by the factor $e^{a\varphi_0}$, and add the constant φ_0 to the scalar field. [4] We also consider only non-negative values of a since

[4]To see why this is true, consider the action (8.2) with the transformation $Q \to Qe^{a\varphi_0}$ and $\varphi \to \varphi + \varphi_0$. The

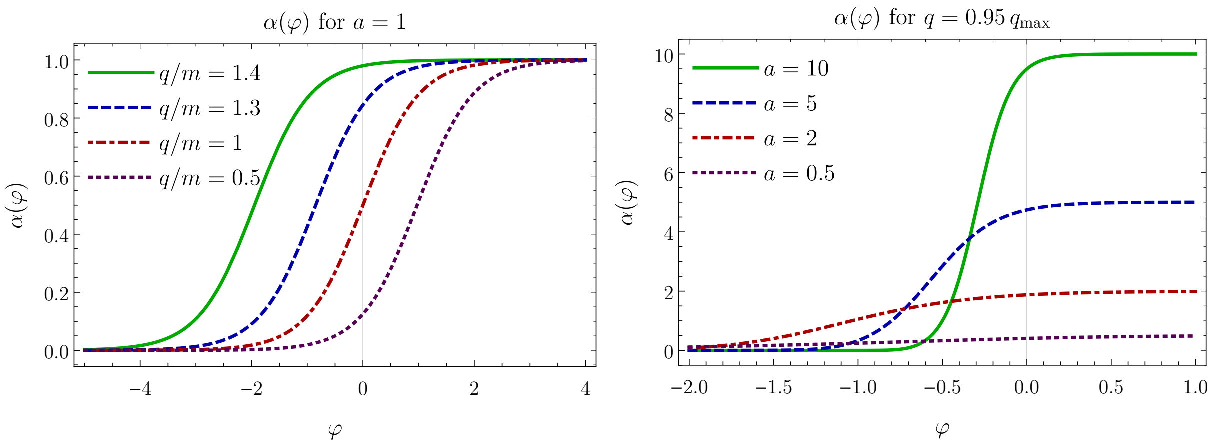

Figure 8.1: $\alpha(\varphi)$ for $a = 1$ with different charge-to-mass ratios (left), and for different values of a with $q = 0.95\, q_{\max}$ (right).

the action (8.2) is invariant under $a \to -a$ and $\varphi \to -\varphi$, so the predictions for negative dilaton couplings are given by changing the sign of the scalar field.

8.2.3 Dynamics of a test black-hole in a background black-hole spacetime

Before turning to the dynamics of a generic two-BH system in EMd theory, it will be useful to study the test-body limit of such a system, i.e., the limit in which one body's mass is negligible compared to the other's. In EM theory (without the dilaton), the test-body limit of a charged BH corresponds simply to a monopolar point-mass with constant mass and constant charge. In EMd theory, however, a BH's mass must retain a dependence on the dilaton field even as its size goes to zero. In the zero-size limit, we can use the local value of the (background) dilaton field φ, at the small BH's location, to determine its mass $\mathfrak{m}(\varphi)$ in the same way that a lone finite-size BH's

vacuum part of the action is symmetric under that transformation, and in the matter action (8.3), the mass $\mathfrak{m}(\varphi)$ is parameterized in terms of the difference $\varphi - \varphi_0$. The electromagnetic part of the matter action is more subtle; it depends on $qv^\mu A_\mu \propto Qqe^{2a\varphi_0}/r$, and hence, one can absorb a factor of $e^{a\varphi_0}$ into each of the two charges. However, since $A_0 = -Qe^{2a\varphi_0}/r$, the transformation $Q \to Qe^{a\varphi_0}$, $\varphi \to \varphi + \varphi_0$ is not valid in equations that depend on A_μ; one first needs to express A_μ in terms of the charges before performing that transformation.

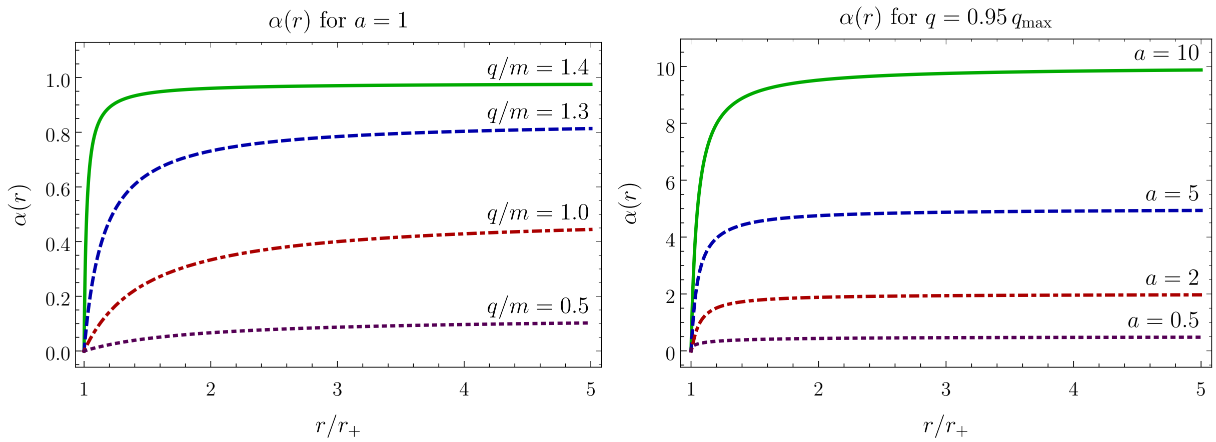

Figure 8.2: $\alpha(r)$ for $a = 1$ with different charge-to-mass ratios (left), and for different values of a (right). In both plots, the charge of the large BH is extremal $Q = \sqrt{1+a^2}M$, and r is scaled by the horizon radius, which is given by Eq. (8.16b). For $a = 1$, the horizon radius is $2M$ independently of the charge or the coupling constant.

mass would be determined by the asymptotic value of the field (as in the previous subsection). This defines what we mean by a "test BH" in EMd theory.[5]

Let us suppose a test BH with mass $\mathfrak{m}(\varphi)$, electric charge q, and dilaton charge d moves in the fixed background spacetime of a larger BH with mass M, electric charge Q, and dilaton charge D. The mass of the test BH $\mathfrak{m}(\varphi)$ depends on the scalar field φ generated by the larger BH. The expansion of $\mathfrak{m}(\varphi)$ is given in terms of the parameters α and β by Eq. (8.7), and the scalar field φ is given by Eq. (8.13).

To find how α and β depend on the mass and charge of the BH, one needs to find the dependence of the mass on the scalar field. We can get a differential equation for $\mathfrak{m}(\varphi)$ from Eq. (8.16a), or Eq. (8.16b), by identifying the mass M and charge Q with those of the test BH,

[5]This is not to be confused with some uses of the phrase "test body" in the context of ST theories, where one means a body with negligible self-gravity (unlike a BH), so that the mass in the Jordan-Fierz frame is constant and the scalar charge is zero.

i.e., $M \to \mathfrak{m}(\varphi)$ and $Q \to q$. The background value of the scalar field can be identified with the field from the more massive BH $\varphi_0 \to \varphi$, and the scalar charge by $D \to d\mathfrak{m}(\varphi)/d\varphi$, as was shown by the matching conditions in Ref. [210]. This leads to the equation

$$\frac{d\mathfrak{m}(\varphi)}{d\varphi} = \frac{a}{1-a^2}\left[\mathfrak{m}(\varphi) - \sqrt{\mathfrak{m}(\varphi)^2 - (1-a^2)q^2 e^{2a\varphi}}\right], \tag{8.19}$$

which, as far as we know, has no analytic solution for arbitrary values of a. Nevertheless, we can still obtain an expression for the dimensionless scalar charge, which is defined by Eq. (8.6),

$$\alpha(\varphi) = \frac{a}{1-a^2}\left[1 - \sqrt{1-(1-a^2)\frac{q^2 e^{2a\varphi}}{\mathfrak{m}^2(\varphi)}}\right], \tag{8.20}$$

and

$$\beta(\varphi) = \frac{a^2 q^2 e^{2a\varphi}}{(1-a^2)\mathfrak{m}^2(\varphi)}\left[1 - \frac{a^2}{\sqrt{1-(1-a^2)\frac{q^2 e^{2a\varphi}}{\mathfrak{m}^2(\varphi)}}}\right], \tag{8.21}$$

in agreement with Ref. [210].

It is interesting to note that an exact analytic solution to the differential equation (8.19) can be found when the coupling constant $a = 1$, that is

$$\mathfrak{m}(\varphi) = \sqrt{\text{const.} + \frac{1}{2}q^2 e^{2\varphi}}\,. \tag{8.22}$$

Since the above expression should give m when $\varphi = 0$, the integration constant is found to be $m^2 - \frac{1}{2}q^2$. Hence,

$$\mathfrak{m}(\varphi) = \sqrt{m^2 - \frac{1}{2}q^2 + \frac{1}{2}q^2 e^{2\varphi}}\,. \tag{8.23}$$

By differentiating $\mathfrak{m}(\varphi)$, we get the parameters

$$\alpha = \frac{q^2}{2m^2}\,, \qquad \beta = \frac{q^2}{m^2} - \frac{q^4}{2m^4}\,. \tag{8.24}$$

In Fig. 8.1, we plot $\alpha(\varphi)$ as a function of φ. We see that the test BH's $\alpha(\varphi)$ transitions between two values: zero and a. The function $\alpha(\varphi)$ reaches its maximum value when the quantity $q^2\, e^{2a\varphi}/\mathfrak{m}^2$ approaches $1 + a^2$, which means that in the Jordan-Fierz frame, the charge q

approaches the extremal value $\sqrt{1+a^2}\tilde{\mathfrak{m}}$, where the mass in the Jordan-Fierz frame $\tilde{\mathfrak{m}}$ is given by Eq. (8.4). Changing the charge-to-mass ratio shifts the curve on the horizontal axis, while changing a changes the maximum value of α and determines how quickly this transition occurs.

We emphasize that the scalar field φ generated by the more massive BH is always negative, as can be seen from Eq. (8.13), so the test BH always descalarizes. Further, because of the logarithm, the magnitude of φ increases slowly with decreasing separation until r approaches the inner horizon r_-, where it diverges. For the scalar charge of the test BH to change dramatically before merging with its much larger companion, both BHs must be close to extremally charged. As discussed in Sec. 8.1, extremally-charged BHs an exist in minicharged dark matter and dark photon models. If the test BH is not sufficiently charged, its scalar charge is close to zero when well separated from its companion, and then monotonically decreases toward zero as the binary evolves. The total shift in the scalar field that the test BH experiences prior to crossing the outer horizon is given by

$$\varphi(r_+) - \varphi(\infty) = \frac{a}{1+a^2} \ln\left[\frac{1 - D/D_{\text{max}}}{1-(1-a^2)D/2D_{\text{max}}}\right]. \tag{8.25}$$

Thus, if the large BH is not also sufficiently charged, then the test BH's scalar charge does not change dramatically.

In Fig. 8.2, we substitute the expression for the scalar field of the larger BH $\varphi(r)$ into that for the scalar charge of the test BH $\alpha(\varphi)$, and plot $\alpha(r)$ versus the separation r scaled by the horizon radius. When setting the charge of the large BH to its extremal value, $Q = \sqrt{1+a^2}M$, we see that the charge of the test BH also needs to be near extremal for the descalarization transition to occur. Yet, the transition only occurs very close to the horizon of the background BH. Hence, we expect this descalarization to drastically affect the GW signature only during the late inspiral and plunge of a test BH into a more massive BH and only when the BHs are nearly-extremally charged, when the horizon, the innermost-stable circular orbit, and the divergence in φ coincide. This result is analogous to extremal Kerr BHs, where the plunge occurs at significantly smaller separations [680]. However, a comparable-mass binary does not perform many orbits at small separations due to stronger radiation reaction, and thus we expect that the transition in the scalar charge would have a negligible effect on GWs from the inspiral of a comparable-mass binary.

We note that, while the descalarization transition occurs for near-extremal BHs, the largest change in the value of α from infinity until, e.g., $r = 2r_+$ occurs when the electric charge is $q/m \sim 1$, as can be seen in the left panel of Fig. 8.2. This is due to the slope of $\alpha(\varphi)$ at the background value of the scalar field $\varphi_0 = 0$. So, in order to increase the change in the scalar charge to observe descalarization, it is important to have a maximal $\beta(\varphi) \equiv d\alpha(\varphi)/d\varphi$.

8.2.4 Compact objects in Einstein-Maxwell-dilaton and scalar-tensor theories

Certain ST theories can exhibit non-perturbative phenomena, known as induced or dynamical scalarization, in binary systems of neutron stars [483–485, 509]. Having established how a BH responds to its scalar environment, we now investigate whether such effects could arise in binary BHs in EMd theory. In Ref. [481], the authors suggested that dynamical and induced scalarization are much less significant in EMd theory than in ST theories. In this subsection, we support this claim using more quantitative arguments by directly comparing the behavior of BHs and neutron stars in the respective theories.

In Ref. [681], the authors argued that the onset of induced and dynamical scalarization coincide with a breakdown of the PN approximation. Specifically, these non-perturbative phenomena indicate that the scalar field has grown beyond the validity of a PN expansion of $\mathfrak{m}$, e.g., Eq. (8.7). A useful diagnostic for determining the onset of such phenomena is to compare the relative size of the coefficients of such a power series to the small parameter with which one constructs the expansion.

While both EMd theory and ST theories include an additional scalar field, the non-minimal coupling of that field to the Jordan-Fierz (physical) metric can differ substantially. To facilitate comparisons between these theories, we consider an expansion of $\mathfrak{m}$ in $G_{\rm N}(\varphi)$, the parameter that characterizes the gravitational force felt between two test bodies placed in the scalar background φ. In both EMd theory and ST theories, this Newton's "constant" is given by

$$G_{\rm N}(\varphi) \equiv \mathcal{A}^2(\varphi)\left[1+\left(\frac{d\log\mathcal{A}}{d\varphi}\right)^2\right]. \tag{8.26}$$

We expand $\mathfrak{m}$ in terms of this quantity

$$\mathfrak{m}(G_{\rm N}) = m\left[1 + C_1\left(\frac{G-G_{\rm N}^0}{G_{\rm N}^0}\right) + C_2\left(\frac{G-G_{\rm N}^0}{G_{\rm N}^0}\right)^2 + \dots\right], \tag{8.27}$$

where we have defined

$$G_{\rm N}^0 \equiv G_{\rm N}(\varphi=0), \tag{8.28a}$$

$$C_1 \equiv \left[\frac{d\log\mathfrak{m}}{d\log G_{\rm N}}\right]_{G_{\rm N}=G_{\rm N}^0}, \tag{8.28b}$$

$$C_2 \equiv \frac{1}{2}\left[\frac{d^2\log\mathfrak{m}}{(d\log G_{\rm N})^2} + \left(\frac{d\log\mathfrak{m}}{d\log G_{\rm N}}\right)^2 - \frac{d\log\mathfrak{m}}{d\log G_{\rm N}}\right]_{G_{\rm N}=G_{\rm N}^0}. \tag{8.28c}$$

We compare these coefficients for BHs in EMd theory to that of neutron stars in Brans-Dicke gravity [682–684], defined by the coupling

$$\mathcal{A}_{\rm BD}(\varphi) = e^{-\alpha_0\varphi}, \tag{8.29}$$

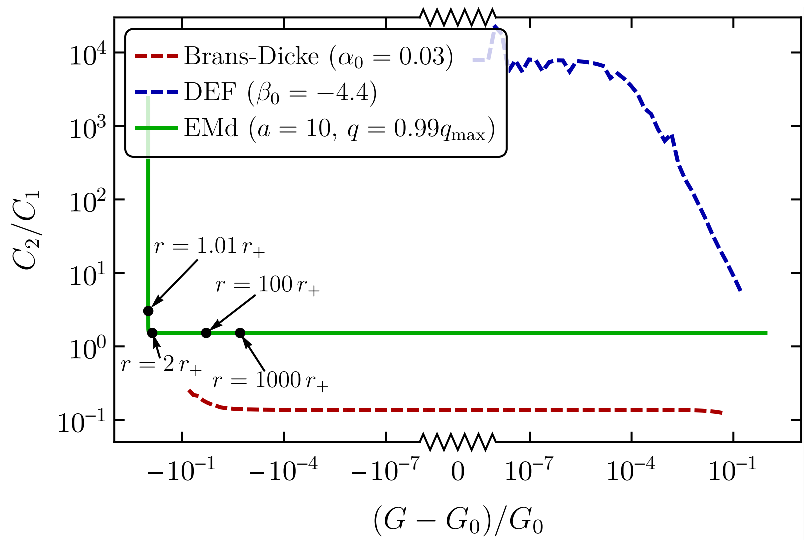

Figure 8.3: Ratio of the coefficients C_2/C_1 defined in Eqs. (8.28b) and (8.28c) as a function of $G_{\rm N}$ for BHs in EMd theory (solid) and neutron stars in various ST theories (dashed). Annotated points depict this ratio at various separations for a test BH with $q = 0.99q_{\rm max}$ in the background of a BH with $Q = Q_{\rm max}$ in EMd theory (r_+ refers to the outer horizon of the background spacetime).

and theories first considered by Damour and Esposito-Farèse (DEF) [200, 482]

$$\mathcal{A}_{\rm DEF}(\varphi) = e^{-\beta_0\varphi^2/2}, \tag{8.30}$$

in which induced and dynamical scalarization can occur when β_0 is sufficiently negative. In Fig. 8.3, we plot the ratio C_2/C_1 for compact objects in the various theories. For the ST theories, we consider neutrons stars with $m = 1.45M_\odot$ with the piecewise polytropic fit to the SLy equation of state constructed in Ref. [685]. The solid curve depicts this ratio for BHs in EMd theory with coupling $a = 10$. By comparison, this same quantity is shown with red and blue dashed curves for neutron stars in Brans-Dicke gravity with $\alpha_0 = 0.03$ and in the theory of Damour and Esposito-Farèse with $\beta_0 = -4.4$, respectively. Note that by inserting Eq. (8.30) into Eq. (8.26), one sees that this theory is only defined for $G_{\rm N}(\varphi) > G_{\rm N}^0$. For reference, we indicate with black points the separation at which these values are achieved in EMd theory when the test BH in placed in the background of an extremally charged BH; r_+ corresponds to the outer horizon of the background BH. We see that the magnitude of the ratio C_2/C_1 drastically differs between ST theories that manifest induced and dynamical scalarization (DEF) and EMd theories. This result indicates that a perturbative expansion of the dynamics has a larger regime of validity, and that non-perturbative phenomena are less likely to emerge during the coalescence of binary BHs in EMd theory.

8.3 Post-Newtonian approximation in Einstein-Maxwell-dilaton theory

8.3.1 Two-body dynamics

To go beyond the test-body limit, treating two-body systems with arbitrary mass ratios, we employ the PN approximation, which is valid in the weak-field, slow-motion regime [130]. In Appendix M, we derive results for the conservative dynamics of a binary BH system in EMd theory, at next-to-leading order in the PN expansion, i.e., at 1PN order. We employ the Fokker action method [686] (see also Ref. [201]), which has been used to treat the 4PN dynamics in GR [425], and the 2PN [201] and 3PN [206] dynamics in ST theories. We begin by considering the PN expansions of the EMd action in Eq. (8.2) and the matter action for point particles in Eq. (8.3), using the mass expansion in terms of the α and β parameters from Eq. (8.7). From the initial full action expanded to 1PN order, we obtain field equations for the scalar field, the metric potential, and the electromagnetic 4-potential. The Fokker action is obtained by plugging the (regularized) solutions to the field equations back into the action, eliminating the field degrees of freedom, yielding an action depending only on the matter variables. We work in the harmonic gauge $g^{\mu\nu}\Gamma^{\lambda}_{\mu\nu} = 0$ and the Lorenz gauge $\partial_\mu A^\mu = 0$ throughout. The final result for the two-body Lagrangian is given by

$$
\begin{aligned}
L = & -m_1 - m_2 + \frac{1}{2}m_1 v_1^2 + \frac{1}{2}m_2 v_2^2 + \left(1 + \alpha_1\alpha_2 - \frac{q_1 q_2}{m_1 m_2}\right)\frac{m_1 m_2}{r} \\
& + \frac{1}{8}m_1 v_1^4 + \frac{1}{8}m_2 v_2^4 + \frac{q_1 q_2}{2r}\left[\boldsymbol{v_1}\cdot\boldsymbol{v_2} + (\boldsymbol{n}\cdot\boldsymbol{v_1})(\boldsymbol{n}\cdot\boldsymbol{v_2})\right] \\
& + \frac{m_1 m_2}{2r}\left[(3-\alpha_1\alpha_2)(v_1^2 + v_2^2) - (7-\alpha_1\alpha_2)(\boldsymbol{v_1}\cdot\boldsymbol{v_2}) - (1+\alpha_1\alpha_2)(\boldsymbol{n}\cdot\boldsymbol{v_1})(\boldsymbol{n}\cdot\boldsymbol{v_2})\right] \\
& - \frac{m_1 m_2}{2r^2}\left[(1+2\alpha_1\alpha_2)(m_1+m_2) + m_1\alpha_1^2(\alpha_2^2+\beta_2) + m_2\alpha_2^2(\alpha_1^2+\beta_1)\right] \\
& + \frac{q_1 q_2}{r^2}\left[m_1(1+a\alpha_1) + m_2(1+a\alpha_2)\right] - \frac{1}{2r^2}\left[m_1 q_2^2(1+a\alpha_1) + m_2 q_1^2(1+a\alpha_2)\right] + \mathcal{O}\left(\frac{1}{c^4}\right),
\end{aligned}
\tag{8.31}
$$

where $\boldsymbol{r} \equiv \boldsymbol{x}_1 - \boldsymbol{x}_2$ is the separation between the two bodies, and $\boldsymbol{n} \equiv \boldsymbol{r}/r$. This Lagrangian agrees with the one derived by Damour and Esposito-Farèse [200, 201] when the Maxwell fields are zero. The standard 1PN Lagrangian in GR is obtained by setting $q_i = \alpha_i = \beta_i = 0$, while the Lagrangian in EM theory is obtained when $\alpha_i = \beta_i = 0$. Note that, since we use the mass expansion in Eq. (8.7) given in terms of generic parameters α and β, our results are not restricted to BHs in EMd theory, but are applicable to more generic bodies as well.

During the course of this project, the same 1PN Lagrangian for a two-body system in EMd theory was derived independently by Julié in Ref. [210]. While our results agree, our derivation differs from that of Ref. [210] in some notable respects. In Ref. [210], the (unexpanded) field equations were directly obtained from the action (8.2), and then those equations were expanded and solved for the fields. The primary difference with our derivation is in how Ref. [210] constructed the two-body Lagrangian: (i) taking (only) the matter action for one body (without the field part of the action, and without the matter action for the other body), which would apply if the body were a test body in some given fields, (ii) inserting for those fields the (regularized) solutions to the field equations resulting from the total (two bodies + fields) action, and (iii) taking the resultant Lagrangian and "symmetrizing" it with respect to the two bodies. While this procedure does produce a correct Lagrangian at 1PN order, it is not justified in general, and it is important to see how the result can be obtained from a consistent treatment of the full action for the two bodies and fields. In Ref. [210], it was also found that it is possible to parameterize the 1PN Lagrangian in EMd theory to have the same structure as the 1PN Lagrangian in ST theories, which means that many results in ST theories can be directly extended to EMd theory at 1PN order. We choose not to use that parameterization to make the dependence on the electric charges more apparent, and because many of our results are specific to EMd theory, such as calculating the vector energy flux and developing the EOB Hamiltonians.

The Hamiltonian in the center-of-mass frame can be derived from the Lagrangian using the Legendre transformation [223]

$$H = \boldsymbol{v} \cdot \boldsymbol{p} - L, \tag{8.32}$$

where the relative velocity $\boldsymbol{v} \equiv \boldsymbol{v}_1 - \boldsymbol{v}_2$ and the center-of-mass momentum

$$p_i = \frac{\partial L}{\partial v^i}. \tag{8.33}$$

This leads to the energy

$$\begin{aligned} E = M &+ \frac{1}{2}\mu v^2 - \frac{G_{12} M\mu}{r} + \frac{3}{8}(1-3\nu)\mu v^4 + \frac{G_{12}M\mu}{2r}\left[\left(\frac{3-\alpha_1\alpha_2}{1+\alpha_1\alpha_2 - \frac{q_1 q_2}{M\mu}} + \nu\right) v^2 + \nu \dot{r}^2\right] \\ &+ \frac{M^2\mu}{2r^2}\left[(1+\alpha_1\alpha_2)^2 + X_2\alpha_2^2\beta_1 + X_1\alpha_1^2\beta_2 + X_1\frac{q_2^2}{M\mu}(1+a\alpha_1) + X_2\frac{q_1^2}{M\mu}(1+a\alpha_2)\right. \\ &\left. - 2\frac{q_1 q_2}{M\mu}\left(1 + a\alpha_1 X_1 + a\alpha_2 X_2\right)\right] + \mathcal{O}\left(\frac{1}{c^4}\right), \end{aligned} \tag{8.34}$$

where $\dot{r} = \boldsymbol{n} \cdot \boldsymbol{v}$, and we defined the total mass M, reduced mass μ, symmetric mass ratio ν, and

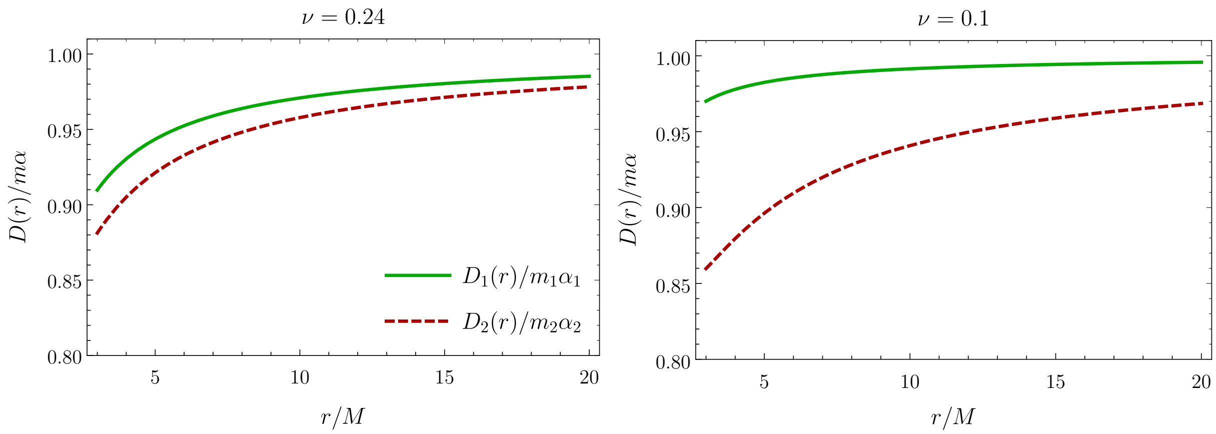

Figure 8.4: Scalar charges scaled by their asymptotic value as a function of the separation r of a binary BH scaled by the total mass. In both plots, the charge-to-mass ratio $q_1/m_1 = q_2/m_2 = 1$ and the dilaton coupling $a = 1$; in the left panel $\nu = 0.24$, while in the right $\nu = 0.1$.

the mass ratios X_i in terms of the constant masses m_1 and m_2 by

$$M \equiv m_1 + m_2\,, \qquad \mu \equiv \frac{m_1 m_2}{M}\,, \qquad \nu \equiv \frac{\mu}{M}\,,$$
$$X_1 \equiv \frac{m_1}{M}, \qquad X_2 \equiv \frac{m_2}{M}. \tag{8.35}$$

We also define the coefficient G_{12} by

$$G_{12} \equiv 1 + \alpha_1\alpha_2 - \frac{q_1 q_2}{M\mu}\,, \tag{8.36}$$

which reduces to the usual definition in ST theories when the electric charges are zero. The advantage of including the charges in G_{12} is that the Newtonian-order acceleration is simply given by $\boldsymbol{a} = -G_{12}M\boldsymbol{n}/r^2 + \mathcal{O}(1/c^2)$.

Expressing the energy in terms of the center-of-mass momentum $\boldsymbol{p} \equiv \boldsymbol{p_1} = -\boldsymbol{p_2}$, instead of the velocity, we obtain the Hamiltonian

$$H = M + \frac{p^2}{2\mu} - \frac{G_{12}M\mu}{r} - \frac{1}{8}(1-3\nu)\frac{p^4}{\mu^3} - \frac{G_{12}M}{2\mu r}\left[\left(\frac{3-\alpha_1\alpha_2}{1+\alpha_1\alpha_2-\frac{q_1q_2}{M\mu}} + \nu\right)p^2 + \nu p_r^2\right]$$

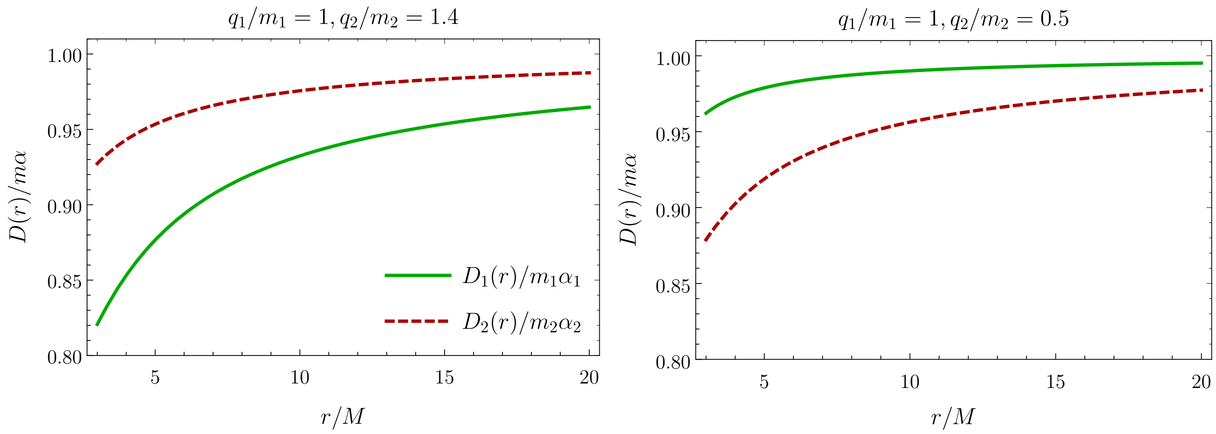

Figure 8.5: Scalar charges of a binary BH as a function of r for equal masses ($\nu = 1/4$), dilaton coupling $a = 1$, and charge-to-mass ratios $q_1/m_1 = 1,\ q_2/m_2 = 1.4$ (left) and $q_1/m_1 = 1,\ q_2/m_2 = 0.5$ (right).

$$+\frac{M^2\mu}{2r^2}\bigg[(1+\alpha_1\alpha_2)^2 + X_2\alpha_2^2\beta_1 + X_1\alpha_1^2\beta_2 + X_1\frac{q_2^2}{M\mu}(1+a\alpha_1) + X_2\frac{q_1^2}{M\mu}(1+a\alpha_2)$$
$$-2\frac{q_1q_2}{M\mu}\left(1+a\alpha_1X_1+a\alpha_2X_2\right)\bigg] + \mathcal{O}\left(\frac{1}{c^4}\right), \tag{8.37}$$

where $p_r = \boldsymbol{n}\cdot\boldsymbol{p}$.

Next, we examine how the scalar charges of the two bodies change with their separation. The dilaton charge is given by

$$D(\varphi) = \frac{d\mathfrak{m}(\varphi)}{d\varphi} = \mathfrak{m}(\varphi)\alpha(\varphi). \tag{8.38}$$

For the two bodies, the dilaton charge as a function of the separation r has the expansion

$$D_1(r) = m_1\Big[\alpha_1 + (\alpha_1^2+\beta_1)\varphi_1(r) + \frac{1}{2}\big(3\beta_1\alpha_1 + \alpha_1^3 + \beta_1'\big)\varphi_1^2(r) + \mathcal{O}\left(1/c^6\right)\Big], \tag{8.39a}$$
$$D_2(r) = m_2\Big[\alpha_2 + (\alpha_2^2+\beta_2)\varphi_2(r) + \frac{1}{2}\big(3\beta_2\alpha_2 + \alpha_2^3 + \beta_2'\big)\varphi_2^2(r) + \mathcal{O}\left(1/c^6\right)\Big], \tag{8.39b}$$

where $\beta' \equiv d\beta(\varphi)/d\varphi|_{\varphi_0}$, φ_1 is the scalar field at the location of body 1, and φ_2 is the scalar field at the location of body 2. From the 1PN scalar field in Eq. (M.32),

$$\varphi_1(r) = -\frac{\alpha_2 m_2}{r} + \frac{m_1 m_2}{r^2}\left(\alpha_2 + \alpha_1\alpha_2^2 + \alpha_1\beta_2\right) - \frac{a q_1 q_2}{r^2} + \frac{a q_2^2}{2r^2} + \frac{1}{2}\alpha_2 m_2(\boldsymbol{n}\cdot\boldsymbol{a}_2) + \mathcal{O}\left(1/c^6\right), \tag{8.40a}$$

$$\varphi_2(r) = -\frac{\alpha_1 m_1}{r} + \frac{m_1 m_2}{r^2}\left(\alpha_1 + \alpha_2\alpha_1^2 + \alpha_2\beta_1\right) - \frac{a q_1 q_2}{r^2} + \frac{a q_1^2}{2r^2} - \frac{1}{2}\alpha_1 m_1(\boldsymbol{n}\cdot\boldsymbol{a}_1) + \mathcal{O}\left(1/c^6\right), \tag{8.40b}$$

where, using $\boldsymbol{a} = -G_{12}M\boldsymbol{n}/r^2 + \mathcal{O}(1/c^2)$ and Eq. (N.19),

$$\boldsymbol{a}_1 = \frac{m_2}{M}\boldsymbol{a} = -\frac{G_{12}m_2}{r^2}\boldsymbol{n} + \mathcal{O}\left(1/c^2\right), \tag{8.41a}$$

$$\boldsymbol{a}_2 = -\frac{m_1}{M}\boldsymbol{a} = \frac{G_{12}m_1}{r^2}\boldsymbol{n} + \mathcal{O}\left(1/c^2\right). \tag{8.41b}$$

In Fig. 8.4, we plot $D_1(r)$ and $D_2(r)$ for charge-to-mass ratios $q_1/m_1 = q_2/m_2 = 1$, dilaton coupling constant $a = 1$, and symmetric mass ratios $\nu = 0.24$ and $\nu = 0.1$. The curves are plotted until $r = 3M$ because the PN expansion becomes inaccurate well before that separation. From the figure, we see that the scalar charge of both bodies decreases as the separation decreases, with the charge of the lighter body decreasing more quickly. Figure 8.5 shows the scalar charge as a function of the separation for equal masses but with different charge-to-mass ratios. We keep $q_1/m_1 = 1$ while q_2/m_2 takes the values 1.4 and 0.5. The scalar charge of the less-charged body decreases more quickly with decreasing separation. These results are consistent with what was found in the previous section for the scalar charge of a test BH, but here, we do not see a transition or a divergence near the horizon.

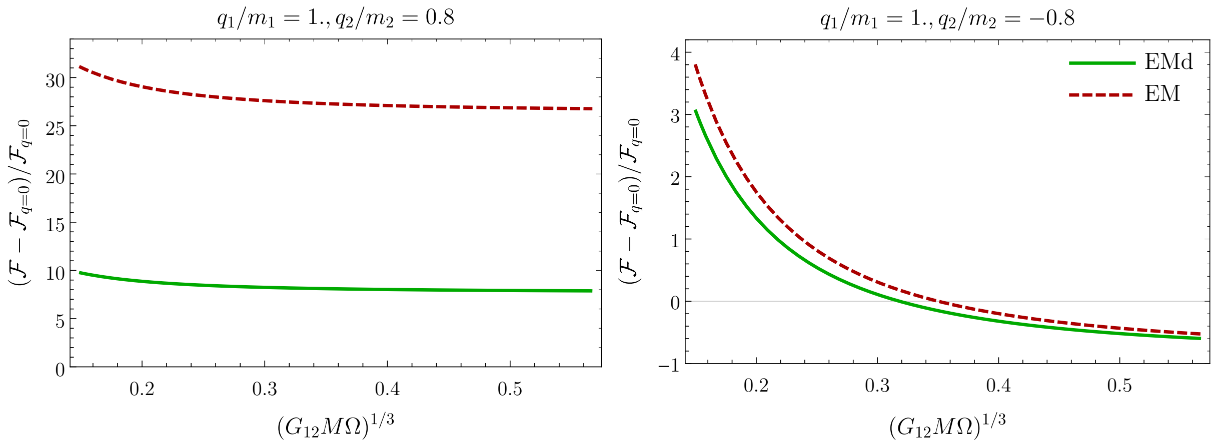

Figure 8.6: Energy flux in EMd theory and EM relative to the uncharged GR flux plotted versus the gauge-invariant velocity for circular orbits $v \equiv (G_{12}M\Omega)^{1/3}$ for coupling constant $a = 1$, for equal masses, and for charge-to-mass ratio $q_1/m_1 = 1, q_2/m_2 = 0.8$ (left) and $q_1/m_1 = 1, q_2/m_2 = -0.8$ (Right).

8.3.2 Gravitational energy flux

From the 1PN expansion, we computed the next-to-leading order scalar, vector, and tensor energy fluxes for general orbits (see Appendix N for the derivation). In a $1/c$ expansion, the leading terms are the scalar and vector dipole fluxes, which are of order $1/c^3$, while the leading order tensor flux is of order $1/c^5$, which is the same as the next-to-leading order scalar and vector fluxes. We computed the next-to-leading order tensor flux, which is of order $1/c^7$, because that is the maximum level of approximation accessible by use of the 1PN near-field equations. The scalar and vector dipole fluxes depend on the difference between the charges of the two bodies. The scalar flux also includes a monopole term that vanishes for circular orbits.

The total energy flux is the sum of the scalar, vector, and tensor fluxes

$$\mathcal{F} = \mathcal{F}_S + \mathcal{F}_V + \mathcal{F}_T, \tag{8.42}$$

where the expressions for the fluxes through next-to-leading order for general orbits are given in Appendix N. The fluxes for circular orbits are given by

$$\mathcal{F}_S = \frac{\nu^2 x^4}{3G_{12}^2}(\alpha_1 - \alpha_2)^2 + \frac{\nu^2 x^5}{15G_{12}^2}\left[20 f_\gamma (\alpha_1 - \alpha_2)^2 + 5\left(f_{v^2}^S + f_{1/r}^S\right) + 16\left(X_1\alpha_2 + X_2\alpha_1\right)^2\right] + \mathcal{O}\left(\frac{1}{c^7}\right), \tag{8.43a}$$

$$\mathcal{F}_V = \frac{2\nu^2 x^4}{3G_{12}^2}\left(\frac{q_1}{m_1} - \frac{q_2}{m_2}\right)^2 + \frac{2\nu^2 x^5}{15G_{12}^2}\left[20 f_\gamma\left(\frac{q_1}{m_1} - \frac{q_2}{m_2}\right)^2 + 8\left(X_2\frac{q_1}{m_1} + X_1\frac{q_2}{m_2}\right)^2 + 5\left(f_{v^2}^V + f_{1/r}^V\right)\right] + \mathcal{O}\left(\frac{1}{c^7}\right), \tag{8.43b}$$

$$\mathcal{F}_T = \frac{32\nu^2 x^5}{5G_{12}^2} + \frac{2\nu^2 x^6}{105G_{12}^2}\left(f_{v^4}^T + f_{v^2/r}^T + f_{1/r^2}^T + 672 f_\gamma\right) + \mathcal{O}\left(\frac{1}{c^9}\right), \tag{8.43c}$$

where the coefficients f are given by Eqs. (N.36), (N.57), (N.80), and (N.86). The energy flux is expressed in terms of the parameter x defined by

$$x \equiv \left(G_{12} M \Omega\right)^{2/3}, \tag{8.44}$$

where Ω is the orbital frequency, which is "perturbatively gauge-invariant" in the sense that it remains fixed under coordinate transformations to arbitrary PN order.

In Figs. 8.6 and 8.7, we plot the total energy flux in EMd theory with $a = 1$ relative to the flux when all charges are zero versus the binary's gauge-invariant velocity $v = (G_{12}M\Omega)^{1/3}$, i.e., we plot $(\mathcal{F} - \mathcal{F}_{q=0})/\mathcal{F}_{q=0}$. For comparison, Fig. 8.6 also includes the energy flux in EM, when scalar charges are zero but not the electric charges. The plots start at $v = (G_{12}M\Omega)^{1/3} = 0.15$ which corresponds to a total mass $M = 20M_\odot$, and a lower GW frequency in the detector of 10 Hz. In the plots, we used the next-to-leading order scalar and vector fluxes, but only used the leading Newtonian order tensor flux, because the 1PN energy flux in GR is given by $\mathcal{F}_{\rm GR} \sim x^5 - \text{const.}\ x^6$; the minus sign of the second term causes the flux to become negative at large frequencies.

From the plots, we see that at small frequencies (large separations), the difference with GR is greater than at larger frequencies because the dipole scalar and vector fluxes dominate ($\mathcal{F}_S \sim x^4$ while $\mathcal{F}_T \sim x^5$). For equal charges, the scalar and vector dipole fluxes are both zero, which means the total energy flux is the tensor flux that is proportional to x^5. Hence, the next-to-leading order flux in EMd theory becomes a constant shift to the GR flux, and the relative flux plotted in the figures becomes a straight line, as can be seen in Fig. 8.7.

In the two panels of Fig. 8.6, we use charge-to-mass ratios $q_1/m_1 = 1,\ q_2/m_2 = 0.8$ (left) and $q_1/m_1 = 1,\ q_2/m_2 = -0.8$ (right). For same-sign charges, at a fixed frequency, there is a greater difference from GR than for opposite-sign charges and also a greater difference between EMd and EM. This is because the energy flux is inversely proportional to $G_{12}^2 = (1 + \alpha_1\alpha_2 - q_1q_2/m_1m_2)^2$, which is larger when the electric charges have opposite signs than when they have the same sign. In the right panel, the plotted curves become negative when $\mathcal{F} < \mathcal{F}_{q=0}$, which occurs because $G_{12} > 1$ for opposite-sign charges, which makes the EMd flux smaller than the GR flux at some frequency.

In Fig. 8.7, we plot the energy flux for several charge-to-mass ratios. In that figure, we do not plot the flux in EM theory, because it is almost the same as the EMd flux for charges $q_i/m_i \lesssim 0.5$ since $\mathcal{F}_S \propto \alpha_i^2 \propto q_i^4/m_i^4$, which is much smaller than $\mathcal{F}_V \propto q_i^2/m_i^2$ for small charges. The plot shows the flux for same-sign charges in a log plot; for small charges $\lesssim 0.01$, the EMd flux decreases significantly and becomes very close to the GR flux.

The most salient feature that differentiates EMd theory from GR from the perspective of GW observations is the presence of dipole radiation. At leading order, the energy flux can be written as

$$\mathcal{F} = \mathcal{F}_{\text{GR}} \left(1 + Bx^{-1}\right), \tag{8.45}$$

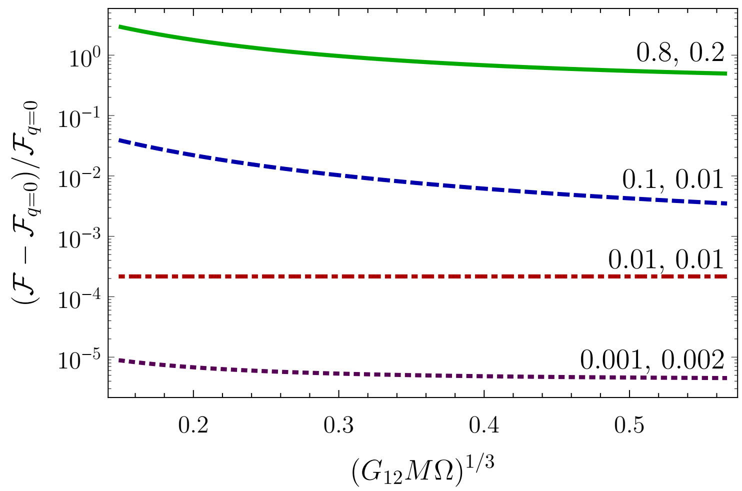

Figure 8.7: Energy flux in EMd theory relative to the uncharged GR flux for coupling constant $a = 1$ plotted versus $v = (G_{12}M\Omega)^{1/3}$, for equal masses, and for various charge-to-mass ratios.

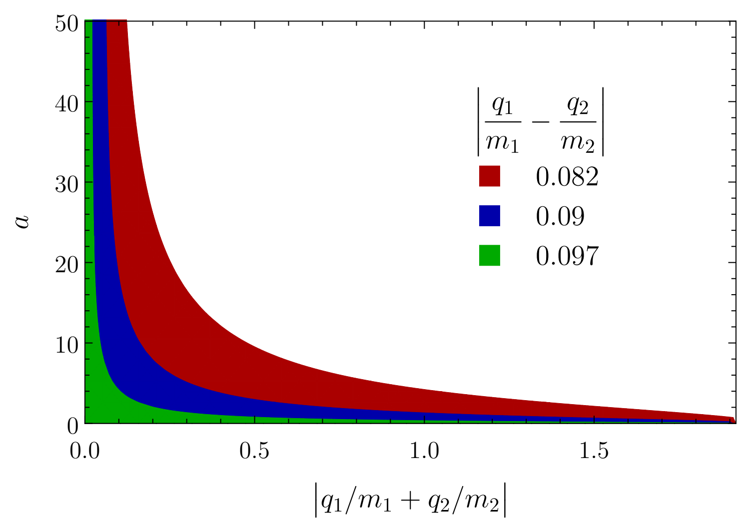

Figure 8.8: Allowed values of EMd coupling a consistent with a dipole flux constraint of $|B| \leq 10^{-3}$ as a function of mass-weighted total electric charge. Colors indicate various possible electric dipoles consistent with the bound on B.

where $\mathcal{F}_{\rm GR}$ is the GR quadrupole flux, and B parameterizes the strength of dipolar emission, which is given by

$$B = \frac{5}{96}\left[(\alpha_1 - \alpha_2)^2 + 2\left(\frac{q_1}{m_1} - \frac{q_2}{m_2}\right)^2\right]. \tag{8.46}$$

The presence of dipole flux has been constrained in several types of binary systems. The best constraints on the B come from radio observations of pulsar–white-dwarf binaries, which lead to the bound $|B| \lesssim 10^{-9}$ [687]. For binaries containing a single BH, the strongest bound comes from low-mass X-ray binaries, in which the companion is a main-sequence star: $|B| \lesssim 2 \times 10^{-3}$ [688]. To date, no bound has been set from GW observations of binary BHs, but at design sensitivity, LIGO could set a bound of $|B| \lesssim 8 \times 10^{-4}$ for a GW150914-like event, and LISA could lower that bound to 10^{-8} [688].

We wish to understand how well such a bound on dipole radiation in binary BHs can constrain EMd theory. Given the discussion above, we consider a hypothetical binary BH observation that constrains the dipole flux to $|B| \lesssim 10^{-3}$. The coupling a that characterizes EMd theory enters the prediction of B through the dimensionless scalar charges of the two bodies. Equation (8.46) demonstrates that for a given value of B, the scalar and electric dipoles are degenerate, and thus no constraint can be set on a directly with only a bound on the dipole flux. However, if an independent measurement of the total charges could be made — e.g., through measurements of the ringdown spectrum of the final remnant—one can potentially break this degeneracy and constrain EMd theory.

In Fig. 8.8, we show the values of a consistent with $|B| \leq 10^{-3}$ as a function of mass-weighted total charge $|q_1/m_1 + q_2/m_2|$ for various possible values of the electric dipole $|q_1/m_1 - q_2/m_2|$. The maximum allowed electric dipole is achieved in the limit that $a = 0$, wherein the scalar charges of the BHs vanish and our bound on the dipole flux translates directly to the bound on the electric dipole $|q_1/m_1 - q_2/m_2| \lesssim 0.098$. Unsurprisingly, we find that the constraint that can be set on a depends primarily on the magnitude of the electric charges in the binary: for equal-mass systems, the strongest constraints can be set when the BHs have large, nearly-equal charges, and the weakest constraints when the BHs have small, opposite charges. We see that for any realistic constraint on dipole flux, the parameter a is completely unbounded without an independent measurement of the electric charges.

8.3.3 Gravitational-wave phase in the stationary-phase approximation

Equipped with PN descriptions of the conservative and dissipative sectors of binary dynamics in EMd theory, we compute a key observable for GW detections: the Fourier-domain gravitational waveform. We utilize the stationary-phase approximation to perform this calculation, relying on the fact the GW phase evolves much more rapidly than its amplitude during the adiabatic inspiral along quasi-circular orbits.

We consider a GW detector a distance $R \gg \lambda_{\rm GR} \sim r/v$ from a binary BH. In the vicinity of the detector, the metric takes the form

$$g_{\mu\nu} = \eta_{\mu\nu} + h_{\mu\nu}, \tag{8.47}$$

where $\eta_{\mu\nu}$ is the Minkowski metric and $h_{\mu\nu}$ contains two propagating, transverse-traceless polarizations h_+ and $h_\times$, which comprise the GW produced by the binary.[6] At the fixed distance R,

[6]A GW detector also responds to the scalar field through the coupling given in Eq. (8.2). These scalar waves represent a transverse breathing polarization of perturbations to the Jordan-Fierz metric. Because standard search techniques are targeted at the transverse-traceless polarizations, we consider only those gravitational modes in this work. Differentiating between the various polarizations of GWs requires a network of detectors; our ability to identify additional GW polarizations will improve as more ground-based detectors come online.

the GW can be decomposed into spin-weighted spherical harmonics

$$h_+ - ih_\times = \sum_{\ell\geq 2}\sum_{m=-\ell}^{\ell} {}_{-2}Y_{\ell m}(\Theta,\Phi)h_{\ell m}(t), \tag{8.48}$$

where Φ, Θ are angular coordinates that define the propagation direction from the source to the detector [130]. We further decompose each mode into an amplitude and complex phase

$$h_{\ell m}(t) = A_{\ell m}(t)e^{im\phi(t)}, \tag{8.49}$$

where $\phi(t)$ is the orbital phase of the binary.

We compute the Fourier-transform of the GW using

$$\tilde{h}_{\ell m}(f) = \int_{-\infty}^{\infty} dt\, h_{\ell m}(t)e^{-2i\pi f t}. \tag{8.50}$$

During the adiabatic inspiral, the amplitude and orbital frequency evolve much more slowly than the orbital phase, i.e., $|\dot{A}_{\ell m}/A_{\ell m}| \ll \Omega$ and $|\dot{\Omega}| \ll \Omega^2$ for $m \neq 0$ modes. Thus, the integral in Eq. (8.50) is highly oscillatory and can be approximated by expanding the integrand about the time at which the complex phase is stationary. Using the stationary-phase approximation, the Fourier-domain waveform is then given by

$$\tilde{h}^{\text{SPA}}_{\ell m}(f) = \mathcal{A}_{\ell m}(f)e^{-i\psi_{\ell m}(f)-i\pi/4}, \tag{8.51}$$

$$\psi_{\ell m}(f) = 2\pi f t_f^{(m)} - m\phi(t_f^{(m)}), \tag{8.52}$$

$$\mathcal{A}_{\ell m}(f) = A_{\ell m}(t_f^{(m)})\sqrt{\frac{2\pi}{m\dot{\Omega}(t_f^{(m)})}}, \tag{8.53}$$

where t_f^m is defined implicitly as the time at which $m\Omega(t_f^{(m)}) = 2\pi f$. Following the notation common in the literature, we employ the binary's gauge-invariant velocity for circular orbits $v \equiv x^{1/2} = (G_{12}M\Omega)^{1/3}$ and introduce a similar notation for the GW frequency f as $v_f \equiv$

$(\pi G_{12} M f)^{1/3}$. Then, by construction, one finds $v(t_f^{(m)}) = (2/m)^{1/3} v_f$ and can rewrite Eq. (8.52) as

$$\psi_{\ell m}(f) = m \left(\frac{1}{G_{12} M} v^3 t(v) - \phi(v) \right) \Bigg|_{v=(2/m)^{1/3} v_f}. \tag{8.54}$$

From here onwards, we focus only on the dominant $\ell = |m| = 2$ modes and drop the explicit mode numbers for notational simplicity; because we restrict our attention to non-spinning systems, the modes obey the symmetry relation

$$h_{\ell m} = (-1)^\ell h^*_{\ell,-m}, \tag{8.55}$$

and thus we can consider only the $m = 2$ mode without loss of generality.

The orbital phase and frequency are computed using the balance equation

$$\frac{dE}{dt} = -\mathcal{F}. \tag{8.56}$$

From this equation, we deduce

$$\phi(v) = \phi_{\text{ref}} - \frac{1}{G_{12} M} \int_{v_{\text{ref}}}^{v} d\hat{v} \hat{v}^3 \frac{E'(\hat{v})}{\mathcal{F}(\hat{v})}, \tag{8.57}$$

$$t(v) = t_{\text{ref}} - \int_{v_{\text{ref}}}^{v} d\hat{v} \frac{dE/d\hat{v}}{\mathcal{F}(\hat{v})}, \tag{8.58}$$

where ϕ_{ref} and t_{ref} refer to an arbitrary reference point in the evolution of the binary. Inserting these results into Eq. (8.54), the Fourier-domain phase is given by

$$\psi(f) = 2\pi f t_{\text{ref}} - \phi_{\text{ref}} + \frac{2}{G_{12} M} \int_{v_f}^{v_{\text{ref}}} \left(v_f^3 - v^3 \right) \frac{E'(v)}{\mathcal{F}(v)} dv. \tag{8.59}$$

The energy flux in terms of x is given by Eq. (8.43a). The energy E is given by Eq. (8.34), and it can be expressed in terms of x using Eqs. (N.83) and (N.86), which leads to

$$E = -\frac{\mu}{2} x \left[1 + f_E x + \mathcal{O}\left(1/c^4\right) \right], \tag{8.60}$$

where the coefficient f_E is given by

$$f_E = \frac{-1}{3G_{12}^2}\left[G_{12}^2\left(\frac{1+\nu}{4}+\frac{3-\alpha_1\alpha_2}{1+\alpha_1\alpha_2-\frac{q_1q_2}{M\mu}}\right)-(1+\alpha_1\alpha_2)^2-X_2\alpha_2^2\beta_1-X_1\alpha_1^2\beta_2\right.$$
$$\left.-X_1\frac{q_2^2}{M\mu}(1+a\alpha_1)-X_2\frac{q_1^2}{M\mu}(1+a\alpha_2)+2\frac{q_1q_2}{M\mu}\left(1+aX_1\alpha_1+aX_2\alpha_2\right)\right]. \tag{8.61}$$

To evaluate the integral in Eq. (8.59), we need to distinguish between two regimes, similarly to what was done in Ref. [209]. In one regime, the electric charges are small and the inspiral is driven by the tensor quadrupole flux. In the other regime, the electric charges are large and the inspiral is driven by the dipole flux.

For the quadrupole-driven (QD) case, we approximate the integrand in Eq. (8.59) by

$$\frac{E'(v)}{\mathcal{F}(v)} \simeq \frac{E'(v)}{\mathcal{F}_T(v)}\left[1-\frac{\mathcal{F}_S(v)+\mathcal{F}_V(v)}{\mathcal{F}_T(v)}\right]. \tag{8.62}$$

Then, we expand the integrand using the next-to-leading order fluxes. Evaluating the integral leads to the phase

$$\psi^{\rm QD}(f) = 2\pi f t_{\rm ref}-\phi_{\rm ref}+\frac{1}{v^5}\left[\rho_0^{\rm QD}+\frac{\rho_{-2}^{\rm QD}}{v^2}+\rho_2^{QD}v^2+\mathcal{O}\left(v^4\right)\right], \tag{8.63}$$

with the coefficients

$$\rho_0^{\rm QD} = -\frac{G_{12}}{4096\nu}\left\{\frac{5}{168}\left(336f_E-672f_\gamma-f^T_{1/r^2}-f^T_{v^2/r}-f^T_{v^4}\right)\left[2\left(\frac{q_1}{m_1}-\frac{q_2}{m_2}\right)^2+(\alpha_1-\alpha_2)^2\right]\right.$$
$$-96+5\left(f^S_{1/r}+f^S_{v^2}\right)+10\left(f^V_{1/r}+f^V_{v^2}\right)+40f_\gamma\left(\frac{q_1}{m_1}-\frac{q_2}{m_2}\right)^2+16\left(X_2\frac{q_1}{m_1}+X_1\frac{q_2}{m_2}\right)^2$$
$$\left.+20f_\gamma(\alpha_1-\alpha_2)^2+16\left(X_2\alpha_1+X_1\alpha_2\right)^2\right\}, \tag{8.64a}$$

$$\rho_{-2}^{\rm QD} = -\frac{5G_{12}}{7168\nu}\left[2\left(\frac{q_1}{m_1}-\frac{q_2}{m_2}\right)^2+(\alpha_1-\alpha_2)^2\right], \tag{8.64b}$$

$$\rho_2^{\rm QD} = -\frac{5G_{12}}{1548288\nu}\left\{-32256f_E+\left[48-20f_E\left(\frac{q_1}{m_1}-\frac{q_2}{m_2}\right)^2-10f_E\left(\alpha_1-\alpha_2\right)^2\right]\right.$$

$$\times\left(672f_\gamma+f^T_{1/r^2}+f^T_{v^2/r}+f^T_{v^4}\right)+\frac{5}{224}\left[2\left(\frac{q_1}{m_1}-\frac{q_2}{m_2}\right)^2+(\alpha_1-\alpha_2)^2\right]$$
$$\times\left(672f_\gamma+f^T_{1/r^2}+f^T_{v^2/r}+f^T_{v^4}\right)^2-\left(672f_\gamma+f^T_{1/r^2}+f^T_{v^2/r}+f^T_{v^4}-336f_E\right)$$
$$\times\left[5\left(f^S_{1/r}+f^S_{v^2}\right)+10\left(f^V_{1/r}+f^V_{v^2}\right)+20f_\gamma(\alpha_1-\alpha_2)^2+40f_\gamma\left(\frac{q_1}{m_1}-\frac{q_2}{m_2}\right)^2\right.$$
$$\left.+16\left(X_2\frac{q_1}{m_1}+X_1\frac{q_2}{m_2}\right)^2+16\left(X_2\alpha_1+X_1\alpha_2\right)^2\right]\Bigg\}, \tag{8.64c}$$

where the coefficients f are given by Eqs. (N.36), (N.57), (N.80), and (N.86). When the charges are zero, this phase reduces to the next-to-leading order GR result, i.e., $\rho_0^{\rm QD}\to 3/128\nu$, $\rho_2^{\rm QD}\to 5(743+924\nu)/32256\nu$, and $\rho_{-2}^{\rm QD}\to 0$.

For the dipole-driven (DD) case, we take the tensor flux at the same order as the scalar and vector fluxes, i.e., to $\mathcal{O}(x^5)$. Evaluating the integral in (8.59) leads to

$$\psi^{\rm DD}(f)=2\pi f t_{\rm ref}-\phi_{\rm ref}+\frac{\rho_0^{\rm DD}}{v^3}\left[1+\rho_2^{\rm DD}v^2+\mathcal{O}(v^4)\right], \tag{8.65}$$

where the coefficients are given by

$$\rho_0^{\rm DD}=\frac{G_{12}}{\nu}\left[2\left(\frac{q_1}{m_1}-\frac{q_2}{m_2}\right)^2+(\alpha_1-\alpha_2)^2\right]^{-1}, \tag{8.66a}$$
$$\rho_2^{\rm DD}=\frac{-9}{10}\left[2\left(\frac{q_1}{m_1}-\frac{q_2}{m_2}\right)^2+(\alpha_1-\alpha_2)^2\right]^{-1}\left[96+10\left(f^V_{1/r}+f^V_{v^2}\right)+5\left(f^S_{1/r}+f^S_{v^2}\right)\right.$$
$$-10(f_E-2f_\gamma)(\alpha_1-\alpha_2)^2+16\left(X_2\alpha_1+X_1\alpha_2\right)^2-20(f_E-2f_\gamma)\left(\frac{q_1}{m_1}+\frac{q_2}{m_2}\right)^2$$
$$\left.+80(f_E-2f_\gamma)\frac{q_1q_1}{m_1m_2}+16\left(X_2\frac{q_1}{m_1}+X_1\frac{q_2}{m_2}\right)^2\right]. \tag{8.66b}$$

When we set the electric charges to zero, but keep the scalar charges nonzero, this result agrees with the (ST) result derived in Ref. [209].

We wish to understand how well a GW signal produced in EMd theory [e.g. Eq. (8.63)] can be distinguished observationally from a signal in GR. Answering this question definitively falls beyond the scope of this paper. To perform such a study, one would need to perform a Bayesian hypothesis test on injections of EMd signals into detectors with realistic noise, comparing the relative evidence that the signal matches template waveforms in either EMd theory or GR; for examples of such analyses for other modifications to GR, see Refs. [667, 689–692]. Instead of this detailed study, we compute two comparatively simple measures of distinguishability: the difference in total phase, and, in Sec. 8.3.4, the number of "useful" GW cycles.

To compare the phase calculated in EMd theory with that in GR, we need to align the waveforms and then compute dephasing from this alignment point. We choose to do the alignment around the "merger frequency," which for simplicity we choose to be the innermost-stable circular orbit (ISCO) frequency $f_{\text{ISCO}} = 6^{-3/2}/\pi M$ for a Schwarzschild BH. Next, we determine t_{ref} and ϕ_{ref} such that the waveform reaches a local maximum at this point and the phase reaches some fixed value, e.g., zero. To satisfy these two conditions, one can choose t_{ref} and ϕ_{ref} such that at f_{ISCO}, $d\psi(f)/df = 0$ and $\psi(f) = 0$. For the QD case, this leads to

$$\begin{aligned} t_{\text{ref}}^{\text{QD}} &= 108 M G_{12}^{-10/3} \left(10 G_{12}^{2/3} \rho_0^{\text{QD}} + G_{12}^{4/3} \rho_2^{\text{QD}} + 84 \rho_{-2}^{\text{QD}}\right), \\ \phi_{\text{ref}}^{\text{QD}} &= 12\sqrt{6} G_{12}^{-7/3} \left(8 G_{12}^{2/3} \rho_0^{\text{QD}} + G_{12}^{4/3} \rho_2^{\text{QD}} + 60 \rho_{-2}^{\text{QD}}\right). \end{aligned} \tag{8.67}$$

Similarly, for the DD case, we get

$$\begin{aligned} t_{\text{ref}}^{\text{DD}} &= 6 M G_{12}^{-2} \rho_0^{\text{DD}} \left(18 + G_{12}^{2/3} \rho_2^{\text{DD}}\right), \\ \phi_{\text{ref}}^{\text{DD}} &= 4\sqrt{\frac{2}{3}} G_{12}^{-1} \rho_0^{\text{DD}} \left(9 + G_{12}^{2/3} \rho_2^{\text{DD}}\right). \end{aligned} \tag{8.68}$$

In Fig. 8.9, we plot the difference between the phase calculated in EMd theory with $a = 1$ and the phase when all charges are zero, which is the phase in GR up to 1PN order. For the configurations considered here, $v = 0.15$ corresponds to approximately 10 Hz for a $20 M_\odot$

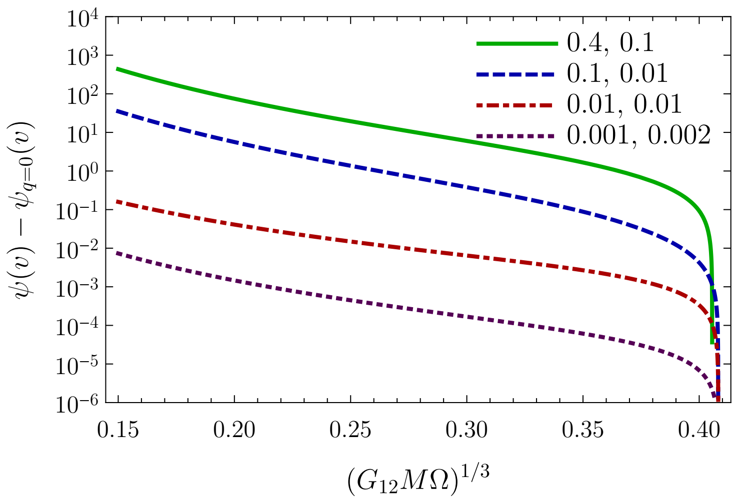

Figure 8.9: Phase difference in radians between EMd theory and GR as a function of v, computed in the quadrupole-driven regime, for various charge-to-mass ratios, and for equal masses ($\nu = 1/4$).

system. Because the charges are relatively small, we compute the phase using Eq. (8.63). For systems whose component's charge-to-mass ratio $q_i/m_i \lesssim 0.01$, the two waveforms differ by less than one radian over the frequency range of a ground-based GW detector. The phase difference does not depend strongly on the value of a; for values of $a \sim 1000$ and charge-to-mass ratios $q_i/m_i \lesssim 10^{-3}$ analogous to those considered in Ref. [481], the phase difference agrees with that shown in Fig. 8.9 within 10%.

8.3.4 Number of useful gravitational-wave cycles

The total number of GW cycles between frequencies $f_{\rm min}$ and $f_{\rm max}$ is given by

$$N_{\rm tot} = \int_{f_{\rm min}}^{f_{\rm max}} \frac{df}{2\pi} \frac{d\phi}{df}, \tag{8.69}$$

where ϕ is the gravitational wave phase. The instantaneous number of cycles spent near some frequency f is defined by multiplying the above integrand by f

$$N(f) \equiv \frac{f}{2\pi} \frac{d\phi}{df}. \tag{8.70}$$

However, GW detectors are not equally sensitive to all parts of the waveform because the noise spectral density of the detector is frequency dependent. A better proxy for how observationally different two waveforms are is to compare the number of "useful" cycles in each. This measure was originally introduced in Ref. [693]. One computes the total phase accumulated in each frequency bin and then weights this estimate by the sensitivity of a detector at that frequency. Because the strain sensitivity of the detector is concentrated in just a window of frequency space, the result would also depend on the mass of the system. The number of useful cycles is defined by [693]

$$N_{\text{useful}}(f) \equiv \left[\int_{f_{\text{min}}}^{f_{\text{max}}} \frac{df}{f} w(f) N(f) \right] \left[\int_{f_{\text{min}}}^{f_{\text{max}}} \frac{df}{f} w(f) \right]^{-1}, \tag{8.71}$$

where the weight $w(f) \equiv A^2(f)/f S_n(f)$, while $A(f)$ is the GW amplitude, and $S_n(f)$ is the noise spectral density of the detector. We use the zero-detuned high-power noise spectral density of Advanced LIGO at design sensitivity [694].

Using the balance equation $dE/dt = -\mathcal{F}$, and the relation between the GW phase and orbital frequency $\dot{\phi} = \Omega$, the instantaneous number of cycles in Eq. (8.70) can be reformulated as

$$N(f) = -\frac{v^4}{3\pi M G_{12}} \frac{E'(v)}{\mathcal{F}(v)}, \tag{8.72}$$

which can be computed in the quadrupole-driven regime using Eq. (8.62). For the GW amplitude, we used the Newtonian order approximation for the transverse-traceless polarizations $A(f) \propto v^2$, since the effect from the amplitude on the number of cycles is small compared to the phase. We can then calculate numerically the number of useful cycles using Eq. (8.71).

In Fig. 8.10, we show the relative difference between N_{useful} in EMd theory with $a = 1$ and the same quantity when all charges are zero (GR to 1PN order). The number of cycles in EMd theory is less than in GR except for equal charges, because the leading dipole radiation dominates the Newtonian order corrections to the binding energy. We find that for systems with $q_i/m_i \sim 0.1$, the number of useful cycles in GR and EMd differs by $\mathcal{O}(1)$.

The quantity plotted in Fig. 8.10 provides a rough estimate of the observable size of deviations from GR relative to the overall GW signal strength. We recast this quantity in terms of the optimal signal-to-noise ratio (SNR) of the waveforms, defined by

$$\text{SNR}^2 = 4\int_{f_{\text{min}}}^{f_{\text{max}}} df \frac{|\mathcal{A}(f)|^2}{S_n(f)}. \tag{8.73}$$

Using Eq. (8.53), this relation can be rewritten as

$$\text{SNR}^2 = 4\int_{f_{\text{min}}}^{f_{\text{max}}} \frac{df}{f} w(f) N(f), \tag{8.74}$$

and thus

$$\frac{|N_{\text{useful}}^{q=0} - N_{\text{useful}}|}{N_{\text{useful}}^{q=0}} = \frac{|\left(\text{SNR}^2\right)^{q=0} - \left(\text{SNR}^2\right)|}{\left(\text{SNR}^2\right)^{q=0}} \tag{8.75}$$

$$= \frac{2|\Delta\text{SNR}|}{\text{SNR}} + \mathcal{O}\left(\left(\frac{\Delta\text{SNR}}{\text{SNR}}\right)^2\right), \tag{8.76}$$

where, $\Delta\text{SNR} = \left(\text{SNR}^{q=0} - \text{SNR}\right)$ is the difference in SNR between signals in GR and EMd theory. Thus, Fig. 8.10 indicates that corrections arising from the presence of electric and scalar charges in EMd theory can account for only a few percent of the total SNR for systems with electric dipole ~ 0.1.

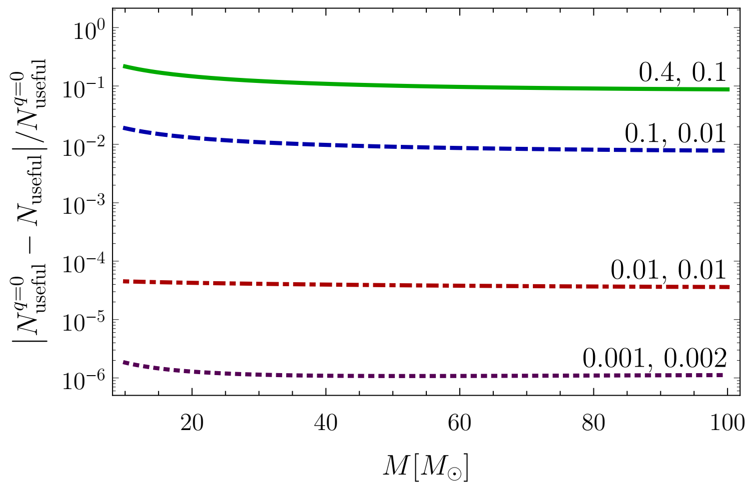

Figure 8.10: Number of useful cycles versus the total mass for various charge-to-mass ratios, and for equal masses ($\nu = 1/4$). The number of cycles in EMd theory is less than in GR except for equal charges.

8.4 Effective-one-body framework

In this section, we construct two EOB Hamiltonians: one based on the EMd metric in Eq. (8.8), in which the potential $C(r) \neq 1$, which we call the GHS gauge; the other is based on an approximation to the EMd metric by making a transformation to a gauge were the potential $C(r) = 1$, which we call the Schwarzschild gauge.

The EOB Hamiltonian in the GHS gauge is more physical in the strong-gravity regime since it exactly reproduces the test-body limit of the two-body dynamics. That is, it belongs to a class of Hamiltonians implementing exact solutions to the field equations for isolated objects/BHs. However, this class of Hamiltonians is very theory specific — for example the analytic ST vacuum metric in Refs. [695, 696] is distinct from the analytic EMd metric when we set the electromagnetic fields to zero. In addition, many BH solutions in alternative theories do not even have an analytic solution that can be used. The advantage of using a Hamiltonian based on the approximate metric in the Schwarzschild gauge, is that it is easier to implement in data-analysis studies of GWs observed by LIGO and Virgo. One would take the existing EOB Hamiltonians in GR as a starting point and add EMd corrections in the same way as, e.g., tidal corrections are added [625]. Within the regime of small deviations from GR, the two EOB Hamiltonians in EMd theory are expected to closely agree.

In Refs. [696, 697], the EOB framework was extended to ST theories. In Ref. [696], the motion of a binary BH was mapped to the motion of a test body, such that the effective metric is a ν-deformation of the ST metric. This approach is similar to our EOB Hamiltonian in the GHS gauge, but we find a different mapping for the scalar charge. In Ref. [697], the motion of the binary in ST theory was mapped to the motion of a test body around an effective BH in GR, but the effective metric does not reproduce exactly the test-body limit of ST theory. In contrast, whereas our EOB Hamiltonian in the Schwarzschild gauge is also not exact in the test-body limit, it still maps the real problem to an effective one in EMd theory (not in GR).

8.4.1 Effective-one-body Hamiltonian in Garfinkle-Horowitz-Strominger gauge

In the EOB framework, the motion of a binary is mapped to the motion of a test body in the background of an effective metric. In the effective problem in EMd theory, we assume that a test body, with mass μ and electric charge q, is moving in the background of a charged BH with mass M and electric charge Q. To relate the real two-body problem to the effective one, we impose the following conditions: (a) M and μ are the total mass and reduced mass of the real description, i.e., $M = m_1 + m_2$ and $\mu = m_1 m_2/M$; (b) the effective charges Q and q are related to the real charges by $Qq = q_1 q_2$, but we do not assume that Q is the total charge; and (c) the mapping between the real and effective Hamiltonians takes the form

$$\frac{H^{\rm NR}_{\rm eff}(\boldsymbol{R},\boldsymbol{P})}{\mu} = \frac{H^{\rm NR}(\boldsymbol{r},\boldsymbol{p})}{\mu}\left[1+\frac{\nu}{2}\frac{H^{\rm NR}(\boldsymbol{r},\boldsymbol{p})}{\mu}\right], \tag{8.77}$$

where the superscript NR means non-relativistic, i.e., $H^{\rm NR} = H - M$, and the real Hamiltonian H is given by Eq. (8.37). The form (8.77) for the "EOB energy map" [380] has proven useful in GR up to 4PN order [80], in classical electrodynamics to 2PN order [698], and in ST gravity to 2PN order [236, 697]. In the first post-Minkowskian approximation, i.e., to all orders in v/c at linear order in G, it can be shown to exactly resum the dynamics, producing the arbitrary-mass-ratio two-body Hamiltonian from the test-body Hamiltonian [236, 264]. For the coordinates in the effective problem, we use uppercase letters, such as R and P, while for the real problem, we keep using lowercase letters, such as r and p.

The effective action for the test body is given by

$$S_{\rm eff} = \int \left[-\mathfrak{m}(\varphi)\, d\tau_{\rm eff} + qA_\mu dX^\mu\right], \tag{8.78}$$

where $\tau_{\rm eff}$ is the proper time of the BH and the effective test-mass $\mathfrak{m}(\varphi)$ depends on the scalar field φ generated by the BH, and has the expansion in terms of the parameters α and β as

$$\mathfrak{m}(\varphi) = \mu\left[1+\alpha\varphi+\frac{1}{2}(\alpha^2+\beta)\varphi^2+\mathcal{O}\left(1/c^6\right)\right]. \tag{8.79}$$

Since we do not know, a priori, how the parameters α and β of the effective test body are related to the real problem, we expand the mass in a $1/R$ expansion

$$\mathfrak{m}(R) = \mu\left[1+\frac{f_1}{R}+\frac{f_2}{R^2}+\mathcal{O}\left(1/c^6\right)\right] \tag{8.80}$$

and solve for the unknown coefficients f_1 and f_2.

We take the effective metric of the background to be a deformation of the EMd metric in the GHS gauge

$$ds^2_{\text{eff}} = -d\tau^2_{\text{eff}} = -A(R)dT^2 + B(R)dR^2 + R^2C(R)d\Omega^2\,, \tag{8.81}$$

with

$$A(R) = \left(1 - \frac{R_+}{R}\right)\left(1 - \frac{R_-}{R}\right)^{\frac{1-a^2}{1+a^2}}\,, \tag{8.82a}$$

$$B(R) = \frac{1}{A(R)}\left(1 + \frac{b_1}{R}\right)\,, \tag{8.82b}$$

$$C(R) = \left(1 - \frac{R_-}{R}\right)^{\frac{2a^2}{1+a^2}}\,, \tag{8.82c}$$

where R_- and R_+ are the radii of the inner and outer horizons of the effective BH, which are given by Eqs. (8.16a) and (8.16b), i.e.,

$$R_- = \frac{1+a^2}{a}D\,, \qquad R_+ = 2M - \frac{1-a^2}{a}D\,. \tag{8.83}$$

We choose to define R_- and R_+ by these relations in terms of D, but not in terms of Q, because the relation between Q and D is deformed by the mapping. We note that in the above metric's ansatz, we have added a deformation to $B(R)$ only because, in EMd theory at 1PN order, the mapping leads to three equations in f_1, f_2, and any deformation to the metric. Thus, we can only determine uniquely one unknown coefficient in the effective metric. So we choose to take that coefficient to be b_1, and assume the possible deformations to $A(R)$ or $C(R)$ to be zero at 1PN order.

The scalar field for a single BH is given by Eq. (8.13); we add a PN deformation g_2/R^2 such that the effective scalar field is given by

$$\varphi(R) = \frac{a}{1+a^2}\ln\left(1 - \frac{R_-}{R} + \frac{1+a^2}{a}\frac{g_2}{R^2}\right)\,. \tag{8.84}$$

The electric potential is given by

$$A_0(R) = -\frac{Q}{R}\,. \tag{8.85}$$

We do not add PN corrections to A_0 because those corrections can be absorbed in the PN corrections to the scalar field or to the relation between D and Q. The coefficient g_2 is not independent of f_1 and f_2, because the mass expansion can also be expanded directly in φ [see Eq. (8.7)]

$$\mathfrak{m}(R) = \mu\left[1 - \frac{D\alpha}{R} + \frac{1}{R^2}\left(g_2\alpha - \frac{D^2\alpha}{2a} - \frac{a}{2}D^2\alpha + \frac{1}{2}D^2\alpha^2 + \frac{1}{2}D^2\beta\right) + \mathcal{O}\left(1/c^6\right)\right]. \tag{8.86}$$

In what follows, we uniquely solve for the coefficients b_1, f_1, and f_2 by matching the real Hamiltonian to the effective one by a canonical transformation. Matching the two mass expansions in Eqs. (8.80) and (8.86) allows us to determine the mapping for the parameters α and β, and for the coefficient g_2. The mapping for α is unique, but the mapping for β and g_2 is not unique at 1PN order.

To find the effective Hamiltonian, we first find the effective Lagrangian, in the equatorial plane $\Theta = \pi/2$,

$$\begin{aligned} L_{\text{eff}} &= qA_0 - \mathfrak{m}(\varphi)\sqrt{-g_{\mu\nu}\frac{dX^\mu}{dT}\frac{dX^\nu}{dT}}, \\ &= qA_0 - \mathfrak{m}(\varphi)\sqrt{A(R) - B(R)\dot{R}^2 - C(R)R^2\dot{\Phi}^2}. \end{aligned} \tag{8.87}$$

Then, applying the Legendre transformation $H_{\text{eff}} = P_R\dot{R} + P_\Phi\dot{\Phi} - L_{\text{eff}}$ yields the effective Hamiltonian

$$H_{\text{eff}} = -qA_0 + \sqrt{A(R)\left[\mathfrak{m}^2(\varphi) + \frac{P_\Phi^2}{C(R)R^2} + \frac{P_R^2}{B(R)}\right]}, \tag{8.88}$$

where $P_\Phi = \partial L_{\text{eff}}/\partial\dot{\Phi}$ is the angular momentum, and $P_R = \partial L_{\text{eff}}/\partial\dot{R}$ is the radial momentum.

Before matching the Hamiltonians, we need to apply a canonical transformation from the real variables, $\boldsymbol{r}$ and $\boldsymbol{p}$, to the effective ones, $\boldsymbol{R}$ and $\boldsymbol{P}$. At 1PN order, this transformation is given by [380]

$$R^i = r^i + \frac{\partial G_{\rm 1PN}}{\partial p_i}\,, \qquad P_i = p_i - \frac{\partial G_{\rm 1PN}}{\partial r^i}\,, \tag{8.89}$$

with the generating function

$$G_{\rm 1PN}(\boldsymbol{r},\boldsymbol{p}) = (\boldsymbol{r}\cdot\boldsymbol{p})\left(c_1\boldsymbol{p}^2 + \frac{c_2}{r}\right), \tag{8.90}$$

where the coefficients c_1 and c_2 are to be determined by the mapping.

Inserting the expansions of the real and effective Hamiltonians into Eq. (8.77), and applying the canonical transformation, we obtain the five equations:

$$2c_1\mu^2 + \nu = 0\,, \tag{8.91a}$$

$$f_1 + M\alpha_1\alpha_2 = 0\,, \tag{8.91b}$$

$$M - c_2 + \mu + \mu\alpha_1\alpha_2 - \frac{qQ}{M} + aD + c_1M\mu^2 - \mu c_1 qQ - \mu c_1 f_1\mu = 0\,, \tag{8.91c}$$

$$b_1 + \frac{qQ}{M} + 2M + 2aD + 4c_1\mu qQ + 4c_1\mu^2 f_1 - 2c_2 - \mu - \mu\alpha_1\alpha_2 - 4c_1M\mu^2 = 0\,, \tag{8.91d}$$

$$\begin{aligned}
&\frac{q^2Q^2}{M^2} + q_2^2X_1\left(1 + a\alpha_1\right) + q_1^2X_2\left(1 + a\alpha_2\right) - 2\mu c_2 + 4\mu f_1 + 2\nu c_2 f_1 + 2M\mu \\
&\quad - \nu f_1^2 - 2\nu f_2 - \frac{2D\mu}{a} + 2aD\mu - \nu D^2 + \nu\frac{D^2}{a^2} + 4M\mu\alpha_1\alpha_2 + 2M\mu\alpha_1^2\alpha_2^2 \\
&\quad + X_2\nu\beta_1\alpha_2^2 + X_1\nu\beta_2\alpha_1^2 + \mu^2 + 2\mu^2\alpha_1\alpha_2 + \mu^2\alpha_1^2\alpha_2^2 \\
&\quad + qQ\left(2\frac{c_2}{M} - 2 - 2\frac{f_1}{M} - 2a\alpha_1X_1 - 2a\alpha_2X_2 - 2\alpha_1\alpha_2 - 2\nu - 2\nu\alpha_1\alpha_2\right) = 0\,.
\end{aligned} \tag{8.91e}$$

Solving these equations respectively for the coefficients c_1, f_1, c_2, b_1, and f_2 yields

$$c_1 = -\frac{\nu}{2\mu^2}\,, \tag{8.92a}$$

$$f_1 = -M\alpha_1\alpha_2\,, \tag{8.92b}$$

$$c_2 = M + \frac{M\nu}{2} + \frac{1}{2}M\nu\alpha_1\alpha_2 - \frac{qQ\nu}{2\mu} + aD\,, \tag{8.92c}$$

$$b_1 = 0\,, \tag{8.92d}$$

$$f_2 = \frac{D^2}{2a^2} - \frac{D^2}{2} - \frac{MD}{a} - aMD\alpha_1\alpha_2 + \frac{aqQD}{\mu} - aM\frac{q_1q_2}{\mu}\left(X_1\alpha_1 + X_2\alpha_2\right)$$
$$- M^2\left[\alpha_1\alpha_2 - \frac{1}{2}(\alpha_1\alpha_2)^2 - \frac{1}{2}\left(X_2\alpha_2^2\beta_1 + X_1\alpha_1^2\beta_2\right)\right]$$
$$+ \frac{M}{2}\left[\frac{q_2^2}{m_2}(1+a\alpha_1) + \frac{q_1^2}{m_1}(1+a\alpha_2)\right]. \tag{8.92e}$$

To find the mapping of the scalar charge, we identify the mass expansion in Eq. (8.80) with the expansion in Eq. (8.86) to give

$$-D\alpha = f_1\,, \tag{8.93a}$$
$$g_2\alpha - \frac{D^2\alpha}{2a} - \frac{a}{2}D^2\alpha + \frac{1}{2}D^2\alpha^2 + \frac{1}{2}D^2\beta = f_2\,. \tag{8.93b}$$

Inserting the solution for f_1 and f_2 gives a unique mapping for α

$$\alpha = \frac{M}{D}\alpha_1\alpha_2\,, \tag{8.94}$$

and suggests the following mapping for β

$$\beta = \frac{M^2}{D^2}\left(X_2\alpha_2^2\beta_1 + X_1\alpha_1^2\beta_2\right). \tag{8.95}$$

Further, we take the mapping of the dilaton charge D of the effective BH to be the sum of the asymptotic value of the scalar charges of the two bodies, i.e.,

$$D = m_1\alpha_1 + m_2\alpha_2\,. \tag{8.96}$$

The mapping for α and β agrees with what was found in Ref. [696], but the mapping for D is different. The reason we choose this mapping for D is that it leads to a simple deformation to the scalar field

$$g_2 = -\frac{1-a^2}{2a^2}\frac{(\alpha_1-\alpha_2)^2}{\alpha_1\alpha_2}DM\nu\,. \tag{8.97}$$

This deformation vanishes in the test-mass-limit $\nu \to 0$, and also when $a = 1$ or $\alpha_1 = \alpha_2$. Other choices for D lead to complicated expressions for g_2. In obtaining this result for g_2, we used the expression for the electric charge in terms of the scalar charge, which is valid for BHs only,

$$\frac{q_i^2}{m_i^2} = \frac{2}{a}\alpha_i - \frac{1-a^2}{a^2}\alpha_i^2\,. \tag{8.98}$$

This relation follows from Eq. (8.20) after solving for q_i in terms of α_i and setting the scalar field to its asymptotic value.

A convenient mapping for the electric charge is

$$Q^2 = M\left(\frac{q_1^2}{m_1} + \frac{q_2^2}{m_2}\right). \tag{8.99}$$

The reasoning behind this choice is that it is symmetric under the exchange of the two bodies; it has the correct test-body limit, $Q \to q_1$ when $m_2/m_1 \to 0$ with q_2/m_2 held constant; and it appears naturally in EM theory as we show in the next subsection. With that mapping for Q and D, the relation between them is given by

$$Q^2 = \frac{2M}{a}D - \frac{1-a^2}{a^2}D^2 - \frac{1-a^2}{a^2}(\alpha_1-\alpha_2)^2M^2\nu\,. \tag{8.100}$$

One could choose to enforce Eq. (8.17) for generic masses by making a different choice for D or Q, but this seems to lead to very complicated expressions for them.

8.4.2 Effective-one-body Hamiltonian in Schwarzschild gauge

In the EMd metric, the potential $C(r) \neq 1$, but the standard EOB gauge is the Schwarzschild gauge $C(r) = 1$. This is the gauge that was used to derive the original EOB Hamiltonian [380], which was then improved by calibrating it to numerical-relativity simulations [582]. Therefore, to profit from the best available EOB Hamiltonian in GR, we need to construct an EMd-EOB Hamiltonian that is also in the Schwarzschild gauge.

The EMd metric can be transformed to the Schwarzschild gauge by the coordinate transformation $\bar{r}^2 = r^2 C(r)$. However, for arbitrary values of the coupling constant a, the metric cannot be analytically transformed. Instead, we expand the EMd metric (8.8) and transform it to get an approximate EMd metric in the Schwarzschild gauge. We make the coordinate transformation, valid to 1PN order,

$$\begin{aligned} \bar{r}^2 &= r^2 \left[1 - \frac{2a^2 r_-}{(1+a^2)r}\right], \\ \Rightarrow \quad r &= \bar{r} + \frac{a^2}{1+a^2} r_- = \bar{r} + aD\,. \end{aligned} \tag{8.101}$$

With that transformation, and inserting the expressions for r_- and r_+ in terms of M and Q [Eqs. (8.16a) and (8.16b)], we get

$$ds^2 = -\left(1 - \frac{2M}{\bar{r}} + \frac{Q^2}{\bar{r}^2}\right) dt^2 + \left(1 + \frac{2M}{\bar{r}}\right) d\bar{r}^2 + \bar{r}^2 d\Omega^2, \tag{8.102}$$

which is the same as the Reissner–Nordström metric to 1PN order.

As an ansatz for the effective metric, we assume a metric based on the approximate metric (8.102)

$$ds^2_{\text{eff}} = -A(R)dt^2 + B(R)dR^2 + R^2 d\Omega^2\,, \tag{8.103}$$

with

$$A(R) = 1 + \frac{a_1}{R} + \frac{a_2}{R^2} + \ldots\,, \tag{8.104a}$$

$$B(R) = 1 + \frac{b_1}{R} + \ldots\,, \tag{8.104b}$$

and we write the mass expansion as

$$\mathfrak{m}(R) = \mu \left[1 + \frac{f_1}{R} + \frac{f_2}{R^2} + \mathcal{O}\left(1/c^6\right)\right], \tag{8.105}$$

where the unknown coefficients a_1, a_2, b_1, f_1, and f_2 are to be determined by the mapping. However, the mapping leads to three equations in those five coefficients, making two of them arbitrary. We choose to take $a_1 = -2M$ and $a_2 = Q^2$ so that the effective metric would agree with the EMd metric in the Schwarzschild gauge to 1PN order. When we solve for b_1, we get $b_1 = 2M$, in agreement with the EMd approximate metric.

For the effective electric potential, we apply the coordinate transformation (8.101) with $\bar{r} = R$ to get

$$A_0(R) = -\frac{Q}{R + aD}\,. \tag{8.106}$$

Applying the same transformation to the scalar field, and adding a PN deformation g_2/R^2, we obtain

$$\varphi(R) = \frac{a}{1+a^2}\ln\left[1 - \frac{1+a^2}{a}\frac{D}{R+aD} + \frac{1+a^2}{a}\frac{g_2}{R^2}\right]. \tag{8.107}$$

The mass expansion in terms of φ, Eq. (8.79), can now be written as an expansion in $1/R$ by

$$\mathfrak{m}(R) = \mu\left[1 - \frac{D\alpha}{R} + \frac{1}{R^2}\left(g_2\alpha - \frac{D^2\alpha}{2a} + \frac{a}{2}D^2\alpha + \frac{1}{2}D^2\alpha^2 + \frac{1}{2}D^2\beta\right) + \mathcal{O}\left(1/c^6\right)\right]. \tag{8.108}$$

Following the same method used in the previous subsection, the effective Hamiltonian is given by Eq. (8.88) with the potential $C(R) = 1$. The relation between the real and effective Hamiltonians is given by Eq. (8.77), and the canonical transformation that relates the real and effective variables is given by Eq. (8.89). Matching the real and effective Hamiltonians, we obtain the five equations:

$$2c_1\mu^2 + \nu = 0\,, \tag{8.109a}$$

$$a_1 + 2f_1 + 2M(1 + \alpha_1\alpha_2) = 0\,, \tag{8.109b}$$

$$2c_2 - a_1 - 4M + c_1 a_1\mu^2 + 2f_1c_1\mu^2 + 2\frac{qQ}{M} - 2\mu(1 + \alpha_1\alpha_2 - c_1qQ) = 0\,, \tag{8.109c}$$

$$b_1 - 2c_2 + 4c_1\mu q Q + 2a_1 c_1 \mu^2 + 4c_1 f_1 \mu^2 - \mu - \mu\alpha_1\alpha_2 + \frac{qQ}{M} = 0\,, \tag{8.109d}$$

$$M^2\alpha_1^2\alpha_2^2 + M^2 X_2\alpha_2\beta_1 + M^2 X_1\alpha_1^2\beta_2 - a_2 - 2M^2\alpha_1\alpha_2 + \frac{2aqQD}{\mu} + \frac{m_1 q_2^2}{\mu}(1+a\alpha_1)$$
$$+ \frac{m_2 q_1^2}{\mu}(1+a\alpha_2) - 2a\frac{qQ}{\mu}(m_1\alpha_1 + m_2\alpha_2) - 2f_2 = 0\,. \tag{8.109e}$$

Solving these equations respectively for the coefficients c_1, f_1, c_2, b_1, and f_2 yields

$$c_1 = -\frac{\nu}{2\mu^2}\,, \tag{8.110a}$$

$$f_1 = -M\alpha_1\alpha_2\,, \tag{8.110b}$$

$$c_2 = M + \frac{M\nu}{2} + \frac{1}{2}M\nu\alpha_1\alpha_2 - \frac{qQ\nu}{2\mu}\,, \tag{8.110c}$$

$$b_1 = 2M\,, \tag{8.110d}$$

$$f_2 = -\frac{a_2}{2} + \frac{aq_1q_2D}{\mu} - a\frac{q_1q_2}{\mu}\left(m_1\alpha_1 + m_2\alpha_2\right) + \frac{M}{2}\left[\frac{q_2^2}{m_2}(1+a\alpha_1) + \frac{q_1^2}{m_1}(1+a\alpha_2)\right]$$
$$- M^2\left[\alpha_1\alpha_2 - \frac{1}{2}(\alpha_1\alpha_2)^2 - \frac{1}{2}\left(X_2\alpha_2^2\beta_1 + X_1\alpha_1^2\beta_2\right)\right]. \tag{8.110e}$$

Choosing $a_2 = Q^2$, so that the effective metric agrees with the EMd metric to 1PN order, the above solution for f_2 leads to the mapping

$$Q^2 = M\left(\frac{q_1^2}{m_1} + \frac{q_2^2}{m_2}\right). \tag{8.111}$$

This is because, for the case of EM theory, when we take the parameters α and β in the solution for f_2 to be zero, we get $f_2 = -a_2/2 + M(q_1^2/m_1 + q_2^2/m_2)/2$. Hence, requiring that $f_2 = 0$ in EM theory and that $a_2 = Q^2$, naturally leads to the charge map (8.111).

Identifying the mass expansion in Eq. (8.105) with that in Eq. (8.108), leads to the following mapping for α and β

$$\alpha = \frac{M}{D}\alpha_1\alpha_2\,, \tag{8.112}$$

$$\beta = \frac{M^2}{D^2}\left(X_2\alpha_2^2\beta_1 + X_1\alpha_1^2\beta_2\right), \tag{8.113}$$

which is the same mapping that was found in the previous subsection. Further, taking the mapping of the dilaton charge to also be given as in the previous subsection

$$D = m_1\alpha_1 + m_2\alpha_2, \tag{8.114}$$

leads to the astonishingly simple result

$$g_2 = 0. \tag{8.115}$$

With that mapping for D and Q, the relation between them is given by Eq. (8.100).

Interestingly, the above mappings also lead to a ST EOB Hamiltonian in Schwarzschild gauge at 1PN order. A 2PN EOB Hamiltonian based on an exact analytic solution for the metric and scalar field can be found in Ref. [696]. The metric in that work also includes a potential $C(R) \neq 1$, Eq. (II.3) in Ref. [696], and that metric is unrelated to the EMd metric when the electric charges are zero. The scalar field is given by

$$\varphi_{\text{ST}} = \frac{D}{a_*}\log\left[1 - \frac{a_*}{r} + \frac{a_*^2 - 2Ma_*}{2r^2}\right], \tag{8.116}$$

where $a_*^2 = 4(M^2 + D^2)$. The author of Ref. [696] found the same mapping for α and β that we got, but used a different mapping for D (at 2PN order). When we approximately transform the metric and the scalar field to the Schwarzschild gauge, in which the potential $C(R) = 1$, and repeat the same analysis in this section, we get an EOB Hamiltonian with the same mapping for the scalar charge given in Eq. (8.114), and with no deformation to the metric or the scalar field to 1PN order. The point is that the mapping of the scalar charge would be the same in EMd theory and ST theory, which is another hint that Eq. (8.114) is a good choice at 1PN order.

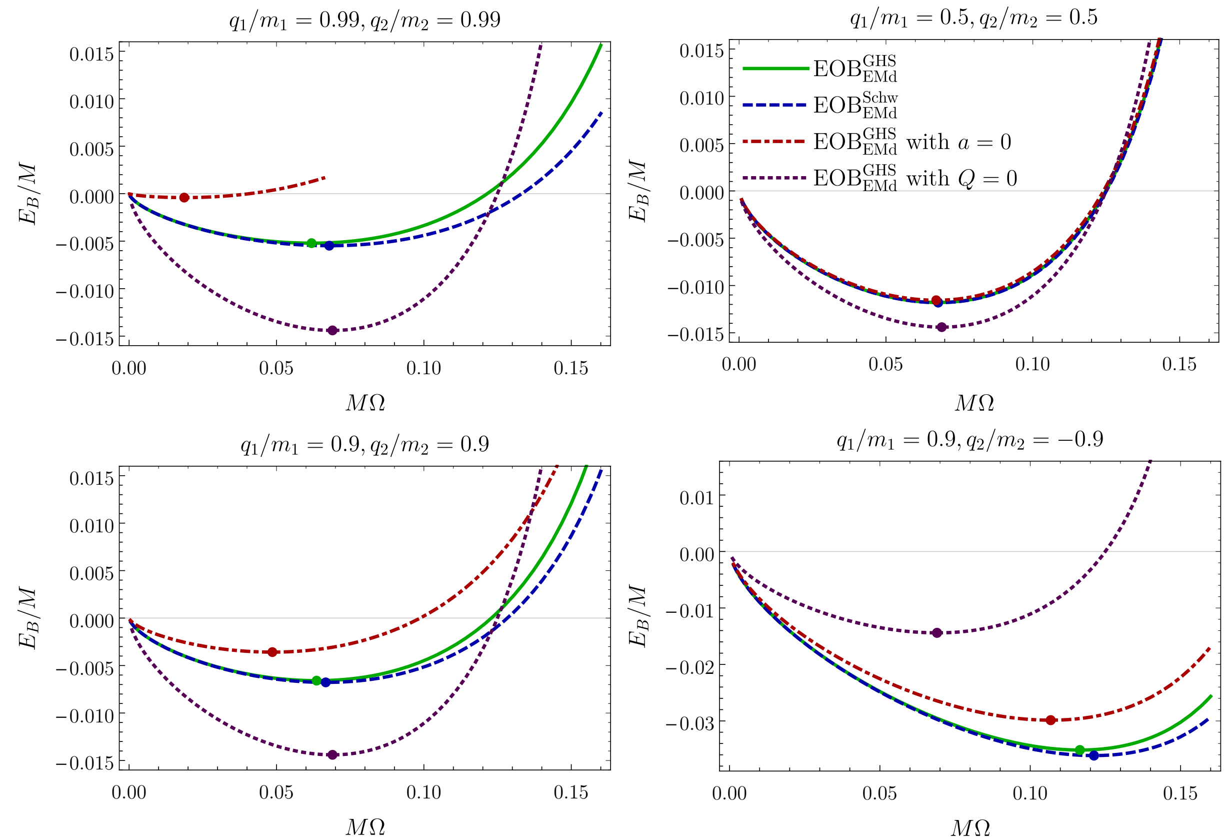

Figure 8.11: Binding energy E_B normalized by the total mass M as a function of $M\Omega$ for equal masses, $\nu = 1/4$, and for charge-to mass-ratios $q_1/m_1 = q_2/m_2 = 0.99,\ 0.9,\ 0.5$, and $q_1/m_1 = -q_2/m_2 = 0.9$. To improve readability, we show the plots only up to the frequency corresponding to $R = 1.05R_{\mathrm{LR}}$ or to energy $E_B/M = 0.015$. The point on each curve indicates the location of the ISCO.

8.4.3 Comparison of two effective-one-body Hamiltonians in Einstein-Maxwell-dilaton theory

In this subsection, we compare the two EMd-EOB Hamiltonians with each other, and also with the EOB Hamiltonian in GR, by calculating the binding energy and the ISCO. The goal is to investigate the range of parameter space where the two EMd-EOB Hamiltonians agree.

The mappings of the electric charge, scalar charge, and the parameters α and β are the same for the two EMd-EOB Hamiltonians, i.e.,

$$Q^2 = M\left(\frac{q_1^2}{m_1}+\frac{q_2^2}{m_2}\right), \qquad D = m_1\alpha_1 + m_2\alpha_2\,,$$
$$\alpha = \frac{M}{D}\alpha_1\alpha_2\,, \qquad \beta = \frac{M^2}{D^2}\left(X_2\alpha_2^2\beta_1 + X_1\alpha_1^2\beta_2\right). \tag{8.117}$$

For the EOB Hamiltonian in the GHS gauge, the effective metric is the GHS metric for $\nu = 0$ [Eqs. (8.81)–(8.83) with $b_1 = 0$]. For the EOB Hamiltonian in the Schwarzschild gauge, the effective metric agrees with the Reissner-Nordström metric for $\nu = 0$ [Eq. (8.102)]. Other differences between the two Hamiltonians are in the parameters of the mass expansion (8.80), the canonical transformation (8.90), and the correction to the scalar field [Eqs. (8.84) and (8.107)]. The parameters in those equations are shown in Table 8.1.

Table 8.1: Difference between the two EOB Hamiltonians in terms of the effective metric and the parameters of the mass expansion, the canonical transformation, and the scalar field.

	EOB in GHS gauge	EOB in Schw gauge
effective metric	Eqs. (8.81)–(8.83)	Eq. (8.102)
c_1	$c_1 = -\nu/2\mu^2$	
c_2	Eq. (8.92c)	Eq. (8.110c)
f_1	$f_1 = -M\alpha_1\alpha_2$	
f_2	Eq. (8.92e)	Eq. (8.110e)
g_2	Eq. (8.97)	$g_2 = 0$

To find the binding energy from the two EOB Hamiltonians, we start with the energy map in Eq. (8.77), which gives the relation between the effective Hamiltonian and the real Hamiltonian. Inverting that relation, we obtain the resummed EOB Hamiltonian

$$H_{\text{EOB}}^{\text{NR}} = M\sqrt{1+2\nu\left(\frac{H_{\text{eff}}}{\mu}-1\right)} - M\,. \tag{8.118}$$

To obtain the binding energy for circular orbits, we set $P_R = 0$, and solve $\dot{P}_R = -\partial H_{\text{eff}}/\partial R = 0$ for the angular momentum P_Φ. However, that equation cannot be solved analytically because of

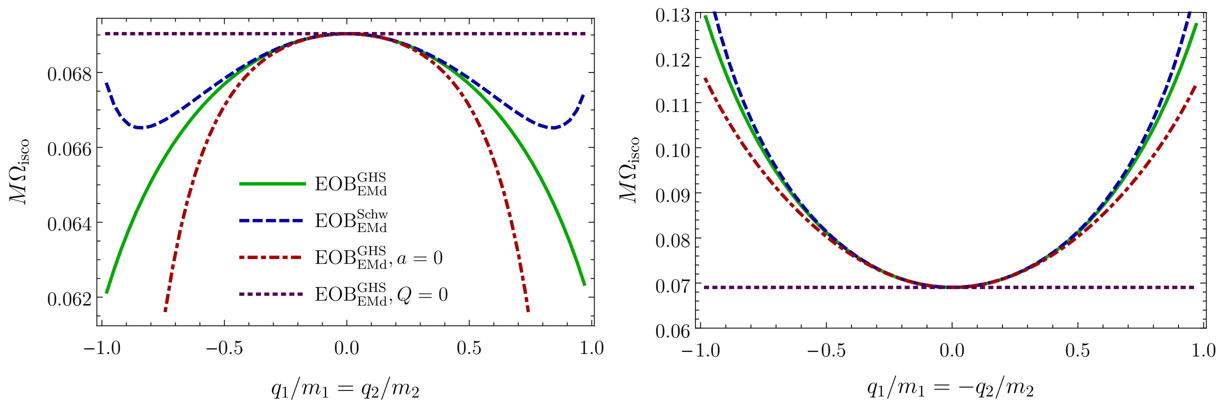

Figure 8.12: Angular frequency at ISCO as a function of the charge-to-mass ratio q_1/m_1 from -0.99 to 0.99. In the left panel, $q_2/m_2 = q_1/m_1$, while in the right, $q_2/m_2 = -q_1/m_1$. An ISCO frequency of 0.062 corresponds to an ISCO radius $\sim 6.4M$, and a frequency of 0.13 corresponds to radius $\sim 3.9M$.

the non-linearity of the Hamiltonian. Hence, we solve the equation numerically for P_Φ at specific values of R. Since we want to plot the binding energy as a function of the orbital frequency Ω, we need to calculate the orbital frequency via

$$\Omega = \frac{\partial H_{\rm EOB}}{\partial P_\Phi} = \frac{\partial H_{\rm EOB}}{\partial H_{\rm eff}} \frac{\partial H_{\rm eff}}{\partial P_\Phi}. \tag{8.119}$$

Then, we calculate the binding energy and orbital frequency as R goes from $100M$ to the radius of the light ring. The light ring (or photon orbit) of a (charged) BH metric in GR is defined as the circular-orbit solution to the geodesic equation of massless particles. This geodesic equation is actually encoded by our effective Hamiltonian if we set $q = 0$ (geodesic motion) and $\mu = 0$ (massless particle). To obtain the light-ring solution in EMd theory, we hence take the effective Hamiltonian for the case $\mu = 0 = q$, and impose the conditions for circular orbits $P_R = 0$ and $\dot{P}_R = 0$. The latter condition means that we look for an extremum of the effective Hamiltonian,

$$0 = \dot{P}_R = -\left.\frac{\partial H_{\rm eff}}{\partial R}\right|_{\mu=q=P_R=0}, \tag{8.120}$$

which is actually a maximum, $\partial^2 H_{\rm eff}/\partial R^2 < 0$, and the light-ring solution is therefore unstable. For the Schwarzschild metric in GR, solving this equation for R gives the known value $R_{\rm LR} = 3M$. For the EMd metric in the GHS gauge

$$R_{\rm LR} = \frac{3}{2}M + \frac{aD}{2} + \frac{1}{2a}\big[9a^2M^2 - 16aMD + 6a^3MD + 8D^2 - 8a^2D^2 + a^4D^2\big]^{1/2}, \tag{8.121}$$

while for the approximate metric in the Schwarzschild gauge

$$R_{\rm LR} = \frac{1}{2}\left[3M + \sqrt{9M^2 - 8Q^2}\right], \tag{8.122}$$

which is the same as the Reissner-Nordström metric since the potential $A(R)$ is the same in both cases.

In Fig. 8.11, we plot the binding energy scaled by the total mass, E_B/M, versus the orbital frequency $M\Omega$ for equal masses, $\nu = 1/4$, and for charge-to mass-ratios $q_1/m_1 = q_2/m_2 = 0.99,\ 0.9,\ 0.5$ and $q_1/m_1 = -q_2/m_2 = 0.9$. The binding energy diverges at the light ring; to improve readability, we show the plots only up to the frequency corresponding to $R = 1.05R_{\rm LR}$ or to energy $E_B/M = 0.015$. We plot the binding energy for four cases: (a) EMd-EOB Hamiltonian in the GHS gauge; (b) EMd-EOB Hamiltonian in the Schwarzschild gauge; (c) EMd-GHS Hamiltonian with $a = 0$, which is EM theory; and (d) EMd-GHS Hamiltonian in the limit where all charges are zero $Q = 0$, which is the standard uncharged GR case. [The effective Hamiltonian for case (c) is that of a charge moving in the Reissner-Nordström spacetime, and for (d) it is that of a reduced mass in Schwarzschild spacetime.] The difference between the EM case ($a = 0$ curve) and the standard astrophysical scenario of uncharged BHs ($Q = 0$ curve) quantifies the effect of the electric charges, while the difference between the EMd Hamiltonian(s) and the EM case quantifies the effect of the scalar charges.

We see from Fig. 8.11 that the electric charges have a larger effect on the binding energy than the additional scalar charges in EMd theory (except for almost extreme charges). For small electric charges $\lesssim 0.5$ (lower left panel of Fig. 8.11), the difference in binding energy between EMd theory and EM theory at the ISCO is only 9% of the difference between EMd theory and GR with no charges, i.e., the scalar charge has a very small effect. The difference between the two EMd-EOB Hamiltonians increases with increasing electric charge and frequency, but they still agree well. The binding energy of the two Hamiltonians at the ISCO differs by $\sim 6\%$ for charge-to-mass ratio 0.99 and by $\sim 0.1\%$ for charge-to-mass ratio 0.5. For charge-to-mass ratios larger than one, a naked singularity appears in the effective metric in the Schwarzschild gauge; this is an unphysical feature arising from the choice of gauge, and thus the EOB Hamiltonian should not be used for small separations (high frequencies) approaching this singularity. Note that, if one is only interested in the inspiral, then the comparison of the Hamiltonians via the binding energy can be stopped already at the ISCO frequency instead of the LR frequency.

The ISCO marks the end of the inspiral phase of the binary coalescence and the beginning of the plunge. To find the value of the ISCO, we set both the first and second derivatives of the effective Hamiltonian to zero $\partial H_{\text{eff}}/\partial R = 0 = \partial^2 H_{\text{eff}}/\partial R^2$ and set $P_R = 0$. Then, we solve the two equations numerically for the ISCO radius and angular momentum. The orbital frequency at ISCO can then be calculated from Eq. (8.119).

In Fig. 8.11, the location of the ISCO is indicated by the point on each curve. In Fig. 8.12, we plot the orbital frequency at ISCO, scaled by the mass, i.e., $M\Omega_{\text{ISCO}}$, versus the charge-to-mass ratio q_1/m_1 with $q_2/m_2 = q_1/m_1$ in the left panel, and $q_2/m_2 = -q_1/m_1$ in the right. From the left panel, we see that for high charge-to-mass ratios, the two EOB Hamiltonians do not agree well at this high frequency. For same-sign charges, the ISCO orbital frequency is lower than the uncharged case, which means the ISCO radius is greater than the Schwarzschild value of $6M$. This is because the binding energy of charged BHs is higher (less bound) than the energy of uncharged BHs, as can be seen from the binding energy in Fig. 8.11. For opposite-sign charges, the ISCO orbital frequency is higher than the uncharged case because the binding energy is lower than the energy of uncharged BHs.

8.5 Conclusions

In this paper, we analytically modeled the dynamics of binary BHs in EMd theory. In this theory, electrically charged BHs also carry a scalar charge, whereas in GR (and many modified theories of gravity) the scalar charge is zero. Thus, the identification of a BH with scalar charge through GW observations could point to modifications of gravity in the strong-field regime and violations of the strong equivalence principle. Observation of a large electric charge on BHs could be a trace of minicharged dark matter and/or dark photons.

We began by considering the case of a test BH in the background of a more massive companion in EMd theory, wherein the scalar charge of the test BH decreases as it moves radially inwards. Consistent with the results of Ref. [210], we found that the dimensionless charge $\alpha(\varphi)$ exhibits a sharp transition [see Figs. 8.1 and 8.2]. However, we showed that in a binary system, the scalar charge of the test BH will change dramatically only very close to the horizon of the background BH and only if both BHs are nearly-extremally charged. Thus, these features can be observationally relevant only in minicharged dark matter and dark photons models, but not in the Standard Model of particle physics. Our study also showed that binary BHs in EMd theory will not exhibit non-perturbative phenomena akin to induced or dynamical scalarization that are found in certain ST theories [see Fig. 8.3].

We then used the PN approximation in EMd theory to study the dynamics of a two-body system with an arbitrary mass ratio. We derived the two-body 1PN Lagrangian and Hamiltonian, and investigated how the bodies' scalar charges decrease with their separation at next-to-leading PN order. As in the test-BH case, we expect that dramatic changes could occur only for nearly-extremal charged BHs on very compact orbits; this is a regime most easily probed by systems with extreme mass ratios and/or rapidly spinning BHs. We derived the scalar, vector, and tensor energy fluxes at next-to-leading PN order. From the energy flux and binding energy, we calculated the Fourier-domain gravitational waveform for binaries on quasi-circular orbits using the stationary-phase approximation.

Using our PN result, we discussed the possibility of constraining EMd theory with GWs. Given current and projected constraints on dipole radiation, we examined how the degeneracies between electric and scalar charges limit the bounds that can be set on the EMd parameter a — constraining this parameter requires one to measure the electric charges of each BH independently, and the strength of this bound improves for larger total electric charge [see Fig. 8.8]. We also estimated the observational deviations from GR predicted in EMd theory with two measures: the dephasing between PN waveforms in the stationary-phase approximation [Fig. 8.9], and the difference in the number of useful GW cycles [Fig. 8.10]. For ground-based GW detectors, we found that the presence of electric and scalar charges contributes $\lesssim 1$ radian to the phase provided the black holes have charge-to-mass ratios of $q_i/m_i \lesssim 0.01$ for coupling constant $a = 1$. We showed that the relative difference in useful cycles between EMd theory and GR provides an estimate of the fractional correction to SNR by non-GR corrections; for systems with $q_i/m_i \lesssim 0.1$, the deviations from GR affect the total SNR by a few percent.

Finally, we constructed two EOB Hamiltonians for binary BHs in EMd theory: an EOB Hamiltonian in the GHS gauge, which is based on the exact BH solution, and an EOB Hamiltonian in the Schwarzschild gauge, which is based on an approximation to that solution. The EOB Hamiltonian in the GHS gauge is more physical in the strong-gravity regime, since it exactly reproduces the dynamics of a test body, and hence will be more accurate for systems with a very asymmetric mass ratio. The EOB Hamiltonian in Schwarzschild gauge is easier to implement by taking the existing EOB Hamiltonians in GR as a starting point and adding to it corrections due to EMd theory. We compared the two Hamiltonians by calculating the binding energy and the innermost stable circular orbit, and found that they agree well, except for nearly-extremal charges at high frequencies [see Figs. 8.11 and 8.12]. The binding energy of the two Hamiltonians at the ISCO differs by $\sim 6\%$ for charge-to-mass ratio 0.99 and by $\sim 0.1\%$ for charge-to-mass ratio 0.5.

An important goal in future continuations of our work would be the construction of a full (inspiral-merger-ringdown) EOB waveform model in EMd theory. For accurate predictions in the late inspiral, one likely needs PN results for the Hamiltonian, fluxes, and modes to the same order as they are available in GR, next to a calibration of the model to NR simulations in EMd theory. Modeling the merger and ringdown requires predictions for the parameters of the final black hole and its quasi-normal modes as a function of the EMd coupling constant a (see, e.g., Refs. [699, 700] for partial results). Since EOB waveform models in existing data-analysis infrastructure are formulated in the Schwarzschild gauge, this gauge is probably the best compromise for the purpose of GW data analysis. This gauge is also better suited for creating a single EOB waveform model covering various alternative theories; for example, we demonstrated that our EOB Hamiltonian in the Schwarzschild gauge can describe both ST and EMd theories. Ultimately, one could aim to construct a generalized EOB framework that uses a physically motivated parameterization to encode a range of possible deviations from GR.

Acknowledgments

M.K. thanks the graduate school and the physics department at the University of Maryland for the International Graduate Research Fellowship. He also thanks the Max Planck Institute for Gravitational Physics for its hospitality and for co-funding his stay during the completion of this work. We thank Sajal Mukherjee for pointing out some typos is Appendix M.

Chapter 9: Theory-agnostic framework for dynamical scalarization of compact binaries

Authors[1]: *Mohammed Khalil, Noah Sennett, Jan Steinhoff, Alessandra Buonanno*

Abstract: Gravitational wave observations can provide unprecedented insight into the fundamental nature of gravity and allow for novel tests of modifications to General Relativity. One proposed modification suggests that gravity may undergo a phase transition in the strong-field regime; the detection of such a new phase would constitute a smoking-gun for corrections to General Relativity at the classical level. Several classes of modified gravity predict the existence of such a transition—known as *spontaneous scalarization*—associated with the spontaneous symmetry breaking of a scalar field near a compact object. Using a strong-field-agnostic effective-field-theory approach, we show that all theories that exhibit spontaneous scalarization can also manifest *dynamical scalarization*, a phase transition associated with symmetry breaking in a binary system. We derive an effective point-particle action that provides a simple parametrization describing both phenomena, which establishes a foundation for theory-agnostic searches for scalarization in gravitational-wave observations. This parametrization can be mapped onto any theory in which scalarization occurs; we demonstrate this point explicitly for binary black holes with a toy model of modified electrodynamics.

[1]Originally published as Phys. Rev. D **100**, no.12, 124013 (2019)

9.1 Introduction

Classical gravity described by General Relativity (GR) has passed many experimental tests, from the scale of the Solar System [50] and binary pulsars [701, 702] to the coalescence of binary black holes (BHs) [12, 519, 579, 660, 668] and neutron stars (NSs) [703]. Despite its observational success, certain theoretical aspects of GR (e.g., its nonrenormalizability and its prediction of singularities [704]) impede progress toward a complete theory of quantum gravity; yet, strong-field modifications of the theory may alleviate these issues [420].

Gravitational wave (GW) observations probe the nonlinear, strong-field behavior of gravity and thus can be used to search for (or constrain) deviations from GR in this regime. Because detectors are typically dominated by experimental noise, sophisticated methods are required to extract GW signals. The most sensitive of these techniques rely on modeled predictions of signals (gravitational waveforms), which are matched against the data. This same approach can be adopted to test gravity with GWs; to do so requires accurate signal models that faithfully incorporate the effects from the strong-field deviations one hopes to constrain [50]. Ideally, these models would be agnostic about details of the strong-field modifications to GR, so that a single test could constrain a variety of alternative theories of gravity.

This work establishes a framework for such tests given the hypothetical scenario in which the gravitational sector manifests phase transitions, with only one phase corresponding to classical GR. This proposal comprises an attractive target for binary pulsar and GW tests of gravity; if the transition between phases arises only in the strong-gravity regime (e.g., in the presence of large curvature, relativistic matter, etc.), then such a theory could generate deviations from GR in compact binary systems while simultaneously evading stringent constraints set by weak-gravity tests. We consider the case wherein the "new" phases arise via spontaneous symmetry breaking in the gravitational sector. Similar phase transitions occur in many areas of contemporary physics—perhaps the most famous example is the electroweak symmetry breaking through the Higgs field [705–707]—so it is sensible to consider their appearance in gravity as well. As a first step, we focus on a simple set of such gravitational theories, in which the transition from GR to a new phase most closely resembles the spontaneous magnetization of a ferromagnet; however, these theories can also be extended to instead replicate the standard Higgs mechanism in the gravitational sector [494, 708].

Specifically, we investigate the nonlinear *scalarization* of nonrotating compact objects (BHs and NSs), which arises from spontaneous symmetry breaking of an additional scalar component of gravity [202, 513]. *Spontaneous scalarization*—the scalarization of a single, isolated object—has been found in several scalar extensions of GR, including massless [482, 514, 709–713] and massive [486, 487, 489] scalar-tensor (ST) theories and extended scalar-tensor-Gauss-Bonnet (ESTGB) theories [497–501, 714]. Similar phenomena can also occur for vector [491, 495], gauge [494], and spinor [493] fields. In contrast, *dynamical scalarization*—scalarization that occurs during the coalescence of a binary system—has been demonstrated and modeled only for NS binaries in ST theories [483–485, 509, 513, 681, 692, 715].

A scalarized compact object emits scalar radiation when accelerated, analogous to an accelerated electric charge. In a binary system, the emission of scalar waves augments the energy dissipation through the (tensor) GWs found in GR, hastening the orbital decay. Radio observations of binary pulsars [701, 702, 716, 717] and GW observations of coalescing BHs and NSs [519, 703] are sensitive to anomalous energy fluxes, and thus can be used to constrain the presence of scalarization in such binaries. Binaries containing spontaneously scalarized components emit scalar radiation throughout their entire evolution. In contrast, dynamically scalarizing binaries transition from an unscalarized (GR) state to a scalarized (non-GR) state at some critical orbital separation, only emitting scalar waves after this point. Because this is a second-order phase transition [513], the emitted GWs contain a sharp feature corresponding to the onset of dynamical scalarization. This feature cannot be replicated within typical theory-agnostic frameworks used to test gravity [664, 665, 667, 718], as these only consider smooth deviations from GR predictions, e.g., modifications to the coefficients of a power-series expansion of the phase evolution.

While one could attempt to model dynamical scalarization phenomenologically by adding nonanalytic functions to such frameworks [692, 719], in this paper, we propose a complementary theory-agnostic approach. We focus on a specific non-GR effect, here scalarization, but remain agnostic toward the particular alternative theory of gravity in which it occurs. The basis for our framework is effective field theory. Scalarization arises from strong-field, nonlinear scalar interactions in the vicinity of compact objects; the details of this short-distance physics depends on the specific alternative to GR that one considers. By integrating out these short-distance scales, we construct an effective point-particle action for scalarizing bodies in which the relevant details of the modification to GR are encapsulated in a small set of form factors. The coefficients of these couplings offer a concise parametrization ideal for searches for scalarization with GWs. The essential step in constructing this effective theory is identifying the fields and symmetries relevant to this phenomenon. Starting from the perspective that scalarization coincides with the appearance of a tachyonic scalar mode of the compact object, we derive the unique leading-order effective action valid near the critical point of the phase transition. Though this effective action matches that of Ref. [513]—which describes the scalarization of NSs in ST theories[2]—the approach described here is valid for a broader range of non-GR theories.

Our proposed parametrization of scalarization is directly analogous to the standard treatment of tidal interactions in compact binary systems. Tidal effects enter GW observables through a set of parameters that characterize the response of each compact object to external tidal fields [191]. These parameters are determined by the structure of the compact bodies—for example, the short-distance nuclear interactions occurring in the interior of a NS. This description of tidal effects is applicable to a broad range of nuclear models (i.e., NS equations of state) and offers a more convenient parametrization of unknown nuclear physics for GW measurements [16, 720] than directly incorporating nuclear physics into GW models. From the perspective of modeling compact binaries, the primary difference between tidal effects and scalarization is that the latter is an inherently nonlinear phenomenon, necessitating higher-order interactions in an effective action.

Beyond offering a convenient parametrization for GW tests of gravity, our effective action also elucidates certain generic properties of scalarization phenomena. Using a simple analysis of energetics based on the effective theory, we argue that *any theory that admits spontaneous scalarization must also admit dynamical scalarization*. Additionally, this type of analysis can provide further insights regarding the (nonperturbative) stability of scalarized configurations and the critical phenomena close to the scalarization phase transition. We illustrate these points by applying our energetics analysis to a simple Einstein-Maxwell-scalar (EMS) theory in which electrically charged BHs can spontaneously scalarize, complementing previous results for NSs in ST theories [513].

The paper is organized as follows. In Sec. 9.2, we first review the mechanism of scalariza-

[2] Dynamical scalarization was also modeled at the level of equations of motion in Refs. [483, 681].

tion as the spontaneous breaking of the $\mathbb{Z}_2$ symmetry of a scalar field driven by a linear scalar-mode instability. Then, we construct an effective worldline action for a compact object interacting with a scalar field valid near the onset of scalarization. In Sec. 9.3, we discuss how the relevant coefficients in the action can be matched to the energetics of an isolated static compact object in an external scalar field, demonstrating the procedure explicitly with BHs in the EMS theory of Ref. [514]. In Sec. 9.4, we employ the effective action to further investigate scalarization in this EMS theory: we examine the stability of scalarized configurations, compute the critical exponents of the scalarization phase transition, and predict the frequency at which dynamical scalarization occurs for binary BHs. We also argue that dynamical scalarization is as ubiquitous as spontaneous scalarization in modified theories of gravity. Finally, in Sec. 9.5, we summarize the main implications of our findings, and discuss future applications of our framework. The appendixes provide a derivation of a more general effective action and details on the construction of numerical solutions for isolated BHs in EMS theory. [3]

9.2 Linear mode instability and effective action close to critical point

In this section, we review the connection between the appearance of an unstable scalar mode in an unscalarized compact object and the existence of a scalarized state for the same body. We then derive an effective action close to this critical point at which this mode becomes unstable.

As an illustrative toy model for this discussion, we consider the modified theory of electrodynamics introduced in Ref. [514] (hereafter referred to as EMS theory for brevity), whose

[3] Throughout this work, we use the conventions of Misner, Thorne, and Wheeler [?] for the metric signature and Riemann tensor and work in units in which the speed of light and bare gravitational constant are unity.

action is given by

$$S_{\text{field}} = \int d^4x \, \frac{\sqrt{-g}}{16\pi} \left[R - 2\partial_\mu\phi\partial^\mu\phi - f(\phi)F^{\mu\nu}F_{\mu\nu} \right], \tag{9.1}$$

where R is the Ricci scalar, g is the determinant of the metric $g_{\mu\nu}$, and $F_{\mu\nu} = \partial_\mu A_\nu - \partial_\nu A_\mu$ is the electromagnetic field tensor. In this paper, we consider two choices of scalar couplings:

$$f_1(\phi) = e^{-\alpha\phi^2}, \tag{9.2}$$

$$f_2(\phi) = \left(1 + \alpha\phi^2 - \frac{1}{2}\alpha^2\phi^4\right)^{-1}, \tag{9.3}$$

where α is a dimensionless coupling constant. While the two couplings have the same behavior near $\phi = 0$, their behavior for large field value differs drastically. The former choice was used in Ref. [514] to construct stable scalarized BH solutions, whereas we introduce the latter in this work to demonstrate a theory in which no stable scalarized BH configurations exist (see Sec. 9.4).

The absence of any linear coupling of ϕ to the Maxwell term implies that any solution in Einstein-Maxwell (EM) theory, i.e., with $\phi = 0$, also solves the field equations of Eq. (9.1); however, stable solutions in EM theory may be unstable in EMS theory. To see this, we write the scalar-field equation schematically as

$$\Box\phi = m_{\text{eff}}^2\,\phi, \qquad m_{\text{eff}}^2 = \frac{f'(\phi)}{4\phi}F^{\mu\nu}F_{\mu\nu}. \tag{9.4}$$

We consider an electrically charged BH, for which $F^{\mu\nu}F_{\mu\nu} < 0$ and thus the effective-mass squared m_{eff}^2 is negative for $\alpha < 0$. One can decompose ϕ into Fourier modes with frequency ω and wave vector $\boldsymbol{k}$, which satisfy the dispersion relation $\omega^2 \approx \boldsymbol{k}^2 + m_{\text{eff}}^2(\boldsymbol{k})$, where curvature corrections have been dropped for simplicity. We see that if $m_{\text{eff}}^2(\boldsymbol{k})$ is sufficiently negative, then ω^2 is also negative, leading to a tachyonic instability. The critical point at which this tachyonic instability first appears can be determined by identifying linearly unstable quasinormal scalar modes

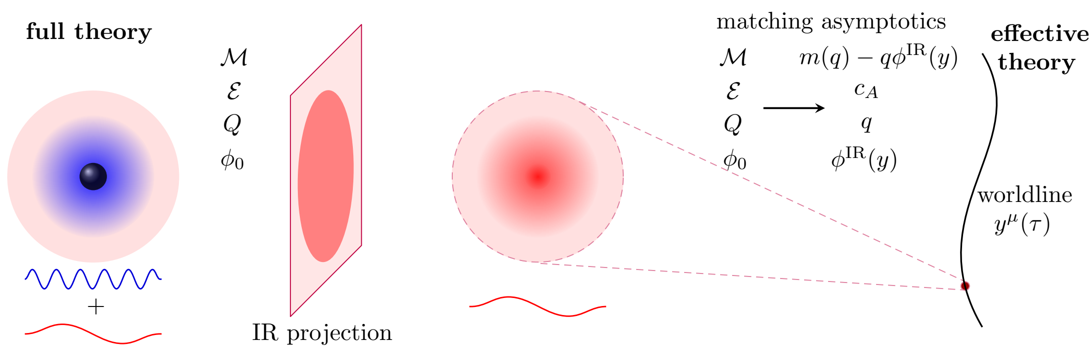

Figure 9.1: An illustration of the approach used in this paper (read from left to right). (*Left*) The fields describing an isolated compact object in equilibrium are decomposed into short- (UV) and long- (IR) wavelength modes, depicted in blue and red, respectively. (*Center*) We integrate out the UV modes via an IR projection. (*Right*) By matching asymptotics, we identify the coarse-grained compact object with an effective point-particle model that describes the IR sector of the full theory. Section 9.3 contains a detailed description of this procedure and the definitions of all quantities shown above.

of the EM solution [499, 721] or by constructing sequences of fully nonlinear, static scalarized solutions (as we do here) [514, 721].

The tachyonic instability drives the body away from the unscalarized solution, thereby breaking the symmetry $\phi \to -\phi$ in Eq. (9.1). For a stable scalarized equilibrium configuration to exist, this instability must saturate in the nonlinear regime [515]. These two conditions—the existence of a tachyonic instability and its eventual saturation—are satisfied in all of the theories discussed previously [482, 486, 487, 489, 491, 493–495, 497–501, 514, 709–714]. The only difference between these theories is the form of $m^2_{\rm eff}$; for example, in ST theories $m^2_{\rm eff}$ depends on the stress-energy tensor, while in ESTGB it depends on the Gauss-Bonnet invariant. Indeed, theories which meet these two criteria can be straightforwardly constructed, which is the reason why scalarization is such a ubiquitous phenomenon.

An even simpler perspective on scalarization arises from a coarse-grained, or effective, theory. Let us derive it explicitly. We start by splitting the fields into the short- (or ultraviolet, UV) and long- (or infrared, IR) wavelength regimes separated by the object's size $\sim R$, i.e., $\phi = \phi^{\mathrm{IR}} + \phi^{\mathrm{UV}}$, and spatially average over (integrate out) the UV parts. This effectively shrinks the compact object to a point and its effective action is given by an integral over a worldline $y^\mu(\tau)$, where τ is the proper time (see Fig. 9.1 for a schematic illustration). Dynamical short-length-scale processes like oscillations of the object are represented by dynamical variables on the worldline. For simplicity, we assume that we can also average over fast oscillation modes and only retain the monopolar mode associated to a linear tachyonic instability, denoted by $q(\tau)$. This mode $q(\tau)$ can indeed be excited by IR fields, since its frequency (or effective mass) vanishes at the critical point.

Effective actions are usually constructed by making an ansatz respecting certain symmetries and including only terms up to a given power in the cutoff between IR and UV scales. The relevant symmetries here are diffeomorphism, U(1)-gauge, worldline-reparametrization, time-reversal[4], and scalar-inversion invariance. The last reads $\phi \to -\phi$ in the full theory, so in the effective action it decomposes into simultaneous IR $\phi^{\mathrm{IR}} \to -\phi^{\mathrm{IR}}$ and UV $q \to -q$ transformations. The IR fields are of order $\phi^{\mathrm{IR}} \sim \mathcal{O}(R/r)$ on the worldline, where r is the typical IR scale (e.g., the separation of a binary). Now, the oscillator equation for the mode $q(\tau)$ driven by the IR field ϕ^{IR} can be schematically written as

$$c_{\dot{q}^2}\ddot{q} + V'(q) = \phi^{\mathrm{IR}}(y), \qquad V(q) = \frac{c_{(2)}}{2}q^2 + \frac{c_{(4)}}{4!}q^4 + \dots, \tag{9.5}$$

where $\dot{} = d/d\tau$ and the $c_{\dots}$ are constant coefficients determined by the UV physics. (The singular self-field contribution to $\phi^{\mathrm{IR}}(y)$ must be removed using some regularization prescription.) The

[4]Time reversal is an approximate symmetry of compact objects in an adiabatic setup, like the inspiral of a binary system. In this case, a compact object's entropy remains approximately constant.

normalization of q is chosen to fix the coefficient of $\phi^{\rm IR}(y)$; for all that follows, we simply assume that $c_{\dot{q}^2} > 0$. Close to the critical point, the quadratic term in V is negligible, and thus from Eq. (9.5), one finds that for equilibrium configurations ($\dot{q} = 0$), q scales as $q^3 \sim \phi^{\rm IR}$. More generally, the mode q oscillates around this equilibrium point provided that the IR field evolves slowly relative to the frequency of the mode, i.e., $\dot{\phi}^{\rm IR} = \dot{y}^\mu \partial_\mu \phi^{\rm IR} \ll \dot{q}/q$; this condition is satisfied for binary systems on quasicircular orbits (which we restrict our attention to in this work), but could be violated for highly eccentric orbits. For small perturbations around equilibrium, one finds that $\dot{q} \sim \delta\sqrt{\phi^{\rm IR}}$ and $\ddot{q} \sim \delta\phi^{\rm IR}$ where $\delta \equiv (q - q_0)/q_0 \ll 1$ is the fractional deviation from the equilibrium point q_0.

Using the scaling relations derived above, we construct the most generic effective action for a nonrotating compact object with a dynamical mode $q(\tau)$ described by Eq. (9.5) close to the critical point, up to order $\mathcal{O}(R^2/r^2)$

$$S_{\rm CO}^{\rm crit} = \int d\tau \left[\frac{c_{\dot{q}^2}}{2}\dot{q}^2 + \phi^{\rm IR}(y)q - c_{(0)} - \frac{c_{(2)}}{2}q^2 - \frac{c_{(4)}}{4!}q^4 + c_A A_\mu^{\rm IR}(y)\dot{y}^\mu + \mathcal{O}\left(\frac{R^2}{r^2}\right)\right], \tag{9.6}$$

$$= \int d\tau \left[\frac{c_{\dot{q}^2}}{2}\dot{q}^2 + \phi^{\rm IR}(y)q - m(q) + c_A A_\mu^{\rm IR}(y)\dot{y}^\mu + \mathcal{O}\left(\frac{R^2}{r^2}\right)\right], \tag{9.7}$$

where CO stands for compact object and for later convenience we define

$$m(q) \equiv c_{(0)} + V(q). \tag{9.8}$$

Terms containing time derivatives of $\phi^{\rm IR}$ all enter at higher order in R/r than we work, e.g., $\ddot{\phi}^{\rm IR}q \sim \dot{\phi}^{\rm IR}\dot{q} \sim \phi^{\rm IR}\ddot{q} \sim \mathcal{O}(R^2/r^2)$, and thus are absent in Eq. (9.7). A reparametrization-invariant action is obtained by inserting $d\tau = d\sigma\sqrt{-g_{\mu\nu}^{\rm IR}(y)dy^\mu/d\sigma dy^\nu/d\sigma}$, where σ is an arbitrary affine parameter, and replacing derivatives $d/d\tau$ accordingly. The complete effective action reads

$$S_{\rm eff} = S_{\rm field}^{\rm IR} + S_{\rm CO}^{\rm crit}, \tag{9.9}$$

where more copies of $S_{\rm CO}^{\rm crit}$ can be added depending on the number of objects in the system and $S_{\rm field}^{\rm IR}$ is given by Eq. (9.1) with IR labels on the fields. The equations of motion and field equations are obtained by independent variations of $y^\mu(\sigma)$, $q(\sigma)$, and $\phi^{\rm IR}(x)$, $g_{\mu\nu}^{\rm IR}(x)$, $A_\mu^{\rm IR}(x)$.

The simplicity of $S_{\rm CO}^{\rm crit}$ is striking, but we recall that it is only valid close to the critical point of a monopolar, tachyonic, linear instability of a scalar mode. (A more generic effective action valid away from the critical point is discussed in Appendix O.) Despite its simplicity, the effective action (9.9) is theory agnostic, in the sense that it is constructed assuming only the scalar-inversion symmetry and that the nonrotating compact object hosts such a mode; in particular, it should hold for the cases studied in Refs. [482, 486, 487, 489, 491, 493–495, 497–501, 514, 709–714] and similar work to come. We emphasize that strong-field UV physics at the body scale is parametrized through the numerical coefficients $c_{\ldots}$, which can be matched to a specific theory and compact object, or be constrained directly from observations (analogous to tidal parameters [703, 720]).

9.3 Matching strong-field physics into black-hole solutions

As an illustrative example of the effective-action framework derived above, we now compute the sought-after coefficients $c_{\ldots}$ for BHs in EMS theory.

For this purpose, we match a BH solution in the full theory (9.1) to a generic solution of the coarse-grained effective theory (9.9) for an isolated body. Schematically, the former represents the full solution at all scales, while the latter only represents its projection onto IR scales. We focus first on BH solutions of the full theory (9.1), restricting our attention to equilibrium/static, electrically charged, spherically symmetric solutions.

In EMS theory, this family of solutions is characterized by three independent parameters, which we take to be the electric charge $\mathcal{E}$, the BH entropy $\mathcal{S}$, and the asymptotic scalar field ϕ_0, assuming a vanishing asymptotic electromagnetic field and an asymptotically flat metric. The electric charge is globally conserved by the U(1) symmetry of the theory and the entropy remains constant under reversible processes, which we have implicitly restricted ourselves to by assuming time-reversal symmetry in the effective action. Thus, we use a sequence of solutions with fixed $\mathcal{E}$ and $\mathcal{S}$ to represent the response of a BH to a varying scalar background ϕ_0. Since EMS theory modifies electrodynamics, but not gravity or the coupling to gravity, the entropy of a charged BH is the same as in GR, i.e., it is proportional to the horizon area. See also Ref. [514] for the first law of BH thermodynamics in EMS theory.

The asymptotic behavior of the fields take the form

$$\begin{pmatrix} \phi \\ \\ A_0 \\ \\ g_{00} \end{pmatrix} = \begin{pmatrix} \phi_0 \\ \\ 0 \\ \\ -1 \end{pmatrix} + \begin{pmatrix} Q(\phi_0) \\ \\ -\mathcal{E} e^{\alpha \phi_0^2} \\ \\ 2\,\mathcal{M}(\phi_0) \end{pmatrix} \frac{1}{|\boldsymbol{X}|} + \mathcal{O}(|\boldsymbol{X}|^{-2}), \tag{9.10}$$

where $Q(\phi_0)$ is the scalar charge of the BH and $\mathcal{M}(\phi_0)$ is its gravitational mass. [5] We construct these solutions numerically (see Appendix P for details), and then compute ϕ_0, $\mathcal{M}$, and Q directly from their asymptotic behavior.

Next, we turn our attention to the description of these BH solutions in the effective theory (9.9). We set up the solution under the same boundary conditions as the numerical sequence described above; in particular, we look at isolated equilibrium configurations, $y^\alpha \partial_\alpha g^{\mathrm{IR}}_{\mu\nu} \approx y^\alpha \partial_\alpha A^{\mathrm{IR}}_0 \approx y^\alpha \partial_\alpha \phi^{\mathrm{IR}} \approx \dot{q} \approx 0$. We construct a coordinate system $\boldsymbol{x}$ in which the worldline has

[5] The quantities $Q(\phi_0)$ and $\mathcal{M}(\phi_0)$ describing the asymptotic behavior of the solution also depend on the parameters $\mathcal{E}$ and $\mathcal{S}$, but we suppress the dependence in our notation for brevity. Derivatives of Q and $\mathcal{M}$ are taken holding $\mathcal{E}$ and $\mathcal{S}$ constant.

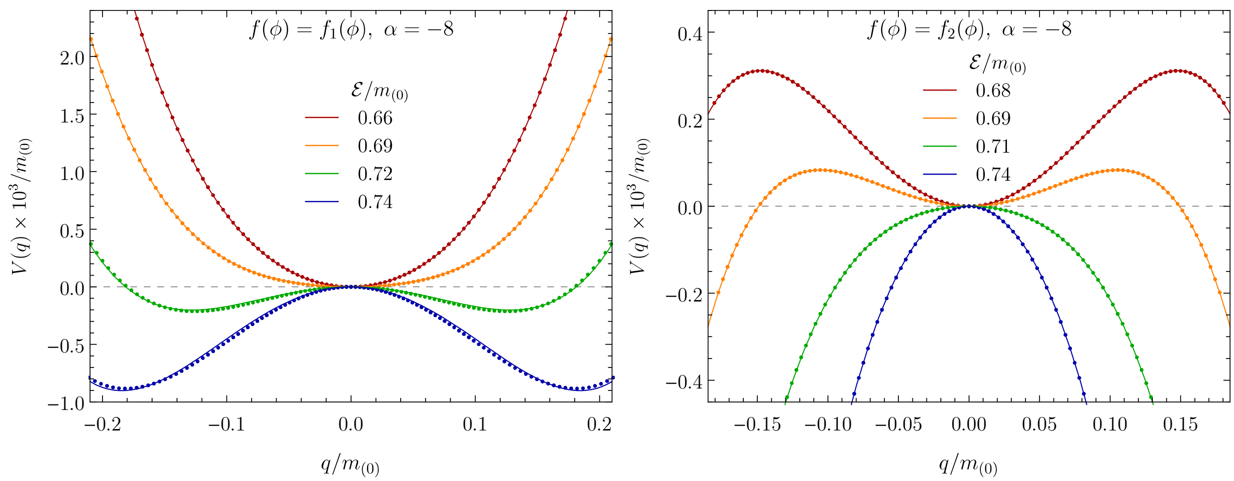

Figure 9.2: The potential $V(q)$ for $\alpha = -8$ and different electric charges $\mathcal{E}$. The left and right panels correspond to BHs in EMS theory with coupling $f_1(\phi)$ [Eq. (9.2)] and $f_2(\phi)$ [Eq. (9.3)], respectively. The numerical solutions and polynomial fits are indicated with points and lines, respectively.

spatial components $\boldsymbol{y} = \boldsymbol{0}$, so that all fields are independent of time. Furthermore, relying on the fact that both solutions are asymptotically flat, we choose the coordinates $\boldsymbol{x}$ such that they match the numerical coordinates $\boldsymbol{X}$ in the asymptotic region, i.e., $\boldsymbol{x} = \boldsymbol{X} + \mathcal{O}(|\boldsymbol{X}|^{-1})$. Then working to linear order in the fields, we find

$$\begin{pmatrix} \phi^{\mathrm{IR}} \\ A_0^{\mathrm{IR}} \\ g_{00}^{\mathrm{IR}} \end{pmatrix} = \begin{pmatrix} \phi_0 \\ 0 \\ -1 \end{pmatrix} + \begin{pmatrix} q \\ -c_A e^{\alpha[\phi^{\mathrm{IR}}(y)]^2} \\ 2[m(q) - \phi^{\mathrm{IR}}(y) q] \end{pmatrix} \frac{1}{|\boldsymbol{x}|} + \ldots. \tag{9.11}$$

These fields are singular when evaluated on the worldline, $\boldsymbol{x} = \boldsymbol{y} = \boldsymbol{0}$. This can be cured by appropriately regularizing the solution; here, we simply keep the finite part and drop the singular self-field part, e.g., $\phi^{\mathrm{IR}}(y) = \phi_0$. The situation is analogous to the singular fields that arise in electrostatics when an extended source is approximated by a point charge.

In addition to a solution for the fields, a variation of q in the effective action leads to

$$\phi_0 = \frac{dm}{dq} = \frac{dV}{dq} = c_{(2)}q + \frac{c_{(4)}q^3}{3!} + \mathcal{O}\left(\frac{R^2}{r^2}\right). \tag{9.12}$$

The matching now consists of identifying the IR-scale fields in the solution of the full theory (9.10) with the fields predicted in the IR effective theory (9.11). We extract the IR-scale fields from the former solution using an appropriate IR projector $P^{\mathrm{IR}}[\cdot]$, such that the matching conditions are given explicitly as $P^{\mathrm{IR}}[\phi] = \phi^{\mathrm{IR}}$ (and likewise for the other fields). Such a projector is most easily formulated in the Fourier domain, so we first compute the (spatial) Fourier transform of the fields (9.10), denoted by a tilde

$$\tilde{\phi}(\boldsymbol{K}) = \phi_0\delta(\boldsymbol{K}) + \frac{4\pi Q(\phi_0)}{\boldsymbol{K}^2} + \mathcal{O}(|\boldsymbol{K}|^{-1}). \tag{9.13}$$

We employ the simple projector $P^{\mathrm{IR}}[\tilde{\phi}] \equiv \tilde{\phi}(\boldsymbol{K})\Theta(K^{\mathrm{IR}} - |\boldsymbol{K}|)$, where Θ is the Heaviside function and K^{IR} is the cutoff scale. Applying this projection to Eq. (9.13) and taking the inverse Fourier transform, one finds that $P^{\mathrm{IR}}[\phi]$ takes the same form as Eq. (9.10) on scales longer than the cutoff, i.e., for $|\boldsymbol{X}| \gg 1/K^{\mathrm{IR}}$. Then, our matching conditions $P^{\mathrm{IR}}[\phi] = \phi^{\mathrm{IR}}$, $P^{\mathrm{IR}}[A_0] = A_0^{\mathrm{IR}}$, $P^{\mathrm{IR}}[g_{00}] = g_{00}^{\mathrm{IR}}$ reduce to

$$Q(\phi_0) = q, \quad \mathcal{E} = c_A, \quad \mathcal{M}(\phi_0) = m(q) - \phi_0 q, \tag{9.14}$$

where we have used $\phi^{\mathrm{IR}}(y) = \phi_0$ as discussed above. Note that the last equation and $m'(q) = \phi_0$ (9.12) reveal that the two measures of energy $\mathcal{M}$ and m are related by a Legendre transformation of the conjugate variables (q, ϕ_0). Hence, we find that $Q = q = -\mathcal{M}'(\phi_0)$, in agreement with the first law of BH thermodynamics [722, 723].

While $\mathcal{M}(\phi_0)$ is the gravitational mass of the system, $m(q)$ represents the "gravitational free energy" of the body (see also Sec. III.A of Ref. [513]). That is, m is the mass/energy with the potential energy $-\phi_0 q$ (due to the external scalar field) subtracted from $\mathcal{M}$. We find below that m—not $\mathcal{M}$—serves as better representation of "point-particle mass" found in the Lagrangian or Hamiltonian description of a binary system; of course, both quantities reduce to the standard ADM mass in GR in the absence of scalarization. Furthermore, away from the critical point, it is not necessary to treat the mode q as a dynamical variable. This means that we can set $\dot{q} = 0$ and remove q from the action (9.7). The latter is achieved by virtue of the Legendre transformation between $m(q)$ in Eq. (9.7) and $\mathcal{M}(\phi^{\text{IR}}(y))$,

$$S_{\text{CO}} = \int d\tau \Big[-\mathcal{M}(\phi^{\text{IR}}(y)) + \mathcal{E} A_\mu^{\text{IR}}(y)\dot{y}^\mu + \dots \Big]. \tag{9.15}$$

We see that $\mathcal{M}$ plays the role of the Eardley mass [480] in the action now. We note that since the Eardley mass and $m(q)$ are related by a Legendre transformation, they contain the same information.

To compute the values of the various $c_{\dots}$, we numerically construct a sequence of BH solutions as described above and extract the functions $\mathcal{M}(\phi_0)$ and $Q(\phi_0)$. From there we obtain $m(q)$ and $V(q)$ numerically from Eq. (9.14), as illustrated in Fig. 9.2. Each curve indicates a BH sequence with a different electric charge-to-mass ratio $\mathcal{E}/m^{(0)}$, where $m^{(0)} \equiv c_{(0)}$ is the mass of the isolated BH with no scalar charge. The points indicate the numerically computed solutions, which are calculated by solving the field equations with different boundary conditions for the scalar field (see Appendix P). The solid lines are polynomial fits of the form (9.5), from which we extract the values of the coefficients $c_{(2)}$ and $c_{(4)}$.

It is remarkable that from equilibrium solutions one can fix the potential of a dynamical (nonequilibrium) mode to order q^4. This connection is nontrivial, and it breaks down when one relaxes the assumption of being close to the critical point. For instance, if terms like $(\phi^{\text{IR}})^2$

are included in Eq. (9.7), then $Q \neq q$; or consider the case of a minimally coupled scalar field ($\alpha = 0$), wherein no-hair theorems [669, 670] guarantee that $\mathcal{M}(\phi_0) = \text{const}$—the energy of an equilibrium BH obviously does not encode any information about dynamical modes.

Having described how to compute the coefficients $c_{\dots}$ in the effective action (9.7), the following section illustrates how this action can be used to study spontaneous and dynamical scalarization.

9.4 Modeling strong-gravity effects within the theory-agnostic framework

In this section, we show how spontaneous and dynamical scalarization can be understood from the effective theory (9.7), based on a simple analysis of energetics. We use this effective action to investigate the properties of these critical phenomena, namely their critical exponents. Though we use EMS theory to make quantitative predictions throughout this section, we emphasize again that the qualitative behavior we find should hold generically for all theories in which spontaneous scalarization occurs. More specifically, theories in which scalarized configurations are stable are analogous to EMS theory with scalar coupling $f_1(\phi)$, whereas those where such configurations are unstable correspond to the coupling $f_2(\phi)$ (see the following subsection for details). Extending the predictions made below to other theories only requires computation of the effective mode potential $V(q)$, as described in the previous section, and the inclusion of any new long-range fields not present in EMS theory that impact the motion of binary systems.

9.4.1 Spontaneous scalarization

Recall that a spontaneously scalarized object is one that hosts a nonzero scalar charge even in the absence of an external scalar field $\phi_0 = 0$. From Eq. (9.12) we see that $\phi_0 = 0$ corresponds to extrema of $V(q)$ for equilibrium configurations. Furthermore, since $V(q)$ is the oscillation-mode potential, q dynamically evolves into a minimum of $V(q)$ [see Eq. (9.5)]. Thus, the existence of spontaneously scalarized configurations is indicated by nontrivial extrema of $V(q)$, and the stability of these configurations depends on whether such points are local minima (stable) or maxima (unstable). For example, the left panel Fig. 9.2 depicts the appearance of spontaneously scalarized BH solutions as one increases the charge-to-mass ratio in EMS theory with coupling $f_1(\phi)$. Without enough electric charge (e.g., the red and orange curves, with $c_{(2)} > 0$), the EM (unscalarized) solutions are the only stable BH solutions, but by increasing the charge beyond a critical value (e.g., the green and blue curves, with $c_{(2)} < 0$), the EM solution becomes unstable and the stable solutions instead occur at nonvanishing values of q.

Our approach allows one to determine the values of the coupling α and the electric charge $\mathcal{E}$ at which spontaneous scalarization first occurs ($c_{(2)} = 0$) using only sequences of equilibrium BH solutions. A more direct approach employed in the past was to search for instabilities of linear, dynamical scalar perturbations on a (GR) Reissner-Nordström background [721]. We find that the two methods provide the same predictions. For the choice of coupling $f_1(\phi)$, we compute the critical coupling as a function of the electric charge $\alpha_{\text{crit}}(\mathcal{E})$ where $c_{(2)} = 0$ and find that our results agree with the predictions of Ref. [721] at the onset of the linear instability of the $\ell = 0$ scalar mode to within 1%. For theories in which scalarized solutions are easy to construct, like the EMS theory considered here, our approach can more efficiently compute this critical point than a perturbative stability analysis. We see that the effective potential $V(q)$ provides strong indications for a linear scalar-mode instability and its nonlinear saturation.

The same energetics argument reveals drastically different behavior in the EMS theory with coupling $f_2(\phi)$, depicted in the right panel of Fig. 9.2. Recall that $f_1(\phi) \approx f_2(\phi)$ for small field values, but the two choices differ in the nonlinear regime, which will dramatically impact the stability of scalarized solutions. This distinction is reflected in our effective action by the sign of $c_{(4)}$; this coefficient is positive for the choice of coupling $f_1(\phi)$ and negative for $f_2(\phi)$. Our simple energetics arguments reveal that above some critical electric charge (e.g., the green and blue curves with $c_{(2)} < 0$), no spontaneously scalarized solutions exist, whereas below this value (e.g., the red and orange curves with $c_{(2)} > 0$) spontaneously scalarized solutions may exist, but are unstable to scalar perturbations. In the former case (the green and blue curves), there is no sign of a nonlinear saturation of the tachyonic instability of the EM solution; no stable equilibrium solutions seem to exist. However, it is impossible to infer how the unstable EM solutions would evolve using our effective theory, since the assumption of time-reversal symmetry (or constant BH entropy) will likely break down. Numerical-relativity simulations are needed to answer this question (or the construction of a more generic effective theory).

The importance of nonlinear interactions in stabilizing spontaneously scalarized solutions has been studied extensively in the context of ESTGB theories [724–726]. For those theories, exponential couplings (equivalent to our f_1) or quartic couplings ($f \sim -\phi^2 + \phi^4$) provide stable scalarized solutions, whereas with quadratic couplings ($f \sim -\phi^2$), all scalarized solutions are unstable. Interestingly, quadratic couplings predict stable scalarized solutions in EMS theories [727], but our analysis suggests that stability is not guaranteed for generic couplings. The stability analyses in these references involve studying linearized perturbations on scalarized backgrounds.

Though technically only valid near the critical point of the spontaneous scalarization phase transition and for small q, our approach offers a much easier alternative for estimating stability. We find that our approach correctly reproduces the findings of these stability analyses for scalarized BHs in EMS theories [727, 728].

9.4.2 Critical exponents of phase transition in gravity

The point-particle action (9.7) also offers some insight into the critical behavior that arises near the onset of spontaneous scalarization. For this discussion, we restrict our attention to the scalar coupling $f_1(\phi)$, for which spontaneously scalarized configurations are stable. Considering the various coefficients $c_{\dots}$ as functions of the electric charge $\mathcal{E}$ and entropy $\mathcal{S}$ of a BH and the overall coupling constant α, the effective potential $V(q)$ corresponds precisely to the standard Landau model of second-order phase transitions [729, 730]. Compared to the archetypal example of ferromagnetism, the role of temperature T is played by either $\mathcal{E}$ or α. This connection reveals that (i) spontaneous scalarization is a second-order phase transition and (ii) the critical exponents characterizing this phase transition match the universal values predicted by the Landau model. Point (i) was already demonstrated for NSs in ST theories in Ref. [513], but point (ii) is new to this work; we elaborate on (ii) below.

Critical exponents dictate how a system behaves close to a critical point (e.g., the location of a second-order phase transition). Such phenomena have first been discovered in GR in the context of critical collapse [731–734], but also appear in perturbations of extremal BHs [735, 736]. Applied to the current example of spontaneous scalarization, we study how the structure of the BH solutions varies as we approach the critical point at which spontaneous scalarization first occurs, parametrized by $\xi \to 0$ where ξ could be either $\xi = (\alpha - \alpha_c)/\alpha_c$ at fixed $\mathcal{E}$ (identifying temperature as $T \sim -1/\alpha$) or $\xi = (\mathcal{E} - \mathcal{E}_c)/\mathcal{E}_c$ at fixed α (identifying $T \sim 1/\mathcal{E}$). For example, the critical exponent β of a Landau model is given by the scaling of the order parameter $q \propto \xi^\beta$ as $\xi \to 0^+$.

The effective potential $V(q)$ in Eq. (9.5) depends on the properties of the BH solution; this dependence is suppressed in the notation used in the previous section, but here we explicitly restore it. In particular, close to the critical point, the potential takes the form

$$V(q;\xi) = \frac{c_{(2)}(\xi)}{2} q^2 + \frac{c_{(4)}(\xi)}{4!} q^4. \tag{9.16}$$

If $c_{(2)}(\xi)$ and $c_{(4)}(\xi)$ are analytic functions, they must take the following form near $\xi = 0$,

$$c_{(2)}(\xi) = a\,\xi + \mathcal{O}\left(\xi^2\right), \qquad c_{(4)}(\xi) = b + \mathcal{O}\left(\xi\right), \tag{9.17}$$

where a and b are positive constants. Then, the minima of $V(q;\xi)$ occur at

$$q = \pm\sqrt{\frac{-6c_{(2)}}{c_{(4)}}} = \pm\sqrt{\frac{-6a}{b}}\,\xi^{1/2}, \tag{9.18}$$

thus, $q \propto \xi^{1/2}$ as $\xi \to 0^+$. For this system, q represents an order parameter, and thus the critical exponent β is 1/2.

We numerically confirm this claim by computing the scalar charge q of electrically charged BHs as a function of ξ near the critical point. Fixing the electric charge $\mathcal{E}$, we first determine the critical coupling α_{crit} at which $c_{(2)}$ vanishes. We then compute q for couplings just below this value, i.e., for $\xi = (\alpha - \alpha_{\text{crit}})/\alpha_{\text{crit}} \gtrsim 0$. The dependence of q on ξ is depicted in Fig. 9.3; we find that $q \propto \xi^{1/2}$ agrees well with our numerical results.

Similarly, we compute the other standard critical exponents describing the phase transition. In particular, both the analytic model (9.16) and our numerical solutions indicate that $\gamma = 1$

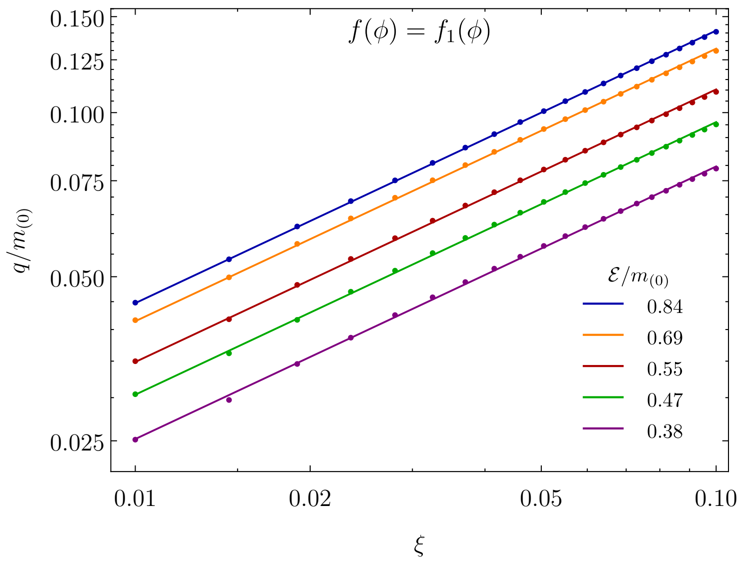

Figure 9.3: Scalar charge q as a function of $\xi \equiv (\alpha - \alpha_c)/\alpha_c$ for different electric charges with coupling $f_1(\phi)$ [Eq. (9.2)]. The numerical solutions are indicated with points, while the solid lines are best fits with slope 1/2. We see that the solutions agree well with the expected scaling $q \propto \xi^{1/2}$.

where $\chi = dq/d\phi_0 \propto |\xi|^{-\gamma}$ for $\xi \to 0^{\pm}$, and $\delta = 3$ where $q \propto \phi_0^{1/\delta}$ at $\xi = 0$. These findings are consistent with the Landau model for phase transitions. It would be interesting to find a correspondence to a correlation length in the future, so that all standard critical exponents can be studied. The introduction of a correlation length (becoming infinite as $c_{(2)} \to 0$) as another scale next to the size of the compact object could also allow for a more formalized power counting for the construction of the effective action close to the critical point.

9.4.3 Dynamical scalarization

We now employ our effective action to study the dynamical scalarization of binary systems in EMS theory, only considering the scalar coupling $f_1(\phi)$ except where noted. For this purpose, we integrate out the remaining IR fields from the complete action (i.e., the field part, suitable gauge-fixing parts, and a copy of $S^{\rm crit}_{\rm CO}$ for each body). [6] We employ a weak-field and slow-motion (i.e., post-Newtonian, PN) approximation. These approximations are not independent here, since a wide separation of the binary (weak field) implies slow motion due to the third Kepler law for bound binaries. The leading order in this approximation is just the Newtonian limit of the relativistic theory we are considering. Therefore, the Lagrangian of the binary to leading order (LO) reads[7]

$$
\begin{aligned}
L^{\rm LO} = &-m_A\left[1-\frac{\dot{\boldsymbol{y}}_A^2}{2}\right]-m_B\left[1-\frac{\dot{\boldsymbol{y}}_B^2}{2}\right]+\frac{c_{\dot{q}^2,A}}{2}\dot{q}_A^2+\frac{c_{\dot{q}^2,B}}{2}\dot{q}_B^2\\
&+\frac{m_Am_B}{r}+\frac{\mathcal{E}_A\mathcal{E}_B}{r}+\frac{q_Aq_B}{r},
\end{aligned}
\tag{9.19}
$$

where A and B label the bodies, $r=|\boldsymbol{y}_A-\boldsymbol{y}_B|$ is their separation, and in this section the dot $\dot{}$ indicates a derivative with respect to coordinate time. We have suppressed the dependence of m_A on q_A for brevity, but recall that the "free energy" of each body takes the form

$$
\begin{aligned}
m_A(q_A) &= m_{(0),A}+V(q_A)\\
&= c_{(0),A}+\frac{c_{(2),A}}{2}q_A^2+\frac{c_{(4),A}}{4!}q_A^4.
\end{aligned}
\tag{9.20}
$$

Notice that $m_A(q_A)$ plays the role of the body's mass in the binary Lagrangian because (i) it couples to gravity like a mass, see Eq. (9.7), and (ii) it is independent of the fields, so that for the purpose of integrating out the fields it can be treated as a constant. The Hamiltonian for the binary can be obtained via a Legendre transformation

$$
H^{\rm LO}=m_A+m_B+\frac{\boldsymbol{p}_A^2}{2m_A}+\frac{\boldsymbol{p}_B^2}{2m_B}+\frac{p_{q,A}^2}{2c_{\dot{q}^2,A}}+\frac{p_{q,B}^2}{2c_{\dot{q}^2,B}}-\frac{m_Am_B}{r}+\frac{\mathcal{E}_A\mathcal{E}_B}{r}-\frac{q_Aq_B}{r},
\tag{9.21}
$$

with the pairs of canonical variables $(\boldsymbol{y}_{A/B},\boldsymbol{p}_{A/B})$ and $(q_{A/B},p_{q,A/B})$.

[6] Strictly speaking, the IR fields are split again into body-scale and radiation-scale parts, and we integrate out the body-scale fields [737]. This would be necessary for a treatment of radiation from the binary using effective-field-theory methods [738].

[7] We have also gauge-fixed the worldline parameters to the coordinate time $\sigma=t$ as usual in the PN approximation.

Following Ref. [513], let us now consider a special case that allows simple analytic solutions for the scalar charges of the bodies. We henceforth assume that the scalar charges evolve adiabatically $p_{q,A/B} \approx 0$ and that the two bodies are identical, i.e., $q \equiv q_A = q_B$, $c_{(2)} \equiv c_{(2),A} = c_{(2),B}$, etc. The Hamiltonian in the center-of-mass system $\boldsymbol{p} \equiv \boldsymbol{p}_A = -\boldsymbol{p}_B$ now reads

$$H^{\text{LO,adiab.}} = 2m + \frac{\boldsymbol{p}^2}{m} - \frac{m^2}{r} + \frac{\mathcal{E}^2}{r} - \frac{q^2}{r}. \tag{9.22}$$

Under these assumptions and recalling again that $m = m(q)$, the equation of motion for the scalar charge q is given by

$$0 \approx \dot{p}_q = \frac{\partial H^{\text{LO,adiab.}}}{\partial q} = 2z\left(c_{(2)}q + \frac{c_{(4)}}{6}q^3\right) - \frac{2q}{r}, \tag{9.23}$$

with the redshift

$$z \equiv 1 - \frac{\mathbf{p}^2}{2m^2} - \frac{m}{r}. \tag{9.24}$$

For simplicity, we neglect relativistic corrections to the redshift from here onward, i.e., $z \approx 1$; restoring these corrections does not affect the qualitative behavior that we describe. Equation (9.23) has three solutions: an unscalarized solution with $q = 0$ and a two scalarized solutions with nonzero q of opposite signs. The condition for stability of these solutions is that they are located at a minimum of the energy of the binary,

$$0 \leq \frac{\partial^2 H^{\text{LO,adiab.}}}{\partial q^2} \approx 2c_{(2)} - \frac{2}{r} + c_{(4)}q^2, \tag{9.25}$$

which is violated for $q = 0$ when $1/r > c_{(2)}$. Hence, the stable solutions are given by

$$q = \begin{cases} 0 & \text{for} \quad 1/r \leq c_{(2)} \\ \pm\sqrt{\dfrac{6}{c_{(4)}}}\sqrt{\dfrac{1}{r} - c_{(2)}} & \text{for} \quad 1/r \geq c_{(2)} \end{cases}, \tag{9.26}$$

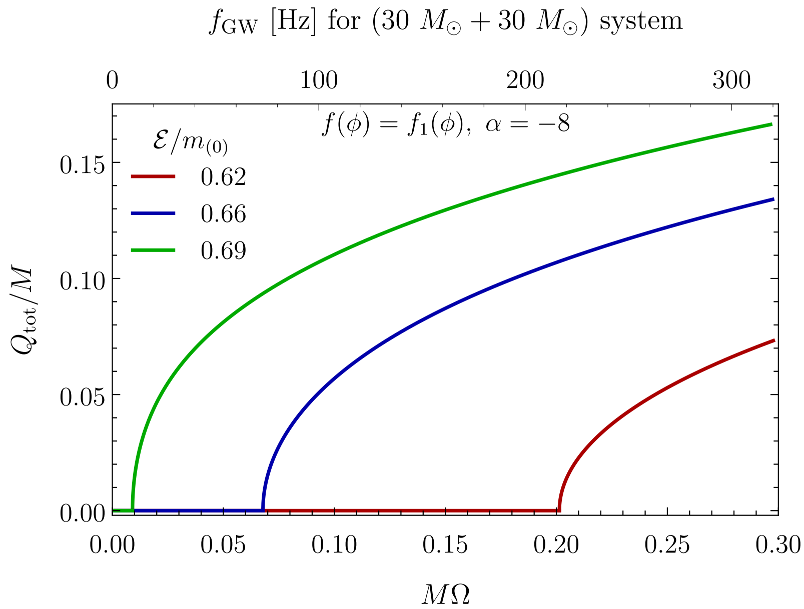

Figure 9.4: Scalar charge $Q_{\rm tot}$ of an equal mass binary as a function of orbital frequency Ω or GW frequency $f_{\rm GW} = \Omega/\pi$ for coupling $f_1(\phi)$ [Eq. (9.2)] with $\alpha = -8$.

which contain a phase transition at $r = 1/c_{(2)}$ corresponding to the spontaneous breaking of the $q \to -q$ symmetry of the effective action. Recall that $c_{(2)} < 0$ corresponds to the case where each object is spontaneously scalarized, for which the bottom condition in Eq. (9.26) always holds, and thus $q \neq 0$ over all separations.

Restricting our attention to circular orbits, we plot in Fig. 9.4 the total scalar charge of the binary $Q_{\rm tot} \equiv q_A + q_B$ as a function of orbital frequency, given by Kepler's law as

$$\Omega^2 = \frac{1}{r^3}(m_A + m_B)\left(1 + \frac{q_A q_B}{m_A m_B} - \frac{\mathcal{E}_A \mathcal{E}_B}{m_A m_B}\right). \tag{9.27}$$

For simplicity, we only show the positive scalar charge branch of solutions. The frequency is shown both as the dimensionless combination $M\Omega$ with $M \equiv m_A^{(0)} + m_B^{(0)}$ and as the equivalent GW frequency $f_{\rm GW} = \Omega/\pi$ for a $(30M_\odot + 30M_\odot)$ binary system. The plotted curves correspond to solutions with coupling constant $\alpha = -8$, and the colors correspond to different values of the electric charge. The scalar charge vanishes below the onset of dynamical scalarization; the scalar charge grows abruptly at some critical frequency Ω_{scal} (as evidenced by kinks in the plotted curves) because dynamical scalarization is a second-order phase transition—see Ref. [513] for a more detailed argument that dynamical scalarization is a phase transition.

In Fig. 9.5, we depict the scalarization of binary systems for various charge-to-mass ratios and couplings α. The solid lines indicate the critical frequency Ω_{scal} at which dynamical scalarization begins; the heavily shaded regions above these lines correspond to dynamically scalarized binaries after the onset of this transition. The critical point $c_{(2)} = 0$, corresponding to $\Omega_{\text{scal}} \to 0$, represents the division between binaries that dynamically scalarize and those whose component BHs (individually) spontaneously scalarize; we depict all spontaneously scalarized configurations with a lighter shading. Thus, we see that our effective action, which was matched to isolated objects and models spontaneous scalarization, predicts dynamical scalarization as well. Refined predictions can be obtained by perturbatively calculating the binary Lagrangian to higher PN orders and also the emitted radiation; both are possible using effective-field-theory techniques [737–739] or more traditional methods where extended bodies are represented by point particles, e.g., Refs. [130, 206].

The same calculation can be repeated for binary systems with the choice $f(\phi) = f_2(\phi)$. As before, the unscalarized $q = 0$ solution is stable for above $r = 1/c_{(2)}$. However, because $c_{(4)} < 0$, no stable dynamically scalarized branch exists below that separation; instead, the system becomes "dynamically" unstable after this critical point. The phase diagram for this choice of coupling takes the same form as Fig. 9.5, but here the shaded regions correspond to scenarios in which no stable configuration exists. At the onset of instability, the scalar radiation will likely grow rapidly

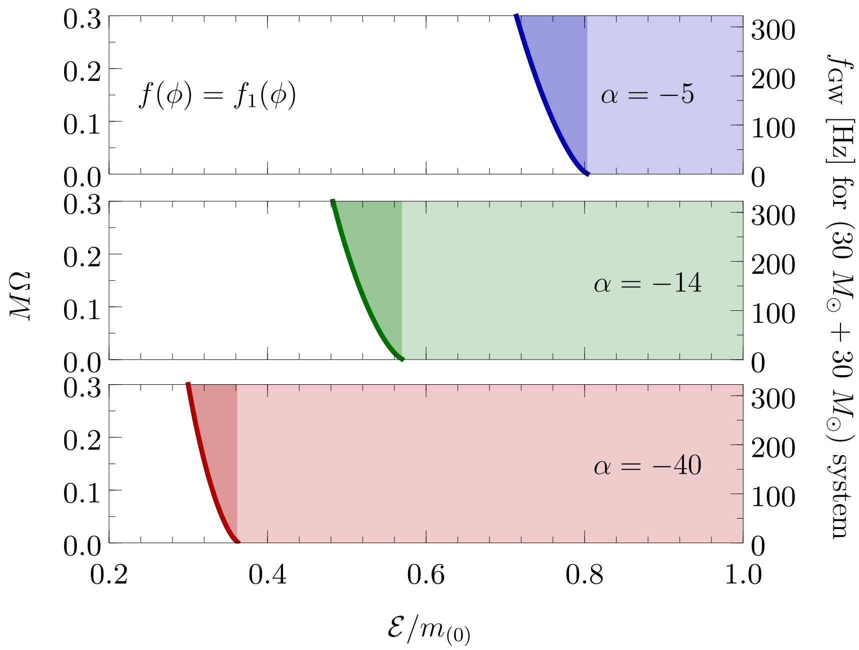

Figure 9.5: Scalarization of binary systems with various electric charges for scalar coupling $f_1(\phi)$ [Eq. (9.2)] with different coupling strengths α. Lightly and heavily shaded regions indicate spontaneously and dynamically scalarized configurations, respectively. The solid lines depict the onset of dynamical scalarization $\Omega_{\rm scal}$ as a function of electric charge.

and the GW frequency will decrease more rapidly compared to the EM case. However, long-term predictions are not possible with our effective theory since the assumption of time-reversal symmetry likely breaks down, as for the unstable isolated BHs.

9.5 Conclusions

In this paper, we developed a simple energetic analysis of spontaneous and dynamical scalarization, based on a strong-field-agnostic effective-field-theory approach (extendable beyond the scalar-field case [491, 493, 494] in the future). We demonstrated our analysis for BHs with modified electrodynamics here, complementing the study of NS in ST gravity from Ref. [513]. The theory-agnostic nature of our approach allowed us to draw general conclusions about scalarization As an example, we found that dynamical scalarization generically occurs in theories that admit spontaneous scalarization. Specific examples of theories for which our findings apply include those discussed in Refs. [487, 491, 493–495, 497–501, 709, 710].

The recent discovery of spontaneous scalarization in ESTGB theories [497–501] has sparked significant interest in this topic. Our work predicts that dynamical scalarization can occur in binary systems in these theories and allows one to straightforwardly estimate the orbital frequency at which it occurs using only information derivable from isolated BH solutions. Such information is valuable for guiding numerical-relativity simulations in these theories, for which there has been recent progress [740]. Eventually higher PN orders in specific theories could be added to our model to derive more accurate predictions, and the framework could be extended to massive scalars or other types of new fields.

We demonstrated how scalarization, as an exemplary strong-gravity modification of GR, is parametrized by just a few constants in the effective action (which vanish in GR). Hence, our effective action provides an ideal foundation for a strong-field-agnostic framework for testing dynamical scalarization. Ultimately, one needs to incorporate self-consistently such effects into gravitational waveform models. This undertaking will require the computation of dissipative effects (analogous to the standard PN treatment in GR) and the mode dynamics during scalarization, characterized (in part) by $c_{\dot{q}^2}$. The effective action can also, in principle, be extended to include other strong-field effects influencing the inspiral of a binary, e.g., phenomena like floating orbits [741, 742] or induced hair growth [743, 744].

Independent of GW tests of GR, further study of dynamical scalarization could offer some insight into the nonlinear behavior of merging binary NSs in GR. As discussed in the Introduction, scalarization and tidal interactions enter models of the inspiral dynamics in a similar manner; in fact, the effective action treatment of dynamical tides (in GR) [587] is completely analogous to the approach adopted here for scalarization. Unlike the case with tides, our model of scalarization includes nonlinear interactions via the q^4 term. Nonlinear tidal effects could be relevant for GW observations of binary NSs [745, 746], but are difficult to handle in GR. Furthermore, mode instabilities also occur for NSs in GR [747, 748]. Dynamical scalarization can be used as a toy model for these types of effects, and further exploration of this non-GR phenomenon could improve gravitational waveform modeling in GR.

Our effective action approach allowed us to study the critical phenomena at the onset of scalarization; further study could also provide insight into critical phenomena in GR. The critical exponents we obtained numerically agree with the analytic predictions from Landau's mean-field treatment of ferromagnetism [729**?**]. Only missing here is a proper definition of correlation length, which we leave for future work. In GR, the BH limit of compact objects has been suggested to play the role of a critical point and lead to the quasiuniversal relations for NS properties [749, 750]. These quasiuniversal relations are invaluable for GW science because they reduce the number of independent parameters needed to describe binary NSs, improving the statistical uncertainty of measurements. In the BH limit (for nonrotating configurations), the leading tidal parameter vanishes [751–753], like $c_{(2)}$ at the critical point here. Better theoretical understanding of the origin of these universal relations could help improve their accuracy; utilizing information from the critical phenomena at the BH limit is a compelling idea, and scalarization could serve as a toy model in that regard.

Acknowledgments

We thank Emanuele Berti, Caio Macedo, Néstor Ortiz, and Fethi Ramazanoğlu for useful discussions.

Chapter 10: Effective-action model for dynamical scalarization beyond the adiabatic approximation

Authors[1]: *Mohammed Khalil, Raissa F. P. Mendes, Néstor Ortiz, Jan Steinhoff*

Abstract: In certain scalar-field extensions to general relativity, scalar charges can develop on compact objects in an inspiraling binary—an effect known as dynamical scalarization. This effect can be modeled using effective-field-theory methods applied to the binary within the post-Newtonian approximation. Past analytic investigations focused on the adiabatic (or quasi-stationary) case for quasi-circular orbits. In this work, we explore the full dynamical evolution around the phase transition to the scalarized regime. This allows for generic (eccentric) orbits and to quantify nonadiabatic (e.g., oscillatory) behavior during the phase transition. We also find that even in the circular-orbit case, the onset of scalarization can only be predicted reliably when taking the full dynamics into account, i.e., the adiabatic approximation is not appropriate. Our results pave the way for accurate post-Newtonian predictions for dynamical scalarization effects in gravitational waves from compact binaries.

[1]Originally published as arXiv:2206.13233 [gr-qc]

10.1 Introduction

Compact astrophysical objects such as black holes and neutron stars offer special environments for tests of general relativity. Not only do perturbative corrections to Newtonian gravity become more pronounced, but gravity might also hold surprises in the strong-field regime, due to the possible onset of nonperturbative effects. A paradigmatic example is the so-called spontaneous scalarization of neutron stars. In the 90's, Damour and Esposito-Farèse (DEF) showed that in a broad class of scalar extensions of general relativity, the scalar field may remain dormant in the weak-field regime, only to be activated around sufficiently compact material bodies such as neutron stars [482]. Although most of the parameter space for spontaneous scalarization in the original DEF model has now been ruled out by pulsar-timing observations [202, 716, 754–756], similar-type effects have been found in other contexts, including massive scalar fields [486–489], more general scalar-tensor theories [490], charged black holes [514, 713, 757], higher-spin fields [491–495, 758], as well as neutron stars [496] and black holes in scalar-tensor-Gauss-Bonnet gravity, in which scalarization can be either curvature-induced [497–503, 714, 759–761] or spin-induced [504–508, 762].

In the original setup of the DEF theory, scalarization was found to be potentialized in a dynamical setting. In Ref. [509], it was shown that two neutron stars which were not compact enough to scalarize in isolation could scalarize dynamically in a close binary system. A similar phenomenon, though different mechanisms are involved, has been observed in scalar-Gauss-Bonnet theories of gravity [510–512]. In the case of DEF theory, dynamical scalarization (DS) was demonstrated in fully nonlinear numerical evolutions, but it appears already in numerically constructed quasi-equilibrium solutions [484, 485], and can be understood as a result of a feedback mechanism between the two neutron stars [483], or more thoroughly, in the context of a resumed post-Newtonian expansion [681].

A particularly elegant way to model DS is by an effective field theory for compact binaries [737, 738, 763] that systematically takes into account the various scales in the problem, including nonperturbative effects in the strong-field regime close to the compact objects. Compact bodies are modeled by point-particles moving along a worldline in the effective theory. Their internal dynamics, in particular from oscillation modes, is encoded in dynamical variables evolved along the worldlines. This allows for the incorporation of scalar oscillation modes; scalarization arises when such modes become linearly unstable [8, 513]. DS is in fact modeled similarly to dynamical tides [191, 587, 764], where fluid oscillation modes are incorporated into the effective theory. See also Refs. [765, 766] for further similarities between tidal effects and finite-size corrections in scalar-tensor theories.

While the effective action approach to DS was first formulated specifically for DEF theory [513], it can be straightforwardly generalized to other gravity theories containing scalar fields. The main ingredient is a monopolar scalar mode close to the critical point of instability, which is included in the effective worldline action [8]. At leading order, the effective action contains only three parameters for each star. These parameters must be matched to a specific gravity theory and compact object, but the form of the effective theory and hence its phenomenology is theory-independent. Past work on this effective-action approach focused on an adiabatic (or quasi-stationary) analysis of the binary on quasi-circular orbits and its energetics, requiring only two of the three parameters of the action [8], finding good qualitative and quantitative agreement with numerical relativity [513]. In the present work, we study the full dynamical evolution of the binary and its scalar charges on generic (eccentric) orbits, where all three parameters become relevant. This is an important step towards improving gravitational waveform models for dynamical-scalarization effects [692, 719].

This work is organized as follows. In Sec. 10.2, we recapitulate the effective action for DS. Section 10.3 develops the leading-order equations of motion for the binary and the scalar modes of the bodies, in particular the radiation-reaction (damping) forces. The matching of all parameters of the effective action to neutron stars is performed in Sec. 10.4, using the DEF class of scalar-tensor gravity as an example. This allows for the investigation of the binary dynamics around the critical point of scalarization in Sec. 10.5. Our conclusions are given in Sec. 8.5, followed by a couple of appendices providing detailed calculations on oscillation equations, as well as fluxes and radiation-reaction forces. We use units such that $c = G = 1$ throughout the text.

10.2 Effective action model

In this section, we briefly review the effective action model for DS of compact objects introduced in Refs. [8, 513]. We emphasize the fact that the following formalism is theory-independent [8]. Let us first recapitulate the widely used "instantaneous" effective action for a neutron star in scalar-tensor gravity given by a point-particle moving along a worldline $y^\mu(\tau)$, which in the Einstein frame reads

$$S_{\text{NS}}^{\text{inst}} = -\int d\tau \, m_E(\varphi), \tag{10.1}$$

where m_E is the Einstein-frame mass depending on the external scalar field $\varphi(y^\mu)$. This action is valid for an instantaneous response of the neutron star to the external scalar field φ, i.e., when internal relaxation timescales are much shorter than external timescales at which φ varies. Small corrections to this approximation can be incorporated through terms involving $\dot{\varphi}$. However, when internal timescales exceed external ones, as for DS, additional dynamical variables representing the internal dynamics need to be evolved along the worldline.

Hence, we include in the effective action a dynamical variable $q(\tau)$ representing the monopolar scalar oscillation mode that becomes linearly unstable at scalarization. That is, the fundamental scalar mode has a frequency that vanishes (its period timescale diverges) at the critical point associated with the transition to a scalarized state. For simplicity, we do not include further dynamical modes such as scalar-mode overtones or fluid oscillation modes in the effective theory (see, e.g., Refs. [587, 764] for the latter), and neglect rotation of the star, but otherwise the model is rather generic or theory-independent. Let us now consider a binary neutron star system. Around the critical point, the action describing the dynamics of q can then be written as [8]

$$S_{\text{NS}}^{\text{crit}} = \int d\tau \left[\frac{c_{\dot{q}^2}}{2} \dot{q}^2 + \varphi(y) q - m(q) + O\left(\frac{R^2}{r^2}\right) \right], \tag{10.2}$$

where $\dot{} = d/d\tau$ and the effective action is expanded in powers of the neutron-star size R over the orbital separation r of the binary. Likewise, $m(q)$ can be expanded as

$$m(q) = c_{(0)} - \varphi_0 q + \underbrace{\frac{c_{(2)}}{2!} q^2 + \frac{c_{(4)}}{4!} q^4 + O\left(\frac{R^2}{r^2}\right)}_{V(q)}, \tag{10.3}$$

where we include a possible cosmological value of the scalar field φ_0 (while φ represents the field at the worldline which emanates from the binary companion); the function $m(q)$ is even in q if $\varphi_0 = 0$. Note that $q^3 = O(R/r)$ close to the critical point where $c_{(2)}$ becomes small. The coefficient $c_{(0)}$ has the interpretation of the body's ADM mass when $q = 0$ (i.e., in general relativity). The Euler-Lagrange equation yields (suppressing the power-counting in R/r from now on)

$$c_{\dot{q}^2}\ddot{q} + V'(q) = \varphi(y) + \varphi_0. \tag{10.4}$$

A stationary-state solution ($\dot{q} \approx 0$) for q can be employed if the external scalar field is not varying too rapidly. In this case it holds $m(q) = m_E(\varphi) + \varphi q$, which can be understood as a Legendre transformation (note that $q = -dm_E/d\varphi$).

By computing the Hamiltonian at leading, Newtonian order, one obtains [8, 513]

$$H = m_A + m_B + \frac{p_{q,A}^2}{2c_{\dot{q}^2,A}} + \frac{p_{q,B}^2}{2c_{\dot{q}^2,B}} + \frac{\boldsymbol{p}_A^2}{2m_A} + \frac{\boldsymbol{p}_B^2}{2m_B} - \frac{m_A m_B}{r} - \frac{q_A q_B}{r}, \tag{10.5}$$

where A, B label the two bodies in the binary, $\boldsymbol{p}_{A/B}$ are their linear momenta, r is the interbody distance, and $p_{q,A/B}$ are the canonical conjugates to the variables $q_{A/B}$. Restricting to the (quasi-)stationary case $p_{q,A/B} \approx 0$, the equation of motion for q_A reads

$$0 = \frac{\partial H}{\partial q_A} = z_A \left(-\varphi_0 + c_{(2),A} q_A + \frac{c_{(4),A}}{6} q_A^3 \right) - \frac{q_B}{r}, \tag{10.6}$$

where $z_A \equiv \partial H/\partial m_A = 1 - \boldsymbol{p}_A^2/(2m_A) - m_B/r$ is the redshift of body A. Assuming, for simplicity, that $\varphi_0 = 0$, that the two bodies are identical ($q \equiv q_A = q_B$), and that we can neglect post-Newtonian corrections to the redshift ($z_A \approx 1$), one obtains

$$0 = \frac{\partial H}{\partial q} = -2q \left(\frac{1}{r} - c_{(2)} - \frac{c_{(4)}}{6} q^2 \right). \tag{10.7}$$

There are three solutions for the equation above, the trivial one, with $q = 0$, and

$$q = \pm \sqrt{\frac{6}{c_{(4)}} \left(\frac{1}{r} - c_{(2)} \right)}. \tag{10.8}$$

The stability condition, $\partial^2 H/\partial q^2 \geq 0$, is violated for the trivial solution if $1/r > c_{(2)}$. This is fulfilled for all r if $c_{(2)} < 0$, which corresponds to the case of spontaneous scalarization. DS is captured in this setup by the fact that even when $c_{(2)} > 0$ the trivial solution can become unstable for sufficiently small binary separations. In the present work, we go beyond the quasi-stationary case and investigate the dynamical evolution of q around the moment of DS.

Let us elaborate on the matching of the coefficients $c_{\dot{q}^2}$, $c_{(n)}$ of the effective theory to the properties of the compact object obtained by solving the inner problem. If one restricts to equilibrium configurations, with $\dot{q} = 0$, the procedure described in Ref. [8] reduces operationally to the one presented for scalar-tensor theories in Ref. [513]. In particular, one can obtain the coefficients $c_{(2)}$ and $c_{(4)}$ through the following steps:

(i) Solve (numerically) the relevant structure equations for an isolated object in the full theory, computing a sequence of solutions at a fixed baryon mass M_b and for different values of the asymptotic scalar field φ_∞, then extract the Einstein-frame ADM mass $m_E(\varphi_\infty)$ and scalar charge $q(\varphi_\infty)$. Note that for each value of φ_∞ more than one equilibrium solution may exist.

(ii) Compute $m(q)$ through

$$m(q) = m_E(\varphi_\infty) + \varphi_\infty q(\varphi_\infty), \tag{10.9}$$

for each each value of φ_∞ and each possible equilibrium solution.

(iii) Fit the polynomial in Eq. (10.3) (with $\varphi_0 = 0$) to the numerical values of $m(q)$, and extract the quadratic $c_{(2)}$ and quartic $c_{(4)}$ coefficients, which encode the existence of spontaneous and dynamical scalarization, as described above.

We can additionally match the coefficient $c_{\dot{q}^2}$ by making the connection to the oscillation frequency of the fundamental scalar mode. For this purpose, we specialize Eq. (10.4) to the force-free case $\varphi + \varphi_0 = 0$ and to small oscillations of frequency ω_0 around the nonscalarized equilibrium $q = 0$,

$$\ddot{q} = -\frac{c_{(2)}}{c_{\dot{q}^2}} q = -\omega_0^2 q. \tag{10.10}$$

However, this picture is not complete, since q also sources monopolar scalar radiation and should include a radiation-reaction force (a damping term involving $\dot{q}$) in the oscillator equation, which is derived in Appendix Q. Now, the parameters in our damped harmonic oscillator q can be matched to the (complex) quasi-normal mode frequency ω_φ obtained from neutron-star perturbation theory, resulting in $\omega_0^2 = |\omega_\varphi|^2 = \Re[\omega_\varphi]^2 + \Im[\omega_\varphi]^2$, which was worked out in detail within a different context in Ref. [767]. We can hence express the remaining coefficient as

$$c_{\dot{q}^2} = \frac{c_{(2)}}{|\omega_\varphi|^2}. \tag{10.11}$$

A different match for $c_{\dot{q}^2}$ can be obtained by comparing damping times from radiation reaction (Appendix Q) and the quasi-normal mode frequency. While this alternative matching is only approximate (with our radiation-reaction force based on a weak-field expansion), we find similar results for $c_{\dot{q}^2}$, at least for the specific model explored in Secs. 10.4 and 10.5.

Finally, one can also expand Eq. (10.4) around a spontaneously scalarized solution q_0 such that $V'(q_0) = 0$, or $q_0 = \pm\sqrt{-6c_{(2)}/c_{(4)}}$. Plugging $q = q_0 + \bar{q}$ in Eq. (10.4) and $\varphi + \varphi_0 = 0$, and expanding to linear order in $\bar{q}$, yields

$$c_{\dot{q}^2}\ddot{\bar{q}} \simeq -\left(c_{(2)} + \frac{c_{(4)}}{2} q_0^2\right)\bar{q}, \tag{10.12}$$

from which we obtain the matching

$$\begin{aligned} c_{\dot{q}^2} &= \frac{1}{|\omega_\varphi|^2}\left(c_{(2)} + \frac{c_{(4)}}{2} q_0^2\right) \\ &= -\frac{2c_{(2)}}{|\omega_\varphi|^2} \qquad \text{(around scalarized solution } q_0\text{)}. \end{aligned} \tag{10.13}$$

10.3 Binary dynamics

In this section, we obtain the set of equations governing the dynamics of a compact binary under the effective action model described in the previous section. Notice that this formalism is still theory-independent.

In the center-of-mass frame, and using polar coordinates, the Hamiltonian for a binary at leading order, Eq. (10.5), can be written as

$$H = m_A + m_B + \frac{\boldsymbol{p}^2}{2\mu} + \frac{p_{q,A}^2}{2c_{\dot{q}^2,A}} + \frac{p_{q,B}^2}{2c_{\dot{q}^2,B}} - \frac{M\mu}{r} - \frac{q_A q_B}{r}, \tag{10.14}$$

where the center-of-mass momentum $\boldsymbol{p} = \boldsymbol{p}_A = -\boldsymbol{p}_B$, $\boldsymbol{p}^2 = p_r^2 + L^2/r^2$, where L is the orbital angular momentum of the system, and the total and reduced masses are defined by

$$M = m_A^0 + m_B^0, \qquad \mu = \frac{m_A^0 m_B^0}{M}, \tag{10.15}$$

i.e., in terms of the constant masses $m^0_{A/B} = c_{(0),A/B}$ to keep the equations of motion at leading order. These equations are given by

$$\begin{aligned}
\dot{r} &= \frac{\partial H}{\partial p_r}, & \dot{p}_r &= -\frac{\partial H}{\partial r} + \mathcal{F}_r^{\text{quad}} + \mathcal{F}_r^{\text{dip}}, \\
\dot{\phi} &= \frac{\partial H}{\partial L}, & \dot{L} &= -\frac{\partial H}{\partial \phi} + \mathcal{F}_\varphi^{\text{quad}} + \mathcal{F}_\varphi^{\text{dip}}, \\
\dot{q}_A &= \frac{\partial H}{\partial p_{q,A}}, & \dot{p}_{q,A} &= -\frac{\partial H}{\partial q_A} + \mathcal{F}_{q_A}^{\text{mon}}, \\
\dot{q}_B &= \frac{\partial H}{\partial p_{q,B}}, & \dot{p}_{q,B} &= -\frac{\partial H}{\partial q_B} + \mathcal{F}_{q_B}^{\text{mon}},
\end{aligned} \tag{10.16}$$

where we add the leading-order tensor quadrupole, scalar dipole, and scalar monopole radiation-reaction forces; the dipole force is expected to dominate in the scalarized phase for binaries with unequal masses and charges, while the quadrupole dominates in the unscalarized phase.

For the tensor quadrupole radiation-reaction force, we use the leading-order expressions given by Eqs. (3.67) and (3.68) in Ref. [402], which read

$$\mathcal{F}_r^{\text{quad}} = \frac{8}{15}\frac{M\mu^2}{r^3}\dot{r}\left(21r^2\dot{\phi}^2 - \frac{M}{r}\right),$$
$$\mathcal{F}_\varphi^{\text{quad}} = -\frac{8}{15}\frac{M\mu^2}{r}\dot{\phi}\left(-\dot{r}^2 + 2r^2\dot{\phi}^2 + 2\frac{M}{r}\right). \tag{10.17}$$

The monopole and dipole radiation-reaction forces are derived in Appendix R, and are given by

$$\mathcal{F}_{q_A}^{\text{mon}} = \mathcal{F}_{q_B}^{\text{mon}} = -\dot{q}_A(t) - \dot{q}_B(t), \tag{10.18}$$
$$\mathcal{F}_r^{\text{dip}} = \frac{2}{3}\frac{M}{\mu r^3}p_r\left(\frac{m_B^0}{M}q_A - \frac{m_A^0}{M}q_B\right)^2\left(1 + \frac{q_A q_B}{M\mu}\right),$$
$$\mathcal{F}_\varphi^{\text{dip}} = -\frac{1}{3}\frac{ML}{\mu r^3}\left(\frac{m_B^0}{M}q_A - \frac{m_A^0}{M}q_B\right)^2\left(1 + \frac{q_A q_B}{M\mu}\right). \tag{10.19}$$

Note that the monopole radiation-reaction force enters the equations of motion for the scalar charges, but not the orbital equations, since the monopole energy flux depends only on $\dot{q}$ but not on the orbital variables.

In order to set initial conditions, the following relations are useful:

$$r = \frac{k}{1 + e\cos\phi}, \qquad k = a(1-e^2) = \frac{L^2}{\mu^2 M}, \tag{10.20}$$

where k is the semilatus rectum, a the semi-major axis, and e the eccentricity of the orbit. The periastron distance is then $r_p = k/(1+e)$ and the apastron distance is $r_a = k/(1-e)$, with the eccentricity $e = (r_a - r_p)/(r_a + r_p)$. If we start the orbit at apastron and assume that the binary starts unscalarized, then the initial conditions read

$$\phi = \pi, \qquad r = r_a, \qquad L = \mu\sqrt{r_a M(1-e)}\,. \tag{10.21}$$

In the absence of radiation reaction, $p_r = 0$ at apastron. However, for slowly varying L due to radiation, and for circular orbits, the initial condition for p_r reads

$$p_r = \mu\dot{r} = \frac{2L}{\mu M}\dot{L} = \frac{2L}{\mu M}\mathcal{F}_{\varphi}^{\text{quad}} = -\frac{64}{15}\frac{\mu^2 M^2}{r^3}. \tag{10.22}$$

This also provides a good approximation for eccentric orbits at apastron.

For the scalar charge, in the presence of a (small) cosmological scalar field φ_0, and assuming stationarity, $\dot{q} = 0$, one gets from Eq. (10.4) that

$$\begin{aligned} c_{(2),A} q_A + O(q_A^3) &= \varphi_0 + \frac{q_B}{r}, \\ c_{(2),B} q_B + O(q_B^3) &= \varphi_0 + \frac{q_A}{r}, \end{aligned} \tag{10.23}$$

leading to

$$q_A = \frac{\varphi_0}{c_{(2),A}} \frac{1 + \frac{1}{c_{(2),B} r}}{1 - \frac{1}{c_{(2),A} c_{(2),B} r^2}} \approx \frac{\varphi_0}{c_{(2),A}}, \tag{10.24}$$

and similarly for q_B. Notice that the last approximation only holds away from the scalarization point, since $c_{(2),B} r \sim 1$ close to scalarization.

Given that we start the evolution in the unscalarized regime, the initial value of p_q is zero. However, if we set the cosmological scalar field $\varphi_0 = 0$, one needs to take p_q as a small but nonzero number to perturb the system away from the unstable solution, $q = 0$, and allow the transition to the DS regime.

10.4 A particular scalar-tensor model

In this section, we illustrate how to compute the effective action coefficients $c_{(2)}$, $c_{(4)}$, and $c_{\dot{q}^2}$ for the case of a massless scalar-tensor theory defined by the (Einstein-frame) action

$$S = \frac{1}{16\pi} \int d^4x \sqrt{-g}\, (\mathcal{R} - 2\nabla_\mu\varphi\nabla^\mu\varphi) + S_{\text{m}}[\Psi_{\text{m}}; a(\varphi)^2 g_{\mu\nu}], \tag{10.25}$$

where $g \equiv \det(g_{\mu\nu})$ and $\mathcal{R}$ is the Ricci scalar. The function $a(\varphi)$ —which defines the Jordan-frame metric $\tilde{g}_{\mu\nu} \equiv a(\varphi)^2 g_{\mu\nu}$ to which matter fields $\Psi_{\rm m}$ couple universally— is fixed to

$$a(\varphi) = \exp(\beta\varphi^2/2). \tag{10.26}$$

This model, introduced by Damour and Esposito-Farèse [482], is arguably the simplest one displaying spontaneous scalarization, and most works on the subject revolve around it. Although most (or all) of the range $\beta \lesssim -4.5$ allowing for spontaneous scalarization in this model [768–771] has now been ruled out by pulsar timing observations [202, 716, 754–756], it is still a good prototype for our discussion. We have analyzed both the cases where $\beta = -5$ and -6, and found very similar behaviors. In what follows, results for $\beta = -5$ will be displayed. Additionally, the stellar fluid will be described by a two-piece polytrope with adiabatic index $\Gamma_1 = 3$ in the core, and $\Gamma_1 = 1.3$ in the crust, with the transition happening at 1.66×10^{13}g/cm^3; this is the same equation of state adopted for the computation of radial mode frequencies in Ref. [516], which will be used in what follows.

10.4.1 Potential coefficients: $c_{(2)}$ and $c_{(4)}$

In order to feed the effective action model with the potential parameters $c_{(2)}$ and $c_{(4)}$, one must consider the "inner" problem of an isolated neutron star with some fixed baryon mass M_b, subject to an external (varying) scalar field —as per item (i) in Sec. 10.2. The structure equations in this case are given, e.g., by Eqs. (31)$-$(34) of Ref. [712]. Next, following item (ii), one computes $m(q)$ in Eq. (10.9) from the ADM mass $m_E(\varphi_\infty)$ and scalar charge $q(\varphi_\infty)$ —in Ref. [712] these are denoted by M and ω, and are given in Eqs. (37) and (38), respectively. For baryon masses close to the critical value for the onset of spontaneous scalarization

($M_{b,cr} = 1.3474 M_\odot$ for the scalar-tensor model and equation of state described above), the potential $V(q) = m(q) - c_{(0)}$ [with $c_{(0)} = m(0)$] is well approximated by the truncated expansion

$$V(q) = \frac{c_{(2)}}{2} q^2 + \frac{c_{(4)}}{4!} q^4. \tag{10.27}$$

The final step (iii) consists in extracting the coefficients $c_{(2)}$ and $c_{(4)}$ of the best fit to the numerical data.

Figure 10.1 illustrates the potential $V(q)$ for some baryon masses around $M_{b,cr}$. Before the critical point, $c_{(2)} > 0$, the potential has a single minimum at $q = 0$. After the critical point, $c_{(2)} < 0$, the potential has a local maximum at $q = 0$ (corresponding to a GR-like unstable equilibrium solution) and two local minima $q \neq 0$ with opposite signs (corresponding to stable scalarized solutions). The local extrema of $V(q)$ correspond to $\varphi_\infty = 0$, since from Eq. (10.9), $V'(q) = \varphi_\infty$.

In Fig. 10.1, the numerically computed points are fitted by a polynomial expression of the form (10.27), with the coefficients $c_{(2)}$ and $c_{(4)}$ represented in Fig. 10.2. Their dependence on the baryon mass is well captured by the following polynomial fits:

$$M_\odot c_{(2)} \approx (x - x_{cr}) \left(-0.3796 + 0.3294x - 0.09174x^2\right), \tag{10.28}$$

$$M_\odot^3 c_{(4)} \approx 4.270 - 7.804x + 5.545x^2 - 1.337x^3, \tag{10.29}$$

where $x \equiv M_b / M_\odot$ and we set $x_{cr} = 1.3474$.

10.4.2 Scalar modes and the coefficient $c_{\dot{q}^2}$

The coefficient $c_{\dot{q}^2}$ determines the strength of the kinetic term in Eq. (10.2); in order to feed the model with this parameter, one can consider the dynamics of scalar field perturbations around

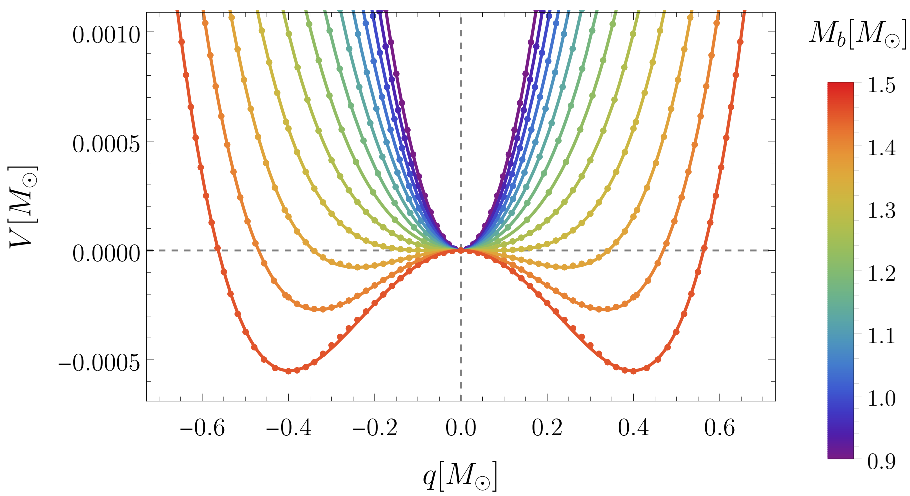

Figure 10.1: $V(q)$ for fixed baryon masses (ranging from 0.9 to $1.5M_\odot$). Points represent the numerically computed values, which are fitted by polynomial expressions of the form (10.27). Fit coefficients are represented in Fig. 10.2.

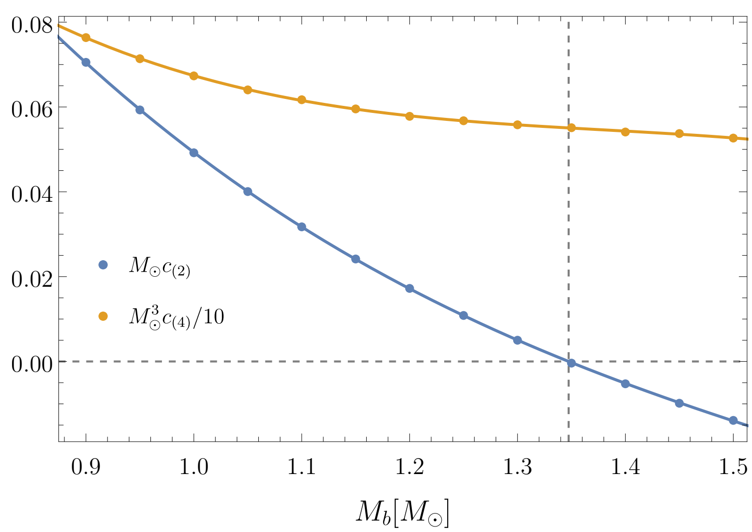

Figure 10.2: Coefficients $c_{(2)}$ and $c_{(4)}$ for some baryon masses around the critical point (represented by the dashed vertical line). Points represent the numerically computed values, which are fitted by expressions (10.28) and (10.29).

a neutron star in equilibrium. As per Eqs. (10.11) and (10.13), $c_{\dot{q}^2}$ depends on the potential coefficients $c_{(2)}$ and $c_{(4)}$, and on the frequency ω_0, which encodes the dynamical timescale of scalar field oscillations. In this work, we adopt the following prescription: $\omega_0^2 \equiv \Re[\omega_\varphi]^2 + \Im[\omega_\varphi]^2$, where ω_φ is the fundamental scalar-led radial mode (or φ-mode) frequency.

The φ-mode frequency was computed in Ref. [516] for stars subject to a vanishing asymptotic scalar field ($\varphi_\infty = 0$), and the result is reproduced in Fig. 10.3 for the range of baryon masses considered previously ($0.9M_\odot \leq M_b \leq 1.5M_\odot$). For $M_b < M_{b,cr}$, i.e. before the onset of spontaneous scalarization, the (radial) perturbation equations for the scalar field and the fluid decouple, and the φ-modes are purely scalar perturbations. For $M_b > M_{b,cr}$, three equilibrium solutions exist. The trivial one, with $q = 0$, is unstable under scalar field perturbations. Correspondingly, its φ-mode has $\Im(\omega) < 0$ and $\Re(\omega) = 0$ (not shown in the plot). The two nontrivial solutions are scalarized, with opposite scalar charges and identical oscillation frequencies (shown in Fig. 10.3). These correspond to coupled scalar and fluid oscillations [516, 772].

Around the critical point, we obtain the following polynomial interpolations for $\Re(\omega_\varphi)$ and $\Im(\omega_\varphi)$ as a function of $x = M_b/M_\odot$:

$$\Re(\omega_\varphi)(x) \approx \begin{cases} (x - x_{cr})^2 \left(0.4465 - 0.9698x + 0.6670x^2\right), & x \leq x_{cr} \\ (x - x_{cr})^2 \left(18.753 - 20.205x + 5.374x^2\right), & x \geq x_{cr} \end{cases} \tag{10.30}$$

and

$$\Im(\omega_\varphi)(x) \approx \begin{cases} (x - x_{cr}) \left(-0.20769 + 0.21629x - 0.11647x^2\right), & x \leq x_{cr} \\ (x - x_{cr}) \left(1.5439 - 1.2407x + 0.20706x^2\right), & x \geq x_{cr} \end{cases} \tag{10.31}$$

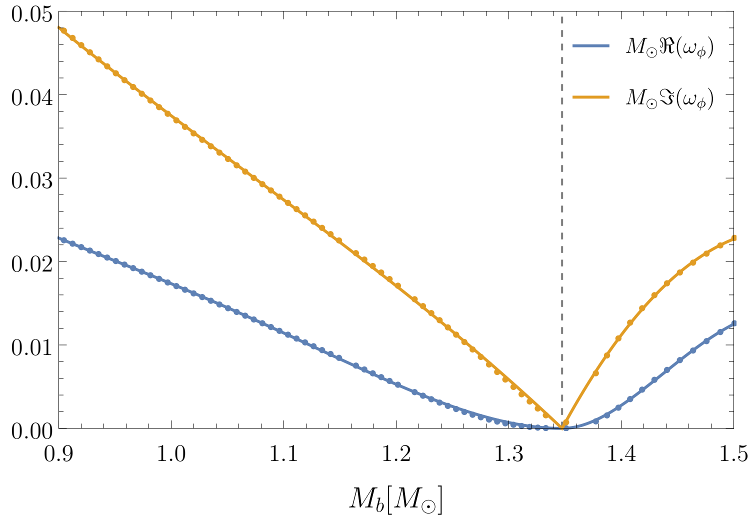

Figure 10.3: Real and imaginary parts of the fundamental scalar-led radial mode frequency (scaled by $M_{\odot}$). Points represent the numerically computed values, and lines represent the polynomial fits (10.30) and (10.31). The dashed vertical line corresponds to the critical point, $M_{b,cr}$.

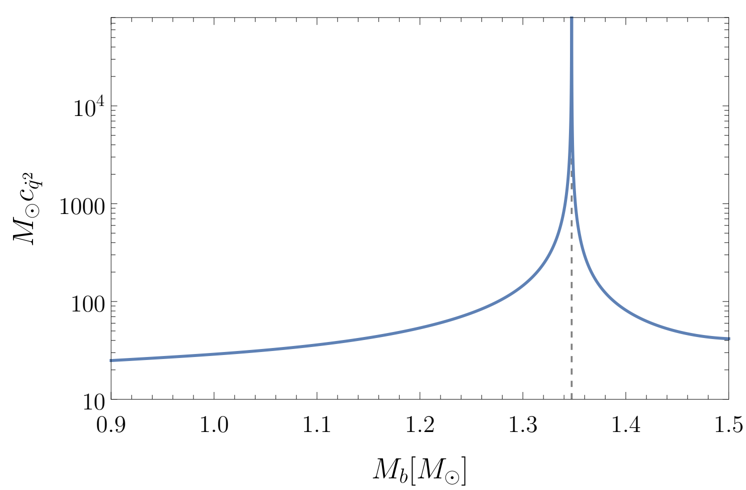

Figure 10.4: Coefficient $c_{\dot{q}^2}$ as a function of baryon mass around the critical point (displayed as a dashed vertical line).

From Eq. (10.11), $c_{\dot{q}^2} = c_{(2)}/|\omega_\varphi|^2$ before the critical point, and from Eq. (10.13), $c_{\dot{q}^2} = -2c_{(2)}/|\omega_\varphi|^2$ after it. [2] Figure 10.4 shows the coefficient $c_{\dot{q}^2}$ as a function of baryon mass, where the polynomial interpolations in Eqs. (10.28), (10.30), and (10.31) were used. From these expressions and our prescription for $c_{\dot{q}^2}$, it is apparent that the coefficient diverges at the critical point. Consequences of this divergence are discussed in Sec. 10.5.2.

10.5 Results for the binary dynamics

In this section, we show results for the binary dynamics in the context of scalar-tensor gravity of the DEF class with $\beta = -5$. We start by considering two representative examples of an equal-mass binary on an eccentric orbit. Then, we show how each of the model parameters affects the scalar charge evolution. After that, we study binaries in a quasi-circular-orbit inspiral; we compare the quasi-stationary approximation with the full dynamical evolution, and compare the binding energy and waveform with general relativity. We finally consider the case of unequal masses to show the effect of the dipole flux.

10.5.1 Eccentric orbits

We recall that, if we assume that the scalar charge evolves adiabatically, i.e., $p_q \approx 0$, then DS occurs for $r < r_{\rm DS} \equiv 1/c_{(2)}$, where we denote the maximum radial separation allowing for DS by $r_{\rm DS}$. We also consider the mean radial separation $\bar{r}$, or the length of the semi-major axis, which we calculate by obtaining interpolating functions for the local maxima $r_a(t)$ and minima

[2] A caveat here is that in the spontaneously-scalarized regime, one has to take into account the coupling between scalar and fluid oscillations, the latter requiring a more sophisticated effective action with further dynamical variables.

$r_p(t)$ of the solution $r(t)$, then evaluating

$$\bar{r}(t) \equiv \frac{r_a(t) + r_p(t)}{2}. \tag{10.32}$$

Figure 10.5 shows an example for an equal-mass binary with baryon mass $M_{bA} = M_{bB} = 1.18 M_\odot$, initial eccentricity $e = 0.3$, and initial radial separation at apastron $r_a = r_{\rm DS} + 22 M_\odot \simeq 33.6 M$. (Equal mass implies that the scalar charges q_A and q_B are identical, thus we refer to only one scalar charge q.) We assume the asymptotic scalar field $\varphi_0 = 0$, which means the initial scalar charge, calculated from Eq. (10.24), is zero. So we take $p_{q,A} = p_{q,B} = 10^{-20}$, representing some small perturbation to move the solution away from the unstable $q = 0$ solution. For all configurations considered in this paper, we stop the numerical evolution of the equations of motion at $r = 10M$.

In the left panel of Fig. 10.5, we plot $r(t)$ and $\bar{r}(t)$. The dashed horizontal line represents the radius $r_{\rm DS}$ at which DS is expected, while the vertical line indicates the time $t_{\rm DS}$ at which $\bar{r}$ crosses that radius. The initial separation is such that $\bar{r} > r_{DS}$. Correspondingly, the scalar charge is initially dominated by an exponential damping, as shown in the middle panel. Even though the periastron distance at the beginning is smaller than $r_{\rm DS}$, the binary does not spend enough time inside $r_{\rm DS}$ for DS to occur. However, the small oscillations in the scalar charge in this phase are due to the binary entering and exiting the DS region.

Shortly after $\bar{r}$ becomes smaller than $r_{\rm DS}$, an exponential growth kicks in, and the scalar charge grows exponentially with small modulations. It eventually saturates, and the saturation point of the exponential growth agrees with the quasi-stationary solution $q^2 \simeq 6/c_{(4)}[1/r(t) - c_{(2)}]$ from Eq. (10.8), as can be seen in the right panel of Fig. 10.5. After reaching saturation, the increase in the scalar charge is proportional to $1/\sqrt{r}$.

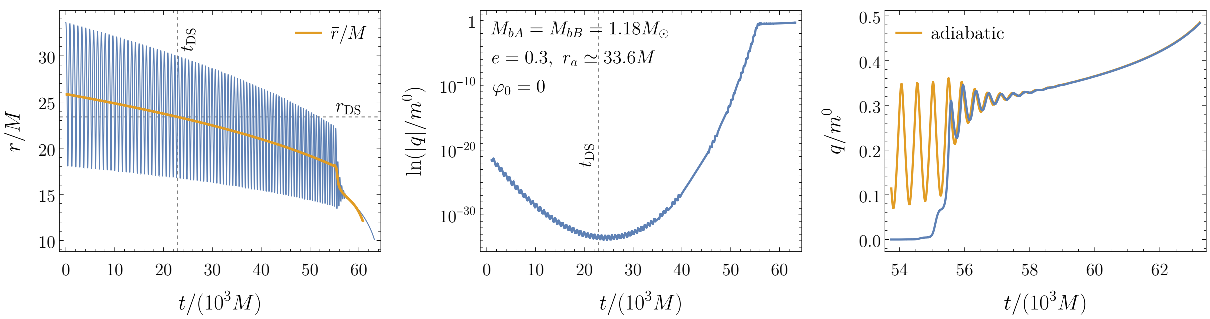

Figure 10.5: Separation and scalar charge for an equal-mass binary with baryon mass $M_{bA} = M_{bB} = 1.18M_\odot$, initial eccentricity $e = 0.3$, initial separation $r_a \simeq 33.6M$, and asymptotic scalar field $\varphi_0 = 0$. The right panel shows the scalar charge around the time it reaches saturation, and compares it with the approximate solution in Eq. (10.8).

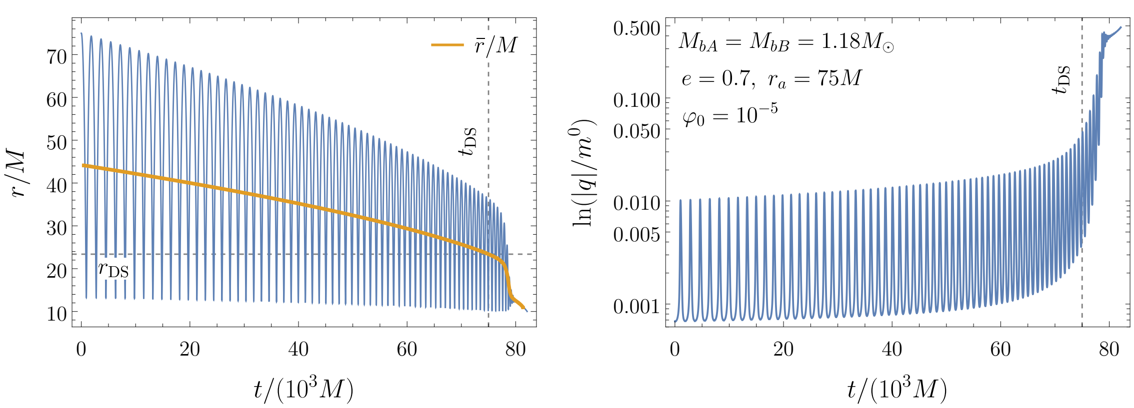

Figure 10.6: Similar to Fig. 10.5 but for initial eccentricity $e = 0.7$ and asymptotic scalar field $\varphi_0 = 10^{-5}$. The local maxima of the scalar charge occur at periastron, which is below the expected separation allowing for DS.

In Fig. 10.6, we consider another example for a binary with the same baryon mass as in Fig. 10.5, but with eccentricity $e = 0.7$ and asymptotic scalar field $\varphi_0 = 10^{-5}$. We see that the high eccentricity and nonzero φ_0 cause the scalar charge to increase at periastron and decrease at apastron. This behavior was first demonstrated in Ref. [483] for eccentric binaries and was dubbed "transient DS". The magnitude of the oscillations of the scalar charge increases with increasing eccentricity and for baryon masses closer to the critical value $M_{b,cr}$. However, the increase in the scalar charge compared to its initial value, given by Eq. (10.24), is mostly independent of φ_0, e.g., for the mass and eccentricity used in Fig. 10.6, the charge increases by about an order of magnitude regardless of the value of φ_0.

10.5.2 Effect of the parameters on the scalar charge

In order to explore the phenomenology of our theory-independent effective action, it makes sense to slightly move away from the specific effective parameters predicted by the DEF theory. In what follows, we focus on an equal-mass binary with baryon mass $M_{bA} = M_{bB} = 1.2M_\odot$, which would be characterized by the parameters $c_{(2)} = 0.01716$, $c_{(4)} = 0.5791$, and $c_{\dot{q}^2} = 53.7$ for the DEF model with $\beta = -5$ (cf. Sec. 10.4).

To explore the effect of each parameter on the scalar charge, we vary one at a time and plot the charge in Fig. 10.7. For all panels in that figure, the middle curve corresponds the DEF values of those parameters. In the first three panels, we take the initial eccentricity as $e = 0.2$ and the asymptotic scalar field as $\varphi_0 = 10^{-20}$, and explore the effects of varying e and φ_0 in the last two panels. We start the evolution with initial separation such that $\bar{r}$ is just above the DS radius, so that the plots focus on the DS transition. In particular, all curves in Fig. 10.7 start at initial

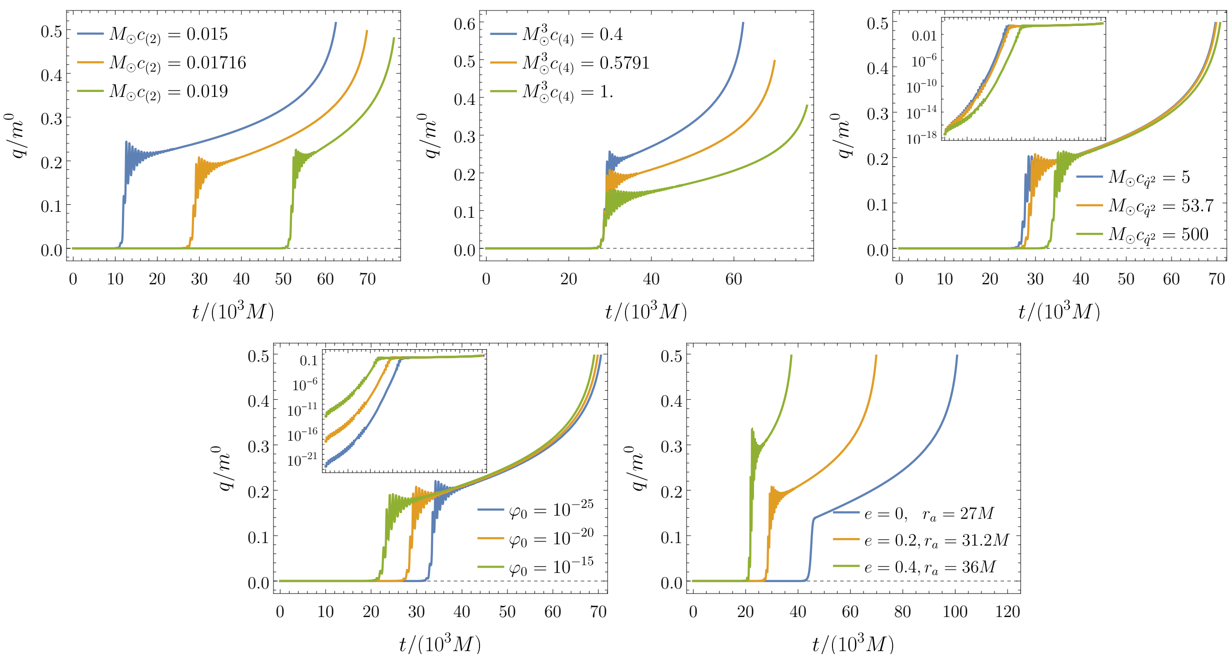

Figure 10.7: Each panel shows the effect on the scalar charge of varying one of the parameters of the effective action ($c_{(2)}$, $c_{(4)}$, and $c_{\dot{q}^2}$), or varying the asymptotic scalar field φ_0 and eccentricity e. The middle orange curve is the same in all panels, representing a configuration with baryon mass $M_{bA} = M_{bB} = 1.2 M_\odot$, initial eccentricity $e = 0.2$, initial separation $r_a \simeq 31.2M$, and asymptotic scalar field $\varphi_0 = 10^{-20}$.

separation $r_a \simeq 31.2M$, except for the last panel, in which we use $r_a = 36M$ for eccentricity $e = 0.4$ and $r_a = 27M$ for $e = 0$ for a better visualization.

From the figure, we observe the following:

- The coefficient $c_{(2)}$ has a significant effect on when scalarization occurs, since $r_{\rm DS} = 1/c_{(2)}$, but it has a small effect on the magnitude of the charge after scalarization, as can be understood from Eq. (10.8).

- The coefficient $c_{(4)}$ affects the magnitude of the charge but not the DS radius, since from Eq. (10.8), we see that the charge after scalarization is proportional to $1/\sqrt{c_{(4)}}$.

- The coefficient $c_{\dot{q}^2}$ affects the time scale for the exponential growth of the scalar charge during scalarization, with smaller values leading to a shorter time. Sufficiently increasing the value of $c_{\dot{q}^2}$, while keeping the other coefficients constant, would increase the scalarization timescale and prevent the binary from scalarizing before merger.

- The asymptotic scalar field φ_0 changes the initial value of the scalar charge, and hence how early it reaches saturation. This is because $q \approx \varphi_0/c_{(2)}$ before scalarization.

- The eccentricity e affects the oscillations near saturation, with larger eccentricity leading to larger oscillations, because the binary spends more orbits going in and out of the DS region.

Note that, as one approaches the critical mass for spontaneous scalarization, $c_{(2)}$ goes to zero, and $r_{\rm DS}$ becomes arbitrarily large. On the other hand, the coefficient $c_{\dot{q}^2}$, which governs the timescale for variations of the scalar charge, diverges at the critical point (cf. Fig. 10.4). These two effects compete in the initial phase of exponential growth of the scalar charge: as the critical

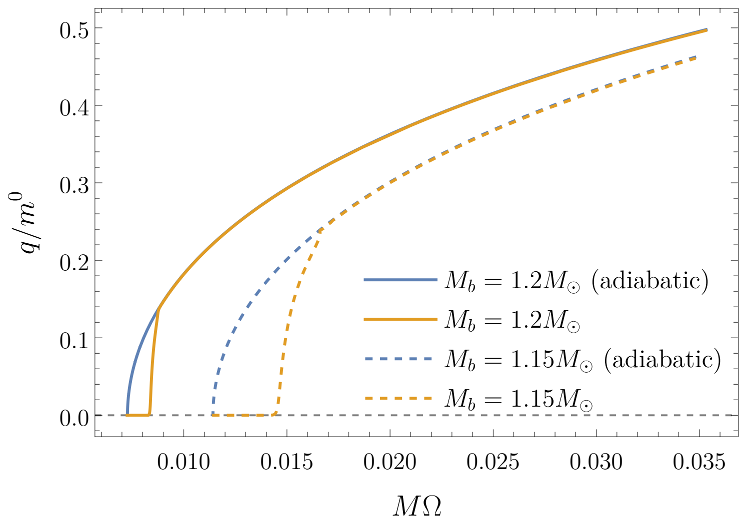

Figure 10.8: Comparison of the quasi-stationary (adiabatic) approximation with the full dynamical evolution of the scalar charges, plotted versus the orbital frequency for equal-mass binaries on quasi-circular orbits.

point is approached, the growth of the scalar charge starts at earlier times due to the increase in $r_{\rm DS}$ (favoring DS), but with a larger timescale due to the increase in $c_{\dot{q}^2}$ (disfavoring DS). Since the growth of the scalar field is exponential and the inspiral timescale is proportional to r^4 one expects DS to be favored as one moves closer to the critical point, which we have checked numerically.

10.5.3 Quasi-circular orbits

If the scalar charge is assumed to change adiabatically ($\dot{q} \approx 0$), then the charge after scalarization is given by Eq. (10.8). In Fig. 10.8, we compare that approximation with the numerical solution of Eqs. (10.16), which include $\dot{q}$, for quasi-circular inspirals.

We consider two configurations: one with baryon mass $M_{bA} = M_{bB} = 1.2M_\odot$, and the other with mass $M_{bA} = M_{bB} = 1.15M_\odot$. For both, we use $\varphi_0 = 10^{-20}$, and start with initial separation $r_a = 1/c_{(2)} + 0.1 M_\odot \simeq 19.8M$, which is just above the expected DS radius. We see very good agreement between the analytical approximation and numerical solution, except at the beginning of the evolution, during the onset of DS. That is because including the $c_{\dot{q}^2}$ coefficient accounts for the time scale of the exponential growth of the scalar charge, and hence delays reaching the saturation point.

For the configuration with mass $M_{bA} = M_{bB} = 1.15 M_\odot$, we plot in Fig. 10.9 the binding energy for the binary, which we define as the value of the Hamiltonian minus the constant ADM mass, that is

$$E_b \equiv H - M. \tag{10.33}$$

To obtain E_b for circular orbits as a function of the orbital frequency, we solve $\partial H/\partial r = 0$ and $\partial H/\partial L = \Omega$ for $r(\Omega)$ and $L(\Omega)$, with $p_r = 0$. Substituting that solution into the Hamiltonian yields

$$E_b = m_A + m_B - M + \frac{p_{q,A}^2}{2c_{\dot{q}^2,A}} + \frac{p_{q,B}^2}{2c_{\dot{q}^2,B}} - \frac{\mu}{2}(M\Omega)^{2/3}\left(1 + \frac{q_A q_B}{\mu M}\right)^{2/3}. \tag{10.34}$$

In Fig. 10.9, we see that the binding energy after scalarization decreases less rapidly than in general relativity, due to the sudden increase in the orbital frequency, causing the binary to become more tightly bound than in general relativity in a very short time. This behavior qualitatively agrees with the quasi-equilibrium numerical calculations of Ref. [485].

We also plot in Fig. 10.10 the Newtonian-order waveform, and compare it with general relativity. The leading order of the $(2,2)$ waveform mode, for general orbits, is given by

$$h_{22} = -4\mu\sqrt{\frac{\pi}{5}}e^{-2i\phi}\left(\frac{M}{r} + \frac{L^2}{\mu^2 r^2} - \frac{p_r^2}{\mu^2} + 2i\frac{Lp_r}{\mu^2 r}\right), \tag{10.35}$$

which can be written as a magnitude and phase $h_{22} \equiv |h_{22}|e^{i\psi_{22}}$. We see from Fig. 10.10 that the

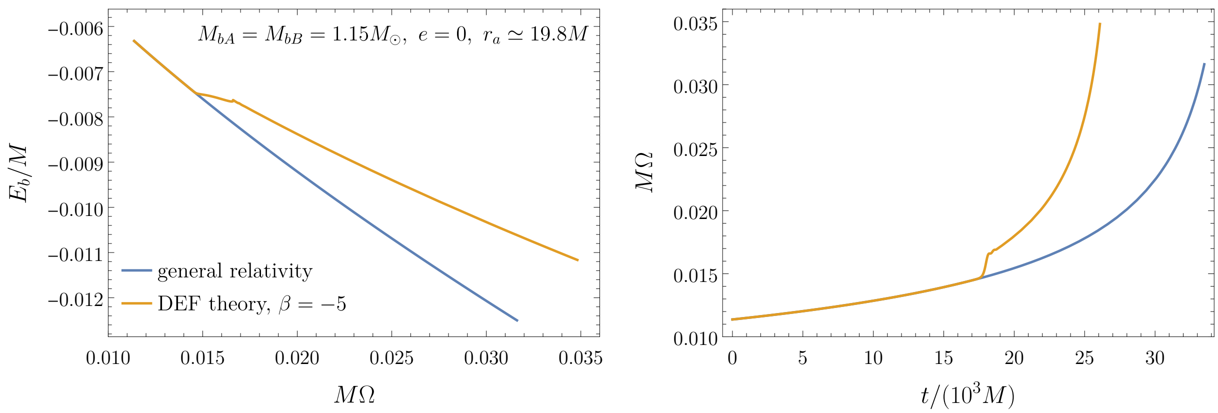

Figure 10.9: Binding energy as a function of the orbital frequency (left panel) and orbital frequency as a function of time (right panel) for masses $M_{bA} = M_{bB} = 1.15M_\odot$ in a quasi-circular inspiral.

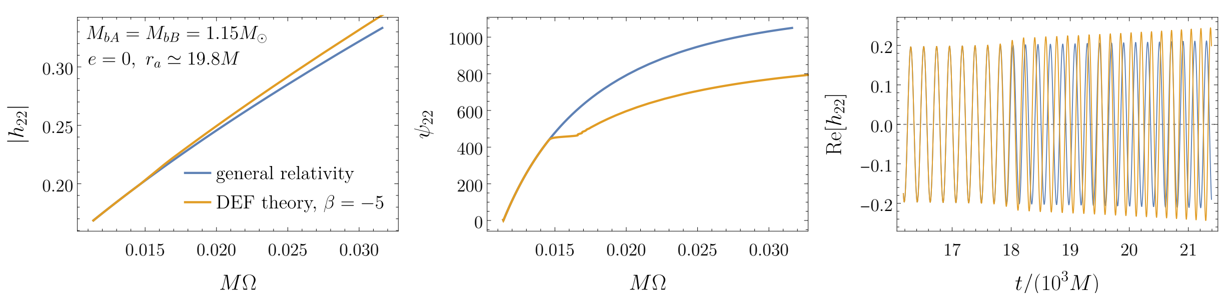

Figure 10.10: The leading order of the (2,2) waveform mode for a quasi-circular inspiral. The left and middle panels show the magnitude and phase of the waveform versus the orbital frequency, while the right panel shows the real part of the waveform around scalarization.

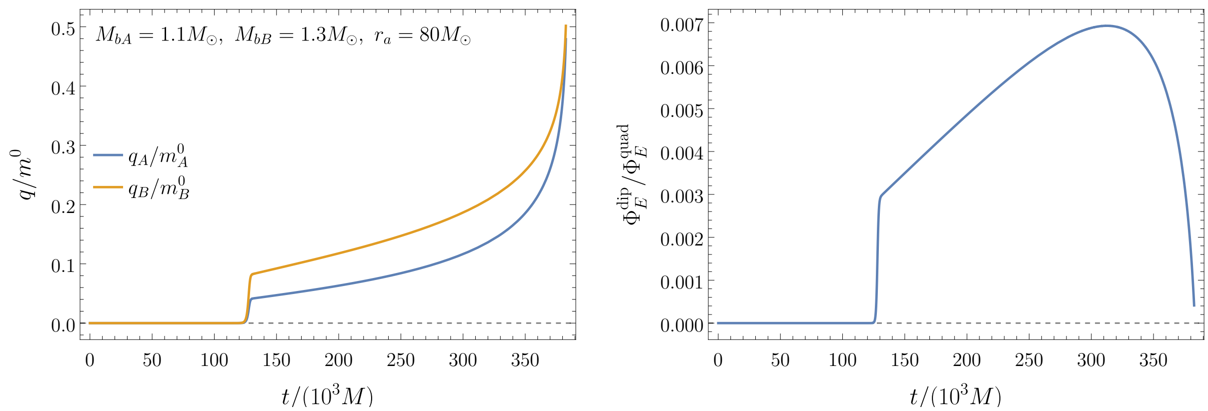

Figure 10.11: Scalar charge (left panel) and the ratio of the scalar dipole flux to the tensor quadrupole flux (right panel), for a configuration with unequal masses on a quasi-circular orbit.

waveform agrees with general relativity until the onset of DS, which leads to a sudden change in the phase of the waveform, causing it to approach merger more quickly.

10.5.4 Dipole flux

So far, we have considered equal-mass systems, for which the leading-order dipole radiation vanishes [cf. Eq. (R.12)]. To see the effect of the dipole flux, we consider a configuration with baryon masses $M_{bA} = 1.1M_\odot$ and $M_{bB} = 1.3M_\odot$, on a quasi-circular orbit with initial separation $r_a = 80M_\odot$, and asymptotic scalar field $\varphi_0 = 0$.

In Fig. 10.11, we plot the two scalar charges and see that they scalarize at almost the same time, with larger magnitude for the larger mass. The right panel of that figure shows the ratio of the leading-order scalar dipole energy flux $\Phi_E^{\rm dip}$, Eq. (R.12), to the tensor quadrupole flux, which is given for quasi-circular orbits by $\Phi_E^{\rm quad} = 32M^3\mu^2/(5r^5)$. That ratio is of order 10^{-3} after scalarization, but decreases at small separations since $\Phi_E^{\rm dip}$ is proportional to $1/r^4$ while $\Phi_E^{\rm quad}$ is proportional to $1/r^5$.

10.6 Conclusions

Dynamical scalarization is a non-perturbative phenomenon that shows up in scalar-tensor theories of gravity, and involves the development of nontrivial scalar charges on inspiraling compact objects. Although this effect was originally discovered in fully nonlinear numerical simulations of neutron stars in scalar-tensor gravity [509], it is captured by compact-binary models that employ effective-field-theory methods [8, 513]. By construction, this effective approach is designed to capture the UV and IR scales of the system, where the UV physics is simplified by modeling the binary components as point-particles, while relevant internal degrees of freedom are captured by variables that evolve along the worldlines. In this way, the model can incorporate physical aspects such as tidal deformations and/or stellar oscillations.

Earlier effective-action models for DS considered the case where the evolution is quasi-stationary, and were restricted to quasi-circular orbits. In this work, we considered the full dynamical evolution predicted by the model for general (eccentric) orbits. This is achieved at leading order in the effective action, which contains only three parameters for each binary component. One of these parameters —the coefficient $c_{\dot{q}^2}$ of the kinetic term in Eq. (10.2)—was neglected in previous works dealing with the quasi-stationary case [8]. Here we suggested a prescription to match this coefficient to properties of the fundamental scalar mode of a neutron star, and considered its effect on the binary evolution. Additionally, radiation-reaction effects were incorporated at the level of the equations of motion. In order to show how the model works in practice, we chose to work with the well-known DEF scalar-tensor theory [cf. Eqs. (10.25) and

(10.26)] with the parameter $\beta = -5$. We have thus worked out the full dynamics of eccentric, oscillatory binary neutron stars in DEF theory, near the phase transition to the scalarized regime.

The main effect of including the $c_{\dot{q}^2}$ term in the model is to account for the initial phase of exponential growth of the scalar charge, before it reaches saturation and the evolution becomes well described by the adiabatic solution. The time spent in the initial phase also depends on the cosmological value of the scalar field (φ_0), which determines the magnitude of the scalar charges prior to scalarization. φ_0 impacts the theory's parameterized post-Newtonian parameters [50] and is thus subject to an upper bound from solar system observations; on the other hand, a lower bound is provided by the scalar field vacuum fluctuations.

General eccentric orbits were also considered. For such orbits, the scalar charge is amplified and suppressed successively as the binary enters and exits the DS radius—defined as the maximum radial separation allowing for DS in the stationary limit—, with the mean radial separation determining the overall behavior (see Fig. 10.5).

By incorporating the effects of mode dynamics and dissipation, our work makes important steps towards improving the accuracy of post-Newtonian waveform models for compact binaries in gravity theories that allow for scalarization, and can thus be useful in constraining scalarization with gravitational-wave observations [692, 716, 719, 773–776].

It is worth emphasizing that, although many of our results were obtained for a specific gravity theory, the effective action model introduced here is theory independent. Thus, it can be used as the basis for both theory-specific and theory-agnostic tests of DS. In the latter case, one could attempt to constrain directly the leading coefficients $(c_{(2)}, c_{(4)}, c_{\dot{q}^2})$ of the effective action— or combinations thereof, taking into account possible degeneracies in their relation to observables. Degeneracies related to uncertainties in the nuclear equation of state may also be relevant for the case of binary neutron star systems, but we note that scalarization also shows up for black holes in some scalar extensions of GR. In any case, waveform models for DS would benefit from higher-order post-Newtonian calculations in specific frameworks (see e.g. Refs. [203, 206, 208] for efforts in a class of scalar-tensor models) and of possible refinements to the effective action, such as accounting for the interplay between fluid and scalar oscillation modes.

Acknowledgments

We thank Robert Benkel for collaboration at an early stage of this work and for insightful discussions, and Hector O. Silva for useful comments on the manuscript. N.O. acknowledges financial support by the CONACyT grants "Ciencia de Frontera" 140630 and 376127, and by the UNAM-PAPIIT grant IA100721. R.M. acknowledges partial funding from the National Council for Scientific and Technological Development (CNPq) and by the Carlos Chagas Filho Research Support Foundation (FAPERJ).

Chapter 11: Conclusions and future work

The work presented in this dissertation targeted improving the analytical approaches for the dynamics of compact binaries, which is important for producing accurate waveforms that can be used in gravitational-wave (GW) detection and parameter estimation. This was achieved by extending the post-Newtonian (PN) approximation for the dynamics of spinning binaries, improving the accuracy of effective-one-body (EOB) waveform models, and identifying some signatures of modified gravity theories on the binary dynamics and waveforms.

11.1 PN approximation for spinning binaries

The PN approximation is the most commonly used analytical approach for describing the motion of comparable-mass binaries, which are the main GW sources for ground-based detectors. Therefore, extending the PN expansion to higher orders and including spin effects can improve the accuracy of waveform models, which are crucial for GW observations.

In Chapters 2, 3, and 4, we presented an approach that combines several analytical approximation methods to derive new PN results from gravitational self-force (GSF) results, by making use of the mass dependence of the scattering angle in a post-Minkowskian (PM) expansion. We used this method to derive the 4.5PN and 5.5PN spin-orbit (SO) conservative dynamics for precessing spins [1, 3], and the 5PN spin$_1$-spin$_2$ dynamics for aligned spins [2].

The 5.5PN SO conservative dynamics involves nonlocal-in-time contributions, due to back-scattered radiation emitted at earlier times. The calculation of these nonlocal contributions in Chapter 4 was done for the first time for the spinning conservative dynamics. For the local-in-time contributions at 5.5PN order, all coefficients have been computed from GSF results at first order in the mass ratio, except for one unknown that has a small effect on the dynamics, as demonstrated by comparing the binding energy with numerical relativity (NR).

The method used to derive these novel results demonstrates the importance of combining PN, PM, and GSF techniques to improve our understanding of the binary dynamics. It also highlights how studying observables for unbound orbits, such as the scattering angle, is also useful for bound orbits. A recent check of this method was the independent calculation of the 5PN spin$_1$-spin$_2$ binding energy for circular orbits in Ref. [777], which is in complete agreement with our results.

Related future work includes the following:

- The remaining unknown coefficient in the 5.5PN SO scattering angle is at second order in the mass ratio, and as such it requires analytical GSF results at second order in the mass ratio, which might become available in the near future since numerical results have already been reported in Refs. [326–328]. Alternatively, that coefficient could be determined through targeted PN calculations, along the lines of Ref. [286], in which the authors related the two missing coefficients at 5PN order to coefficients that can be calculated from an effective-field-theory approach.

- The 5PN quadratic-in-spin dynamics for aligned spins can be fully determined from GSF results. This requires the derivation of new results for the spin-precession frequency at first order in the mass ratio, in a Schwarzschild background to linear order in the secondary spin, which is something we are working on. Another important point in this calculation is extending the first law of binary mechanics to spin-quadrupole, and relating it to tidal invariants [344, 353, 354].

- It would be interesting to investigate how to obtain PN results for *precessing* spins from invariants calculated in GSF. The PM expansion of the impulse (net change in momentum) and the spin kick (net change in the spin vector) should have a similar mass dependence as in the aligned-spin case, which could make it possible to relate arbitrary-mass-ratio PN results to GSF invariants. However, the challenge would be in obtaining analytical GSF results for generic orbits in a Kerr background, which are currently only available numerically [318].

11.2 Effective-one-body formalism

PN expansions become inaccurate in the late inspiral. However, resumming PN results in the EOB formalism extends their applicability in the strong field regime. This is because EOB combines information from several analytical approximations with NR results, while recovering the strong-field test-body limit, thus providing a more accurate description of the binary dynamics throughout the parameter space.

In Chapter 5, we obtained EOB Hamiltonians that include the complete 4PN conservative dynamics for precessing spins and generic compact objects, i.e. black holes or neutron stars. We considered four Hamiltonians, which are variations of the Hamiltonians often used in EOB models, and compared their circular-orbit binding-energy to NR simulations finding good agreement.

In Chapter 6, we dealt with the dissipative dynamics for eccentric orbits. We derived the radiation-reaction force and waveform modes in EOB coordinates through 2PN order, including tail and spin effects. We recast those results in a factorized form and used them to extend the quasi-circular–orbit model `SEOBNRv4HM` [397, 398], which is currently used in LIGO-Virgo analyses. We compared our eccentric model `SEOBNRv4EHM` [10] with NR simulations with initial orbital eccentricities up to $e \simeq 0.3$, finding good agreement.

In Chapter 7, we assessed the accuracy of the 4PM conservative dynamics, which were derived in Refs. [246, 247, 258, 259], through comparisons with the PN approximation and NR simulations for the circular-orbit binding energy and the scattering angle. We also incorporated the PM results in EOB Hamiltonians, which significantly improves the accuracy over PM-expanded Hamiltonians. We found that while the 4PM approximation gives comparable results to the 3PN approximation for bound orbits, it performs better for scattering encounters.

Related future work includes the following:

- The results in Chapters 5 and 6 have been employed in building the next-generation EOB waveform model for use in the upcoming LIGO-Virgo-KAGRA runs in 2023. For example, we used a variation of one of the 4PN Hamiltonians in Chapter 5, based on the Hamiltonian for a test mass in Kerr, and extended it by including higher PN orders. In addition, the results obtained in Chapter 6 are being used to extend the model to eccentric orbits.

- In Chapter 6, we restricted to the case of binaries with aligned spins. Extending our calculation for the radiation-reaction force to precessing spins is straightforward, as outlined in Sec. 6.2. However, the waveform modes for precessing spins are only known for spherical orbits at leading PN order [169], so it would be important to extend them to generic orbits and higher PN orders.

- The study of PM results in Chapter 7 would be useful in developing a full inspiral-merger-ringdown EOB waveform model, combining PN and PM results, and including radiation-reaction effects, with a particular emphasis on hyperbolic orbits. All GW detections so far have been consistent with bound-orbit inspirals. However, the detection of hyperbolic encounters can be useful in determining the binary formation channels; using waveform models that are accurate for scattering orbits may increase the likelihood of detecting them.

- Furthermore, it would be interesting to incorporate spin information in EOB Hamiltonians in a PM expansion. For spinning binaries, PM results were derived in Refs. [262–276], and NR simulations have been reported in Ref. [778], which noted that PN EOB models do not give satisfactory agreement for spinning configurations. Therefore, it could be that combining PN and PM results might improve the agreement with NR.

11.3 Modified gravity theories

GW observations offer a unique opportunity to test gravity in the strong-field regime, which requires incorporating potential deviations from GR in waveform models, either in a theory-specific or theory-agnostic approach. Therefore, the PN techniques and EOB formalism discussed above are important when trying to identify the effect of modified gravity theories on GW observations.

In Chapter 8, we used a theory-specific approach and focused on the binary dynamics in Einstein-Maxwell-dilaton (EMd) theory, deriving the 1PN Lagrangian governing the conservative binary dynamics, and the next-to-leading order energy flux. We also computed the Fourier-domain gravitational waveform in the stationary-phase approximation, and the number of useful cycles measurable by Advanced LIGO.

In Chapters 9 and 10, we presented a theory-agnostic effective-field-theory approach for describing spontaneous and dynamical scalarization, showing that all theories that exhibit spontaneous scalarization for isolated compact objects also manifest dynamical scalarization in binary inspirals. We applied this approach to black holes in Einstein-Maxwell-scalar theory using a quasi-stationary approximation, examined the stability of scalarized solutions, computed the critical exponents of the scalarization phase transition, and estimated the frequency at which dynamical scalarization occurs. Then, we extended our approach to account for the dynamical evolution of the scalar charge during scalarization, and applied it to binary neutron stars in a scalar-tensor theory, demonstrating how eccentric-orbit inspirals cause oscillations in the scalar charge.

Related future work includes the following:

- The construction of a full (inspiral-merger-ringdown) EOB waveform model in EMd theory. This can be done by incorporating the PN results from Chapter 8 into waveform models that include higher PN orders in GR.

- Applying the effective-action approach to other theories. In particular, ongoing work concerns studying scalarization in scalar-Gauss-Bonnet theories, and we were able to recover some results in the literature [499] using this simpler method.

- Incorporating the effects of dynamical scalarization in existing waveform models to constrain theories that exhibit scalarization with GW observations. This can be done in either a theory-agnostic or theory-specific approach through the coefficients of the effective action.

Appendix A: Redshift and spin-precession frequency

In this Appendix, we outline how the redshift and spin-precession frequency are computed, first for a spinning test body, then at first order in the mass ratio in terms of the metric perturbations. We follow the derivation from Refs. [338, 342, 347, 779].

A.1 Spinning test body in a Schwarzschild background

We start from the MPD equations (1.120) and (1.121) at linear order in spin, and assume that a spinning test body in a Schwarzschild background has a spin vector along the z direction given by $\boldsymbol{S} = s\hat{\boldsymbol{e}}_z$, where s is the spin magnitude, and that it moves along a circular orbit in the equatorial plane. Because of the helical symmetry of the problem, the 4-velocity can be written as [336]

$$\bar{u}^\mu = \bar{u}^t(\partial_t + \Omega\partial_\phi), \tag{A.1}$$

where Ω is the angular frequency, and $\bar{u}^\mu$ coincides with $\dot{z}^\mu = \mathrm{d}x^\mu/\mathrm{d}\tau$ at linear order in spin [366]. In this Appendix, we use a bar to denote quantities evaluated on the background Schwarzschild metric.

The normalization condition $\bar{u}^\mu\bar{u}_\mu = -1$ leads to

$$-\left(1 - \frac{2M}{r}\right) + \Omega^2 r^2 = -(\bar{u}^t)^{-2}, \tag{A.2}$$

while the r-component of Eq. (1.120) leads to

$$\bar{u}^t \left(-M\mu + 3sM\Omega + \mu\Omega^2 r^3\right) = 0. \tag{A.3}$$

Solving these two equations yields

$$\bar{u}^t = \frac{1}{\sqrt{1-3u}}\left(1 - \frac{3}{2}\hat{s}\frac{u^{5/2}}{1-3u}\right), \tag{A.4}$$

$$M\Omega = u^{3/2}\left(1 - \frac{3}{2}\hat{s}u^{3/2}\right), \tag{A.5}$$

where we define $u \equiv M/r$ and $\hat{s} \equiv s/(M\mu)$. From the solution for Ω, we define the frequency variable $y \equiv (M\Omega)^{2/3}$, leading to

$$y = u(1 - \hat{s}u^{3/2}), \qquad u = y(1 + \hat{s}y^{3/2}). \tag{A.6}$$

The gauge-invariant redshift is defined as $\bar{z} \equiv \mathrm{d}\tau/\mathrm{d}t = 1/\bar{u}^t$, and from Eq. (A.4) it reads

$$\begin{aligned}\bar{z} &= \sqrt{1-3u} + \frac{3}{2}\hat{s}\frac{u^{5/2}}{\sqrt{1-3u}} \\ &= \sqrt{1-3y}\,.\end{aligned} \tag{A.7}$$

For the spin-precession frequency Ω_S, it was shown in Ref. [347] that it is related to the helical Killing vector $k^\mu \equiv \partial_t + \Omega\partial_\phi$ via

$$\Omega_S = \Omega - |\nabla k|\,, \tag{A.8}$$

where the quantity $|\nabla k|$ is defined by

$$|\nabla k|^2 \equiv \frac{1}{2}K_{\mu\nu}K^{\mu\nu}, \tag{A.9}$$

with the antisymmetric tensor $K_{\mu\nu} \equiv \nabla_\mu k_\nu$. To zeroth-order in spin, we obtain

$$M|\nabla k| = y^{3/2}\sqrt{1-3y}\,, \tag{A.10}$$

leading to the spin-precession invariant

$$\bar{\psi} \equiv \frac{\Omega_S}{\Omega} = 1 - \sqrt{1 - 3y}\,. \tag{A.11}$$

A.2 Spinning body in a perturbed Schwarzschild background

Equations (A.7) and (A.11) give the redshift and spin-precession invariants for a test spin in a Schwarzschild background. To account for the perturbation caused by the small mass μ of the test body on the background metric, we write the perturbed metric as

$$g^R_{\mu\nu} = \bar{g}_{\mu\nu} + q h^R_{\mu\nu}, \tag{A.12}$$

where $q \equiv \mu/M$ is the mass ratio, and $h^R_{\mu\nu}$ is the regularized metric perturbation, which we write as the sum of a nonspinning and a linear-in-spin term

$$h^R_{\mu\nu} \equiv h^{(0)}_{\mu\nu} + \hat{s} h^{(\hat{s})}_{\mu\nu}. \tag{A.13}$$

The normalization condition for the perturbed 4-velocity $u^\mu u_\mu = -1$ leads to

$$-\left(u^t\right)^{-2} = \left(-1 + \frac{2M}{r} + \Omega^2 r^2 + q h_{kk}\right), \tag{A.14}$$

where $h_{kk} \equiv h_{\alpha\beta} k^\alpha k^\beta$, which can be solved for u^t in terms of r and Ω. To solve for $\Omega(r)$, we write

$$M\Omega = u^{3/2}\left[1 - \frac{3}{2}\hat{s} u^{3/2} + q\left(\tilde{\Omega}_1 + \hat{s}\tilde{\Omega}_{1s}\right)\right], \tag{A.15}$$

then the r-component of Eq. (1.120) yields the solution

$$\tilde{\Omega}_1 = -\frac{M}{4u^2}\partial_r h^{(0)}_{kk}, \tag{A.16}$$

and $\tilde{\Omega}_{1s}$ is given by Eq. (B11) of Ref. [342].

From the solution for u^t given in Eq. (A.14), the redshift reads

$$z = \frac{1}{u^t} = \sqrt{1 - \frac{2M}{r} - \Omega^2 r^2}\left[1 + \frac{q\left(h^{(0)}_{kk} - \hat{s}h^{(\hat{s})}_{kk}\right)}{2\left(1 - \frac{2M}{r} - \Omega^2 r^2\right)}\right]$$
$$= \sqrt{1-3y} - q\left[\frac{h^{(0)}_{kk}}{2\sqrt{1-3y}} + \frac{\hat{s}\left(M\sqrt{y}\partial_r h^{(0)}_{kk} + h^{(\hat{s})}_{kk}\right)}{2\sqrt{1-3y}}\right]. \tag{A.17}$$

The first-order regularized metric perturbations can be computed by solving the Regge-Wheeler-Zerilli equation [51, 52] in a series expansion over modes using the Mano, Suzuki and Takasugi (MST) method [334]. The first few PN terms in the redshift read [337, 342]

$$z = \sqrt{1-3y} + q\Bigg[y - y^2 - y^3 + \left(\frac{76}{3} - \frac{41\pi^2}{32}\right)y^4 + \ldots$$
$$+ \hat{s}\left(y^{7/2} - 3y^{9/2} - \frac{15y^{11/2}}{2} + \ldots\right)\Bigg]. \tag{A.18}$$

For the spin precession, to zeroth order in spin, we calculate $|\nabla k|$ in the perturbed metric and obtain

$$M|\nabla k| = y^{3/2}\sqrt{1-3y}\,[1 + q\delta_0] \tag{A.19}$$

where

$$\delta_0 \equiv -\frac{\partial_{\bar{\phi}} h^{(0)}_{rk}}{2\sqrt{y}} + \frac{\partial_r h^{(0)}_{\phi k}}{2\sqrt{y}} - \frac{h^{(0)}_{kk}\,y}{2\left(6y^2 - 5y + 1\right)} + h^{(0)}_{rr}\left(y - \frac{1}{2}\right)$$
$$- \frac{h^{(0)}_{\phi k}\,y^{3/2}}{M - 2My} + \frac{h^{(0)}_{\phi\phi}(1-3y)y^2}{2M^2(2y-1)}, \tag{A.20}$$

The spin-precession invariant is then given by

$$\psi = \bar{\psi} - q\sqrt{1-3y}\delta_0, \tag{A.21}$$

with $\bar{\psi}$ given by Eq. (A.11). In a PN expansion, the first few terms are given by [347]

$$\psi = 1 - \sqrt{1-3y} + q\left[y^2 - 3y^3 - \frac{15}{2}y^4 + \ldots\right]. \tag{A.22}$$

Appendix B: The nonspinning 4PN terms in the bound radial action through sixth order in eccentricity

Here we present the additional 4PN-order terms in the radial action for bound orbits, computed via (3.70) applied to the 4PN EOB Hamiltonian given in [80], valid to sixth order in the orbital eccentricity e. Note that the expansion in eccentricity has occurred only in the 4PN terms, at $\mathcal{O}(c^{-8})$, where it is sufficient to use the Newtonian relation $e = \sqrt{1+\varepsilon(L/GM\mu)^2} + \mathcal{O}(c^{-2})$. The complete radial action we employ above, through 4PN order for the nonspinning terms and through NNNLO for the spin terms, is obtained by replacing the first two lines of (3.80) with

$$
\begin{aligned}
I_r = {} & -L + GM\mu\frac{1+2\varepsilon}{c\sqrt{-\varepsilon}} + \frac{1}{c^2}\frac{(GM\mu)^2}{\pi\Gamma L_{\rm cov}}\mathsf{X}_2 \\
& + \frac{1}{\pi}\sum_{l=2}^{4}\frac{1}{c^{2l}}\frac{(GM\mu)^{2l}}{(\Gamma L_{\rm cov})^{2l-1}}\frac{\bar{\mathsf{X}}_{2l}}{2l-1} + \frac{1}{c^8}\mathcal{O}(e^8) + \mathcal{O}(\frac{1}{c^{10}}),
\end{aligned}
\tag{B.1}
$$

where

$$
\begin{aligned}
\frac{\bar{\mathsf{X}}_4}{3\pi} = {} & \frac{5}{4}(7-2\nu) + \left[\frac{105}{4} + \Big(\frac{41}{128}\pi^2 - \frac{557}{24}\Big)\nu\right]\varepsilon + \left[\frac{1155}{64} + \Big(\frac{65383}{1440} + \frac{33601}{24576}\pi^2\right. \\
& \left. - \frac{74}{15}\gamma_{\rm E} - \frac{6122}{3}\ln 2 + \frac{24057}{20}\ln 3 + \frac{74}{15}\ln\frac{cL_{\rm cov}}{GM\mu}\Big)\nu - \frac{81}{32}\nu^2 + \frac{45}{16}\nu^3\right]\varepsilon^2 + \mathcal{O}(\varepsilon^3),
\end{aligned}
\tag{B.2}
$$

$$
\begin{aligned}
\frac{\bar{\mathsf{X}}_6}{5\pi} = {} & \frac{231}{4} + \Big(\frac{123}{128}\pi^2 - \frac{125}{2}\Big)\nu + \frac{21}{8}\nu^2 + \left[\frac{9009}{32} + \Big(-\frac{64739}{240} + \frac{51439}{4096}\pi^2 - \frac{244}{5}\gamma_{\rm E}\right. \\
& \left. - \frac{60172}{15}\ln 2 + \frac{22599}{10}\ln 3 + \frac{244}{5}\ln\frac{cL_{\rm cov}}{GM\mu}\Big)\nu + \Big(\frac{483}{8} - \frac{369}{256}\pi^2\Big)\nu^2 + \frac{45}{16}\nu^3\right]\varepsilon + \mathcal{O}(\varepsilon^2),
\end{aligned}
\tag{B.3}
$$

and

$$\frac{\bar{\mathsf{X}}_8}{7\pi} = \frac{32175}{64} + \Big(-\frac{534089}{720} + \frac{425105}{24576}\pi^2 - \frac{170}{3}\gamma_\mathrm{E} - \frac{9982}{5}\ln 2 + \frac{21141}{20}\ln 3 \\ + \frac{170}{3}\ln\frac{cL_\mathrm{cov}}{GM\mu}\Big)\nu + \Big(\frac{4711}{24} - \frac{1025}{256}\pi^2\Big)\nu^2 - \frac{15}{8}\nu^3 + \mathcal{O}(\varepsilon). \tag{B.4}$$

Appendix C: Kerr-geodesic variables

We provide here the relevant details to compute the change of variables from (y, λ) to (u_p, e) needed for comparison with the 1SF calculations of the perturbed redshift and spin precession invariants. Since we are working with perturbed quantities we need only compute this change of variables at the geodesic level.

The geodesic equations in Kerr spacetime when specialized to the equator $\theta = \frac{\pi}{2}$ are

$$\dot{t} = \frac{1}{\Sigma}\left[E\left(\frac{(r^2+a^2)^2}{\Delta} - a^2\right) + aL\left(1 - \frac{r^2+a^2}{\Delta}\right)\right], \tag{C.1}$$

$$\dot{r} = \frac{1}{\Sigma}\sqrt{\left(E(r^2+a^2) - aL\right)^2 - \Delta(r^2 + (L-aE)^2)}, \tag{C.2}$$

$$\dot{\phi} = \frac{1}{\Sigma}\left[(L-aE) + \frac{a}{\Delta}\left(r^2 E - a(L-aE)\right)\right], \tag{C.3}$$

where $\dot{} \equiv \frac{d}{d\tau}$. The radial motion is commonly parametrized using the Darwin relativistic anomaly χ as

$$r = \frac{m_2 p}{(1 + e\cos\chi)}, \tag{C.4}$$

where e is the eccentricity and p the (dimensionless) semilatus rectum. This defines the turning points of the orbit to be at $\chi = 0, \pi$. Note that here we use p instead of $u_p \equiv 1/p$ from the text since it makes the equations below simpler. To determine the constants of motion E, L as functions of (p, e) we set $\dot{r} = 0$ at the turning points. While these simultaneous equations can be solved fully, we give their expansion in a, which will be sufficient for this work,

$$E = \sqrt{\frac{(p-2)^2 - 4e^2}{p(p-3-e^2)}} - \frac{(e^2-1)^2}{p(p-3-e^2)^{3/2}} a + \mathcal{O}(a^2), \tag{C.5}$$

$$L = \frac{p}{\sqrt{p-3-e^2}} + (3+e^2)\sqrt{\frac{(p-2)^2-4e^2}{p(p-3-e^2)^3}} a + \mathcal{O}(a^2). \tag{C.6}$$

Next, we calculate the radial and azimuthal periods T_{r0} and Φ_0 in the Kerr background geometry

$$T_{r0} = \oint dt = \int_0^{2\pi} \frac{dt}{d\chi} d\chi \,, \tag{C.7}$$

$$\Phi_0 = \oint d\phi = \int_0^{2\pi} \frac{d\phi}{d\chi} d\chi \,, \tag{C.8}$$

where

$$\frac{dt}{d\chi} = \frac{\dot{t}}{\dot{r}} \frac{dr}{d\chi}, \qquad \frac{d\phi}{d\chi} = \frac{\dot{\phi}}{\dot{r}} \frac{dr}{d\chi}. \tag{C.9}$$

Further expanding the integrands in eccentricity, and integrating order by order in a and e gives for the periods a result of the form

$$T_{r0}(p,e) = T^0_{r0}(p,e) + T^1_{r0}(p,e) a + \mathcal{O}(a^2) \,, \tag{C.10}$$

$$\Phi_0(p,e) = \Phi^0_0(p,e) + \Phi^1_0(p,e) a + \mathcal{O}(a^2) \,, \tag{C.11}$$

with

$$\begin{aligned} T^0_{r0} = & \frac{2\pi p^2}{\sqrt{p-6}} \Bigg[1 + \frac{3\,(2p^3 - 32p^2 + 165p - 266)}{4(p-6)^2(p-2)} e^2 \\ & + \frac{3e^4}{64(p-6)^4(p-2)^3} \Big(40p^7 - 1296p^6 + 17556p^5 - 128448p^4 + 546523p^3 - 1350786p^2 \\ & + 1803396p - 1016920 \Big) + \mathcal{O}(e^6) \Bigg], \end{aligned} \tag{C.12}$$

$$T^1_{r0} = -\frac{6\pi\sqrt{p}(p+2)}{(p-6)^{3/2}} \Bigg[1 + \frac{(2p^3 - 32p^2 + 139p + 6)}{4(p-6)^2(p+2)} e^2$$

$$+ \frac{(24p^5 - 656p^4 + 6844p^3 - 32576p^2 + 60889p + 210)}{64(p-6)^4(p+2)} e^4 + \mathcal{O}(e^6)\Bigg], \tag{C.13}$$

and

$$\Phi_0^0 = 2\pi\sqrt{\frac{p}{p-6}}\left[1 + \frac{3}{4(p-6)^2}e^2 + \frac{105}{64(p-6)^4}e^4 + \mathcal{O}(e^6)\right], \tag{C.14}$$

$$\Phi_0^1 = -\frac{8\pi}{(p-6)^{3/2}}\Bigg[1 + \frac{3(9p-34)}{4(p-6)^2(p-2)}e^2 + \frac{3\,(739p^3 - 6962p^2 + 23332p - 28824)}{64(p-6)^4(p-2)^3}e^4 + \mathcal{O}(e^6)\Bigg]. \tag{C.15}$$

With these we can use Eq. (4.57) to obtain (y, λ) to the desired 4.5PN accuracy by expanding about small $u_p = 1/p$ as

$$y(u_p, e) = y^0(u_p, e) + a\, y^a(u_p, e) + \mathcal{O}(a^2, u_p^6)\,, \tag{C.16}$$

$$\lambda(u_p, e) = \lambda^0(u_p, e) + a\, \lambda^a(u_p, e) + \mathcal{O}(a^2, u_p^5)\,, \tag{C.17}$$

with

$$y^0(u_p, e) = \left(1 - e^2\right) u_p - 2e^2\left(-1 + e^2\right) u_p^2 + \left(6e^2 - \frac{23e^4}{8}\right) u_p^3 + \left(24e^2 - \frac{13e^4}{4}\right) u_p^4 - \frac{1}{4}e^2\left(-480 + e^2\right) u_p^5\,, \tag{C.18}$$

$$y^a(u_p, e) = \frac{2}{3}\left(-1 - 2e^2 + 3e^4\right) u_p^{5/2} + \frac{1}{3}e^2\left(-52 + 37e^2\right) u_p^{7/2} + \left(-102e^2 + \frac{353e^4}{12}\right) u_p^{9/2} + \left(-704e^2 + \frac{763e^4}{6}\right) u_p^{11/2}\,, \tag{C.19}$$

$$\begin{aligned}\lambda^0(u_p, e) ={}& 1 - e^2 + \frac{1}{4}\left(-18 + 25e^2 - 7e^4\right) u_p + \frac{1}{16}\left(-36 - 36e^2 + 115e^4\right) u_p^2 \\ &+ \frac{3}{64}\left(-144 - 220e^2 + 421e^4\right) u_p^3 + \frac{1}{16}\left(-405 - 807e^2 + 1007e^4\right) u_p^4 \\ &+ \frac{3}{256}\left(-9072 - 24772e^2 + 22501e^4\right) u_p^5\,,\end{aligned} \tag{C.20}$$

$$\begin{aligned}\lambda^a(u_p, e) ={}& \frac{4}{3}\left(1 - e^2\right)\sqrt{u_p} - \frac{2}{3}\left(1 - e^2\right) u_p^{3/2} + \left(6 - \frac{25e^2}{6} - \frac{13e^4}{4}\right) u_p^{5/2} \\ &+ \left(\frac{39}{2} + 32e^2 - \frac{202e^4}{3}\right) u_p^{7/2} + \left(\frac{423}{4} + \frac{1761e^2}{8} - \frac{26243e^4}{96}\right) u_p^{9/2}\,.\end{aligned} \tag{C.21}$$

Appendix D: Quasi-Keplerian parametrization

D.1 Elliptic orbits

For a binary in a bound orbit in the orbital plane, and using polar coordinates (r, ϕ), the quasi-Keplerian parametrization [427], up to 1.5PN, reads

$$r = a_r(1 - e_r \cos u), \tag{D.1}$$

$$\ell \equiv nt = u - e_t \sin u, \tag{D.2}$$

$$\phi = 2K \arctan\left[\sqrt{\frac{1+e_\phi}{1-e_\phi}} \tan\frac{u}{2}\right], \tag{D.3}$$

where a_r is the semi-major axis, u is the eccentric anomaly, ℓ is the mean anomaly, n is the mean motion (radial angular frequency), K is the periastron advance, and (e_r, e_t, e_ϕ) are the radial, time and phase eccentricities. Spin was included in the quasi-Keplerian parametrization in Refs. [571, 572]. (See Fig. 2 of Ref. [572] for a geometric picture for some of these quantities.)

The (dimensionless) harmonic-coordinates Hamiltonian with LO SO reads

$$H = \frac{c^2}{\nu} + \frac{p^2}{2} - \frac{1}{r} + \frac{L}{c^3 r^3}\left[2\delta\chi_A - (\nu - 2)\chi_S\right]. \tag{D.4}$$

By inserting $r = a_r(1 - e_r \cos u)$ into the Hamiltonian at periastron ($u = 0$) and apastron ($u = \pi$), one can solve for the energy and angular momentum (with $p_r = 0$) as a function of a_r and e_r, i.e.,

$$\bar{E} = \frac{-1}{2a_r} + \frac{(\nu - 2)\chi_S - 2\delta\chi_A}{2\sqrt{a_r^5\,(1 - e_r^2)}}, \tag{D.5}$$

$$L = \sqrt{a_r\left(1-e_r^2\right)} + \frac{\left(e_r^2+3\right)\left[2\delta\chi_A + (2-\nu)\chi_S\right]}{2a_r\left(e_r^2-1\right)},$$

where $\bar{E} \equiv E - 1/\nu < 0$ is the dimensionless binding energy, which is negative for bound orbits, and we only include the LO nonspinning and SO terms. These expansions can be inverted to obtain $e_r(\bar{E}, L)$ and $a_r(\bar{E}, L)$ leading to

$$\begin{aligned} e_r &= \sqrt{1+2\bar{E}L^2} + \frac{4E\left(1+\bar{E}L^2\right)\left[2\delta\chi_A + (2-\nu)\chi_S\right]}{L\sqrt{1+2\bar{E}L^2}}, \\ a_r &= \frac{-1}{2\bar{E}} + \frac{2\delta\chi_A + (2-\nu)\chi_S}{L}. \end{aligned} \tag{D.6}$$

The radial period T_r and periastron advance K can be calculated from the integrals

$$\begin{aligned} T_r &= \oint \frac{dr}{\dot{r}} = 2\int_{r_p}^{r_a} \frac{dr}{\partial H/\partial p_r}, \\ K &= \frac{1}{2\pi}\oint dr \frac{\dot{\phi}}{\dot{r}} = 2\int_{r_p}^{r_a} dr \frac{\partial H/\partial L}{\partial H/\partial p_r}, \end{aligned} \tag{D.7}$$

where r_p and r_a are the periastron and apastron separations calculated from the solution of $p_r = 0$, which yields the PN expansion

$$\begin{aligned} n = \frac{2\pi}{T_r} &= 2\sqrt{2}(-\bar{E})^{3/2} \\ &= \frac{1}{a_r^{3/2}} + \frac{3\left[2\delta\chi_A + (2-\nu)\chi_S\right]}{2a_r^3\sqrt{1-e_t^2}}, \end{aligned} \tag{D.8}$$

$$\begin{aligned} K &= 1 + \frac{2(\nu-2)\chi_S - 4\delta\chi_A}{L^3} \\ &= 1 - \frac{4\delta\chi_A + 2(2-\nu)\chi_S}{a_r^{3/2}\left(1-e_t^2\right)^{3/2}}. \end{aligned} \tag{D.9}$$

The three eccentricities (e_r, e_t, e_ϕ) agree at LO, and can be related to each other, and to the energy and angular momentum, via

$$e_t = \sqrt{1+2\bar{E}L^2} + \frac{2\bar{E}\left[2\delta\chi_A + (2-\nu)\chi_S\right]}{L\sqrt{1+2\bar{E}L^2}}, \tag{D.10}$$

$$e_\phi = \sqrt{1+2\bar{E}L^2} + \frac{4\bar{E}\left(1+\bar{E}L^2\right)\left[2\delta\chi_A + (2-\nu)\chi_S\right]}{L\sqrt{1+2\bar{E}L^2}}, \tag{D.11}$$

$$\frac{e_r}{e_t} = 1 + \frac{2\bar{E}}{L}\left[2\delta\chi_A + (2-\nu)\chi_S\right], \tag{D.12}$$

$$\frac{e_\phi}{e_t} = 1 + \frac{2\bar{E}}{L}\left[2\delta\chi_A + (2-\nu)\chi_S\right]. \tag{D.13}$$

D.2 Hyperbolic motion

The quasi-Keplerian parametrization for hyperbolic motion [427, 575] can be summarized, up to 1.5PN, by the following equations:

$$r = \bar{a}_r(e_r \cosh \bar{u} - 1), \tag{D.14}$$

$$\bar{n}t = e_t \sinh \bar{u} - \bar{u}, \tag{D.15}$$

$$\phi = 2K \arctan\left[\sqrt{\frac{e_\phi + 1}{e_\phi - 1}} \tanh\frac{\bar{u}}{2}\right]. \tag{D.16}$$

The equations for hyperbolic motion are related to the elliptic-orbit equations via analytic continuation from $\bar{E} < 0$ to $\bar{E} > 0$, and $u \to i\bar{u}$ [427]. In particular, the energy and angular momentum are given by

$$\begin{aligned}
\bar{E} &= \frac{1}{2\bar{a}_r} + \frac{(\nu-2)\chi_S - 2\delta\chi_A}{2\sqrt{\bar{a}_r^5\left(e_r^2-1\right)}}, \\
L &= \sqrt{\bar{a}_r\left(e_r^2-1\right)} - \frac{\left(e_r^2+3\right)\left[2\delta\chi_A + (2-\nu)\chi_S\right]}{2\bar{a}_r\left(e_r^2-1\right)}.
\end{aligned} \tag{D.17}$$

Inverting these expansions, we obtain

$$\bar{a}_r = \frac{1}{2\bar{E}} - \frac{2\delta\chi_A + (2-\nu)\chi_S}{L}, \tag{D.18}$$

and $e_r(\bar{E}, L)$ the same as in Eq. (D.6).

The mean motion $\bar{n}$ and periastron advance K are given by

$$\bar{n} = \frac{2\pi}{T_r} = 2\sqrt{2}\bar{E}^{3/2}$$

$$= \frac{1}{\bar{a}_r^{3/2}} - \frac{3\left[2\delta\chi_A + (2-\nu)\chi_S\right]}{2\bar{a}_r^3\sqrt{e_t^2-1}}, \tag{D.19}$$

$$\begin{aligned} K &= 1 + \frac{2(\nu-2)\chi_S - 4\delta\chi_A}{L^3} \\ &= 1 - \frac{4\delta\chi_A + 2(2-\nu)\chi_S}{\bar{a}_r^{3/2}\left(e_t^2-1\right)^{3/2}}. \end{aligned} \tag{D.20}$$

The eccentricities e_t and e_ϕ are given in terms of energy and angular momentum by Eqs. (D.10) and (D.11), respectively.

Appendix E: SEOB Hamiltonian coefficients

In this Appendix, we present the results of matching the SEOB Hamiltonians using the procedure described in Sec. 5.2.2. Here, we express the multipole constants as

$$\tilde{C}_{i(\mathrm{ES}^2)} \equiv C_{i(\mathrm{ES}^2)} - 1, \quad \tilde{C}_{i(\mathrm{BS}^2)} \equiv C_{i(\mathrm{BS}^2)} - 1, \quad \text{etc.} \tag{E.1}$$

such that the black hole results are easily obtained by setting $\tilde{C}_{\dots} = 0$.

E.1 Coefficients of the $\mathrm{SEOB}^{r_c}_{\mathrm{TM}}$ Hamiltonian

The spin-orbit and spin-cubed PN corrections in Eq. (5.31a) are given by

$$\begin{aligned} G_S = 2\bigg[&1 + \frac{1}{\hat{r}_c}\frac{5\nu}{16} + \frac{27\nu}{16}\hat{p}_r^2 + \frac{1}{\hat{r}_c^2}\left(\frac{41\nu^2}{256} + \frac{51\nu}{8}\right) + \frac{\hat{p}_r^2}{\hat{r}_c}\left(\frac{21\nu}{4} - \frac{49\nu^2}{128}\right) \\ &+ \left(\frac{169\nu^2}{256} - \frac{5\nu}{16}\right)\hat{p}_r^4\bigg]^{-1}, \end{aligned} \tag{E.2a}$$

$$\begin{aligned} G_{S^*} = \frac{3}{2}\bigg[&1 + \frac{1}{\hat{r}_c}\left(\frac{\nu}{2} + \frac{3}{4}\right) + \left(\frac{3\nu}{2} + \frac{5}{4}\right)\hat{p}_r^2 + \frac{\hat{p}_r^2}{\hat{r}_c}\left(-\frac{7\nu^2}{8} + 5\nu - 1\right) \\ &+ \frac{1}{\hat{r}_c^2}\left(\frac{3\nu^2}{8} + \frac{29\nu}{4} + \frac{27}{16}\right) + \left(\frac{3\nu^2}{8} + \frac{25\nu}{12} + \frac{5}{48}\right)\hat{p}_r^4\bigg]^{-1}, \end{aligned} \tag{E.2b}$$

$$\begin{aligned} G_{S^3} = \frac{1}{\hat{r}_c}\bigg\{ &(\boldsymbol{n}\cdot\boldsymbol{\chi}_1)^2\left[(5\nu + (5\nu - 5)X_1)\,\tilde{C}_{1(\mathrm{BS}^3)} + \left(\frac{9\nu X_1}{4} - \frac{9\nu^2}{4}\right)\tilde{C}_{1(\mathrm{ES}^2)} + \left(\frac{9\nu}{2} - 2\right)X_1 \right. \\ &\left. - \frac{5\nu^2}{2} + 2\nu\right] + \boldsymbol{\chi}_1^2\left[((1-\nu)X_1 - \nu)\,\tilde{C}_{1(\mathrm{BS}^3)} + \left(\frac{3\nu^2}{4} - \frac{3\nu X_1}{4}\right)\tilde{C}_{1(\mathrm{ES}^2)} - \frac{\nu^2}{4} + \frac{\nu X_1}{4}\right] \\ &+ \boldsymbol{n}\cdot\boldsymbol{\chi}_1\,\boldsymbol{n}\cdot\boldsymbol{\chi}_2\left[\left(-6\nu^2 - \frac{15\nu X_1}{2}\right)\tilde{C}_{1(\mathrm{ES}^2)} - \frac{5\nu^2}{3} - \frac{2\nu X_1}{3}\right] \\ &+ \boldsymbol{\chi}_1\cdot\boldsymbol{\chi}_2\left[\left(\frac{3\nu^2}{2} + \frac{3\nu X_1}{2}\right)\tilde{C}_{1(\mathrm{ES}^2)} + \frac{4\nu^2}{3} - \frac{5\nu X_1}{12}\right] \end{aligned}$$

$$
\begin{aligned}
&+ \boldsymbol{\chi}_2^2 \left[\left(\frac{3\nu X_2}{4} - \frac{3\nu^2}{4}\right)\tilde{C}_{2(\mathrm{ES}^2)} - \frac{13\nu^2}{12} + \frac{2\nu X_2}{3}\right] \\
&+ (\boldsymbol{n}\cdot\boldsymbol{\chi}_2)^2 \left[\left(\frac{3\nu^2}{4} - \frac{15\nu X_2}{4}\right)\tilde{C}_{2(\mathrm{ES}^2)} + \frac{25\nu^2}{6} - \frac{17\nu X_2}{6}\right]\Bigg\} \\
&+ \frac{\hat{L}^2}{\hat{r}^2}\left[(\boldsymbol{n}\cdot\boldsymbol{\chi}_1)^2\left(\frac{\nu^2}{2} - \frac{\nu X_1}{2}\right) + \boldsymbol{n}\cdot\boldsymbol{\chi}_1\,\boldsymbol{n}\cdot\boldsymbol{\chi}_2\left(\nu^2 - \nu X_1\right) + (\boldsymbol{n}\cdot\boldsymbol{\chi}_2)^2\left(\frac{\nu X_2}{2} - \frac{3\nu^2}{2}\right)\right] \\
&+ \hat{p}_r^2\Bigg[(\boldsymbol{n}\cdot\boldsymbol{\chi}_1)^2\left(\frac{5\nu X_1}{2} - \frac{5\nu^2}{2}\right) + \boldsymbol{n}\cdot\boldsymbol{\chi}_1\,\boldsymbol{n}\cdot\boldsymbol{\chi}_2\left(3\nu X_1 - \nu^2\right) \\
&\qquad + (\boldsymbol{n}\cdot\boldsymbol{\chi}_2)^2\left(\frac{7\nu^2}{2} - \frac{\nu X_2}{2}\right)\Bigg],
\end{aligned} \tag{E.2c}
$$

$$
\tilde{G}_{S^3} = G_{S^3} \text{ with } 1 \leftrightarrow 2. \tag{E.2d}
$$

The spin-squared corrections in Eq. (5.29) are given by

$$
\begin{aligned}
A^{SS} &= \frac{1}{\hat{r}_c^3}\boldsymbol{\chi}_1^2\left(\nu - X_1\right)\tilde{C}_{1(\mathrm{ES}^2)} \\
&+ \frac{1}{\hat{r}_c^4}\Bigg\{\boldsymbol{\chi}_1^2\left[\left(6\nu + (2\nu - 6)X_1\right)\tilde{C}_{1(\mathrm{ES}^2)} - \frac{\nu^2}{2} + 3\nu X_1\right] + \frac{1}{2}\boldsymbol{\chi}_1\cdot\boldsymbol{\chi}_2\left(2\nu - \nu^2\right)\Bigg\} \\
&+ \frac{1}{\hat{r}_c^5}\Bigg\{\boldsymbol{\chi}_1^2\Bigg[\left(-\frac{207\nu^2}{28} + \frac{275\nu}{14} + \left(\frac{533\nu}{28} - \frac{275}{14}\right)X_1\right)\tilde{C}_{1(\mathrm{ES}^2)} + \frac{3\nu^3}{8} - \frac{157\nu^2}{8} \\
&\qquad + \left(\frac{123\nu}{4} - \frac{45\nu^2}{8}\right)X_1\Bigg] + \frac{1}{2}\boldsymbol{\chi}_1\cdot\boldsymbol{\chi}_2\left(\frac{3\nu^3}{4} + \frac{145\nu^2}{8} + \frac{25\nu}{2}\right)\Bigg\} + 1 \leftrightarrow 2,
\end{aligned} \tag{E.3a}
$$

$$
\begin{aligned}
A^{nS} &= \frac{1}{\hat{r}_c^3}\left(\boldsymbol{n}\cdot\boldsymbol{\chi}_1\right)^2\left(3X_1 - 3\nu\right)\tilde{C}_{1(\mathrm{ES}^2)} \\
&+ \frac{1}{\hat{r}_c^4}\Bigg\{(\boldsymbol{n}\cdot\boldsymbol{\chi}_1)^2\left[\left(-3\nu^2 - 9\nu + (9 - 3\nu)X_1\right)\tilde{C}_{1(\mathrm{ES}^2)} - \frac{5\nu^2}{4} - 7\nu X_1\right] \\
&+ \frac{1}{2}(\boldsymbol{n}\cdot\boldsymbol{\chi}_2)(\boldsymbol{n}\cdot\boldsymbol{\chi}_1)\left(\frac{9\nu^2}{2} - \frac{27\nu}{4}\right)\Bigg\} \\
&+ \frac{1}{\hat{r}_c^5}\Bigg\{(\boldsymbol{n}\cdot\boldsymbol{\chi}_1)^2\Bigg[\left(-\frac{7\nu^3}{8} - \frac{641\nu^2}{56} - \frac{150\nu}{7} + \left(-\frac{47\nu^2}{8} + \frac{22\nu}{7} + \frac{150}{7}\right)X_1\right)\tilde{C}_{1(\mathrm{ES}^2)} \\
&\qquad + \frac{11\nu^3}{4} - \frac{71\nu^2}{12} + \left(-\frac{63\nu^2}{4} - \frac{79\nu}{3}\right)X_1\Bigg] \\
&\qquad + \frac{1}{2}(\boldsymbol{n}\cdot\boldsymbol{\chi}_2)(\boldsymbol{n}\cdot\boldsymbol{\chi}_1)\left(\frac{3\nu^3}{2} - \frac{265\nu^2}{6} - \frac{387\nu}{16}\right)\Bigg\} + 1 \leftrightarrow 2,
\end{aligned} \tag{E.3b}
$$

$$
B_p^{nS} = \frac{1}{\hat{r}_c^3}\Bigg\{(\boldsymbol{n}\cdot\boldsymbol{\chi}_1)^2\left[\left(-3\nu^2 + 3\nu + (3\nu - 3)X_1\right)\tilde{C}_{1(\mathrm{ES}^2)} - \frac{5\nu^2}{2} + 4\nu X_1\right]
$$

$$
\begin{aligned}
&\quad + \frac{1}{2}\boldsymbol{n}\cdot\boldsymbol{\chi}_1\,\boldsymbol{n}\cdot\boldsymbol{\chi}_2\left(2\nu^2+\frac{9\nu}{4}\right)\Bigg\}\\
&+\frac{1}{\hat{r}_c^4}\Bigg\{(\boldsymbol{n}\cdot\boldsymbol{\chi}_1)^2\Bigg[\left(\left(-\frac{7\nu^3}{8}-\frac{221\nu^2}{8}+\frac{15\nu}{2}+\left(-\frac{47\nu^2}{8}+\frac{169\nu}{4}-\frac{15}{2}\right)X_1\right)\tilde{C}_{1(\mathrm{ES}^2)}\right.\\
&\quad\left.-\frac{889\nu^2}{24}+\frac{27\nu^3}{8}+\left(\frac{323\nu}{12}-\frac{217\nu^2}{8}\right)X_1\right]\\
&\quad+\frac{1}{2}\boldsymbol{n}\cdot\boldsymbol{\chi}_1\,\boldsymbol{n}\cdot\boldsymbol{\chi}_2\left(\frac{11\nu^3}{4}-\frac{427\nu^2}{24}+\frac{57\nu}{16}\right)\Bigg\}+1\leftrightarrow 2, \qquad \text{(E.3c)}
\end{aligned}
$$

$$
\begin{aligned}
B_{np}^{nS}&=\frac{1}{\hat{r}_c^3}\Bigg\{(\boldsymbol{n}\cdot\boldsymbol{\chi}_1)^2\left(\frac{15\nu^2}{4}-15\nu X_1\right)+\frac{1}{2}\boldsymbol{n}\cdot\boldsymbol{\chi}_1\,\boldsymbol{n}\cdot\boldsymbol{\chi}_2\left(-\frac{15\nu^2}{2}-\frac{45\nu}{4}\right)\Bigg\}\\
&+\frac{1}{\hat{r}_c^4}\Bigg\{(\boldsymbol{n}\cdot\boldsymbol{\chi}_1)^2\Bigg[\left(-\frac{7\nu^3}{2}-\frac{\nu^2}{4}+\frac{9\nu}{2}+\left(\frac{25\nu^2}{2}+\frac{121\nu}{4}-\frac{9}{2}\right)X_1\right)\tilde{C}_{1(\mathrm{ES}^2)}\\
&\quad+\frac{17\nu^3}{8}+\frac{185\nu^2}{24}+\left(-\frac{23\nu^2}{8}-\frac{619\nu}{12}\right)X_1\Bigg]\\
&\quad+\frac{1}{2}\boldsymbol{n}\cdot\boldsymbol{\chi}_1\,\boldsymbol{n}\cdot\boldsymbol{\chi}_2\left(-\frac{47\nu^3}{4}-\frac{4411\nu^2}{24}-\frac{39\nu}{2}\right)\Bigg\}+1\leftrightarrow 2, \qquad \text{(E.3d)}
\end{aligned}
$$

$$
\begin{aligned}
B_{np}^{SS}&=\frac{1}{\hat{r}_c^3}\Bigg\{\boldsymbol{\chi}_1^2\left[\left(-3\nu^2+3\nu+(3\nu-3)X_1\right)\tilde{C}_{1(\mathrm{ES}^2)}-\frac{15\nu^2}{4}+9\nu X_1\right]\\
&\quad+\frac{1}{2}\left(\frac{9\nu^2}{2}+6\nu\right)\boldsymbol{\chi}_1\cdot\boldsymbol{\chi}_2\Bigg\}+\frac{1}{\hat{r}_c^4}\Bigg\{\frac{1}{2}\left(10\nu^3+38\nu^2+20\nu\right)\boldsymbol{\chi}_1\cdot\boldsymbol{\chi}_2\\
&\quad+\boldsymbol{\chi}_1^2\Bigg[\left(-\frac{159\nu^2}{4}+\frac{23\nu}{2}+\left(-12\nu^2+\frac{197\nu}{4}-\frac{23}{2}\right)X_1\right)\tilde{C}_{1(\mathrm{ES}^2)}\\
&\quad+5\nu^3-61\nu^2+\left(\frac{275\nu}{4}-37\nu^2\right)X_1\Bigg]\Bigg\}+1\leftrightarrow 2, \qquad \text{(E.3e)}
\end{aligned}
$$

$$
\begin{aligned}
Q^{S^2}&=\frac{\hat{p}_r^3}{\hat{r}_c^3}\Bigg\{\boldsymbol{n}\cdot\boldsymbol{\chi}_1\,\hat{\boldsymbol{p}}\cdot\boldsymbol{\chi}_1\Bigg[\left(20\nu^3-35\nu^2+\left(35\nu-20\nu^2\right)X_1\right)\tilde{C}_{1(\mathrm{ES}^2)}+\frac{199\nu^3}{8}-\frac{1085\nu^2}{24}\\
&\quad+\left(\frac{130\nu}{3}-\frac{517\nu^2}{8}\right)X_1\Bigg]+\boldsymbol{n}\cdot\boldsymbol{\chi}_1\,\hat{\boldsymbol{p}}\cdot\boldsymbol{\chi}_2\left(-\frac{79\nu^3}{8}+\frac{79\nu^2}{12}+\frac{45\nu}{16}\right)\Bigg\}\\
&+\frac{\hat{p}_r^4}{\hat{r}_c^3}\Bigg\{\boldsymbol{\chi}_1^2\Bigg[\left(5\nu^3-\frac{35\nu^2}{4}+\left(\frac{35\nu}{4}-5\nu^2\right)X_1\right)\tilde{C}_{1(\mathrm{ES}^2)}+\frac{55\nu^3}{8}-\frac{105\nu^2}{8}\\
&\quad+\left(\frac{55\nu}{4}-\frac{145\nu^2}{8}\right)X_1\Bigg]+(\boldsymbol{n}\cdot\boldsymbol{\chi}_1)^2\Bigg[\left(119\nu^2-\frac{1015\nu}{12}\right)X_1-\frac{91\nu^3}{2}+\frac{1015\nu^2}{12}\\
&\quad+\left(\frac{245\nu^2}{4}-35\nu^3+\left(35\nu^2-\frac{245\nu}{4}\right)X_1\right)\tilde{C}_{1(\mathrm{ES}^2)}\Bigg]\\
&\quad+\frac{1}{2}\boldsymbol{\chi}_1\cdot\boldsymbol{\chi}_2\left(-\frac{25\nu^3}{4}+\frac{45\nu^2}{8}+\frac{5\nu}{2}\right)
\end{aligned}
$$

$$+\frac{1}{2}\boldsymbol{n}\cdot\boldsymbol{\chi}_1\,\boldsymbol{n}\cdot\boldsymbol{\chi}_2\left(\frac{77\nu^3}{2}-\frac{721\nu^2}{24}-\frac{105\nu}{8}\right)\Bigg\}+1\leftrightarrow 2. \tag{E.3f}$$

The spin-quartic corrections in Eq. (5.30) are given by

$$\begin{aligned}
A^{S^4}=\frac{1}{\hat{r}_c^5}\Bigg\{&\left(\boldsymbol{n}\cdot\boldsymbol{\chi}_1\right)^4\Bigg[\left(\frac{21\nu^2}{2}-\frac{21\nu}{2}+\left(\frac{21}{2}-21\nu\right)X_1\right)\tilde{C}_{1(\mathrm{ES}^2)}\\
&+\left(-\frac{35\nu^2}{4}+\frac{35\nu}{4}+\left(\frac{35\nu}{2}-\frac{35}{4}\right)X_1\right)\tilde{C}_{1(\mathrm{ES}^4)}\Bigg]\\
&+\boldsymbol{n}\cdot\boldsymbol{\chi}_2\left(\boldsymbol{n}\cdot\boldsymbol{\chi}_1\right)^3\left[\left(35\nu^2-35\nu X_1\right)\tilde{C}_{1(\mathrm{BS}^3)}+\left(21\nu X_1-21\nu^2\right)\tilde{C}_{1(\mathrm{ES}^2)}\right]\\
&+\boldsymbol{\chi}_1\cdot\boldsymbol{\chi}_2\left(\boldsymbol{n}\cdot\boldsymbol{\chi}_1\right)^2\left[\left(15\nu X_1-15\nu^2\right)\tilde{C}_{1(\mathrm{BS}^3)}+\left(3\nu^2-3\nu X_1\right)\tilde{C}_{1(\mathrm{ES}^2)}\right]\\
&+\boldsymbol{\chi}_1^2\left(\boldsymbol{n}\cdot\boldsymbol{\chi}_1\right)^2\Bigg[\left(-\frac{9\nu^2}{2}+\frac{9\nu}{2}+\left(9\nu-\frac{9}{2}\right)X_1\right)\tilde{C}_{1(\mathrm{ES}^2)}\\
&+\left(\frac{15\nu^2}{2}-\frac{15\nu}{2}+\left(\frac{15}{2}-15\nu\right)X_1\right)\tilde{C}_{1(\mathrm{ES}^4)}\Bigg]\\
&+\boldsymbol{\chi}_2^2\left(\boldsymbol{n}\cdot\boldsymbol{\chi}_1\right)^2\left[6\tilde{C}_{2(\mathrm{ES}^2)}\nu^2+\tilde{C}_{1(\mathrm{ES}^2)}\left(\frac{15}{2}\tilde{C}_{2(\mathrm{ES}^2)}\nu^2+\frac{15\nu^2}{2}\right)\right]\\
&+\frac{1}{2}\left(\boldsymbol{n}\cdot\boldsymbol{\chi}_2\right)^2\left(\boldsymbol{n}\cdot\boldsymbol{\chi}_1\right)^2\left[\tilde{C}_{1(\mathrm{ES}^2)}\left(-\frac{1}{2}105\tilde{C}_{2(\mathrm{ES}^2)}\nu^2-42\nu^2\right)-42\nu^2\tilde{C}_{2(\mathrm{ES}^2)}\right]\\
&+\boldsymbol{\chi}_1^2\,\boldsymbol{n}\cdot\boldsymbol{\chi}_2\,\boldsymbol{n}\cdot\boldsymbol{\chi}_1\left[\left(15\nu X_1-15\nu^2\right)\tilde{C}_{1(\mathrm{BS}^3)}+\left(6\nu^2-6\nu X_1\right)\tilde{C}_{1(\mathrm{ES}^2)}\right]\\
&+\frac{1}{2}\boldsymbol{n}\cdot\boldsymbol{\chi}_2\,\boldsymbol{\chi}_1\cdot\boldsymbol{\chi}_2\,\boldsymbol{n}\cdot\boldsymbol{\chi}_1\left[27\tilde{C}_{2(\mathrm{ES}^2)}\nu^2+\tilde{C}_{1(\mathrm{ES}^2)}\left(30\tilde{C}_{2(\mathrm{ES}^2)}\nu^2+27\nu^2\right)\right]\\
&+\boldsymbol{\chi}_1\cdot\boldsymbol{\chi}_2\,\boldsymbol{\chi}_1^2\left(3\nu^2-3\nu X_1\right)\tilde{C}_{1(\mathrm{BS}^3)}+\boldsymbol{\chi}_1^4\left[-\frac{3\nu^2}{4}+\frac{3\nu}{4}+\left(\frac{3\nu}{2}-\frac{3}{4}\right)X_1\right]\tilde{C}_{1(\mathrm{ES}^4)}\\
&+\frac{1}{2}\boldsymbol{\chi}_1^2\boldsymbol{\chi}_2^2\left[\tilde{C}_{1(\mathrm{ES}^2)}\left(-\frac{1}{2}3\tilde{C}_{2(\mathrm{ES}^2)}\nu^2-\frac{3\nu^2}{2}\right)-\frac{3}{2}\nu^2\tilde{C}_{2(\mathrm{ES}^2)}\right]\\
&+\frac{1}{2}\left(\boldsymbol{\chi}_1\cdot\boldsymbol{\chi}_2\right)^2\left[\tilde{C}_{1(\mathrm{ES}^2)}\left(-3\tilde{C}_{2(\mathrm{ES}^2)}\nu^2-3\nu^2\right)-3\nu^2\tilde{C}_{2(\mathrm{ES}^2)}\right]\Bigg\}+1\leftrightarrow 2.
\end{aligned} \tag{E.4}$$

E.2 Coefficients of the $\mathrm{SEOB_{TM}}$ Hamiltonian

The spin-orbit and spin-cubed PN corrections in Eq. (5.34a) are given by

$$G_S=2\Bigg[1-\frac{27}{16}\nu\hat{p}_r^2-\frac{5\nu}{16\hat{r}}+\left(\frac{35\nu^2}{16}+\frac{5\nu}{16}\right)\hat{p}_r^4+\frac{\hat{p}_r^2}{\hat{r}}\left(\frac{23\nu^2}{16}-\frac{21\nu}{4}\right)$$

$$
+\frac{1}{\hat{r}^2}\left(-\frac{\nu^2}{16}-\frac{51\nu}{8}\right)\Bigg], \tag{E.5a}
$$

$$
\begin{aligned}
G_{S^*} = \frac{3}{2}\Bigg[&1-\left(\frac{3\nu}{2}+\frac{5}{4}\right)\hat{p}_r^2-\frac{1}{\hat{r}}\left(\frac{3}{4}+\frac{\nu}{2}\right)+\left(\frac{15\nu^2}{8}+\frac{5\nu}{3}+\frac{35}{24}\right)\hat{p}_r^4 \\
&+\frac{\hat{p}_r^2}{\hat{r}}\left(\frac{19\nu^2}{8}-\frac{3\nu}{2}+\frac{23}{8}\right)+\frac{1}{\hat{r}^2}\left(-\frac{\nu^2}{8}-\frac{13\nu}{2}-\frac{9}{8}\right)\Bigg],
\end{aligned} \tag{E.5b}
$$

$$
\begin{aligned}
G_{S^3} = \frac{1}{\hat{r}}\Bigg\{&\left(\boldsymbol{n}\cdot\boldsymbol{\chi}_1\right)^2\left[\left(5\nu+(5\nu-5)X_1\right)\tilde{C}_{1(\mathrm{BS}^3)}+\left(\frac{9\nu X_1}{4}-\frac{9\nu^2}{4}\right)\tilde{C}_{1(\mathrm{ES}^2)}-2\nu^2+2\nu X_1\right] \\
&+\boldsymbol{\chi}_1^2\left[\left((1-\nu)X_1-\nu\right)\tilde{C}_{1(\mathrm{BS}^3)}+\left(\frac{3\nu^2}{4}-\frac{3\nu X_1}{4}\right)\tilde{C}_{1(\mathrm{ES}^2)}+\frac{\nu^2}{2}-\frac{\nu X_1}{2}\right] \\
&+\boldsymbol{\chi}_1\cdot\boldsymbol{\chi}_2\left[\left(\frac{3\nu^2}{2}+\frac{3\nu X_1}{2}\right)\tilde{C}_{1(\mathrm{ES}^2)}-\frac{\nu^2}{6}-\frac{5\nu X_1}{12}\right] \\
&+\boldsymbol{\chi}_2^2\left[\left(\frac{3\nu X_2}{4}-\frac{3\nu^2}{4}\right)\tilde{C}_{2(\mathrm{ES}^2)}-\frac{\nu^2}{3}-\frac{\nu X_2}{12}\right] \\
&+\boldsymbol{n}\cdot\boldsymbol{\chi}_1\,\boldsymbol{n}\cdot\boldsymbol{\chi}_2\left[\left(-6\nu^2-\frac{15\nu X_1}{2}\right)\tilde{C}_{1(\mathrm{ES}^2)}-\frac{8\nu^2}{3}+\frac{10\nu X_1}{3}\right] \\
&+\left(\boldsymbol{n}\cdot\boldsymbol{\chi}_2\right)^2\left[\left(\frac{3\nu^2}{4}-\frac{15\nu X_2}{4}\right)\tilde{C}_{2(\mathrm{ES}^2)}+\frac{14\nu^2}{3}-\frac{4\nu X_2}{3}\right]\Bigg\} \\
+\frac{\hat{L}^2}{r^2}&\left[\left(\boldsymbol{n}\cdot\boldsymbol{\chi}_1\right)^2\left(\frac{\nu^2}{2}-\frac{\nu X_1}{2}\right)+\boldsymbol{n}\cdot\boldsymbol{\chi}_1\,\boldsymbol{n}\cdot\boldsymbol{\chi}_2\left(\nu^2-\nu X_1\right)+\left(\boldsymbol{n}\cdot\boldsymbol{\chi}_2\right)^2\left(\frac{\nu X_2}{2}-\frac{3\nu^2}{2}\right)\right] \\
+\hat{p}_r^2&\Bigg[\left(\boldsymbol{n}\cdot\boldsymbol{\chi}_1\right)^2\left(\frac{5\nu X_1}{2}-\frac{5\nu^2}{2}\right)+\boldsymbol{n}\cdot\boldsymbol{\chi}_1\,\boldsymbol{n}\cdot\boldsymbol{\chi}_2\left(3\nu X_1-\nu^2\right) \\
&+\left(\boldsymbol{n}\cdot\boldsymbol{\chi}_2\right)^2\left(\frac{7\nu^2}{2}-\frac{\nu X_2}{2}\right)\Bigg],
\end{aligned} \tag{E.5c}
$$

$$
\tilde{G}_{S^3} = G_{S^3} \text{ with } 1 \leftrightarrow 2. \tag{E.5d}
$$

The spin-squared and spin-quartic corrections in Eq. (5.33) read

$$
\begin{aligned}
A^{SS} = &\frac{1}{\hat{r}^3}\boldsymbol{\chi}_1^2\left(\nu-X_1\right)\tilde{C}_{1(\mathrm{ES}^2)} \\
&+\frac{1}{\hat{r}^4}\left\{\boldsymbol{\chi}_1^2\left[\left(4\nu+(2\nu-4)X_1\right)\tilde{C}_{1(\mathrm{ES}^2)}-\frac{\nu^2}{2}+3\nu X_1\right]+\frac{1}{2}\boldsymbol{\chi}_1\cdot\boldsymbol{\chi}_2\left(2\nu-\nu^2\right)\right\} \\
&+\frac{1}{\hat{r}^5}\Bigg\{\boldsymbol{\chi}_1^2\Bigg[\left(-\frac{207\nu^2}{28}+\frac{163\nu}{14}+\left(\frac{421\nu}{28}-\frac{163}{14}\right)X_1\right)\tilde{C}_{1(\mathrm{ES}^2)}+\frac{3\nu^3}{8}-\frac{125\nu^2}{8}
\end{aligned}
$$

$$+\left(\frac{87\nu}{4}-\frac{45\nu^2}{8}\right)X_1\Big] + \frac{1}{2}\boldsymbol{\chi}_1\cdot\boldsymbol{\chi}_2\left(\frac{3\nu^3}{4}+\frac{113\nu^2}{8}+\frac{17\nu}{2}\right)\Bigg\} + 1\leftrightarrow 2, \tag{E.6a}$$

$$\begin{aligned}
A^{nS} &= \frac{1}{\hat{r}^3}\left(\boldsymbol{n}\cdot\boldsymbol{\chi}_1\right)^2\left(3X_1-3\nu\right)\tilde{C}_{1(\mathrm{ES}^2)} \\
&+\frac{1}{\hat{r}^4}\Bigg\{\left(\boldsymbol{n}\cdot\boldsymbol{\chi}_1\right)^2\left[\left(-3\nu^2-9\nu+(9-3\nu)X_1\right)\tilde{C}_{1(\mathrm{ES}^2)}-\frac{5\nu^2}{4}-7\nu X_1\right] \\
&\qquad+\frac{1}{2}\boldsymbol{n}\cdot\boldsymbol{\chi}_1\,\boldsymbol{n}\cdot\boldsymbol{\chi}_2\left(\frac{9\nu^2}{2}-\frac{27\nu}{4}\right)\Bigg\} \\
&+\frac{1}{\hat{r}^5}\Bigg\{\left(\boldsymbol{n}\cdot\boldsymbol{\chi}_1\right)^2\Bigg[\left(-\frac{7\nu^3}{8}-\frac{641\nu^2}{56}-\frac{150\nu}{7}+\left(-\frac{47\nu^2}{8}+\frac{22\nu}{7}+\frac{150}{7}\right)X_1\right)\tilde{C}_{1(\mathrm{ES}^2)} \\
&\qquad\quad+\frac{11\nu^3}{4}-\frac{71\nu^2}{12}+\left(-\frac{63\nu^2}{4}-\frac{79\nu}{3}\right)X_1\Bigg] \\
&\qquad+\frac{1}{2}\boldsymbol{n}\cdot\boldsymbol{\chi}_1\,\boldsymbol{n}\cdot\boldsymbol{\chi}_2\left(\frac{3\nu^3}{2}-\frac{265\nu^2}{6}-\frac{387\nu}{16}\right)\Bigg\}+1\leftrightarrow 2,
\end{aligned} \tag{E.6b}$$

$$\begin{aligned}
B_p^{nS} &= \frac{1}{\hat{r}^3}\Bigg\{\left(\boldsymbol{n}\cdot\boldsymbol{\chi}_1\right)^2\left[\left(3\nu^2-3\nu+(3-3\nu)X_1\right)\tilde{C}_{1(\mathrm{ES}^2)}+\frac{5\nu^2}{2}-4\nu X_1\right] \\
&\qquad+\frac{1}{2}\boldsymbol{n}\cdot\boldsymbol{\chi}_1\,\boldsymbol{n}\cdot\boldsymbol{\chi}_2\left(-2\nu^2-\frac{9\nu}{4}\right)\Bigg\} \\
&+\frac{1}{\hat{r}^4}\Bigg\{\left(\boldsymbol{n}\cdot\boldsymbol{\chi}_1\right)^2\Bigg[\left(\frac{7\nu^3}{8}+\frac{221\nu^2}{8}-\frac{15\nu}{2}+\left(\frac{47\nu^2}{8}-\frac{169\nu}{4}+\frac{15}{2}\right)X_1\right)\tilde{C}_{1(\mathrm{ES}^2)} \\
&\qquad\quad-\frac{27\nu^3}{8}+\frac{889\nu^2}{24}+\left(\frac{217\nu^2}{8}-\frac{323\nu}{12}\right)X_1\Bigg] \\
&\qquad+\frac{1}{2}\boldsymbol{n}\cdot\boldsymbol{\chi}_1\,\boldsymbol{n}\cdot\boldsymbol{\chi}_2\left(-\frac{11\nu^3}{4}+\frac{427\nu^2}{24}-\frac{57\nu}{16}\right)\Bigg\}+1\leftrightarrow 2,
\end{aligned} \tag{E.6c}$$

$$\begin{aligned}
B_{np}^{nS} &= \frac{1}{\hat{r}^3}\Bigg\{\left(\boldsymbol{n}\cdot\boldsymbol{\chi}_1\right)^2\left(\frac{15\nu^2}{4}-15\nu X_1\right)+\frac{1}{2}\boldsymbol{n}\cdot\boldsymbol{\chi}_1\,\boldsymbol{n}\cdot\boldsymbol{\chi}_2\left(-\frac{15\nu^2}{2}-\frac{45\nu}{4}\right)\Bigg\} \\
&+\frac{1}{\hat{r}^4}\Bigg\{\left(\boldsymbol{n}\cdot\boldsymbol{\chi}_1\right)^2\Bigg[\left(-\frac{7\nu^3}{2}-\frac{\nu^2}{4}+\frac{9\nu}{2}+\left(\frac{25\nu^2}{2}+\frac{121\nu}{4}-\frac{9}{2}\right)X_1\right)\tilde{C}_{1(\mathrm{ES}^2)} \\
&\qquad\quad+\frac{17\nu^3}{8}+\frac{365\nu^2}{24}+\left(-\frac{23\nu^2}{8}-\frac{979\nu}{12}\right)X_1\Bigg] \\
&\qquad+\frac{1}{2}\left(-\frac{47\nu^3}{4}-\frac{4771\nu^2}{24}-42\nu\right)\boldsymbol{n}\cdot\boldsymbol{\chi}_1\,\boldsymbol{n}\cdot\boldsymbol{\chi}_2\Bigg\}+1\leftrightarrow 2,
\end{aligned} \tag{E.6d}$$

$$B_{np}^{SS} = \frac{1}{\hat{r}^3}\Bigg\{\boldsymbol{\chi}_1^2\left[\left(-3\nu^2+3\nu+(3\nu-3)X_1\right)\tilde{C}_{1(\mathrm{ES}^2)}-\frac{15\nu^2}{4}+9\nu X_1\right]$$

$$
\begin{aligned}
&\quad + \frac{1}{2}\boldsymbol{\chi}_1\cdot\boldsymbol{\chi}_2\left(\frac{9\nu^2}{2}+6\nu\right)\Bigg\}\\
&+\frac{1}{\hat r^4}\Bigg\{\boldsymbol{\chi}_1^2\Bigg[\left(\left(-\frac{159\nu^2}{4}+\frac{23\nu}{2}+\left(-12\nu^2+\frac{197\nu}{4}-\frac{23}{2}\right)X_1\right)\tilde C_{1(\mathrm{ES}^2)}+5\nu^3-55\nu^2\right.\\
&\quad\left.+\left(\frac{251\nu}{4}-37\nu^2\right)X_1\right]+\frac{1}{2}\boldsymbol{\chi}_1\cdot\boldsymbol{\chi}_2\left(10\nu^3+26\nu^2+20\nu\right)\Bigg\}+1\leftrightarrow 2, \qquad \text{(E.6e)}
\end{aligned}
$$

$$
\begin{aligned}
Q^{S^2}=&\frac{\hat p_r^3}{\hat r^3}\Bigg\{\boldsymbol{n}\cdot\boldsymbol{\chi}_1\,\hat{\boldsymbol{p}}\cdot\boldsymbol{\chi}_1\Bigg[\left(20\nu^3-35\nu^2+\left(35\nu-20\nu^2\right)X_1\right)\tilde C_{1(\mathrm{ES}^2)}+\frac{199\nu^3}{8}-\frac{1085\nu^2}{24}\\
&\quad+\left(\frac{130\nu}{3}-\frac{517\nu^2}{8}\right)X_1\Bigg]+\boldsymbol{n}\cdot\boldsymbol{\chi}_1\,\hat{\boldsymbol{p}}\cdot\boldsymbol{\chi}_2\left(-\frac{79\nu^3}{8}+\frac{79\nu^2}{12}+\frac{45\nu}{16}\right)\Bigg\}\\
&+\frac{\hat p_r^4}{\hat r^3}\Bigg\{\boldsymbol{\chi}_1^2\Bigg[\left(5\nu^3-\frac{35\nu^2}{4}+\left(\frac{35\nu}{4}-5\nu^2\right)X_1\right)\tilde C_{1(\mathrm{ES}^2)}+\frac{55\nu^3}{8}-\frac{105\nu^2}{8}\\
&\quad+\left(\frac{55\nu}{4}-\frac{145\nu^2}{8}\right)X_1\Bigg]+\left(\boldsymbol{n}\cdot\boldsymbol{\chi}_1\right)^2\Bigg[\left(119\nu^2-\frac{1015\nu}{12}\right)X_1-\frac{91\nu^3}{2}\\
&\quad+\frac{1015\nu^2}{12}+\left(\frac{245\nu^2}{4}-35\nu^3+\left(35\nu^2-\frac{245\nu}{4}\right)X_1\right)\tilde C_{1(\mathrm{ES}^2)}\Bigg]\\
&+\frac{1}{2}\boldsymbol{\chi}_1\cdot\boldsymbol{\chi}_2\left(-\frac{25\nu^3}{4}+\frac{45\nu^2}{8}+\frac{5\nu}{2}\right)\\
&+\frac{1}{2}\boldsymbol{n}\cdot\boldsymbol{\chi}_1\,\boldsymbol{n}\cdot\boldsymbol{\chi}_2\left(\frac{77\nu^3}{2}-\frac{721\nu^2}{24}-\frac{105\nu}{8}\right)\Bigg\}+1\leftrightarrow 2, \qquad \text{(E.6f)}
\end{aligned}
$$

$$
\begin{aligned}
A^{S^4}=&\frac{1}{\hat r^5}\Bigg\{\left(\boldsymbol{n}\cdot\boldsymbol{\chi}_1\right)^4\Bigg[\left(\frac{15\nu^2}{2}-\frac{15\nu}{2}+\left(\frac{15}{2}-15\nu\right)X_1\right)\tilde C_{1(\mathrm{ES}^2)}\\
&\quad+\left(\frac{35\nu}{4}-\frac{35\nu^2}{4}+\left(\frac{35\nu}{2}-\frac{35}{4}\right)X_1\right)\tilde C_{1(\mathrm{ES}^4)}\Bigg]\\
&+\boldsymbol{n}\cdot\boldsymbol{\chi}_2\left(\boldsymbol{n}\cdot\boldsymbol{\chi}_1\right)^3\left[\left(35\nu^2-35\nu X_1\right)\tilde C_{1(\mathrm{BS}^3)}+\left(15\nu X_1-15\nu^2\right)\tilde C_{1(\mathrm{ES}^2)}\right]\\
&+\boldsymbol{\chi}_1\cdot\boldsymbol{\chi}_2\left(\boldsymbol{n}\cdot\boldsymbol{\chi}_1\right)^2\left[\left(15\nu X_1-15\nu^2\right)\tilde C_{1(\mathrm{BS}^3)}+\left(12\nu^2-12\nu X_1\right)\tilde C_{1(\mathrm{ES}^2)}\right]\\
&+\boldsymbol{\chi}_1^2\left(\boldsymbol{n}\cdot\boldsymbol{\chi}_1\right)^2\Bigg[\left(-9\nu^2+9\nu+(18\nu-9)X_1\right)\tilde C_{1(\mathrm{ES}^2)}\\
&\quad+\left(\frac{15\nu^2}{2}-\frac{15\nu}{2}+\left(\frac{15}{2}-15\nu\right)X_1\right)\tilde C_{1(\mathrm{ES}^4)}\Bigg]\\
&+\boldsymbol{\chi}_2^2\left(\boldsymbol{n}\cdot\boldsymbol{\chi}_1\right)^2\left[6\tilde C_{2(\mathrm{ES}^2)}\nu^2+\tilde C_{1(\mathrm{ES}^2)}\left(\frac{15}{2}\tilde C_{2(\mathrm{ES}^2)}\nu^2+3\nu^2\right)\right]\\
&+\frac{1}{2}\left(\boldsymbol{n}\cdot\boldsymbol{\chi}_2\right)^2\left(\boldsymbol{n}\cdot\boldsymbol{\chi}_1\right)^2\left[\tilde C_{1(\mathrm{ES}^2)}\left(-\frac{1}{2}105\tilde C_{2(\mathrm{ES}^2)}\nu^2-45\nu^2\right)-45\nu^2\tilde C_{2(\mathrm{ES}^2)}\right]
\end{aligned}
$$

$$
\begin{aligned}
&+ \boldsymbol{n}\cdot\boldsymbol{\chi}_2\,\boldsymbol{\chi}_1^2\boldsymbol{n}\cdot\boldsymbol{\chi}_1\left[\left(15\nu X_1-15\nu^2\right)\tilde{C}_{1(\mathrm{BS}^3)}+\left(6\nu^2-6\nu X_1\right)\tilde{C}_{1(\mathrm{ES}^2)}\right]\\
&+\frac{1}{2}\boldsymbol{n}\cdot\boldsymbol{\chi}_2\,\boldsymbol{\chi}_1\cdot\boldsymbol{\chi}_2\,\boldsymbol{n}\cdot\boldsymbol{\chi}_1\left[27\tilde{C}_{2(\mathrm{ES}^2)}\nu^2+\tilde{C}_{1(\mathrm{ES}^2)}\left(30\tilde{C}_{2(\mathrm{ES}^2)}\nu^2+27\nu^2\right)\right]\\
&+\boldsymbol{\chi}_1\cdot\boldsymbol{\chi}_2\,\boldsymbol{\chi}_1^2\left[\left(3\nu^2-3\nu X_1\right)\tilde{C}_{1(\mathrm{BS}^3)}+\left(3\nu X_1-3\nu^2\right)\tilde{C}_{1(\mathrm{ES}^2)}\right]\\
&-\frac{3}{4}\nu^2\boldsymbol{\chi}_1^2\boldsymbol{\chi}_2^2\tilde{C}_{1(\mathrm{ES}^2)}\tilde{C}_{2(\mathrm{ES}^2)}+\boldsymbol{\chi}_1^4\Bigg[\left(\frac{3\nu^2}{2}-\frac{3\nu}{2}+\left(\frac{3}{2}-3\nu\right)X_1\right)\tilde{C}_{1(\mathrm{ES}^2)}\\
&\qquad+\left(-\frac{3\nu^2}{4}+\frac{3\nu}{4}+\left(\frac{3\nu}{2}-\frac{3}{4}\right)X_1\right)\tilde{C}_{1(\mathrm{ES}^4)}\Bigg]\\
&+\frac{1}{2}\left(\boldsymbol{\chi}_1\cdot\boldsymbol{\chi}_2\right)^2\left[\tilde{C}_{1(\mathrm{ES}^2)}\left(-3\tilde{C}_{2(\mathrm{ES}^2)}\nu^2-3\nu^2\right)-3\nu^2\tilde{C}_{2(\mathrm{ES}^2)}\right]\Bigg\}+1\leftrightarrow 2. \qquad \text{(E.6g)}
\end{aligned}
$$

E.3 Coefficients of the $\mathrm{SEOB}^{r_c,\mathrm{align}}_{\mathrm{TM}}$ Hamiltonian

The coefficients of the $\mathrm{SEOB}^{r_c,\mathrm{align}}_{\mathrm{TM}}$ Hamiltonian are given in Ref. [400], but we rewrite them here for convenience in the notation used in the rest of the paper.

The spin-orbit and spin-cubic correction in Eq. (5.39) are given by

$$
\begin{aligned}
G_S &= 2\Bigg[1+\frac{27}{16}\nu\hat{p}_{r_*}^2+\frac{5\nu}{16\hat{r}_c}+\left(\frac{169\nu^2}{256}-\frac{5\nu}{16}\right)\hat{p}_{r_*}^4+\frac{\hat{p}_{r_*}^2}{\hat{r}_c}\left(12\nu-\frac{49\nu^2}{128}\right)\\
&\qquad+\frac{1}{\hat{r}_c^2}\left(\frac{41\nu^2}{256}+\frac{51\nu}{8}\right)\Bigg]^{-1},\\
G_{S^*} &= \frac{3}{2}\Bigg[1+\frac{1}{\hat{r}_c}\left(\frac{\nu}{2}+\frac{3}{4}\right)+\left(\frac{3\nu}{2}+\frac{5}{4}\right)\hat{p}_{r_*}^2+\left(\frac{3\nu^2}{8}+\frac{25\nu}{12}+\frac{5}{48}\right)\hat{p}_{r_*}^4\\
&\qquad+\frac{\hat{p}_{r_*}^2}{\hat{r}_c}\left(-\frac{7\nu^2}{8}+11\nu+4\right)+\frac{1}{\hat{r}_c^2}\left(\frac{3\nu^2}{8}+\frac{29\nu}{4}+\frac{27}{16}\right)\Bigg]^{-1}, \qquad \text{(E.7a)}\\
G_{S^3} &= \frac{1}{\hat{r}_c}\Bigg\{\chi_1^2\Bigg[\left(1-2\nu+(\nu-1)X_1\right)\tilde{C}_{1(\mathrm{BS}^3)}+\left(\frac{\nu^2}{4}+\frac{5\nu}{4}+\left(\frac{3}{4}-\frac{\nu}{2}\right)X_1-\frac{3}{4}\right)\tilde{C}_{1(\mathrm{ES}^2)}\\
&\qquad+\frac{\nu^2}{4}-\frac{3\nu}{4}+\frac{1}{4}+\left(\frac{\nu}{2}-\frac{1}{4}\right)X_1\Bigg]+\chi_1\chi_2\Bigg[\left(\frac{\nu^2}{4}+2\nu-2\nu X_1\right)\tilde{C}_{1(\mathrm{ES}^2)}\\
&\qquad-\frac{\nu^2}{4}+\frac{\nu}{2}-\frac{\nu X_1}{2}\Bigg]\Bigg\},
\end{aligned}
$$

$$\tilde{G}_{S^3} = G_{S^3} \text{ with } 1\leftrightarrow 2. \qquad \text{(E.7b)}$$

The spin-squared and spin-quartic corrections in Eq. (5.37) are given by

$$\delta a^2_{\rm NLO} = \chi_1^2 \left[\left((4-2\nu)X_1 - 4\nu\right)\tilde{C}_{1({\rm ES}^2)} + \frac{\nu^2}{2} - 3\nu X_1\right] + \frac{1}{2}\chi_1\chi_2\left(\nu^2 - 2\nu\right) + 1 \leftrightarrow 2, \tag{E.8a}$$

$$\begin{aligned}\delta a^2_{\rm NNLO} = \chi_1^2\bigg[&\left(\frac{207\nu^2}{28} - \frac{275\nu}{14} + \left(\frac{275}{14} - \frac{533\nu}{28}\right)X_1\right)\tilde{C}_{1({\rm ES}^2)}\\ &- \frac{3\nu^3}{8} + \frac{157\nu^2}{8} + \left(\frac{45\nu^2}{8} - \frac{123\nu}{4}\right)X_1\bigg]\\ &+ \frac{1}{2}\chi_1\chi_2\left(-\frac{3\nu^3}{4} - \frac{145\nu^2}{8} - \frac{25\nu}{2}\right) + 1 \leftrightarrow 2,\end{aligned} \tag{E.8b}$$

$$\begin{aligned}\delta a^4_{\rm LO} = \chi_1^3\chi_2&\left[\left(3\nu X_1 - 3\nu^2\right)\tilde{C}_{1({\rm BS}^3)} + \left(3\nu^2 - 3\nu X_1\right)\tilde{C}_{1({\rm ES}^2)}\right]\\ &+ \frac{1}{2}\chi_1^2\chi_2^2\left[\tilde{C}_{1({\rm ES}^2)}\left(3\nu^2\tilde{C}_{2({\rm ES}^2)} + 3\nu^2\right) + 3\nu^2\tilde{C}_{2({\rm ES}^2)}\right]\\ &+ \chi_1^4\bigg[\left(-\frac{3\nu^2}{4} + \frac{9\nu}{4} + \left(\frac{3}{4} - \frac{3\nu}{2}\right)X_2 - \frac{3}{4}\right)\tilde{C}^2_{1({\rm ES}^2)}\\ &\quad + \left(-\frac{3\nu^2}{2} + \frac{9\nu}{2} + \left(\frac{3}{2} - 3\nu\right)X_2 - \frac{3}{2}\right)\tilde{C}_{1({\rm ES}^2)}\\ &\quad + \left(\frac{3\nu^2}{4} - \frac{9\nu}{4} + \left(\frac{3\nu}{2} - \frac{3}{4}\right)X_2 + \frac{3}{4}\right)\tilde{C}_{1({\rm ES}^4)}\bigg] + 1 \leftrightarrow 2.\end{aligned} \tag{E.8c}$$

E.4 Coefficients of the SEOB$_{\rm TS}$ Hamiltonian

The spin-squared corrections in Eq. (5.49) are given by

$$\begin{aligned}A^{SS} = &\frac{1}{\hat{r}^3}\boldsymbol{\chi}_1^2\left(\nu - X_1\right)\tilde{C}_{1({\rm ES}^2)}\\ &+ \frac{1}{\hat{r}^4}\left\{\boldsymbol{\chi}_1^2\left[\left(2\nu + (2\nu-2)X_1\right)\tilde{C}_{1({\rm ES}^2)} + \frac{17\nu^2}{6} + \left(\frac{23\nu^2}{6} + \frac{\nu}{6}\right)X_1\right] + \frac{37}{12}\nu^2\boldsymbol{\chi}_1\cdot\boldsymbol{\chi}_2\right\}\\ &+ \frac{1}{\hat{r}^5}\bigg\{\boldsymbol{\chi}_1^2\bigg[\left(-\frac{207\nu^2}{28} + \frac{51\nu}{14} + \left(\frac{309\nu}{28} - \frac{51}{14}\right)X_1\right)\tilde{C}_{1({\rm ES}^2)} + \frac{529\nu^4}{144} - \frac{2353\nu^3}{144} + \frac{55\nu^2}{4}\\ &\quad + \left(\frac{143\nu^3}{72} + \frac{7015\nu^2}{144} - \frac{155\nu}{8}\right)X_1\bigg] + \frac{1}{2}\boldsymbol{\chi}_1\cdot\boldsymbol{\chi}_2\left(\frac{529\nu^4}{72} - \frac{112\nu^3}{3} + \frac{51\nu^2}{8}\right)\bigg\}\\ &+ 1 \leftrightarrow 2,\end{aligned} \tag{E.9a}$$

$$
\begin{aligned}
A^{nS} &= \frac{1}{\hat{r}^3}\left(3X_1-3\nu\right)\tilde{C}_{1(\mathrm{ES}^2)}\left(\boldsymbol{n}\cdot\boldsymbol{\chi}_1\right)^2 \\
&\quad+\frac{1}{\hat{r}^4}\bigg\{\left(\boldsymbol{n}\cdot\boldsymbol{\chi}_1\right)^2\bigg[\left(-3\nu^2-3\nu+(3-3\nu)X_1\right)\tilde{C}_{1(\mathrm{ES}^2)}-\frac{5\nu^3}{4}+\frac{3\nu^2}{2} \\
&\qquad\quad+\left(-\frac{15\nu^2}{4}-6\nu\right)X_1\bigg]+\frac{1}{2}\boldsymbol{n}\cdot\boldsymbol{\chi}_1\,\boldsymbol{n}\cdot\boldsymbol{\chi}_2\left(-\frac{5\nu^3}{2}-\frac{67\nu^2}{4}\right)\bigg\} \\
&\quad+\frac{1}{\hat{r}^5}\bigg\{\left(\boldsymbol{n}\cdot\boldsymbol{\chi}_1\right)^2\bigg[\left(\frac{\nu^3}{4}-\frac{205\nu^2}{28}-\frac{24\nu}{7}+\left(-\frac{37\nu^2}{4}+\frac{64\nu}{7}+\frac{24}{7}\right)X_1\right)\tilde{C}_{1(\mathrm{ES}^2)} \\
&\qquad\quad-\frac{109\nu^4}{12}+\frac{113\nu^3}{4}-\frac{515\nu^2}{12}+\left(-\frac{13\nu^3}{2}-\frac{374\nu^2}{3}+\frac{149\nu}{3}\right)X_1\bigg] \\
&\qquad\quad+\frac{1}{2}\boldsymbol{n}\cdot\boldsymbol{\chi}_1\,\boldsymbol{n}\cdot\boldsymbol{\chi}_2\left(-\frac{109\nu^4}{6}+\frac{133\nu^3}{12}-\frac{1301\nu^2}{48}\right)\bigg\}+1\leftrightarrow 2,
\end{aligned}
\tag{E.9b}
$$

$$
\begin{aligned}
B_p^{nS} &= \frac{1}{\hat{r}^3}\bigg\{\left(\boldsymbol{n}\cdot\boldsymbol{\chi}_1\right)^2\bigg[\left(3\nu^2-3\nu+(3-3\nu)X_1\right)\tilde{C}_{1(\mathrm{ES}^2)}+\frac{5\nu^3}{4}-\frac{29\nu^2}{4}+\left(\frac{13\nu}{2}-\frac{31\nu^2}{4}\right)X_1\bigg] \\
&\qquad+\frac{1}{2}\boldsymbol{n}\cdot\boldsymbol{\chi}_1\,\boldsymbol{n}\cdot\boldsymbol{\chi}_2\left(\frac{5\nu^3}{2}+\frac{15\nu^2}{4}\right)\bigg\} \\
&\quad+\frac{1}{\hat{r}^4}\bigg\{\left(\boldsymbol{n}\cdot\boldsymbol{\chi}_1\right)^2\bigg[\left(-\frac{\nu^3}{4}+\frac{59\nu^2}{2}-\frac{15\nu}{2}+\left(\frac{37\nu^2}{4}-\frac{169\nu}{4}+\frac{15}{2}\right)X_1\right)\tilde{C}_{1(\mathrm{ES}^2)} \\
&\qquad\quad-\frac{31\nu^4}{16}-\frac{413\nu^3}{48}-\frac{101\nu^2}{24}+\left(\frac{13\nu^3}{24}+\frac{763\nu^2}{48}+\frac{155\nu}{24}\right)X_1\bigg] \\
&\qquad\quad+\frac{1}{2}\boldsymbol{n}\cdot\boldsymbol{\chi}_1\,\boldsymbol{n}\cdot\boldsymbol{\chi}_2\left(-\frac{31\nu^4}{8}+\frac{217\nu^3}{6}+\frac{1493\nu^2}{48}\right)\bigg\}+1\leftrightarrow 2,
\end{aligned}
\tag{E.9c}
$$

$$
\begin{aligned}
B_{np}^{nS} &= \frac{1}{\hat{r}^3}\bigg\{\left(\boldsymbol{n}\cdot\boldsymbol{\chi}_1\right)^2\left(-\frac{15\nu^3}{4}+15\nu^2+\left(\frac{75\nu^2}{4}-15\nu\right)X_1\right) \\
&\qquad\quad+\frac{1}{2}\boldsymbol{n}\cdot\boldsymbol{\chi}_1\,\boldsymbol{n}\cdot\boldsymbol{\chi}_2\left(-\frac{15\nu^3}{2}-\frac{45\nu^2}{4}\right)\bigg\} \\
&\quad+\frac{1}{\hat{r}^4}\bigg\{\left(\boldsymbol{n}\cdot\boldsymbol{\chi}_1\right)^2\bigg[\left(\nu^3-\frac{31\nu^2}{4}+\frac{9\nu}{2}+\left(-\nu^2+\frac{121\nu}{4}-\frac{9}{2}\right)X_1\right)\tilde{C}_{1(\mathrm{ES}^2)} \\
&\qquad\quad-\frac{63\nu^4}{16}+\frac{2615\nu^3}{48}-\frac{899\nu^2}{24}+\left(\frac{509\nu^3}{24}-\frac{1331\nu^2}{16}+\frac{1223\nu}{24}\right)X_1\bigg] \\
&\qquad\quad+\frac{1}{2}\boldsymbol{n}\cdot\boldsymbol{\chi}_1\,\boldsymbol{n}\cdot\boldsymbol{\chi}_2\left(-\frac{63\nu^4}{8}-\frac{455\nu^3}{12}+\frac{63\nu^2}{4}\right)\bigg\}+1\leftrightarrow 2,
\end{aligned}
\tag{E.9d}
$$

$$
\begin{aligned}
B_{np}^{SS} &= \frac{1}{\hat{r}^3}\boldsymbol{\chi}_1^2\left[\left(-3\nu^2+3\nu+(3\nu-3)X_1\right)\tilde{C}_{1(\mathrm{ES}^2)}+\frac{9\nu^2}{4}+\left(\frac{3\nu^2}{2}-\frac{3\nu}{2}\right)X_1\right] \\
&\quad+\frac{1}{\hat{r}^4}\bigg\{\boldsymbol{\chi}_1^2\bigg[\left(-\frac{135\nu^2}{4}+\frac{11\nu}{2}+\left(-12\nu^2+\frac{173\nu}{4}-\frac{11}{2}\right)X_1\right)\tilde{C}_{1(\mathrm{ES}^2)}
\end{aligned}
$$

$$
\begin{aligned}
&+\frac{187\nu^4}{48}-\frac{409\nu^3}{48}+\frac{781\nu^2}{72}+\left(-\frac{187\nu^3}{24}+\frac{605\nu^2}{144}-\frac{1807\nu}{72}\right)X_1\Big]\\
&+\frac{1}{2}\boldsymbol{\chi}_1\cdot\boldsymbol{\chi}_2\left(\frac{187\nu^4}{24}-\frac{181\nu^3}{4}-\frac{1213\nu^2}{18}\right)\Bigg\}+1\leftrightarrow 2,
\end{aligned}
\tag{E.9e}
$$

$$
\begin{aligned}
Q^{S^2}=\frac{\hat{p}_r^3}{\hat{r}^3}\Bigg\{&\boldsymbol{n}\cdot\boldsymbol{\chi}_1\hat{\boldsymbol{p}}\cdot\boldsymbol{\chi}_1\Big[\left(20\nu^3-35\nu^2+\left(35\nu-20\nu^2\right)X_1\right)\tilde{C}_{1(\mathrm{ES}^2)}+\frac{45\nu^4}{8}-\frac{425\nu^3}{12}+\frac{35\nu^2}{6}\\
&+\left(-\frac{100\nu^3}{3}+\frac{145\nu^2}{4}-\frac{35\nu}{6}\right)X_1\Big]+\boldsymbol{n}\cdot\boldsymbol{\chi}_1\hat{\boldsymbol{p}}\cdot\boldsymbol{\chi}_2\left[\frac{45\nu^4}{8}+\frac{10\nu^3}{3}-\frac{25\nu^2}{16}\right]\Bigg\}\\
+\frac{\hat{p}_r^4}{\hat{r}^3}\Bigg\{&\left(\boldsymbol{n}\cdot\boldsymbol{\chi}_1\right)^2\Bigg[\left(-35\nu^3+\frac{245\nu^2}{4}+\left(35\nu^2-\frac{245\nu}{4}\right)X_1\right)\tilde{C}_{1(\mathrm{ES}^2)}-\frac{105\nu^4}{16}\\
&+\frac{2135\nu^3}{48}-\frac{35\nu^2}{24}+\left(\frac{1085\nu^3}{24}-\frac{595\nu^2}{16}+\frac{35\nu}{24}\right)X_1\Bigg]\\
&+\boldsymbol{\chi}_1^2\Bigg[\left(5\nu^3-\frac{35\nu^2}{4}+\left(\frac{35\nu}{4}-5\nu^2\right)X_1\right)\tilde{C}_{1(\mathrm{ES}^2)}+\frac{5\nu^4}{16}-\frac{145\nu^3}{48}-\frac{35\nu^2}{24}\\
&\quad+\left(-\frac{95\nu^3}{24}+\frac{5\nu^2}{16}+\frac{35\nu}{24}\right)X_1\Bigg]+\frac{1}{2}\boldsymbol{\chi}_1\cdot\boldsymbol{\chi}_2\left[\frac{5\nu^4}{8}+\frac{55\nu^3}{12}-\frac{5\nu^2}{12}\right]\\
&+\frac{1}{2}\boldsymbol{n}\cdot\boldsymbol{\chi}_1\,\boldsymbol{n}\cdot\boldsymbol{\chi}_2\left[-\frac{105\nu^4}{8}-\frac{245\nu^3}{12}+\frac{35\nu^2}{8}\right]\Bigg\}+1\leftrightarrow 2.
\end{aligned}
\tag{E.9f}
$$

The spin-cubed corrections in Eq. (5.49b) are

$$
\begin{aligned}
G_{S^3}=\frac{1}{\hat{r}}\Bigg\{&\left(\boldsymbol{n}\cdot\boldsymbol{\chi}_1\right)^2\Bigg[\left(5\nu+(5\nu-5)X_1\right)\tilde{C}_{1(\mathrm{BS}^3)}+\left(\left(3\nu^2+\frac{9\nu}{4}\right)X_1-\frac{3\nu^3}{2}-\frac{9\nu^2}{4}\right)\tilde{C}_{1(\mathrm{ES}^2)}\\
&-\nu^4+7\nu^3+\frac{5\nu^2}{4}+\left(3\nu^3-7\nu^2-\frac{5\nu}{4}\right)X_1\Bigg]\\
&+\boldsymbol{\chi}_1^2\left[\left((1-\nu)X_1-\nu\right)\tilde{C}_{1(\mathrm{BS}^3)}+\left(\frac{3\nu^2}{4}-\frac{3\nu X_1}{4}\right)\tilde{C}_{1(\mathrm{ES}^2)}-\frac{5\nu^3}{4}+\frac{3\nu^2X_1}{2}\right]\\
&+\boldsymbol{n}\cdot\boldsymbol{\chi}_1\,\boldsymbol{n}\cdot\boldsymbol{\chi}_2\Bigg[\left(-\frac{7\nu^3}{2}-\frac{5\nu^2}{2}-\frac{15\nu X_1}{2}\right)\tilde{C}_{1(\mathrm{ES}^2)}-2\nu^4+\frac{37\nu^3}{6}-5\nu^2\\
&+\left(\frac{\nu^3}{3}-\frac{11\nu^2}{3}\right)X_1\Bigg]+\boldsymbol{\chi}_1\cdot\boldsymbol{\chi}_2\Bigg[\left(\nu^3+\frac{\nu^2}{2}+\frac{3\nu X_1}{2}\right)\tilde{C}_{1(\mathrm{ES}^2)}\\
&+\frac{17\nu^3}{12}+\nu^2+\left(\frac{5\nu^3}{6}-\frac{7\nu^2}{6}\right)X_1\Bigg]+\left(\boldsymbol{n}\cdot\boldsymbol{\chi}_2\right)^2\Bigg[\left(2\nu^3-\frac{5\nu^2}{4}-\frac{15\nu X_2}{4}\right)\tilde{C}_{2(\mathrm{ES}^2)}\\
&-\nu^4+\frac{89\nu^3}{6}-\frac{5\nu^2}{2}+\left(\frac{8\nu^3}{3}-\frac{25\nu^2}{3}\right)X_2\Bigg]\\
&+\boldsymbol{\chi}_2^2\left[\left(-\nu^3+\frac{\nu^2}{4}+\frac{3\nu X_2}{4}\right)\tilde{C}_{2(\mathrm{ES}^2)}-\frac{31\nu^3}{6}+\frac{\nu^2}{2}+\left(\frac{8\nu^2}{3}-\frac{5\nu^3}{6}\right)X_2\right]\Bigg\}
\end{aligned}
$$

$$
+\frac{\hat{L}^2}{\hat{r}^2}\Bigg[(\boldsymbol{n}\cdot\boldsymbol{\chi}_1)^2\left(\frac{\nu^4}{2}-\frac{3\nu^3}{2}+\frac{\nu^2}{2}+\left(-\frac{3\nu^3}{2}+2\nu^2-\frac{\nu}{2}\right)X_1\right)
$$

$$
+\boldsymbol{n}\cdot\boldsymbol{\chi}_1\,\boldsymbol{n}\cdot\boldsymbol{\chi}_2\left(\nu^4-\nu^3X_1\right)+(\boldsymbol{n}\cdot\boldsymbol{\chi}_2)^2\left(\frac{\nu^4}{2}-\frac{\nu^3X_2}{2}\right)\Bigg]
$$

$$
+\hat{p}_r^2\Bigg[(\boldsymbol{n}\cdot\boldsymbol{\chi}_1)^2\left(-\frac{5\nu^4}{2}+\frac{15\nu^3}{2}-\frac{5\nu^2}{2}+\left(\frac{15\nu^3}{2}-10\nu^2+\frac{5\nu}{2}\right)X_1\right)
$$

$$
+\boldsymbol{n}\cdot\boldsymbol{\chi}_1\,\boldsymbol{n}\cdot\boldsymbol{\chi}_2\left(5\nu^3X_1-5\nu^4\right)+(\boldsymbol{n}\cdot\boldsymbol{\chi}_2)^2\left(\frac{5\nu^3X_2}{2}-\frac{5\nu^4}{2}\right)\Bigg], \tag{E.10a}
$$

$$
\tilde{G}_{S^3}=G_{S^3}\text{ with }1\leftrightarrow 2. \tag{E.10b}
$$

The spin-quartic corrections in Eq. (5.49) read

$$
A^{S^4}=\frac{1}{\hat{r}^5}\Bigg\{(\boldsymbol{n}\cdot\boldsymbol{\chi}_1)^4\Bigg[\left(-\frac{15\nu^3}{2}+\frac{45\nu^2}{2}-\frac{15\nu}{2}+\left(\frac{45\nu^2}{2}-30\nu+\frac{15}{2}\right)X_1\right)\tilde{C}_{1(\mathrm{ES}^2)}
$$

$$
-\frac{63\nu^4}{4}+36\nu^3+3\nu^2+\left(46\nu^3-33\nu^2-3\nu\right)X_1
$$

$$
+\left(-\frac{35\nu^2}{4}+\frac{35\nu}{4}+\left(\frac{35\nu}{2}-\frac{35}{4}\right)X_1\right)\tilde{C}_{1(\mathrm{ES}^4)}\Bigg]
$$

$$
+\boldsymbol{n}\cdot\boldsymbol{\chi}_2\,(\boldsymbol{n}\cdot\boldsymbol{\chi}_1)^3\Big[-3\nu^4+3\nu^3+\left(6\nu^3-6\nu^2\right)X_1+\left(3\nu^2-3\nu X_1\right)\tilde{C}_{1(\mathrm{BS}^3)}
$$

$$
+\left(3\nu^2X_1-3\nu^3\right)\tilde{C}_{1(\mathrm{ES}^2)}\Big]+\boldsymbol{\chi}_1^2\,(\boldsymbol{n}\cdot\boldsymbol{\chi}_1)^2\Bigg[\frac{21\nu^4}{2}-27\nu^3-3\nu^2
$$

$$
+\left(9\nu^3-27\nu^2+9\nu+\left(-27\nu^2+36\nu-9\right)X_1\right)\tilde{C}_{1(\mathrm{ES}^2)}
$$

$$
+\left(-33\nu^3+24\nu^2+3\nu\right)X_1+\left(\frac{15\nu^2}{2}-\frac{15\nu}{2}+\left(\frac{15}{2}-15\nu\right)X_1\right)\tilde{C}_{1(\mathrm{ES}^4)}\Bigg]
$$

$$
+\boldsymbol{\chi}_2^2\,(\boldsymbol{n}\cdot\boldsymbol{\chi}_1)^2\Big[-63\nu^4+58\nu^3+\left(35\nu^2-35\nu X_2\right)\tilde{C}_{2(\mathrm{BS}^3)}
$$

$$
+\left(104\nu^3-93\nu^2\right)X_2+\left(\left(6\nu^3+12\nu^2\right)X_2-12\nu^3\right)\tilde{C}_{2(\mathrm{ES}^2)}\Big]
$$

$$
+\boldsymbol{\chi}_1\cdot\boldsymbol{\chi}_2\,(\boldsymbol{n}\cdot\boldsymbol{\chi}_1)^2\Bigg[\left(-\frac{21\nu^3}{2}-\frac{105\nu^2}{2}+\left(\frac{21\nu^2}{2}-6\nu^3\right)X_1\right)\tilde{C}_{2(\mathrm{ES}^2)}
$$

$$
+\tilde{C}_{1(\mathrm{ES}^2)}\left(-\frac{33\nu^3}{2}-\frac{105}{2}\tilde{C}_{2(\mathrm{ES}^2)}\nu^2-42\nu^2+\left(6\nu^3-\frac{21\nu^2}{2}\right)X_1\right)
$$

$$
-\frac{189\nu^4}{2}+54\nu^3-42\nu^2\Bigg]
$$

$$
\begin{aligned}
&+\frac{1}{2}\left(\boldsymbol{n}\cdot\boldsymbol{\chi}_2\right)^2\left(\boldsymbol{n}\cdot\boldsymbol{\chi}_1\right)^2\bigg[\left(9\nu^3-27\nu^2+9\nu+\left(-27\nu^2+36\nu-9\right)X_2\right)\tilde{C}_{2(\mathrm{ES}^2)}\\
&\quad+\frac{21\nu^4}{2}-27\nu^3-3\nu^2+\left(-33\nu^3+24\nu^2+3\nu\right)X_2\\
&\quad+\left(\frac{15\nu^2}{2}-\frac{15\nu}{2}+\left(\frac{15}{2}-15\nu\right)X_2\right)\tilde{C}_{2(\mathrm{ES}^4)}\bigg]\\
&+\boldsymbol{n}\cdot\boldsymbol{\chi}_2\,\boldsymbol{\chi}_1^2\boldsymbol{n}\cdot\boldsymbol{\chi}_1\bigg[\left(-2\nu^4-6\nu^3+\frac{9\nu^2}{2}\right)X_1+\left(\frac{3\nu^3}{2}-\frac{3X_1\nu^2}{2}+\frac{15\nu^2}{2}\right)\tilde{C}_{2(\mathrm{ES}^2)}\\
&\quad+\frac{23\nu^4}{2}-\frac{15\nu^3}{2}+\frac{9\nu^2}{2}+\tilde{C}_{1(\mathrm{ES}^2)}\left(\frac{9\nu^3}{2}+\frac{9X_1\nu^2}{2}+\frac{15}{2}\tilde{C}_{2(\mathrm{ES}^2)}\nu^2+3\nu^2\right)\bigg]\\
&+\frac{1}{2}\boldsymbol{n}\cdot\boldsymbol{\chi}_2\,\boldsymbol{\chi}_1\cdot\boldsymbol{\chi}_2\,\boldsymbol{n}\cdot\boldsymbol{\chi}_1\bigg[\left(\frac{9\nu^2}{2}-2\nu^4-6\nu^3\right)X_2+\left(\frac{9\nu^3}{2}+\frac{9X_2\nu^2}{2}+3\nu^2\right)\tilde{C}_{2(\mathrm{ES}^2)}\\
&\quad+\frac{23\nu^4}{2}-\frac{15\nu^3}{2}+\frac{9\nu^2}{2}+\tilde{C}_{1(\mathrm{ES}^2)}\left(\frac{3\nu^3}{2}+\frac{15}{2}\tilde{C}_{2(\mathrm{ES}^2)}\nu^2-\frac{3X_2\nu^2}{2}+\frac{15\nu^2}{2}\right)\bigg]\\
&+\boldsymbol{\chi}_1^4\bigg[\left(3\nu^3-3\nu^2\right)X_1+\left(-\frac{3\nu^3}{2}+\frac{9\nu^2}{2}-\frac{3\nu}{2}+\left(\frac{9\nu^2}{2}-6\nu+\frac{3}{2}\right)X_1\right)\tilde{C}_{1(\mathrm{ES}^2)}\\
&\quad-\frac{3\nu^4}{4}+3\nu^3+\left(-\frac{3\nu^2}{4}+\frac{3\nu}{4}+\left(\frac{3\nu}{2}-\frac{3}{4}\right)X_1\right)\tilde{C}_{1(\mathrm{ES}^4)}\bigg]\\
&+\frac{1}{2}\left(\boldsymbol{\chi}_1\cdot\boldsymbol{\chi}_2\right)^2\Big[-3\nu^4+3\nu^3+\left(6\nu^3-6\nu^2\right)X_2+\left(3\nu^2-3\nu X_2\right)\tilde{C}_{2(\mathrm{BS}^3)}\\
&\quad+\left(3\nu^2X_2-3\nu^3\right)\tilde{C}_{2(\mathrm{ES}^2)}\Big]\\
&+\frac{1}{2}\boldsymbol{\chi}_1^2\boldsymbol{\chi}_2^2\bigg[18\nu^4-\frac{55\nu^3}{2}+\left(-2\nu^4-47\nu^3+\frac{85\nu^2}{2}\right)X_2+\left(15\nu X_2-15\nu^2\right)\tilde{C}_{2(\mathrm{BS}^3)}\\
&\quad+\left(9\nu^3+\left(-6\nu^3-9\nu^2\right)X_2\right)\tilde{C}_{2(\mathrm{ES}^2)}\bigg]\\
&+\boldsymbol{\chi}_1\cdot\boldsymbol{\chi}_2\,\boldsymbol{\chi}_1^2\bigg[-\frac{3\nu^4}{2}+3\nu^3-\frac{3\nu^2}{2}+\left(-\frac{3\nu^3}{2}+\frac{3X_1\nu^2}{2}-\frac{3\nu^2}{2}\right)\tilde{C}_{2(\mathrm{ES}^2)}\\
&\quad+\tilde{C}_{1(\mathrm{ES}^2)}\left(-\frac{3\nu^3}{2}-\frac{3}{2}\tilde{C}_{2(\mathrm{ES}^2)}\nu^2-\frac{3X_1\nu^2}{2}\right)\bigg]\bigg\}+1\leftrightarrow2, \qquad \text{(E.11a)}
\end{aligned}
$$

$$
\begin{aligned}
Q^{S^4}=\;&\frac{\hat{p}_r^2}{\hat{r}^4}\Big\{\boldsymbol{\chi}_1\cdot\boldsymbol{\chi}_2\left(\boldsymbol{n}\cdot\boldsymbol{\chi}_1\right)^2\left[9\nu^4-3\nu^3+\left(6\nu^4-12\nu^3+3\nu^2\right)X_1\right]\\
&\quad+\boldsymbol{\chi}_1^2\boldsymbol{n}\cdot\boldsymbol{\chi}_1\,\boldsymbol{n}\cdot\boldsymbol{\chi}_2\left[-9\nu^4+3\nu^3+\left(-6\nu^4+12\nu^3-3\nu^2\right)X_1\right]\\
&\quad+\boldsymbol{\chi}_2^2\left(\boldsymbol{n}\cdot\boldsymbol{\chi}_1\right)^2\left(3\nu^4-6\nu^4X_2\right)\Big\}\\
&+\frac{\hat{p}_r}{\hat{r}^4}\Big\{\hat{\boldsymbol{p}}\cdot\boldsymbol{\chi}_1\Big[\left(\boldsymbol{n}\cdot\boldsymbol{\chi}_2\right)^3\left(-12\nu^4+4\nu^3+\left(-8\nu^4+16\nu^3-4\nu^2\right)X_2\right)
\end{aligned}
$$

$$
\begin{aligned}
&+ \boldsymbol{n}\cdot\boldsymbol{\chi}_1\boldsymbol{\chi}_2^2\left(8\nu^4 X_2 - 4\nu^4\right) + \boldsymbol{n}\cdot\boldsymbol{\chi}_1\left(\boldsymbol{n}\cdot\boldsymbol{\chi}_2\right)^2\left(8\nu^4 - 16\nu^4 X_2\right)\\
&+ \boldsymbol{\chi}_2^2\boldsymbol{n}\cdot\boldsymbol{\chi}_2\left(12\nu^4 - 4\nu^3 + \left(8\nu^4 - 16\nu^3 + 4\nu^2\right)X_2\right)\\
&+ \left(\boldsymbol{n}\cdot\boldsymbol{\chi}_1\right)^2\boldsymbol{n}\cdot\boldsymbol{\chi}_2\left(20\nu^4 - 20\nu^3 + 4\nu^2 + \left(-8\nu^4 + 16\nu^3 - 4\nu^2\right)X_2\right)\\
&+ \boldsymbol{n}\cdot\boldsymbol{\chi}_1\boldsymbol{\chi}_1\cdot\boldsymbol{\chi}_2\left(-20\nu^4 + 20\nu^3 - 4\nu^2 + \left(8\nu^4 - 16\nu^3 + 4\nu^2\right)X_2\right)\Bigg]\Bigg\} + 1 \leftrightarrow 2.
\end{aligned}
\tag{E.11b}
$$

Appendix F: Coordinate transformation from harmonic to EOB coordinates

The coordinate transformation from harmonic to EOB coordinates with no spin is given in Appendix A of Ref. [402]. In this appendix, we include LO SO and SS contributions to the transformation. We label harmonic, ADM, and EOB coordinates by $(\boldsymbol{x}_h, \boldsymbol{v}_h)$, $(\boldsymbol{x}_a, \boldsymbol{p}_a)$, and $(\boldsymbol{x}, \boldsymbol{p})$, respectively.

F.1 ADM to EOB transformation

To find the canonical transformation from the ADM Hamiltonian with LO SO and SS using the NW SSC (see e.g. Refs. [101, 384, 780]) and the 2PN expansion of the EOB Hamiltonian of Ref. [382], we write an ansatz with unknown coefficients for the generating function $G(\boldsymbol{x}, \boldsymbol{p})$, perform the following transformation on the ADM Hamiltonian [380]:

$$\begin{aligned} x_a^i &= x^i + \frac{\partial G}{\partial p_i} - \frac{\partial G}{\partial x^j}\frac{\partial^2 G}{\partial p_j \partial p_i} + \mathcal{O}\left(\frac{1}{c^6}\right), \\ p_a^i &= p^i - \frac{\partial G}{\partial x_i} + \frac{\partial G}{\partial x^j}\frac{\partial^2 G}{\partial p_j \partial x^i} + \mathcal{O}\left(\frac{1}{c^6}\right), \end{aligned} \tag{F.1}$$

and match it to the EOB Hamiltonian to solve for the unknowns.

The result for the generating function is given by

$$\begin{aligned} G(x,p) = \frac{p_r}{c^2}\left[-1 - \frac{\nu}{2} + \frac{1}{2}\nu p^2 r\right] + \frac{p_r}{c^4}\left[\frac{1}{8}\nu(3\nu-1)p^4 r - \frac{1}{8}\nu(\nu+14)p^2 - \frac{\nu^2 - 7\nu + 1}{4r}\right. \\ \left. + \frac{1}{8}\nu^2 p_r^2\right] + \frac{\nu^2}{2c^4 r}\left[p_r(\hat{\boldsymbol{S}}_1 + \hat{\boldsymbol{S}}_2)^2 - (\boldsymbol{n}\cdot\hat{\boldsymbol{S}}_1 + \boldsymbol{n}\cdot\hat{\boldsymbol{S}}_2)(\boldsymbol{p}\cdot\hat{\boldsymbol{S}}_1 + \boldsymbol{p}\cdot\hat{\boldsymbol{S}}_2)\right], \end{aligned} \tag{F.2}$$

which has no LO SO terms since the ADM and EOB Hamiltonian are the same at that order. This generating function yields

$$
\begin{aligned}
\boldsymbol{x}_a = \boldsymbol{x} &+ \frac{1}{c^2}\left[\boldsymbol{x}\left(\frac{\nu p^2}{2} - \frac{\nu+2}{2r}\right) + \nu r p_r \boldsymbol{p}\right] + \frac{1}{c^4}\Bigg\{\boldsymbol{x}\left[\frac{3(\nu-2)\nu p^2}{8r} - \frac{1}{8}\nu(\nu+1)p^4\right.\\
&\left. - \frac{\nu(5\nu+16)p_r^2}{8r} - \frac{\nu^2-7\nu+1}{4r^2}\right] + \boldsymbol{p}p_r\left[\frac{1}{2}(\nu-1)\nu p^2 r + \frac{(\nu-10)\nu}{4}\right]\\
&+ \frac{\nu^2}{2r}\left[(\hat{\boldsymbol{S}}_1+\hat{\boldsymbol{S}}_2)^2\frac{\boldsymbol{x}}{r} - (\hat{\boldsymbol{S}}_1+\hat{\boldsymbol{S}}_2)(\boldsymbol{n}\cdot\hat{\boldsymbol{S}}_1 + \boldsymbol{n}\cdot\hat{\boldsymbol{S}}_2)\right]\Bigg\},\\
\boldsymbol{p}_a = \boldsymbol{p} &+ \frac{1}{c^2}\left[\boldsymbol{p}\left(\frac{\nu+2}{2r} - \frac{\nu p^2}{2}\right) - \boldsymbol{x}\frac{(\nu+2)p_r}{2r^2}\right] + \frac{1}{c^4}\Bigg\{\boldsymbol{p}\left[\frac{1}{8}\nu(3\nu+1)p^4 - \frac{\nu(7\nu+2)p^2}{8r}\right.\\
&\left. + \frac{\nu(\nu+8)p_r^2}{8r} + \frac{2\nu^2-3\nu+5}{4r^2}\right] + \boldsymbol{x}p_r\left[\frac{3(\nu-2)\nu p^2}{8r^2} - \frac{3\nu^2-10\nu+6}{4r^3} + \frac{3\nu^2 p_r^2}{8r^2}\right]\\
&+ \frac{\nu^2\boldsymbol{x}}{r^3}\left[(\hat{\boldsymbol{S}}_1+\hat{\boldsymbol{S}}_2)^2 p_r - (\boldsymbol{n}\cdot\hat{\boldsymbol{S}}_1 + \boldsymbol{n}\cdot\hat{\boldsymbol{S}}_2)(\boldsymbol{p}\cdot\hat{\boldsymbol{S}}_1 + \boldsymbol{p}\cdot\hat{\boldsymbol{S}}_2)\right]\\
&+ \frac{\nu^2}{2r^2}\left[-(\hat{\boldsymbol{S}}_1+\hat{\boldsymbol{S}}_2)^2\boldsymbol{p} + (\hat{\boldsymbol{S}}_1+\hat{\boldsymbol{S}}_2)(\boldsymbol{p}\cdot\hat{\boldsymbol{S}}_1 + \boldsymbol{p}\cdot\hat{\boldsymbol{S}}_2)\right]\Bigg\}.
\end{aligned}
\tag{F.3}
$$

F.2 Harmonic to EOB transformation

The transformation from harmonic to ADM coordinates is given by Eq. (E1) of Ref. [402], which is independent of spin since the ADM and harmonic coordinates agree at LO SO and SS. Using that equation together with Eq. (F.3), we obtain the following transformation from harmonic to EOB coordinates:

$$
\begin{aligned}
\boldsymbol{x}_h = \boldsymbol{x} &+ \frac{1}{c^2}\left[\boldsymbol{x}\left(\frac{\nu p^2}{2} - \frac{\nu+2}{2r}\right) + \nu r p_r \boldsymbol{p}\right] + \frac{1}{c^4}\Bigg\{\boldsymbol{x}\left[-\frac{1}{8}\nu(\nu+1)p^4 + \frac{(3\nu-1)\nu p^2}{8r}\right.\\
&\left. - \frac{\nu(5\nu+17)p_r^2}{8r} - \frac{(\nu-19)\nu}{4r^2}\right] + \boldsymbol{p}p_r\left[\frac{1}{4}(\nu-19)\nu + \frac{1}{2}(\nu-1)\nu p^2 r\right]\\
&+ \frac{\nu^2}{2r}\left[(\hat{\boldsymbol{S}}_1+\hat{\boldsymbol{S}}_2)^2\frac{\boldsymbol{x}}{r} - (\hat{\boldsymbol{S}}_1+\hat{\boldsymbol{S}}_2)(\boldsymbol{n}\cdot\hat{\boldsymbol{S}}_1 + \boldsymbol{n}\cdot\hat{\boldsymbol{S}}_2)\right]\Bigg\},\\
\boldsymbol{v}_h = \boldsymbol{p} &+ \frac{1}{c^2}\left[\boldsymbol{p}\left(\left(\nu - \frac{1}{2}\right)p^2 - \frac{\nu+4}{2r}\right) - \boldsymbol{x}\frac{(3\nu+2)p_r}{2r^2}\right]\\
&- \frac{1}{4c^3 r^2}\left[\boldsymbol{n}\times\hat{\boldsymbol{S}}_1(3-3\delta+2\nu) + \boldsymbol{n}\times\hat{\boldsymbol{S}}_2(3+3\delta+2\nu)\right]
\end{aligned}
$$

$$
\begin{aligned}
&+\frac{1}{c^4}\Bigg\{\boldsymbol{p}\left[\left(\frac{3}{8}-\nu\right)p^4+\frac{(7\nu^2-41\nu+8)\,p^2}{8r}+\frac{(-15\nu^2+29\nu+8)\,p_r^2}{8r}+\frac{-\nu^2+15\nu+1}{2r^2}\right]\\
&+\boldsymbol{x}p_r\left[\frac{(4-7\nu^2-23\nu)\,p^2}{8r^2}+\frac{4-3\nu^2+9\nu}{4r^3}+\frac{3\nu(5\nu+1)p_r^2}{8r^2}\right]\\
&+\frac{\nu^2}{2r^2}\left[(\hat{\boldsymbol{S}}_1+\hat{\boldsymbol{S}}_2)(\boldsymbol{p}\cdot\hat{\boldsymbol{S}}_1+\boldsymbol{p}\cdot\hat{\boldsymbol{S}}_2)-(\hat{\boldsymbol{S}}_1+\hat{\boldsymbol{S}}_2)^2\boldsymbol{p}\right]\\
&+\frac{\nu^2\boldsymbol{x}}{r^3}\left[(\hat{\boldsymbol{S}}_1+\hat{\boldsymbol{S}}_2)^2p_r-(\boldsymbol{n}\cdot\hat{\boldsymbol{S}}_1+\boldsymbol{n}\cdot\hat{\boldsymbol{S}}_2)(\boldsymbol{p}\cdot\hat{\boldsymbol{S}}_1+\boldsymbol{p}\cdot\hat{\boldsymbol{S}}_2)\right]\Bigg\},
\end{aligned}
\tag{F.4}
$$

and for the scalars $(\phi, r, \dot{\phi}, \dot{r})$, we obtain

$$
\begin{aligned}
\phi_h &= \phi+\frac{p_\phi\nu p_r}{c^2r}+\frac{p_rp_\phi}{c^4}\left[\frac{3(\nu-5)\nu}{4r^2}-\frac{\nu p^2}{2r}-\frac{\nu^2p_r^2}{r}\right],\\
r_h &= r+\frac{1}{c^2}\left(\frac{\nu}{2}p^2r+\nu rp_r^2-1-\frac{\nu}{2}\right)+\frac{1}{c^4}\bigg[\frac{\nu}{8}(3\nu-1)p^2-\frac{\nu}{8}(\nu+1)p^4r-\frac{\nu}{4r}(\nu-19)\\
&\quad+\frac{\nu}{2}(2\nu-1)p^2p_r^2r-\frac{\nu}{8}(3\nu+55)p_r^2-\frac{1}{2}\nu^2rp_r^4+\frac{1}{2r}\left(X_1^4\chi_1^2+2\nu^2\chi_1\chi_2+X_2^4\chi_2^2\right)\bigg],\\
\dot{\phi}_h &= \frac{p_\phi}{r^2}+\frac{p_\phi}{c^2r^2}\left[\frac{\nu-1}{2}p^2-2\nu p_r^2-\frac{1}{r}\right]+\frac{1}{2r^3c^3}\Big[\chi_1(2+2\delta-\nu)+\chi_2(2-2\delta-\nu)\Big]\\
&\quad+\frac{p_\phi}{c^4r^2}\bigg[4\nu^2p_r^4+\frac{(3\nu^2-17\nu+2)\,p^2}{4r}-2(\nu-1)\nu p_r^2p^2-\frac{(\nu^2+5\nu-3)\,p^4}{8}\\
&\quad+\frac{4-5\nu^2+65\nu}{4r}p_r^2-\frac{\nu^2-9\nu+2}{4r^2}+\frac{1}{2r^2}\left(X_1^4\chi_1^2+2\nu^2\chi_1\chi_2+X_2^4\chi_2^2\right)\bigg],\\
\dot{r}_h &= p_r+\frac{p_r}{c^2}\left[\left(2\nu-\frac{1}{2}\right)p^2-(2\nu+3)\frac{1}{r}-\nu p_r^2\right]+\frac{p_r}{c^4}\bigg[\left(\nu^2-2\nu+\frac{3}{8}\right)p^4\\
&\quad+\frac{(\nu^2-55\nu+6)\,p^2}{4r}+\left(\nu-\frac{5\nu^2}{2}\right)p_r^2p^2+\frac{4-\nu^2+39\nu}{4r}p_r^2+\frac{3}{2}\nu^2p_r^4\\
&\quad+\frac{6-5\nu^2+39\nu}{4r^2}+\frac{1}{2r^2}\left(X_1^4\chi_1^2+2\nu^2\chi_1\chi_2+X_2^4\chi_2^2\right)\bigg].
\end{aligned}
\tag{F.5}
$$

F.3 Transformation for the SSC

When calculating the spin contributions to the waveform modes, we used the source moments from Refs. [166, 173] which are in terms of the covariant SSC. To transform the resulting modes to the NW SSC, we use the center-of-mass shift [164]

$$x^i_{A(\text{cov})} \to x^i_A + \frac{1}{2c^3 m_A}(\boldsymbol{v}_A \times \boldsymbol{S}_A)^i, \tag{F.6}$$

and the spin transformation [97]

$$\boldsymbol{S}_1^{\text{cov}} = \left(1 - \frac{m_2}{c^2 r}\right)\boldsymbol{S}_1 + \frac{1}{2c^2}\boldsymbol{v}_1(\boldsymbol{v}_1 \cdot \boldsymbol{S}_1), \tag{F.7}$$

where the spin transformation is only required for the NLO SO part of the 2PN $(2,1)$ mode.

For the scalars $(r, \phi, \dot{r}, \dot{\phi}, \chi_1, \chi_2)$, we obtain the transformations

$$\begin{aligned}
r_{\text{cov}} &= r - \frac{\nu r \dot{\phi}}{2c^3}(\chi_1 + \chi_2),\\
\phi_{\text{cov}} &= \phi + \frac{\nu \dot{r}}{2c^3 r}(\chi_1 + \chi_2),\\
\dot{r}_{\text{cov}} &= \dot{r} + \frac{\nu \dot{r}\dot{\phi}}{2c^3}(\chi_1 + \chi_2),\\
\dot{\phi}_{\text{cov}} &= \dot{\phi} - \frac{\nu}{2c^3 r^3}\left(1 + r\dot{r}^2 - r^3\dot{\phi}^2\right)(\chi_1 + \chi_2),\\
\chi_1^{\text{cov}} &= \chi_1 - \frac{\chi_1}{2c^2 r}(1 - \delta),\\
\chi_2^{\text{cov}} &= \chi_2 - \frac{\chi_2}{2c^2 r}(1 + \delta).
\end{aligned} \tag{F.8}$$

Appendix G: Angular momentum flux at leading-order spin-squared

In this appendix, we derive the angular momentum flux at leading spin-squared (S_i^2) order. Here, we use unscaled variables in *harmonic* coordinates, but we drop the subscript 'h' to simplify the notation. We denote the orbital angular momentum $\boldsymbol{L} = \mu\boldsymbol{r}\times\boldsymbol{v}$, the relative position $\boldsymbol{r} = \boldsymbol{x}_1 - \boldsymbol{x}_2$, and relative velocity $\boldsymbol{v} = d\boldsymbol{r}/dt$.

The relative acceleration $\boldsymbol{a} \equiv \boldsymbol{a}_1 - \boldsymbol{a}_2$ with LO SO and SS contributions, in harmonic coordinates and the NW SSC, is given by [164]

$$\begin{aligned}\boldsymbol{a} = -M\frac{\boldsymbol{n}}{r^2} + \frac{1}{c^3}\Bigg[3\left(2+\frac{3m_2}{2m_1}\right)\boldsymbol{n}\cdot(\boldsymbol{v}\times\boldsymbol{S}_1)\frac{\boldsymbol{n}}{r^3} - \left(4+\frac{3m_2}{m_1}\right)\\ \frac{\boldsymbol{v}\times\boldsymbol{S}_1}{r^3} + 3\left(2+\frac{3m_2}{2m_1}\right)\frac{\dot{r}}{r^3}\boldsymbol{n}\times\boldsymbol{S}_1 + 1\leftrightarrow 2\Bigg]\\ - \frac{3}{c^4\mu r^4}\Big[\boldsymbol{n}(\boldsymbol{S}_1\cdot\boldsymbol{S}_2) + \boldsymbol{S}_1(\boldsymbol{n}\cdot\boldsymbol{S}_2) + \boldsymbol{S}_2(\boldsymbol{n}\cdot\boldsymbol{S}_1) - 5\boldsymbol{n}(\boldsymbol{n}\cdot\boldsymbol{S}_1)(\boldsymbol{n}\cdot\boldsymbol{S}_2)\Big]\\ + \frac{3}{2c^4r^4}\left[\frac{m_2C_{1\mathrm{ES}^2}}{m_1\mu}\Big(-\boldsymbol{n}\,\boldsymbol{S}_1^2 + 5\boldsymbol{n}(\boldsymbol{n}\cdot\boldsymbol{S}_1)^2 - 2\boldsymbol{S}_1(\boldsymbol{n}\cdot\boldsymbol{S}_1)\Big) + 1\leftrightarrow 2\right].\end{aligned} \tag{G.1}$$

Since the spin evolution equations start at 1PN order, we can assume $\dot{\boldsymbol{S}}_1 = 0 = \dot{\boldsymbol{S}}_2$ for the calculation of the LO fluxes.

The source multipole moments needed are the spin quadrupole I^{ij} and the current quadrupole J^{ij}, which are given by [164, 166, 179]

$$I^{ij} = m_1 x_1^{\langle i}x_1^{j\rangle} + \frac{3}{c^3}x_1^{\langle i}(\boldsymbol{v}_1\times\boldsymbol{S}_1)^{j\rangle} - \frac{4}{3c^3}\frac{d}{dt}x_1^{\langle i}(\boldsymbol{x}_1\times\boldsymbol{S}_1)^{j\rangle} - \frac{C_{1\mathrm{ES}^2}}{c^4m_1}S_1^{\langle i}S_1^{j\rangle} + 1\leftrightarrow 2 \tag{G.2}$$

$$J^{ij} = m_1 x_1^{\langle i}(\boldsymbol{x}_1\times\boldsymbol{v}_1)^{j\rangle} + \frac{3}{2c}x_1^{\langle i}S_1^{j\rangle} + 1\leftrightarrow 2, \tag{G.3}$$

where the indices in angle brackets denote a symmetric trace-free part.

To transform from the coordinates of the two bodies x_1^i and x_2^i to the center-of-mass relative coordinates $x^i = x_1^i - x_2^i$, we use [165]

$$x_1^i = \frac{m_2}{M}x^i + \delta x^i, \quad x_2^i = -\frac{m_1}{M}x^i + \delta x^i, \tag{G.4}$$

where

$$\delta x^i = -\frac{\nu}{2c^3}\left[\frac{(\boldsymbol{v}\times\boldsymbol{S}_1)^i}{m_1} - \frac{(\boldsymbol{v}\times\boldsymbol{S}_2)^i}{m_2}\right]. \tag{G.5}$$

The energy and angular momentum fluxes in terms of the multipole moments, to the order needed for the LO fluxes, are then calculated from [135, 164]

$$\Phi_E = \frac{1}{5}I_{ij}^{(3)}I_{ij}^{(3)} + \frac{16}{45c^2}J_{ij}^{(3)}J_{ij}^{(3)}, \tag{G.6}$$

$$\Phi_J^i = \frac{2}{5}\epsilon_{ijk}I_{jl}^{(2)}I_{kl}^{(3)} + \frac{32}{45c^2}\epsilon_{ijk}J_{jl}^{(2)}J_{kl}^{(3)}. \tag{G.7}$$

This yields the LO SO and S_1S_2 fluxes derived in Refs. [164, 167, 168], in addition to the S_i^2 energy flux from Ref. [179]. For the S_i^2 angular momentum flux, we obtain

$$\begin{aligned}
\boldsymbol{\Phi}_J^{S_i^2} &= \frac{2m_2^2}{5c^4r^5}\left[\frac{\boldsymbol{L}}{\mu r}\boldsymbol{S}_1^2 - \boldsymbol{n}\cdot\boldsymbol{S}_1(\boldsymbol{v}\times\boldsymbol{S}_1) + \boldsymbol{v}\cdot\boldsymbol{S}_1(\boldsymbol{n}\times\boldsymbol{S}_1)\right] \\
&\quad + \frac{2m_2^2C_{1\mathrm{ES}^2}}{5c^4Mr^4}\left[\frac{\boldsymbol{L}}{\mu r}\boldsymbol{S}_1^2\left(-30\dot{r}^2 + 12v^2 + 24\frac{M}{r}\right) + \frac{\boldsymbol{L}}{\mu r}(\boldsymbol{n}\cdot\boldsymbol{S}_1)^2\left(210\dot{r}^2 - 60v^2 - 90\frac{M}{r}\right)\right. \\
&\quad + \boldsymbol{v}\times\boldsymbol{S}_1(\boldsymbol{n}\cdot\boldsymbol{S}_1)\left(30\dot{r}^2 - 18v^2 - 12\frac{M}{r}\right) + 6\boldsymbol{n}\times\boldsymbol{S}_1(\boldsymbol{v}\cdot\boldsymbol{S}_1 - \dot{r}\boldsymbol{n}\cdot\boldsymbol{S}_1)\frac{M}{r} \\
&\quad \left. - 90\frac{\boldsymbol{L}}{\mu r}\dot{r}(\boldsymbol{n}\cdot\boldsymbol{S}_1)(\boldsymbol{v}\cdot\boldsymbol{S}_1) + 6\frac{\boldsymbol{L}}{\mu r}(\boldsymbol{v}\cdot\boldsymbol{S}_1)^2 - 6\dot{r}(\boldsymbol{v}\cdot\boldsymbol{S}_1)\boldsymbol{v}\times\boldsymbol{S}_1\right] + 1\leftrightarrow 2.
\end{aligned} \tag{G.8}$$

This is in agreement with the recent results of Ref. [181], although our expression appears simpler because of using the individual spins S_i and masses m_i, instead of different combinations of them.

Appendix H: Aligned-spin contributions to the modes in harmonic coordinates

The modes calculated from the source moments of Refs. [166, 173] in *harmonic* coordinates and using the *covariant* SSC have the following spin contributions:

$$\hat{H}^{20}_{\text{spin}} = \frac{\dot{\phi}}{\sqrt{6}c^3 r}\left[\chi_1(1+\delta+\nu) + \chi_2(1-\delta+\nu)\right] \\ - \frac{\sqrt{3}}{2\sqrt{2}c^4 r^3}\left[C_{1\text{ES}^2}X_1^2\chi_1^2 + 2\nu\chi_1\chi_2 + C_{2\text{ES}^2}X_2^2\chi_2^2\right], \tag{H.1}$$

$$\hat{H}^{21}_{\text{spin}} = -\frac{i}{4r^2}\left[(1+\delta)\chi_1 + (\delta-1)\chi_2\right] + \frac{i}{168c^4 r^3}\Bigg\{\chi_1\Big[154 + 22\delta(\nu+7) + 34\nu \\ + 4r^3\dot{\phi}^2(4\nu\delta - 21\delta + 66\nu - 21) - 2i\dot{r}r^2\dot{\phi}(13\nu\delta + 147\delta - 83\nu + 147) \\ + \dot{r}^2 r(-60\delta\nu + 105\delta - 52\nu + 105)\Big] + \chi_2\Big[-154 + 22\delta(\nu+7) - 34\nu \\ + 4r^3\dot{\phi}^2(4\nu\delta - 21\delta - 66\nu + 21) - 2i\dot{r}r^2\dot{\phi}(13\nu\delta + 147\delta + 83\nu - 147) \\ + \dot{r}^2 r(-60\delta\nu + 105\delta + 52\nu - 105)\Big]\Bigg\}, \tag{H.2}$$

$$\hat{H}^{22}_{\text{spin}} = -\frac{1}{6c^3 r^2}\Bigg\{\chi_1\left[r\dot{\phi}(3\delta - 5\nu + 3) + i\dot{r}(3\delta - 8\nu + 3)\right] \\ + \chi_2\left[r\dot{\phi}(-3\delta - 5\nu + 3) - i\dot{r}(3\delta + 8\nu - 3)\right]\Bigg\} \\ + \frac{3}{4c^4 r^3}\left[C_{1\text{ES}^2}\chi_1^2 X_1^2 + C_{2\text{ES}^2}\chi_2^2 X_2^2 + 2\nu\chi_2\chi_1\right], \tag{H.3}$$

$$\hat{H}^{30}_{\text{spin}} = -\frac{i\nu\dot{r}}{\sqrt{42}c^3 r^2}(\chi_1 + \chi_2), \tag{H.4}$$

$$\hat{H}^{31}_{\text{spin}} = \frac{i}{48\sqrt{14}c^4 r^3}\Bigg\{\chi_1\Big[-4 + 20\delta\nu - 4\delta + 20\nu + r^3\dot{\phi}^2(-31\delta\nu - 24\delta + 87\nu - 24) \\ + i\dot{r}r^2\dot{\phi}(-70\delta\nu - 12\delta + 62\nu - 12) + \dot{r}^2 r(-30\delta\nu + 12\delta - 50\nu + 12)\Big]$$

$$+ \chi_2\Bigg[4 + 20\delta\nu - 4\delta - 20\nu + r^3\dot{\phi}^2(-31\delta\nu - 24\delta - 87\nu + 24)$$

$$+ i\dot{r}r^2\dot{\phi}(-70\delta\nu - 12\delta - 62\nu + 12) + \dot{r}^2 r(-30\delta\nu + 12\delta + 50\nu - 12)\Bigg]\Bigg\}, \quad \text{(H.5)}$$

$$\hat{H}^{32}_{\text{spin}} = \sqrt{\frac{5}{7}}\frac{\nu}{6c^3r^2}\left(4r\dot{\phi} + i\dot{r}\right)(\chi_1 + \chi_2)\,, \quad \text{(H.6)}$$

$$\hat{H}^{33}_{\text{spin}} = \sqrt{\frac{5}{42}}\frac{i}{16c^4r^3}\Bigg\{\chi_1\Bigg[4 - 20\delta\nu + 4\delta - 20\nu + r^3\dot{\phi}^2(-33\delta\nu + 24\delta - 119\nu + 24)$$

$$+ i\dot{r}r^2\dot{\phi}(-78\delta\nu + 36\delta - 154\nu + 36) + \dot{r}^2 r(30\delta\nu - 12\delta + 50\nu - 12)\Bigg]$$

$$+ \chi_2\Bigg[-4 - 20\delta\nu + 4\delta + 20\nu + r^3\dot{\phi}^2(-33\delta\nu + 24\delta + 119\nu - 24)$$

$$+ i\dot{r}r^2\dot{\phi}(-78\delta\nu + 36\delta + 154\nu - 36) + \dot{r}^2 r(30\delta\nu - 12\delta - 50\nu + 12)\Bigg]\Bigg\}, \quad \text{(H.7)}$$

$$\hat{H}^{41}_{\text{spin}} = -i\sqrt{\frac{5}{2}}\frac{\nu}{336c^4r^3}\left(11r^3\dot{\phi}^2 - 10i\dot{r}r^2\dot{\phi} + 6\dot{r}^2 r - 12\right)\left[(\delta - 1)\chi_1 + (\delta + 1)\chi_2\right], \quad \text{(H.8)}$$

$$\hat{H}^{43}_{\text{spin}} = \sqrt{\frac{5}{14}}\frac{\nu}{48c^4r^3}\left(-23ir^3\dot{\phi}^2 + 10\dot{r}r^2\dot{\phi} + 2i\dot{r}^2 r - 4i\right)\left[(\delta - 1)\chi_1 + (\delta + 1)\chi_2\right]. \quad \text{(H.9)}$$

Appendix I: Keplerian parametrization

This appendix provides expressions for some orbital quantities in the Keplerian parametrization that are needed for calculating the initial conditions, and the tail part of the RR force and waveform modes.

In the Keplerian parametrization,

$$r = \frac{1}{u_p(1 + e\cos\chi)}, \tag{I.1}$$

where u_p is the inverse semilatus rectum and χ is the relativistic anomaly. Inverting the Hamiltonian at the turning points $r_\pm = 1/(u_p(1 \pm e))$ and solving for the energy and angular momentum to 2PN order yields

$$\begin{aligned}
E &= \frac{1}{2}\left(e^2-1\right)u_p - \frac{u_p^2}{8c^2}\left(e^2-1\right)^2(\nu-3) \\
&\quad + \frac{u_p^3}{16c^4}\left(e^2-1\right)^2\left[e^2\left(\nu^2-3\nu+5\right)-\nu^2-5\nu+27\right] \\
&\quad + \frac{\left(1-e^2\right)^2 u_p^{5/2}}{4c^3}\left[\chi_1(\nu-2\delta-2)+\chi_2(\nu+2\delta-2)\right] \\
&\quad + \frac{\left(1-e^2\right)^2 u_p^3}{4c^4}\Big[\chi_1^2\left(C_{1\mathrm{ES}^2}X_1^2+X_1^4\right)+2\nu(1+\nu)\chi_2\chi_1+\chi_2^2\left(C_{2\mathrm{ES}^2}X_2^2+X_2^4\right)\Big], \\
p_\phi &= \frac{1}{\sqrt{u_p}} + \frac{\sqrt{u_p}}{2c^2}\left(e^2+3\right) + \frac{u_p^{3/2}}{8c^4}\left(e^2+3\right)\left(3e^2-4\nu+9\right) \\
&\quad + \frac{u_p}{4c^3}\left(e^2+3\right)\left[\chi_1(-2\delta+\nu-2)+\chi_2(2\delta+\nu-2)\right] \\
&\quad + \frac{\left(e^2+3\right)u_p^{3/2}}{4c^4}\Big[\chi_1^2\left(C_{1\mathrm{ES}^2}X_1^2+X_1^4\right)+\chi_2^2\left(C_{2\mathrm{ES}^2}X_2^2+X_2^4\right)\Big] \\
&\quad + \frac{\nu u_p^{3/2}\chi_1\chi_2}{2c^4}\left[e^2(3\nu+1)+\nu+3\right].
\end{aligned} \tag{I.2}$$

Inverting $p_\phi(u_p, e)$, we obtain $u_p(p_\phi, e)$

$$\begin{aligned}
u_p(p_\phi, e) &= \frac{1}{p_\phi^2} + \frac{(e^2+3)}{c^2 p_\phi^4} + \frac{(e^2+3)(2e^2-\nu+6)}{c^4 p_\phi^6} \\
&\quad + \frac{3+e^2}{2p_\phi^5 c^3}\left[(\nu-2\delta-2)\chi_1 + (\nu+2\delta-2)\chi_2\right] \\
&\quad + \frac{1}{2p_\phi^6 c^4}\Big\{\nu\chi_1\chi_2\left[e^2(3\nu+1)+\nu+3\right] + \chi_1^2\left[C_{1\mathrm{ES}^2}\left(e^2+3\right)X_1^2 + \left(3e^2+1\right)X_1^4\right] \\
&\quad\quad + 1 \leftrightarrow 2\Big\}.
\end{aligned} \tag{I.3}$$

Inverting the Hamiltonian to obtain $p_r(E, p_\phi)$, and plugging $E(e, u_p)$ and $p_\phi(e, u_p)$, yields

$$p_r = e\sqrt{u_p}\sin\chi + \frac{e u_p^{3/2}}{2c^2}\sin\chi\left(e^2 + 2e\cos\chi + 1\right) + \ldots \tag{I.4}$$

The radial and azimuthal periods are given, respectively, by

$$\begin{aligned}
T_r &= \oint dt = \oint \left(\frac{\partial H}{\partial p_r}\right)^{-1} dr = 2\int_0^\pi \left(\frac{\partial H}{\partial p_r}\right)^{-1} \frac{dr}{d\chi} d\chi \\
&= \frac{2\pi}{\left(u_p - e^2 u_p\right)^{3/2}} - \frac{\pi(\nu-6)}{c^2\sqrt{u_p - e^2 u_p}} + \ldots, \\
T_\phi &= \oint \dot{\phi}\, dt = \oint \frac{\partial H}{\partial p_\phi} dt = 2\pi + \frac{6\pi u_p}{c^2} + \ldots.
\end{aligned} \tag{I.5}$$

The associated frequencies are

$$\omega_r = \frac{2\pi}{T_r}, \qquad \omega_\phi = \frac{T_\phi}{T_r}. \tag{I.6}$$

The dimensionless frequency variable $x \equiv \omega_\phi^{2/3}$ to 2PN order is given by

$$\begin{aligned}
x &= u_p - e^2 u_p + \frac{u_p^2}{3c^2}\left(e^2-1\right)\left(e^2(\nu-6)-\nu\right) \\
&\quad - \frac{u_p^3}{36c^4}\left(e^2-1\right)\Big\{e^4\left(8\nu^2 - 33\nu + 180\right) + 8\nu^2 \\
&\quad - 2e^2\left[3\left(12\sqrt{1-e^2}+5\right)\nu - 90\sqrt{1-e^2} + 8\nu^2 + 27\right] \\
&\quad + 9\left(8\sqrt{1-e^2}-13\right)\nu - 180\left(\sqrt{1-e^2}-1\right)\Big\}
\end{aligned}$$

$$
\begin{aligned}
&+\frac{u_p^{5/2}}{6c^3}\left(e^2-1\right)\left(3e^2+1\right)\left[\chi_1(2+2\delta-\nu)+1\leftrightarrow 2\right]\\
&-\frac{u_p^3}{2c^4}\Big\{\chi_1^2\left[C_{1\mathrm{ES}^2}\left(e^4-1\right)X_1^2+\left(e^2-1\right)^2X_1^4\right]\\
&\quad+\nu\chi_1\chi_2\left[e^4(\nu+1)-2e^2\nu+\nu-1\right]+1\leftrightarrow 2\Big\},
\end{aligned}
\tag{I.7}
$$

which can be inverted to obtain $u_p(x,e)$, the 1PN part of which reads

$$
u_p=-\frac{x}{e^2-1}+\frac{x^2\left[e^2(\nu-6)-\nu\right]}{3c^2\left(e^2-1\right)^2}+\dots. \tag{I.8}
$$

Appendix J: $\dot{p}_r$ in tortoise coordinates

The tortoise-coordinate r_* is defined by [411, 582]

$$\frac{dr_*}{dr} = \frac{\sqrt{D(r)}}{A(r)} \equiv \frac{1}{\xi(r)}, \tag{J.1}$$

where $A(r)$ and $D(r)$ are the metric potentials

$$ds^2_{\text{eff}} = -A(r)dt^2 + \frac{D(r)}{A(r)}dr^2 + r^2 d\Omega^2. \tag{J.2}$$

The conjugate momentum to r_* is denoted p_{r_*}, and invariance of the action gives the relation

$$p_{r_*} = p_r \xi(r). \tag{J.3}$$

The Hamiltonian and EOMs used in SEOBNRv4 (see Eqs. (10) of Ref. [387]) are expressed in terms of the variables $(r, p_{r_*}, \phi, p_\phi)$. However, the RR force we derived in Sec. 6.2 is expressed in terms of $(r, p_r, \dot{p}_r)$. We use Eq. (J.3) to replace p_r with p_{r_*}, and to obtain a relation between $\dot{p}_r$ and the derivatives of $H_{\text{EOB}}(r, p_{r_*}, p_\phi)$. We use the following relations:

$$\begin{aligned} dH &= \left(\frac{\partial H}{\partial r}\right)_{p_{r_*}} dr + \left(\frac{\partial H}{\partial p_{r_*}}\right)_r dp_{r_*} + \frac{\partial H}{\partial p_\phi} dp_\phi \\ &= \left(\frac{\partial H}{\partial r}\right)_{p_r} dr + \left(\frac{\partial H}{\partial p_r}\right)_r dp_r + \frac{\partial H}{\partial p_\phi} dp_\phi, \end{aligned} \tag{J.4}$$

$$dp_{r_*} = \left(\frac{\partial p_{r_*}}{\partial r}\right)_{p_r} dr + \left(\frac{\partial p_{r_*}}{\partial r}\right)_r dp_r, \tag{J.5}$$

leading to

$$\left(\frac{\partial H}{\partial r}\right)_{p_r} = \left(\frac{\partial H}{\partial r}\right)_{p_{r_*}} + \left(\frac{\partial H}{\partial p_{r_*}}\right)_r \left(\frac{\partial p_{r_*}}{\partial r}\right)_{p_r}, \tag{J.6}$$

where

$$\left(\frac{\partial p_{r_*}}{\partial r}\right)_{p_r} = p_r \frac{d\xi(r)}{dr}. \tag{J.7}$$

Hence,

$$\begin{aligned} \dot{p}_r &= -\left(\frac{\partial H}{\partial r}\right)_{p_r} \\ &= -\left[\left(\frac{\partial H}{\partial r}\right)_{p_{r_*}} + \left(\frac{\partial H}{\partial p_{r_*}}\right)_r \frac{p_{r_*}}{\xi(r)} \frac{d\xi(r)}{dr}\right]. \end{aligned} \tag{J.8}$$

Appendix K: PN Hamiltonian for bound orbits in isotropic gauge

In this appendix, we canonically transform the 6PN-EOB Hamiltonian of Refs. [92, 93] to the isotropic gauge, in which the Hamiltonian only depends on r and p^2 with no explicit dependence on the angular momentum.

We start by writing an ansatz with unknown coefficients for the Hamiltonian

$$\hat{H}^{\text{iso}}_{\text{6PN}} = \frac{1}{\nu} + \frac{p^2}{2} - \frac{1}{r} + \sum_{i=2}^{7}\sum_{j=0}^{i} \alpha_{ij} \frac{p^{2(i-j)}}{r^j} + \sum_{i=5}^{7}\sum_{j=1}^{i} \alpha_{ij} \frac{p^{2(i-j)}}{r^j} \ln r, \tag{K.1}$$

where the 0PM coefficients are given by the PN expansion of

$$H^{\text{iso}}_{\text{0PM}} = \sqrt{m_1^2 + P^2} + \sqrt{m_2^2 + P^2}. \tag{K.2}$$

Then, we write an ansatz for the generating function $\mathcal{G}$, perform a canonical transformation using Poisson brackets, and match to the 6PN EOB Hamiltonian, i.e.,

$$H^{\text{EOB}}_{\text{6PN}} = H^{\text{iso}}_{\text{6PN}} + \{\mathcal{G}, H^{\text{iso}}_{\text{6PN}}\} + \frac{1}{2!}\{\mathcal{G}, \{\mathcal{G}, H^{\text{iso}}_{\text{6PN}}\}\} + \frac{1}{3!}\{\mathcal{G}, \{\mathcal{G}, \{\mathcal{G}, H^{\text{iso}}_{\text{6PN}}\}\}\} + \dots, \tag{K.3}$$

where each bracket introduces a factor of $1/c^2$.

The result for the full 6PN Hamiltonian, which contains 6 coefficients that have not yet been determined in Refs. [92, 93], is provided in the Supplemental Material. Here, we write that Hamiltonian truncated at $\mathcal{O}(G^4)$

$$\hat{H}^{\text{ell,iso}}_{\text{4PN(4PM)}} = \hat{H}^{\text{iso}}_{\text{3PN}} + \left[\frac{7}{256} + \frac{63\nu^4}{256} - \frac{105\nu^3}{128} + \frac{189\nu^2}{256} - \frac{63\nu}{256}\right] p^{10}$$

$$+\frac{Gp^8}{r}\left[\frac{45}{128}+\nu\left(-\frac{294051}{2800}+\frac{10834496\ln 2}{45}+\frac{6591861\ln 3}{700}-\frac{27734375\ln 5}{252}\right)\right.$$
$$\left.-\nu^4-3\nu^3+\frac{51\nu^2}{8}\right]+\frac{G^2p^6}{r^2}\left[\frac{13}{8}+\frac{35\nu^4}{32}+\frac{337\nu^3}{16}+\frac{453\nu^2}{32}\right.$$
$$\left.+\nu\left(\frac{9062513}{16800}-\frac{21212984}{15}\ln 2+\frac{1296484375\ln 5}{2016}-\frac{282031389\ln 3}{5600}\right)\right]$$
$$+\frac{G^3p^4}{r^3}\left[\frac{105}{32}+\nu\left(-\frac{2872367}{2400}+\frac{233388968\ln 2}{75}+\frac{16351713\ln 3}{160}-\frac{405859375\ln 5}{288}\right)\right.$$
$$\left.-\frac{487\nu^3}{16}-\frac{2589\nu^2}{32}\right]+\frac{G^4p^2}{r^4}\left[\frac{105}{32}-\frac{5\nu^4}{16}+\frac{27\nu^3}{2}+\left(\frac{2957}{48}-\frac{41\pi^2}{64}\right)\nu^2\right.$$
$$+\nu\left(-\frac{74\ln r}{15}+\frac{4086409}{3600}-\frac{29665\pi^2}{12288}+\frac{148\gamma_E}{15}-\frac{680106004}{225}\ln 2+\frac{196484375\ln 5}{144}\right.$$
$$\left.\left.-\frac{37122381\ln 3}{400}\right)\right], \tag{K.4}$$

$$\hat{H}^{\text{ell,iso}}_{\text{5PN(4PM)}}=\hat{H}^{\text{ell,iso}}_{\text{4PN(4PM)}}+\left[-\frac{21}{1024}+\frac{231\nu^5}{1024}-\frac{1155\nu^4}{1024}+\frac{1617\nu^3}{1024}-\frac{231\nu^2}{256}+\frac{231\nu}{1024}\right]p^{12}$$
$$+\frac{Gp^{10}}{r}\left[-\frac{77}{256}-\nu^5+\nu^2\left(-\frac{18236}{35}+\frac{10834496\ln 2}{9}+\frac{6591861\ln 3}{140}-\frac{138671875\ln 5}{252}\right)\right.$$
$$\left.-\frac{5\nu^4}{2}+\frac{95\nu^3}{8}+\nu\left(\frac{1212079}{22400}-\frac{5417248}{45}\ln 2+\frac{27734375\ln 5}{504}-\frac{6591861\ln 3}{1400}\right)\right]$$
$$+\frac{G^2p^8}{r^2}\left[-\frac{425}{256}+\frac{315\nu^5}{256}+\frac{7107\nu^4}{256}+\frac{2625\nu^3}{256}\right.$$
$$+\nu^2\left(\frac{48228101}{13440}-\frac{2125906693}{378}\ln 2+\frac{242787134673\ln 3}{286720}+\frac{3671798828125\ln 5}{1548288}\right.$$
$$\left.-\frac{96889010407\ln 7}{221184}\right)+\nu\left(\frac{82224409}{53760}-\frac{249145033}{60}\ln 2+\frac{12166079921875\ln 5}{6193152}\right.$$
$$\left.\left.+\frac{96889010407\ln 7}{884736}-\frac{103980982797\ln 3}{229376}\right)\right]$$
$$+\frac{G^3p^6}{r^3}\left[-\frac{273}{64}-\frac{6607\nu^4}{128}-\frac{1527\nu^3}{8}\right.$$
$$+\nu^2\left(-\frac{5713223}{560}+\frac{105895904239\ln 2}{13230}+\frac{2588320706587\ln 7}{1105920}-\frac{10808816520303\ln 3}{2007040}\right.$$
$$\left.-\frac{28119126171875\ln 5}{10838016}\right)+\nu\left(\frac{2922687496621\ln 2}{132300}-\frac{4523914911}{627200}\right.$$
$$\left.\left.+\frac{13469503195629\ln 3}{5734400}-\frac{2588320706587\ln 7}{4423680}-\frac{150369012359375\ln 5}{14450688}\right)\right]$$

$$
\begin{aligned}
&+\frac{G^4p^4}{r^4}\bigg[-\frac{165}{32}-\frac{35\nu^5}{64}+\frac{2055\nu^4}{64}+\left(\frac{56249}{192}-\frac{41\pi^2}{64}\right)\nu^3\\
&\quad+\nu^2\bigg(\frac{72487381}{5040}-\frac{148\ln r}{15}-\frac{27697\pi^2}{6144}+\frac{296\gamma_E}{15}-\frac{9735062548\ln 2}{33075}\\
&\qquad+\frac{14337306321183\ln 3}{1254400}-\frac{650540498447\ln 7}{138240}-\frac{2701666015625\ln 5}{1354752}\bigg)\\
&\quad+\nu\bigg(-\frac{107\ln r}{140}-\frac{10889\pi^2}{4096}+\frac{976047931}{78400}+\frac{107\gamma_E}{70}-\frac{526259559517\ln 2}{13230}\\
&\qquad+\frac{33874913921875\ln 5}{1806336}+\frac{650540498447\ln 7}{552960}-\frac{641012819877\ln 3}{143360}\bigg)\bigg],
\end{aligned}
\tag{K.5}
$$

$$
\begin{aligned}
\hat{H}^{\text{ell,iso}}_{\text{6PN(4PM)}}&=\hat{H}^{\text{ell,iso}}_{\text{5PN(4PM)}}+\left[\frac{33}{2048}+\frac{429\nu^6}{2048}-\frac{3003\nu^5}{2048}+\frac{3003\nu^4}{1024}-\frac{1287\nu^3}{512}+\frac{2145\nu^2}{2048}-\frac{429\nu}{2048}\right]p^{14}\\
&+\frac{Gp^{12}}{r}\bigg[\frac{273}{1024}+\nu^3\left(-\frac{218307}{140}+\frac{10834496\ln 2}{3}+\frac{19775583\ln 3}{140}-\frac{138671875\ln 5}{84}\right)\\
&\quad+\nu^2\left(\frac{10614711}{22400}-\frac{1}{5}5417248\ln 2+\frac{27734375\ln 5}{56}-\frac{59326749\ln 3}{1400}\right)-\nu^6-\frac{3\nu^5}{2}\\
&\quad+\nu\left(-\frac{1860381}{44800}+\frac{1354312\ln 2}{15}+\frac{19775583\ln 3}{5600}-\frac{27734375\ln 5}{672}\right)+\frac{75\nu^4}{4}\bigg]\\
&+\frac{G^2p^{10}}{r^2}\bigg[\frac{441}{256}+\frac{693\nu^6}{512}+\frac{17175\nu^5}{512}-\frac{2505\nu^4}{256}\\
&\quad+\nu^3\bigg(\frac{1752882443}{134400}-\frac{50772177511\ln 2}{3780}+\frac{15140243287719\ln 3}{2867200}+\frac{15746212109375\ln 5}{3096576}\\
&\qquad-\frac{1065779114477\ln 7}{442368}\bigg)+\nu^2\bigg(\frac{930216823}{107520}-\frac{188966394467\ln 2}{7560}+\frac{147239183828125\ln 5}{12386304}\\
&\qquad+\frac{484445052035\ln 7}{589824}-\frac{7125985899279\ln 3}{2293760}\bigg)+\nu\bigg(-\frac{29016839}{35840}+\frac{154094423\ln 2}{72}\\
&\qquad+\frac{527065116993\ln 3}{2293760}-\frac{96889010407\ln 7}{1769472}-\frac{12533579921875\ln 5}{12386304}\bigg)\bigg]\\
&+\frac{G^3p^8}{r^3}\bigg[\frac{2805}{512}-\frac{19425\nu^5}{256}-\frac{168131\nu^4}{512}+\nu^3\bigg(-\frac{5539742599}{120960}+\frac{38790406370519\ln 2}{1786050}\\
&\qquad+\frac{1009279694921875\ln 5}{877879296}+\frac{453841966033589\ln 7}{89579520}-\frac{244047465883413\ln 3}{10035200}\bigg)\\
&\quad+\nu^2\bigg(-\frac{180308862367}{2822400}+\frac{116606471572979\ln 2}{1071630}+\frac{3680972377512689\ln 7}{358318080}\\
&\qquad-\frac{448065058976289\ln 3}{40140800}-\frac{181279182489765625\ln 5}{3511517184}\bigg)
\end{aligned}
$$

$$
\begin{aligned}
&+\nu\bigg(-\frac{3456473588783}{304819200}+\frac{369057536315537\ln 2}{9185400}+\frac{6074018303706627\ln 3}{80281600}\\
&\quad-\frac{1267373911442149\ln 7}{429981696}-\frac{44240036362654375\ln 5}{2341011456}\bigg)\bigg]\\
&+\frac{G^4p^6}{r^4}\bigg[\frac{2275}{256}-\frac{105\nu^6}{128}+\frac{1855\nu^5}{32}+\left(\frac{146987}{192}-\frac{41\pi^2}{64}\right)\nu^4\\
&+\nu^3\bigg(-\frac{74\ln r}{5}-\frac{25729\pi^2}{4096}+\frac{1701353519}{20160}+\frac{148\gamma_E}{5}-\frac{2348423027149\ln 2}{51030}\\
&\quad+\frac{8674336284777\ln 3}{286720}+\frac{250707235071713\ln 7}{17915904}-\frac{2232609748046875\ln 5}{125411328}\bigg)\\
&+\nu^2\bigg(\frac{197\ln r}{140}-\frac{197\gamma_E}{70}-\frac{104939\pi^2}{16384}+\frac{2714159093323}{16934400}-\frac{126132398166437\ln 2}{1071630}\\
&\quad+\frac{763693932388383\ln 3}{8028160}+\frac{204623745011171875\ln 5}{3511517184}-\frac{4304025048065071\ln 7}{71663616}\bigg)\\
&+\nu\bigg(-\frac{5827\ln r}{1008}-\frac{2337139\pi^2}{25165824}+\frac{3571766093993}{76204800}+\frac{5827\gamma_E}{504}-\frac{616925145960877\ln 2}{3214890}\\
&\quad+\frac{52541416380715625\ln 5}{585252864}+\frac{1554400159532395\ln 7}{107495424}-\frac{144912376553769\ln 3}{4014080}\bigg)\bigg].
\end{aligned}
\tag{K.6}
$$

This Hamiltonian can be used to check the PN expansion of a bound-orbit isotropic-gauge 4PM Hamiltonian, once the latter is computed in the future. Currently, it only agrees with the hyperbolic-orbit Hamiltonian of Ref. [246] at 3PN order.

In Sec. 7.4, we complement the 4PM Hamiltonian $H^{\text{hyp}}_{\text{4PM}}$ with bound-orbit PN corrections $\Delta H^{\text{ell}}_{\text{4PM(nPN)}}$ to get an estimate for its effect on the circular-orbit binding energy. We obtain those bound-orbit corrections using

$$
\Delta H^{\text{ell}}_{\text{4PM(nPN)}} = H^{\text{ell,iso}}_{\text{nPN(4PM)}} - H^{\text{hyp}}_{\text{4PM}}\Big|_{\text{nPN}}, \tag{K.7}
$$

i.e., we subtract the nPN expansion of $H^{\text{hyp}}_{\text{4PM}}$ from the isotropic-coordinate Hamiltonian in Eq. (K.6).

Appendix L: Coefficients of the 4PM-EOB Hamiltonians

In this appendix, we list the coefficients of the PM-EOB Hamiltonians, in the PS gauge of Eq. (7.17) and the PS* gauge of Eq. (7.18).

L.1 Hamiltonian in the PS gauge

When matching the scattering angle calculated from the EOB Hamiltonians to the PM-expanded scattering angle in Eq. (7.10), we solve for the coefficients $q_{n\mathrm{PM}}(\gamma)$ as functions of the effective energy.

The 2PM coefficient was derived in Ref. [237], and it reads

$$q_{2\mathrm{PM}}(\gamma) = \frac{3\left(5\gamma^2-1\right)\left(\Gamma-1\right)}{2\Gamma}. \tag{L.1}$$

When working up to 3PM order, as in Ref. [405], it was enough to replace γ by the Schwarzschild Hamiltonian $\hat{H}_S$. However, at 4PM order, we need to replace γ by the 2PM effective energy, which we take to be the 2PM expansion of Eq. (7.17), i.e.,

$$\gamma \to \hat{H}_S + \frac{q_{2\mathrm{PM}}(\hat{H}_S)}{2\hat{H}_S}u^2. \tag{L.2}$$

In the 3PM and 4PM coefficients, we simply replace γ by $\hat{H}_S$.

The 3PM coefficient is given by Eq. (2.17) of Ref. [405], which reads

$$q_{3\mathrm{PM}}(\gamma) = \frac{8\left(4\gamma^4-12\gamma^2-3\right)\nu}{\sqrt{\gamma^2-1}\Gamma^2}\sinh^{-1}\left(\frac{\sqrt{\gamma-1}}{\sqrt{2}}\right)$$

$$+\frac{1}{6\left(\gamma^2-1\right)\Gamma^2}\Big[9\left(10\gamma^4-7\gamma^2+1\right)\Gamma-9\left(10\gamma^4-7\gamma^2+1\right)\Gamma^2$$
$$+8\gamma\left(14\gamma^4+11\gamma^2-25\right)\nu\Big]. \tag{L.3}$$

The 4PM coefficient we obtain reads

$$\begin{aligned}
\frac{\Gamma^3\varepsilon}{\nu}q_{\text{4PM}}(\gamma) &= \frac{7}{8}\left(380\gamma^3+380\gamma^2+169\gamma+169\right)\mathrm{E}\left(\frac{\gamma-1}{\gamma+1}\right)^2 \\
&+\left(300\gamma^2+\frac{2095\gamma}{4}+\frac{417}{2}\right)\mathrm{K}\left(\frac{\gamma-1}{\gamma+1}\right)^2 \\
&-\left(300\gamma^3+665\gamma^2+\frac{2929\gamma}{4}+\frac{1183}{4}\right)\mathrm{E}\left(\frac{\gamma-1}{\gamma+1}\right)\mathrm{K}\left(\frac{\gamma-1}{\gamma+1}\right) \\
&-\frac{8\left(12\gamma^6-40\gamma^4+3\gamma^2+3\right)\Gamma\ln\left(\sqrt{\gamma-1}+\sqrt{\gamma+1}\right)}{\sqrt{\varepsilon}} \\
&-\frac{\gamma^2\left(3-2\gamma^2\right)^2\left(35\gamma^6-65\gamma^4+41\gamma^2-11\right)\ln^2\left(\gamma+\sqrt{\gamma-1}\sqrt{\gamma+1}\right)}{8\varepsilon^3} \\
&+\frac{2\gamma\left(75\gamma^8-215\gamma^6-143\gamma^4-569\gamma^2+852\right)\ln\gamma}{3\varepsilon} \\
&+\frac{1}{4}\left(-25\gamma^8+125\gamma^6+180\gamma^5-49\gamma^4+48\gamma^3-9\gamma^2-228\gamma-42\right)\ln^2(\gamma+1) \\
&+\frac{(\gamma^2-1)\ln\varepsilon}{12\varepsilon}\Big[210\gamma^6-552\gamma^5+3\gamma^4(70\varepsilon\ln 2+113)+24\gamma^3(15\varepsilon\ln 2-38) \\
&\quad+\gamma^2(3148-900\varepsilon\ln 2)+24\gamma(19\varepsilon\ln 2-139)-30\varepsilon\ln 2+1151\Big] \\
&+\ln(\gamma+1)\ln\varepsilon\frac{1}{2}\left(-35\gamma^6-60\gamma^5+185\gamma^4-16\gamma^3-145\gamma^2+76\gamma-5\right) \\
&\quad-\ln(\gamma+1)\frac{(\gamma^2-1)}{6\varepsilon}\Big[150\gamma^7-75\gamma^6\varepsilon\ln 2-832\gamma^5 \\
&\quad+18\gamma^4(5\varepsilon\ln 2-68)+2\gamma^3(90\varepsilon\ln 2-739)+\gamma^2(1053\varepsilon\ln 2-272) \\
&\quad+12\gamma(19\varepsilon\ln 2-420)+4(39\varepsilon\ln 2-76)\Big] \\
&+\ln\left(\gamma+\sqrt{\gamma-1}\sqrt{\gamma+1}\right)\Bigg[\frac{\gamma\ln\varepsilon}{4\varepsilon^{3/2}}\left(70\gamma^8-235\gamma^6+277\gamma^4-145\gamma^2+33\right) \\
&\quad-\frac{4\gamma\ln(\gamma+1)}{\varepsilon^{3/2}}\left(30\gamma^6-71\gamma^4+35\gamma^2+6\right) \\
&\quad-\frac{\gamma\left(2\gamma^4-5\gamma^2+3\right)}{12\varepsilon^{5/2}}\Big(210\gamma^6-720\gamma^5+3\gamma^4(70\varepsilon\ln 2+113)-576\gamma^3
\end{aligned}$$

$$
\left. \left. + \gamma^2(3148 - 900\varepsilon \ln 2) - 3504\gamma - 30\varepsilon \ln 2 + 1151 \right) \right]
$$

$$
+ \frac{2\gamma}{\sqrt{\varepsilon}} \mathrm{Li}_2 \left(-\sqrt{\frac{\gamma - 1}{\gamma + 1}} \right) \left(30\gamma^5 - 60\gamma^4 - 7\gamma^3 + 82\gamma^2 - 57\gamma + 12 \right)
$$

$$
+ \left(-25\gamma^8 + 55\gamma^6 + 81\gamma^4 - 91\gamma^2 - 20 \right) \mathrm{Li}_2 \left(\frac{1 - \gamma}{\gamma + 1} \right)
$$

$$
- \frac{1}{2}(\gamma + 1)^2 \left(25\gamma^6 - 50\gamma^5 + 20\gamma^4 + 70\gamma^3 - \gamma^2 - 52\gamma - 12 \right) \mathrm{Li}_2 \left(\frac{1 - \gamma}{2} \right)
$$

$$
- \frac{2\gamma \mathrm{Li}_2 \left(\sqrt{\frac{\gamma - 1}{\gamma + 1}} \right)}{\sqrt{\varepsilon}} \left(30\gamma^5 - 60\gamma^4 - 7\gamma^3 + 82\gamma^2 - 57\gamma + 12 \right), \tag{L.4}
$$

where we recall that $\varepsilon \equiv \gamma^2 - 1$.

The bound-orbit 4PN correction term $\Delta^Q_{\rm 4PN}$ in Eq. (7.17) is given by

$$
\begin{aligned}
\Delta^Q_{\rm 4PN}(\hat{H}_S, r) &= \frac{(\hat{H}_S^2 - 1)^3 \nu}{r^2} \left(-\frac{1027}{12} - \frac{147432}{5} \ln 2 + \frac{1399437 \ln 3}{160} + \frac{1953125 \ln 5}{288} \right) \\
&+ \frac{(\hat{H}_S^2 - 1)^2 \nu}{r^3} \left(-\frac{78917}{300} - \frac{14099512}{225} \ln 2 + \frac{14336271 \ln 3}{800} + \frac{4296875 \ln 5}{288} \right) \\
&+ \frac{(\hat{H}_S^2 - 1) \nu}{r^4} \left(\frac{296\gamma_E}{15} - \frac{27139}{75} - \frac{9766576}{225} \ln 2 + \frac{1182681 \ln 3}{100} + \frac{390625 \ln 5}{36} \right) \\
&+ \frac{1}{r^5} \left[\nu \left(\frac{136\gamma_E}{3} - \frac{34499}{1800} - \frac{29917\pi^2}{6144} - \frac{254936}{25} \ln 2 + \frac{1061181 \ln 3}{400} + \frac{390625 \ln 5}{144} \right) \right. \\
&\quad \left. + \left(\frac{205\pi^2}{64} - \frac{2387}{24} \right) \nu^2 + \frac{9\nu^3}{4} \right] \\
&- \frac{68}{3r^5} \nu \ln r - \frac{148(\hat{H}_S^2 - 1)\nu}{15r^4} \ln(\hat{H}_S^2 - 1) - \frac{148(\hat{H}_S^2 - 1)}{15r^4} \nu \ln r.
\end{aligned} \tag{L.5}
$$

L.2 Hamiltonian in the PS* gauge

For the EOB Hamiltonian in the gauge in Eq. (7.18), the 2PM coefficient is given by

$$
a_{\rm 2PM}(\gamma) = \frac{3\,(5\gamma^2 - 1)\,(\Gamma - 1)}{2\Gamma\gamma^2}, \tag{L.6}
$$

and we replace γ by the 2PM-expanded effective Hamiltonian, i.e.,

$$
\gamma \to \hat{H}_S + \frac{a_{\rm 2PM}(\hat{H}_S)}{2\hat{H}_S} \left(1 + p_r^2 + l^2 u^2 \right) u^2. \tag{L.7}
$$

The 3PM coefficient is given by

$$a_{3\mathrm{PM}}(\gamma) = \frac{q_{3\mathrm{PM}}(\gamma)}{\gamma^2} - \frac{6\left(5\gamma^2-1\right)(\Gamma-1)}{\Gamma\gamma^2}, \tag{L.8}$$

where we replace γ by $\hat{H}_S$. Similarly, for the 4PM coefficient, we obtain

$$\begin{aligned}
a_{4\mathrm{PM}}(\gamma) = \frac{q_{4\mathrm{PM}}(\gamma)}{\gamma^2} + \frac{1}{12\gamma^4\Gamma^3\varepsilon}\Big\{ & 9\left(195\gamma^6 - 209\gamma^4 + 49\gamma^2 - 3\right)\Gamma^3 \\
& - 18\left(135\gamma^6 - 157\gamma^4 + 41\gamma^2 - 3\right)\Gamma^2 + \gamma^2\nu\ln 2\Big[75\gamma^8\ln 2 - 300\gamma^7 + 45\gamma^6\ln 2 \\
& \quad + 4\gamma^5(416 + 45\ln 2) - 3\gamma^4(691\ln 2 - 816) + 4\gamma^3(739 + 12\ln 2) \\
& \quad + \gamma^2(544 + 1767\ln 2) - 12\gamma(19\ln 2 - 840) + 608 + 186\ln 2\Big] \\
& - \Gamma\Big[896\gamma^7\nu - 3\gamma^6\left(256\sqrt{\varepsilon}\nu\ln 2 + 225\right) + 704\gamma^5\nu \\
& \quad + 9\gamma^4\left(256\sqrt{\varepsilon}\nu\ln 2 + 105\right) - 1600\gamma^3\nu + 9\gamma^2\left(64\sqrt{\varepsilon}\nu\ln 2 - 33\right) + 27\Big] \\
& + 4\gamma^2\nu\ln\left(\frac{\gamma+1}{2}\right)\Big[152 - 75\gamma^7 + 105\gamma^6\ln 2 + 4\gamma^5(104 + 45\ln 2) \\
& \quad + \gamma^4(612 - 555\ln 2) + \gamma^3(739 + 48\ln 2) + \gamma^2(136 + 435\ln 2) \\
& \quad + \gamma(2520 - 228\ln 2) + 15\ln 2\Big] \\
& + 3\gamma^2\left(25\gamma^6 - 100\gamma^4 - 180\gamma^3 - 51\gamma^2 - 228\gamma - 42\right)\varepsilon\nu\ln^2(\gamma+1) \\
& - 3\gamma^2\nu\ln^2\left(\frac{\gamma+1}{2}\right)\Big[25\gamma^8 - 125\gamma^6 - 180\gamma^5 + 49\gamma^4 - 48\gamma^3 + 9\gamma^2 + 228\gamma + 42\Big] \\
& + 384\gamma^2\left(-4\gamma^4 + 12\gamma^2 + 3\right)\Gamma\sqrt{\varepsilon}\nu\ln\left(\sqrt{\gamma-1} + \sqrt{\gamma+1}\right) \\
& - 2\gamma^2\nu\ln(\gamma+1)\Big[75\gamma^8\ln 2 - 150\gamma^7 - 165\gamma^6\ln 2 + \gamma^5(832 - 180\ln 2) \\
& \quad - 9\gamma^4(117\ln 2 - 2(68 + 5\ln 2)) + \gamma^3(1478 - 48\ln 2) + \gamma^2(272 + 897\ln 2) \\
& \quad + 12\gamma(420 + 19\ln 2) + 4(76 + 39\ln 2)\Big]\Big\}.
\end{aligned} \tag{L.9}$$

The bound-orbit 4PN correction term $\Delta^A_{4\mathrm{PN}}$ in Eq. (7.18) is given by

$$\Delta^A_{4\mathrm{PN}}(\hat{H}_S, r) = \Delta^Q_{4\mathrm{PN}}(\hat{H}_S, r) + u^5\left[\left(\frac{640}{3} - \frac{41\pi^2}{8}\right)\nu - 14\nu^2\right]. \tag{L.10}$$

Appendix M: The 1PN two-body Lagrangian in Einstein-Maxwell-dilaton theory

In this appendix, we derive the 1PN two-body Lagrangian in EMd theory using the Fokker action method [686] (see also Refs. [201, 206, 425]). To derive the Lagrangian, we expand the EMd action in Eq. (8.2), together with the matter action for point particles in Eq. (8.3) and the mass expansion from Eq. (8.7). After that, we obtain the field equations for the potentials, solve them, and plug the solutions back into the action to get the Lagrangian. Throughout, we work in the harmonic gauge $g^{\mu\nu}\Gamma^{\lambda}_{\mu\nu} = 0$ and the Lorenz gauge $\partial_\mu A^\mu = 0$. Also, in this appendix and the next, we explicitly write c and G for bookkeeping.

M.1 Expanding the metric and connection coefficients

Before expanding the EMd action, we start by expanding the metric in powers of v/c [222],

$$
\begin{aligned}
g_{00} &= -1 + 2V - 2V^2 + \ldots, \\
g_{0i} &= -4V_i + \ldots, \\
g_{ij} &= \delta_{ij} + 2V\delta_{ij} + \ldots,
\end{aligned} \tag{M.1}
$$

where the potentials $V \sim \mathcal{O}(1/c^2)$, and $V_i \sim \mathcal{O}(1/c^3)$. The inverse metric satisfies $g^{\mu\lambda}g_{\lambda\nu} = \delta^{\mu}_{\ \nu}$.

The connection coefficients in terms of the metric are given by

$$\Gamma^{\mu}{}_{\nu\lambda} = \frac{1}{2} g^{\mu\rho} \left(\partial_\lambda g_{\rho\nu} + \partial_\nu g_{\rho\lambda} - \partial_\rho g_{\nu\lambda} \right) . \tag{M.2}$$

Plugging the metric expansion in terms of the potentials yields the connection coefficients to $\mathcal{O}(1/c^4)$

$$\begin{aligned}
\Gamma^0{}_{00} &= -\partial_0 V \, , \\
\Gamma^0{}_{0i} &= -\partial_i V \, , \\
\Gamma^i{}_{00} &= -\partial_i V + 2\partial_i V^2 - 4\partial_0 V_i \, , \\
\Gamma^0{}_{ij} &= 2\left(\partial_j V_i + \partial_i V_j \right) + \delta_{ij}\partial_0 V \, , \\
\Gamma^i{}_{0j} &= 2\left(\partial_i V_j - \partial_j V_i \right) + \delta_{ij}\partial_0 V \, , \\
\Gamma^i{}_{jk} &= (1 - 2V)\left(\delta_{ij}\partial_k V + \delta_{ik}\partial_j V - \delta_{jk}\partial_i V \right) .
\end{aligned} \tag{M.3}$$

M.2 Expanding the action

The action of EMd theory is given by Eq. (8.2). We can divide that action into four pieces

$$S = S_g + S_\varphi + S_{\text{em}} + S_m \, , \tag{M.4}$$

where S_g is the gravitational action, S_φ is the dilaton action, S_{em} is the electromagnetic action with the dilaton coupling, and S_m is the matter action.

In the Einstein frame, the gravitational action is the same as in GR. The Einstein-Hilbert gravitational action can be written in the Landau-Lifshitz form

$$S_g = \frac{c^4}{16\pi G} \int dt d^3\boldsymbol{x} \, \sqrt{-g} g^{\mu\nu} \left(\Gamma^\rho_{\mu\lambda}\Gamma^\lambda_{\nu\rho} - \Gamma^\rho_{\mu\nu}\Gamma^\lambda_{\rho\lambda} \right) . \tag{M.5}$$

Substituting the connection coefficients from Eq. (M.3) in terms of the potentials leads to

$$S_g = \frac{c^4}{16\pi G}\int dtd^3\boldsymbol{x}\Big[-2\partial_i V\partial_i V - 16\partial_i V\partial_0 V_i - 6\partial_0 V\partial_0 V \\ + 8\partial_i V_j\partial_i V_j - 8\partial_i V_j\partial_j V_i\Big]. \tag{M.6}$$

Imposing the harmonic gauge condition $g^{\mu\nu}\Gamma^{\lambda}_{\mu\nu} = 0$ gives $\partial_0 V + \partial_i V_i = 0$. Applying that condition in the action and integrating by parts yields

$$S_g = \frac{c^4}{16\pi G}\int dtd^3\boldsymbol{x}\Big[-2\partial_i V\partial_i V + 2\partial_0 V\partial_0 V + 8\partial_i V_j\partial_i V_j\Big]. \tag{M.7}$$

The dilaton action is given by

$$S_\varphi = -\frac{c^4}{8\pi G}\int dtd^3\boldsymbol{x}\sqrt{-g}g^{\mu\nu}\partial_\mu\varphi\partial_\nu\varphi\,. \tag{M.8}$$

Since φ is of order $1/c^2$, then to $\mathcal{O}(1/c^2)$

$$S_\varphi = -\frac{c^4}{8\pi G}\int dtd^3\boldsymbol{x}\left(-\partial_0\varphi\partial_0\varphi + \partial_i\varphi\partial_i\varphi\right). \tag{M.9}$$

The electromagnetic action including the dilaton coupling is given by

$$S_{\text{em}} = \frac{-1}{16\pi}\int dtd^3\boldsymbol{x}\sqrt{-g}e^{-2a\varphi}F_{\mu\nu}F^{\mu\nu}\,, \tag{M.10}$$

with the electromagnetic field $F_{\mu\nu} = \nabla_\mu A_\nu - \nabla_\nu A_\mu = \partial_\mu A_\nu - \partial_\nu A_\mu$ and the vector potential $A_\mu = (A_0, A_i)$. The component $A_0 = \mathcal{O}(1) + \mathcal{O}(1/c^2) + \ldots$, while the components $A_i = \mathcal{O}(1/c) + \ldots$. Therefore, expanding $F_{\mu\nu}F^{\mu\nu}$ to $\mathcal{O}(1/c^2)$ leads to

$$F_{\mu\nu}F^{\mu\nu} = -2\partial_i A_0\partial_i A_0 + 2\partial_j A_i\partial_j A_i + 4\partial_0 A_i\partial_i A_0 - 2\partial_i A_j\partial_j A_i\,. \tag{M.11}$$

Because the last two terms in Eq. (M.11) are of order $1/c^2$, we can use integration by parts and the Lorentz gauge condition ($\partial_\mu A^\mu = 0$) to replace these last two terms by $2\partial_0 A_0\partial_0 A_0$. Since

$\sqrt{-g} = 1 + 2V$, and $e^{-2a\varphi} \simeq 1 - 2a\varphi + \ldots$, the action becomes

$$S_{\text{em}} = \frac{1}{8\pi} \int dt d^3\boldsymbol{x} \big[(1 + 2V - 2a\varphi)\partial_i A_0 \partial_i A_0 - \partial_j A_i \partial_j A_i - \partial_0 A_0 \partial_0 A_0\big]. \tag{M.12}$$

The matter action S_m for point particles at monopolar order (dipole/spin and higher multipoles neglected) is given by

$$S_m = -\sum_A \int dt \left[\mathfrak{m}_A(\varphi) c^2 \sqrt{-g_{\mu\nu}\, v_A^\mu v_A^\nu / c^2} - \frac{1}{c} q_A A_\mu \frac{dx^\mu}{dt}\right], \tag{M.13}$$

where the field-dependent mass of each body has the expansion given by Eq. (8.7)

$$\mathfrak{m}(\varphi) = m \left[1 + \alpha\varphi + \frac{1}{2}(\alpha^2 + \beta)\varphi^2 + \mathcal{O}\left(1/c^6\right)\right]. \tag{M.14}$$

Defining the mass density ρ_g in terms of the constant masses

$$\rho_g \equiv \sum_A m_A \delta^3(\boldsymbol{x} - \boldsymbol{x}_A), \tag{M.15}$$

and defining the electric charge density by

$$\rho_e \equiv \sum_A q_A \delta^3(\boldsymbol{x} - \boldsymbol{x}_A), \tag{M.16}$$

then the matter action to $\mathcal{O}(1/c^2)$ can be written as

$$\begin{aligned} S_m = \int dt d^3\boldsymbol{x} \bigg[\rho_g \bigg(- c^2 + \frac{1}{2} v^2 + V c^2 + \frac{1}{8}\frac{v^4}{c^2} + \frac{3}{2} V v^2 - \frac{1}{2} V^2 c^2 - 4 V_i v^i c\bigg) \\ + \rho_g \alpha\varphi \left(-c^2 + \frac{1}{2} v^2 + V c^2\right) - \frac{1}{2} c^2 \rho_g (\alpha^2 + \beta)\varphi^2 + \rho_e \left(A_0 + \frac{1}{c} A_i v^i\right)\bigg]. \end{aligned} \tag{M.17}$$

The parameters α and β will be assigned a subscript when multiplied by the delta functions in ρ_g.

M.3 The field equations

Combining the expansion of the action from the previous section, the total action at 1PN order is given by

$$S = \int dt d^3\boldsymbol{x} \left\{ \frac{c^4}{16\pi G} \left[-2\partial_i V \partial_i V + 2\partial_0 V \partial_0 V + 8 \partial_i V_j \partial_i V_j\right] \right. \tag{M.18}$$

$$+\rho_g\left[-c^2+\frac{1}{2}v^2+Vc^2+\frac{1}{8}\frac{v^4}{c^2}+\frac{3}{2}Vv^2-\frac{1}{2}V^2c^2-4V_iv^ic\right]$$
$$-\frac{c^4}{8\pi G}\left(-\partial_0\varphi\partial_0\varphi+\partial_i\varphi\partial_i\varphi\right)+\rho_g\alpha\varphi\left(-c^2+\frac{1}{2}v^2+Vc^2\right)-\frac{1}{2}c^2\rho_g(\alpha^2+\beta)\varphi^2$$
$$+\frac{1}{8\pi}\left[(1+2V-2a\varphi)\partial_iA_0\partial_iA_0-\partial_jA_i\partial_jA_i-\partial_0A_0\partial_0A_0\right]+\rho_e\left(A_0+\frac{1}{c^2}A_iv^i\right)\Bigg\}.$$

Varying the action with respect to the potentials V_i, A_i, V, φ, and A_0 respectively yields the field equations

$$\nabla^2V_i=-\frac{4\pi G}{c^3}\rho_gv^i\,, \tag{M.19}$$

$$\nabla^2A_i=-\frac{4\pi}{c}\rho_ev^i\,, \tag{M.20}$$

$$\Box V=-\frac{4\pi G}{c^2}\rho_g-\frac{4\pi G}{c^4}\rho_g\left(\frac{3}{2}v^2-Vc^2\right)-\frac{4\pi G}{c^2}\rho_g\alpha\varphi-\frac{G}{c^4}\partial_iA_0\partial_iA_0\,, \tag{M.21}$$

$$\Box\varphi=-\frac{4\pi G}{c^4}\rho_g\left[-\alpha+\frac{1}{2}\alpha v^2+\alpha V-(\alpha^2+\beta)\varphi\right]+\frac{Ga}{c^4}\partial_iA_0\partial_iA_0\,, \tag{M.22}$$

$$\Box A_0=4\pi\rho_e-2V\nabla^2A_0-2\partial_iV\partial_iA_0+2a\varphi\nabla^2A_0+2a\partial_i\varphi\partial_iA_0\,, \tag{M.23}$$

where $\Box=-\partial_0^2+\nabla^2$ is the flat d'Alembertian.

The first two equations can be solved directly for V_i, and A_i

$$V_i=\frac{G}{c^3}\left(\frac{m_1v_1^i}{|\boldsymbol{x}-\boldsymbol{x}_1|}+\frac{m_2v_2^i}{|\boldsymbol{x}-\boldsymbol{x}_2|}\right), \tag{M.24}$$

$$A_i=\frac{1}{c}\left(\frac{q_1v_1^i}{|\boldsymbol{x}-\boldsymbol{x}_1|}+\frac{q_2v_2^i}{|\boldsymbol{x}-\boldsymbol{x}_2|}\right). \tag{M.25}$$

To solve the other three equations, we first rewrite the terms $\partial_iA_0\partial_iA_0$, $\partial_i\varphi\partial_iA_0$, and $\partial_iV\partial_iA_0$ using the identity

$$\nabla^2(\chi\xi)=\chi\nabla^2\xi+\xi\nabla^2\chi+2\partial_i\chi\partial_i\xi\,, \tag{M.26}$$

where χ and ξ are any scalar functions. Using that identity, Eqs. (M.21), (M.22), and (M.23) can be written as

$$\Box V=-\frac{4\pi G}{c^2}\rho_g-\frac{4\pi G}{c^4}\rho_g\left(\frac{3}{2}v^2-Vc^2\right)-\frac{4\pi G}{c^2}\rho_g\alpha\varphi$$

$$-\frac{G}{2c^4}\nabla^2(A_0)^2+\frac{G}{c^4}A_0\nabla^2A_0\,, \tag{M.27}$$

$$\Box\varphi=-\frac{4\pi G}{c^4}\rho_g\left[-c^2\alpha+\frac{1}{2}\alpha v^2+c^2\alpha V-c^2(\alpha^2+\beta)\varphi\right]$$
$$-\frac{Ga}{c^4}A_0\nabla^2A_0+\frac{Ga}{2c^4}\nabla^2(A_0)^2\,, \tag{M.28}$$

$$\Box A_0=4\pi\rho_e-\nabla^2(VA_0)-V\nabla^2A_0+A_0\nabla^2V+a\nabla^2(\varphi A_0)+a\varphi\nabla^2A_0-aA_0\nabla^2\varphi\,. \tag{M.29}$$

At this point, one could split the fields into separate PN orders, followed by further simplifications of the action through partial integrations and use of the field equations. Eventually one would only need an explicit expression for the leading order solution to the field equations here in order to obtain the 1PN Fokker action. This is essentially the "n+2" method from Ref. [425]. However, at this order this does overall not provide a big simplification, and we need a solution for the 1PN scalar field for Figs. 8.4 and 8.5. We therefore proceed by solving the 1PN field equations and straightforwardly insert the solution into the complete action.

To solve those three equations, we first solve for the leading order terms of V, φ, and A_0, and then insert that solution back into the right hand side of the equations. Equation (M.27) yields

$$\begin{aligned}V=&\frac{G}{c^2}\left(\frac{m_1}{|\boldsymbol{x}-\boldsymbol{x}_1|}+\frac{m_2}{|\boldsymbol{x}-\boldsymbol{x}_2|}\right)+\frac{G}{2c^4}\left(m_1\frac{\partial^2}{\partial t^2}|\boldsymbol{x}-\boldsymbol{x}_1|+m_2\frac{\partial^2}{\partial t^2}|\boldsymbol{x}-\boldsymbol{x}_2|\right)\\&+\frac{3G}{2c^4}\left(\frac{m_1v_1^2}{|\boldsymbol{x}-\boldsymbol{x}_1|}+\frac{m_2v_2^2}{|\boldsymbol{x}-\boldsymbol{x}_2|}\right)-\frac{G^2}{c^4}m_1m_2\left(\frac{1}{r|\boldsymbol{x}-\boldsymbol{x}_1|}+\frac{1}{r|\boldsymbol{x}-\boldsymbol{x}_2|}\right)\\&-\frac{G^2}{c^4}\alpha_1\alpha_2m_1m_2\left(\frac{1}{r|\boldsymbol{x}-\boldsymbol{x}_1|}+\frac{1}{r|\boldsymbol{x}-\boldsymbol{x}_2|}\right)-\frac{G}{2c^4}\left(\frac{q_1}{|\boldsymbol{x}-\boldsymbol{x}_1|}+\frac{q_2}{|\boldsymbol{x}-\boldsymbol{x}_2|}\right)^2\\&+\frac{G}{c^4}q_1q_2\left(\frac{1}{r|\boldsymbol{x}-\boldsymbol{x}_1|}+\frac{1}{r|\boldsymbol{x}-\boldsymbol{x}_2|}\right),\end{aligned} \tag{M.30}$$

where $r\equiv|\boldsymbol{x}_1-\boldsymbol{x}_2|$ and

$$\frac{\partial^2}{\partial t^2}|\boldsymbol{x}-\boldsymbol{x}_1|=\frac{v_1^2}{|\boldsymbol{x}-\boldsymbol{x}_1|}-\boldsymbol{n}_1\cdot\boldsymbol{a}_1-\frac{(\boldsymbol{n}_1\cdot\boldsymbol{v}_1)^2}{|\boldsymbol{x}-\boldsymbol{x}_1|}\,, \tag{M.31}$$

with $\boldsymbol{n}_1\equiv(\boldsymbol{x}-\boldsymbol{x}_1)/|\boldsymbol{x}-\boldsymbol{x}_1|$, and $\boldsymbol{a}_1=d\boldsymbol{v}_1/dt$ is the acceleration.

Solving Eq. (M.28) and using Eq. (M.31), we get

$$\varphi = -\frac{G}{c^2}\left(\frac{\alpha_1 m_1}{|\boldsymbol{x}-\boldsymbol{x}_1|}+\frac{\alpha_2 m_2}{|\boldsymbol{x}-\boldsymbol{x}_2|}\right)+\frac{G}{2c^4}\alpha_1 m_1\left(\boldsymbol{n}_1\cdot\boldsymbol{a}_1+\frac{(\boldsymbol{n}_1\cdot\boldsymbol{v}_1)^2}{|\boldsymbol{x}-\boldsymbol{x}_1|}\right)$$
$$+\frac{G\alpha_2 m_2}{2c^4}\left(\boldsymbol{n}_2\cdot\boldsymbol{a}_2+\frac{(\boldsymbol{n}_2\cdot\boldsymbol{v}_2)^2}{|\boldsymbol{x}-\boldsymbol{x}_2|}\right)+\frac{G^2 m_1 m_2}{c^4}\left(\frac{\alpha_1+\alpha_2(\alpha_1^2+\beta_1)}{r|\boldsymbol{x}-\boldsymbol{x}_1|}+\frac{\alpha_2+\alpha_1(\alpha_2^2+\beta_2)}{r|\boldsymbol{x}-\boldsymbol{x}_2|}\right)$$
$$-\frac{Ga}{c^4}q_1 q_2\left(\frac{1}{r|\boldsymbol{x}-\boldsymbol{x}_1|}+\frac{1}{r|\boldsymbol{x}-\boldsymbol{x}_2|}\right)+\frac{a}{2}\left(\frac{q_1}{|\boldsymbol{x}-\boldsymbol{x}_1|}+\frac{q_2}{|\boldsymbol{x}-\boldsymbol{x}_2|}\right)^2. \tag{M.32}$$

The solution of Eq. (M.29) for A_0 is given by

$$A_0 = -\left(\frac{q_1}{|\boldsymbol{x}-\boldsymbol{x}_1|}+\frac{q_2}{|\boldsymbol{x}-\boldsymbol{x}_2|}\right)-\frac{q_1}{2c^2}\left(\frac{v_1^2}{|\boldsymbol{x}-\boldsymbol{x}_1|}-\boldsymbol{n}_1\cdot\boldsymbol{a}_1-\frac{(\boldsymbol{n}_1\cdot\boldsymbol{v}_1)^2}{|\boldsymbol{x}-\boldsymbol{x}_1|}\right)$$
$$-\frac{q_2}{2c^2}\left(\frac{v_2^2}{|\boldsymbol{x}-\boldsymbol{x}_2|}-\boldsymbol{n}_2\cdot\boldsymbol{a}_2-\frac{(\boldsymbol{n}_2\cdot\boldsymbol{v}_2)^2}{|\boldsymbol{x}-\boldsymbol{x}_2|}\right)$$
$$+\frac{G}{c^2}\left((1+a\alpha_1)\frac{m_1}{|\boldsymbol{x}-\boldsymbol{x}_1|}+(1+a\alpha_2)\frac{m_2}{|\boldsymbol{x}-\boldsymbol{x}_2|}\right)\left(\frac{q_1}{|\boldsymbol{x}-\boldsymbol{x}_1|}+\frac{q_2}{|\boldsymbol{x}-\boldsymbol{x}_2|}\right)$$
$$+\frac{G}{c^2}\left((1+a\alpha_2)\frac{q_1 m_2}{r|\boldsymbol{x}-\boldsymbol{x}_1|}+(1+a\alpha_1)\frac{q_2 m_1}{r|\boldsymbol{x}-\boldsymbol{x}_2|}\right)$$
$$-\frac{G}{c^2}\left((1+a\alpha_1)\frac{m_1 q_2}{r|\boldsymbol{x}-\boldsymbol{x}_1|}+(1+a\alpha_2)\frac{m_2 q_1}{r|\boldsymbol{x}-\boldsymbol{x}_2|}\right). \tag{M.33}$$

M.4 The 1PN Lagrangian

The total action, after using the field equations and integrating by parts, can be written as

$$S=\int dt d^3\boldsymbol{x}\Bigg[\rho_g\left(-c^2+\frac{1}{2}v^2+\frac{v^4}{8c^2}+\frac{1}{2}Vc^2+\frac{3}{4}Vv^2-2V_i v^i c\right)+\rho_e\left(\frac{1}{2}A_0+\frac{1}{2c}A_i v^i\right)$$
$$+\frac{1}{2}\rho_g\alpha\varphi\left(-c^2+\frac{1}{2}v^2\right)+\frac{1}{2}\rho_e A_0 V-\frac{1}{2}a\rho_e A_0\varphi+\frac{G}{4c^2}\rho_g(1+a\alpha)A_0^2\Bigg]. \tag{M.34}$$

Substituting the potentials gives acceleration terms that can be eliminated using integration by parts in the action

$$\int dt\,(\boldsymbol{n}\cdot\boldsymbol{a}_1)=\int dt\left(-\frac{v_1^2}{r}+\frac{(\boldsymbol{n}\cdot\boldsymbol{v}_1)^2}{r}-\frac{(\boldsymbol{n}\cdot\boldsymbol{v}_1)(\boldsymbol{n}\cdot\boldsymbol{v}_2)}{r}+\frac{\boldsymbol{v}_1\cdot\boldsymbol{v}_2}{r}\right), \tag{M.35}$$

where $\boldsymbol{n} \equiv (\boldsymbol{x}_1 - \boldsymbol{x}_2)/|\boldsymbol{x}_1 - \boldsymbol{x}_2|$, and $\boldsymbol{a}_1 = \dot{\boldsymbol{v}}_1$. Finally, integrating over space term by term and simplifying leads to the 1PN Lagrangian

$$L = -m_1 c^2 - m_2 c^2 + L_0 + \frac{1}{c^2} L_1 \,, \tag{M.36}$$

with

$$\begin{aligned}
L_0 =& \frac{1}{2} m_1 v_1^2 + \frac{1}{2} m_2 v_2^2 + G(1+\alpha_1\alpha_2)\frac{m_1 m_2}{r} - \frac{q_1 q_2}{r}, \\
L_1 =& \frac{1}{8} m_1 v_1^4 + \frac{1}{8} m_2 v_2^4 + \frac{q_1 q_2}{2r}\left[\boldsymbol{v_1}\cdot\boldsymbol{v_2} + (\boldsymbol{n}\cdot\boldsymbol{v_1})(\boldsymbol{n}\cdot\boldsymbol{v_2})\right] \\
&+ \frac{G m_1 m_2}{2r}\Big[(3-\alpha_1\alpha_2)(v_1^2+v_2^2) - (7-\alpha_1\alpha_2)(\boldsymbol{v_1}\cdot\boldsymbol{v_2}) - (1+\alpha_1\alpha_2)(\boldsymbol{n}\cdot\boldsymbol{v_1})(\boldsymbol{n}\cdot\boldsymbol{v_2})\Big] \\
&- \frac{G^2 m_1 m_2}{2r^2}\Big[(1+2\alpha_1\alpha_2)(m_1+m_2) + m_1\alpha_1^2(\alpha_2^2+\beta_2) + m_2\alpha_2^2(\alpha_1^2+\beta_1)\Big] \\
&+ \frac{G q_1 q_2}{r^2}\left[m_1(1+a\alpha_1) + m_2(1+a\alpha_2)\right] - \frac{G}{2r^2}\Big[m_1 q_2^2(1+a\alpha_1) + m_2 q_1^2(1+a\alpha_2)\Big] \,.
\end{aligned} \tag{M.37}$$

Appendix N: Energy flux to next-to-leading PN order in Einstein-Maxwell-dilaton theory

In this appendix, we derive the next-to-leading order scalar, vector, and tensor energy fluxes for general orbits. The derivation follows the one used in Ref. [200] in the context of ST theory.

N.1 Scalar energy flux

The scalar field in a radiative coordinate system can be written as

$$\varphi(\boldsymbol{X}^\mu) = \varphi_0 + \frac{1}{R}\psi(U, \boldsymbol{N}) + \mathcal{O}\left(\frac{1}{R^2}\right), \tag{N.1}$$

where $R \equiv |\boldsymbol{X}|$, $U \equiv T - R/c$, $\boldsymbol{N} \equiv \boldsymbol{X}/R$, and the Einstein-frame radiative scalar multipole moments are defined by

$$\psi(U, \boldsymbol{N}) = G \sum_{\ell \geq 0} \frac{1}{\ell! c^{\ell+2}} N^L \Psi_L^{(\ell)}(U). \tag{N.2}$$

In this notation, an uppercase index denotes a multi-index, such as $N^L = N^{i_1} N^{i_2} \ldots N^{i_\ell}$. A superscript in parentheses denotes derivative, such as $\Psi^{(\ell)}(U) = d^\ell \Psi / dU^\ell$.

Next, to relate the radiative moments to the source moments, one defines 'algorithmic' moments that serve as functional parameters for a general external metric. Based on the arguments in Refs. [138, 200], the radiative moments coincide with the algorithmic ones to $\mathcal{O}(1/c^3)$, and the algorithmic moments agree with the source moments K_L to order $\mathcal{O}(1/c^4)$

$$\Psi_L = \Psi_L^{\text{(alg)}} + \mathcal{O}(1/c^3), \tag{N.3}$$

$$\Psi_L^{\text{(alg)}} = K_L + \mathcal{O}(1/c^4). \tag{N.4}$$

The source moments are defined by

$$K_L = \int d^3x \left[\widehat{x}_L S + \frac{1}{2(2\ell+3)c^2}\boldsymbol{x}^2\widehat{x}_L\frac{\partial^2 S}{\partial t^2}\right], \tag{N.5}$$

where the hat on x_L denotes a symmetric trace-free projection on the ℓ indices. The source function S is defined by the field equation for φ as

$$\Box\varphi = -\frac{4\pi G}{c^2}S. \tag{N.6}$$

The scalar energy flux

$$\mathcal{F}_S = -cR^2\oint T^S_{0i}N^i d\Omega, \tag{N.7}$$

where the scalar part of the stress-energy tensor is given by

$$T^S_{\mu\nu} = \frac{c^4}{4\pi G}\left[\nabla_\mu\varphi\nabla_\nu\varphi - \frac{1}{2}g_{\mu\nu}(\nabla\varphi)^2\right]. \tag{N.8}$$

In the far zone,

$$T^S_{0i} \simeq \frac{c^4}{4\pi G}\partial_0\varphi\partial_i\varphi \simeq -\frac{c^4}{4\pi G}N_i(\partial_0\varphi)^2, \tag{N.9}$$

where, in the last step, we used the relation

$$\partial_i\varphi = -N_i\partial_0\varphi + \mathcal{O}(r/R^2). \tag{N.10}$$

The scalar flux becomes

$$\mathcal{F}_S = \frac{c^3}{4\pi G}\int d\Omega\left(\frac{\partial\psi}{\partial U}\right)^2$$

$$= G\sum_{\ell\geq 0}\frac{1}{c^{2\ell+1}(\ell!)^2}\int\frac{d\Omega}{4\pi}N^L N^P \Psi_L^{(\ell+1)}(U)\Psi_P^{(\ell+1)}(U). \tag{N.11}$$

To integrate over the solid angle, we use the integration formula given by Eq. (A 29a) in Ref. [137], which yields

$$\begin{aligned}\mathcal{F}_S &= G\sum_{\ell\geq 0}\frac{1}{c^{2\ell+1}\ell!(2\ell+1)!!}\Psi_L^{(\ell+1)}(U)\Psi_L^{(\ell+1)}(U)\\ &= G\left[\frac{\Psi^{(1)}\Psi^{(1)}}{c}+\frac{\Psi_i^{(2)}\Psi_i^{(2)}}{3c^3}+\frac{\Psi_{ij}^{(3)}\Psi_{ij}^{(3)}}{30c^5}+\dots\right],\end{aligned} \tag{N.12}$$

where the first term is the monopole flux, the second is the dipole flux, and the third is the quadrupole flux. In terms of the source function S, those multipole moments needed for the calculation of the next-to-leading order flux are given by

$$\Psi = \int d^3x\left[S+\frac{1}{6c^2}\frac{d}{dt}(x^2 S)\right], \tag{N.13}$$

$$\Psi_i = \int d^3x\left[x^i S+\frac{1}{10c^2}\frac{d}{dt}\left(x^2 x^i S\right)\right], \tag{N.14}$$

$$\Psi_{ij} = \int d^3x\left(x^i x^j-\frac{1}{3}x^2\delta_{ij}\right)S. \tag{N.15}$$

The 1PN field equation for φ is given by Eq. (M.28)

$$\Box\varphi = -\frac{4\pi G}{c^2}\rho_g\left[-\alpha+\frac{1}{2c^2}\alpha v^2+\alpha V-(\alpha^2+\beta)\varphi\right]-\frac{Ga}{c^4}A_0\nabla^2 A_0+\frac{Ga}{2c^4}\nabla^2(A_0)^2. \tag{N.16}$$

The last term in that equation can be moved to the left hand side by a redefinition of the field, and since $A_0^2\sim 1/R^2$, we can neglect that term to $\mathcal{O}(1/R)$. The other terms are expressed in terms of delta functions. Hence, we can write the source function S as

$$S(\boldsymbol{x},t) = \sum_A \sigma_A\delta^3(\boldsymbol{x}-\boldsymbol{x}_A), \tag{N.17}$$

with

$$\sigma_1 = -m_1\alpha_1\left(1-\frac{v_1^2}{2c^2}\right)+\frac{m_1 m_2}{c^2 r}\left(\alpha_1+\alpha_1^2\alpha_2+\beta_1\alpha_2\right)-\frac{aq_1q_2}{c^2 r}, \tag{N.18}$$

and similarly for σ_2, where $\boldsymbol{r} \equiv \boldsymbol{x}_1 - \boldsymbol{x}_2$. In the center-of-mass coordinates, we define

$$\begin{aligned}
\boldsymbol{v} &\equiv \frac{d\boldsymbol{r}}{dt}\,, \qquad \boldsymbol{a} \equiv \frac{d\boldsymbol{v}}{dt}\,, \\
\boldsymbol{x}_1 &= \frac{m_2}{M}\boldsymbol{r} + \mathcal{O}\left(\frac{1}{c^2}\right), \\
\boldsymbol{x}_2 &= -\frac{m_1}{M}\boldsymbol{r} + \mathcal{O}\left(\frac{1}{c^2}\right).
\end{aligned} \tag{N.19}$$

Thus, σ_1 can be written as

$$\sigma_1 = -\, m_1\alpha_1 + \frac{\nu}{2c^2} m_1\alpha_1 v^2 + \frac{M^2\nu}{c^2 r}\left[\alpha_1 + \alpha_1^2\alpha_2 + \beta_1\alpha_2 - \frac{aq_1q_2}{M\mu}\right]. \tag{N.20}$$

The multipole moments can now be written in terms of σ after integrating the delta functions

$$\Psi^{(1)} = \frac{d\sigma_1}{dt} - \frac{m_1\alpha_1}{6c^2}\frac{d^2}{dt^2}x_1^2 + 1 \leftrightarrow 2, \tag{N.21}$$

$$\Psi_i^{(2)} = \frac{d^2}{dt^2}(x_1^i\sigma_1) - \frac{m_1\alpha_1}{10c^2}\frac{d^4}{dt^4}x_1^2 x_1^i + 1 \leftrightarrow 2, \tag{N.22}$$

$$\Psi_{ij}^{(3)} = -m_1\alpha_1\frac{d^3}{dt^3}\left(x_1^i x_1^j - \frac{1}{3}x_1^2\delta_{ij}\right) + 1 \leftrightarrow 2, \tag{N.23}$$

where, in the higher order terms, we used $\sigma_1 = -m_1\alpha_1$.

For the monopole and quadrupole fluxes, the multipole moments in the center-of-mass coordinates can be written as

$$\Psi^{(1)} = \frac{d}{dt}(\sigma_1 + \sigma_2) - \frac{\nu}{6c^2}\left(m_2\alpha_1 + m_1\alpha_2\right)\frac{d^3 r^2}{dt^3}\,, \tag{N.24}$$

$$\Psi_{ij}^{(3)} = -\nu(m_2\alpha_1 + m_1\alpha_2)\frac{d^3}{dt^3}\left(r^i r^j - \frac{1}{3}r^2\delta_{ij}\right). \tag{N.25}$$

Differentiating, and using the relations

$$\begin{aligned}
\frac{d^2\boldsymbol{r}}{dt^2} &= -\frac{G_{12}M}{r^2}\boldsymbol{n} + \mathcal{O}\left(\frac{1}{c^2}\right), \\
\frac{d\boldsymbol{n}}{dt} &= \frac{\boldsymbol{v} - \dot{r}\boldsymbol{n}}{r}\,,
\end{aligned} \tag{N.26}$$

where

$$G_{12} \equiv G\left(1 + \alpha_1\alpha_2 - \frac{q_1 q_2}{M\mu}\right), \tag{N.27}$$

we get

$$\begin{aligned}
\Psi^{(1)} &= -\frac{2}{3}\frac{G_{12}M\mu}{c^2 r^2}\dot{r}\left(X_2\alpha_1 + X_1\alpha_2\right) \\
&\quad - \frac{M\mu}{c^2 r^2}\dot{r}\left[\alpha_1 + \alpha_2 + \alpha_1^2\alpha_2 + \alpha_2^2\alpha_1 + \beta_1\alpha_2 + \beta_2\alpha_1 - \frac{2aq_1q_2}{M\mu}\right], \\
\Psi^{(3)}_{ij} &= -\frac{G_{12}M\mu}{r^2}\left(X_1\alpha_2 + X_2\alpha_1\right)\left[6\dot{r}n^i n^j - 4(n^i v^j + n^j v^i) + \frac{2}{3}\dot{r}\delta_{ij}\right].
\end{aligned} \tag{N.28}$$

Squaring leads to the monopole and quadrupole scalar fluxes

$$\begin{aligned}
\mathcal{F}_S^{\text{Mon}} &= G\frac{\Psi^{(1)}\Psi^{(1)}}{c} \\
&= \frac{G}{c^5}\left(\frac{G_{12}M\mu}{r^2}\right)^2 \dot{r}^2\left[\frac{\alpha_1 + \alpha_2 + \alpha_1^2\alpha_2 + \alpha_2^2\alpha_1 + \beta_1\alpha_2 + \beta_2\alpha_1 - \frac{2aq_1q_2}{M\mu}}{1 + \alpha_1\alpha_2 - \frac{q_1q_2}{M\mu}}\right. \\
&\qquad \left. + \frac{2}{3}\left(X_2\alpha_1 + X_1\alpha_2\right)\right]^2.
\end{aligned} \tag{N.29}$$

$$\begin{aligned}
\mathcal{F}_S^{\text{Quad}} &= G\frac{\Psi^{(3)}_{ij}\Psi^{(3)}_{ij}}{c^5} \\
&= \frac{G}{30c^5}\left(\frac{G_{12}M\mu}{r^2}\right)^2 \left(X_1\alpha_2 + X_2\alpha_1\right)^2\left(32v^2 - \frac{88}{3}\dot{r}^2\right).
\end{aligned} \tag{N.30}$$

For the dipole flux, we need to write $\boldsymbol{x}_1$ and $\boldsymbol{x}_2$ in the center-of-mass coordinates to 1PN order. From the boost invariance of the Lagrangian, we obtain [200]

$$\begin{aligned}
\boldsymbol{x}_1 &= \frac{\mu_2}{\mu_1 + \mu_2}\boldsymbol{r} + \mathcal{O}\left(\frac{1}{c^4}\right), \\
\boldsymbol{x}_2 &= -\frac{\mu_1}{\mu_1 + \mu_2}\boldsymbol{r} + \mathcal{O}\left(\frac{1}{c^4}\right),
\end{aligned} \tag{N.31}$$

where

$$\mu_1 \equiv m_1\left(1 + \frac{v_1^2}{2c^2} - \frac{G_{12}m_2}{2c^2 r}\right) + \mathcal{O}\left(\frac{1}{c^4}\right)$$

$$= M\left(X_1 + X_2\frac{\nu v^2}{2c^2} - \frac{G_{12}M\nu}{2c^2 r}\right) + \mathcal{O}\left(\frac{1}{c^4}\right), \tag{N.32}$$

and similarly for μ_2. This leads to the dipole moment Ψ_i in the center-of-mass coordinates

$$\Psi_i^{(2)} = \frac{d^2}{dt^2}\left(\frac{\mu_2}{\mu_1+\mu_2} r^i \sigma_1\right) - \frac{d^2}{dt^2}\left(\frac{\mu_1}{\mu_1+\mu_2} r^i \sigma_2\right) + \frac{\mu}{10c^2}\left(X_1^2\alpha_2 - X_2^2\alpha_1\right)\frac{d^4}{dt^4}(r^2 r^i). \tag{N.33}$$

To calculate the dipole flux, we also need the 1PN acceleration, which can be derived from the 1PN Lagrangian, and we obtain

$$\begin{aligned}
\frac{d^2\boldsymbol{r}}{dt^2} =& -\frac{G_{12}M}{r^2}\boldsymbol{n}\Bigg\{1 + \frac{v^2}{c^2}\left[3\nu + \frac{1-\alpha_1\alpha_2 + q_1q_2/2M\mu}{1+\alpha_1\alpha_2 - q_1q_2/M\mu}\right] - \frac{3}{2c^2}\nu\dot{r}^2 - 2\nu\frac{G_{12}M}{c^2 r} \\
&- \frac{G_{12}M}{c^2 r}\frac{1}{\left(1+\alpha_1\alpha_2 - \frac{q_1q_2}{M\mu}\right)^2}\Bigg[2\nu\left(1+\alpha_1\alpha_2 - \frac{q_1q_2}{M\mu}\right)^2 + X_2\frac{q_1^2}{M\mu}(1+a\alpha_2) \\
&+ X_1\frac{q_2^2}{M\mu}(1+a\alpha_1) - 2a\frac{q_1q_2}{M\mu}\left(X_1\alpha_1 + X_2\alpha_2\right) - \frac{q_1q_2}{M\mu}(5-\alpha_1\alpha_2) + 4(1+\alpha_1\alpha_2) \\
&+ X_2\beta_1\alpha_2^2 + X_1\beta_2\alpha_1^2\Bigg]\Bigg\} - \frac{G_{12}M}{c^2r^2}\dot{r}\boldsymbol{v}\left[2\nu - \frac{4-q_1q_2/M\mu}{1+\alpha_1\alpha_2 - q_1q_2/M\mu}\right] + \mathcal{O}\left(\frac{1}{c^4}\right).
\end{aligned} \tag{N.34}$$

Finally, we obtain the dipole scalar flux

$$\mathcal{F}_S^{\text{dip}} = \frac{G}{3c^3}\left(\frac{G_{12}M\mu}{r^2}\right)^2\left\{(\alpha_1-\alpha_2)^2 + f^S_{\dot{r}^2}\frac{\dot{r}^2}{c^2} + f^S_{v^2}\frac{v^2}{c^2} + f^S_{1/r}\frac{G_{12}M}{c^2 r}\right\}, \tag{N.35}$$

with the coefficients

$$\begin{aligned}
f^S_{\dot{r}^2} =& \frac{-1}{1+\alpha_1\alpha_2 - \frac{q_1q_2}{M\mu}}\Bigg\{8(\alpha_1-\alpha_2)^2 - 2\nu(\alpha_1-\alpha_2)^2(1+\alpha_1\alpha_2) \\
&+ (\alpha_1-\alpha_2)(1+\alpha_1\alpha_2)\left[X_1(\alpha_1+3\alpha_2) - X_2(\alpha_2+3\alpha_1)\right] + 2(\alpha_1-\alpha_2)\left(X_1\alpha_1\beta_2 - X_2\alpha_2\beta_1\right) \\
&- \frac{q_1q_2}{M\mu}\left[2(1-\nu)(\alpha_1-\alpha_2)^2 + \left(X_1-X_2\right)(\alpha_1-\alpha_2)(2a+\alpha_1+\alpha_2)\right]\Bigg\},
\end{aligned} \tag{N.36a}$$

$$f^S_{v^2} = \frac{2}{5\left(1+\alpha_1\alpha_2 - \frac{q_1q_2}{M\mu}\right)}\Bigg\{5(\alpha_1-\alpha_2)^2(1-\alpha_1\alpha_2) + 5(\alpha_1-\alpha_2)\left(X_1\alpha_1\beta_2 - X_2\alpha_2\beta_1\right)$$

$$
\begin{aligned}
&+(\alpha_1-\alpha_2)(1+\alpha_1\alpha_2)\left[-\frac{25}{2}(1-\nu)(\alpha_1-\alpha_2)+\frac{11}{2}\left(X_2^2\alpha_1-X_1^2\alpha_2\right)+\frac{35}{2}\left(X_1\alpha_1-X_2\alpha_2\right)\right]\\
&+\frac{q_1q_2}{2M\mu}(\alpha_1-\alpha_2)\left[5(1-5\nu)(\alpha_1-\alpha_2)-10a\left(X_1-X_2\right)-11\left(X_2^2\alpha_1-X_1^2\alpha_2\right)\right]\\
&-\frac{5q_1q_2}{2M\mu}(\alpha_1-\alpha_2)\left[2\left(X_1\alpha_1-X_2\alpha_2\right)+3\left(X_1\alpha_2-X_2\alpha_1\right)\right]\Bigg\},
\end{aligned}
\tag{N.36b}
$$

$$
\begin{aligned}
f^S_{1/r}=-\frac{2}{5}\Bigg\{&5\nu(\alpha_1-\alpha_2)^2+5(\alpha_1^2-\alpha_2^2)\left(X_1-X_2\right)+6(\alpha_1-\alpha_2)\left(X_2^2\alpha_1-X_1^2\alpha_2\right)\\
&+\frac{5(\alpha_1-\alpha_2)^2}{\left(1+\alpha_1\alpha_2-\frac{q_1q_2}{M\mu}\right)^2}\left[-\frac{q_1q_2}{M\mu}\left(5-\alpha_1\alpha_2+2aX_1\alpha_1+2aX_2\alpha_2\right)+X_2\frac{q_1^2}{M\mu}(1+a\alpha_2)\right.\\
&\left.+X_1\frac{q_2^2}{M\mu}(1+a\alpha_1)\right]+\frac{5(\alpha_1-\alpha_2)^2}{\left(1+\alpha_1\alpha_2-\frac{q_1q_2}{M\mu}\right)^2}\left[4(1+\alpha_1\alpha_2)+X_2\alpha_2^2\beta_1+X_1\alpha_1^2\beta_2\right]\Bigg\}.
\end{aligned}
\tag{N.36c}
$$

This flux reduces to the ST dipole flux derived in Ref. [200] in the limit where the electric charges are zero.

N.2 Vector energy flux

The calculation of the vector flux is similar to that of the scalar flux. The vector potential can be written in terms of radiative multipole moments as [139]

$$
\begin{aligned}
A_0(\boldsymbol{X},T)&=\frac{1}{R}\sum_{\ell\geq 0}\frac{1}{\ell!c^\ell}N^LQ_L^{(\ell)}(U),\\
A_i(\boldsymbol{X},T)&=\frac{1}{R}\sum_{\ell\geq 1}\frac{1}{\ell!c^\ell}\left[N_{L-1}Q^{(\ell)}_{iL-1}(U)-\frac{\ell}{(\ell+1)c}\varepsilon_{iab}N_{aL-1}M^{(\ell)}_{bL-1}\right].
\end{aligned}
\tag{N.37}
$$

As was done in the previous section, the radiative moments can be related to the source moments using algorithmic moments. At leading order, the three agree, and we can express the electric and magnetic multipole moments directly in terms of the source moments

$$Q_L(U) = \int d^3x \left[\widehat{x}_L\rho + \frac{1}{2(2\ell+3)c^2}x^2\widehat{x}_L\frac{d^2\rho}{dt^2} - \frac{2\ell+1}{(\ell+1)(2\ell+1)c^2}\widehat{x}_{aL}\frac{dJ_a}{dt}\right], \quad \ell \geq 0\,, \tag{N.38}$$

$$M_L(U) = \int d^3x \left[\widehat{x}_{\langle L-1}m_{i_\ell\rangle} + \frac{1}{2(2\ell+3)c^2}x^2\widehat{x}_{\langle L-1}\frac{d}{dt^2}m_{i_\ell\rangle}\right], \quad \ell \geq 1\,, \tag{N.39}$$

where the magnetization density $\boldsymbol{m} = \boldsymbol{x} \times \boldsymbol{J}$. The source functions ρ and J_i are defined by

$$\Box A_0 = 4\pi\rho\,, \qquad \Box A_i = -\frac{4\pi}{c}J_i. \tag{N.40}$$

The vector flux

$$\mathcal{F}_V = -cR^2 \oint N^i T^{\rm EM}_{0i} d\Omega, \tag{N.41}$$

where the electromagnetic part of the stress-energy tensor is given by

$$T^{\rm EM}_{\mu\nu} = \frac{1}{8\pi}e^{-2a\varphi}\left(2F_{\mu\alpha}F_\nu{}^\alpha - \frac{1}{2}g_{\mu\nu}F^2\right). \tag{N.42}$$

In the far zone,

$$\begin{aligned} T^{\rm EM}_{0i} &= \frac{1}{4\pi}F_{0j}F_i{}^j \\ &= \frac{1}{4\pi}\left(\partial_0 A_j - \partial_j A_0\right)\left(\partial_i A_j - \partial_j A_i\right). \end{aligned} \tag{N.43}$$

The vector flux becomes

$$\mathcal{F}_V = \frac{R^2}{4\pi c}\int d\Omega \left[\frac{\partial A_i}{\partial U}\frac{\partial A_i}{\partial U} - N^i N^j \frac{\partial A_i}{\partial U}\frac{\partial A_j}{\partial U}\right]. \tag{N.44}$$

The vector potential A_i, to the required order, has the multipole expansion

$$A_i = \frac{1}{R}\left[\frac{1}{c}Q_i^{(1)} - \frac{1}{2c^2}\varepsilon_{ijk}N^j M_k^{(1)} + \frac{1}{2c^2}N^j Q_{ij}^{(2)}\right], \tag{N.45}$$

which leads to

$$\frac{R^2}{4\pi c}\int d\Omega\left(\frac{\partial A_i}{\partial U}\right)^2 = \frac{Q_i^{(2)}Q_i^{(2)}}{c^3} + \frac{M_i^{(2)}M_i^{(2)}}{6c^5} + \frac{Q_{ij}^{(3)}Q_{ij}^{(3)}}{12c^5} + \mathcal{O}\left(\frac{1}{c^7}\right)$$
$$= \sum_{\ell\geq 1}\frac{1}{c^{2\ell+1}\ell!(2\ell+1)!!}\left[\frac{2\ell+1}{\ell}Q_L^{(\ell+1)}Q_L^{(\ell+1)} + \frac{\ell}{c^2(\ell+1)}M_L^{(\ell+1)}M_L^{(\ell+1)}\right], \tag{N.46}$$

and

$$\frac{R^2}{4\pi c}\int d\Omega N^i N^j \frac{\partial A_i}{\partial U}\frac{\partial A_j}{\partial U} = \sum_{\ell\geq 1}\frac{1}{c^{2\ell+1}\ell!(2\ell+1)!!}Q_L^{(\ell+1)}Q_L^{(\ell+1)}$$
$$= \frac{Q_i^{(2)}Q_i^{(2)}}{3c^3} + \frac{Q_{ij}^{(3)}Q_{ij}^{(3)}}{30c^5} + \mathcal{O}\left(\frac{1}{c^7}\right). \tag{N.47}$$

Hence, the vector flux

$$\mathcal{F}_V = \sum_{\ell\geq 1}\frac{1}{c^{2\ell+1}\ell!(2\ell+1)!!}\left[\frac{\ell+1}{\ell}Q_L^{(\ell+1)}Q_L^{(\ell+1)} + \frac{\ell}{c^2(\ell+1)}M_L^{(\ell+1)}M_L^{(\ell+1)}\right] \tag{N.48}$$
$$= \frac{2Q_i^{(2)}Q_i^{(2)}}{3c^3} + \frac{M_i^{(2)}M_i^{(2)}}{6c^5} + \frac{Q_{ij}^{(3)}Q_{ij}^{(3)}}{20c^5} + \dots. \tag{N.49}$$

The first two terms give the dipole flux, and the third term is the quadrupole flux. There is no monopole flux because of the conservation of the total electric charge.

The 1PN field equations are given by Eqs. (M.20) and (M.29), which are

$$\Box A_i = -\frac{4\pi}{c}\rho_e v^i\,, \tag{N.50}$$
$$\Box A_0 = 4\pi\rho_e - V\nabla^2 A_0 + A_0\nabla^2 V + a\varphi\nabla^2 A_0 - aA_0\nabla^2\varphi$$
$$- \nabla^2(VA_0) + a\nabla^2(\varphi A_0). \tag{N.51}$$

The last two terms in the above equation are of order $1/R^2$, and hence do not contribute to the next-to-leading order flux. The source functions ρ and J^i are then given by

$$\rho = \rho_e = q_1\delta^3(\boldsymbol{x}-\boldsymbol{x}_1) + q_2\delta^3(\boldsymbol{x}-\boldsymbol{x}_2), \tag{N.52}$$

$$J^i = \rho_e v^i = q_1 v_1^i \delta^3(\boldsymbol{x} - \boldsymbol{x}_1) + q_2 v_2^i \delta^3(\boldsymbol{x} - \boldsymbol{x}_2). \tag{N.53}$$

The function ρ is simply the electric charge density because the higher order terms from the field equation cancel when summed over the two bodies.

For the dipole flux, we need Q_i and M_i to $\mathcal{O}(1/c^2)$

$$\begin{aligned}
Q_i =& \int d^3x \left[x_i \rho_e + \frac{1}{10c^2} \rho_e \frac{d^2}{dt^2} \left(x^2 x^i \right) - \frac{3}{10c^2} \frac{d}{dt} \left(\widehat{x}_{ij} J_j \right) \right] \\
=& \left(q_1 \frac{\mu_2}{\mu_1 + \mu_2} - q_2 \frac{\mu_1}{\mu_1 + \mu_2} \right) r^i + \frac{1}{10c^2} \left(q_1 \frac{m_2^3}{M^3} - q_2 \frac{m_1^3}{M^3} \right) \frac{d^2}{dt^2} \left(r^i r^2 \right) \\
& - \frac{3}{10c^2} \left(q_1 \frac{m_2^3}{M^3} - q_2 \frac{m_1^3}{M^3} \right) \frac{d}{dt} \left(r^i r^j - \frac{1}{3} r^2 \delta^{ij} \right) v^j \,,
\end{aligned} \tag{N.54}$$

$$\begin{aligned}
M_i =& \, q_1 \varepsilon_{ijk} x_1^j v_1^k + q_2 \varepsilon_{ijk} x_2^j v_2^k \\
=& \left(q_1 \frac{m_2^2}{M^2} + q_2 \frac{m_1^2}{M^2} \right) \varepsilon_{ijk} r^j v^k \,.
\end{aligned} \tag{N.55}$$

Differentiating and using the 1PN acceleration from Eq. (N.34), we obtain the next-to-leading order vector dipole flux

$$\mathcal{F}_V^{\mathrm{Dip}} = \frac{2}{3c^3} \left(\frac{G_{12} M \mu}{r^2} \right)^2 \left[\left(\frac{q_1}{m_1} - \frac{q_2}{m_2} \right)^2 + f_{v^2}^V \frac{v^2}{c^2} + f_{\dot{r}^2}^V \frac{\dot{r}^2}{c^2} + f_{1/r}^V \frac{G_{12} M}{c^2 r} \right], \tag{N.56}$$

with the coefficients

$$\begin{aligned}
f_{v^2}^V =& \frac{2}{5} \left(X_2^2 \frac{q_1}{m_1} - X_1^2 \frac{q_2}{m_2} \right) \left(\frac{q_1}{m_1} - \frac{q_2}{m_2} \right) + \frac{2}{M} (X_1 - X_2) \left(q_1 + q_2 \right) \left(\frac{q_1}{m_1} - \frac{q_2}{m_2} \right) \\
& + \frac{1}{1 + \alpha_1 \alpha_2 - \frac{q_1 q_2}{M\mu}} \left(\frac{q_1}{m_1} - \frac{q_2}{m_2} \right)^2 \left[2 + 6\nu + 2\alpha_1 \alpha_2 (3\nu - 1) + \frac{q_1 q_2}{M\mu} (1 - 6\nu) \right],
\end{aligned} \tag{N.57a}$$

$$f_{\dot{r}^2}^V = - \left(\frac{q_1}{m_1} - \frac{q_2}{m_2} \right)^2 \left[3\nu + \frac{(X_1 - X_2)(q_1 + q_2)}{M \left(\frac{q_1}{m_1} - \frac{q_2}{m_2} \right)} + \frac{8 - 4\nu (1 + \alpha_1 \alpha_2) - 2 \frac{q_1 q_2}{M\mu} (1 - 2\nu)}{1 + \alpha_1 \alpha_2 - \frac{q_1 q_2}{M\mu}} \right], \tag{N.57b}$$

$$f_{1/r}^V = -2 \left(\frac{q_1}{m_1} - \frac{q_2}{m_2} \right)^2 \left[2\nu + \frac{2}{5} \frac{X_2^2 q_1/m_1 - X_1^2 q_2/m_2}{q_1/m_1 - q_2/m_2} - \frac{q_1 q_2}{M\mu} \frac{5 - \alpha_1 \alpha_2 + 2a \left(X_1 \alpha_1 + X_2 \alpha_2 \right)}{\left(1 + \alpha_1 \alpha_2 - \frac{q_1 q_2}{M\mu} \right)^2} \right.$$

$$+\frac{4(1+\alpha_1\alpha_2)+X_2\frac{q_1^2}{M\mu}(1+a\alpha_2)+X_1\frac{q_2^2}{M\mu}(1+a\alpha_1)+X_2\alpha_2^2\beta_1+X_1\alpha_1^2\beta_2}{\left(1+\alpha_1\alpha_2-\frac{q_1q_2}{M\mu}\right)^2}$$

$$+\left.\frac{(X_1-X_2)(q_1+q_2)}{M\left(\frac{q_1}{m_1}-\frac{q_2}{m_2}\right)}\right]. \tag{N.57c}$$

For the quadrupole flux,

$$Q_{ij}^{(3)}=\int d^3x\left(x_ix_j-\frac{1}{3}x^2\delta_{ij}\right)\rho_e=\left(X_2^2q_1+X_1^2q_2\right)\frac{d^3}{dt^3}\left(r^ir^j-\frac{1}{3}r^2\delta^{ij}\right), \tag{N.58}$$

which leads to

$$\mathcal{F}_V^{\text{Quad}}=\frac{Q_{ij}^{(3)}Q_{ij}^{(3)}}{30c^5}=\frac{1}{30c^5}\left(\frac{G_{12}M\mu}{r^2}\right)^2\left(X_2\frac{q_1}{M}+X_1\frac{q_2}{m_2}\right)^2\left(32v^2-\frac{88}{3}\dot{r}^2\right). \tag{N.59}$$

N.3 Tensor energy flux

The metric in radiative coordinates

$$G_{\mu\nu}(\boldsymbol{X}^\mu)=\eta_{\mu\nu}+\frac{1}{R}H_{\mu\nu}(U,\boldsymbol{N})+\mathcal{O}\left(\frac{1}{R^2}\right), \tag{N.60}$$

where the radiative multipole moments M_L and S_L are defined by

$$H_{ij}^{\text{TT}}(U,\boldsymbol{N})=4G\sum_{\ell\geq 2}\frac{1}{\ell!c^{\ell+2}}\left[N_{L-2}M_{ijL-2}^{(\ell)}(U)-\frac{2\ell}{(\ell+1)c}N_{hL-2}\varepsilon_{hk(i}S_{j)kL-2}^{(\ell)}\right]^{\text{TT}}. \tag{N.61}$$

The radiative multipoles agree with the source multipoles I_L and J_L up to order

$$M_L=I_L+\mathcal{O}(1/c^3),\qquad S_L=J_L+\mathcal{O}(1/c^2), \tag{N.62}$$

where [139, 200]

$$I_L(t)=\int d^3x\left[\widehat{x}_L\sigma+\frac{1}{2(2\ell+3)c^2}x^2\widehat{x}_L\frac{\partial^2\sigma}{\partial t^2}-\frac{4(2\ell+1)}{(\ell+1)(2\ell+3)c^2}\widehat{x}_{Ls}\frac{\partial\sigma^s}{\partial t}\right], \tag{N.63}$$

$$J_L(t)=\int d^3x\,\varepsilon_{hk\langle i_\ell}\widehat{x}_{L-1\rangle h}\sigma^k. \tag{N.64}$$

In terms of the multipole moments, the tensor flux is given by

$$\begin{aligned}
F_g &= \frac{c^3}{32\pi G}\int d\Omega\left(\frac{\partial H^{\mathrm{TT}}_{ij}}{\partial U}\right)^2 \\
&= G\sum_{\ell\geq 2}\frac{1}{c^{2\ell+1}\ell!(2\ell+1)!!}\Bigg[\frac{(\ell+1)(\ell+2)}{\ell(\ell-1)}M_L^{(\ell+1)}(U)M_L^{(\ell+1)}(U) \\
&\qquad + \frac{4\ell(\ell+2)}{c^2(\ell-1)(\ell+1)}S_L^{\ell+1}(U)S_L^{(\ell+1)}(U)\Bigg] \\
&= \frac{G}{5c^5}M^{(3)}_{ij}M^{(3)}_{ij} + \frac{G}{189c^7}M^{(4)}_{ijk}M^{(4)}_{ijk} + \frac{16G}{45c^7}S^{(3)}_{ij}S^{(3)}_{ij} + \mathcal{O}\left(1/c^9\right),
\end{aligned} \tag{N.65}$$

where the first term is the mass quadrupole flux, the second is the mass octopole, and the third is the current quadrupole.

The source functions σ and σ^i are given by

$$\sigma \equiv \frac{T^{00}+T^{ss}}{c^2}, \qquad \sigma^i \equiv \frac{T^{0i}}{c}, \tag{N.66}$$

and from the 1PN field equations (M.27) and (M.19)

$$\Box V = -\frac{4\pi G}{c^2}\sigma, \qquad \Box V^i = -\frac{4\pi G}{c^3}\sigma^i, \tag{N.67}$$

with

$$\sigma^i = m_1 v_1^i\delta^3(\boldsymbol{x}-\boldsymbol{x}_1) + m_2 v_2^i\delta^3(\boldsymbol{x}-\boldsymbol{x}_2), \tag{N.68}$$

$$\sigma = \left[m_1 + \frac{3}{2c^2}m_1v_1^2 - \frac{G_{12}m_1m_2}{c^2 r}\right]\delta(\boldsymbol{x}-\boldsymbol{x}_1) + 1 \leftrightarrow 2. \tag{N.69}$$

The multipole moments needed for the next-to-leading order flux are M_{ij}, M_{ijk}, and S_{ij}, which are given by

$$M_{ij} = \left(m_1 + \frac{3}{2c^2}m_1v_1^2 - \frac{G_{12}m_1m_2}{c^2r}\right)\widehat{x}_1^{ij} + \frac{m_1}{14c^2}\frac{d^2}{dt^2}x_1^2\widehat{x}_1^{ij} - \frac{20m_1}{21c^2}\frac{d}{dt}v_1^k\widehat{x}_1^{ijk} + 1 \leftrightarrow 2, \tag{N.70}$$

$$M_{ijk} = m_1 \widehat{x}_1^{ijk} + m_2 \widehat{x}_2^{ijk}, \tag{N.71}$$

$$S_{ij} = m_1 \varepsilon^{hk\langle j} x_1^{i\rangle} x_1^h v_1^k + 1 \leftrightarrow 2. \tag{N.72}$$

In the center-of-mass coordinates, this becomes

$$\begin{aligned} M_{ij} &= \mu \left[1 + \frac{3}{2c^2}(1-3\nu)v^2 - \frac{G_{12}M}{c^2 r}(1-2\nu)\right] + \frac{\mu}{14c^2}(1-3\nu)\frac{d^2}{dt^2} r^2 \widehat{r}^{ij} \\ &\quad - \frac{20\mu}{21c^2}(1-3\nu)\frac{d}{dt} v^k \widehat{r}^{ijk}, \end{aligned} \tag{N.73}$$

$$M_{ijk} = \mu \left[\frac{m_2^2}{M^2} - \frac{m_1^2}{M^2}\right] \widehat{r}^{ijk}, \tag{N.74}$$

$$S_{ij} = \mu \left[\frac{m_2^2}{M^2} - \frac{m_1^2}{M^2}\right] \varepsilon^{hk\langle j} r^{i\rangle} r^h v^k, \tag{N.75}$$

where

$$\widehat{r}^{ij} = r^i r^j - \frac{1}{3} r^2 \delta_{ij}, \tag{N.76}$$

$$\widehat{r}^{ijk} = r^i r^j r^k - \frac{r^2}{5}\left(r^i \delta^{jk} + r^j \delta^{ik} + r^k \delta^{ij}\right), \tag{N.77}$$

$$\varepsilon^{hk\langle j} r^{i\rangle} r^h v^k = \left[\frac{1}{2}\varepsilon^{hkj} r^i + \frac{1}{2}\varepsilon^{hki} r^j - \frac{1}{3}\varepsilon^{hkm} r^m\right] r^h v^k. \tag{N.78}$$

Taking the time derivatives of the multipole moments and squaring, we obtain the tensor flux

$$\begin{aligned} \mathcal{F}_T = \frac{8G}{15c^5}\left(\frac{G_{12}M\mu}{r^2}\right)^2 \left[12v^2 - 11\dot{r}^2\right] + \frac{8G}{420c^7}\left(\frac{G_{12}M\mu}{r^2}\right)^2 \Big[f^T_{v^4} v^4 + f^T_{v^2\dot{r}^2} v^2 \dot{r}^2 \\ + f^T_{\dot{r}^4}\dot{r}^4 + f^T_{v^2/r}\frac{G_{12}Mv^2}{r} + f^T_{\dot{r}^2/r}\frac{G_{12}M\dot{r}^2}{r} + f^T_{1/r^2}\frac{G_{12}^2M^2}{r^2}\Big], \end{aligned} \tag{N.79}$$

with the coefficients

$$f^T_{v^4} = \left[\frac{785 + 113\alpha_1\alpha_2 - 281\frac{q_1q_2}{M\mu}}{1 + \alpha_1\alpha_2 - \frac{q_1q_2}{M\mu}} - 852\nu\right], \tag{N.80a}$$

$$f^T_{v^2\dot{r}^2} = -2\left[\frac{1487 + 255\alpha_1\alpha_2 - 563\frac{q_1q_2}{M\mu}}{1 + \alpha_1\alpha_2 - \frac{q_1q_2}{M\mu}} - 1392\nu\right], \tag{N.80b}$$

$$f^T_{\dot{r}^4} = 3\left[\frac{687 + 127\alpha_1\alpha_2 - 267\frac{q_1q_2}{M\mu}}{1 + \alpha_1\alpha_2 - \frac{q_1q_2}{M\mu}} - 620\nu\right], \tag{N.80c}$$

$$f^T_{1/r^2} = 16(1-4\nu), \tag{N.80d}$$

$$\begin{aligned}
f^T_{v^2/r} = &-\frac{8}{\left(1+\alpha_1\alpha_2-\frac{q_1q_2}{M\mu}\right)^2}\Bigg[20(1+\alpha_1\alpha_2)(17-\nu)+4\alpha_1\alpha_2(1+\alpha_1\alpha_2)(22-5\nu)\\
&+84\frac{q_1^2}{M\mu}X_2(1+a\alpha_2)+84\frac{q_2^2}{M\mu}X_1(1+a\alpha_1)+\frac{q_1^2q_2^2}{M^2\mu^2}(67-20\nu)\\
&-168\frac{aq_1q_2}{M\mu}\left(X_1\alpha_1+X_2\alpha_2\right)-\frac{q_1q_2}{M\mu}(491-40\nu)-\alpha_1\alpha_2\frac{q_1q_2}{M\mu}(71-40\nu)\\
&+84\left(X_1\alpha_1^2\beta_2+X_2\alpha_2^2\beta_1\right)\Bigg],
\end{aligned} \tag{N.80e}$$

$$\begin{aligned}
f^T_{\dot{r}^2/r} = &\frac{8}{\left(1+\alpha_1\alpha_2-\frac{q_1q_2}{M\mu}\right)^2}\Bigg[(1+\alpha_1\alpha_2)(367-15\nu)+3\alpha_1\alpha_2(1+\alpha_1\alpha_2)(29-5\nu)\\
&+84\frac{q_1^2}{M\mu}X_2(1+a\alpha_2)+84\frac{q_2^2}{M\mu}X_1(1+a\alpha_1)+\frac{q_1^2q_2^2}{M^2\mu^2}(73-15\nu)\\
&-168\frac{aq_1q_2}{M\mu}\left(X_1\alpha_1+X_2\alpha_2\right)-\frac{2q_1q_2}{M\mu}(262-15\nu)-2\frac{q_1q_2}{M\mu}\alpha_1\alpha_2(38-15\nu)\\
&+84\left(X_1\alpha_1^2\beta_2+X_2\alpha_2^2\beta_1\right)\Bigg].
\end{aligned} \tag{N.80f}$$

This flux reduces to the one derived in Ref. [205], in the context of ST theory, when the electric charges are zero and after converting the notation to the Jordan-Fierz frame.

N.4 Energy flux for circular orbits

In this section, we express the energy flux for circular orbits in terms of the gauge-independent parameter x, which is defined by

$$x \equiv \left(\frac{G_{12}M\Omega}{c^3}\right)^{2/3}, \tag{N.81}$$

where Ω is the orbital frequency. To do that, we need to find the relation between r and Ω to 1PN order (Kepler's third law). We start by writing the Lagrangian (8.31) in the center-of-mass coordinates

$$L = -Mc^2 + \frac{1}{2}\mu v^2 + \frac{G_{12}M\mu}{r} + \frac{1}{c^2}\Bigg\{\frac{G_{12}M\mu}{2r}\left[\left(\frac{3-\alpha_1\alpha_2}{1+\alpha_1\alpha_2-\frac{q_1q_2}{M\mu}}+\nu\right)v^2+\nu\dot{r}^2\right]$$
$$+\frac{1}{8}(1-3\nu)\mu v^4 - \frac{M^2\mu}{2r^2}\bigg[(1+\alpha_1\alpha_2)^2 - 2\frac{q_1q_2}{M\mu}(1+a\alpha_1X_1+a\alpha_2X_2)$$
$$+X_2\alpha_2^2\beta_1 + X_1\alpha_1^2\beta_2 + \frac{q_2^2}{M\mu}X_1(1+a\alpha_1) + \frac{q_1^2}{M\mu}X_2(1+a\alpha_2)\bigg]\Bigg\}. \tag{N.82}$$

Applying the Euler-Lagrange equation and using $\dot{r} = 0$ and $v = r\Omega$ leads to

$$\Omega^2 = \frac{G_{12}M}{r^3}\left[1 - 3f_\gamma\gamma + \mathcal{O}\left(\frac{1}{c^4}\right)\right], \tag{N.83}$$

where the parameter γ is defined by

$$\gamma \equiv \frac{G_{12}M}{c^2r}, \tag{N.84}$$

and the the coefficient f_γ is defined by

$$f_\gamma \equiv \frac{1}{6G_{12}^2}\bigg[G_{12}^2(1-2\nu) + G_{12}(3-\alpha_1\alpha_2) + 2(1+\alpha_1\alpha_2)^2 + 2X_2\alpha_2^2\beta_1 + 2X_1\alpha_1^2\beta_2$$
$$+2\frac{q_2^2}{M\mu}X_1(1+a\alpha_1) + 2\frac{q_1^2}{M\mu}X_2(1+a\alpha_2) - 4\frac{q_1q_2}{M\mu}(1+aX_1\alpha_1+aX_2\alpha_2)\bigg]. \tag{N.85}$$

Substituting x instead of Ω and inverting Eq. (N.83), we obtain

$$\gamma = x\left[1 + f_\gamma x + \mathcal{O}\left(1/c^4\right)\right]. \tag{N.86}$$

To express the flux for circular orbits in terms of γ, we set $\dot{r} = 0$ and $v = r\Omega$ and then use Eqs. (N.83) to obtain

$$\mathcal{F}_S = \frac{Gc^5}{3G_{12}^2}\nu^2\gamma^4(\alpha_1-\alpha_2)^2 + \frac{Gc^5}{3G_{12}^2}\nu^2\gamma^5\left[f_{v^2}^S + f_{1/r}^S + \frac{16}{5}(X_1\alpha_2+X_2\alpha_1)^2\right], \tag{N.87a}$$

$$\mathcal{F}_V = \frac{2Gc^5}{3G_{12}^2}\nu^2\gamma^4\left(\frac{q_1}{m_1}-\frac{q_2}{m_2}\right)^2 + \frac{2Gc^5}{3G_{12}^2}\nu^2\gamma^5\left[\frac{8}{5}\left(X_2\frac{q_1}{m_1}+X_1\frac{q_2}{m_2}\right)^2 + f_{v^2}^V + f_{1/r}^V\right], \tag{N.87b}$$

$$\mathcal{F}_T = \frac{32Gc^5}{5G_{12}^2}\nu^2\gamma^5 + \frac{2Gc^5}{105G_{12}^2}\nu^2\gamma^6 \left(f_{v^4}^T + f_{v^2/r}^T + f_{1/r^2}^T + 1008 f_\gamma \right). \tag{N.87c}$$

Using Eq. (N.86) to express the energy flux in terms of x instead of γ leads to Eq. (8.43a).

Appendix O: Effective action for compact objects away from critical point

A crucial assumption made in the construction of the effective action (9.7) is the near-criticality of the scalar mode q. The power counting used in the main text to formulate this relatively simple effective theory is not valid without this assumption. For example, if $c_{(2)} > 0$ (i.e., the object does not spontaneously scalarize), then away from the critical point one finds $q \sim \phi^{\text{IR}}(y) \sim \mathcal{O}(R/r)$ and must include terms like $[\phi^{\text{IR}}(y)]^2$ to the action to work consistently at the given order in R/r. For scalarized compact objects $c_{(2)} < 0$ far from the critical point, the scalar field $\phi^{\text{IR}}(y)$ and mode q reach values too large for our polynomial expansion around zero to be valid. If one expands the fields around their true (nonzero) equilibrium values instead, the effective action no longer respects the spontaneously broken scalar-inversion symmetry of the underlying theory.

In this appendix, we relax this assumption that the scalar mode q is nearly critical. We construct an effective action valid in this broader context, and then show that the model (9.7) is recovered as one approaches the critical point. We still ignore derivative couplings involving $\partial_\mu \phi^{\text{IR}}(y)$ since they belong to multipoles above the monopole ($\ell > 0$) and we are only interested in a monopolar mode q. The most generic effective action in the scalar-inversion-symmetric (unbroken) phase then reads

$$S_{\text{CO}}^{\text{unbroken}} = \int d\tau \left[\frac{c_{\dot{q}^2}}{2} \dot{q}^2 - c_{(0,0)} - V - V^{\phi} - V^{q\phi} + c_A A_\mu^{\text{IR}}(y) \dot{y}^\mu \right], \tag{O.1}$$

$$V = \frac{c_{(0,2)}}{2} q^2 + \frac{c_{(0,4)}}{4!} q^4 + \dots , \tag{O.2}$$

$$V^{\phi} = \frac{c_{(2,0)}}{2} [\phi^{\mathrm{IR}}(y)]^2 + \frac{c_{(4,0)}}{4!} [\phi^{\mathrm{IR}}(y)]^4 + \text{time derivatives} + \dots , \tag{O.3}$$

$$\begin{aligned} V^{q\phi} = & -\phi^{\mathrm{IR}}(y) q + \frac{c_{(1,3)}}{3!} \phi^{\mathrm{IR}}(y) q^3 + \frac{c_{(2,2)}}{4} [\phi^{\mathrm{IR}}(y)]^2 q^2 \\ & + \frac{c_{(3,1)}}{3!} [\phi^{\mathrm{IR}}(y)]^3 q + \text{time derivatives} + \dots , \end{aligned} \tag{O.4}$$

where the subscripts in $c_{(i,j)}$ indicate the powers of ϕ^{IR} and q, respectively; the coefficients $c_{(n)}$ in the main text correspond to $c_{(0,n)}$ in this notation. All terms must be even polynomials in ϕ^{IR}, q due to scalar-inversion symmetry and must contain an even number of time derivatives due to time-reversal symmetry. Higher time derivatives that would appear in V can always be removed by appropriate redefinition of q [781]; we assume that such field redefinition has been done. This allows for an interpretation of V as an ordinary potential for the mode q in the absence of an external driving field ϕ^{IR}.

To fix all coefficients in the action, one needs to match against the exact solution for an isolated body in a generic time-dependent external scalar field. In general, this is a complicated endeavor, and we do not attempt it here. [1] Instead, we explore what information can be gleaned from the sequences of equilibrium solutions considered in the main text. Using only this restricted class of solutions, we do not expect to find a unique match for all coefficients in the effective action above, but rather a series of relations relating them to the exact solutions.

Solutions for compact objects in equilibrium are manifestly time independent, and thus cannot inform the terms containing time derivatives in the effective action; we omit these terms from the action below for brevity. We perform the same procedure outlined in the main text to match the IR fields of the effective theory (O.1) to the IR projection of the UV solutions (9.10)

[1] Note that our assumption of time-reversal symmetry needs to be imposed on the exact solution as well, so, in the case of a BH, one must impose somewhat unphysical (reflecting) boundary conditions at the horizon.

and find $c_A = \mathcal{E}$, $\phi_0 = \phi^{\text{IR}}(y)$, and

$$Q(\phi_0) = -\frac{\partial V^{q\phi}(q, \phi^{\text{IR}})}{\partial \phi^{\text{IR}}} - \frac{dV^{\phi}(\phi^{\text{IR}})}{d\phi^{\text{IR}}}, \tag{O.5}$$

$$\mathcal{M}(\phi_0) = c_{(0,0)} + V + V^{\phi} + V^{q\phi}. \tag{O.6}$$

Together with the equation of motion for q,

$$0 = \frac{dV(q)}{dq} + \frac{\partial V^{q\phi}(q, \phi^{\text{IR}})}{\partial q}, \tag{O.7}$$

we see that

$$d\,\mathcal{M} = \left[\frac{dV(q)}{dq} + \frac{\partial V^{q\phi}(q, \phi^{\text{IR}})}{\partial q}\right] dq + \left[\frac{\partial V^{q\phi}(q, \phi^{\text{IR}})}{\partial \phi^{\text{IR}}} + \frac{dV^{\phi}(\phi^{\text{IR}})}{d\phi^{\text{IR}}}\right] d\phi^{\text{IR}} \tag{O.8}$$

$$= -Q\, d\phi_0, \tag{O.9}$$

in agreement with the first law of BH thermodynamics [722, 723]. We see that ϕ_0 and Q are conjugate variables, and therefore we can construct the "gravitational free energy" $\mathbb{M}(Q)$ via a Legendre transformation of $\mathcal{M}(\phi_0)$,

$$\mathbb{M}(Q) \equiv \mathcal{M}(\phi_0) + \phi_0 Q, \tag{O.10}$$

such that $\phi_0 = d\mathbb{M}/dQ$. As in the main text, from a sequence of exact compact-object solutions in the full theory, one obtains $\mathcal{M}(\phi_0)$ and $Q(\phi_0)$ and then can compute $\mathbb{M}(Q)$ numerically from Eq. (O.10).

To aid comparison, we also define

$$\mathbb{V}(Q) \equiv \mathbb{M}(Q) - c_{(0,0)}, \tag{O.11}$$

which represents the component of the "free energy" due to the scalar charge Q. It admits an expansion around $Q = 0$

$$\mathbb{V}(Q) = \frac{C_{(2)}}{2} Q^2 + \frac{C_{(4)}}{4!} Q^4 + \ldots, \tag{O.12}$$

whose coefficients can be extracted numerically. Unlike V, this quantity does not correspond to the potential of any dynamical variable, but instead simply represents the energetics of a sequence of equilibrium solutions. While these two quantities are not directly related in general, in the vicinity of the critical point it is possible to reconstruct the potential V from the energetics $\mathbb{V}$ (as we found in the main text). In the remainder of this appendix, we demonstrate this connection explicitly by expressing the $C_{(n)}$ in terms of the coefficients in the effective action $c_{(i,j)}$, and then take the limit that q becomes unstable $c_{(0,2)} \to 0$, i.e., approaches the critical point.

Working perturbatively in $\phi_0 = \phi^{\rm IR}$, we solve the equation of motion (O.7) for q, relate this solution to Q and $\mathcal{M}$ via Eqs. (O.5) and (O.6), and then insert these solutions into Eq. (O.11) and read off the coefficients $C_{(n)}$ from the expansion in Eq. (O.12). We find that

$$\begin{aligned} C_{(2)} =& \frac{c_{(0,2)}}{1 - c_{(0,2)}c_{(2,0)}}, \\ C_{(4)} =& \frac{1}{(1 - c_{(0,2)}c_{(2,0)})^4}\left[c_{(0,4)} + 4c_{(0,2)}c_{(1,3)} + 6c^2_{(0,2)}c_{(2,2)} + 4c^3_{(0,2)}c_{(3,1)} + c^4_{(0,2)}c_{(4,0)}\right]. \end{aligned} \tag{O.13}$$

We see that, in general, an instability in the mode q cannot be inferred directly from $\mathbb{V}(Q)$, i.e., $C_{(2)} < 0 \not\Rightarrow c_{(0,2)} < 0$ and $c_{(0,2)} < 0 \not\Rightarrow C_{(2)} < 0$. However, close to the critical point $c_{(0,2)} \approx 0$, we find

$$C_{(2)} = c_{(0,2)} + \mathcal{O}(c^2_{(0,2)}), \tag{O.14}$$

$$C_{(4)} = c_{(0,4)} + \mathcal{O}(c_{(0,2)}), \tag{O.15}$$

which confirms the link between the dynamical mode potential $V(q)$ and the energetics of equilibrium solutions $\mathbb{V}(Q)$, close to the critical point.

The relation between the mode q and the scalar charge Q along a sequence of equilibrium solutions reads

$$
\begin{aligned}
q =& \frac{Q}{1-c_{(0,2)}c_{(2,0)}} + \frac{Q^3}{3!(1-c_{(0,2)}c_{(2,0)})^4}\Big[c_{(1,3)} + c_{(2,0)}c_{(0,4)} + 3c_{(0,2)}(c_{(2,2)} + c_{(2,0)}c_{(1,3)}) \\
&+ 3c_{(0,2)}^2(c_{(3,1)} + c_{(2,0)}c_{(2,2)}) + c_{(0,2)}^3(c_{(4,0)} + c_{(2,0)}c_{(3,1)})\Big] + \dots
\end{aligned}
\tag{O.16}
$$

Note that Eq. (O.16) does not lead to $Q = q$ as in the main text when $c_{(0,2)} = 0$. But full agreement with the main text (ignoring higher orders in $c_{(0,2)}$ throughout) is achieved if we redefine

$$
q \to q + \frac{q^3}{3!}\left[c_{(1,3)} + c_{(2,0)}c_{(0,4)}\right] + \mathcal{O}(c_{(0,2)}, Q^5). \tag{O.17}
$$

Appendix P: Numerical calculation of $V(q)$

In this appendix, we detail the numerical calculation of equilibrium BH solutions in EMS theory used to construct $V(q)$ through the matching procedure discussed in the main text. A Mathematica code that illustrates this calculation is provided as supplemental material [**?**]. We consider the class of theories in Eq. (9.1) and restrict our attention to static, spherically symmetric configurations. Starting with the ansatz for vector potential and metric

$$A = \lambda(r)\, dt, \tag{P.1}$$

$$ds^2 = -N(r)e^{-2\delta(r)}dt^2 + \frac{dr^2}{N(r)} + r^2(d\theta^2 + \sin^2\theta d\varphi^2), \tag{P.2}$$

where $N(r) \equiv 1 - 2m(r)/r$ and $m(r)$ is the Misner-Sharp mass (not to be confused with $m(q)$ introduced in the main text), the field equations reduce to

$$\lambda' = -\frac{e^{-\delta}}{f(\phi)}\frac{\mathcal{E}}{r^2}, \tag{P.3a}$$

$$m' = \frac{1}{2}r^2 N\phi'^2 + \frac{\mathcal{E}^2}{2f(\phi)r^2}, \tag{P.3b}$$

$$\delta' + r\phi'^2 = 0, \tag{P.3c}$$

$$(e^{-\delta}r^2 N\phi')' = -e^{-\delta}\frac{f'(\phi)\mathcal{E}^2}{2(f(\phi))^2 r^2}, \tag{P.3d}$$

where $' = d/dr$ and $\mathcal{E}$ is the electric charge of the BH. Here, the field equation for the electric potential λ was already integrated once, introducing the electric charge $\mathcal{E}$ as an integration constant.

We impose the following boundary conditions at the horizon

$$
\begin{aligned}
m(r_H) =& \frac{r_H}{2}, \qquad \delta(r_H) = \delta_H, \qquad \phi(r_H) = \phi_H, \\
\phi'(r_H) =& -\frac{f'(\phi_H)}{2f(\phi_H)r_H}\left(\frac{\mathcal{E}^2}{f(\phi_H)r_H^2 - \mathcal{E}^2}\right).
\end{aligned} \tag{P.4}
$$

Note that δ_H represents a simple rescaling of the time coordinate, and thus can be chosen arbitrarily; we ultimately rescale t such that $\delta(r = \infty) = 0$. For computational simplicity, we rescale all dimensional quantities by the horizon radius r_H, i.e., $\tilde{r} \equiv r/r_H$, $\tilde{m} \equiv m/r_H$, and $\tilde{\mathcal{E}} = \mathcal{E}/r_H$, and then compactify the domain over which they are solved using the variable

$$
x \equiv \frac{r - r_H}{r + br_H} = \frac{\tilde{r} - 1}{\tilde{r} + b}, \tag{P.5}
$$

where the constant b is chosen to adequately resolve the solution.

As discussed in the main text, we consider sequences of BH solutions with fixed electric charge $\mathcal{E}$ and entropy $\mathcal{S}$ (or horizon area), which is equivalent to fixed $\tilde{\mathcal{E}}$ and r_H. Fixing these two parameters, we generate a sequence of solutions by solving Eqs. (P.3) and (P.4) for several values of ϕ_H. We then extract the mass $\mathcal{M}$, asymptotic field ϕ_0, and scalar charge Q from the asymptotic behavior of the solution

$$
m(r) \to \mathcal{M} + \mathcal{O}\left(\frac{1}{r}\right), \qquad \phi(r) \to \phi_0 + \frac{Q}{r} + \mathcal{O}\left(\frac{1}{r^2}\right), \tag{P.6}
$$

allowing us to implicitly construct the functions $\mathcal{M}(\phi_0)$ and $Q(\phi_0)$ used in the main text to compute the effective potential $V(q)$.

Appendix Q: Oscillator equation with damping term

In Sec. 10.2, we approximated $\dot{q} \simeq 0$ and used the oscillator equation $c_{\dot{q}^2}\ddot{q} \simeq -c_{(2)}q$ to relate $c_{\dot{q}^2}$ to the φ-mode frequency as in Eq. (10.11). In this appendix, we investigate the effect of the monopole radiation-reaction force as a damping term.

In Appendix R, we show that the radiation-reaction force for an isolated compact object is given by $\mathcal{F}_q = -\dot{q}$. Inserting that force on the right-hand side of the oscillator equation (10.4) yields

$$c_{\dot{q}^2}\ddot{q} + V'(q) = \varphi_0 + \mathcal{F}_q. \tag{Q.1}$$

Assuming vanishing cosmological scalar field $\varphi_0 = 0$, and keeping only the leading term in $V'(q)$, we get

$$c_{\dot{q}^2}\ddot{q} + \dot{q} + c_{(2)}q = 0, \tag{Q.2}$$

which is the equation for a damped harmonic oscillator and can be written as

$$\ddot{q} + \gamma_0\dot{q} + \omega_0^2 q = 0, \tag{Q.3}$$

with the definitions

$$\gamma_0 \equiv \frac{1}{c_{\dot{q}^2}}, \qquad \omega_0^2 \equiv \frac{c_{(2)}}{c_{\dot{q}^2}}. \tag{Q.4}$$

The solution of this equation is given by

$$q(t) = e^{-\omega_I t}\left[a\cos(\omega_R t) + b\sin(\omega_R t)\right], \tag{Q.5}$$

where

$$\omega_I \equiv \frac{\gamma_0}{2}\,, \qquad \omega_R \equiv \sqrt{\omega_0^2 - (\gamma_0/2)^2}\,, \tag{Q.6}$$

leading to $\omega_0^2 = \omega_R^2 + \omega_I^2$. These relations can be inverted to obtain $c_{\dot{q}^2}$ and $c_{(2)}$ in terms of ω_R and ω_I, i.e.,

$$c_{\dot{q}^2} = \frac{1}{2\omega_I}, \qquad c_{(2)} = \frac{\omega_0^2}{2\omega_I}. \tag{Q.7}$$

It was argued in Ref. [767] that ω_R and ω_I can be identified as the real and imaginary parts, respectively, of the mode frequency. Hence, the relation (Q.7) for $c_{\dot{q}^2}$, obtained by including a damping term in the oscillator equation, is the same as the one in Eq. (10.11), which was obtained by assuming $\dot{q} \simeq 0$. However, $c_{(2)}$ calculated from the φ-mode frequency in Eq. (Q.7) gives a different result from the one calculated from the quartic fit in Fig. 10.1, with a relative difference of about $\sim 50\%$. Such a difference would then propagate to $c_{\dot{q}^2}$, but we showed in Fig. 10.7 that the scalarization time has a weak dependence on the value of $c_{\dot{q}^2}$. Thus, we choose to identify $c_{\dot{q}^2} = c_{(2)}/\omega_0^2$, with $c_{(2)}$ calculated from the quartic fit, which is more accurate.

Appendix R: Scalar fluxes and radiation-reaction force

In this appendix, we derive the leading order scalar monopole energy flux, and the scalar dipole energy and angular momentum fluxes, following the steps in Ref. [200]. From the fluxes, we obtain the radiation-reaction force that enters the equations of motion (6.4).

R.1 Energy flux

The scalar-field equation is given by

$$\Box\varphi = -4\pi S, \tag{R.1}$$

with the source term

$$S = q_A(t)\delta^3(\boldsymbol{x} - \boldsymbol{x}_A) + q_B(t)\delta^3(\boldsymbol{x} - \boldsymbol{x}_B). \tag{R.2}$$

The scalar field has the solution

$$\varphi = \int d^3x' \, \frac{S(x', t_{\text{ret}})}{|\boldsymbol{x} - \boldsymbol{x}'|} \,, \tag{R.3}$$

where $\boldsymbol{x}$ is the distance to the detector at near spatial infinity, and the retarded time $t_{\text{ret}} = t - |\boldsymbol{x} - \boldsymbol{x}'|$.

Defining $R \equiv |\boldsymbol{x}|$, $\boldsymbol{N} \equiv \boldsymbol{x}/R$, and $t' \equiv t - R$, we expand the scalar field, in the far zone, in terms of multipole moments such that

$$\varphi = \int d^3x' \left[\frac{S(x', t')}{R} + \frac{1}{R}\frac{\partial}{\partial t}S(x', t')\boldsymbol{x} \cdot \boldsymbol{N} + \ldots\right]$$

$$\equiv \frac{1}{R}\left(\Psi + \dot{\Psi}^i N^i + \dots\right), \tag{R.4}$$

where the monopole and dipole moments are defined by

$$\Psi \equiv \int d^3x\, S = q_A + q_B, \tag{R.5}$$

$$\Psi^i \equiv \int d^3x\, x^i S = \left(\frac{m_B^0}{M} q_A - \frac{m_A^0}{M} q_B\right) r^i, \tag{R.6}$$

and we have used the center-of-mass relations $\boldsymbol{x}_A = m_B^0 \boldsymbol{r}/M$, $\boldsymbol{x}_B = -m_A^0 \boldsymbol{r}/M$, and $\boldsymbol{r} = \boldsymbol{x}_A - \boldsymbol{x}_B$.

The energy flux due to scalar radiation is related to the stress-energy tensor via

$$\Phi_E = -R^2 \int d\Omega\, T_{0i} N^i, \tag{R.7}$$

where $T_{0i} = \partial_0\varphi\partial_i\varphi/4\pi \simeq -N_i(\partial_0\varphi)^2/4\pi$, since $\partial_i\varphi \simeq -N_i\partial_0\varphi + \mathcal{O}(r/R)$, which yields

$$\begin{aligned} \Phi_E &= \frac{1}{4\pi}\int d\Omega\, (\dot{\Psi} + \ddot{\Psi}^i N_i + \dots)^2 \\ &= \dot{\Psi}^2 + \frac{1}{3}\ddot{\Psi}^i\ddot{\Psi}^i + \dots . \end{aligned} \tag{R.8}$$

The first term in this equation is the monopole flux, while the second is the dipole flux. To evaluate the angular integral, we have used the relation $\int d\Omega\, N^i N^j = 4\pi\delta^{ij}/3$.

In taking the time derivatives, we assume that $\dot{q}$ is small compared to q. So we neglect terms with $\dot{q}$ in the dipole part of the energy flux, but we keep them in the leading-order monopole flux. Hence, we obtain

$$\Phi_E \simeq (\dot{q}_A + \dot{q}_B)^2 + \frac{1}{3}\left(\frac{m_B^0}{M} q_A - \frac{m_A^0}{M} q_B\right)^2 \ddot{\boldsymbol{r}}^2, \tag{R.9}$$

with

$$\ddot{\boldsymbol{r}} = -\frac{M}{r^2}\left(1 + \frac{q_A q_B}{M\mu}\right)\hat{\boldsymbol{r}}, \tag{R.10}$$

leading to the monopole and dipole energy fluxes

$$\Phi_E^{\rm mon} = \left(\dot{q}_A + \dot{q}_B\right)^2, \tag{R.11}$$

$$\Phi_E^{\rm dip} = \frac{M^2}{3r^4}\left(\frac{m_B^0}{M}q_A - \frac{m_A^0}{M}q_B\right)^2\left(1 + \frac{q_A q_B}{M\mu}\right)^2. \tag{R.12}$$

The dipole flux vanishes for equal masses and charges, in which case, the next-to-leading order monopole flux and the leading order quadrupole flux become the leading contributions. The scalar quadrupole flux can be computed following the same steps outlined above, with the additional contribution $\dddot{\Psi}^{ij}\dddot{\Psi}^{ij}/15$ in Eq. (R.8). However, it is at the same post-Newtonian order as the next-to-leading monopole flux, which requires the equations of motion at next-to-leading order, and is thus beyond the scope of this work.

R.2 Angular momentum flux

The angular momentum carried by the scalar field is related to the stress-energy tensor via

$$\begin{aligned} J^i &= \epsilon^{ikl}\int d^3x\, x^k T^{0l} \\ &= \frac{1}{4\pi}\epsilon^{ikl}\int d^3x\ (\partial_0\varphi)x^k(\partial^l\varphi). \end{aligned} \tag{R.13}$$

Using $\partial^j N^i = (\delta^{ij} - N^j N^j)/R$, and $d^3x = R^2 dt d\Omega$, the above equation yields

$$\begin{aligned} \frac{dJ^i}{dt} = \frac{1}{4\pi}\epsilon^{ikl}&\int d\Omega R N^k\left[\dot{\Psi} + \ddot{\Psi}^j N^j\right] \\ &\times\left[-N^l\dot{\Psi} - N^l N^m\ddot{\Psi}^m + \frac{1}{R}\left(\delta^{ml} - N^m N^l\right)\dot{\Psi}^m\right]. \end{aligned} \tag{R.14}$$

Due to the antisymmetry of ϵ^{ikl}, the only term that does not vanish is

$$\frac{dJ^i}{dt} = \frac{1}{4\pi}\epsilon^{ikl}\int d\Omega\, N^k N^l \ddot{\Psi}^j\dot{\Psi}^l$$

$$= \frac{1}{3}\epsilon^{ikl}\ddot{\Psi}^k\dot{\Psi}^l\,. \tag{R.15}$$

Differentiating the dipole moment, while assuming $\dot{q} \simeq 0$, leads to

$$\frac{dJ^i}{dt} = \frac{1}{3}\epsilon^{ikl}\left(\frac{m_B^0}{M}q_A - \frac{m_A^0}{M}q_B\right)^2 \ddot{r}^k\dot{r}^l. \tag{R.16}$$

Thus, we obtain the angular momentum flux

$$\begin{aligned}\Phi_J^{\text{dip}} &= -\frac{dJ^\theta}{dt}\\ &\simeq \frac{1}{3}\frac{ML}{\mu r^3}\left(\frac{m_B^0}{M}q_A - \frac{m_A^0}{M}q_B\right)^2\left(1+\frac{q_Aq_B}{M\mu}\right).\end{aligned} \tag{R.17}$$

R.3 Radiation-reaction force

To obtain the monopole radiation-reaction force, we use the balance equation $\dot{E}^{\text{mon}}_{\text{system}} = -\Phi_E^{\text{mon}}$, where the energy loss by the system is the time derivative of the Hamiltonian in Eq. (10.14) after substituting the equations of motion (6.4) without the dipole or quadrupole radiation-reaction force, leading to

$$\dot{E}^{\text{mon}}_{\text{system}} = \mathcal{F}^{\text{mon}}_{q_A}\dot{q}_A + \mathcal{F}^{\text{mon}}_{q_B}\dot{q}_B. \tag{R.18}$$

Setting this equal to the energy flux in Eq. (R.11), and solving for the radiation-reaction force yields

$$\mathcal{F}^{\text{mon}}_{q_A} = \mathcal{F}^{\text{mon}}_{q_B} = -\dot{q}_A - \dot{q}_B. \tag{R.19}$$

This force is the same for both q_A and q_B, which implies that the equation of motion for the combination $q_A - q_B$ does not have a damping term at that order. Therefore, for equal masses but opposite charges, such that the sum $q_A + q_B$ vanishes, the monopole force would not affect the charges. The damping in this case would be provided by terms in the scalar *dipole* flux with time derivatives of the scalar charges. We dropped these contributions in Eq. (R.12) for simplicity, but we checked that they have negligible effect on the results considered in this paper.

For the dipole radiation-reaction forces, we follow the arguments in Ref. [402], and use the energy and angular momentum balance equations including Schott terms, which represent additional contributions to energy and angular momentum due to interaction with the radiation field, i.e.,

$$\begin{aligned} \dot{E}^{\text{dip}}_{\text{system}} + \dot{E}_{\text{Schott}} + \Phi^{\text{dip}}_E &= 0, \\ \dot{J}^{\text{dip}}_{\text{system}} + \dot{J}_{\text{Schott}} + \Phi^{\text{dip}}_J &= 0. \end{aligned} \tag{R.20}$$

The energy and angular momentum losses by the system are given by

$$\begin{aligned} \dot{E}^{\text{dip}}_{\text{system}} &= \frac{dH}{dt} = \dot{r}\mathcal{F}^{\text{dip}}_r + \dot{\varphi}\mathcal{F}^{\text{dip}}_\varphi \\ \dot{J}^{\text{dip}}_{\text{system}} &= \frac{dL}{dt} = \mathcal{F}^{\text{dip}}_\varphi. \end{aligned} \tag{R.21}$$

We choose to set $\dot{J}_{\text{Schott}} = 0$, which corresponds to part of the coordinate gauge freedom. The components of the radiation-reaction force are then related to the fluxes via

$$\begin{aligned} \dot{r}\mathcal{F}^{\text{dip}}_r + \dot{E}_{\text{schott}} &= -\Phi_{EJ}, \\ \mathcal{F}^{\text{dip}}_\varphi &= -\Phi_J, \end{aligned} \tag{R.22}$$

where we define $\Phi_{EJ} \equiv \Phi_E - \dot{\phi}\Phi_J$ with $\dot{\phi}$ being the orbital frequency.

For circular orbits $\Phi_{EJ} = 0$ since $\Phi_E = \dot{\phi}\Phi_J$. Hence, Φ_{EJ} can be written in terms of quantities that vanish for circular orbits, such as p_r^2 and $\dot{p}_r$, which also satisfy time-reversal symmetry,

$$\begin{aligned} \Phi_{EJ} &= f_1 p_r^2 + f_2 \dot{p}_r \\ &= p_r \left(p_r f_1 - \frac{df_2}{dt} \right) + \frac{d}{dt}(f_2 p_r), \end{aligned} \tag{R.23}$$

for some arbitrary functions f_1 and f_2, which leads to

$$\begin{aligned} E_{\text{Schott}} &= -f_2 p_r, \\ \mathcal{F}_r^{\text{dip}} &= -\frac{p_r}{\dot{r}}\left(p_r f_1 - \frac{df_2}{dt}\right). \end{aligned} \tag{R.24}$$

Applying that approach using the dipole fluxes from Eq. (R.12) leads to

$$\begin{aligned} f_1 &= 0, \\ f_2 &= -\frac{M}{3\mu r^2}\left(\frac{m_B^0}{M}q_A - \frac{m_A^0}{M}q_B\right)^2\left(1 + \frac{q_A q_B}{M\mu}\right). \end{aligned} \tag{R.25}$$

Thus, we obtain the Schott energy and $\mathcal{F}_r^{\text{dip}}$

$$E_{\text{Schott}} = \frac{M}{3\mu r^2}p_r\left(\frac{m_B^0}{M}q_A - \frac{m_A^0}{M}q_B\right)^2\left(1 + \frac{q_A q_B}{M\mu}\right), \tag{R.26}$$

$$\mathcal{F}_r^{\text{dip}} = \frac{2}{3}\frac{M}{\mu r^3}p_r\left(\frac{m_B^0}{M}q_A - \frac{m_A^0}{M}q_B\right)^2\left(1 + \frac{q_A q_B}{M\mu}\right). \tag{R.27}$$

Bibliography

[1] A. Antonelli, C. Kavanagh, M. Khalil, J. Steinhoff, and J. Vines, Gravitational spin-orbit coupling through third-subleading post-Newtonian order: from first-order self-force to arbitrary mass ratios, Phys. Rev. Lett. **125**, 011103 (2020), arXiv:2003.11391 [gr-qc] .

[2] A. Antonelli, C. Kavanagh, M. Khalil, J. Steinhoff, and J. Vines, Gravitational spin-orbit and aligned spin$_1$-spin$_2$ couplings through third-subleading post-Newtonian orders, Phys. Rev. D **102**, 124024 (2020), arXiv:2010.02018 [gr-qc] .

[3] M. Khalil, Gravitational spin-orbit dynamics at the fifth-and-a-half post-Newtonian order, Phys. Rev. D **104**, 124015 (2021), arXiv:2110.12813 [gr-qc] .

[4] M. Khalil, J. Steinhoff, J. Vines, and A. Buonanno, Fourth post-Newtonian effective-one-body Hamiltonians with generic spins, Phys. Rev. D **101**, 104034 (2020), arXiv:2003.04469 [gr-qc] .

[5] M. Khalil, A. Buonanno, J. Steinhoff, and J. Vines, Radiation-reaction force and multipolar waveforms for eccentric, spin-aligned binaries in the effective-one-body formalism, Phys. Rev. D **104**, 024046 (2021), arXiv:2104.11705 [gr-qc] .

[6] M. Khalil, A. Buonanno, J. Steinhoff, and J. Vines, Energetics and scattering of gravitational two-body systems at fourth post-Minkowskian order, Phys. Rev. D **106**, 024042 (2022), arXiv:2204.05047 [gr-qc] .

[7] M. Khalil, N. Sennett, J. Steinhoff, J. Vines, and A. Buonanno, Hairy binary black holes in Einstein-Maxwell-dilaton theory and their effective-one-body description, Phys. Rev. D **98**, 104010 (2018), arXiv:1809.03109 [gr-qc] .

[8] M. Khalil, N. Sennett, J. Steinhoff, and A. Buonanno, Theory-agnostic framework for dynamical scalarization of compact binaries, Phys. Rev. D **100**, 124013 (2019), arXiv:1906.08161 [gr-qc] .

[9] M. Khalil, R. F. P. Mendes, N. Ortiz, and J. Steinhoff, Effective-action model for dynamical scalarization beyond the adiabatic approximation, (2022), arXiv:2206.13233 [gr-qc] .

[10] A. Ramos-Buades, A. Buonanno, M. Khalil, and S. Ossokine, Effective-one-body multipolar waveforms for eccentric binary black holes with nonprecessing spins, Phys. Rev. D **105**, 044035 (2022), arXiv:2112.06952 [gr-qc] .

[11] A. Buonanno, M. Khalil, D. O'Connell, R. Roiban, M. P. Solon, and M. Zeng, Snowmass White Paper: Gravitational Waves and Scattering Amplitudes, in *2022 Snowmass Summer Study* (2022) arXiv:2204.05194 [hep-th] .

[12] B. P. Abbott *et al.* (LIGO Scientific, Virgo), Observation of Gravitational Waves from a Binary Black Hole Merger, Phys. Rev. Lett. **116**, 061102 (2016), arXiv:1602.03837 [gr-qc] .

[13] B. P. Abbott *et al.* (LIGO Scientific, Virgo), GWTC-1: A Gravitational-Wave Transient Catalog of Compact Binary Mergers Observed by LIGO and Virgo during the First and Second Observing Runs, Phys. Rev. X **9**, 031040 (2019), arXiv:1811.12907 [astro-ph.HE] .

[14] R. Abbott *et al.* (LIGO Scientific, Virgo), GWTC-2: Compact Binary Coalescences Observed by LIGO and Virgo During the First Half of the Third Observing Run, Phys. Rev. X **11**, 021053 (2021), arXiv:2010.14527 [gr-qc] .

[15] R. Abbott *et al.* (LIGO Scientific, VIRGO, KAGRA), GWTC-3: Compact Binary Coalescences Observed by LIGO and Virgo During the Second Part of the Third Observing Run, (2021), arXiv:2111.03606 [gr-qc] .

[16] B. P. Abbott *et al.* (LIGO Scientific, Virgo), GW170817: Observation of Gravitational Waves from a Binary Neutron Star Inspiral, Phys. Rev. Lett. **119**, 161101 (2017), arXiv:1710.05832 [gr-qc] .

[17] R. Abbott *et al.* (LIGO Scientific, KAGRA, VIRGO), Observation of Gravitational Waves from Two Neutron Star–Black Hole Coalescences, Astrophys. J. Lett. **915**, L5 (2021), arXiv:2106.15163 [astro-ph.HE] .

[18] B. P. Abbott *et al.* (LIGO Scientific, Virgo), Binary Black Hole Population Properties Inferred from the First and Second Observing Runs of Advanced LIGO and Advanced Virgo, Astrophys. J. Lett. **882**, L24 (2019), arXiv:1811.12940 [astro-ph.HE] .

[19] R. Abbott *et al.* (LIGO Scientific, Virgo), Population Properties of Compact Objects from the Second LIGO-Virgo Gravitational-Wave Transient Catalog, Astrophys. J. Lett. **913**, L7 (2021), arXiv:2010.14533 [astro-ph.HE] .

[20] R. Abbott *et al.* (LIGO Scientific, VIRGO, KAGRA), The population of merging compact binaries inferred using gravitational waves through GWTC-3, (2021), arXiv:2111.03634 [astro-ph.HE] .

[21] M. Maggiore, *Gravitational Waves. Volume 1: theory and experiments* (Oxford University Press, 2008).

[22] J. D. Creighton and W. G. Anderson, Gravitational-wave physics and astronomy, Wiley-VCH **2**, 1 (2011).

[23] A. Buonanno, Gravitational waves, in *Les Houches Summer School - Session 86: Particle Physics and Cosmology: The Fabric of Spacetime* (2007) arXiv:0709.4682 [gr-qc] .

[24] C. W. Misner, K. S. Thorne, and J. A. Wheeler, *Gravitation* (W H Freeman and Company, 1973).

[25] J. Aasi *et al.* (LIGO Scientific), Advanced LIGO, Class. Quant. Grav. **32**, 074001 (2015), arXiv:1411.4547 [gr-qc] .

[26] B. P. Abbott *et al.*, Sensitivity of the Advanced LIGO detectors at the beginning of gravitational wave astronomy, Phys. Rev. D **93**, 112004 (2016), [Addendum: Phys.Rev.D 97, 059901 (2018)], arXiv:1604.00439 [astro-ph.IM] .

[27] F. Acernese *et al.* (VIRGO), Advanced Virgo: a second-generation interferometric gravitational wave detector, Class. Quant. Grav. **32**, 024001 (2015), arXiv:1408.3978 [gr-qc] .

[28] K. Somiya (KAGRA), Detector configuration of KAGRA: The Japanese cryogenic gravitational-wave detector, Class. Quant. Grav. **29**, 124007 (2012), arXiv:1111.7185 [gr-qc] .

[29] T. Akutsu *et al.* (KAGRA), KAGRA: 2.5 Generation Interferometric Gravitational Wave Detector, Nature Astron. **3**, 35 (2019), arXiv:1811.08079 [gr-qc] .

[30] B. P. Abbott *et al.* (KAGRA, LIGO Scientific, Virgo, VIRGO), Prospects for observing and localizing gravitational-wave transients with Advanced LIGO, Advanced Virgo and KAGRA, Living Rev. Rel. **21**, 3 (2018), arXiv:1304.0670 [gr-qc] .

[31] B. P. Abbott *et al.* (LIGO Scientific, Virgo), A guide to LIGO–Virgo detector noise and extraction of transient gravitational-wave signals, Class. Quant. Grav. **37**, 055002 (2020), arXiv:1908.11170 [gr-qc] .

[32] R. L. Arnowitt, S. Deser, and C. W. Misner, Dynamical Structure and Definition of Energy in General Relativity, Phys. Rev. **116**, 1322 (1959).

[33] R. L. Arnowitt, S. Deser, and C. W. Misner, The Dynamics of general relativity, Gen. Rel. Grav. **40**, 1997 (2008), arXiv:gr-qc/0405109 .

[34] F. Pretorius, Evolution of binary black hole spacetimes, Phys. Rev. Lett. **95**, 121101 (2005), arXiv:gr-qc/0507014 [gr-qc] .

[35] M. Campanelli, C. O. Lousto, P. Marronetti, and Y. Zlochower, Accurate evolutions of orbiting black-hole binaries without excision, Phys. Rev. Lett. **96**, 111101 (2006), arXiv:gr-qc/0511048 .

[36] J. G. Baker, J. Centrella, D.-I. Choi, M. Koppitz, and J. van Meter, Gravitational wave extraction from an inspiraling configuration of merging black holes, Phys. Rev. Lett. **96**, 111102 (2006), arXiv:gr-qc/0511103 .

[37] J. A. Gonzalez, U. Sperhake, and B. Bruegmann, Black-hole binary simulations: The Mass ratio 10:1, Phys. Rev. D **79**, 124006 (2009), arXiv:0811.3952 [gr-qc] .

[38] L. T. Buchman, H. P. Pfeiffer, M. A. Scheel, and B. Szilagyi, Simulations of non-equal mass black hole binaries with spectral methods, Phys. Rev. D **86**, 084033 (2012), arXiv:1206.3015 [gr-qc] .

[39] T. Chu, H. P. Pfeiffer, and M. A. Scheel, High accuracy simulations of black hole binaries: Spins anti-aligned with the orbital angular momentum, Phys. Rev. D **80**, 124051 (2009), arXiv:0909.1313 [gr-qc] .

[40] A. H. Mroue *et al.*, Catalog of 174 Binary Black Hole Simulations for Gravitational Wave Astronomy, Phys. Rev. Lett. **111**, 241104 (2013), arXiv:1304.6077 [gr-qc] .

[41] M. Boyle *et al.*, The SXS Collaboration catalog of binary black hole simulations, Class. Quant. Grav. **36**, 195006 (2019), arXiv:1904.04831 [gr-qc] .

[42] J. Healy, C. O. Lousto, Y. Zlochower, and M. Campanelli, The RIT binary black hole simulations catalog, Class. Quant. Grav. **34**, 224001 (2017), arXiv:1703.03423 [gr-qc] .

[43] J. Healy and C. O. Lousto, Fourth RIT binary black hole simulations catalog: Extension to eccentric orbits, Phys. Rev. D **105**, 124010 (2022), arXiv:2202.00018 [gr-qc] .

[44] K. Jani, J. Healy, J. A. Clark, L. London, P. Laguna, and D. Shoemaker, Georgia Tech Catalog of Gravitational Waveforms, Class. Quant. Grav. **33**, 204001 (2016), arXiv:1605.03204 [gr-qc] .

[45] F. Foucart *et al.*, Gravitational waveforms from spectral Einstein code simulations: Neutron star-neutron star and low-mass black hole-neutron star binaries, Phys. Rev. D **99**, 044008 (2019), arXiv:1812.06988 [gr-qc] .

[46] L. Lehner and F. Pretorius, Numerical Relativity and Astrophysics, Ann. Rev. Astron. Astrophys. **52**, 661 (2014), arXiv:1405.4840 [astro-ph.HE] .

[47] T. W. Baumgarte and S. L. Shapiro, *Numerical relativity: solving Einstein's equations on the computer* (Cambridge University Press, 2010).

[48] M. Alcubierre, *Introduction to 3+ 1 numerical relativity*, Vol. 140 (OUP Oxford, 2008).

[49] C. Palenzuela, Introduction to numerical relativity, Frontiers in Astronomy and Space Sciences **7**, 58 (2020).

[50] C. M. Will, The Confrontation between General Relativity and Experiment, Living Rev. Rel. **17**, 4 (2014), arXiv:1403.7377 [gr-qc] .

[51] T. Regge and J. A. Wheeler, Stability of a Schwarzschild singularity, Phys. Rev. **108**, 1063 (1957).

[52] F. J. Zerilli, Gravitational field of a particle falling in a schwarzschild geometry analyzed in tensor harmonics, Phys. Rev. D **2**, 2141 (1970).

[53] F. J. Zerilli, Effective potential for even parity Regge-Wheeler gravitational perturbation equations, Phys. Rev. Lett. **24**, 737 (1970).

[54] C. V. Vishveshwara, Stability of the schwarzschild metric, Phys. Rev. D **1**, 2870 (1970).

[55] C. V. Vishveshwara, Scattering of Gravitational Radiation by a Schwarzschild Black-hole, Nature **227**, 936 (1970).

[56] S. A. Teukolsky, Perturbations of a rotating black hole. 1. Fundamental equations for gravitational electromagnetic and neutrino field perturbations, Astrophys. J. **185**, 635 (1973).

[57] W. H. Press and S. A. Teukolsky, Perturbations of a Rotating Black Hole. II. Dynamical Stability of the Kerr Metric, Astrophys. J. **185**, 649 (1973).

[58] S. A. Teukolsky and W. H. Press, Perturbations of a rotating black hole. III - Interaction of the hole with gravitational and electromagnet ic radiation, Astrophys. J. **193**, 443 (1974).

[59] S. Chandrasekhar and S. L. Detweiler, The quasi-normal modes of the Schwarzschild black hole, Proc. Roy. Soc. Lond. A **344**, 441 (1975).

[60] A. Einstein, Explanation of the Perihelion Motion of Mercury from the General Theory of Relativity, Sitzungsber. Preuss. Akad. Wiss. Berlin (Math. Phys.) **1915**, 831 (1915).

[61] W. de Sitter, Einstein's theory of gravitation and its astronomical consequences, Second Paper, Mon. Not. Roy. Astron. Soc. **77**, 155 (1916).

[62] H. A. Lorentz and J. Droste, De beweging van een stelsel lichamen onder den invloed van hunne onderlinge aantrekking, behandeld volgens de theorie van einstein, i, Versl. K. Akad. Wet.(Amsterdam) **26**, 392 (1917).

[63] H. Lorentz and J. Droste, The motion of a system of bodies under the influence of their mutual attraction, according to einstein's theory, in *Collected papers* (Springer, 1937) pp. 330–355.

[64] A. Einstein, L. Infeld, and B. Hoffmann, The Gravitational equations and the problem of motion, Annals Math. **39**, 65 (1938).

[65] S. Chandrasekhar, The Post-Newtonian Equations of Hydrodynamics in General Relativity., Astrophys. J. **142**, 1488 (1965).

[66] S. Chandrasekhar, Post-Newtonian Methods and Conservation Laws, in *Relativity Conference in the Midwest* (1970) pp. 81–108.

[67] R. A. Hulse and J. H. Taylor, Discovery of a pulsar in a binary system, Astrophys. J. Lett. **195**, L51 (1975).

[68] J. Ehlers, A. Rosenblum, J. N. Goldberg, and P. Havas, Comments on Gravitational Radiation Damping and Energy Loss in Binary Systems, Astrophys. J. Lett. **208**, L77 (1976).

[69] C. M. Will, On the unreasonable effectiveness of the post-Newtonian approximation in gravitational physics, Proc. Nat. Acad. Sci. **108**, 5938 (2011), arXiv:1102.5192 [gr-qc] .

[70] D. Kennefick, The binary pulsar and the quadrupole formula controversy, Eur. Phys. J. H **42**, 293 (2017).

[71] D. Kennefick, *Traveling at the speed of thought: Einstein and the quest for gravitational waves* (2007).

[72] T. Ohta, H. Okamura, K. Hiida, and T. Kimura, Higher order gravitational potential for many-body system, Prog. Theor. Phys. **51**, 1220 (1974).

[73] T. Damour and G. Schäfer, Lagrangians for$n$ point masses at the second post-Newtonian approximation of general relativity, Gen. Rel. Grav. **17**, 879 (1985).

[74] L. Blanchet and G. Faye, General relativistic dynamics of compact binaries at the third postNewtonian order, Phys. Rev. D **63**, 062005 (2001), arXiv:gr-qc/0007051 .

[75] L. Blanchet and G. Faye, Equations of motion of point particle binaries at the third post-Newtonian order, Phys. Lett. A **271**, 58 (2000), arXiv:gr-qc/0004009 .

[76] P. Jaranowski and G. Schaefer, Third postNewtonian higher order ADM Hamilton dynamics for two-body point mass systems, Phys. Rev. D **57**, 7274 (1998), [Erratum: Phys.Rev.D 63, 029902 (2001)], arXiv:gr-qc/9712075 .

[77] P. Jaranowski and G. Schaefer, The Binary black hole dynamics at the third postNewtonian order in the orbital motion, Annalen Phys. **9**, 378 (2000), arXiv:gr-qc/0003054 .

[78] Y. Itoh and T. Futamase, New derivation of a third postNewtonian equation of motion for relativistic compact binaries without ambiguity, Phys. Rev. D **68**, 121501 (2003), arXiv:gr-qc/0310028 .

[79] T. Damour, P. Jaranowski, and G. Schäfer, Nonlocal-in-time action for the fourth post-Newtonian conservative dynamics of two-body systems, Phys. Rev. **D89**, 064058 (2014), arXiv:1401.4548 [gr-qc] .

[80] T. Damour, P. Jaranowski, and G. Schäfer, Fourth post-Newtonian effective one-body dynamics, Phys. Rev. **D91**, 084024 (2015), arXiv:1502.07245 [gr-qc] .

[81] T. Damour, P. Jaranowski, and G. Schäfer, Conservative dynamics of two-body systems at the fourth post-Newtonian approximation of general relativity, Phys. Rev. D **93**, 084014 (2016), arXiv:1601.01283 [gr-qc] .

[82] L. Bernard, L. Blanchet, G. Faye, and T. Marchand, Center-of-Mass Equations of Motion and Conserved Integrals of Compact Binary Systems at the Fourth Post-Newtonian Order, Phys. Rev. D **97**, 044037 (2018), arXiv:1711.00283 [gr-qc] .

[83] T. Marchand, L. Bernard, L. Blanchet, and G. Faye, Ambiguity-Free Completion of the Equations of Motion of Compact Binary Systems at the Fourth Post-Newtonian Order, Phys. Rev. D **97**, 044023 (2018), arXiv:1707.09289 [gr-qc] .

[84] S. Foffa and R. Sturani, Conservative dynamics of binary systems to fourth Post-Newtonian order in the EFT approach I: Regularized Lagrangian, Phys. Rev. **D100**, 024047 (2019), arXiv:1903.05113 [gr-qc] .

[85] S. Foffa, R. A. Porto, I. Rothstein, and R. Sturani, Conservative dynamics of binary systems to fourth Post-Newtonian order in the EFT approach II: Renormalized Lagrangian, Phys. Rev. D **100**, 024048 (2019), arXiv:1903.05118 [gr-qc] .

[86] J. Blümlein, A. Maier, P. Marquard, and G. Schäfer, Fourth post-Newtonian Hamiltonian dynamics of two-body systems from an effective field theory approach, Nucl. Phys. B **955**, 115041 (2020), arXiv:2003.01692 [gr-qc] .

[87] J. Blümlein, A. Maier, P. Marquard, and G. Schäfer, The fifth-order post-Newtonian Hamiltonian dynamics of two-body systems from an effective field theory approach: potential contributions, Nucl. Phys. B **965**, 115352 (2021), arXiv:2010.13672 [gr-qc] .

[88] J. Blümlein, A. Maier, P. Marquard, and G. Schäfer, The fifth-order post-Newtonian Hamiltonian dynamics of two-body systems from an effective field theory approach, (2021), arXiv:2110.13822 [gr-qc] .

[89] S. Foffa, P. Mastrolia, R. Sturani, C. Sturm, and W. J. Torres Bobadilla, Static two-body potential at fifth post-Newtonian order, Phys. Rev. Lett. **122**, 241605 (2019), arXiv:1902.10571 [gr-qc] .

[90] D. Bini, T. Damour, and A. Geralico, Novel approach to binary dynamics: application to the fifth post-Newtonian level, Phys. Rev. Lett. **123**, 231104 (2019), arXiv:1909.02375 [gr-qc] .

[91] D. Bini, T. Damour, and A. Geralico, Binary dynamics at the fifth and fifth-and-a-half post-Newtonian orders, Phys. Rev. D **102**, 024062 (2020), arXiv:2003.11891 [gr-qc] .

[92] D. Bini, T. Damour, and A. Geralico, Sixth post-Newtonian nonlocal-in-time dynamics of binary systems, Phys. Rev. D **102**, 084047 (2020), arXiv:2007.11239 [gr-qc] .

[93] D. Bini, T. Damour, and A. Geralico, Sixth post-Newtonian local-in-time dynamics of binary systems, Phys. Rev. D **102**, 024061 (2020), arXiv:2004.05407 [gr-qc] .

[94] J. Blümlein, A. Maier, P. Marquard, and G. Schäfer, The 6th post-Newtonian potential terms at $O(G_N^4)$, Phys. Lett. B **816**, 136260 (2021), arXiv:2101.08630 [gr-qc] .

[95] W. Tulczyjew, Motion of multipole particles in general relativity theory, Acta Phys. Pol. **18**, 393 (1959).

[96] W. Tulczyjew, Equations of motion of rotating bodies in general relativity theory, Acta Phys. Polon. **18**, 37 (1959), [Erratum: Acta Phys. Polon. **18**, 534 (1959)].

[97] H. Tagoshi, A. Ohashi, and B. J. Owen, Gravitational field and equations of motion of spinning compact binaries to 2.5 postNewtonian order, Phys. Rev. D **63**, 044006 (2001), arXiv:gr-qc/0010014 .

[98] R. A. Porto, Post-Newtonian corrections to the motion of spinning bodies in NRGR, Phys. Rev. D **73**, 104031 (2006), arXiv:gr-qc/0511061 .

[99] G. Faye, L. Blanchet, and A. Buonanno, Higher-order spin effects in the dynamics of compact binaries. I. Equations of motion, Phys. Rev. D **74**, 104033 (2006), arXiv:gr-qc/0605139 .

[100] T. Damour, P. Jaranowski, and G. Schaefer, Hamiltonian of two spinning compact bodies with next-to-leading order gravitational spin-orbit coupling, Phys. Rev. D **77**, 064032 (2008), arXiv:0711.1048 [gr-qc] .

[101] J. Steinhoff, G. Schaefer, and S. Hergt, ADM canonical formalism for gravitating spinning objects, Phys. Rev. D **77**, 104018 (2008), arXiv:0805.3136 [gr-qc] .

[102] J. Hartung and J. Steinhoff, Next-to-next-to-leading order post-Newtonian spin-orbit Hamiltonian for self-gravitating binaries, Ann. Phys. (Berlin) **523**, 783 (2011), arXiv:1104.3079 [gr-qc] .

[103] D. L. Perrodin, Subleading Spin-Orbit Correction to the Newtonian Potential in Effective Field Theory Formalism, in *12th Marcel Grossmann Meeting on General Relativity* (2010) pp. 725–727, arXiv:1005.0634 [gr-qc] .

[104] R. A. Porto, Next to leading order spin-orbit effects in the motion of inspiralling compact binaries, Class. Quant. Grav. **27**, 205001 (2010), arXiv:1005.5730 [gr-qc] .

[105] J. Hartung, J. Steinhoff, and G. Schafer, Next-to-next-to-leading order post-Newtonian linear-in-spin binary Hamiltonians, Annalen Phys. **525**, 359 (2013), arXiv:1302.6723 [gr-qc] .

[106] S. Marsat, A. Bohe, G. Faye, and L. Blanchet, Next-to-next-to-leading order spin-orbit effects in the equations of motion of compact binary systems, Class. Quant. Grav. **30**, 055007 (2013), arXiv:1210.4143 [gr-qc] .

[107] A. Bohe, S. Marsat, G. Faye, and L. Blanchet, Next-to-next-to-leading order spin-orbit effects in the near-zone metric and precession equations of compact binaries, Class. Quant. Grav. **30**, 075017 (2013), arXiv:1212.5520 [gr-qc] .

[108] M. Levi and J. Steinhoff, Next-to-next-to-leading order gravitational spin-orbit coupling via the effective field theory for spinning objects in the post-Newtonian scheme, JCAP **1601**, 011, arXiv:1506.05056 [gr-qc] .

[109] M. Levi, A. J. Mcleod, and M. Von Hippel, N^{3}LO gravitational spin-orbit coupling at order G^4, JHEP **07**, 115, arXiv:2003.02827 [hep-th] .

[110] B. M. Barker and R. F. O'Connell, Gravitational Two-Body Problem with Arbitrary Masses, Spins, and Quadrupole Moments, Phys. Rev. **D12**, 329 (1975).

[111] B. M. Barker and R. F. O'Connell, The gravitational interaction: Spin, rotation, and quantum effects—a review, Gen. Relativ. Gravit. **11**, 149 (1979).

[112] P. D. D'Eath, Interaction of two black holes in the slow-motion limit, Phys. Rev. D **12**, 2183 (1975).

[113] S. Hergt and G. Schäfer, Higher-order-in-spin interaction Hamiltonians for binary black holes from Poincare invariance, Phys. Rev. **D78**, 124004 (2008), arXiv:0809.2208 [gr-qc] .

[114] R. A. Porto and I. Z. Rothstein, The Hyperfine Einstein-Infeld-Hoffmann potential, Phys. Rev. Lett. **97**, 021101 (2006), arXiv:gr-qc/0604099 [gr-qc] .

[115] R. A. Porto and I. Z. Rothstein, Next to Leading Order Spin(1)Spin(1) Effects in the Motion of Inspiralling Compact Binaries, Phys. Rev. D **78**, 044013 (2008), [Erratum: Phys.Rev.D 81, 029905 (2010)], arXiv:0804.0260 [gr-qc] .

[116] R. A. Porto and I. Z. Rothstein, Spin(1)Spin(2) Effects in the Motion of Inspiralling Compact Binaries at Third Order in the Post-Newtonian Expansion, Phys. Rev. D **78**, 044012 (2008), [Erratum: Phys.Rev.D 81, 029904 (2010)], arXiv:0802.0720 [gr-qc] .

[117] J. Steinhoff, S. Hergt, and G. Schäfer, On the next-to-leading order gravitational spin(1)-spin(2) dynamics, Phys. Rev. **D77**, 081501 (2008), arXiv:0712.1716 [gr-qc] .

[118] J. Steinhoff and G. Schaefer, Comment on 'Spin(1)spin(2) effects in the motion of inspiralling compact binaries at third order in the post-Newtonian expansion' and 'Next to leading order spin(1)spin(1) effects in the motion of inspiralling compact binaries', Phys. Rev. D **80**, 088501 (2009), arXiv:0903.4772 [gr-qc] .

[119] S. Hergt, J. Steinhoff, and G. Schäfer, Reduced Hamiltonian for next-to-leading order Spin-Squared Dynamics of General Compact Binaries, Class. Quant. Grav. **27**, 135007 (2010), arXiv:1002.2093 [gr-qc] .

[120] J. Hartung and J. Steinhoff, Next-to-next-to-leading order post-Newtonian spin(1)-spin(2) Hamiltonian for self-gravitating binaries, Annalen Phys. **523**, 919 (2011), arXiv:1107.4294 [gr-qc] .

[121] M. Levi, Binary dynamics from spin1-spin2 coupling at fourth post-Newtonian order, Phys. Rev. **D85**, 064043 (2012), arXiv:1107.4322 [gr-qc] .

[122] M. Levi and J. Steinhoff, Next-to-next-to-leading order gravitational spin-squared potential via the effective field theory for spinning objects in the post-Newtonian scheme, JCAP **1601**, 008, arXiv:1506.05794 [gr-qc] .

[123] M. Levi and J. Steinhoff, Leading order finite size effects with spins for inspiralling compact binaries, JHEP **06**, 059, arXiv:1410.2601 [gr-qc] .

[124] M. Levi and J. Steinhoff, Complete conservative dynamics for inspiralling compact binaries with spins at the fourth post-Newtonian order, JCAP **09**, 029, arXiv:1607.04252 [gr-qc] .

[125] M. Levi, S. Mougiakakos, and M. Vieira, Gravitational cubic-in-spin interaction at the next-to-leading post-Newtonian order, JHEP **01**, 036, arXiv:1912.06276 [hep-th] .

[126] M. Levi and F. Teng, NLO gravitational quartic-in-spin interaction, JHEP **01**, 066, arXiv:2008.12280 [hep-th] .

[127] J. Vines and J. Steinhoff, Spin-multipole effects in binary black holes and the test-body limit, Phys. Rev. D **97**, 064010 (2018), arXiv:1606.08832 [gr-qc] .

[128] N. Siemonsen and J. Vines, Test black holes, scattering amplitudes and perturbations of Kerr spacetime, Phys. Rev. D **101**, 064066 (2020), arXiv:1909.07361 [gr-qc] .

[129] T. Futamase and Y. Itoh, The post-Newtonian approximation for relativistic compact binaries, Living Rev. Rel. **10**, 2 (2007).

[130] L. Blanchet, Gravitational Radiation from Post-Newtonian Sources and Inspiralling Compact Binaries, Living Rev. Rel. **17**, 2 (2014), arXiv:1310.1528 [gr-qc] .

[131] G. Schäfer and P. Jaranowski, Hamiltonian formulation of general relativity and post-Newtonian dynamics of compact binaries, Living Rev. Rel. **21**, 7 (2018), arXiv:1805.07240 [gr-qc] .

[132] M. Levi and J. Steinhoff, Spinning gravitating objects in the effective field theory in the post-Newtonian scheme, JHEP **09**, 219, arXiv:1501.04956 [gr-qc] .

[133] R. A. Porto, The effective field theorist's approach to gravitational dynamics, Phys. Rept. **633**, 1 (2016), arXiv:1601.04914 [hep-th] .

[134] M. Levi, Effective Field Theories of Post-Newtonian Gravity: A comprehensive review, Rept. Prog. Phys. **83**, 075901 (2020), arXiv:1807.01699 [hep-th] .

[135] K. S. Thorne, Multipole Expansions of Gravitational Radiation, Rev. Mod. Phys. **52**, 299 (1980).

[136] T. Damour and N. Deruelle, Radiation Reaction and Angular Momentum Loss in Small Angle Gravitational Scattering, Phys. Lett. A **87**, 81 (1981).

[137] L. Blanchet and T. Damour, Radiative gravitational fields in general relativity I. general structure of the field outside the source, Phil. Trans. Roy. Soc. Lond. A **320**, 379 (1986).

[138] L. Blanchet and T. Damour, Postnewtonian Generation of Gravitational Waves, Ann. Inst. H. Poincare Phys. Theor. **50**, 377 (1989).

[139] T. Damour and B. R. Iyer, Multipole analysis for electromagnetism and linearized gravity with irreducible cartesian tensors, Phys. Rev. **D43**, 3259 (1991).

[140] C. W. Lincoln and C. M. Will, Coalescing Binary Systems of Compact Objects to (Post)5/2 Newtonian Order: Late Time Evolution and Gravitational Radiation Emission, Phys. Rev. D **42**, 1123 (1990).

[141] A. G. Wiseman, Coalescing binary systems of compact objects to (post)5/2 Newtonian order. 2. Higher order wave forms and radiation recoil, Phys. Rev. D **46**, 1517 (1992).

[142] A. G. Wiseman, Coalescing binary systems of compact objects to (post)Newtonian**5/2 order. 4V: The Gravitational wave tail, Phys. Rev. D **48**, 4757 (1993).

[143] L. Blanchet and T. Damour, Hereditary effects in gravitational radiation, Phys. Rev. D **46**, 4304 (1992).

[144] L. Blanchet, T. Damour, and B. R. Iyer, Gravitational waves from inspiralling compact binaries: Energy loss and wave form to second postNewtonian order, Phys. Rev. D **51**, 5360 (1995), [Erratum: Phys.Rev.D 54, 1860 (1996)], arXiv:gr-qc/9501029 .

[145] L. Blanchet, T. Damour, B. R. Iyer, C. M. Will, and A. G. Wiseman, Gravitational radiation damping of compact binary systems to second postNewtonian order, Phys. Rev. Lett. **74**, 3515 (1995), arXiv:gr-qc/9501027 .

[146] B. R. Iyer and C. Will, PostNewtonian gravitational radiation reaction for two-body systems, Phys. Rev. Lett. **70**, 113 (1993).

[147] B. R. Iyer and C. Will, PostNewtonian gravitational radiation reaction for two-body systems: Nonspinning bodies, Phys. Rev. D **52**, 6882 (1995).

[148] C. M. Will and A. G. Wiseman, Gravitational radiation from compact binary systems: Gravitational wave forms and energy loss to second postNewtonian order, Phys. Rev. D **54**, 4813 (1996), arXiv:gr-qc/9608012 .

[149] A. Gopakumar and B. R. Iyer, Gravitational waves from inspiralling compact binaries: Angular momentum flux, evolution of the orbital elements and the wave form to the second postNewtonian order, Phys. Rev. D **56**, 7708 (1997), arXiv:gr-qc/9710075 .

[150] A. Gopakumar, B. R. Iyer, and S. Iyer, Second postNewtonian gravitational radiation reaction for two-body systems: Nonspinning bodies, Phys. Rev. D **55**, 6030 (1997), [Erratum: Phys.Rev.D 57, 6562 (1998)], arXiv:gr-qc/9703075 .

[151] A. Gopakumar and B. R. Iyer, Second postNewtonian gravitational wave polarizations for compact binaries in elliptical orbits, Phys. Rev. D **65**, 084011 (2002), arXiv:gr-qc/0110100 .

[152] M. E. Pati and C. M. Will, PostNewtonian gravitational radiation and equations of motion via direct integration of the relaxed Einstein equations. 1. Foundations, Phys. Rev. D **62**, 124015 (2000), arXiv:gr-qc/0007087 .

[153] L. Blanchet, T. Damour, G. Esposito-Farese, and B. R. Iyer, Gravitational radiation from inspiralling compact binaries completed at the third post-Newtonian order, Phys. Rev. Lett. **93**, 091101 (2004), arXiv:gr-qc/0406012 .

[154] T. Damour, A. Gopakumar, and B. R. Iyer, Phasing of gravitational waves from inspiralling eccentric binaries, Phys. Rev. D **70**, 064028 (2004), arXiv:gr-qc/0404128 .

[155] K. Arun, L. Blanchet, B. R. Iyer, and M. S. Qusailah, Inspiralling compact binaries in quasi-elliptical orbits: The Complete 3PN energy flux, Phys. Rev. D **77**, 064035 (2008), arXiv:0711.0302 [gr-qc] .

[156] K. Arun, L. Blanchet, B. R. Iyer, and M. S. Qusailah, Tail effects in the 3PN gravitational wave energy flux of compact binaries in quasi-elliptical orbits, Phys. Rev. D **77**, 064034 (2008), arXiv:0711.0250 [gr-qc] .

[157] K. Arun, L. Blanchet, B. R. Iyer, and S. Sinha, Third post-Newtonian angular momentum flux and the secular evolution of orbital elements for inspiralling compact binaries in quasi-elliptical orbits, Phys. Rev. D **80**, 124018 (2009), arXiv:0908.3854 [gr-qc] .

[158] G. Faye, S. Marsat, L. Blanchet, and B. R. Iyer, The third and a half post-Newtonian gravitational wave quadrupole mode for quasi-circular inspiralling compact binaries, Class. Quant. Grav. **29**, 175004 (2012), arXiv:1204.1043 [gr-qc] .

[159] C. K. Mishra, K. Arun, and B. R. Iyer, Third post-Newtonian gravitational waveforms for compact binary systems in general orbits: Instantaneous terms, Phys. Rev. D **91**, 084040 (2015), arXiv:1501.07096 [gr-qc] .

[160] N. Loutrel and N. Yunes, Hereditary Effects in Eccentric Compact Binary Inspirals to Third Post-Newtonian Order, Class. Quant. Grav. **34**, 044003 (2017), arXiv:1607.05409 [gr-qc] .

[161] Y. Boetzel, C. K. Mishra, G. Faye, A. Gopakumar, and B. R. Iyer, Gravitational-wave amplitudes for compact binaries in eccentric orbits at the third post-Newtonian order: Tail contributions and postadiabatic corrections, Phys. Rev. D **100**, 044018 (2019), arXiv:1904.11814 [gr-qc] .

[162] K. S. Thorne and J. B. Hartle, Laws of motion and precession for black holes and other bodies, Phys. Rev. D **31**, 1815 (1984).

[163] L. E. Kidder, C. M. Will, and A. G. Wiseman, Spin effects in the inspiral of coalescing compact binaries, Phys. Rev. D **47**, R4183 (1993), arXiv:gr-qc/9211025 .

[164] L. E. Kidder, Coalescing binary systems of compact objects to postNewtonian 5/2 order. 5. Spin effects, Phys. Rev. D **52**, 821 (1995), arXiv:gr-qc/9506022 .

[165] C. M. Will, Post-Newtonian gravitational radiation and equations of motion via direct integration of the relaxed Einstein equations. III. Radiation reaction for binary systems with spinning bodies, Phys. Rev. D **71**, 084027 (2005), arXiv:gr-qc/0502039 .

[166] L. Blanchet, A. Buonanno, and G. Faye, Higher-order spin effects in the dynamics of compact binaries. II. Radiation field, Phys. Rev. D **74**, 104034 (2006), [Erratum: Phys.Rev.D 75, 049903 (2007), Erratum: Phys.Rev.D 81, 089901 (2010)], arXiv:gr-qc/0605140 .

[167] J. Zeng and C. M. Will, Application of energy and angular momentum balance to gravitational radiation reaction for binary systems with spin-orbit coupling, Gen. Rel. Grav. **39**, 1661 (2007), arXiv:0704.2720 [gr-qc] .

[168] H. Wang and C. M. Will, Post-Newtonian gravitational radiation and equations of motion via direct integration of the relaxed Einstein equations. IV. Radiation reaction for binary systems with spin-spin coupling, Phys. Rev. D **75**, 064017 (2007), arXiv:gr-qc/0701047 .

[169] K. G. Arun, A. Buonanno, G. Faye, and E. Ochsner, Higher-order spin effects in the amplitude and phase of gravitational waveforms emitted by inspiraling compact binaries: Ready-to-use gravitational waveforms, Phys. Rev. **D79**, 104023 (2009), [Erratum: Phys. Rev.D84,049901(2011)], arXiv:0810.5336 [gr-qc] .

[170] L. Blanchet, G. Faye, B. R. Iyer, and S. Sinha, The Third post-Newtonian gravitational wave polarisations and associated spherical harmonic modes for inspiralling compact binaries in quasi-circular orbits, Class. Quant. Grav. **25**, 165003 (2008), [Erratum: Class.Quant.Grav. 29, 239501 (2012)], arXiv:0802.1249 [gr-qc] .

[171] R. A. Porto, A. Ross, and I. Z. Rothstein, Spin induced multipole moments for the gravitational wave flux from binary inspirals to third Post-Newtonian order, JCAP **03**, 009, arXiv:1007.1312 [gr-qc] .

[172] L. Blanchet, A. Buonanno, and G. Faye, Tail-induced spin-orbit effect in the gravitational radiation of compact binaries, Phys. Rev. D **84**, 064041 (2011), arXiv:1104.5659 [gr-qc] .

[173] A. Buonanno, G. Faye, and T. Hinderer, Spin effects on gravitational waves from inspiraling compact binaries at second post-Newtonian order, Phys. Rev. **D87**, 044009 (2013), arXiv:1209.6349 [gr-qc] .

[174] A. Bohé, S. Marsat, and L. Blanchet, Next-to-next-to-leading order spin–orbit effects in the gravitational wave flux and orbital phasing of compact binaries, Class. Quant. Grav. **30**, 135009 (2013), arXiv:1303.7412 [gr-qc] .

[175] S. Marsat, A. Bohé, L. Blanchet, and A. Buonanno, Next-to-leading tail-induced spin–orbit effects in the gravitational radiation flux of compact binaries, Class. Quant. Grav. **31**, 025023 (2014), arXiv:1307.6793 [gr-qc] .

[176] S. Marsat, Cubic order spin effects in the dynamics and gravitational wave energy flux of compact object binaries, Class. Quant. Grav. **32**, 085008 (2015), arXiv:1411.4118 [gr-qc] .

[177] A. Bohé, G. Faye, S. Marsat, and E. K. Porter, Quadratic-in-spin effects in the orbital dynamics and gravitational-wave energy flux of compact binaries at the 3PN order, Class. Quant. Grav. **32**, 195010 (2015), arXiv:1501.01529 [gr-qc] .

[178] N. T. Maia, C. R. Galley, A. K. Leibovich, and R. A. Porto, Radiation reaction for spinning bodies in effective field theory I: Spin-orbit effects, Phys. Rev. D **96**, 084064 (2017), arXiv:1705.07934 [gr-qc] .

[179] N. T. Maia, C. R. Galley, A. K. Leibovich, and R. A. Porto, Radiation reaction for spinning bodies in effective field theory II: Spin-spin effects, Phys. Rev. D **96**, 084065 (2017), arXiv:1705.07938 [gr-qc] .

[180] N. Siemonsen, J. Steinhoff, and J. Vines, Gravitational waves from spinning binary black holes at the leading post-Newtonian orders at all orders in spin, Phys. Rev. D **97**, 124046 (2018), arXiv:1712.08603 [gr-qc] .

[181] G. Cho, B. Pardo, and R. A. Porto, Gravitational radiation from inspiralling compact objects: Spin-spin effects completed at the next-to-leading post-Newtonian order, Phys. Rev. D **104**, 024037 (2021), arXiv:2103.14612 [gr-qc] .

[182] G. Cho, R. A. Porto, and Z. Yang, Gravitational radiation from inspiralling compact objects: Spin effects to fourth Post-Newtonian order, (2022), arXiv:2201.05138 [gr-qc] .

[183] L. Blanchet and T. Damour, Tail Transported Temporal Correlations in the Dynamics of a Gravitating System, Phys. Rev. D **37**, 1410 (1988).

[184] L. Blanchet, Gravitational wave tails of tails, Class. Quant. Grav. **15**, 113 (1998), [Erratum: Class.Quant.Grav. 22, 3381 (2005)], arXiv:gr-qc/9710038 .

[185] J. E. Vines and É. É. Flanagan, Post-1-Newtonian quadrupole tidal interactions in binary systems, Phys. Rev. **D88**, 024046 (2013), arXiv:1009.4919 [gr-qc] .

[186] J. Vines, É. É. Flanagan, and T. Hinderer, Post-1-Newtonian tidal effects in the gravitational waveform from binary inspirals, Phys. Rev. **D83**, 084051 (2011), arXiv:1101.1673 [gr-qc] .

[187] D. Bini, T. Damour, and G. Faye, Effective action approach to higher-order relativistic tidal interactions in binary systems and their effective one body description, Phys. Rev. **D85**, 124034 (2012), arXiv:1202.3565 [gr-qc] .

[188] T. Abdelsalhin, L. Gualtieri, and P. Pani, Post-Newtonian spin-tidal couplings for compact binaries, Phys. Rev. D **98**, 104046 (2018), arXiv:1805.01487 [gr-qc] .

[189] B. Banihashemi and J. Vines, Gravitomagnetic tidal effects in gravitational waves from neutron star binaries, Phys. Rev. D **101**, 064003 (2020), arXiv:1805.07266 [gr-qc] .

[190] Q. Henry, G. Faye, and L. Blanchet, Hamiltonian for tidal interactions in compact binary systems to next-to-next-to-leading post-Newtonian order, Phys. Rev. D **102**, 124074 (2020), arXiv:2009.12332 [gr-qc] .

[191] É. É. Flanagan and T. Hinderer, Constraining neutron star tidal Love numbers with gravitational wave detectors, Phys. Rev. **D77**, 021502 (2008), arXiv:0709.1915 [astro-ph] .

[192] T. Damour, A. Nagar, and L. Villain, Measurability of the tidal polarizability of neutron stars in late-inspiral gravitational-wave signals, Phys. Rev. D **85**, 123007 (2012), arXiv:1203.4352 [gr-qc] .

[193] M. Favata, Systematic parameter errors in inspiraling neutron star binaries, Phys. Rev. Lett. **112**, 101101 (2014), arXiv:1310.8288 [gr-qc] .

[194] P. Landry, Rotational-tidal phasing of the binary neutron star waveform, (2018), arXiv:1805.01882 [gr-qc] .

[195] Q. Henry, G. Faye, and L. Blanchet, Tidal effects in the equations of motion of compact binary systems to next-to-next-to-leading post-Newtonian order, Phys. Rev. D **101**, 064047 (2020), arXiv:1912.01920 [gr-qc] .

[196] Q. Henry, G. Faye, and L. Blanchet, Tidal effects in the gravitational-wave phase evolution of compact binary systems to next-to-next-to-leading post-Newtonian order, Phys. Rev. D **102**, 044033 (2020), arXiv:2005.13367 [gr-qc] .

[197] T. Dietrich, T. Hinderer, and A. Samajdar, Interpreting Binary Neutron Star Mergers: Describing the Binary Neutron Star Dynamics, Modelling Gravitational Waveforms, and Analyzing Detections, Gen. Rel. Grav. **53**, 27 (2021), arXiv:2004.02527 [gr-qc] .

[198] C. Will, *Theory and Experiment in Gravitational Physics* (Cambridge University Press, 1993).

[199] K. Nordtvedt, Jr., PostNewtonian metric for a general class of scalar tensor gravitational theories and observational consequences, Astrophys. J. **161**, 1059 (1970).

[200] T. Damour and G. Esposito-Farese, Tensor multiscalar theories of gravitation, Class. Quant. Grav. **9**, 2093 (1992).

[201] T. Damour and G. Esposito-Farese, Testing gravity to second postNewtonian order: A Field theory approach, Phys. Rev. **D53**, 5541 (1996), arXiv:gr-qc/9506063 [gr-qc] .

[202] T. Damour and G. Esposito-Farese, Tensor - scalar gravity and binary pulsar experiments, Phys. Rev. **D54**, 1474 (1996), arXiv:gr-qc/9602056 [gr-qc] .

[203] S. Mirshekari and C. M. Will, Compact binary systems in scalar-tensor gravity: Equations of motion to 2.5 post-Newtonian order, Phys. Rev. **D87**, 084070 (2013), arXiv:1301.4680 [gr-qc] .

[204] R. N. Lang, Compact binary systems in scalar-tensor gravity. II. Tensor gravitational waves to second post-Newtonian order, Phys. Rev. D **89**, 084014 (2014), arXiv:1310.3320 [gr-qc] .

[205] R. N. Lang, Compact binary systems in scalar-tensor gravity. III. Scalar waves and energy flux, Phys. Rev. **D91**, 084027 (2015), arXiv:1411.3073 [gr-qc] .

[206] L. Bernard, Dynamics of compact binary systems in scalar-tensor theories: Equations of motion to the third post-Newtonian order, Phys. Rev. D **98**, 044004 (2018), arXiv:1802.10201 [gr-qc] .

[207] L. Bernard, Dynamics of compact binary systems in scalar-tensor theories: II. Center-of-mass and conserved quantities to 3PN order, Phys. Rev. D **99**, 044047 (2019), arXiv:1812.04169 [gr-qc] .

[208] L. Bernard, L. Blanchet, and D. Trestini, Gravitational waves in scalar-tensor theory to one-and-a-half post-Newtonian order, (2022), arXiv:2201.10924 [gr-qc] .

[209] N. Sennett, S. Marsat, and A. Buonanno, Gravitational waveforms in scalar-tensor gravity at 2PN relative order, Phys. Rev. **D94**, 084003 (2016), arXiv:1607.01420 [gr-qc] .

[210] F.-L. Julié, On the motion of hairy black holes in Einstein-Maxwell-dilaton theories, JCAP **1801**, 026, arXiv:1711.10769 [gr-qc] .

[211] T. P. Sotiriou and E. Barausse, Post-Newtonian expansion for Gauss-Bonnet gravity, Phys. Rev. D **75**, 084007 (2007), arXiv:gr-qc/0612065 .

[212] S. Alexander and N. Yunes, Parametrized post-Newtonian expansion of Chern-Simons gravity, Phys. Rev. D **75**, 124022 (2007), arXiv:0704.0299 [hep-th] .

[213] K. Yagi, L. C. Stein, N. Yunes, and T. Tanaka, Post-Newtonian, Quasi-Circular Binary Inspirals in Quadratic Modified Gravity, Phys. Rev. D **85**, 064022 (2012), [Erratum: Phys.Rev.D 93, 029902 (2016)], arXiv:1110.5950 [gr-qc] .

[214] F.-L. Julié and E. Berti, Post-Newtonian dynamics and black hole thermodynamics in Einstein-scalar-Gauss-Bonnet gravity, Phys. Rev. D **100**, 104061 (2019), arXiv:1909.05258 [gr-qc] .

[215] P. Guilleminot, F.-L. Julié, N. Merino, and R. Olea, First-order Lagrangian and Hamiltonian of Lovelock gravity, Class. Quant. Grav. **38**, 105004 (2021), arXiv:2011.01296 [gr-qc] .

[216] C. Zhang, X. Zhao, A. Wang, B. Wang, K. Yagi, N. Yunes, W. Zhao, and T. Zhu, Gravitational waves from the quasicircular inspiral of compact binaries in Einstein-aether theory, Phys. Rev. D **101**, 044002 (2020), [Erratum: Phys.Rev.D 104, 069905 (2021)], arXiv:1911.10278 [gr-qc] .

[217] M. De Laurentis and A. J. Lopez-Revelles, Newtonian, Post Newtonian and Parameterized Post Newtonian limits of f(R, G) gravity, Int. J. Geom. Meth. Mod. Phys. **11**, 1450082 (2014), arXiv:1311.0206 [gr-qc] .

[218] A. Einstein, Über Gravitationswellen, Sitzungsber. Preuss. Akad. Wiss. Berlin (Math. Phys.) **1918**, 154 (1918).

[219] A. Einstein, The Foundation of the General Theory of Relativity, Annalen Phys. **49**, 769 (1916).

[220] A. Einstein, Hamilton's Principle and the General Theory of Relativity, Sitzungsber. Preuss. Akad. Wiss. Berlin (Math. Phys.) **1916**, 1111 (1916).

[221] L. D. Landau and E. M. Lifshitz, *The Classical Theory of Fields*, Course of Theoretical Physics, Vol. Volume 2 (Pergamon Press, Oxford, 1975).

[222] T. Damour, M. Soffel, and C. Xu, General relativistic celestial mechanics. 1. Method and definition of reference systems, Phys. Rev. **D43**, 3273 (1991).

[223] L. Blanchet and B. R. Iyer, Third postNewtonian dynamics of compact binaries: Equations of motion in the center-of-mass frame, Class. Quant. Grav. **20**, 755 (2003), arXiv:gr-qc/0209089 [gr-qc] .

[224] L. Blanchet, Energy losses by gravitational radiation in inspiraling compact binaries to five halves postNewtonian order, Phys. Rev. D **54**, 1417 (1996), [Erratum: Phys.Rev.D 71, 129904 (2005)], arXiv:gr-qc/9603048 .

[225] L. E. Kidder, Using full information when computing modes of post-Newtonian waveforms from inspiralling compact binaries in circular orbit, Phys. Rev. D **77**, 044016 (2008), arXiv:0710.0614 [gr-qc] .

[226] B. Bertotti, On gravitational motion, Nuovo Cim. **4**, 898 (1956).

[227] B. Bertotti and J. Plebanski, Theory of gravitational perturbations in the fast motion approximation, Annals Phys. **11**, 169 (1960).

[228] K. Westpfahl and M. Goller, Gravitational scattering of two relativistic particles in post-linear approximation, Lett. Nuovo Cim. **26**, 573 (1979).

[229] K. Westpfahl and H. Hoyler, Gravitational bremsstrahlung in post-linear fast-motion approximation, Lett. Nuovo Cim. **27**, 581 (1980).

[230] M. Portilla, SCATTERING OF TWO GRAVITATING PARTICLES: CLASSICAL APPROACH, J. Phys. A **13**, 3677 (1980).

[231] A. Rosenblum, Gravitational Radiation Energy Loss in Scattering Problems and the Einstein Quadrupole Formula, Phys. Lett. A **81**, 1 (1981).

[232] L. Bel, T. Damour, N. Deruelle, J. Ibanez, and J. Martin, Poincaré-invariant gravitational field and equations of motion of two pointlike objects: The postlinear approximation of general relativity, Gen. Rel. Grav. **13**, 963 (1981).

[233] G. Schäfer, The adm hamiltonian at the postlinear approximation, General relativity and gravitation **18**, 255 (1986).

[234] K. Westpfahl, High-Speed Scattering of Charged and Uncharged Particles in General Relativity, Fortsch. Phys. **33**, 417 (1985).

[235] K. Westpfahl, R. Mohles, and H. Simonis, Energy-momentum conservation for gravitational two-body scattering in the post-linear approximation, Class. Quant. Grav. **4**, L185 (1987).

[236] T. Damour, Gravitational scattering, post-Minkowskian approximation and Effective One-Body theory, Phys. Rev. **D94**, 104015 (2016), arXiv:1609.00354 [gr-qc] .

[237] T. Damour, High-energy gravitational scattering and the general relativistic two-body problem, Phys. Rev. **D97**, 044038 (2018), arXiv:1710.10599 [gr-qc] .

[238] N. Arkani-Hamed, T.-C. Huang, and Y.-t. Huang, Scattering amplitudes for all masses and spins, JHEP **11**, 070, arXiv:1709.04891 [hep-th] .

[239] N. J. Bjerrum-Bohr, P. H. Damgaard, G. Festuccia, L. Planté, and P. Vanhove, General Relativity from Scattering Amplitudes, Phys. Rev. Lett. **121**, 171601 (2018), arXiv:1806.04920 [hep-th] .

[240] D. A. Kosower, B. Maybee, and D. O'Connell, Amplitudes, Observables, and Classical Scattering, JHEP **02**, 137, arXiv:1811.10950 [hep-th] .

[241] C. Cheung, I. Z. Rothstein, and M. P. Solon, From Scattering Amplitudes to Classical Potentials in the Post-Minkowskian Expansion, Phys. Rev. Lett. **121**, 251101 (2018), arXiv:1808.02489 [hep-th] .

[242] Y. F. Bautista and A. Guevara, From Scattering Amplitudes to Classical Physics: Universality, Double Copy and Soft Theorems, (2019), arXiv:1903.12419 [hep-th] .

[243] Z. Bern, C. Cheung, R. Roiban, C.-H. Shen, M. P. Solon, and M. Zeng, Scattering Amplitudes and the Conservative Hamiltonian for Binary Systems at Third Post-Minkowskian Order, Phys. Rev. Lett. **122**, 201603 (2019), arXiv:1901.04424 [hep-th] .

[244] N. E. J. Bjerrum-Bohr, A. Cristofoli, and P. H. Damgaard, Post-Minkowskian Scattering Angle in Einstein Gravity, JHEP **08**, 038, arXiv:1910.09366 [hep-th] .

[245] A. Cristofoli, P. H. Damgaard, P. Di Vecchia, and C. Heissenberg, Second-order Post-Minkowskian scattering in arbitrary dimensions, JHEP **07**, 122, arXiv:2003.10274 [hep-th] .

[246] Z. Bern, J. Parra-Martinez, R. Roiban, M. S. Ruf, C.-H. Shen, M. P. Solon, and M. Zeng, Scattering Amplitudes and Conservative Binary Dynamics at $\mathcal{O}(G^4)$, Phys. Rev. Lett. **126**, 171601 (2021), arXiv:2101.07254 [hep-th] .

[247] Z. Bern, J. Parra-Martinez, R. Roiban, M. S. Ruf, C.-H. Shen, M. P. Solon, and M. Zeng, Scattering Amplitudes, the Tail Effect, and Conservative Binary Dynamics at O(G4), Phys. Rev. Lett. **128**, 161103 (2022), arXiv:2112.10750 [hep-th] .

[248] G. Travaglini *et al.*, The SAGEX Review on Scattering Amplitudes, (2022), arXiv:2203.13011 [hep-th] .

[249] N. E. J. Bjerrum-Bohr, P. H. Damgaard, L. Plante, and P. Vanhove, The SAGEX Review on Scattering Amplitudes, Chapter 13: Post-Minkowskian expansion from Scattering Amplitudes, (2022), arXiv:2203.13024 [hep-th] .

[250] D. A. Kosower, R. Monteiro, and D. O'Connell, The SAGEX Review on Scattering Amplitudes, Chapter 14: Classical Gravity from Scattering Amplitudes, (2022), arXiv:2203.13025 [hep-th] .

[251] T. Ledvinka, G. Schaefer, and J. Bicak, Relativistic Closed-Form Hamiltonian for Many-Body Gravitating Systems in the Post-Minkowskian Approximation, Phys. Rev. Lett. **100**, 251101 (2008), arXiv:0807.0214 [gr-qc] .

[252] T. Damour, Classical and quantum scattering in post-Minkowskian gravity, Phys. Rev. D **102**, 024060 (2020), arXiv:1912.02139 [gr-qc] .

[253] L. Blanchet and A. S. Fokas, Equations of motion of self-gravitating N-body systems in the first post-Minkowskian approximation, Phys. Rev. D **98**, 084005 (2018), arXiv:1806.08347 [gr-qc] .

[254] S. Foffa, Gravitating binaries at 5PN in the post-Minkowskian approximation, Phys. Rev. D **89**, 024019 (2014), arXiv:1309.3956 [gr-qc] .

[255] G. Kälin and R. A. Porto, From Boundary Data to Bound States, JHEP **01**, 072, arXiv:1910.03008 [hep-th] .

[256] G. Kälin, Z. Liu, and R. A. Porto, Conservative Dynamics of Binary Systems to Third Post-Minkowskian Order from the Effective Field Theory Approach, Phys. Rev. Lett. **125**, 261103 (2020), arXiv:2007.04977 [hep-th] .

[257] G. Kälin and R. A. Porto, Post-Minkowskian Effective Field Theory for Conservative Binary Dynamics, JHEP **11**, 106, arXiv:2006.01184 [hep-th] .

[258] C. Dlapa, G. Kälin, Z. Liu, and R. A. Porto, Dynamics of binary systems to fourth Post-Minkowskian order from the effective field theory approach, Phys. Lett. B **831**, 137203 (2022), arXiv:2106.08276 [hep-th] .

[259] C. Dlapa, G. Kälin, Z. Liu, and R. A. Porto, Conservative Dynamics of Binary Systems at Fourth Post-Minkowskian Order in the Large-Eccentricity Expansion, Phys. Rev. Lett. **128**, 161104 (2022), arXiv:2112.11296 [hep-th] .

[260] G. Mogull, J. Plefka, and J. Steinhoff, Classical black hole scattering from a worldline quantum field theory, JHEP **02**, 048, arXiv:2010.02865 [hep-th] .

[261] G. U. Jakobsen, G. Mogull, J. Plefka, and J. Steinhoff, Classical Gravitational Bremsstrahlung from a Worldline Quantum Field Theory, Phys. Rev. Lett. **126**, 201103 (2021), arXiv:2101.12688 [gr-qc] .

[262] D. Bini and T. Damour, Gravitational spin-orbit coupling in binary systems, post-Minkowskian approximation and effective one-body theory, Phys. Rev. **D96**, 104038 (2017), arXiv:1709.00590 [gr-qc] .

[263] D. Bini and T. Damour, Gravitational spin-orbit coupling in binary systems at the second post-Minkowskian approximation, Phys. Rev. **D98**, 044036 (2018), arXiv:1805.10809 [gr-qc] .

[264] J. Vines, Scattering of two spinning black holes in post-Minkowskian gravity, to all orders in spin, and effective-one-body mappings, Class. Quant. Grav. **35**, 084002 (2018), arXiv:1709.06016 [gr-qc] .

[265] J. Vines, J. Steinhoff, and A. Buonanno, Spinning-black-hole scattering and the test-black-hole limit at second post-Minkowskian order, Phys. Rev. **D99**, 064054 (2019), arXiv:1812.00956 [gr-qc] .

[266] A. Guevara, A. Ochirov, and J. Vines, Black-hole scattering with general spin directions from minimal-coupling amplitudes, Phys. Rev. **D100**, 104024 (2019), arXiv:1906.10071 [hep-th] .

[267] G. Kälin and R. A. Porto, From Boundary Data to Bound States II: Scattering Angle to Dynamical Invariants (with Twist), JHEP **02**, 120, arXiv:1911.09130 [hep-th] .

[268] Z. Bern, A. Luna, R. Roiban, C.-H. Shen, and M. Zeng, Spinning black hole binary dynamics, scattering amplitudes, and effective field theory, Phys. Rev. D **104**, 065014 (2021), arXiv:2005.03071 [hep-th] .

[269] M.-Z. Chung, Y.-t. Huang, J.-W. Kim, and S. Lee, Complete Hamiltonian for spinning binary systems at first post-Minkowskian order, JHEP **05**, 105, arXiv:2003.06600 [hep-th] .

[270] B. Maybee, D. O'Connell, and J. Vines, Observables and amplitudes for spinning particles and black holes, JHEP **12**, 156, arXiv:1906.09260 [hep-th] .

[271] Y. F. Bautista, A. Guevara, C. Kavanagh, and J. Vines, From Scattering in Black Hole Backgrounds to Higher-Spin Amplitudes: Part I, (2021), arXiv:2107.10179 [hep-th] .

[272] D. Kosmopoulos and A. Luna, Quadratic-in-spin Hamiltonian at $\mathcal{O}(\mathrm{G}^2)$ from scattering amplitudes, JHEP **07**, 037, arXiv:2102.10137 [hep-th] .

[273] Z. Liu, R. A. Porto, and Z. Yang, Spin Effects in the Effective Field Theory Approach to Post-Minkowskian Conservative Dynamics, JHEP **06**, 012, arXiv:2102.10059 [hep-th] .

[274] G. U. Jakobsen, G. Mogull, J. Plefka, and J. Steinhoff, Gravitational Bremsstrahlung and Hidden Supersymmetry of Spinning Bodies, Phys. Rev. Lett. **128**, 011101 (2022), arXiv:2106.10256 [hep-th] .

[275] G. U. Jakobsen, G. Mogull, J. Plefka, and J. Steinhoff, SUSY in the sky with gravitons, JHEP **01**, 027, arXiv:2109.04465 [hep-th] .

[276] R. Aoude, K. Haddad, and A. Helset, Classical gravitational spinning-spinless scattering at $\mathcal{O}(G^2S^\infty)$, (2022), arXiv:2205.02809 [hep-th] .

[277] D. Bini, T. Damour, and A. Geralico, Scattering of tidally interacting bodies in post-Minkowskian gravity, Phys. Rev. D **101**, 044039 (2020), arXiv:2001.00352 [gr-qc] .

[278] C. Cheung and M. P. Solon, Tidal Effects in the Post-Minkowskian Expansion, Phys. Rev. Lett. **125**, 191601 (2020), arXiv:2006.06665 [hep-th] .

[279] G. Kälin, Z. Liu, and R. A. Porto, Conservative Tidal Effects in Compact Binary Systems to Next-to-Leading Post-Minkowskian Order, Phys. Rev. D **102**, 124025 (2020), arXiv:2008.06047 [hep-th] .

[280] Z. Bern, J. Parra-Martinez, R. Roiban, E. Sawyer, and C.-H. Shen, Leading Nonlinear Tidal Effects and Scattering Amplitudes, JHEP **05**, 188, arXiv:2010.08559 [hep-th] .

[281] C. Cheung, N. Shah, and M. P. Solon, Mining the Geodesic Equation for Scattering Data, Phys. Rev. D **103**, 024030 (2021), arXiv:2010.08568 [hep-th] .

[282] K. Haddad and A. Helset, Tidal effects in quantum field theory, JHEP **12**, 024, arXiv:2008.04920 [hep-th] .

[283] R. Aoude, K. Haddad, and A. Helset, Tidal effects for spinning particles, JHEP **03**, 097, arXiv:2012.05256 [hep-th] .

[284] S. Mougiakakos, M. M. Riva, and F. Vernizzi, Gravitational Bremsstrahlung with tidal effects in the post-Minkowskian expansion, (2022), arXiv:2204.06556 [hep-th] .

[285] T. Damour, Radiative contribution to classical gravitational scattering at the third order in G, Phys. Rev. D **102**, 124008 (2020), arXiv:2010.01641 [gr-qc] .

[286] D. Bini, T. Damour, and A. Geralico, Radiative contributions to gravitational scattering, Phys. Rev. D **104**, 084031 (2021), arXiv:2107.08896 [gr-qc] .

[287] D. Bini and A. Geralico, Higher-order tail contributions to the energy and angular momentum fluxes in a two-body scattering process, Phys. Rev. D **104**, 104020 (2021), arXiv:2108.05445 [gr-qc] .

[288] P. Di Vecchia, C. Heissenberg, R. Russo, and G. Veneziano, The eikonal approach to gravitational scattering and radiation at $\mathcal{O}(\mathrm{G}^3)$, JHEP **07**, 169, arXiv:2104.03256 [hep-th] .

[289] N. E. J. Bjerrum-Bohr, P. H. Damgaard, L. Planté, and P. Vanhove, The amplitude for classical gravitational scattering at third Post-Minkowskian order, JHEP **08**, 172, arXiv:2105.05218 [hep-th] .

[290] A. Brandhuber, G. Chen, G. Travaglini, and C. Wen, Classical gravitational scattering from a gauge-invariant double copy, JHEP **10**, 118, arXiv:2108.04216 [hep-th] .

[291] P. H. Damgaard, L. Plante, and P. Vanhove, On an exponential representation of the gravitational S-matrix, JHEP **11**, 213, arXiv:2107.12891 [hep-th] .

[292] E. Herrmann, J. Parra-Martinez, M. S. Ruf, and M. Zeng, Gravitational Bremsstrahlung from Reverse Unitarity, Phys. Rev. Lett. **126**, 201602 (2021), arXiv:2101.07255 [hep-th] .

[293] E. Herrmann, J. Parra-Martinez, M. S. Ruf, and M. Zeng, Radiative classical gravitational observables at $\mathcal{O}(\mathrm{G}^3)$ from scattering amplitudes, JHEP **10**, 148, arXiv:2104.03957 [hep-th] .

[294] P. Di Vecchia, C. Heissenberg, R. Russo, and G. Veneziano, Radiation Reaction from Soft Theorems, Phys. Lett. B **818**, 136379 (2021), arXiv:2101.05772 [hep-th] .

[295] M. M. Riva and F. Vernizzi, Radiated momentum in the post-Minkowskian worldline approach via reverse unitarity, JHEP **11**, 228, arXiv:2110.10140 [hep-th] .

[296] M. V. S. Saketh, J. Vines, J. Steinhoff, and A. Buonanno, Conservative and radiative dynamics in classical relativistic scattering and bound systems, Phys. Rev. Res. **4**, 013127 (2022), arXiv:2109.05994 [gr-qc] .

[297] G. Cho, G. Kälin, and R. A. Porto, From boundary data to bound states. Part III. Radiative effects, JHEP **04**, 154, arXiv:2112.03976 [hep-th] .

[298] A. V. Manohar, A. K. Ridgway, and C.-H. Shen, Radiated Angular Momentum and Dissipative Effects in Classical Scattering, (2022), arXiv:2203.04283 [hep-th] .

[299] Z. Bern, C. Cheung, R. Roiban, C.-H. Shen, M. P. Solon, and M. Zeng, Black Hole Binary Dynamics from the Double Copy and Effective Theory, JHEP **10**, 206, arXiv:1908.01493 [hep-th] .

[300] H. Goldstein, C. Poole, and J. Safko, *Classical Mechanics*, 3rd ed. (Addison-Wesley, Boston, 2000).

[301] P. Amaro-Seoane *et al.* (LISA), Laser Interferometer Space Antenna, (2017), arXiv:1702.00786 [astro-ph.IM] .

[302] Y. Mino, M. Sasaki, and T. Tanaka, Gravitational radiation reaction to a particle motion, Phys. Rev. **D55**, 3457 (1997), arXiv:gr-qc/9606018 [gr-qc] .

[303] T. C. Quinn and R. M. Wald, An Axiomatic approach to electromagnetic and gravitational radiation reaction of particles in curved space-time, Phys. Rev. **D56**, 3381 (1997), arXiv:gr-qc/9610053 [gr-qc] .

[304] S. L. Detweiler and B. F. Whiting, Selfforce via a Green's function decomposition, Phys. Rev. D **67**, 024025 (2003), arXiv:gr-qc/0202086 .

[305] L. Barack and A. Ori, Mode sum regularization approach for the selfforce in black hole space-time, Phys. Rev. D **61**, 061502 (2000), arXiv:gr-qc/9912010 .

[306] L. Barack, Gravitational selfforce by mode sum regularization, Phys. Rev. D **64**, 084021 (2001), arXiv:gr-qc/0105040 .

[307] L. Barack and D. A. Golbourn, Scalar-field perturbations from a particle orbiting a black hole using numerical evolution in 2+1 dimensions, Phys. Rev. D **76**, 044020 (2007), arXiv:0705.3620 [gr-qc] .

[308] L. Barack, D. A. Golbourn, and N. Sago, m-Mode Regularization Scheme for the Self Force in Kerr Spacetime, Phys. Rev. D **76**, 124036 (2007), arXiv:0709.4588 [gr-qc] .

[309] L. Barack, Y. Mino, H. Nakano, A. Ori, and M. Sasaki, Calculating the gravitational selfforce in Schwarzschild space-time, Phys. Rev. Lett. **88**, 091101 (2002), arXiv:gr-qc/0111001 .

[310] L. Barack and A. Ori, Regularization parameters for the selfforce in Schwarzschild space-time. 2. Gravitational and electromagnetic cases, Phys. Rev. D **67**, 024029 (2003), arXiv:gr-qc/0209072 .

[311] L. Barack and N. Sago, Gravitational self force on a particle in circular orbit around a Schwarzschild black hole, Phys. Rev. **D75**, 064021 (2007), arXiv:gr-qc/0701069 [gr-qc] .

[312] A. G. Shah, T. S. Keidl, J. L. Friedman, D.-H. Kim, and L. R. Price, Conservative, gravitational self-force for a particle in circular orbit around a Schwarzschild black hole in a Radiation Gauge, Phys. Rev. D **83**, 064018 (2011), arXiv:1009.4876 [gr-qc] .

[313] L. Barack and N. Sago, Gravitational self-force on a particle in eccentric orbit around a Schwarzschild black hole, Phys. Rev. **D81**, 084021 (2010), arXiv:1002.2386 [gr-qc] .

[314] L. Barack and N. Sago, Beyond the geodesic approximation: conservative effects of the gravitational self-force in eccentric orbits around a Schwarzschild black hole, Phys. Rev. D **83**, 084023 (2011), arXiv:1101.3331 [gr-qc] .

[315] L. Barack and A. Ori, Gravitational selfforce on a particle orbiting a Kerr black hole, Phys. Rev. Lett. **90**, 111101 (2003), arXiv:gr-qc/0212103 .

[316] A. G. Shah, J. L. Friedman, and T. S. Keidl, EMRI corrections to the angular velocity and redshift factor of a mass in circular orbit about a Kerr black hole, Phys. Rev. D **86**, 084059 (2012), arXiv:1207.5595 [gr-qc] .

[317] M. van de Meent, Gravitational self-force on eccentric equatorial orbits around a Kerr black hole, Phys. Rev. **D94**, 044034 (2016), arXiv:1606.06297 [gr-qc] .

[318] M. van de Meent, Gravitational self-force on generic bound geodesics in Kerr spacetime, Phys. Rev. **D97**, 104033 (2018), arXiv:1711.09607 [gr-qc] .

[319] E. Rosenthal, Second-order gravitational self-force, Phys. Rev. D **74**, 084018 (2006), arXiv:gr-qc/0609069 .

[320] A. Pound, Second-order gravitational self-force, Phys. Rev. Lett. **109**, 051101 (2012), arXiv:1201.5089 [gr-qc] .

[321] A. Pound, Nonlinear gravitational self-force. I. Field outside a small body, Phys. Rev. D **86**, 084019 (2012), arXiv:1206.6538 [gr-qc] .

[322] S. E. Gralla, Second Order Gravitational Self Force, Phys. Rev. D **85**, 124011 (2012), arXiv:1203.3189 [gr-qc] .

[323] A. Pound, Conservative effect of the second-order gravitational self-force on quasicircular orbits in Schwarzschild spacetime, Phys. Rev. D **90**, 084039 (2014), arXiv:1404.1543 [gr-qc] .

[324] J. Miller, B. Wardell, and A. Pound, Second-order perturbation theory: the problem of infinite mode coupling, Phys. Rev. D **94**, 104018 (2016), arXiv:1608.06783 [gr-qc] .

[325] A. Pound, Nonlinear gravitational self-force: second-order equation of motion, Phys. Rev. D **95**, 104056 (2017), arXiv:1703.02836 [gr-qc] .

[326] A. Pound, B. Wardell, N. Warburton, and J. Miller, Second-order self-force calculation of the gravitational binding energy in compact binaries, Phys. Rev. Lett. **124**, 021101 (2020), arXiv:1908.07419 [gr-qc] .

[327] N. Warburton, A. Pound, B. Wardell, J. Miller, and L. Durkan, Gravitational-Wave Energy Flux for Compact Binaries through Second Order in the Mass Ratio, Phys. Rev. Lett. **127**, 151102 (2021), arXiv:2107.01298 [gr-qc] .

[328] B. Wardell, A. Pound, N. Warburton, J. Miller, L. Durkan, and A. Le Tiec, Gravitational waveforms for compact binaries from second-order self-force theory, (2021), arXiv:2112.12265 [gr-qc] .

[329] E. Poisson, The Gravitational self-force, in *17th International Conference on General Relativity and Gravitation* (2004) pp. 119–141, arXiv:gr-qc/0410127 .

[330] L. Barack, Gravitational self force in extreme mass-ratio inspirals, Class. Quant. Grav. **26**, 213001 (2009), arXiv:0908.1664 [gr-qc] .

[331] A. Pound, Motion of small objects in curved spacetimes: An introduction to gravitational self-force, Fund. Theor. Phys. **179**, 399 (2015), arXiv:1506.06245 [gr-qc] .

[332] L. Barack and A. Pound, Self-force and radiation reaction in general relativity, Rept. Prog. Phys. **82**, 016904 (2019), arXiv:1805.10385 [gr-qc] .

[333] A. Pound and B. Wardell, Black hole perturbation theory and gravitational self-force, (2021), arXiv:2101.04592 [gr-qc] .

[334] S. Mano, H. Suzuki, and E. Takasugi, Analytic solutions of the Regge-Wheeler equation and the postMinkowskian expansion, Prog. Theor. Phys. **96**, 549 (1996), arXiv:gr-qc/9605057 .

[335] S. Mano, H. Suzuki, and E. Takasugi, Analytic solutions of the Teukolsky equation and their low frequency expansions, Prog. Theor. Phys. **95**, 1079 (1996), arXiv:gr-qc/9603020 .

[336] S. L. Detweiler, A Consequence of the gravitational self-force for circular orbits of the Schwarzschild geometry, Phys. Rev. **D77**, 124026 (2008), arXiv:0804.3529 [gr-qc] .

[337] D. Bini and T. Damour, High-order post-Newtonian contributions to the two-body gravitational interaction potential from analytical gravitational self-force calculations, Phys. Rev. D **89**, 064063 (2014), arXiv:1312.2503 [gr-qc] .

[338] C. Kavanagh, A. C. Ottewill, and B. Wardell, Analytical high-order post-Newtonian expansions for extreme mass ratio binaries, Phys. Rev. **D92**, 084025 (2015), arXiv:1503.02334 [gr-qc] .

[339] S. Hopper, C. Kavanagh, and A. C. Ottewill, Analytic self-force calculations in the post-Newtonian regime: eccentric orbits on a Schwarzschild background, Phys. Rev. **D93**, 044010 (2016), arXiv:1512.01556 [gr-qc] .

[340] D. Bini, T. Damour, and A. Geralico, Confirming and improving post-Newtonian and effective-one-body results from self-force computations along eccentric orbits around a Schwarzschild black hole, Phys. Rev. D **93**, 064023 (2016), arXiv:1511.04533 [gr-qc] .

[341] C. Kavanagh, A. C. Ottewill, and B. Wardell, Analytical high-order post-Newtonian expansions for spinning extreme mass ratio binaries, Phys. Rev. **D93**, 124038 (2016), arXiv:1601.03394 [gr-qc] .

[342] D. Bini, T. Damour, A. Geralico, and C. Kavanagh, Detweiler's redshift invariant for spinning particles along circular orbits on a Schwarzschild background, Phys. Rev. D **97**, 104022 (2018), arXiv:1801.09616 [gr-qc] .

[343] D. Bini and A. Geralico, New gravitational self-force analytical results for eccentric equatorial orbits around a Kerr black hole: redshift invariant, Phys. Rev. **D100**, 104002 (2019), arXiv:1907.11080 [gr-qc] .

[344] D. Bini, A. Geralico, and J. Steinhoff, Detweiler's redshift invariant for extended bodies orbiting a Schwarzschild black hole, Phys. Rev. D **102**, 024091 (2020), arXiv:2003.12887 [gr-qc] .

[345] C. Munna and C. R. Evans, High-order post-Newtonian expansion of the redshift invariant for eccentric-orbit non-spinning extreme-mass-ratio inspirals, (2022), arXiv:2203.13832 [gr-qc] .

[346] S. R. Dolan, N. Warburton, A. I. Harte, A. Le Tiec, B. Wardell, and L. Barack, Gravitational self-torque and spin precession in compact binaries, Phys. Rev. **D89**, 064011 (2014), arXiv:1312.0775 [gr-qc] .

[347] D. Bini and T. Damour, Two-body gravitational spin-orbit interaction at linear order in the mass ratio, Phys. Rev. **D90**, 024039 (2014), arXiv:1404.2747 [gr-qc] .

[348] S. Akcay, D. Dempsey, and S. R. Dolan, Spin–orbit precession for eccentric black hole binaries at first order in the mass ratio, Class. Quant. Grav. **34**, 084001 (2017), arXiv:1608.04811 [gr-qc] .

[349] C. Kavanagh, D. Bini, T. Damour, S. Hopper, A. C. Ottewill, and B. Wardell, Spin-orbit precession along eccentric orbits for extreme mass ratio black hole binaries and its effective-one-body transcription, Phys. Rev. **D96**, 064012 (2017), arXiv:1706.00459 [gr-qc] .

[350] D. Bini, T. Damour, A. Geralico, C. Kavanagh, and M. van de Meent, Gravitational self-force corrections to gyroscope precession along circular orbits in the Kerr spacetime, Phys. Rev. **D98**, 104062 (2018), arXiv:1809.02516 [gr-qc] .

[351] D. Bini and A. Geralico, New gravitational self-force analytical results for eccentric equatorial orbits around a Kerr black hole: gyroscope precession, Phys. Rev. **D100**, 104003 (2019), arXiv:1907.11082 [gr-qc] .

[352] C. Munna and C. R. Evans, Post-Newtonian expansion of the spin-precession invariant for eccentric-orbit non-spinning extreme-mass-ratio inspirals to 9PN and e^{16}, (2022), arXiv:2206.04085 [gr-qc] .

[353] S. R. Dolan, P. Nolan, A. C. Ottewill, N. Warburton, and B. Wardell, Tidal invariants for compact binaries on quasicircular orbits, Phys. Rev. **D91**, 023009 (2015), arXiv:1406.4890 [gr-qc] .

[354] D. Bini and T. Damour, Gravitational self-force corrections to two-body tidal interactions and the effective one-body formalism, Phys. Rev. **D90**, 124037 (2014), arXiv:1409.6933 [gr-qc] .

[355] P. Nolan, C. Kavanagh, S. R. Dolan, A. C. Ottewill, N. Warburton, and B. Wardell, Octupolar invariants for compact binaries on quasicircular orbits, Phys. Rev. D **92**, 123008 (2015), arXiv:1505.04447 [gr-qc] .

[356] D. Bini and A. Geralico, Gravitational self-force corrections to tidal invariants for spinning particles on circular orbits in a Schwarzschild spacetime, Phys. Rev. D **98**, 084021 (2018), arXiv:1806.03495 [gr-qc] .

[357] D. Bini and A. Geralico, Gravitational self-force corrections to tidal invariants for particles on circular orbits in a Kerr spacetime, Phys. Rev. D **98**, 064040 (2018), arXiv:1806.08765 [gr-qc] .

[358] D. Bini and A. Geralico, Gravitational self-force corrections to tidal invariants for particles on eccentric orbits in a Schwarzschild spacetime, Phys. Rev. D **98**, 064026 (2018), arXiv:1806.06635 [gr-qc] .

[359] T. A. Apostolatos, C. Cutler, G. J. Sussman, and K. S. Thorne, Spin induced orbital precession and its modulation of the gravitational wave forms from merging binaries, Phys. Rev. **D49**, 6274 (1994).

[360] J. Steinhoff, Canonical formulation of spin in general relativity, Ann. Phys. (Berlin) **523**, 296 (2011), arXiv:1106.4203 [gr-qc] .

[361] W. G. Dixon, Extended bodies in general relativity: their description and motion, in *Isolated Gravitating Systems in General Relativity*, edited by J. Ehlers (North Holland, Amsterdam, 1979) pp. 156–219.

[362] J. Steinhoff, Spin and quadrupole contributions to the motion of astrophysical binaries, *Proceedings, 524th WE-Heraeus-Seminar: Equations of Motion in Relativistic Gravity (EOM 2013)*, Fund. Theor. Phys. **179**, 615 (2015), arXiv:1412.3251 [gr-qc] .

[363] A. D. Fokker, *Relativiteitstheorie* (P. Noordhoff, 1929).

[364] M. H. L. Pryce, The mass-centre in the restricted theory of relativity and its connexion with the quantum theory of elementary particles, Proceedings of the Royal Society of London. Series A. Mathematical and Physical Sciences **195**, 62 (1948).

[365] T. D. Newton and E. P. Wigner, Localized states for elementary systems, Reviews of Modern Physics **21**, 400 (1949).

[366] J. Vines, D. Kunst, J. Steinhoff, and T. Hinderer, Canonical Hamiltonian for an extended test body in curved spacetime: To quadratic order in spin, Phys. Rev. **D93**, 103008 (2016), arXiv:1601.07529 [gr-qc] .

[367] M. Mathisson, Neue mechanik materieller systemes, Acta Phys. Polon. **6**, 163 (1937).

[368] A. Papapetrou, Spinning test particles in general relativity. 1., Proc. Roy. Soc. Lond. A **A209**, 248 (1951).

[369] W. Dixon, Dynamics of extended bodies in general relativity. I. Momentum and angular momentum, Proc. Roy. Soc. Lond. A **314**, 499 (1970).

[370] T. Damour, Coalescence of two spinning black holes: an effective one-body approach, Phys. Rev. D **64**, 124013 (2001), arXiv:gr-qc/0103018 .

[371] W. G. Laarakkers and E. Poisson, Quadrupole moments of rotating neutron stars, Astrophys. J. **512**, 282 (1999), arXiv:gr-qc/9709033 .

[372] G. Pappas and T. A. Apostolatos, Revising the multipole moments of numerical spacetimes, and its consequences, Phys. Rev. Lett. **108**, 231104 (2012), arXiv:1201.6067 [gr-qc] .

[373] B. M. Barker, G. G. Byrd, and R. Oconnell, Spin nutation in binary systems due to general relativistic and quadrupole effects, The Astrophysical Journal **253**, 309 (1982).

[374] A. Buonanno, Y. Chen, and T. Damour, Transition from inspiral to plunge in precessing binaries of spinning black holes, Phys. Rev. D **74**, 104005 (2006), arXiv:gr-qc/0508067 .

[375] D. Gerosa, A. Lima, E. Berti, U. Sperhake, M. Kesden, and R. O'Shaughnessy, Wide nutation: binary black-hole spins repeatedly oscillating from full alignment to full anti-alignment, Class. Quant. Grav. **36**, 105003 (2019), arXiv:1811.05979 [gr-qc] .

[376] X. Zhao, M. Kesden, and D. Gerosa, Nutational resonances, transitional precession, and precession-averaged evolution in binary black-hole systems, Phys. Rev. D **96**, 024007 (2017), arXiv:1705.02369 [gr-qc] .

[377] E. Racine, Analysis of spin precession in binary black hole systems including quadrupole-monopole interaction, Phys. Rev. D **78**, 044021 (2008), arXiv:0803.1820 [gr-qc] .

[378] M. Kesden, D. Gerosa, R. O'Shaughnessy, E. Berti, and U. Sperhake, Effective potentials and morphological transitions for binary black-hole spin precession, Phys. Rev. Lett. **114**, 081103 (2015), arXiv:1411.0674 [gr-qc] .

[379] D. Gangardt, N. Steinle, M. Kesden, D. Gerosa, and E. Stoikos, A taxonomy of black-hole binary spin precession and nutation, Phys. Rev. D **103**, 124026 (2021), arXiv:2103.03894 [gr-qc] .

[380] A. Buonanno and T. Damour, Effective one-body approach to general relativistic two-body dynamics, Phys. Rev. **D59**, 084006 (1999), arXiv:gr-qc/9811091 [gr-qc] .

[381] A. Buonanno and T. Damour, Transition from inspiral to plunge in binary black hole coalescences, Phys. Rev. **D62**, 064015 (2000), arXiv:gr-qc/0001013 [gr-qc] .

[382] E. Barausse and A. Buonanno, An Improved effective-one-body Hamiltonian for spinning black-hole binaries, Phys. Rev. **D81**, 084024 (2010), arXiv:0912.3517 [gr-qc] .

[383] E. Barausse and A. Buonanno, Extending the effective-one-body Hamiltonian of black-hole binaries to include next-to-next-to-leading spin-orbit couplings, Phys. Rev. **D84**, 104027 (2011), arXiv:1107.2904 [gr-qc] .

[384] T. Damour, P. Jaranowski, and G. Schäfer, On the determination of the last stable orbit for circular general relativistic binaries at the third post-Newtonian approximation, Phys. Rev. **D62**, 084011 (2000), arXiv:gr-qc/0005034 [gr-qc] .

[385] A. Buonanno, Y. Pan, J. G. Baker, J. Centrella, B. J. Kelly, S. T. McWilliams, and J. R. van Meter, Toward faithful templates for non-spinning binary black holes using the effective-one-body approach, Phys. Rev. **D76**, 104049 (2007), arXiv:0706.3732 [gr-qc] .

[386] T. Damour, B. R. Iyer, and A. Nagar, Improved resummation of post-Newtonian multipolar waveforms from circularized compact binaries, Phys. Rev. **D79**, 064004 (2009), arXiv:0811.2069 [gr-qc] .

[387] Y. Pan, A. Buonanno, M. Boyle, L. T. Buchman, L. E. Kidder, H. P. Pfeiffer, and M. A. Scheel, Inspiral-merger-ringdown multipolar waveforms of nonspinning black-hole binaries using the effective-one-body formalism, Phys. Rev. **D84**, 124052 (2011), arXiv:1106.1021 [gr-qc] .

[388] A. Nagar, G. Pratten, G. Riemenschneider, and R. Gamba, Multipolar effective one body model for nonspinning black hole binaries, Phys. Rev. D **101**, 024041 (2020), arXiv:1904.09550 [gr-qc] .

[389] T. Damour, P. Jaranowski, and G. Schäfer, Effective one body approach to the dynamics of two spinning black holes with next-to-leading order spin-orbit coupling, Phys. Rev. **D78**, 024009 (2008), arXiv:0803.0915 [gr-qc] .

[390] A. Nagar, Effective one body Hamiltonian of two spinning black-holes with next-to-next-to-leading order spin-orbit coupling, Phys. Rev. **D84**, 084028 (2011), [Erratum: Phys. Rev.D88,no.8,089901(2013)], arXiv:1106.4349 [gr-qc] .

[391] T. Damour and A. Nagar, New effective-one-body description of coalescing nonprecessing spinning black-hole binaries, Phys. Rev. **D90**, 044018 (2014), arXiv:1406.6913 [gr-qc] .

[392] S. Balmelli and T. Damour, New effective-one-body Hamiltonian with next-to-leading order spin-spin coupling, Phys. Rev. D **92**, 124022 (2015), arXiv:1509.08135 [gr-qc] .

[393] Y. Pan, A. Buonanno, A. Taracchini, L. E. Kidder, A. H. Mroué, H. P. Pfeiffer, M. A. Scheel, and B. Szilágyi, Inspiral-merger-ringdown waveforms of spinning, precessing black-hole binaries in the effective-one-body formalism, Phys. Rev. **D89**, 084006 (2014), arXiv:1307.6232 [gr-qc] .

[394] A. Taracchini, Y. Pan, A. Buonanno, E. Barausse, M. Boyle, T. Chu, G. Lovelace, H. P. Pfeiffer, and M. A. Scheel, Prototype effective-one-body model for nonprecessing spinning inspiral-merger-ringdown waveforms, Phys. Rev. **D86**, 024011 (2012), arXiv:1202.0790 [gr-qc] .

[395] A. Taracchini *et al.*, Effective-one-body model for black-hole binaries with generic mass ratios and spins, Phys. Rev. **D89**, 061502 (2014), arXiv:1311.2544 [gr-qc] .

[396] S. Babak, A. Taracchini, and A. Buonanno, Validating the effective-one-body model of spinning, precessing binary black holes against numerical relativity, Phys. Rev. D **95**, 024010 (2017), arXiv:1607.05661 [gr-qc] .

[397] A. Bohé *et al.*, Improved effective-one-body model of spinning, nonprecessing binary black holes for the era of gravitational-wave astrophysics with advanced detectors, Phys. Rev. **D95**, 044028 (2017), arXiv:1611.03703 [gr-qc] .

[398] R. Cotesta, A. Buonanno, A. Bohé, A. Taracchini, I. Hinder, and S. Ossokine, Enriching the Symphony of Gravitational Waves from Binary Black Holes by Tuning Higher Harmonics, Phys. Rev. **D98**, 084028 (2018), arXiv:1803.10701 [gr-qc] .

[399] S. Ossokine *et al.*, Multipolar Effective-One-Body Waveforms for Precessing Binary Black Holes: Construction and Validation, Phys. Rev. D **102**, 044055 (2020), arXiv:2004.09442 [gr-qc] .

[400] A. Nagar, F. Messina, P. Rettegno, D. Bini, T. Damour, A. Geralico, S. Akcay, and S. Bernuzzi, Nonlinear-in-spin effects in effective-one-body waveform models of spin-aligned, inspiralling, neutron star binaries, Phys. Rev. **D99**, 044007 (2019), arXiv:1812.07923 [gr-qc] .

[401] A. Nagar *et al.*, Time-domain effective-one-body gravitational waveforms for coalescing compact binaries with nonprecessing spins, tides and self-spin effects, Phys. Rev. **D98**, 104052 (2018), arXiv:1806.01772 [gr-qc] .

[402] D. Bini and T. Damour, Gravitational radiation reaction along general orbits in the effective one-body formalism, Phys. Rev. D **86**, 124012 (2012), arXiv:1210.2834 [gr-qc] .

[403] T. Hinderer and S. Babak, Foundations of an effective-one-body model for coalescing binaries on eccentric orbits, Phys. Rev. D **96**, 104048 (2017), arXiv:1707.08426 [gr-qc] .

[404] A. Nagar, A. Bonino, and P. Rettegno, Effective one-body multipolar waveform model for spin-aligned, quasicircular, eccentric, hyperbolic black hole binaries, Phys. Rev. D **103**, 104021 (2021), arXiv:2101.08624 [gr-qc] .

[405] A. Antonelli, A. Buonanno, J. Steinhoff, M. van de Meent, and J. Vines, Energetics of two-body Hamiltonians in post-Minkowskian gravity, Phys. Rev. **D99**, 104004 (2019), arXiv:1901.07102 [gr-qc] .

[406] P. H. Damgaard and P. Vanhove, Remodeling the effective one-body formalism in post-Minkowskian gravity, Phys. Rev. D **104**, 104029 (2021), arXiv:2108.11248 [hep-th] .

[407] T. Damour, Gravitational Self Force in a Schwarzschild Background and the Effective One Body Formalism, Phys. Rev. D **81**, 024017 (2010), arXiv:0910.5533 [gr-qc] .

[408] E. Barausse, A. Buonanno, and A. Le Tiec, The complete non-spinning effective-one-body metric at linear order in the mass ratio, Phys. Rev. **D85**, 064010 (2012), arXiv:1111.5610 [gr-qc] .

[409] S. Akcay, L. Barack, T. Damour, and N. Sago, Gravitational self-force and the effective-one-body formalism between the innermost stable circular orbit and the light ring, Phys. Rev. **D86**, 104041 (2012), arXiv:1209.0964 [gr-qc] .

[410] A. Antonelli, M. van de Meent, A. Buonanno, J. Steinhoff, and J. Vines, Quasicircular inspirals and plunges from nonspinning effective-one-body Hamiltonians with gravitational self-force information, Phys. Rev. **D101**, 024024 (2020), arXiv:1907.11597 [gr-qc] .

[411] T. Damour and A. Nagar, Faithful effective-one-body waveforms of small-mass-ratio coalescing black-hole binaries, Phys. Rev. **D76**, 064028 (2007), arXiv:0705.2519 [gr-qc] .

[412] T. Damour and A. Nagar, Comparing Effective-One-Body gravitational waveforms to accurate numerical data, Phys. Rev. **D77**, 024043 (2008), arXiv:0711.2628 [gr-qc] .

[413] Y. Pan, A. Buonanno, R. Fujita, E. Racine, and H. Tagoshi, Post-Newtonian factorized multipolar waveforms for spinning, non-precessing black-hole binaries, Phys. Rev. **D83**, 064003 (2011), [Erratum: Phys. Rev.D87,no.10,109901(2013)], arXiv:1006.0431 [gr-qc] .

[414] E. Poisson, Gravitational radiation from a particle in circular orbit around a black hole. 1: Analytical results for the nonrotating case, Phys. Rev. D **47**, 1497 (1993).

[415] H. Asada and T. Futamase, Propagation of gravitational waves from slow motion sources in Coulomb type potential, Phys. Rev. D **56**, R6062 (1997), arXiv:gr-qc/9711009 .

[416] E. Barausse, V. Morozova, and L. Rezzolla, On the mass radiated by coalescing black-hole binaries, Astrophys. J. **758**, 63 (2012), [Erratum: Astrophys.J. 786, 76 (2014)], arXiv:1206.3803 [gr-qc] .

[417] D. A. Hemberger, G. Lovelace, T. J. Loredo, L. E. Kidder, M. A. Scheel, B. Szilágyi, N. W. Taylor, and S. A. Teukolsky, Final spin and radiated energy in numerical simulations of binary black holes with equal masses and equal, aligned or anti-aligned spins, Phys. Rev. D **88**, 064014 (2013), arXiv:1305.5991 [gr-qc] .

[418] F. Hofmann, E. Barausse, and L. Rezzolla, The final spin from binary black holes in quasi-circular orbits, Astrophys. J. **825**, L19 (2016), arXiv:1605.01938 [gr-qc] .

[419] W. Del Pozzo and A. Nagar, Analytic family of post-merger template waveforms, Phys. Rev. D **95**, 124034 (2017), arXiv:1606.03952 [gr-qc] .

[420] K. S. Stelle, Renormalization of Higher Derivative Quantum Gravity, Phys. Rev. D **16**, 953 (1977).

[421] S. W. Hawking and R. Penrose, The Singularities of gravitational collapse and cosmology, Proc. Roy. Soc. Lond. A **314**, 529 (1970).

[422] D. Lovelock, The Einstein tensor and its generalizations, J. Math. Phys. **12**, 498 (1971).

[423] D. Lovelock, The four-dimensionality of space and the einstein tensor, J. Math. Phys. **13**, 874 (1972).

[424] E. Berti *et al.*, Testing General Relativity with Present and Future Astrophysical Observations, Class. Quant. Grav. **32**, 243001 (2015), arXiv:1501.07274 [gr-qc] .

[425] L. Bernard, L. Blanchet, A. Bohé, G. Faye, and S. Marsat, Fokker action of nonspinning compact binaries at the fourth post-Newtonian approximation, Phys. Rev. D **93**, 084037 (2016), arXiv:1512.02876 [gr-qc] .

[426] L. Blanchet and T. Damour, Post-newtonian generation of gravitational waves, in *Annales de l'IHP Physique théorique*, Vol. 50 (1989) pp. 377–408.

[427] T. Damour and N. Deruelle, General relativistic celestial mechanics of binary systems. i. the post-newtonian motion, in *Annales de l'IHP Physique théorique*, Vol. 43 (1985) pp. 107–132.

[428] D. Bini, A. Geralico, and J. Vines, Hyperbolic scattering of spinning particles by a Kerr black hole, Phys. Rev. **D96**, 084044 (2017), arXiv:1707.09814 [gr-qc] .

[429] A. Le Tiec, L. Blanchet, and B. F. Whiting, The First Law of Binary Black Hole Mechanics in General Relativity and Post-Newtonian Theory, Phys. Rev. **D85**, 064039 (2012), arXiv:1111.5378 [gr-qc] .

[430] L. Blanchet, A. Buonanno, and A. Le Tiec, First law of mechanics for black hole binaries with spins, Phys. Rev. **D87**, 024030 (2013), arXiv:1211.1060 [gr-qc] .

[431] A. Le Tiec, First Law of Mechanics for Compact Binaries on Eccentric Orbits, Phys. Rev. **D92**, 084021 (2015), arXiv:1506.05648 [gr-qc] .

[432] L. Blanchet and A. Le Tiec, First Law of Compact Binary Mechanics with Gravitational-Wave Tails, Class. Quant. Grav. **34**, 164001 (2017), arXiv:1702.06839 [gr-qc] .

[433] D. Bini, T. Damour, and A. Geralico, High post-Newtonian order gravitational self-force analytical results for eccentric equatorial orbits around a Kerr black hole, Phys. Rev. **D93**, 124058 (2016), arXiv:1602.08282 [gr-qc] .

[434] T. Damour, A. Nagar, D. Pollney, and C. Reisswig, Energy versus Angular Momentum in Black Hole Binaries, Phys. Rev. Lett. **108**, 131101 (2012), arXiv:1110.2938 [gr-qc] .

[435] A. Nagar, T. Damour, C. Reisswig, and D. Pollney, Energetics and phasing of non-precessing spinning coalescing black hole binaries, Phys. Rev. **D93**, 044046 (2016), arXiv:1506.08457 [gr-qc] .

[436] M. Ruiz, R. Takahashi, M. Alcubierre, and D. Nunez, Multipole expansions for energy and momenta carried by gravitational waves, Gen. Rel. Grav. **40**, 2467 (2008), arXiv:0707.4654 [gr-qc] .

[437] T. Dietrich, S. Bernuzzi, M. Ujevic, and W. Tichy, Gravitational waves and mass ejecta from binary neutron star mergers: Effect of the stars' rotation, Phys. Rev. **D95**, 044045 (2017), arXiv:1611.07367 [gr-qc] .

[438] S. Ossokine, T. Dietrich, E. Foley, R. Katebi, and G. Lovelace, Assessing the Energetics of Spinning Binary Black Hole Systems, Phys. Rev. **D98**, 104057 (2018), arXiv:1712.06533 [gr-qc] .

[439] B. Abbott *et al.* (LIGO Scientific, Virgo), Search for Eccentric Binary Black Hole Mergers with Advanced LIGO and Advanced Virgo during their First and Second Observing Runs, Astrophys. J. **883**, 149 (2019), arXiv:1907.09384 [astro-ph.HE] .

[440] I. M. Romero-Shaw, P. D. Lasky, and E. Thrane, Searching for Eccentricity: Signatures of Dynamical Formation in the First Gravitational-Wave Transient Catalogue of LIGO and Virgo, Mon. Not. Roy. Astron. Soc. **490**, 5210 (2019), arXiv:1909.05466 [astro-ph.HE] .

[441] A. H. Nitz, A. Lenon, and D. A. Brown, Search for Eccentric Binary Neutron Star Mergers in the first and second observing runs of Advanced LIGO, Astrophys. J. **890**, 1 (2019), arXiv:1912.05464 [astro-ph.HE] .

[442] I. M. Romero-Shaw, P. D. Lasky, E. Thrane, and J. C. Bustillo, GW190521: orbital eccentricity and signatures of dynamical formation in a binary black hole merger signal, Astrophys. J. Lett. **903**, L5 (2020), arXiv:2009.04771 [astro-ph.HE] .

[443] P. C. Peters, Gravitational Radiation and the Motion of Two Point Masses, Phys. Rev. **136**, B1224 (1964).

[444] I. Hinder, B. Vaishnav, F. Herrmann, D. Shoemaker, and P. Laguna, Universality and final spin in eccentric binary black hole inspirals, Phys. Rev. D **77**, 081502 (2008), arXiv:0710.5167 [gr-qc] .

[445] K. Gultekin, M. Coleman Miller, and D. P. Hamilton, Three-body dynamics with gravitational wave emission, Astrophys. J. **640**, 156 (2006), arXiv:astro-ph/0509885 .

[446] J. Samsing, Eccentric Black Hole Mergers Forming in Globular Clusters, Phys. Rev. D **97**, 103014 (2018), arXiv:1711.07452 [astro-ph.HE] .

[447] C. L. Rodriguez, P. Amaro-Seoane, S. Chatterjee, and F. A. Rasio, Post-Newtonian Dynamics in Dense Star Clusters: Highly-Eccentric, Highly-Spinning, and Repeated Binary Black Hole Mergers, Phys. Rev. Lett. **120**, 151101 (2018), arXiv:1712.04937 [astro-ph.HE] .

[448] L. Gondán and B. Kocsis, High eccentricities and high masses characterize gravitational-wave captures in galactic nuclei as seen by Earth-based detectors, Mon. Not. Roy. Astron. Soc. **506**, 1665 (2021), arXiv:2011.02507 [astro-ph.HE] .

[449] J. Samsing and E. Ramirez-Ruiz, On the Assembly Rate of Highly Eccentric Binary Black Hole Mergers, Astrophys. J. Lett. **840**, L14 (2017), arXiv:1703.09703 [astro-ph.HE] .

[450] J. Samsing, M. MacLeod, and E. Ramirez-Ruiz, The Formation of Eccentric Compact Binary Inspirals and the Role of Gravitational Wave Emission in Binary-Single Stellar Encounters, Astrophys. J. **784**, 71 (2014), arXiv:1308.2964 [astro-ph.HE] .

[451] M. Zevin, J. Samsing, C. Rodriguez, C.-J. Haster, and E. Ramirez-Ruiz, Eccentric Black Hole Mergers in Dense Star Clusters: The Role of Binary–Binary Encounters, Astrophys. J. **871**, 91 (2019), arXiv:1810.00901 [astro-ph.HE] .

[452] F. Antonini and H. B. Perets, Secular evolution of compact binaries near massive black holes: Gravitational wave sources and other exotica, Astrophys. J. **757**, 27 (2012), arXiv:1203.2938 [astro-ph.GA] .

[453] F. Antonini, S. Chatterjee, C. L. Rodriguez, M. Morscher, B. Pattabiraman, V. Kalogera, and F. A. Rasio, Black hole mergers and blue stragglers from hierarchical triples formed in globular clusters, Astrophys. J. **816**, 65 (2016), arXiv:1509.05080 [astro-ph.GA] .

[454] J. H. VanLandingham, M. C. Miller, D. P. Hamilton, and D. C. Richardson, The Role of the Kozai–lidov Mechanism in Black Hole Binary Mergers in Galactic Centers, Astrophys. J. **828**, 77 (2016), arXiv:1604.04948 [astro-ph.HE] .

[455] D. Britt, B. Johanson, L. Wood, M. C. Miller, and E. Michaely, Binary black hole mergers from hierarchical triples in open clusters, Mon. Not. Roy. Astron. Soc. **505**, 3844 (2021), arXiv:2103.14706 [astro-ph.HE] .

[456] L. Gondán, B. Kocsis, P. Raffai, and Z. Frei, Accuracy of Estimating Highly Eccentric Binary Black Hole Parameters with Gravitational-Wave Detections, Astrophys. J. **855**, 34 (2018), arXiv:1705.10781 [astro-ph.HE] .

[457] R. Abbott *et al.* (LIGO Scientific, Virgo), GW190521: A Binary Black Hole Merger with a Total Mass of $150M_{\odot}$, Phys. Rev. Lett. **125**, 101102 (2020), arXiv:2009.01075 [gr-qc] .

[458] `https://data.black-holes.org/waveforms`.

[459] B. Kocsis, M. E. Gaspar, and S. Marka, Detection rate estimates of gravity-waves emitted during parabolic encounters of stellar black holes in globular clusters, Astrophys. J. **648**, 411 (2006), arXiv:astro-ph/0603441 .

[460] N. Ivanova, C. Heinke, F. A. Rasio, K. Belczynski, and J. Fregeau, Formation and evolution of compact binaries in globular clusters: II. Binaries with neutron stars, Mon. Not. Roy. Astron. Soc. **386**, 553 (2008), arXiv:0706.4096 [astro-ph] .

[461] R. M. O'Leary, B. Kocsis, and A. Loeb, Gravitational waves from scattering of stellar-mass black holes in galactic nuclei, Mon. Not. Roy. Astron. Soc. **395**, 2127 (2009), arXiv:0807.2638 [astro-ph] .

[462] S. Capozziello, M. De Laurentis, F. De Paolis, G. Ingrosso, and A. Nucita, Gravitational waves from hyperbolic encounters, Mod. Phys. Lett. A **23**, 99 (2008), arXiv:0801.0122 [gr-qc] .

[463] D. Tsang, Shattering Flares During Close Encounters of Neutron Stars, Astrophys. J. **777**, 103 (2013), arXiv:1307.3554 [astro-ph.HE] .

[464] K. Kremer, C. S. Ye, N. Z. Rui, N. C. Weatherford, S. Chatterjee, G. Fragione, C. L. Rodriguez, M. Spera, and F. A. Rasio, Modeling Dense Star Clusters in the Milky Way and Beyond with the CMC Cluster Catalog, Astrophys. J. Suppl. **247**, 48 (2020), arXiv:1911.00018 [astro-ph.HE] .

[465] S. Mukherjee, S. Mitra, and S. Chatterjee, Gravitational wave observatories may be able to detect hyperbolic encounters of black holes, Mon. Not. Roy. Astron. Soc. **508**, 5064 (2021), arXiv:2010.00916 [gr-qc] .

[466] T. Damour, F. Guercilena, I. Hinder, S. Hopper, A. Nagar, and L. Rezzolla, Strong-Field Scattering of Two Black Holes: Numerics Versus Analytics, Phys. Rev. D **89**, 081503 (2014), arXiv:1402.7307 [gr-qc] .

[467] G. W. Gibbons and K.-i. Maeda, Black Holes and Membranes in Higher Dimensional Theories with Dilaton Fields, Nucl. Phys. **B298**, 741 (1988).

[468] D. Garfinkle, G. T. Horowitz, and A. Strominger, Charged black holes in string theory, Phys. Rev. **D43**, 3140 (1991), [Erratum: Phys. Rev.D45,3888(1992)].

[469] G. W. Gibbons, Vacuum Polarization and the Spontaneous Loss of Charge by Black Holes, Commun. Math. Phys. **44**, 245 (1975).

[470] D. M. Eardley and W. H. Press, Astrophysical processes near black holes, Ann. Rev. Astron. Astrophys. **13**, 381 (1975).

[471] A. De Rujula, S. L. Glashow, and U. Sarid, Charged dark matter, Nucl. Phys. **B333**, 173 (1990).

[472] M. L. Perl and E. R. Lee, The search for elementary particles with fractional electric charge and the philosophy of speculative experiments, Am. J. Phys. **65**, 698 (1997).

[473] S. D. McDermott, H.-B. Yu, and K. M. Zurek, Turning off the Lights: How Dark is Dark Matter?, Phys. Rev. **D83**, 063509 (2011), arXiv:1011.2907 [hep-ph] .

[474] L. Ackerman, M. R. Buckley, S. M. Carroll, and M. Kamionkowski, Dark Matter and Dark Radiation, *Proceedings, 7th International Heidelberg Conference on Dark Matter in Astro and Particle Physics (DARK 2009): Christchurch, New Zealand, January 18-24, 2009*, Phys. Rev. **D79**, 023519 (2009), [,277(2008)], arXiv:0810.5126 [hep-ph] .

[475] J. L. Feng, H. Tu, and H.-B. Yu, Thermal Relics in Hidden Sectors, JCAP **0810**, 043, arXiv:0808.2318 [hep-ph] .

[476] J. L. Feng, M. Kaplinghat, H. Tu, and H.-B. Yu, Hidden Charged Dark Matter, JCAP **0907**, 004, arXiv:0905.3039 [hep-ph] .

[477] V. Cardoso, C. F. B. Macedo, P. Pani, and V. Ferrari, Black holes and gravitational waves in models of minicharged dark matter, JCAP **1605**, 054, arXiv:1604.07845 [hep-ph] .

[478] I. Banerjee, B. Mandal, and S. SenGupta, Implications of Einstein–Maxwell dilaton–axion gravity from the black hole continuum spectrum, Mon. Not. Roy. Astron. Soc. **500**, 481 (2020), arXiv:2007.13980 [gr-qc] .

[479] A. Tripathi, B. Zhou, A. B. Abdikamalov, D. Ayzenberg, and C. Bambi, Constraints on Einstein-Maxwell dilaton-axion gravity from X-ray reflection spectroscopy, JCAP **07**, 002, arXiv:2103.07593 [astro-ph.HE] .

[480] D. M. Eardley, Observable effects of a scalar gravitational field in a binary pulsar, The Astrophysical Journal **196**, L59 (1975).

[481] E. W. Hirschmann, L. Lehner, S. L. Liebling, and C. Palenzuela, Black Hole Dynamics in Einstein-Maxwell-Dilaton Theory, Phys. Rev. **D97**, 064032 (2018), arXiv:1706.09875 [gr-qc] .

[482] T. Damour and G. Esposito-Farese, Nonperturbative strong field effects in tensor - scalar theories of gravitation, Phys. Rev. Lett. **70**, 2220 (1993).

[483] C. Palenzuela, E. Barausse, M. Ponce, and L. Lehner, Dynamical scalarization of neutron stars in scalar-tensor gravity theories, Phys. Rev. **D89**, 044024 (2014), arXiv:1310.4481 [gr-qc] .

[484] M. Shibata, K. Taniguchi, H. Okawa, and A. Buonanno, Coalescence of binary neutron stars in a scalar-tensor theory of gravity, Phys. Rev. **D89**, 084005 (2014), arXiv:1310.0627 [gr-qc] .

[485] K. Taniguchi, M. Shibata, and A. Buonanno, Quasiequilibrium sequences of binary neutron stars undergoing dynamical scalarization, Phys. Rev. **D91**, 024033 (2015), arXiv:1410.0738 [gr-qc] .

[486] P. Chen, T. Suyama, and J. Yokoyama, Spontaneous scalarization: asymmetron as dark matter, Phys. Rev. **D92**, 124016 (2015), arXiv:1508.01384 [gr-qc] .

[487] F. M. Ramazanoğlu and F. Pretorius, Spontaneous Scalarization with Massive Fields, Phys. Rev. **D93**, 064005 (2016), arXiv:1601.07475 [gr-qc] .

[488] U. Sperhake, C. J. Moore, R. Rosca, M. Agathos, D. Gerosa, and C. D. Ott, Long-lived inverse chirp signals from core collapse in massive scalar-tensor gravity, Phys. Rev. Lett. **119**, 201103 (2017), arXiv:1708.03651 [gr-qc] .

[489] L. Sagunski, J. Zhang, M. C. Johnson, L. Lehner, M. Sakellariadou, S. L. Liebling, C. Palenzuela, and D. Neilsen, Neutron star mergers as a probe of modifications of general relativity with finite-range scalar forces, Phys. Rev. **D97**, 064016 (2018), arXiv:1709.06634 [gr-qc] .

[490] N. Andreou, N. Franchini, G. Ventagli, and T. P. Sotiriou, Spontaneous scalarization in generalised scalar-tensor theory, Phys. Rev. D **99**, 124022 (2019), [Erratum: Phys.Rev.D 101, 109903 (2020)], arXiv:1904.06365 [gr-qc] .

[491] F. M. Ramazanoğlu, Spontaneous growth of vector fields in gravity, Phys. Rev. **D96**, 064009 (2017), arXiv:1706.01056 [gr-qc] .

[492] H. O. Silva, A. Coates, F. M. Ramazanoğlu, and T. P. Sotiriou, Ghost of vector fields in compact stars, Phys. Rev. D **105**, 024046 (2022), arXiv:2110.04594 [gr-qc] .

[493] F. M. Ramazanoğlu, Spontaneous growth of spinor fields in gravity, Phys. Rev. **D98**, 044011 (2018), arXiv:1804.00594 [gr-qc] .

[494] F. M. Ramazanoğlu, Spontaneous growth of gauge fields in gravity through the Higgs mechanism, Phys. Rev. **D98**, 044013 (2018), arXiv:1804.03158 [gr-qc] .

[495] F. M. Ramazanoğlu, Spontaneous tensorization from curvature coupling and beyond, Phys. Rev. **D99**, 084015 (2019), arXiv:1901.10009 [gr-qc] .

[496] R. Xu, Y. Gao, and L. Shao, Neutron stars in massive scalar-Gauss-Bonnet gravity: Spherical structure and time-independent perturbations, Phys. Rev. D **105**, 024003 (2022), arXiv:2111.06561 [gr-qc] .

[497] D. D. Doneva and S. S. Yazadjiev, New Gauss-Bonnet Black Holes with Curvature-Induced Scalarization in Extended Scalar-Tensor Theories, Phys. Rev. Lett. **120**, 131103 (2018), arXiv:1711.01187 [gr-qc] .

[498] D. D. Doneva and S. S. Yazadjiev, Neutron star solutions with curvature induced scalarization in the extended Gauss-Bonnet scalar-tensor theories, JCAP **1804** (04), 011, arXiv:1712.03715 [gr-qc] .

[499] H. O. Silva, J. Sakstein, L. Gualtieri, T. P. Sotiriou, and E. Berti, Spontaneous scalarization of black holes and compact stars from a Gauss-Bonnet coupling, Phys. Rev. Lett. **120**, 131104 (2018), arXiv:1711.02080 [gr-qc] .

[500] G. Antoniou, A. Bakopoulos, and P. Kanti, Evasion of No-Hair Theorems and Novel Black-Hole Solutions in Gauss-Bonnet Theories, Phys. Rev. Lett. **120**, 131102 (2018), arXiv:1711.03390 [hep-th] .

[501] G. Antoniou, A. Bakopoulos, and P. Kanti, Black-Hole Solutions with Scalar Hair in Einstein-Scalar-Gauss-Bonnet Theories, Phys. Rev. **D97**, 084037 (2018), arXiv:1711.07431 [hep-th] .

[502] P. V. P. Cunha, C. A. R. Herdeiro, and E. Radu, Spontaneously Scalarized Kerr Black Holes in Extended Scalar-Tensor–Gauss-Bonnet Gravity, Phys. Rev. Lett. **123**, 011101 (2019), arXiv:1904.09997 [gr-qc] .

[503] L. G. Collodel, B. Kleihaus, J. Kunz, and E. Berti, Spinning and excited black holes in Einstein-scalar-Gauss–Bonnet theory, Class. Quant. Grav. **37**, 075018 (2020), arXiv:1912.05382 [gr-qc] .

[504] A. Dima, E. Barausse, N. Franchini, and T. P. Sotiriou, Spin-induced black hole spontaneous scalarization, Phys. Rev. Lett. **125**, 231101 (2020), arXiv:2006.03095 [gr-qc] .

[505] C. A. R. Herdeiro, E. Radu, H. O. Silva, T. P. Sotiriou, and N. Yunes, Spin-induced scalarized black holes, Phys. Rev. Lett. **126**, 011103 (2021), arXiv:2009.03904 [gr-qc] .

[506] E. Berti, L. G. Collodel, B. Kleihaus, and J. Kunz, Spin-induced black-hole scalarization in Einstein-scalar-Gauss-Bonnet theory, Phys. Rev. Lett. **126**, 011104 (2021), arXiv:2009.03905 [gr-qc] .

[507] D. D. Doneva, L. G. Collodel, C. J. Krüger, and S. S. Yazadjiev, Black hole scalarization induced by the spin: 2+1 time evolution, Phys. Rev. D **102**, 104027 (2020), arXiv:2008.07391 [gr-qc] .

[508] D. D. Doneva and S. S. Yazadjiev, Dynamics of the nonrotating and rotating black hole scalarization, Phys. Rev. D **103**, 064024 (2021), arXiv:2101.03514 [gr-qc] .

[509] E. Barausse, C. Palenzuela, M. Ponce, and L. Lehner, Neutron-star mergers in scalar-tensor theories of gravity, Phys. Rev. **D87**, 081506 (2013), arXiv:1212.5053 [gr-qc] .

[510] H. O. Silva, H. Witek, M. Elley, and N. Yunes, Dynamical Descalarization in Binary Black Hole Mergers, Phys. Rev. Lett. **127**, 031101 (2021), arXiv:2012.10436 [gr-qc] .

[511] M. Elley, H. O. Silva, H. Witek, and N. Yunes, Spin-induced dynamical scalarization, de-scalarization and stealthness in scalar-Gauss-Bonnet gravity during black hole coalescence, (2022), arXiv:2205.06240 [gr-qc] .

[512] L. Annulli, Close limit approximation for modified gravity: Scalar instabilities in binary black hole spacetimes, Phys. Rev. D **104**, 124028 (2021), arXiv:2105.08728 [gr-qc] .

[513] N. Sennett, L. Shao, and J. Steinhoff, Effective action model of dynamically scalarizing binary neutron stars, Phys. Rev. **D96**, 084019 (2017), arXiv:1708.08285 [gr-qc] .

[514] C. A. R. Herdeiro, E. Radu, N. Sanchis-Gual, and J. A. Font, Spontaneous Scalarization of Charged Black Holes, Phys. Rev. Lett. **121**, 101102 (2018), arXiv:1806.05190 [gr-qc] .

[515] F. M. Ramazanoğlu, Regularization of instabilities in gravity theories, Phys. Rev. **D97**, 024008 (2018), arXiv:1710.00863 [gr-qc] .

[516] R. F. P. Mendes and N. Ortiz, New class of quasinormal modes of neutron stars in scalar-tensor gravity, Phys. Rev. Lett. **120**, 201104 (2018), arXiv:1802.07847 [gr-qc] .

[517] J. Aasi *et al.* (LIGO Scientific), Advanced LIGO, Class. Quant. Grav. **32**, 074001 (2015), arXiv:1411.4547 [gr-qc] .

[518] F. Acernese *et al.* (VIRGO), Advanced Virgo: a second-generation interferometric gravitational wave detector, Class. Quant. Grav. **32**, 024001 (2015), arXiv:1408.3978 [gr-qc] .

[519] B. P. Abbott *et al.* (LIGO Scientific, Virgo), Tests of General Relativity with the Binary Black Hole Signals from the LIGO-Virgo Catalog GWTC-1, Phys. Rev. **D100**, 104036 (2019), arXiv:1903.04467 [gr-qc] .

[520] B. P. Abbott *et al.* (LIGO Scientific, Virgo, VIRGO), A Gravitational-wave Measurement of the Hubble Constant Following the Second Observing Run of Advanced LIGO and Virgo, Astrophys. J. **909**, 218 (2021), arXiv:1908.06060 [astro-ph.CO] .

[521] M. Pürrer and C.-J. Haster, Gravitational waveform accuracy requirements for future ground-based detectors, Phys. Rev. Res. **2**, 023151 (2020), arXiv:1912.10055 [gr-qc] .

[522] L. Bernard, L. Blanchet, A. Bohé, G. Faye, and S. Marsat, Energy and periastron advance of compact binaries on circular orbits at the fourth post-Newtonian order, Phys. Rev. **D95**, 044026 (2017), arXiv:1610.07934 [gr-qc] .

[523] J. Blümlein, A. Maier, and P. Marquard, Five-Loop Static Contribution to the Gravitational Interaction Potential of Two Point Masses, Phys. Lett. **B800**, 135100 (2020), arXiv:1902.11180 [gr-qc] .

[524] J. Blümlein, A. Maier, P. Marquard, and G. Schäfer, Testing binary dynamics in gravity at the sixth post-Newtonian level, Phys. Lett. B **807**, 135496 (2020), arXiv:2003.07145 [gr-qc] .

[525] C. Cheung and M. P. Solon, Classical gravitational scattering at $\mathcal{O}(G^3)$ from Feynman diagrams, JHEP **06**, 144, arXiv:2003.08351 [hep-th] .

[526] T. Aoyama, M. Hayakawa, T. Kinoshita, and M. Nio, Tenth-Order QED Contribution to the Electron g-2 and an Improved Value of the Fine Structure Constant, Phys. Rev. Lett. **109**, 111807 (2012), arXiv:1205.5368 [hep-ph] .

[527] B. C. Odom, D. Hanneke, B. D'Urso, and G. Gabrielse, New Measurement of the Electron Magnetic Moment Using a One-Electron Quantum Cyclotron, Phys. Rev. Lett. **97**, 030801 (2006), [Erratum: Phys. Rev. Lett.99,039902(2007)].

[528] B. Zackay, T. Venumadhav, L. Dai, J. Roulet, and M. Zaldarriaga, Highly spinning and aligned binary black hole merger in the Advanced LIGO first observing run, Phys. Rev. **D100**, 023007 (2019), arXiv:1902.10331 [astro-ph.HE] .

[529] Y. Huang, C.-J. Haster, S. Vitale, A. Zimmerman, J. Roulet, T. Venumadhav, B. Zackay, L. Dai, and M. Zaldarriaga, Source properties of the lowest signal-to-noise-ratio binary black hole detections, Phys. Rev. D **102**, 103024 (2020), arXiv:2003.04513 [gr-qc] .

[530] C. W. F. Everitt *et al.*, Gravity Probe B: Final Results of a Space Experiment to Test General Relativity, Phys. Rev. Lett. **106**, 221101 (2011), arXiv:1105.3456 [gr-qc] .

[531] D. Bini, T. Damour, and a. Geralico, New gravitational self-force analytical results for eccentric orbits around a Schwarzschild black hole, Phys. Rev. **D93**, 104017 (2016), arXiv:1601.02988 [gr-qc] .

[532] D. Bini and T. Damour, Analytic determination of high-order post-Newtonian self-force contributions to gravitational spin precession, Phys. Rev. **D91**, 064064 (2015), arXiv:1503.01272 [gr-qc] .

[533] S. Akcay, Self-force correction to geodetic spin precession in Kerr spacetime, Phys. Rev. **D96**, 044024 (2017), arXiv:1705.03282 [gr-qc] .

[534] D. Bini, T. Damour, and A. Geralico, Spin-orbit precession along eccentric orbits: improving the knowledge of self-force corrections and of their effective-one-body counterparts, Phys. Rev. **D97**, 104046 (2018), arXiv:1801.03704 [gr-qc] .

[535] R. Fujita, S. Isoyama, A. Le Tiec, H. Nakano, N. Sago, and T. Tanaka, Hamiltonian Formulation of the Conservative Self-Force Dynamics in the Kerr Geometry, Class. Quant. Grav. **34**, 134001 (2017), arXiv:1612.02504 [gr-qc] .

[536] M. Hannam, P. Schmidt, A. Bohé, L. Haegel, S. Husa, F. Ohme, G. Pratten, and M. Pürrer, Simple Model of Complete Precessing Black-Hole-Binary Gravitational Waveforms, Phys. Rev. Lett. **113**, 151101 (2014), arXiv:1308.3271 [gr-qc] .

[537] S. Husa, S. Khan, M. Hannam, M. Pürrer, F. Ohme, X. Jiménez Forteza, and A. Bohé, Frequency-domain gravitational waves from nonprecessing black-hole binaries. I. New numerical waveforms and anatomy of the signal, Phys. Rev. D **93**, 044006 (2016), arXiv:1508.07250 [gr-qc] .

[538] S. Khan, S. Husa, M. Hannam, F. Ohme, M. Pürrer, X. Jiménez Forteza, and A. Bohé, Frequency-domain gravitational waves from nonprecessing black-hole binaries. II. A phenomenological model for the advanced detector era, Phys. Rev. **D93**, 044007 (2016), arXiv:1508.07253 [gr-qc] .

[539] S. Khan, F. Ohme, K. Chatziioannou, and M. Hannam, Including higher order multipoles in gravitational-wave models for precessing binary black holes, Phys. Rev. D **101**, 024056 (2020), arXiv:1911.06050 [gr-qc] .

[540] C. García-Quirós, M. Colleoni, S. Husa, H. Estellés, G. Pratten, A. Ramos-Buades, M. Mateu-Lucena, and R. Jaume, Multimode frequency-domain model for the gravitational wave signal from nonprecessing black-hole binaries, Phys. Rev. D **102**, 064002 (2020), arXiv:2001.10914 [gr-qc] .

[541] G. Pratten, S. Husa, C. Garcia-Quiros, M. Colleoni, A. Ramos-Buades, H. Estelles, and R. Jaume, Setting the cornerstone for a family of models for gravitational waves from compact binaries: The dominant harmonic for nonprecessing quasicircular black holes, Phys. Rev. D **102**, 064001 (2020), arXiv:2001.11412 [gr-qc] .

[542] G. Pratten *et al.*, Computationally efficient models for the dominant and subdominant harmonic modes of precessing binary black holes, Phys. Rev. D **103**, 104056 (2021), arXiv:2004.06503 [gr-qc] .

[543] N. S. Foundation, The A+ Upgrade to Advanced LIGO (2018), retrieved online on 18-04-2020.

[544] Y. Aso, Y. Michimura, K. Somiya, M. Ando, O. Miyakawa, T. Sekiguchi, D. Tatsumi, and H. Yamamoto (KAGRA), Interferometer design of the KAGRA gravitational wave detector, Phys. Rev. **D88**, 043007 (2013), arXiv:1306.6747 [gr-qc] .

[545] B. Iyer *et al.* (LIGO Collaboration), LIGO-India, Proposal of the Consortium for Indian Initiative in Gravitational-wave Observations (2011), LIGO Document M1100296-v2.

[546] I. Z. Rothstein, Progress in effective field theory approach to the binary inspiral problem, Gen. Rel. Grav. **46**, 1726 (2014).

[547] W. D. Goldberger, Effective field theories and gravitational radiation, in *Les Houches Summer School - Session 86: Particle Physics and Cosmology: The Fabric of Spacetime* (2007) pp. 351–353, 355–396, arXiv:hep-ph/0701129 [hep-ph] .

[548] D. Bini, T. Damour, A. Geralico, S. Laporta, and P. Mastrolia, Gravitational dynamics at $O(G^6)$: perturbative gravitational scattering meets experimental mathematics, (2020), arXiv:2008.09389 [gr-qc] .

[549] M. Levi and J. Steinhoff, Equivalence of ADM Hamiltonian and Effective Field Theory approaches at next-to-next-to-leading order spin1-spin2 coupling of binary inspirals, JCAP **12**, 003, arXiv:1408.5762 [gr-qc] .

[550] M. Levi, A. J. Mcleod, and M. Von Hippel, N^3LO gravitational quadratic-in-spin interactions at G^4, JHEP **07**, 116, arXiv:2003.07890 [hep-th] .

[551] N. K. Johnson-McDaniel, A. G. Shah, and B. F. Whiting, Experimental mathematics meets gravitational self-force, Phys. Rev. D **92**, 044007 (2015), arXiv:1503.02638 [gr-qc] .

[552] L. Blanchet, S. Detweiler, A. Le Tiec, and B. F. Whiting, High-Accuracy Comparison between the Post-Newtonian and Self-Force Dynamics of Black-Hole Binaries, *Mass and motion in general relativity. Proceedings, School on Mass, Orleans, France, June 23-25, 2008*, Fundam. Theor. Phys. **162**, 415 (2011), [,415(2010)], arXiv:1007.2614 [gr-qc] .

[553] S. Akcay, A. Le Tiec, L. Barack, N. Sago, and N. Warburton, Comparison Between Self-Force and Post-Newtonian Dynamics: Beyond Circular Orbits, Phys. Rev. D **91**, 124014 (2015), arXiv:1503.01374 [gr-qc] .

[554] S. Akcay and M. van de Meent, Numerical computation of the effective-one-body potential q using self-force results, Phys. Rev. **D93**, 064063 (2016), arXiv:1512.03392 [gr-qc] .

[555] R. Aoude, K. Haddad, and A. Helset, On-shell heavy particle effective theories, JHEP **05**, 051, arXiv:2001.09164 [hep-th] .

[556] A. Guevara, A. Ochirov, and J. Vines, Scattering of Spinning Black Holes from Exponentiated Soft Factors, JHEP **09**, 056, arXiv:1812.06895 [hep-th] .

[557] E. Barausse, E. Racine, and A. Buonanno, Hamiltonian of a spinning test-particle in curved spacetime, Phys. Rev. **D80**, 104025 (2009), [Erratum: Phys. Rev. **D85**, 069904 (2012)], arXiv:0907.4745 [gr-qc] .

[558] D. Bini and T. Damour, Gravitational scattering of two black holes at the fourth post-Newtonian approximation, Phys. Rev. D **96**, 064021 (2017), arXiv:1706.06877 [gr-qc] .

[559] D. N. Kabat and M. Ortiz, Eikonal quantum gravity and Planckian scattering, Nucl. Phys. B **388**, 570 (1992), arXiv:hep-th/9203082 .

[560] R. Akhoury, R. Saotome, and G. Sterman, High Energy Scattering in Perturbative Quantum Gravity at Next to Leading Power, (2013), arXiv:1308.5204 [hep-th] .

[561] T. Hinderer and E. E. Flanagan, Two timescale analysis of extreme mass ratio inspirals in Kerr. I. Orbital Motion, Phys. Rev. D **78**, 064028 (2008), arXiv:0805.3337 [gr-qc] .

[562] B. Carter, Republication of: Black hole equilibrium states Part II. General theory of stationary black hole states, General Relativity and Gravitation **42**, 653 (2010).

[563] F. Larrouturou, Q. Henry, L. Blanchet, and G. Faye, The Quadrupole Moment of Compact Binaries to the Fourth post-Newtonian Order: I. Non-Locality in Time and Infra-Red Divergencies, (2021), arXiv:2110.02240 [gr-qc] .

[564] G. L. Almeida, S. Foffa, and R. Sturani, Tail contributions to gravitational conservative dynamics, Phys. Rev. D **104**, 124075 (2021), arXiv:2110.14146 [gr-qc] .

[565] D. Bini and A. Geralico, Frequency domain analysis of the gravitational wave energy loss in hyperbolic encounters, Phys. Rev. D **104**, 104019 (2021), arXiv:2108.02472 [gr-qc] .

[566] S. L. Detweiler, Perspective on gravitational self-force analyses, Class. Quant. Grav. **22**, S681 (2005), arXiv:gr-qc/0501004 .

[567] S. E. Gralla and R. M. Wald, A Rigorous Derivation of Gravitational Self-force, Class. Quant. Grav. **25**, 205009 (2008), [Erratum: Class.Quant.Grav. 28, 159501 (2011)], arXiv:0806.3293 [gr-qc] .

[568] T. S. Keidl, A. G. Shah, J. L. Friedman, D.-H. Kim, and L. R. Price, Gravitational Self-force in a Radiation Gauge, Phys. Rev. D **82**, 124012 (2010), [Erratum: Phys.Rev.D 90, 109902 (2014)], arXiv:1004.2276 [gr-qc] .

[569] A. Pound, Singular perturbation techniques in the gravitational self-force problem, Phys. Rev. D **81**, 124009 (2010), arXiv:1003.3954 [gr-qc] .

[570] R.-M. Memmesheimer, A. Gopakumar, and G. Schaefer, Third post-Newtonian accurate generalized quasi-Keplerian parametrization for compact binaries in eccentric orbits, Phys. Rev. D **70**, 104011 (2004), arXiv:gr-qc/0407049 .

[571] M. Tessmer, J. Hartung, and G. Schafer, Motion and gravitational wave forms of eccentric compact binaries with orbital-angular-momentum-aligned spins under next-to-leading order in spin-orbit and leading order in spin(1)-spin(2) and spin-squared couplings, Class. Quant. Grav. **27**, 165005 (2010), arXiv:1003.2735 [gr-qc] .

[572] M. Tessmer, J. Hartung, and G. Schafer, Aligned Spins: Orbital Elements, Decaying Orbits, and Last Stable Circular Orbit to high post-Newtonian Orders, Class. Quant. Grav. **30**, 015007 (2013), arXiv:1207.6961 [gr-qc] .

[573] Black Hole Perturbation Toolkit, (bhptoolkit.org).

[574] D. Bini, T. Damour, A. Geralico, S. Laporta, and P. Mastrolia, Gravitational scattering at the seventh order in G: nonlocal contribution at the sixth post-Newtonian accuracy, Phys. Rev. D **103**, 044038 (2021), arXiv:2012.12918 [gr-qc] .

[575] G. Cho, A. Gopakumar, M. Haney, and H. M. Lee, Gravitational waves from compact binaries in post-Newtonian accurate hyperbolic orbits, Phys. Rev. D **98**, 024039 (2018), arXiv:1807.02380 [gr-qc] .

[576] M. Punturo *et al.*, The Einstein Telescope: A third-generation gravitational wave observatory, Class. Quant. Grav. **27**, 194002 (2010).

[577] S. Kawamura *et al.*, The Japanese space gravitational wave antenna DECIGO, Class. Quant. Grav. **23**, S125 (2006).

[578] D. Reitze *et al.*, Cosmic Explorer: The U.S. Contribution to Gravitational-Wave Astronomy beyond LIGO, Bull. Am. Astron. Soc. **51**, 035 (2019), arXiv:1907.04833 [astro-ph.IM] .

[579] B. P. Abbott *et al.* (LIGO Scientific, Virgo), Binary Black Hole Mergers in the first Advanced LIGO Observing Run, Phys. Rev. **X6**, 041015 (2016), [erratum: Phys. Rev.X8,no.3,039903(2018)], arXiv:1606.04856 [gr-qc] .

[580] S. Balmelli and P. Jetzer, Effective-one-body Hamiltonian with next-to-leading order spin-spin coupling for two nonprecessing black holes with aligned spins, Phys. Rev. D **87**, 124036 (2013), [Erratum: Phys.Rev.D 90, 089905 (2014)], arXiv:1305.5674 [gr-qc] .

[581] S. Balmelli and P. Jetzer, Effective-one-body Hamiltonian with next-to-leading order spin-spin coupling, Phys. Rev. **D91**, 064011 (2015), arXiv:1502.01343 [gr-qc] .

[582] Y. Pan, A. Buonanno, L. T. Buchman, T. Chu, L. E. Kidder, H. P. Pfeiffer, and M. A. Scheel, Effective-one-body waveforms calibrated to numerical relativity simulations: coalescence of non-precessing, spinning, equal-mass black holes, Phys. Rev. D **81**, 084041 (2010), arXiv:0912.3466 [gr-qc] .

[583] A. Nagar, G. Riemenschneider, and G. Pratten, Impact of Numerical Relativity information on effective-one-body waveform models, Phys. Rev. **D96**, 084045 (2017), arXiv:1703.06814 [gr-qc] .

[584] S. Akcay, S. Bernuzzi, F. Messina, A. Nagar, N. Ortiz, and P. Rettegno, Effective-one-body multipolar waveform for tidally interacting binary neutron stars up to merger, Phys. Rev. **D99**, 044051 (2019), arXiv:1812.02744 [gr-qc] .

[585] A. Nagar and P. Rettegno, Efficient effective one body time-domain gravitational waveforms, Phys. Rev. D **99**, 021501 (2019), arXiv:1805.03891 [gr-qc] .

[586] T. Hinderer *et al.*, Effects of neutron-star dynamic tides on gravitational waveforms within the effective-one-body approach, Phys. Rev. Lett. **116**, 181101 (2016), arXiv:1602.00599 [gr-qc] .

[587] J. Steinhoff, T. Hinderer, A. Buonanno, and A. Taracchini, Dynamical Tides in General Relativity: Effective Action and Effective-One-Body Hamiltonian, Phys. Rev. D **94**, 104028 (2016), arXiv:1608.01907 [gr-qc] .

[588] N. Yunes, A. Buonanno, S. A. Hughes, Y. Pan, E. Barausse, M. C. Miller, and W. Throwe, Extreme Mass-Ratio Inspirals in the Effective-One-Body Approach: Quasi-Circular, Equatorial Orbits around a Spinning Black Hole, Phys. Rev. D **83**, 044044 (2011), [Erratum: Phys.Rev.D 88, 109904 (2013)], arXiv:1009.6013 [gr-qc] .

[589] T. Hinderer *et al.*, Periastron advance in spinning black hole binaries: comparing effective-one-body and Numerical Relativity, Phys. Rev. **D88**, 084005 (2013), arXiv:1309.0544 [gr-qc] .

[590] P. Rettegno, F. Martinetti, A. Nagar, D. Bini, G. Riemenschneider, and T. Damour, Comparing Effective One Body Hamiltonians for spin-aligned coalescing binaries, Phys. Rev. D **101**, 104027 (2020), arXiv:1911.10818 [gr-qc] .

[591] M. Mathisson, Republication of: New mechanics of material systems, Gen. Relativ. Gravit. **42**, 1011 (2010).

[592] E. Corinaldesi and A. Papapetrou, Spinning test particles in general relativity. 2., Proc. Roy. Soc. Lond. **A209**, 259 (1951).

[593] D. Bini, T. Damour, and A. Geralico, Spin-dependent two-body interactions from gravitational self-force computations, Phys. Rev. **D92**, 124058 (2015), [Erratum: Phys. Rev.D93,no.10,109902(2016)], arXiv:1510.06230 [gr-qc] .

[594] B. M. Barker and R. F. O'Connell, Derivation of the equations of motion of a gyroscope from the quantum theory of gravitation, Phys. Rev. **D2**, 1428 (1970).

[595] P. D. D'Eath, Interaction of two black holes in the slow-motion limit, Phys. Rev. **D12**, 2183 (1975).

[596] T. Damour, Probléme des deux corps et freinage de rayonnement en relativité générale, C. R. Acad. Sci. Paris Sér. II **294**, 1355 (1982).

[597] T. Damour and G. Schäfer, Higher Order Relativistic Periastron Advances and Binary Pulsars, Nuovo Cim. **B101**, 127 (1988).

[598] M. Levi, Next to Leading Order gravitational Spin-Orbit coupling in an Effective Field Theory approach, Phys. Rev. D **82**, 104004 (2010), arXiv:1006.4139 [gr-qc] .

[599] E. Poisson, Gravitational waves from inspiraling compact binaries: The Quadrupole moment term, Phys. Rev. **D57**, 5287 (1998), arXiv:gr-qc/9709032 [gr-qc] .

[600] M. Levi, Next to Leading Order gravitational Spin1-Spin2 coupling with Kaluza-Klein reduction, Phys. Rev. **D82**, 064029 (2010), arXiv:0802.1508 [gr-qc] .

[601] J. Steinhoff, S. Hergt, and G. Schäfer, Spin-squared Hamiltonian of next-to-leading order gravitational interaction, Phys. Rev. D **78**, 101503 (2008), arXiv:0809.2200 [gr-qc] .

[602] S. Hergt, J. Steinhoff, and G. Schäfer, Elimination of the spin supplementary condition in the effective field theory approach to the post-Newtonian approximation, Annals Phys. **327**, 1494 (2012), arXiv:1110.2094 [gr-qc] .

[603] S. Hergt and G. Schäfer, Higher-order-in-spin interaction Hamiltonians for binary black holes from source terms of Kerr geometry in approximate ADM coordinates, Phys. Rev. **D77**, 104001 (2008), arXiv:0712.1515 [gr-qc] .

[604] V. Vaidya, Gravitational spin Hamiltonians from the S matrix, Phys. Rev. **D91**, 024017 (2015), arXiv:1410.5348 [hep-th] .

[605] J. B. Gilmore and A. Ross, Effective field theory calculation of second post-Newtonian binary dynamics, Phys. Rev. **D78**, 124021 (2008), arXiv:0810.1328 [gr-qc] .

[606] A. Sesana, Self consistent model for the evolution of eccentric massive black hole binaries in stellar environments: implications for gravitational wave observations, Astrophys. J. **719**, 851 (2010), arXiv:1006.0730 [astro-ph.CO] .

[607] K. Breivik, C. L. Rodriguez, S. L. Larson, V. Kalogera, and F. A. Rasio, Distinguishing Between Formation Channels for Binary Black Holes with LISA, Astrophys. J. Lett. **830**, L18 (2016), arXiv:1606.09558 [astro-ph.GA] .

[608] B. Willems, V. Kalogera, A. Vecchio, N. Ivanova, F. Rasio, J. Fregeau, and K. Belczynski, Eccentric double white dwarfs as LISA sources in globular clusters, Astrophys. J. Lett. **665**, L59 (2007), arXiv:0705.4287 [astro-ph] .

[609] J. Samsing and D. J. D'Orazio, Black Hole Mergers From Globular Clusters Observable by LISA I: Eccentric Sources Originating From Relativistic N-body Dynamics, Mon. Not. Roy. Astron. Soc. **481**, 5445 (2018), arXiv:1804.06519 [astro-ph.HE] .

[610] V. Cardoso, C. F. B. Macedo, and R. Vicente, Eccentricity evolution of compact binaries and applications to gravitational-wave physics, Phys. Rev. D **103**, 023015 (2021), arXiv:2010.15151 [gr-qc] .

[611] Y. Boetzel, A. Susobhanan, A. Gopakumar, A. Klein, and P. Jetzer, Solving post-Newtonian accurate Kepler Equation, Phys. Rev. D **96**, 044011 (2017), arXiv:1707.02088 [gr-qc] .

[612] N. Loutrel and N. Yunes, Eccentric Gravitational Wave Bursts in the Post-Newtonian Formalism, Class. Quant. Grav. **34**, 135011 (2017), arXiv:1702.01818 [gr-qc] .

[613] S. Tanay, M. Haney, and A. Gopakumar, Frequency and time domain inspiral templates for comparable mass compact binaries in eccentric orbits, Phys. Rev. D **93**, 064031 (2016), arXiv:1602.03081 [gr-qc] .

[614] N. Yunes, K. Arun, E. Berti, and C. M. Will, Post-Circular Expansion of Eccentric Binary Inspirals: Fourier-Domain Waveforms in the Stationary Phase Approximation, Phys. Rev. D **80**, 084001 (2009), [Erratum: Phys.Rev.D 89, 109901 (2014)], arXiv:0906.0313 [gr-qc] .

[615] E. A. Huerta, P. Kumar, S. T. McWilliams, R. O'Shaughnessy, and N. Yunes, Accurate and efficient waveforms for compact binaries on eccentric orbits, Phys. Rev. D **90**, 084016 (2014), arXiv:1408.3406 [gr-qc] .

[616] S. Tiwari, G. Achamveedu, M. Haney, and P. Hemantakumar, Ready-to-use Fourier domain templates for compact binaries inspiraling along moderately eccentric orbits, Phys. Rev. D **99**, 124008 (2019), arXiv:1905.07956 [gr-qc] .

[617] A. Klein, Y. Boetzel, A. Gopakumar, P. Jetzer, and L. de Vittori, Fourier domain gravitational waveforms for precessing eccentric binaries, Phys. Rev. D **98**, 104043 (2018), arXiv:1801.08542 [gr-qc] .

[618] C. Konigsdorffer and A. Gopakumar, Phasing of gravitational waves from inspiralling eccentric binaries at the third-and-a-half post-Newtonian order, Phys. Rev. D **73**, 124012 (2006), arXiv:gr-qc/0603056 .

[619] B. Moore, M. Favata, K. Arun, and C. K. Mishra, Gravitational-wave phasing for low-eccentricity inspiralling compact binaries to 3PN order, Phys. Rev. D **93**, 124061 (2016), arXiv:1605.00304 [gr-qc] .

[620] I. Hinder, L. E. Kidder, and H. P. Pfeiffer, Eccentric binary black hole inspiral-merger-ringdown gravitational waveform model from numerical relativity and post-Newtonian theory, Phys. Rev. D **98**, 044015 (2018), arXiv:1709.02007 [gr-qc] .

[621] E. Huerta *et al.*, Complete waveform model for compact binaries on eccentric orbits, Phys. Rev. D **95**, 024038 (2017), arXiv:1609.05933 [gr-qc] .

[622] A. Ramos-Buades, S. Husa, G. Pratten, H. Estellés, C. García-Quirós, M. Mateu-Lucena, M. Colleoni, and R. Jaume, First survey of spinning eccentric black hole mergers: Numerical relativity simulations, hybrid waveforms, and parameter estimation, Phys. Rev. D **101**, 083015 (2020), arXiv:1909.11011 [gr-qc] .

[623] E. A. Huerta *et al.*, Physics of eccentric binary black hole mergers: A numerical relativity perspective, Phys. Rev. **D100**, 064003 (2019), arXiv:1901.07038 [gr-qc] .

[624] T. Islam, V. Varma, J. Lodman, S. E. Field, G. Khanna, M. A. Scheel, H. P. Pfeiffer, D. Gerosa, and L. E. Kidder, Eccentric binary black hole surrogate models for the gravitational waveform and remnant properties: comparable mass, nonspinning case, Phys. Rev. D **103**, 064022 (2021), arXiv:2101.11798 [gr-qc] .

[625] T. Damour and A. Nagar, Effective One Body description of tidal effects in inspiralling compact binaries, Phys. Rev. **D81**, 084016 (2010), arXiv:0911.5041 [gr-qc] .

[626] Z. Cao and W.-B. Han, Waveform model for an eccentric binary black hole based on the effective-one-body-numerical-relativity formalism, Phys. Rev. D **96**, 044028 (2017), arXiv:1708.00166 [gr-qc] .

[627] X. Liu, Z. Cao, and L. Shao, Validating the Effective-One-Body Numerical-Relativity Waveform Models for Spin-aligned Binary Black Holes along Eccentric Orbits, Phys. Rev. **D101**, 044049 (2020), arXiv:1910.00784 [gr-qc] .

[628] X. Liu, Z. Cao, and Z.-H. Zhu, A higher-multipole gravitational waveform model for an eccentric binary black holes based on the effective-one-body-numerical-relativity formalism, Class. Quant. Grav. **39**, 035009 (2022), arXiv:2102.08614 [gr-qc] .

[629] D. Chiaramello and A. Nagar, Faithful analytical effective-one-body waveform model for spin-aligned, moderately eccentric, coalescing black hole binaries, Phys. Rev. D **101**, 101501 (2020), arXiv:2001.11736 [gr-qc] .

[630] A. Nagar, G. Riemenschneider, G. Pratten, P. Rettegno, and F. Messina, Multipolar effective one body waveform model for spin-aligned black hole binaries, Phys. Rev. D **102**, 024077 (2020), arXiv:2001.09082 [gr-qc] .

[631] S. Habib and E. Huerta, Characterization of numerical relativity waveforms of eccentric binary black hole mergers, Phys. Rev. D **100**, 044016 (2019), arXiv:1904.09295 [gr-qc] .

[632] T. Mora and C. M. Will, Numerically generated quasiequilibrium orbits of black holes: Circular or eccentric?, Phys. Rev. D **66**, 101501 (2002), arXiv:gr-qc/0208089 .

[633] S. Drasco, E. E. Flanagan, and S. A. Hughes, Computing inspirals in Kerr in the adiabatic regime. I. The Scalar case, Class. Quant. Grav. **22**, S801 (2005), arXiv:gr-qc/0505075 .

[634] T. Akutsu *et al.* (KAGRA), Overview of KAGRA: Calibration, detector characterization, physical environmental monitors, and the geophysics interferometer, PTEP **2021**, 05A102 (2021), arXiv:2009.09305 [gr-qc] .

[635] M.-Z. Chung, Y.-T. Huang, and J.-W. Kim, Classical potential for general spinning bodies, JHEP **09**, 074, arXiv:1908.08463 [hep-th] .

[636] W.-M. Chen, M.-Z. Chung, Y.-t. Huang, and J.-W. Kim, The 2PM Hamiltonian for binary Kerr to quartic in spin, (2021), arXiv:2111.13639 [hep-th] .

[637] G. U. Jakobsen and G. Mogull, Conservative and Radiative Dynamics of Spinning Bodies at Third Post-Minkowskian Order Using Worldline Quantum Field Theory, Phys. Rev. Lett. **128**, 141102 (2022), arXiv:2201.07778 [hep-th] .

[638] Z. Bern, D. Kosmopoulos, A. Luna, R. Roiban, and F. Teng, Binary Dynamics Through the Fifth Power of Spin at $\mathcal{O}(G^2)$, (2022), arXiv:2203.06202 [hep-th] .

[639] R. Aoude, K. Haddad, and A. Helset, Searching for Kerr in the 2PM amplitude, (2022), arXiv:2203.06197 [hep-th] .

[640] P. Di Vecchia, C. Heissenberg, R. Russo, and G. Veneziano, Universality of ultra-relativistic gravitational scattering, Phys. Lett. B **811**, 135924 (2020), arXiv:2008.12743 [hep-th] .

[641] S. E. Gralla and K. Lobo, Self-force effects in post-Minkowskian scattering, Class. Quant. Grav. **39**, 095001 (2022), arXiv:2110.08681 [gr-qc] .

[642] S. Clesse and J. García-Bellido, Massive Primordial Black Holes from Hybrid Inflation as Dark Matter and the seeds of Galaxies, Phys. Rev. D **92**, 023524 (2015), arXiv:1501.07565 [astro-ph.CO] .

[643] J. Garcia-Bellido and S. Nesseris, Gravitational wave bursts from Primordial Black Hole hyperbolic encounters, Phys. Dark Univ. **18**, 123 (2017), arXiv:1706.02111 [astro-ph.CO] .

[644] J. García-Bellido and S. Nesseris, Gravitational wave energy emission and detection rates of Primordial Black Hole hyperbolic encounters, Phys. Dark Univ. **21**, 61 (2018), arXiv:1711.09702 [astro-ph.HE] .

[645] G. Morrás, J. García-Bellido, and S. Nesseris, Search for black hole hyperbolic encounters with gravitational wave detectors, Phys. Dark Univ. **35**, 100932 (2022), arXiv:2110.08000 [astro-ph.HE] .

[646] B. McKernan, K. E. S. Ford, W. Lyra, and H. B. Perets, Intermediate mass black holes in AGN disks: I. Production & Growth, Mon. Not. Roy. Astron. Soc. **425**, 460 (2012), arXiv:1206.2309 [astro-ph.GA] .

[647] N. C. Stone, B. D. Metzger, and Z. Haiman, Assisted inspirals of stellar mass black holes embedded in AGN discs: solving the ‘final au problem’, Mon. Not. Roy. Astron. Soc. **464**, 946 (2017), arXiv:1602.04226 [astro-ph.GA] .

[648] N. W. C. Leigh *et al.*, On the rate of black hole binary mergers in galactic nuclei due to dynamical hardening, Mon. Not. Roy. Astron. Soc. **474**, 5672 (2018), arXiv:1711.10494 [astro-ph.GA] .

[649] S. Repetto, A. P. Igoshev, and G. Nelemans, The Galactic distribution of X-ray binaries and its implications for compact object formation and natal kicks, Mon. Not. Roy. Astron. Soc. **467**, 298 (2017), arXiv:1701.01347 [astro-ph.HE] .

[650] A. S. Hamers, B. Bar-Or, C. Petrovich, and F. Antonini, The impact of vector resonant relaxation on the evolution of binaries near a massive black hole: implications for gravitational wave sources, Astrophys. J. **865**, 2 (2018), arXiv:1805.10313 [astro-ph.HE] .

[651] C. L. Rodriguez, P. Amaro-Seoane, S. Chatterjee, K. Kremer, F. A. Rasio, J. Samsing, C. S. Ye, and M. Zevin, Post-Newtonian Dynamics in Dense Star Clusters: Formation, Masses, and Merger Rates of Highly-Eccentric Black Hole Binaries, Phys. Rev. D **98**, 123005 (2018), arXiv:1811.04926 [astro-ph.HE] .

[652] C. P. L. Berry and J. R. Gair, Gravitational wave energy spectrum of a parabolic encounter, Phys. Rev. D **82**, 107501 (2010), arXiv:1010.3865 [gr-qc] .

[653] L. De Vittori, P. Jetzer, and A. Klein, Gravitational wave energy spectrum of hyperbolic encounters, Phys. Rev. D **86**, 044017 (2012), arXiv:1207.5359 [gr-qc] .

[654] L. De Vittori, A. Gopakumar, A. Gupta, and P. Jetzer, Gravitational waves from spinning compact binaries in hyperbolic orbits, Phys. Rev. D **90**, 124066 (2014), arXiv:1410.6311 [gr-qc] .

[655] M. Gröbner, P. Jetzer, M. Haney, S. Tiwari, and W. Ishibashi, A note on the gravitational wave energy spectrum of parabolic and hyperbolic encounters, Class. Quant. Grav. **37**, 067002 (2020), arXiv:2001.05187 [gr-qc] .

[656] A. Nagar, P. Rettegno, R. Gamba, and S. Bernuzzi, Effective-one-body waveforms from dynamical captures in black hole binaries, Phys. Rev. D **103**, 064013 (2021), arXiv:2009.12857 [gr-qc] .

[657] A. Nagar and P. Rettegno, Next generation: Impact of high-order analytical information on effective one body waveform models for noncircularized, spin-aligned black hole binaries, Phys. Rev. D **104**, 104004 (2021), arXiv:2108.02043 [gr-qc] .

[658] R. Gamba, M. Breschi, G. Carullo, P. Rettegno, S. Albanesi, S. Bernuzzi, and A. Nagar, GW190521: A dynamical capture of two black holes, (2021), arXiv:2106.05575 [gr-qc] .

[659] B. P. Abbott *et al.* (Virgo, LIGO Scientific), GW151226: Observation of Gravitational Waves from a 22-Solar-Mass Binary Black Hole Coalescence, Phys. Rev. Lett. **116**, 241103 (2016), arXiv:1606.04855 [gr-qc] .

[660] B. P. Abbott *et al.* (VIRGO, LIGO Scientific), GW170104: Observation of a 50-Solar-Mass Binary Black Hole Coalescence at Redshift 0.2, Phys. Rev. Lett. **118**, 221101 (2017), [Erratum: Phys. Rev. Lett.121,no.12,129901(2018)], arXiv:1706.01812 [gr-qc] .

[661] B. P. Abbott *et al.* (Virgo, LIGO Scientific), GW170608: Observation of a 19-solar-mass Binary Black Hole Coalescence, Astrophys. J. **851**, L35 (2017), arXiv:1711.05578 [astro-ph.HE] .

[662] B. P. Abbott *et al.* (LIGO Scientific, Virgo), GW170814: A Three-Detector Observation of Gravitational Waves from a Binary Black Hole Coalescence, Phys. Rev. Lett. **119**, 141101 (2017), arXiv:1709.09660 [gr-qc] .

[663] N. Yunes, K. Yagi, and F. Pretorius, Theoretical Physics Implications of the Binary Black-Hole Mergers GW150914 and GW151226, Phys. Rev. **D94**, 084002 (2016), arXiv:1603.08955 [gr-qc] .

[664] K. G. Arun, B. R. Iyer, M. S. S. Qusailah, and B. S. Sathyaprakash, Probing the non-linear structure of general relativity with black hole binaries, Phys. Rev. **D74**, 024006 (2006), arXiv:gr-qc/0604067 [gr-qc] .

[665] N. Yunes and F. Pretorius, Fundamental Theoretical Bias in Gravitational Wave Astrophysics and the Parameterized Post-Einsteinian Framework, Phys. Rev. **D80**, 122003 (2009), arXiv:0909.3328 [gr-qc] .

[666] C. K. Mishra, K. G. Arun, B. R. Iyer, and B. S. Sathyaprakash, Parametrized tests of post-Newtonian theory using Advanced LIGO and Einstein Telescope, Phys. Rev. **D82**, 064010 (2010), arXiv:1005.0304 [gr-qc] .

[667] T. G. F. Li, W. Del Pozzo, S. Vitale, C. Van Den Broeck, M. Agathos, J. Veitch, K. Grover, T. Sidery, R. Sturani, and A. Vecchio, Towards a generic test of the strong field dynamics of general relativity using compact binary coalescence, Phys. Rev. **D85**, 082003 (2012), arXiv:1110.0530 [gr-qc] .

[668] B. P. Abbott *et al.* (Virgo, LIGO Scientific), Tests of general relativity with GW150914, Phys. Rev. Lett. **116**, 221101 (2016), arXiv:1602.03841 [gr-qc] .

[669] S. W. Hawking, Black holes in the Brans-Dicke theory of gravitation, Commun. Math. Phys. **25**, 167 (1972).

[670] T. P. Sotiriou and V. Faraoni, Black holes in scalar-tensor gravity, Phys. Rev. Lett. **108**, 081103 (2012), arXiv:1109.6324 [gr-qc] .

[671] J. H. Horne and G. T. Horowitz, Rotating dilaton black holes, Phys. Rev. **D46**, 1340 (1992), arXiv:hep-th/9203083 [hep-th] .

[672] V. P. Frolov, A. I. Zelnikov, and U. Bleyer, Charged Rotating Black Hole From Five-dimensional Point of View, Annalen Phys. **44**, 371 (1987).

[673] S. Davidson, S. Hannestad, and G. Raffelt, Updated bounds on millicharged particles, JHEP **05**, 003, arXiv:hep-ph/0001179 [hep-ph] .

[674] C. Burrage, J. Jaeckel, J. Redondo, and A. Ringwald, Late time CMB anisotropies constrain mini-charged particles, JCAP **0911**, 002, arXiv:0909.0649 [astro-ph.CO] .

[675] M. Ahlers, The Hubble diagram as a probe of mini-charged particles, Phys. Rev. **D80**, 023513 (2009), arXiv:0904.0998 [hep-ph] .

[676] K. Kadota, T. Sekiguchi, and H. Tashiro, A new constraint on millicharged dark matter from galaxy clusters, (2016), arXiv:1602.04009 [astro-ph.CO] .

[677] M. Zilhao, V. Cardoso, C. Herdeiro, L. Lehner, and U. Sperhake, Collisions of charged black holes, Phys. Rev. **D85**, 124062 (2012), arXiv:1205.1063 [gr-qc] .

[678] M. Zilhão, V. Cardoso, C. Herdeiro, L. Lehner, and U. Sperhake, Collisions of oppositely charged black holes, Phys. Rev. **D89**, 044008 (2014), arXiv:1311.6483 [gr-qc] .

[679] E. E. Flanagan, The Conformal frame freedom in theories of gravitation, Class. Quant. Grav. **21**, 3817 (2004), arXiv:gr-qc/0403063 [gr-qc] .

[680] A. Taracchini, A. Buonanno, G. Khanna, and S. A. Hughes, Small mass plunging into a Kerr black hole: Anatomy of the inspiral-merger-ringdown waveforms, Phys. Rev. **D90**, 084025 (2014), arXiv:1404.1819 [gr-qc] .

[681] N. Sennett and A. Buonanno, Modeling dynamical scalarization with a resummed post-Newtonian expansion, Phys. Rev. **D93**, 124004 (2016), arXiv:1603.03300 [gr-qc] .

[682] P. Jordan, *Schwerkraft und Weltall* (F. Vieweg, Braunschweig, 1955).

[683] M. Fierz, On the physical interpretation of P.Jordan's extended theory of gravitation, Helv. Phys. Acta **29**, 128 (1956).

[684] C. Brans and R. H. Dicke, Mach's principle and a relativistic theory of gravitation, Phys. Rev. **124**, 925 (1961).

[685] J. S. Read, B. D. Lackey, B. J. Owen, and J. L. Friedman, Constraints on a phenomenologically parameterized neutron-star equation of state, Phys. Rev. **D79**, 124032 (2009), arXiv:0812.2163 [astro-ph] .

[686] A. D. Fokker, Ein invarianter Variationssatz für die Bewegung mehrerer elektrischer Massenteilchen, Z. Phys. **58**, 386 (1929).

[687] N. Yunes and S. A. Hughes, Binary Pulsar Constraints on the Parameterized post-Einsteinian Framework, Phys. Rev. **D82**, 082002 (2010), arXiv:1007.1995 [gr-qc] .

[688] E. Barausse, N. Yunes, and K. Chamberlain, Theory-Agnostic Constraints on Black-Hole Dipole Radiation with Multiband Gravitational-Wave Astrophysics, Phys. Rev. Lett. **116**, 241104 (2016), arXiv:1603.04075 [gr-qc] .

[689] W. Del Pozzo, J. Veitch, and A. Vecchio, Testing General Relativity using Bayesian model selection: Applications to observations of gravitational waves from compact binary systems, Phys. Rev. **D83**, 082002 (2011), arXiv:1101.1391 [gr-qc] .

[690] N. Cornish, L. Sampson, N. Yunes, and F. Pretorius, Gravitational Wave Tests of General Relativity with the Parameterized Post-Einsteinian Framework, Phys. Rev. **D84**, 062003 (2011), arXiv:1105.2088 [gr-qc] .

[691] S. Gossan, J. Veitch, and B. S. Sathyaprakash, Bayesian model selection for testing the no-hair theorem with black hole ringdowns, Phys. Rev. **D85**, 124056 (2012), arXiv:1111.5819 [gr-qc] .

[692] L. Sampson, N. Yunes, N. Cornish, M. Ponce, E. Barausse, A. Klein, C. Palenzuela, and L. Lehner, Projected Constraints on Scalarization with Gravitational Waves from Neutron Star Binaries, Phys. Rev. **D90**, 124091 (2014), arXiv:1407.7038 [gr-qc] .

[693] T. Damour, B. R. Iyer, and B. S. Sathyaprakash, Frequency domain P approximant filters for time truncated inspiral gravitational wave signals from compact binaries, Phys. Rev. **D62**, 084036 (2000), arXiv:gr-qc/0001023 [gr-qc] .

[694] LIGO-T1800042-v5: Updated Advanced LIGO sensitivity design curve, `https://dcc.ligo.org/LIGO-T1800044/public`.

[695] R. Coquereaux and G. Esposito-Farese, The Theory of Kaluza-Klein-Jordan-Thiry revisited, Ann. Inst. H. Poincare Phys. Theor. **52**, 113 (1990).

[696] F.-L. Julié, Reducing the two-body problem in scalar-tensor theories to the motion of a test particle : a scalar-tensor effective-one-body approach, Phys. Rev. **D97**, 024047 (2018), arXiv:1709.09742 [gr-qc] .

[697] F.-L. Julié and N. Deruelle, Two-body problem in Scalar-Tensor theories as a deformation of General Relativity : an Effective-One-Body approach, Phys. Rev. **D95**, 124054 (2017), arXiv:1703.05360 [gr-qc] .

[698] A. Buonanno, Reduction of the two-body dynamics to a one-body description in classical electrodynamics, Phys. Rev. **D62**, 104022 (2000), arXiv:hep-th/0004042 [hep-th] .

[699] P. Jai-akson, A. Chatrabhuti, O. Evnin, and L. Lehner, Black hole merger estimates in Einstein-Maxwell and Einstein-Maxwell-dilaton gravity, Phys. Rev. **D96**, 044031 (2017), arXiv:1706.06519 [gr-qc] .

[700] V. Ferrari, M. Pauri, and F. Piazza, Quasinormal modes of charged, dilaton black holes, Phys. Rev. **D63**, 064009 (2001), arXiv:gr-qc/0005125 [gr-qc] .

[701] N. Wex, Testing Relativistic Gravity with Radio Pulsars, (2014), arXiv:1402.5594 [gr-qc] .

[702] M. Kramer, Pulsars as probes of gravity and fundamental physics, Int. J. Mod. Phys. **D25**, 1630029 (2016), arXiv:1606.03843 [astro-ph.HE] .

[703] B. P. Abbott *et al.* (LIGO Scientific, Virgo), Tests of General Relativity with GW170817, Phys. Rev. Lett. **123**, 011102 (2019), arXiv:1811.00364 [gr-qc] .

[704] S. W. Hawking and R. Penrose, The Singularities of gravitational collapse and cosmology, Proc. Roy. Soc. Lond. **A314**, 529 (1970).

[705] F. Englert and R. Brout, Broken Symmetry and the Mass of Gauge Vector Mesons, Phys. Rev. Lett. **13**, 321 (1964).

[706] P. W. Higgs, Broken Symmetries and the Masses of Gauge Bosons, Phys. Rev. Lett. **13**, 508 (1964).

[707] G. S. Guralnik, C. R. Hagen, and T. W. B. Kibble, Global Conservation Laws and Massless Particles, Phys. Rev. Lett. **13**, 585 (1964).

[708] A. Coates, M. W. Horbartsch, and T. P. Sotiriou, Gravitational Higgs Mechanism in Neutron Star Interiors, Phys. Rev. **D95**, 084003 (2017), arXiv:1606.03981 [gr-qc] .

[709] I. Z. Stefanov, S. S. Yazadjiev, and M. D. Todorov, Phases of 4D scalar-tensor black holes coupled to Born-Infeld nonlinear electrodynamics, Mod. Phys. Lett. **A23**, 2915 (2008), arXiv:0708.4141 [gr-qc] .

[710] D. D. Doneva, S. S. Yazadjiev, K. D. Kokkotas, and I. Z. Stefanov, Quasi-normal modes, bifurcations and non-uniqueness of charged scalar-tensor black holes, Phys. Rev. **D82**, 064030 (2010), arXiv:1007.1767 [gr-qc] .

[711] C. Palenzuela and S. L. Liebling, Constraining scalar-tensor theories of gravity from the most massive neutron stars, Phys. Rev. **D93**, 044009 (2016), arXiv:1510.03471 [gr-qc] .

[712] R. F. P. Mendes and N. Ortiz, Highly compact neutron stars in scalar-tensor theories of gravity: Spontaneous scalarization versus gravitational collapse, Phys. Rev. **D93**, 124035 (2016), arXiv:1604.04175 [gr-qc] .

[713] P. G. S. Fernandes, C. A. R. Herdeiro, A. M. Pombo, E. Radu, and N. Sanchis-Gual, Spontaneous Scalarisation of Charged Black Holes: Coupling Dependence and Dynamical Features, Class. Quant. Grav. **36**, 134002 (2019), arXiv:1902.05079 [gr-qc] .

[714] Y. Brihaye and B. Hartmann, Spontaneous scalarization of charged black holes at the approach to extremality, Phys. Lett. **B792**, 244 (2019), arXiv:1902.05760 [gr-qc] .

[715] P. Zimmerman, Gravitational self-force in scalar-tensor gravity, Phys. Rev. **D92**, 064051 (2015), arXiv:1507.04076 [gr-qc] .

[716] L. Shao, N. Sennett, A. Buonanno, M. Kramer, and N. Wex, Constraining nonperturbative strong-field effects in scalar-tensor gravity by combining pulsar timing and laser-interferometer gravitational-wave detectors, Phys. Rev. **X7**, 041025 (2017), arXiv:1704.07561 [gr-qc] .

[717] D. Anderson, P. Freire, and N. Yunes, Binary Pulsar constraints on massless scalar-tensor theories using Bayesian statistics, Class. Quant. Grav. **36**, 225009 (2019), arXiv:1901.00938 [gr-qc] .

[718] M. Agathos, W. Del Pozzo, T. G. F. Li, C. Van Den Broeck, J. Veitch, and S. Vitale, TIGER: A data analysis pipeline for testing the strong-field dynamics of general relativity with gravitational wave signals from coalescing compact binaries, Phys. Rev. **D89**, 082001 (2014), arXiv:1311.0420 [gr-qc] .

[719] L. Sampson, N. Cornish, and N. Yunes, Mismodeling in gravitational-wave astronomy: The trouble with templates, Phys. Rev. **D89**, 064037 (2014), arXiv:1311.4898 [gr-qc] .

[720] B. P. Abbott *et al.* (LIGO Scientific, Virgo), Properties of the binary neutron star merger GW170817, Phys. Rev. **X9**, 011001 (2019), arXiv:1805.11579 [gr-qc] .

[721] Y. S. Myung and D.-C. Zou, Instability of Reissner–Nordström black hole in Einstein-Maxwell-scalar theory, Eur. Phys. J. C **79**, 273 (2019), arXiv:1808.02609 [gr-qc] .

[722] G. W. Gibbons, R. Kallosh, and B. Kol, Moduli, scalar charges, and the first law of black hole thermodynamics, Phys. Rev. Lett. **77**, 4992 (1996), arXiv:hep-th/9607108 [hep-th] .

[723] M. Cárdenas, F.-L. Julié, and N. Deruelle, Thermodynamics sheds light on black hole dynamics, Phys. Rev. D **97**, 124021 (2018), arXiv:1712.02672 [gr-qc] .

[724] J. L. Blázquez-Salcedo, D. D. Doneva, J. Kunz, and S. S. Yazadjiev, Radial perturbations of the scalarized Einstein-Gauss-Bonnet black holes, Phys. Rev. **D98**, 084011 (2018), arXiv:1805.05755 [gr-qc] .

[725] M. Minamitsuji and T. Ikeda, Scalarized black holes in the presence of the coupling to Gauss-Bonnet gravity, Phys. Rev. **D99**, 044017 (2019), arXiv:1812.03551 [gr-qc] .

[726] H. O. Silva, C. F. B. Macedo, T. P. Sotiriou, L. Gualtieri, J. Sakstein, and E. Berti, Stability of scalarized black hole solutions in scalar-Gauss-Bonnet gravity, Phys. Rev. **D99**, 064011 (2019), arXiv:1812.05590 [gr-qc] .

[727] Y. S. Myung and D.-C. Zou, Stability of scalarized charged black holes in the Einstein–Maxwell–Scalar theory, Eur. Phys. J. **C79**, 641 (2019), arXiv:1904.09864 [gr-qc] .

[728] Y. S. Myung and D.-C. Zou, Quasinormal modes of scalarized black holes in the Einstein–Maxwell–Scalar theory, Phys. Lett. **B790**, 400 (2019), arXiv:1812.03604 [gr-qc] .

[729] L. D. Landau, Theory of phase transformations. I, Zh. Eksp. Teor. Fiz. **7**, 19 (1937).

[730] L. D. Landau, Ukr. J. Phys **53**, 25 (2008), (English translation).

[731] M. W. Choptuik, Universality and scaling in gravitational collapse of a massless scalar field, Phys. Rev. Lett. **70**, 9 (1993).

[732] A. M. Abrahams and C. R. Evans, Critical behavior and scaling in vacuum axisymmetric gravitational collapse, Phys. Rev. Lett. **70**, 2980 (1993).

[733] C. R. Evans and J. S. Coleman, Observation of critical phenomena and selfsimilarity in the gravitational collapse of radiation fluid, Phys. Rev. Lett. **72**, 1782 (1994), arXiv:gr-qc/9402041 [gr-qc] .

[734] M. W. Choptuik, T. Chmaj, and P. Bizon, Critical behavior in gravitational collapse of a Yang-Mills field, Phys. Rev. Lett. **77**, 424 (1996), arXiv:gr-qc/9603051 [gr-qc] .

[735] S. E. Gralla and P. Zimmerman, Critical Exponents of Extremal Kerr Perturbations, Class. Quant. Grav. **35**, 095002 (2018), arXiv:1711.00855 [gr-qc] .

[736] S. E. Gralla and P. Zimmerman, Scaling and Universality in Extremal Black Hole Perturbations, JHEP **06**, 061, arXiv:1804.04753 [gr-qc] .

[737] W. D. Goldberger and I. Z. Rothstein, An Effective field theory of gravity for extended objects, Phys. Rev. **D73**, 104029 (2006), arXiv:hep-th/0409156 [hep-th] .

[738] W. D. Goldberger and A. Ross, Gravitational radiative corrections from effective field theory, Phys. Rev. **D81**, 124015 (2010), arXiv:0912.4254 [gr-qc] .

[739] A. Kuntz, F. Piazza, and F. Vernizzi, Effective field theory for gravitational radiation in scalar-tensor gravity, JCAP **1905** (05), 052, arXiv:1902.04941 [gr-qc] .

[740] H. Witek, L. Gualtieri, P. Pani, and T. P. Sotiriou, Black holes and binary mergers in scalar Gauss-Bonnet gravity: scalar field dynamics, Phys. Rev. **D99**, 064035 (2019), arXiv:1810.05177 [gr-qc] .

[741] V. Cardoso, S. Chakrabarti, P. Pani, E. Berti, and L. Gualtieri, Floating and sinking: The Imprint of massive scalars around rotating black holes, Phys. Rev. Lett. **107**, 241101 (2011), arXiv:1109.6021 [gr-qc] .

[742] S. Endlich and R. Penco, A Modern Approach to Superradiance, JHEP **05**, 052, arXiv:1609.06723 [hep-th] .

[743] M. W. Horbatsch and C. P. Burgess, Cosmic Black-Hole Hair Growth and Quasar OJ287, JCAP **1205**, 010, arXiv:1111.4009 [gr-qc] .

[744] L. K. Wong, A.-C. Davis, and R. Gregory, Effective field theory for black holes with induced scalar charges, Phys. Rev. **D100**, 024010 (2019), arXiv:1903.07080 [hep-th] .

[745] S. Reyes and D. A. Brown, Constraints on Nonlinear Tides due to p–g Mode Coupling from the Neutron Star Merger GW170817, Astrophys. J. **894**, 41 (2020), arXiv:1808.07013 [astro-ph.HE] .

[746] B. P. Abbott *et al.* (LIGO Scientific, Virgo), Constraining the p-Mode–g-Mode Tidal Instability with GW170817, Phys. Rev. Lett. **122**, 061104 (2019), arXiv:1808.08676 [astro-ph.HE] .

[747] E. Gaertig, K. Glampedakis, K. D. Kokkotas, and B. Zink, The f-mode instability in relativistic neutron stars, Phys. Rev. Lett. **107**, 101102 (2011), arXiv:1106.5512 [astro-ph.SR] .

[748] N. Andersson and K. D. Kokkotas, The R mode instability in rotating neutron stars, Int. J. Mod. Phys. **D10**, 381 (2001), arXiv:gr-qc/0010102 [gr-qc] .

[749] K. Yagi and N. Yunes, Approximate Universal Relations for Neutron Stars and Quark Stars, Phys. Rept. **681**, 1 (2017), arXiv:1608.02582 [gr-qc] .

[750] K. Yagi and N. Yunes, I-Love-Q, Science **341**, 365 (2013), arXiv:1302.4499 [gr-qc] .

[751] T. Damour and A. Nagar, Relativistic tidal properties of neutron stars, Phys. Rev. **D80**, 084035 (2009), arXiv:0906.0096 [gr-qc] .

[752] T. Binnington and E. Poisson, Relativistic theory of tidal Love numbers, Phys. Rev. **D80**, 084018 (2009), arXiv:0906.1366 [gr-qc] .

[753] B. Kol and M. Smolkin, Black hole stereotyping: Induced gravito-static polarization, JHEP **02**, 010, arXiv:1110.3764 [hep-th] .

[754] P. C. C. Freire, N. Wex, G. Esposito-Farese, J. P. W. Verbiest, M. Bailes, B. A. Jacoby, M. Kramer, I. H. Stairs, J. Antoniadis, and G. H. Janssen, The relativistic pulsar-white dwarf binary PSR J1738+0333 II. The most stringent test of scalar-tensor gravity, Mon. Not. Roy. Astron. Soc. **423**, 3328 (2012), arXiv:1205.1450 [astro-ph.GA] .

[755] M. Kramer *et al.*, Strong-Field Gravity Tests with the Double Pulsar, Phys. Rev. X **11**, 041050 (2021), arXiv:2112.06795 [astro-ph.HE] .

[756] J. Zhao, P. C. C. Freire, M. Kramer, L. Shao, and N. Wex, Closing a spontaneous-scalarization window with binary pulsars 10.1088/1361-6382/ac69a3 (2022), arXiv:2201.03771 [astro-ph.HE] .

[757] T. Ikeda, T. Nakamura, and M. Minamitsuji, Spontaneous scalarization of charged black holes in the Scalar-Vector-Tensor theory, Phys. Rev. D **100**, 104014 (2019), arXiv:1908.09394 [gr-qc] .

[758] S. Barton, B. Hartmann, B. Kleihaus, and J. Kunz, Spontaneously vectorized Einstein-Gauss-Bonnet black holes, Phys. Lett. B **817**, 136336 (2021), arXiv:2103.01651 [gr-qc] .

[759] D. D. Doneva, S. Kiorpelidi, P. G. Nedkova, E. Papantonopoulos, and S. S. Yazadjiev, Charged Gauss-Bonnet black holes with curvature induced scalarization in the extended scalar-tensor theories, Phys. Rev. D **98**, 104056 (2018), arXiv:1809.00844 [gr-qc] .

[760] C. F. B. Macedo, J. Sakstein, E. Berti, L. Gualtieri, H. O. Silva, and T. P. Sotiriou, Self-interactions and Spontaneous Black Hole Scalarization, Phys. Rev. D **99**, 104041 (2019), arXiv:1903.06784 [gr-qc] .

[761] W. E. East and J. L. Ripley, Dynamics of Spontaneous Black Hole Scalarization and Mergers in Einstein-Scalar-Gauss-Bonnet Gravity, Phys. Rev. Lett. **127**, 101102 (2021), arXiv:2105.08571 [gr-qc] .

[762] S. Hod, Onset of spontaneous scalarization in spinning Gauss-Bonnet black holes, Phys. Rev. D **102**, 084060 (2020), arXiv:2006.09399 [gr-qc] .

[763] W. D. Goldberger and I. Z. Rothstein, Towers of Gravitational Theories, Gen. Rel. Grav. **38**, 1537 (2006), arXiv:hep-th/0605238 .

[764] P. K. Gupta, J. Steinhoff, and T. Hinderer, Relativistic effective action of dynamical gravitomagnetic tides for slowly rotating neutron stars, Phys. Rev. Res. **3**, 013147 (2021), arXiv:2011.03508 [gr-qc] .

[765] L. Bernard, Dipolar tidal effects in scalar-tensor theories, Phys. Rev. D **101**, 021501 (2020), arXiv:1906.10735 [gr-qc] .

[766] G. Creci, T. Hinderer, and J. Steinhoff, Tidal response from scattering and the role of analytic continuation, Phys. Rev. D **104**, 124061 (2021), arXiv:2108.03385 [gr-qc] .

[767] M. Maggiore, The Physical interpretation of the spectrum of black hole quasinormal modes, Phys. Rev. Lett. **100**, 141301 (2008), arXiv:0711.3145 [gr-qc] .

[768] T. Harada, Stability analysis of spherically symmetric star in scalar - tensor theories of gravity, Prog. Theor. Phys. **98**, 359 (1997), arXiv:gr-qc/9706014 .

[769] J. Novak, Neutron star transition to strong scalar field state in tensor scalar gravity, Phys. Rev. D **58**, 064019 (1998), arXiv:gr-qc/9806022 .

[770] H. O. Silva, C. F. B. Macedo, E. Berti, and L. C. B. Crispino, Slowly rotating anisotropic neutron stars in general relativity and scalar–tensor theory, Class. Quant. Grav. **32**, 145008 (2015), arXiv:1411.6286 [gr-qc] .

[771] Z. Altaha Motahar, J. L. Blázquez-Salcedo, B. Kleihaus, and J. Kunz, Scalarization of neutron stars with realistic equations of state, Phys. Rev. D **96**, 064046 (2017), arXiv:1707.05280 [gr-qc] .

[772] H. Sotani, Scalar gravitational waves from relativistic stars in scalar-tensor gravity, Phys. Rev. D **89**, 064031 (2014), arXiv:1402.5699 [astro-ph.HE] .

[773] J. Zhao, L. Shao, Z. Cao, and B.-Q. Ma, Reduced-order surrogate models for scalar-tensor gravity in the strong field regime and applications to binary pulsars and GW170817, Phys. Rev. D **100**, 064034 (2019), arXiv:1907.00780 [gr-qc] .

[774] R. Niu, X. Zhang, B. Wang, and W. Zhao, Constraining Scalar-tensor Theories Using Neutron Star–Black Hole Gravitational Wave Events, Astrophys. J. **921**, 149 (2021), arXiv:2105.13644 [gr-qc] .

[775] M. Guo, J. Zhao, and L. Shao, Extended reduced-order surrogate models for scalar-tensor gravity in the strong field and applications to binary pulsars and gravitational waves, Phys. Rev. D **104**, 104065 (2021), arXiv:2106.01622 [gr-qc] .

[776] L. K. Wong, C. A. R. Herdeiro, and E. Radu, Constraining spontaneous black hole scalarization in scalar-tensor-Gauss-Bonnet theories with current gravitational-wave data, Phys. Rev. D **106**, 024008 (2022), arXiv:2204.09038 [gr-qc] .

[777] J.-W. Kim, M. Levi, and Z. Yin, Quadratic-in-spin interactions at fifth post-Newtonian order probe new physics, (2021), arXiv:2112.01509 [hep-th] .

[778] S. Hopper, A. Nagar, and P. Rettegno, Strong-field scattering of two spinning black holes: Numerics versus Analytics, (2022), arXiv:2204.10299 [gr-qc] .

[779] D. Bini, A. Geralico, and R. T. Jantzen, Spin-geodesic deviations in the Schwarzschild spacetime, Gen. Rel. Grav. **43**, 959 (2011), arXiv:1408.4946 [gr-qc] .

[780] T. Damour and G. Schäeer, Higher-order relativistic periastron advances and binary pulsars, Il Nuovo Cimento B (1971-1996) **101**, 127 (1988).

[781] T. Damour and G. Schäfer, Redefinition of position variables and the reduction of higher order Lagrangians, J. Math. Phys. **32**, 127 (1991).